PHOTOCURRENT IMAGING USING A SCANNING LASER MICROSCOPE

PHOTOCURRENT IMAGING USING A SCANNING LASER MICROSCOPE

BY

TASNEEM FATIMA MOHIUDDIN

University College London

Autumn 1998

Presented in fulfilment of the requirements for the degree of Doctor of Philosophy of the University of London

Acknowledgements

I would like to thank all the staff in the Chemistry Department at UCL, in particular my supervisor Prof. D.E. Williams for all his inspiration and words of wisdom, and Dr Keith Pratt for his practical advice and encouragement, and John Cresswell for his help with the photography of some of the apparatus shown in this thesis, as well as all the members of the electronics and mechanical workshops for their help in the construction of many custom made apparatus with out which it would not have been possible to carry out my work.

I would also like to make a special thank you to Kevin Reeves of the Institute of Archaeology, UCL, for his considerable help with the electron probe x-ray microanalyser.

Last of all I wish to thank all my friends and family for their help and encouragement through my PhD, in particular my mum and dad.

ABSTRACT

This thesis explores the direct photocurrent imaging technique using a gaussian scanning laser spot. This includes advancements to the technique, its uses and, a study of effects produced by surface heating by the laser.

A confocal scanning laser microscope (Bio-Rad MRC 600) which had been adapted to record photocurrent images, as well as confocal optical images was used. The photocurrent image showed the function at electroactive areas, where as the optical image just showed the topography. In addition, to explore further the features seen on the photocurrent image an electron probe microanalyser was used to record microprobe element concentration maps and SEM images.

Basics of this technique and the resolution possible were shown by taking photocurrent images at different laser intensities for a Si-memory chip and a p-type Si electrode in HCl. Features on the photocurrent image changed in both cases with increasing light intensity, with which the penetration depth of the laser into the sample increases. The effects of electrode geometry and poisoning on image contrast in photoelectrochemical microscopy were studied using gold microband and disc electrodes in Fe $(CN)_6^{4-}$ solution. It was found the image contrast developed as a consequence of the temperature induced transient produced by a rapidly scanned focussed laser spot, the theory for which is given here. Finally as a detailed example of the application this technique, the processes leading to the initiation of the corrosion of stainless steel in dilute Cl^- were studied. Changes in the photocurrent image, correlating to the initiation of pitting corrosion, were found to occur at certain inclusions.

PREFACE

This thesis is concerned with the technique of photocurrent imaging using the laser spot scanning technique, with the laser being operated in a continuously scanning fixed intensity mode. This is more commonly known as the continuous-scan-direct-method of photocurrent imaging. Therefore this thesis hopes to explain the resolution, advantages and advancements made to this technique. This was done by primarily examining electrochemical systems, although a little work looking at a solid-state physics system was also carried out.

As many vastly different areas of research ranging from photothermal effects to corrosion have been studied, each results chapter (Chapters 3 - 6) contains its own introduction, aims, results, discussion and conclusion for each particular system. The general introduction (Chapter 1) therefore does not go into specific detail on each system studied but explains everything about the laser spot scanning technique, and in particular how it has been used for photocurrent imaging. For completion the first part of Chapter 1 deals with some introductory concepts involved in both electrochemistry and solid state physics as it is hoped that this thesis will be read by people in a wide range of scientific disciplines to whom the photocurrent imaging technique may be of interest. So readers of expertise in a particular area may miss out their area of expertise when reading the introduction.

A detailed list of references including: the author names, journal title, year, volume, page numbers, title of book or paper and further notes are given in Chapter 8 of this thesis. In this chapter the references are listed firstly by subject and then by year. The references have been numbered through this thesis as a section (topic) letter followed by a reference number (see Chapter 8). For example if 'ref. D-6' is given, when this is looked up in Chapter 8 we can see that section D, is the section on 'Laser spot scanning in photocurrent imaging via photothermal effects' and reference number 6 in this section gives the authors: T.F. Mohiuddin, R.S. Hutton, D.E. Williams, the journal title: Electrochimica Acta, year: 1996, volume: 41, pages: 2025-2034 and the title: 'Effect of electrode geometry and poisoning on image contrast in photoelectrochemical microscopy'.

The final part of this thesis contains a comprehensive set of appendices. These include a list of the apparatus used and the contact addresses for the suppliers. In addition detailed information on the custom built apparatus has also been given. This includes technical diagrams (showing sizes, electronic circuitry and materials used), block diagrams and photographs as required. The custom made apparatus shown here includes: the cell and surrounding faraday cage, a battery operated potentiostat, a battery operated voltage offset-box, a Ni-Cd battery charger and discharger. Preparation of the working electrodes and purified water has also been given here in great detail. In addition, summary notes on the symbols, equations, physical properties, and specific experimental settings, for the work shown in this thesis has also been listed here.

It should be noted that the abbreviation SSE has been used to represent the mercury / mercurous sulphate electrode (Hg/Hg_2SO_4, sat. K_2SO_4) and the abbreviation SCE has been used to represent the saturated calomel electrode (Hg/Hg_2Cl_2, sat. KCl), in many places in this thesis.

Notes about the author

Name-

Miss Tasneem Fatima Mohiuddin

Institution of study-

Department of Chemistry,
University College London,
20 Gordon Street,
London WC1H OAJ, England, UK.

PhD Supervisor-

Professor David E Williams (University College London).

Previous Degrees-

BSc Honours in Chemistry from King's College, University of London in 1992 and an MSc with Distinction from King's College, University of London in 1993.

PHOTOGRAPH ,

MISSING FROM THIS

DIGITAL COPY, HAVE BEEN

EXCLUDED AT THE

REQUEST OF THE

UNIVERSITY

CONTENTS SUMMARY

CONTENTS

Chapter 2.

Chapter 3.

Chapter 6.

Chapter 7.

Chapter 8.

1. GENERAL INTRODUCTION

1. GENERAL INTRODUCTION

This is a general introduction to the area of study and general objectives of this thesis. In this work the laser spot scanning technique was used to generate photocurrents at either electrode-electrolyte interfaces in electrochemical systems or electroactive junctions between two types of material in solid state systems. During image data collection the laser was left at continuous intensity and not pulsed (modulated / chopped), with the images being collected in real time. This work was conducted using a confocal scanning laser microscope system (Bio-Rad MRC 600) containing a 25 mW argon ion laser (of which 10 mW is at $\lambda = 488$ nm, 10 mW is at $\lambda = 512$ nm, and 5 mW is at other similar wavelengths).

The main objective of the work shown in this thesis was to improve the technique and to explore its application, as well as to improve the understanding of spatial features produced on the photocurrent images. This system was used in particular to understand the effects seen in electrochemical systems by variation of parameters such as electrode potential, laser intensity, laser velocity, and geometry and extent of reversibility of the system being studied.

1.1 BASIC PRINCIPLES OF PHOTOCURRENT GENERATION

When the surface of a material is illuminated an electronic excitation may be caused, generating a current: the photocurrent. This change in current can be detected and measured and recorded. In order to describe exactly how the photocurrent is generated by the movement of electrons and holes (positive vacancies left by electrons moving away in the lattice) a little of the background information about how the electrons are arranged in solids must be understood. This information follows.

Behaviour of Electrons in Solids

In an atom the electrons fill up the energy levels in an orderly fashion by the PAULI EXCLUSION PRINCIPLE. This states that only one electron can occupy each quantum state i.e. electrons cannot occupy the same level unless spin opposed. So two electrons of opposite spin may occupy each energy level.

For example the electrons in a metal at absolute zero fill a succession of energy levels up to a particular level, and this is known as the FERMI LEVEL and the energy of this upper most state is known as the Fermi Energy E_F

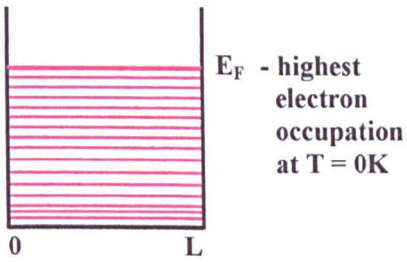

figure 1.1

If a regular network of many atoms is brought close together as in the case of a solid, the interaction of electron energy levels gives rise to the formation of energy bands rather than discrete energy levels. The theory explaining this effect is known as BAND THEORY.

For example, if 5 atoms are placed in a row  with equal separation, each with five atomic orbitals, five energy levels split from the originating energy level, as illustrated below.

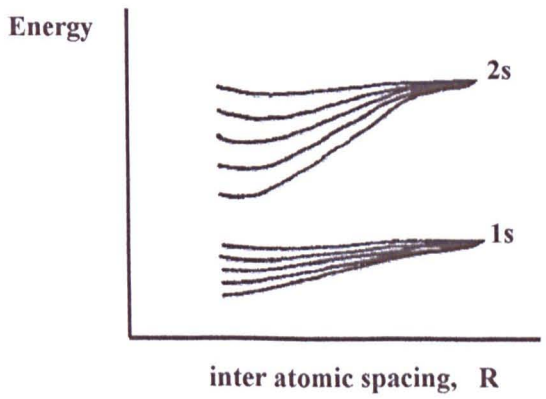

figure 1.2

So if there are N atoms and N becomes large the energy appears as a CONTINUUM of energy levels, the energy separation between the energy levels becomes infinitesimal. Such a group of levels is called an ENERGY BAND. Each energy band has a definite lower and upper limit called band edges. There is only a small separation of energy levels within a band, but between energy band levels (e.g. 1s and 2s) the separation is large.

For a regular lattice spacing (a), there is no solution where Bragg reflection of the electron wave function occurs, i.e. there is no solution for $k = \frac{n\pi}{a}$ where $n = 0 \pm 1$, and λ denotes the wavelength of the electron wave function.

$$k = \frac{2\pi}{\lambda}$$

$$\frac{n\pi}{a} = \frac{2\pi}{\lambda} \rightarrow n\lambda = 2a \qquad \textbf{Bragg's Law} \quad (1.1)$$

Hence the behaviour of a free electron in a box is modified in the presence of a regular lattice of scattering centres (the nuclei) as illustrated in figure 1.3.

Eventually when all the electrons available in the solid fill up the energy bands there will be upper energy bands which may be ; completely full, partially filled or completely empty, which correspond to the **valence** and **conductance bands**. Full bands can not conduct electrons as there is no where for the electrons to go.

A variety of different circumstances may pertain with respect to the occupancy and overlap of energy bands as illustrated in figure 1.4

The separation between the conductance and valence bands is known as the band gap energy ($E_{bg} = E_C - E_V$). Incident light of an energy greater than E_{bg} is required to separate the electron hole pair ($h\nu > E_{bg}$). The materials used can be classified by the magnitude of band gap between the conductance and valence bands.

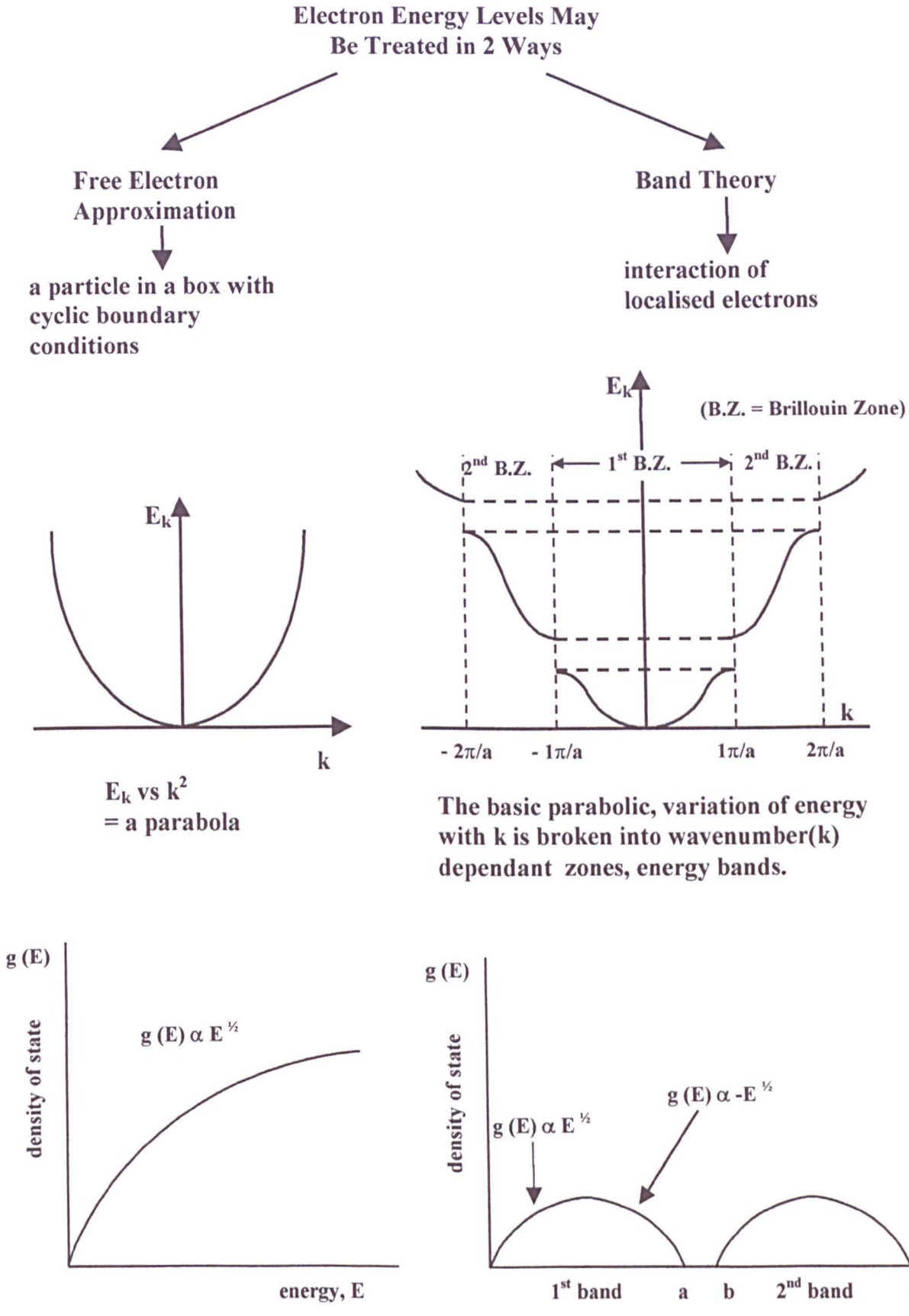
Electron Energy Levels May
Be Treated in 2 Ways
Free Electron
Approximation
a particle in a box with
cyclic boundary
conditions
Band Theory
interaction of
localised electrons
E_k
k
E_k vs k^2
= a parabola
E_k
(B.Z. = Brillouin Zone)
2nd B.Z.
1st B.Z.
2nd B.Z.
k
- 2π/a
- 1π/a
1π/a
2π/a
The basic parabolic, variation of energy
with k is broken into wavenumber(k)
dependant zones, energy bands.
g (E)
density of state
g (E) α E ½
energy, E
g (E)
density of state
g (E) α E ½
g (E) α -E ½
E
1st band
a
b
2nd band
c

figure 1.3

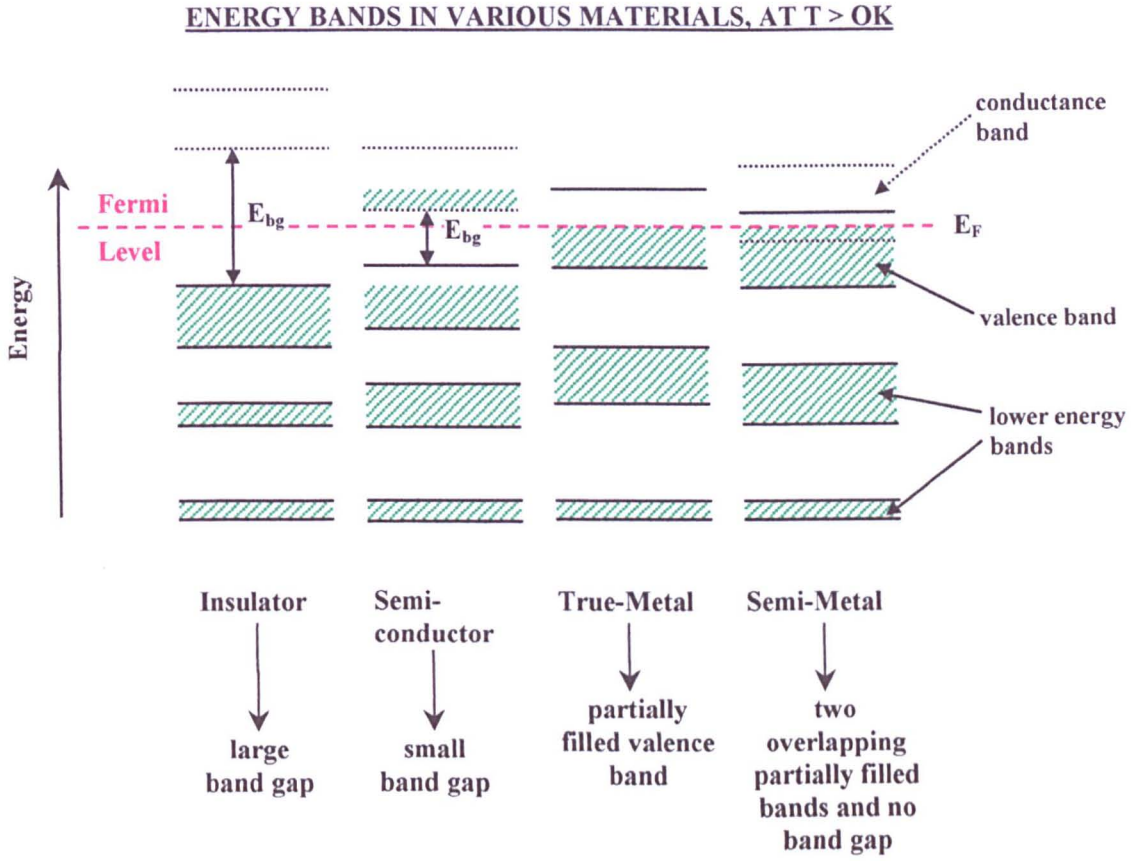

figure 1.4

In order for the electrons to be able to move and therefore a current to be generated the electrons must be able to move to a partially empty level within an energy band. In a metal empty levels are directly above the filled ones, so application of a potential difference at room temperature can easily make these electrons move up to a higher energy level. However in the case of a semiconductor the movement of electrons needs to occur from the upper most filled level (valence band) to the lower most empty level (conductance band). In order to get from the valence to conductance band enough energy has to be provided to allow the transaction to occur.

To summarise semi-metals (conductors) tend to have an overlap in the conductance and valence bands; true metals (conductors) have no band gap or on occasion very small band gaps (> 0.1 eV); semiconductors have a small band gap of less than 3 eV and insulators have a large band gap of more than 3 eV.

DIAGRAMS REPRESENTING MATERIALS AT ABSOLUTE TEMPERATURE

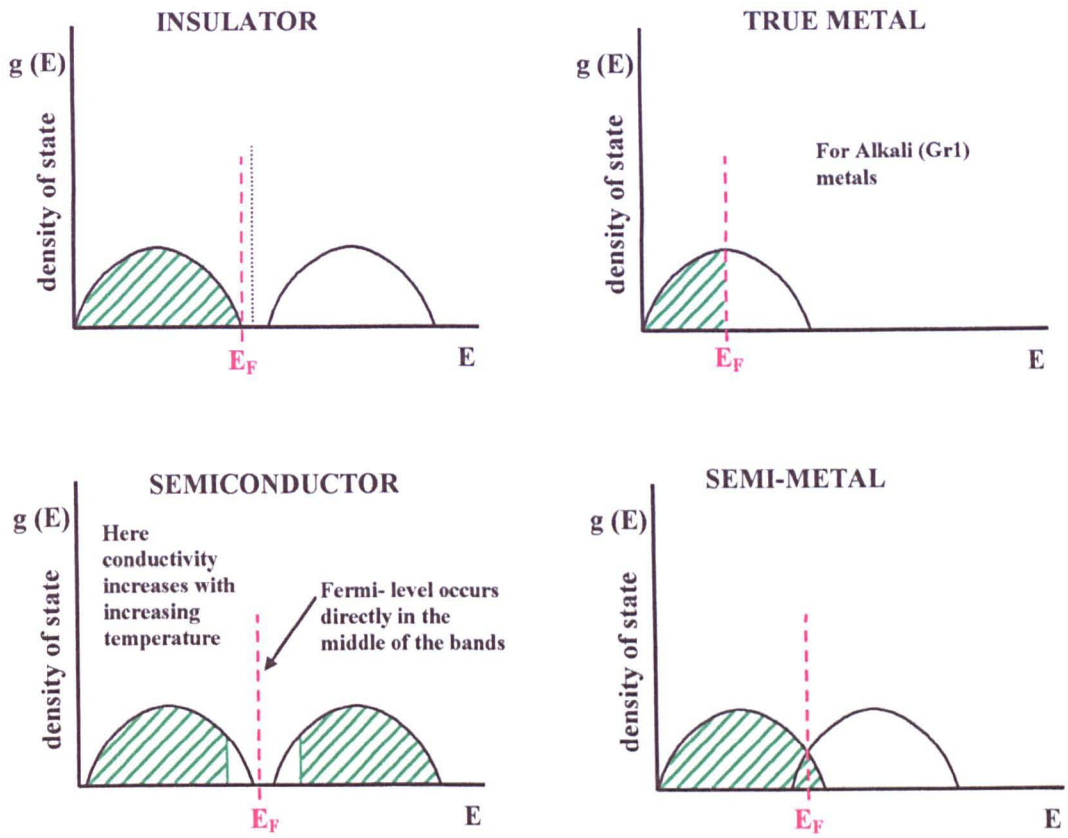

figure 1.5

Mechanisms of Photocurrent Generation

Under the influence of light there are two mechanisms which can lead to **photoexcitation**: these are the photoelectric effect and photoemission; and there is one mechanism leading to **thermal excitation**: the photothermal effect.

Photoelectric effect

In this process light gives rise to current directly by the creation of electron-hole pairs, therefore increasing the electrical conductivity. In this process enough light energy is absorbed to cause the excitation of electrons to the conductance band.

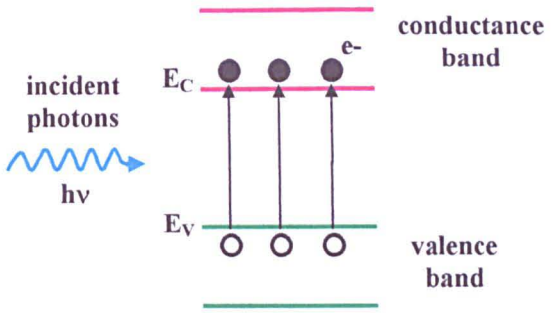

PHOTOEXCITATION OF ELECTRONS FROM THE VALENCE BAND TO THE CONDUCTANCE BAND

figure 1.6

Photoemission

In a vacuum the photoelectric effect can lead to photoemission of an electron from the solid into a vacuum. This occurs provided the kinetic energy of the electron after the absorption of light is large enough to allow the electron to escape the solid.

PHOTOELECTRIC EMISSION

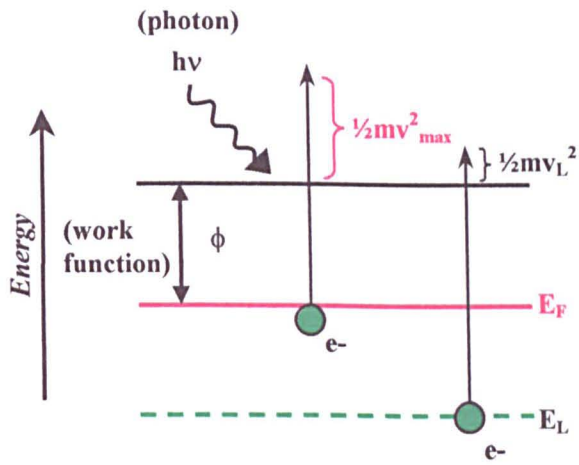

figure 1.7

For photoelectric emission, the photonic-energy, hν, has to be greater than or equal to the work function, ϕ, which is the work required to free the electron from the solid. An electron from near the Fermi-level would leave the surface with a maximum kinetic energy:

$$\frac{1}{2}mv_{max}^{2} = h\nu - \phi \qquad (1.2)$$

Incident photons can also cause emissions from lower energy levels e.g.

$$\tfrac{1}{2}mv_L{}^2 = h\nu - [\phi(E_F - E_L)] \qquad (1.3)$$

Photoemission between condensed phases

In this process a charge carrier moves from one condensed phase to another condensed phase. This is a much less efficient process than electron hole-pair generation so it occurs much less frequently and generates much smaller photocurrents. There are two principal types of photoemission which occur between condensed phases in electrochemical experiments, distinguished by the terms: internal photoemission and external photoemission. In external photoemission an electron is excited across the electrode-electrolyte interface, where it has to be captured by the solution or returns to the electrode. This is an inefficient process. In internal photoemission the electron ejected moves from solid to solid which is much more favourable. Examples of internal photoemission are, the movement of an ejected electron from a metal to a metal-oxide at the surface, or from on type of metal to another at a metal-metal junction.

A DIAGRAM SHOWING EXAMPLES OF INTERNAL PHOTOEMISSION

eg.1

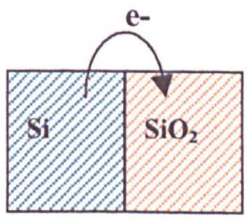

eg. 2

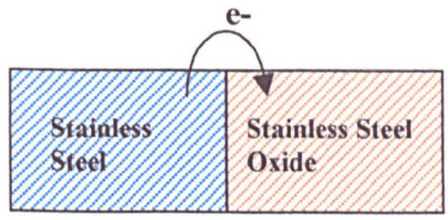

figure 1.8

Photothermal effect

Here the light absorbed causes a temperature change in the electrode. The consequences for electrochemical systems have been discussed in much greater detail in the introduction to chapter 4.

1. 2 PHOTOCURRENT GENERATION IN ELECTROCHEMISTRY

Basic Concepts in Electrochemistry

Photocurrent generation can not only be monitored in solid state physics systems, but in electrochemical systems as well. Electrochemistry is the study of phases containing ions (electrolyte) in contact with phases containing electrons (electrodes). In a electrochemical system an electrode is placed in an electrolyte solution an accumulation of electrons will occur near / at the interface to the electrolyte, and on the electrolyte side of the interface positive ions are drawn towards the metal as a result of electrostatic attraction.

THE ELECTRODE / ELECTROLYTE INTERFACE

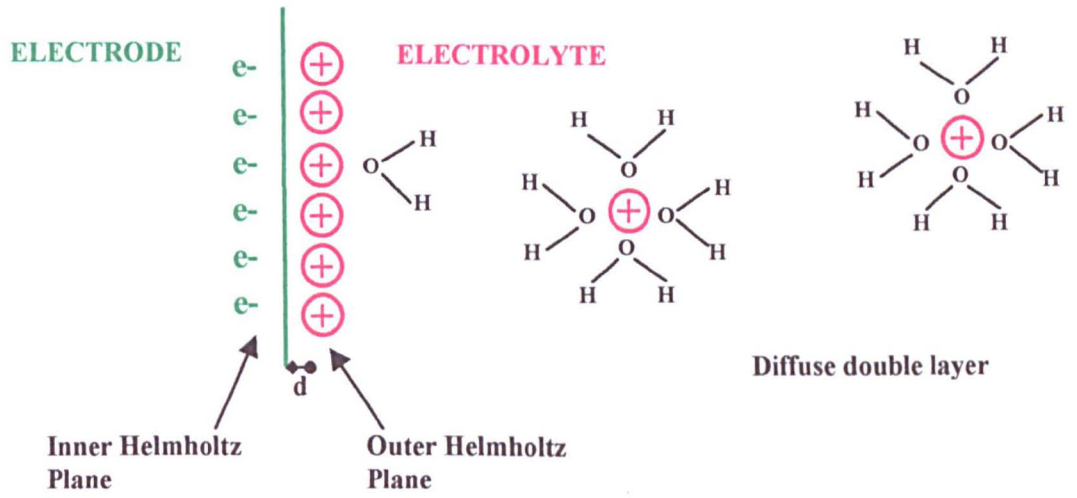

Notes: The Helmholtz plane is a rigid double layer of opposing charges with a linear potential drop across it. This on its own can be compared to an electrical capacitor: Capacitance (F) = Charge (C) ÷ Potential Difference (Volts) = [surface area (m^2) x permitivity (Fm^{-1})] ÷ the distance between the 2 oppositely charged layers (m). The diffuse (Gouy and Chapman) layer shows a diffuse layer of ions of a particular charge spreading out in to the solution. The capacitance of the diffuse layer alone would depend on the potential and concentration of the electrolyte. The overall combination of the capacitance of the fixed and diffused layers (the Stern Model) may be given by [1 ÷ capacitance] = [1 ÷ fixed layer capacitance] + [1 ÷ diffuse layer capacitance].

figure 1.9

In electrochemical reactions, properties of the electrode and electrolyte which are influenced by the nature of the double layer can be measured. The voltage (E) which arises as a species in the electrolyte solution (e.g. a metal ion) equilibriates with the electrons in the solid electrode. As charge separation occurs across the interface potential arises, but this can not be measured directly for one electrode alone. Instead it has to be measured as a value relative to other interfaces. Therefore to measure a voltage at least two interfaces must be created. In this way two electrodes (electronic conductors) can be brought together in an electrolyte solution containing ions, in order to form an electrochemical cell. In this situation ions can: 1) set up as double layers, 2) adsorb, 3) react.

Many species react at the electrodes. If an reaction occurs at an electrode this results in current flow. This allows voltage measurement across the cell. Diffusion of any species to the electrode surface can occur if a concentration difference arises, when a reaction occurs at the electrode surface, resulting in a depletion of the reactant material at the surface.

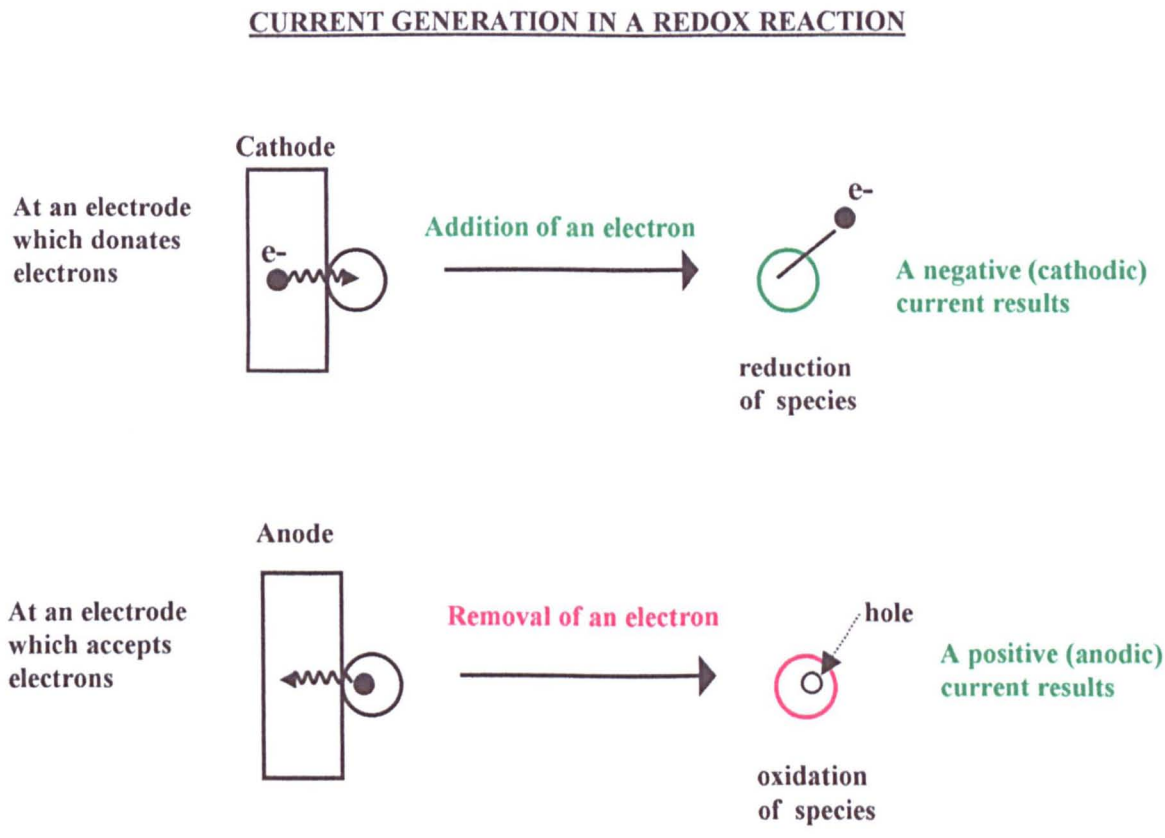

figure 1.10

Effect of Light on Electrochemical Systems

In an electrochemical system an electrolyte solution is present, in comparison to a solid-state system where there is not. In an electrochemical system light still causes photoexcitation and thermal excitation in the electrode but in addition the electronic excitation caused by the adsorption of light can also have an impact on the reactions occurring in the surrounding solution at the electrode-electrolyte interface.

In electrochemical systems currents which result, due to the transfer of electrons between the electrode and electrolyte and the occurrence of subsequent reactions at the surface of the electrodes, are influenced by the action of the light. The action of the laser may therefore significantly increase the currents. Currents due to electrochemical effects add to currents produced by photocurrent generation in the solid itself. Often the light induced current in the solid triggers the following current generation at the electrode-electrolyte interface. So the electrons may be excited by the solid (electrode) and then these electrons are easily captured by the surrounding solution (electrolyte) allowing a subsequent chemical reaction to occur. This method can therefore allow any reaction occurring at the surface of an electrode to be studied.

The change in current produced in a system on application of a laser beam is termed the **photocurrent**. For a current to be sustained a reaction must occur to transfer the charge across the interface. However there may also be transient currents induced immediately following the illumination, associated with charge separation and trapping in the solid. The transient signals do not necessarily involve a reaction across the interface.

1.3 THE LASER SPOT SCANNING (LSS) TECHNIQUE

Laser Spot Scanning and its Applications

Laser spot scanning is a technique that can be used to probe the electrode-electrolyte interface with a scanning focused laser spot, allowing spatial resolution and optical properties to be monitored. The electrode used is typically a semiconductor. The light source can be the laser from a modified scanning laser microscope, which allows the reflected light and photocurrent (or any other property which changes with the contact of the laser on the sample surface) to be monitored as images. This experimental technique has been referred to most commonly as the laser spot scanning (LSS) or less frequently as the scanning light / laser spot technique (SLS).

This technique can be used to measure the local photocurrents generated on a surface of by using a laser beam that is focused to a small spot size (~1 μm) and moving it from point to point across the electrode surface forming a raster image. Photocurrent imaging can be used to investigate to photoelectrochemical systems or solid-state systems. When applied to photoelectrochemistry it is most commonly known as **photoelectrochemical microscopy (PEM)**.

The raster image (see Appendix H) may be formed by using a stepper motor controlled x-y coordinate table which moves the cell or by using scanning mirrors, which move the illuminating beam from one image point to the next. The advantage in using a fixed table and therefore cell position, and a moving beam is that less problems are caused in not having a cell containing solution moving around resulting in vibrations which would cause noise in the resulting image.

The wide range of lasers are available ranging from infra-red to ultra violet, allows the excitation energy required to cause; photoexcitation, photothermal effects or a particular chemical reaction, to be easily selected. Useful lasers are listed in figure 1.11. For photoexcitation to occur the wavelength of the laser has to be below a value known as the threshold wavelength (λ_{bg}), in order that the energy supplied is greater than the band gap energy (where λ_{bg} in 'nm' = $1240 \div E_{bg}$ in 'eV').

EXAMPLES OF LASERS USED IN THE LASER SPOT SCANNING TECHNIQUE

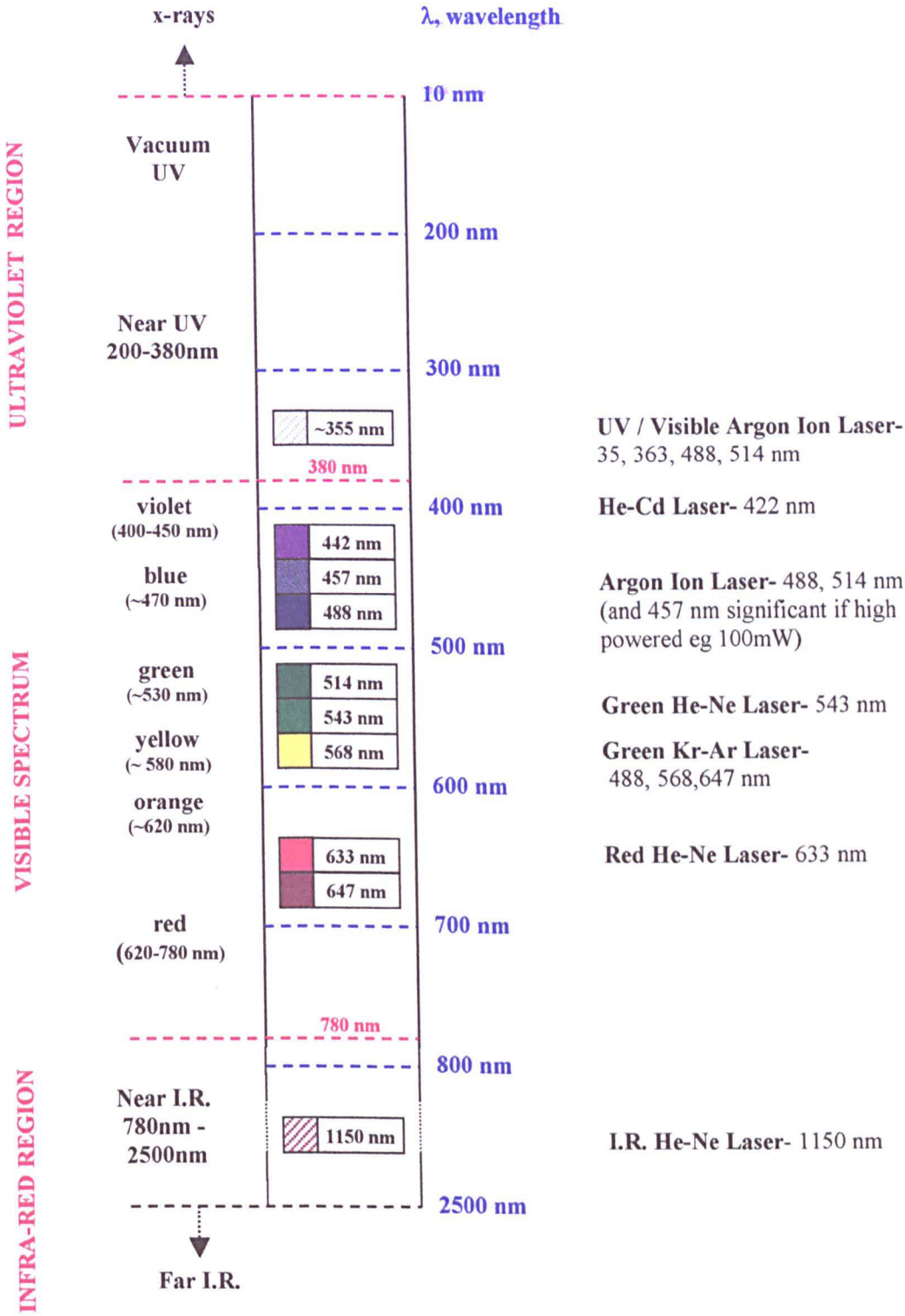

Notes: The word laser is an acronym for light amplification by the stimulated emission of radiation. Electrons in the atoms of the laser medium are excited by an energy source and then stimulated by external photons to emit energy as photons. The photons emitted have a frequency characteristic of the atoms and travel in step with the stimulating photons. These photons in turn interact with other excited atoms to release more photons. Light amplification is achieved as the photons move back and fourth between two parallel mirrors triggering further stimulated emissions. Intense, directional and monochromatic light finally leaves through a partially silvered mirror.

figure 1.11

Laser spot scanning first became popular as a technique in the late-1970's / early 1980's. In this early work (refs. C1-1, C1-2, C1-3, C2-1, C2-2) this technique was used to record crude line maps. As experimental techniques then became more sophisticated video images (ref. C1-4, M.A. Bulter, 1994) were recorded using point by point raster scanning of a laser beam over the surface. This allowed near photographic quality video images to be recorded. On these video images, the extent of photocurrent magnitude at any specific location on the surface is represented by the use of a grey scale ('black & white') or colour where the different values of photocurrent are shown as differing shades of grey or differing colours.

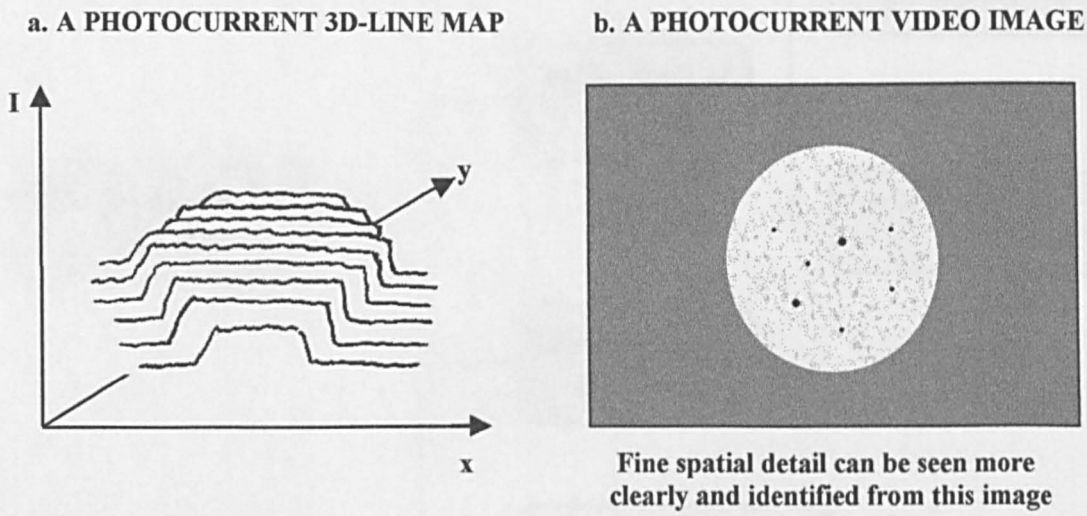

figure 1.12

The basic apparatus used for laser spot scanning has been varied from one research group to another in a number of ways. The two main techniques of laser spot scanning to produce a rastered image are the continuous scan direct method and the step-scan lock in method. These are further described in the next section (Section 1.4).

Laser spot scanning has since been applied to other detection methods, in order to give spatially resolved images of these other properties as well. The changes that can be monitored using the laser spot scanning technique include; the change in current (photocurrent imaging), change in voltage (photovoltage imaging), change in the current to voltage ratio (photoconductance imaging), emission of light at a new wavelength

(photoluminescence imaging) and the emission of sound vibrations due to thermal effects (photoacoustic imaging).

APPLICATIONS OF THE LASER SPOT SCANNING TECHNIQUE

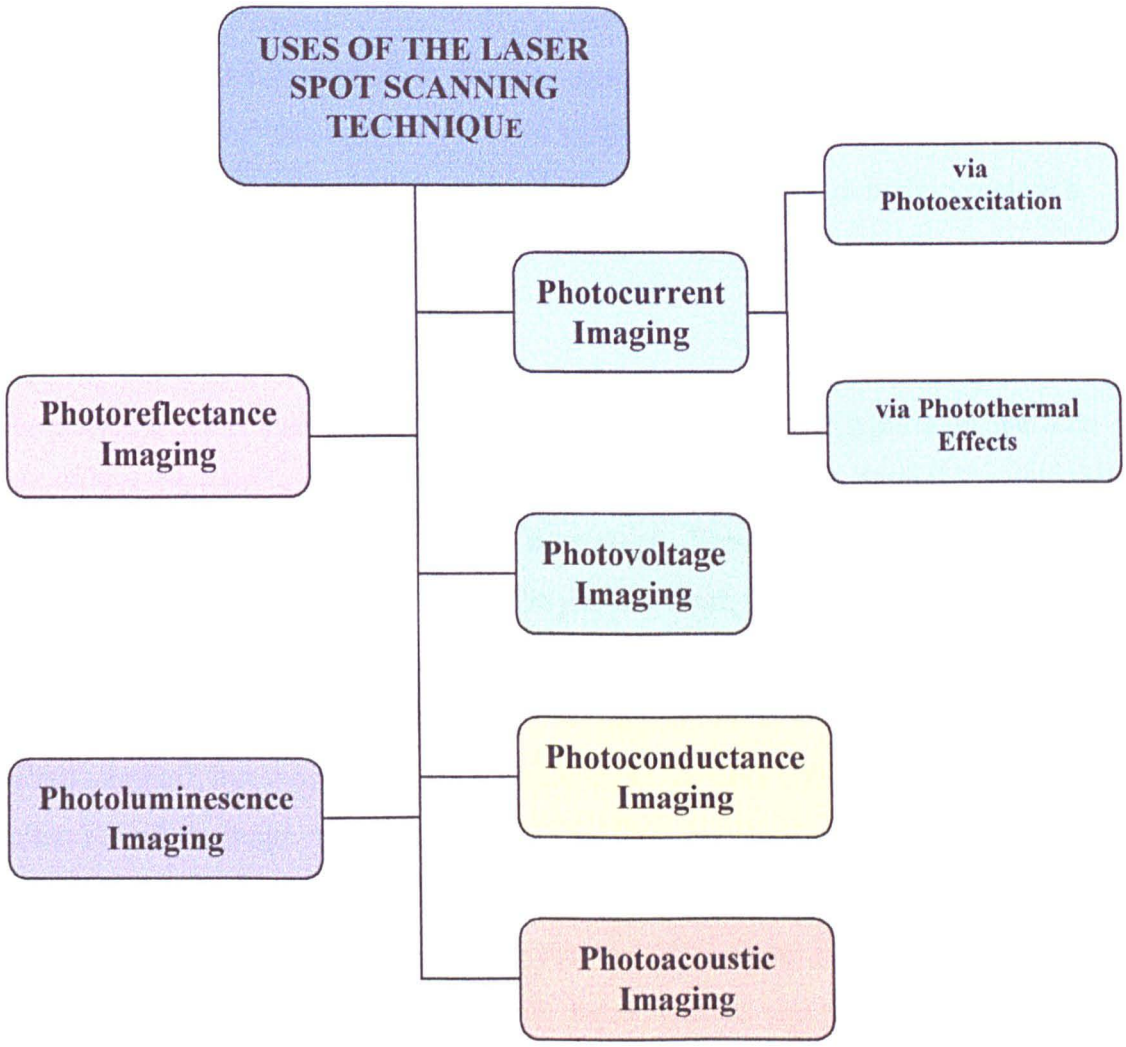

figure 1.13

Other similar techniques using scanning probe methods include **scanning tunnelling microscopy** and **scanning electrochemical microscopy (SECM)**. Scanning tunnelling microscopy involves using a small tunnelling current between the, tip of a sharp probe and the surface of interest. By scanning the tip across the surface atomic resolved images can be obtained. In scanning electrochemical microscopy a semiconductor is immersed in an electrolyte solution and an ultra-microelectrode is taken and moved

(scanned) across the surface of the semiconductor allowing information about the surface by redox species diffusing to the electrode due to its close proximity to the surface as it scans.

The Pulsed Beam Step-Scan Lock-in Method

In the step-scan lock in method an intensity modulated beam is produced by means of a chopper which chops the light on and of at a chosen frequency, or by an acousto-optic modulator which allows a sinusoidal variation of light intensity to be imposed on a static level. This signal is sent to a lock in amplifier which compares the photocurrent to the reference signal.

The photocurrent is measured by recording the current when the light is on and then again when the light is off. This is repeated a sufficient number of times for adequate noise reduction before moving on to the next point. The advantage of using this method is that it gives a direct measurement of the photocurrent, which is given by the difference between light on and off. However the disadvantage is the long time required to collect and process this data. Not only are many data points recorded at both light on and off, but they then have to be stored in memory until all the points have been collected and an image can be produced. The times involved are in the range of several hours for one image (ref. C1-4, M. A. Butler). There have been some recent publications referring to the use of this technique using faster line scan times, in the region of 10-25 s per line, where the work is described as real time imaging (ref. C1-26, G. Razzini et al., 1995, using an electrochemical system, and ref. C2-9, J. Bajaj et al. 1993, using a solid state system). Provided that the reaction variation is slow enough, images showing how the photocurrent changes with time may be recorded. Both the scanning mirror technique and the moving table techniques have been used for this method of sampling photocurrents. The important fact is that noise reduction is carried out point by point.

The Continuous Beam Direct Method

In the continuous - scan direct method, mirrors rapidly scan the laser beam across the surface. Variations in the total current are used to form the image. In this method the laser light is not chopped on and off but kept on continuously at a fixed intensity. Changes arising in the photocurrent from one point to the next are measured, by high-pass filtering the signal to remove the background current, which varies on a time scales longer than the frame time. The signals are sent via a pre-amplifier and black level (offset box) directly to a monitor where they can be viewed as an image as they are collected. Noise reduction is carried out by frame averaging.

This method has the advantage of collecting images quickly, the time involved ranging from seconds to several minutes (10 - 15 min) at the most, even when several frames of the image are collected and averaged. Typical line scan times are in the range of a few milliseconds. The image improvement on averaging can be viewed directly as each frame is collected so the laser can be stopped from scanning any more frames when no more improvement can be seen. The advantage in this technique is that images can be directly observed as they are collected. Other merits of this method include the fact that the images contain information on real time and real space effects, such as blurring, dark (negative photocurrent) regions following the electrode, and information on how subsequent points on the electrode depend on the previous ones. These effects all go to provide important information about the system being studied. The disadvantage of this method is that we do not obtain direct photocurrent measurements.

Use of a Scanning Laser Microscope System

The laser spot scanning technique has been implemented using a true microscope system in only a few research groups in both electrochemistry and solid-state physics. This apparatus makes use of a microscope system which allows optical images of the surface topography (via reflectivity measurements) to be recorded as well as photocurrents.

Many research groups have used simpler systems which do not use a microscope but never the less still form a photocurrent image by the using a collection of lenses, a beam splitter, and an x-y positioner to move the stage the specimen is on. In addition in some cases an optical fibre has been used to direct the light / laser beam source.

The fibre-optic laser direction technique was used by Ogura and coworkers (ref. C2-3, 1985) in order to examine semiconductor defects in a silicon solar cell and GaAs: an optical fibre with a core diameter of 80 μm was employed. Later work by P.Carlsson and coworkers (refs. C1-9, C1-10, 1988), used a 4 μm optical fibre drawn from a bunch of fibres used to collect all the light efficiently to examine properties of $InSe_2$ in 0.1M K_2SO_4. More recently the technique of using an optical fibre has been adapted further to allow simultaneous scanning electrochemical and photoelectrochemical microscopy by use of a metalised fibre (ref. C1-33, W.H. Smyrl and coworkers, 1996). This technique combined the scanning electrochemical microscopy (using a scanning microelectrode) and a photoelectrochemical microscopy (using a scanning laser) techniques. In this work a laser beam was passed down a commercial polyamide encased gold coated optical fibre (core diameter 80 μm) which was held in place by a rubber wedge in the mouth of a hypodermic needle. The gold ring in this system formed a SECM ring. This technique was then named the scanning photoelectrochemical microscopy technique (SPECM) and it was used to investigate the Ti/TiO_2 system in 1M KBr and 0.05M H_2SO_4.

A review of published work using advanced instrumentation employing true microscope systems allowing multiple imaging applications (as used in electrochemistry and solid-state physics) follows.

Early work by D.E. Williams and coworkers (refs. C1-11, C1-14, C1-15, C1-17 to C1-23, 1989-1994) involved a homemade scanning laser microscope system of moving mirrors directing a laser beam (He-Cd : λ = 442 nm or He-Ne : λ = 633 nm or Ar^+: λ = 488 nm) through a microscope onto a specimen surface. The image data recorded was typically of a size 512 x 512 pixels with 8 bit (256 levels) of resolution. This system was used to record images using either a the step-scan lock-in method, or continuous scan direct detection method. This system was used to study a wide variety of

electrochemical systems ranging from work studying the effects on semiconductors to the effects on passive films, by recording photovoltage, photocurrent and optical images.

Later work by the Williams research group (refs. C1-24, C1-32, C1-34, C1-35, C1-39 and D-2 to D-6) involved the use of a commercial confocal scanning laser microscope system (Bio-Rad MRC-600) using a 25 mW Ar^+ ion laser beam in a continuously scanning fixed intensity mode. Again this system allowed the collection of both the photocurrents and optical reflectivity, the first showing the function at the electroactive region and the latter the topography at the surface of the sample in its surroundings. The images recorded by this technique were 768 x 512 pixels in size and of 8 bit resolution. Work carried out with this included photocurrent imaging of semiconductors and examination of thermal effects on metal electrodes such as gold (refs. D-2, D-3, D-5, D-6) and platinised carbon (ref. D-4).

A.M. Chapparro and coworkers (refs. C1-36,C1-37, 1997) have recently published work using a scanning laser microscope system. They used the step-scan lock-in technique to apply a light beam through the objective of an inverted (Nikon, Epiphot) microscope. The light sources used were either a 10 mW He-Ne laser (632.8 nm) or a 5 mW diode at 780 nm or a 50 W quartz-tungsten lamp. This set-up was used for semiconductor characterisation (n-$MoSe_2$ or n-WSe_2 / I^- interface) by carrying out photocurrent, photovoltage and electroreflectance imaging.

J. Bajaj and coworkers (ref. C2-8, 1990 and ref. C2-9, 1993) employed a commercial non-confocal scanning laser microscope system (Waterloo Scientific Inc., WSI-1000) equipped with multiple lasers (Nd-YLF: λ = 1047 nm, Ne-He: λ = 632.8 nm, He-Ne: λ = 1520 nm). The laser was chopped at 3000 Hz and the image was collected in real time using a stepper motor translation stage with a minimum step size of 0.5 μm. This technique was used to record photocurrent, reflected light, photoluminescence and infrared features, in order to carry out spatially resolved characterisation of HgCdTe alloy semiconductor materials and p-n junctions made of this system (a solid-state system).

A new system has been developed by Ribes and coworkers (ref. C2-10, 1996), who further developed the scanning laser microscope system to give large photocurrent images (macro-images) as well as the regular photocurrent images. In this work reflected light, photoluminescence and photocurrent imaging was carried out on $Cds/CuInSe_2$ thin film solar cells using a confocal scanning laser microscope system. The larger images were achieved by using a slightly different apparatus setup. This involved the removal of the normally used microscope objective (x5, N.A. = 0.14, 2r = beam diameter = 5.5 μm, 3.5 cm working distance or x20, N.A. = 0.42, 2r = 1.8 μm, 2 cm working distance) as well as a unitary telescope which preceded it and then fitting a laser scan unit in their place. The laser scan unit was very large in size compared to a regular microscope objective (30 cm in length and 12.5 cm in diameter with a working distance of 22 cm and a numerical aperture equal to 0.05) and it focussed the laser beam down to 10 μm (2r). So in this case the confocal scanning laser microscope could be used to image sample areas from submicron resolution, depending on the objective magnification, right up to large sample sizes of 7x7 cm when used in the macroscope mode.

Differences Between Conventional and Scanning Laser Techniques

There are two main differences between recording photocurrents using the laser spot scanning technique, from that using a conventional technique such as cyclic voltammetry by recording the photocurrent by chopping the light on then off.

1. The most obvious difference is that recording the data as a image provides spatial information whereas only one total current reading would be acquired by the conventional technique, so any great differences due to surface composition or topography would not be recognised.

2. A less obvious difference results from the difference in time scales which may be employed. This is since a scanning laser system can be made to scan at very fast speeds with sampling times to match. The sampling times for the laser system are typically in the region of microseconds whereas the sampling time in a conventional experiment

using a chart recorder would be in the region of a tenth of a second. This means that the cyclic voltammetry technique, which employs a slower detection time, will not be sensitive to the capacitors in the system. This results as there is a complex system of capacitors, storing electrical charge in the electrode-electrolyte interface, which delay the effects that are observed. Capacitors can therefore cause a change in the laser scanned signal but not in the total current observed in cyclic voltammetry. So the photocurrent image contrast may not always be obvious from the general theory and results obtained by cyclic voltammetry on the chart recorder.

Added complications arise in photocurrent imaging using the continuously scanning system as the signal from a perturbed laser irradiation point may subsequently go on to add to the signal in the point which follows if the time it takes to return to steady-state conditions, as present prior to laser irradiation, is slower that the time to sample the data point involved. In the imaging system variations in the image are embedded in the transient characteristics of the photocurrent. The characteristics of the photocurrent with time are described by a transfer function (ref. C1-21, D. E. Williams et al.,1993). The transfer function being a function of frequency (f).

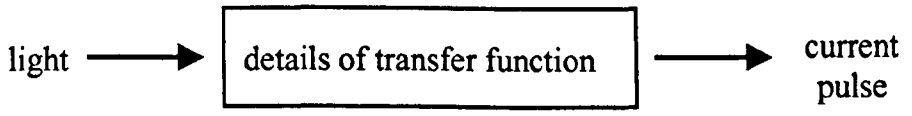

figure 1.14

The frequency of the signal generated however can be limited by the method of detection due to the response of the detection instrument. The limiting response time (τ_{inst}) can be given by $\tau_{inst} = 1 \div 2\pi f$. If several instruments are connected together in the detection system (e.g. potentiostat, voltage offset box and pre-amplifier) then the component instrument in the detection system with the slowest response time will give value of value of τ_{inst} for the whole instrumental setup. The response time may be controlled using built in high frequency cut-off filters in some apparatus, to limit the amount of background noise pick up which may occur at higher frequencies, in order to improve the signal to noise ratio.

1.4 PREVIOUS WORK USING THE LASER SPOT SCANNING TECHNIQUE

This section deals with the research areas which have already been examined and possible areas of interest which may be examined in the future using the laser spot scanning technique. Scanning laser spot techniques can be used to gain the information on the photoelectrochemistry and optical properties of the semiconductor - electrolyte interface. As laser spot scanning helps in our understanding of local structure and electronic properties, it is important in areas of research including: corrosion, areas of catalysis, optical films, microelectronics and even in the development of alternative methods of energy conversion. This technique has been used to examine such things as solid state devices (e.g. solar cells), semiconductors such as Si and GaAs, and corrosion films.

Photoelectochemical properties of semiconductor electrodes are to a large extent determined by the surface morphology. The presence of surface defects such as scratches, grain boundaries and in layered compounds are known to reduce photocurrents as they cause recombination of the photogenerated charge carriers.

This method has been used to look at such things as variations in thickness of surface films. Laser spot scanning has been used to generate photocurrent images / maps to identify the local character of films with a resolution of about 1 μm. Where oxide films on metals are concerned this technique can be used to identify the nature and distribution of oxide heterogeneities and therefore, may be help to identify how these heterogeneities are related to the breakdown of the oxide and to determine how these films may be stabilised in order to protect the metal underneath the film. As well as looking at the film thickness the role of alloying in corrosion and resistance and the effect on the electronic properties of the passivating layer can be observed.

In the **photocurrent imaging technique** an image is recorded at a fixed potential and the current is generated on the illumination of each point, the data from each point is then recorded and displayed as an image by assigning a shade of grey or a particular colour to represent different amount of current generated. The photocurrents can be

generated by photoexcitation or photothermal effects as mentioned previously. Details of research work using laser spot scanning by these techniques of recording photocurrent images, with particular reference to the study of electrochemical systems, as well as some other uses the laser spot scanning technique follows.

Photocurrent Imaging via Photoexcitation

Most of the work carried out using the LSS technique, in order to investigate the electroactive function of various systems, has been conducted by the method of photocurrent imaging, with the image being generated as a result of photoexcitation. This work has included the study of semiconductor electrodes, passive films on metal electrodes and more recently the metabolic processes of live micro-organisms on chemically adapted semiconductors.

Early work using semiconductor electrodes was primarily concerned with identifying good and dead areas and the analysis of charge carrier efficiency of solar energy converters. Later on the technique was applied more thoroughly for measuring as well as mapping inhomogenities in semiconductors as well as semiconductor parameters such as minority carrier lifetime, resistivity and surface recombination ability. It was found that defect regions such as scratches or grain boundaries could be easily identified as they reduced the photocurrent generated due to a higher rate of recombination of charge carriers

Semiconductor / electrolyte systems which have been studied include: Se containing alloys such as n-WSe_2 (refs. C1-1, C1-30, C1-31, C1-36) and InSe (ref. C1-9) and CdSe (ref. C1-28) thin films. Ga containing semiconductors which have been studied include: n- GaAs (refs. C1-19, C1-20, C1-23, C1-24) and GaP (ref. C1-4). Silicon is another substrate that has been studied by electrochemical photocurrent imaging both in the form of n-type (refs. C1-5, C1-14, C1-15) and p-type (refs. C1-6, C1-10, C1-32) silicon.

Passive films which typically exist as metal oxides on metals have been studied extensively by photocurrent imaging as they have semiconducting properties, and therefore are semiconducting oxides. Passive films have been studied in order to investigate their properties and to map out any defects present as well as to carry out the in-situ study of corroding surfaces in order to determine possible sites where break down of the passive film and pitting corrosion may occur in various electrolytes. Passive films which have been utilised include oxides on: Ti, stainless steel, Bi, Cu, Fe, and Pb. Details of this work follows.

Much work has been done on the photoelectrochemical imaging of oxide layers on titanium (n-type, rutile phase). Initially this work was carried out by M.A. Butler (ref. C1-3, 1988) where the line map images were recorded using the a krypton ion laser and the step-scan lock-in method with an x-y digitally moved stage. This was then improved by subsequent work by Butler and coworkers in order to record a video image (ref. C1-4,1984) using 256 x 256 data points. The work by M.A. Butler investigated the TiO_2/Ti system in Na_2SO_4 with a pulsed krypton laser. Yet more work was done by M.R. Kozowski and coworkers (ref. C1-8, 1988 and ref. C1-12, 1989) recording the effects of photoresponse of thin TiO_2 films on polycrystalline titanium in 0.05M H_2SO_4. The results from the work carried out as shown above gave photocurrent images which showed that the photoelectrochemical properties of the film were different on individual grains of metal of different orientation under the film (figure 1.15).

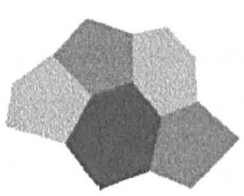

THE PHOTOCURRENT IMAGE OF TiO_2 SHOWS DIFFERENT GRAIN ORIENTATIONS ON THE METAL

figure 1.15

In addition the photocurrents seen were found to be very sensitive to the rate of the oxide growth (ref. C1-13, M.R Kozowski et al., 1990). This work showed that slowly grown films (by slow voltage ramping) showed varied photocurrents on the image but fast grown films showed more homogeneous photocurrents, with the average photocurrent and contrast range decreased. This therefore suggested that the image depends on surface preparation as well as the crystallisation. The thin film grown on Ti

showed variations in photoresponse due to variations of defect density which acts as recombination centres in the oxide lowering the photocurrent where the density of defects is determined by oxide growth rate and substrate orientation. In addition work was carried out by S. Kudelk and J.W. Shultze (ref. C1-38, 1997), which specifically showed how different grain orientations which contained different package densities of atoms to be present effected the photocurrent. This effect was investigated by examining the effects of Fe^{2+} oxidation and oxygen evolution at the Ti/O_2 surface. It was found that the photocurrents generated were the greatest on the particular orientation of the Ti metal (0001) which allowed the highest package density and were found to be very much slower or completely inhibited on other particular (xxx0) orientations. Corrosion effects of KBr on the TiO_2 film has also been investigated. This showed that the photocurrent was fairly evenly distributed on a freshly passivated surface by holding the sample and solution (0.5M KBr) at +9 V vs SHE for a few seconds. The photocurrent showed great uneveness (ref. C1-7, U. Stimming et al. 1987). In addition studies in acidic KBr (ref. C1-35, W. H. Smyrl et al. 1996) showed the occurrence of pre-pitting sites with a reduction of photocurrent on the image.

Another area of study involving passive films is investigating the effects of oxides on stainless steel (an iron, nickel, chromium alloy). Effects investigated include the dissolution (breakdown) of the oxide film and reactions at the surface of the film. The dissolution and reaction of sulphide inclusions in stainless steel has been investigated by D. E. Williams and coworkers (ref. C1-18, 1992). In this work stainless steel was placed in $NaClO_4$ and photocurrent images were taken immediately after polarising at 1.1V vs NHE and then 2 hours later at 1.1V vs NHE. Images obtained showed bands of negative photocurrents. These were thought to be at inclusions which were two small too be seen. Rings of larger positive photocurrents and negative photocurrents were found to develop around some inclusions, behaviour being attributed to the effects of thiosulphate and sulphide in solution and sulphur on the surface, all these species having been formed by dissolution of MnS inclusions contained in the stainless steel. The large area photocurrent behaviour and laser spot scanning of passivated stainless steels was also investigated by P. Schumi and H. Bohni (ref. C1-25) In this work photocurrent images were collected in Na_2SO_4 using a He-Cd laser. It was found that the photocurrents increased (becoming more positive) and pit initiation increased with

increasing potential. There was found to be a critical potential (+400 mV vs SCE). This was explained by Cr(III), Cr(VI) oxidation starting at this potential.
As well as investigating the effects of corrosion at the stainless steel surface, photocurrent imaging of hydrogen diffusing into 304 stainless steel foil (100 μm thick) was also investigated (ref. C1-26, G.Razzini and coworkers, 1995). This technique could be used because when a metal covered by a passive film is loaded with hydrogen and illuminated, an increase in the current generated occurs due to the occurrence of hydrogen photo-oxidation. In this work a pulsed laser beam technique was used with fairly fast scanning rates (10-25 s / line and a illumination time between 30 to 100 ms per point). The stainless steel foil was suspended between two cells. In one cell the hydrogen was created at the surface and then diffused through the foil to the other cell which had a window in it. A photocurrent image was taken before hydrogen loading and then after hydrogen loading. A positive increase in photocurrent occurred. The photocurrent image formed because the passivating oxide layer in contact with an alkaline solution behaved as a n-type semiconductor which produces a photocurrent under polarisation, the photo-anodic process occurring at the semiconductor - electrolyte interface being : $2OH^- + 4h^+ \longrightarrow O_2 + 2H^+$. It was also shown that the area of hydrogen loading could be selectively reduced. This was done by attaching a 'H' shaped sticky letter on the foil, then varnishing over it, then removing the letter leaving only the 'H' shaped area in contact with the electrolyte. A few hours later a white 'H' shaped area could be seen on the photocurrent image. This work overall showed that the photoelectrochemical microscopy technique allowed detection of hydrogen diffusion into a passive metal, and that a sequence of images could be taken in time to see this process developing.

Other metals with passive films investigated included Bi, Cu, Fe and Pb. Photocurrent images produced on bismuth (ref. C1-8), like the images produced for Ti, showed different photocurrents on different crystal planes. This difference in photocurrent reflected the different properties of anodic oxides formed on different crystal planes of a polycrystalline specimen. Corrosion of Cu in 0.1M NaCl (ref. C1-17) was also investigated: the photocurrent sign changed where pits appeared. Work with Fe (refs. C1-17, C1-22) showed the heterogeneity of the surface chemistry on pure and impure samples. The photocurrent was not uniform all over the sample and in addition there

was a strong dependence on the electrolyte solution composition. The photocurrent changed in the presence of ferrocyanide (0.01M) in solution as it acted as a hole acceptor (Fe^{2+} + hole $\longrightarrow$ Fe^{3+}). Lead monoxide on lead has also been studied (ref. C1-29) in acid solution (1M H_2SO_4) using an argon ion laser. This was studied because PbO formation in lead acid batteries causes a loss in capacity of the battery. The formation of the PbO caused a rise in the photocurrent. From this work it was found that oxide growth was uniform at early stages of the growth of the PbO layer

One novel use of the photocurrent imaging technique has recently been developed in order to allow the examination of the electrochemical processes in micro-organisms such as yeast colonies (*Saccharmyces cervisdae*). In this work Nakao and coworkers. (ref. section C3, 1994-1998) were able to adapt the photocurrent imaging technique for use as a scanning laser- pH imaging sensor. Calibration curves showing how the photocurrent decreases with increasing potential were recorded at various pH values for this system. It was found that the curve shifted to a more positive voltage along the potential difference axis as the pH was increased. The shift in the curve was 56 mV per pH. From these calibration curves correlation it was possible to have grey scale images depicting the pH. In one particular experiment (ref. C3-1) the yeast was cultured for 48 hours in an agar medium containing pletone, glucose and yeast extract. This medium was then used as the electrolyte in the experiment with a Pt electrode (used counter and reference electrodes) in it. The electrode used was n-Si - SiO_2 - SiN_4 , with the SiN_4 in contact with the electrolyte and the n-Si had a small ohmic contact on its underside on one very small corner of the electrode. In the electrochemical cell the yeast cells consume glucose and excrete acidic products such as lactic acid and carbon dioxide produced during aerobic respiration. The electrode-electrolyte interface was imaged by a focussed laser beam (1 μm) and a modulated (1-10 kHz) 10 mW He-Ne laser beam scanning from the underneath of the cell through the semiconductor. It was found that the thinner the Si wafer, the better the resolution was. Yeast colonies were indicated by dark areas on the image showing low photocurrents (and pH). The inner part of the colony was darker than the perimeter. So it was found that the laser spot scanning technique could be used to observe H^+ distribution produced by living cells. So this technique could be used to give an insight into the metabolic activity of micro-

organisms on the microscopic scale which would not be otherwise possible with optical imaging.

Photocurrent Imaging via Photothermal Effects

Some work has been carried out more recently in connection with photothermal imaging of electrochemical reaction dynamics (ref. section D and refs. C1-21, C1-35). Thermal imaging offers a means by which systems which are not photoactive may be studied. By this method the way an increase in temperature changes the rate of a reaction can be monitored. Systems which have been studied include gold, platinised carbon and stainless steel.

Scanning laser photothermal electrochemical microscopy has been used to look at reaction dynamics of Fe(II) oxidation at a gold (disc) electrode (refs. D-2, D-3, D-5, D.E. Williams and coworkers, 1991-1995). In this method the electrochemical response arises as a consequence of the temperature rise induced by the focused laser spot. The temperature rise depends on the physical properties of the electrode material and the solution it is in, as well as the time spent at a particular point and the shape and size of the laser spot. The laser scans across the surface with time and the slower the scan the greater the temperature build up should be. This work has been continued in this thesis in order to examine many other effects including effects of electrode geometry and electrode poisoning. Intense illumination of the gold by scanning the laser over a very small zoomed in area repeatedly at potentials $\geq +800$ mV, resulted in the electrode being photo-deactivated in this area.

The photothermal effects on a platinised carbon paper electrode were used to monitor the effect that would be produced on attaching glucose oxidase (an enzyme that breaks down glucose) to it in the presence of glucose (ref. D-4, D.E. Williams et al.). When the platinised carbon paper (with nm size particles) was imaged in glucose the photocurrent generated was found to be uniform over the surface but in the presence of glucose oxidase imobilized on to the platinum carbon paper the photocurrents generated were found to be non-uniform.

Photothermal Effects on stainless steel were investigated by Fujimoto and coworkers (ref. D-1,1991) by inducing a temperature jump with the use of an infra-red laser beam (λ = 830 nm, P = 40 mW). This work showed that the laser induced current was dependent on chromium content and potential. It was concluded that differences in chromium content in the grain boundary or in the different phase of an inclusion are responsible for localised corrosion attack.

LSS work which involved looking at parameters other than photocurrent, i.e. photovoltage, photoconductance, photoluminescence, and photoacoustic imaging follows.

Photovoltage Imaging

In photovoltage imaging (ref. sec. E1) the current is fixed or the circuit can be left open, so that no net current flows. The photovoltage maps the voltage change which occurs at the electrode surface as a function of the position of the illuminating spot. This technique has been termed scanning photovoltage imaging (SPV). Photovoltage imaging work has included, looking at photovoltage images of Cu electrodes in NaCl to study the effects of corrosion (ref. C1-17, D.E. Williams et al. 1992) and in the study of the n-$MoSe_2$ / I^- interface (ref. C1-37, A.M. Chaparro, 1997).

Photoconductance Imaging

The change in conductance (ratio of I/V = 1/R) has not been used in conjunction with the laser spot scanning technique very often. One such experiment (ref. E3-1) which involved this technique used this method to study polysilicon defect passivation using a pulsed He-Ne laser. In this system copper or H^+ ions were implanted into the surface under vacuum. This showed significant reduction in the photoconductance peaks at the grain boundaries particularly in the case of H^+. The reduction of the photoconductance showed that the activity of the defects was reduced and that a high degree of passivation had been achieved.

Photoluminescence Imaging

In the photoluminescence imaging technique (ref. section. E2) when the laser contacts the electrode surface this excites the charge carriers allowing radiation to be emitted from the excited species. This emission of radiation (light) occurs as the photogenerated electron-hole pairs combine, at the electrode electrolyte interface in the electrochemical system, or at defect regions in the solid state system. The wavelength of the emitted light is different to the wavelength of the light which goes in. Therefore a filter which can only let through the light of a particular wavelength is used in order to stop any reflected light from reaching the detector. The information from the light detector (PMT) can be used to show which areas of the surface are emitting photoluminescence.

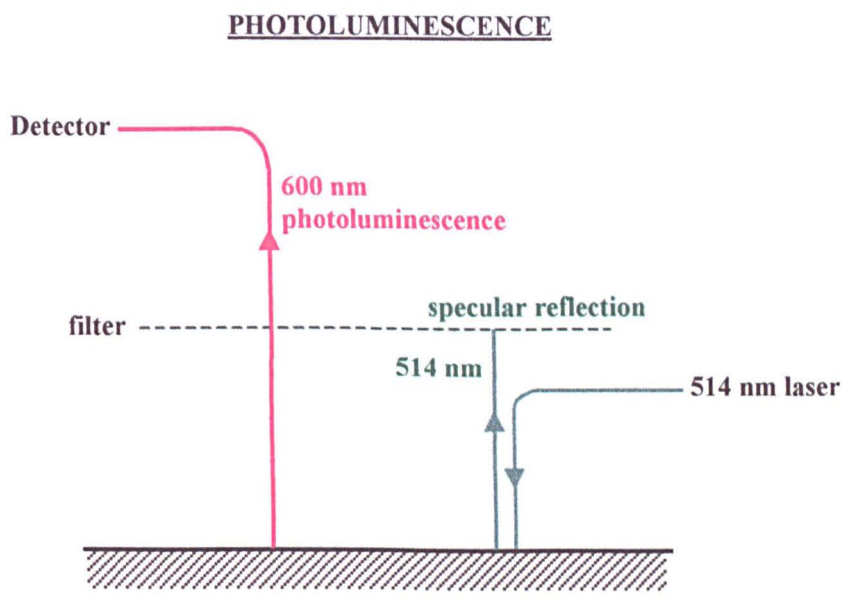

figure 1.16

Photoluminescence has been used to obtain spatially resolved images of semi-insulating (i.e. an undoped, pure as possible, sample with a high resistance) GaAs (refs. E2-1, E2-2, E2-4). In these experiments it was shown that dark spots were centred on dislocation regions and just outside any dark spot on an image a bright ring could be seen which was three times higher in intensity than the background area which surrounds it. These features were explained by knowing that electrically active defects and impurities are non-radiative recombination centres in semi-insulating GaAs. So in

the region of dislocation there is a higher concentration of non-radioactive centres so resulting in a dark appearance on the photoluminescence image and as a larger area around this will be depleted of these non-radiative recombination centres they appear bright on the image. Other systems which have been examined include the study of the stress and defects in Gallium nitride films (ref. E2-6) as well as the examination of polymer layers on indium-tin-oxide (ref. E2-5). InP (ref. E2-3) was also studied by this method to show the action of chemical treatments on the surface with HF, NH_4OH^-, NHO_3 and H_2O_2. In this work non-uniform spatial characteristics were found in many cases on the microscopic scale and photoluminescence was found to increase after HF and HNO_3 treatments and reduce after H_2O_2 or NH_4OH^- treatments which had been carried out prior to the imaging work.

Photoacoustic Imaging

The photoacoustic imaging technique can be used (ref. section. E4) when the light absorbed by a material results in sound being produced as a response. The sound generated can then be measured with a microphone. In this case the image generated represents variations in the absorption coefficients of the material at particular wavelengths of the laser. In this technique illumination of the surface results in local heating and therefore expansion in the material. If the laser beam is intensity modulated (by chopping the laser beam), the resulting modulated expansion is transmitted through the solid as a sound wave which can be detected. Image contrast arises in this case firstly due to variation in absorption coefficients, and secondly because of scattering absorption of sound waves by sub-surface defects.

One such early experiment carried out (ref. E4-1) involved adapting a He-Ne scanning laser microscope in order to give a 128 x 128 data point image. The object imaged as an example, was a photographic glass plate with a mask structure for an interdigital acoustic-surface-wave transducer on it. In more recent work (ref. E4-7) it was found that changing the laser frequency changed the thermal diffusion length of the heat waves in the sample probing different layers beneath the sample, allowing features to be seen below the optically opaque surface of layered microcircuits.

1.6 OTHER COMPLIMENTARY IMAGING TECHNIQUES

Optical Imaging (confocal reflective and colour video imaging)

The optical imaging technique is a method which shows the surface topography of the sample. Optical imaging is used along side methods of spatial monitoring of the function at electroactive regions, such as photocurrent imaging. So this allows a feature which may be seen on a photocurrent image to be possibly equated with a feature seen on the optical image.

Reflective imaging using the laser spot scanning technique

Reflective imaging is a form of optical imaging which can make use of the laser spot scanning technique and a scanning laser microscope system. In this technique the reflectance (photoreflectance) is the property which is recorded. This occurs as not all of the light shone on a sample is absorbed. The light which is not absorbed, is reflected. The reflected light can be specular, when it travels straight up the path it came down, when it is reflected or it can go back up along other paths at a different angle and direction in which it originally came from in which case it is diffuse. The extent of reflectivity is then detected by a photomultiplier tube (PMT) in the scanning laser microscope system where it is converted into a voltage reading and then subsequently into a digital signal in the computer where it is displayed as an image.

If a confocal scanning laser microscope is used then the depth of the field is small. This means that the image is only focussed for a short depth (height). So confocal images allow a greater sensitivity to height.

Use of a scanning laser microscope to record optical images allows fairly high magnifications (depending on the objective magnification and electronic zoom capabilities of both the microscope equipment and software) without destruction of the surface as well as allowing a method of wet-surface non-vacuum imaging.

Colour video imaging

In colour video imaging (or microscopy) the images are collected using an ordinary (non-scanning laser) microscope with an attached video camera. The signal from the video camera may then be sent to a monitor to view as well as to a video printer so that a photograph may be printed. In some cases instead of a video camera and printer system a regular camera was attached to the microscope or if the sample is large enough it may be photographed directly using a camera with a close focussing lens.

This type of imaging is important as it allows the changes in colour and hence the change in composition to be monitored and equated to any changes picked up on the photocurrent image. This is useful particularly when there is only a slightly change in the reflectance between different regions but an obvious change in the colour, so the changes on the colour optical micrograph may show up more easily by this method than on a greyscale / false colour reflective image as given in the previous technique. The colour seen in various places may also be indicative of a particular product if its colour is known. In addition this imaging technique allows a greater depth of field to be measured in one image, than would be possible using a confocal system.

Microprobe Imaging (concentration maps and SEM)

An electron probe x-ray microanalyser, known more commonly as a microprobe analyser, can be used to record concentration maps (images) of any selected element in order to show the variation of an element over the surface. This instrument can also be used to record SEM images as well.

In this method a beam of electrons is made to move over the sample surface, in a vacuum. The electron beam in this technique is comparable to the laser in the LSS technique. The contact of the electron beam results in various emissions from the sample surface which can be measured. These emissions may include backscattered electrons, secondary electrons, x-rays, auger electrons, phonons, transmitted electrons and cathode luminescence.

Electron beam generation in a microprobe analyser

In a microprobe instrument (see chapter 2, figure 2.25 for a cross sectional diagram of the microprobe apparatus which was used in this work) the electron beam is generated by means of an electron gun. In the electron gun a 'V' shaped tungsten filament is heated electrically to over 2700K. At this high temperature many of the electrons in the tungsten are excited enough to free them to escape (thermonic emission). Once freed in order to stop the electrons going back into the filament a high negative voltage (2-25 kV) is applied between the filament and nearby anodic disc, this allows the electrons to be accelerated away from the filament. The resulting velocity of these electrons therefore depends on the accelerating voltage. The tungsten filament is enclosed in a metal cylinder known as the Wehnelt (or cathode) this shapes the electrons into a beam which emerges with a diameter between 10-50 μm. A vacuum system is connected to the column containing this apparatus, so that the gas molecules (in air) are removed from the electron beam's pathway, so allowing it to travel unhindered to the target specimen. If the air is not removed the electron beam will only travel a few millimetres before diminishing due to collisions with the gas molecules. The beam diameter is reduced further still by means of a set of two lenses known as the condenser, and a third lens known as the objective lens is used to insure that the beam has its smallest diameter when it strikes the specimen surface and this third lens is used to focus the image.

Results of specimen - electron beam interactions

Emissions caused by an electron beam contacting the surface of a sample in a vacuum follow:

1. Backscattered Electrons

This is due to elastic scattering which occurs when the electron beam comes to close to the positive atomic nucleus it where it may be attracted by its opposite charge. This results in the electron changing the direction in which it is moving by deflecting through an angle between 0 and 180 °. So the electron is affected very little or made to travel back in the direction in which it came. Many of the electrons with large defection angles (> 90 °) end up being re-emitted from the specimen with high energy. These electrons are called reflected primary electrons or backscattered electrons. This is useful for specimens with little topographic contrast but high atomic number contrast.

2. Secondary Electrons

This results due to inelastic collisions, and it occurs when incident electrons knock loosely bound conduction electrons out of the sample. This technique is widely used in SEM topographic imaging.

3. X-rays

This results due to inelastic collisions if an inner shell electron is knocked out of its orbit by the incidental beam results in an outer shell electron dropping down to fill this vacancy with the accompanied release of a high energy photon with energy in the x-ray part of the electromagnetic spectrum.

4. Auger Electrons

Auger electrons are produced as a result of inelastic collisions. This occurs if an inner shell electron is knocked out of its orbit by the incident beam and then the atom rearranges its self and if an outer shell electron moves to an inner shell one the atom gets excited or ionised and this energy is transferred to a second outer shell electron which can then be emitted from the atom. These are the Auger electrons. These emitted electrons have energies which are specific to the elements which produce them and detection by Auger electron spectrometers (AES) can be used to find composition information.

5. Phonons

This is again the result of inelastic collisions. Phonons are lattice oscillations set up due to electron bombardment, this results in a considerable amount of heating of the sample. If this occurs on delicate specimens a method of removing the heat must be present so as not to damage them.

6. Transmitted electrons

This results due to inelastic collisions. These can occur when the specimen is very thin. If the specimen is very thin electrons from the beam will pass through the sample some without interaction but the majority having undergone inelastic scattering. When they emerge from the other side of the specimen they will have lost an amount of energy which is characteristic of the elements present. The transmission microscope (TEM) is

fitted with an electron energy loss spectrometer (EELS) which can analyse the elements present in the specimens using this process.

7. Cathode Luminescence

This results from inelastic collisions as when exposed to the incident electron beam some specimens emit long wavelength photons in the UV or visible range of the spectrum.

Techniques in detection and image formation in microprobe analysis

Electron probe x-ray microanalysis is carried out on a small pre-selected area of the surface of a solid specimen which is bombarded by electrons. In microprobe analysis, **x-ray emission** is the product that is measured and used in the production of an image by the movement of the electron beam or specimen holding stage from point to point.

In this work the sample is coated over with a thin layer of carbon, to provide good conductivity of the whole sample surface right to the edge up to and including the resin and on any non-metallic impurities and products present (due to surface reactions etc). As this is a destructive technique, requiring the samples to be carbon coated, this method was only used after stopping an electrochemical experiment completely, since polishing the surface after this analysis results in any fine features on the surface changing.

The SEM images are taken in the 1st instant to locate and compare the region of interest to that seen on the optical image. Even though this technique shows compositional information by the change in grey scale it is primarily used to provide information on topographic features present when used in conjunction with the recording of microprobe elemental concentration maps. The SEM technique however is not sensitive enough to pick up small differences in element concentration as a microprobe image is. Microprobe element concentration maps can be recorded for any selected element in order to show how the concentration varies over the surface of a sample. The highs and lows on this image can then be compared with the highs and lows of the features seen on the photocurrent images to see how the electrode composition relates to the photocurrents seen.

The characteristic x-ray emission produced is superimposed on a background of continuum-radiation. In a solid target the x-ray spectrum originates typically from a volume of a few μm^3. In microprobe analysis the emitted spectrum from the specimen is recorded routinely by an x-ray detector and a crystal spectrometer or an energy dispersive system.

1. Detection by an Wavelength Dispersive Spectrometer

The wavelength dispersive method of detection, analyses the characteristic x-rays emitted from the sample by accurate measurement of the x-ray wavelengths (energies) and intensities. In this system the x-ray spectrometer emission is dispersed by an analysing crystal via Bragg diffraction from its crystal lattice planes. This is usually referred to as wavelength dispersive spectrometry (WDS) as the wavelength of the characteristic lines are measured. The simplest type of wavelength dispersive spectrometer consists of a flat crystal placed in the x-ray beam and an x-ray counter positioned so that it collects x-rays reflected from a low index plane of the crystal according to the Bragg equation: $n\lambda = 2d \sin \theta$, where d = interplanar spacing, n = order of reflection and θ = Bragg angle. However as with the small x-ray source sizes involved in microanalysis would only equal the Bragg angle over a small part of a flat crystal making it in efficient the analysing crystal is curved in most systems to increase the useful working area whilst maintaining a constant Bragg angle. Further more to ensure that a high proportion of the x-rays are emitted from the sample entering the spectrometer also enter the counter after diffraction by the system a focussing system is used.

2. Detection by the Energy Dispersive Spectrometer

In this system the x-ray detector is positioned before the dispersing system to collect a sample of all or most of the distribution of emitted x-ray energies. Dispersion of the x-ray signal from the detector then takes place by the electronic processing using pulse-height analysis equipment, the measured height of a pulse being related to the energy of the incoming x-ray photon. Hence the term energy dispersive spectrometry (EDS) is used. In an energy dispersive spectrometer x-rays are detected by a device which produces pulses proportional in height to the x-ray photon energy. Electronic pulse height analysis is then used to analyse the pulse and produce an x-ray spectrum. Earlier

instruments of this sort made use of a gas filled proportion counter to detect ultra-light element x-rays but these days solid-state detectors are employed which give a better resolution.

Comparing the WDS and EDS techniques we may see that they are distinctly different therefore there performance also differs. The energy dispersive system is inferior to the wavelength dispersive system even with more modern solid state detection techniques, but never the less still has a few advantageous features which include the parallel collection of the whole spectrum (where as the WD spectrometers operate in sequential mode) giving a greater collection efficiency. As it is easy to attach an ED detector to a scanning electron microscope this has lead to the wide spread adaptation of these basically image forming instruments for analytical purposes. So much so that there are far more SEM-EDS instruments in use than true microprobes. Even though both WD and ED spectrometers can be fitted to most electron-optical columns the main advantage is in using a wavelength dispersive spectrometer is in the resolution of the apparatus. In the wavelength dispersive spectrometer the resolution depends on the Bragg angle and spectrometer focussing. This is typically expressed in terms of an energy region of a few electron volts which usually suffices to separate major emission lines completely and as a result over lap problems are extremely rare compared with the WDS. One disadvantage of the WDS apparatus is that it costs considerably more to purchase than a EDS apparatus.

In the work shown in this PhD thesis the microprobe elemental concentration imaging as well as quantitative analysis were carried out using a electron probe x-ray microanalyser with a wavelength dispersive spectrometer detection system. This system was used as it was found that the SEM instrument was not sensitive enough to distinguish between elements of similar atomic weight and to give the resolution involved for the small percentages of elements involved. A cross section diagram of the microprobe instrument and the method of operation are given in Chapter 2 (Experimental Method) of this thesis.

This chapter showed how various instruments can be used in the collection of data to form images such as the photocurrent, confocal reflective (optical), and microprobe

element concentration images. Details explaining how the data can be collected and converted into an image using computer techniques has been given in Appendix H.

1.6 OVERALL AIMS

The overall aims of this work was to use a confocal scanning laser microscope in order to spatially map photocurrents as video images, primarily to carry out a wide variety of photoelectrochemical investigations including:

1. To examine the effectiveness and limitations of the technique and the resolutions obtainable.

2. To study photocurrent mapping of electrochemical reactions under varying conditions. The various conditions may include changing the potential applied, changing the laser velocity, changing the incident laser (light) intensity and changing the concentration of the reactants / species in the solution.

3. To examine the presence of surface non-uniformities such as; trace impurities present on screen printed gold microband electrodes, and MnS and MnO inclusions in stainless steels, and various different semiconductors present in compound semiconductor devices such as a silicon memory chip, or defects present in on mono-crystalline semiconductor.

4. To clarify the sources of image contrast in photothermal imaging in electrochemical systems.

5. To examine and compare images of electrochemical reversible and irreversible systems.

6. To investigate the effect of electrode geometry on the photocurrent images produced by the comparison of macrodisc and microband electrodes

7. To improve the apparatus and technique involved in order to make the apparatus more efficient such as by reducing the background noise.

8. To carry out real time experiments by rapid data collection once the efficiency of the apparatus has been enhanced enough to allow so with very little signal averaging for background noise. This was carried out by following the corrosion of stainless steel.

9. To show how various features on the photocurrent image can be related to the topography and the element composition at a particular area by comparing with other complimentary imaging techniques namely; reflective optical imaging, true colour imaging, SEM imaging and microprobe element concentration imaging.

These aims were demonstrated by studying a variety of different systems including; a silicon memory chip, p-type silicon in 1M HCl, gold disc and gold microband electrodes in 5mM $Fe(CN)_6^{4-}$ and stainless steels in $NaClO_4$ and various $NaClO_4$ / NaCl mixtures. More detailed aims relating to the science for each particular system are given in the results chapters related to each system (Chapters 3, 4, 5, and 6).

The general method of how the work was carried out follows in chapter 2 and the specific experimental details for each particular system studied are given in the results chapters (Chapters 3, 4, 5, and 6).

2. EXPERIMENTAL METHOD

2. EXPERIMENTAL METHOD

This chapter deals with how, why and what the instruments were used for in the experiments carried out as well as the procedures that were used. Further technical details of the custom made apparatus, such as circuit diagrams, and technical drawings, including dimensions and materials used have been given in Appendix C. In addition general notes on the properties of the commercial instruments have also been listed in the Appendix E, as well as a list of the apparatus used in the experimental work in Appendix A and a list of suppliers and addresses in Appendix L.

In the experiments conducted, a working electrode was prepared and then polished or etched to give a smooth finish. Electrochemical experiments were carried out, firstly showing how the DC current for the electrode as a whole varies with potential (by cyclic voltammetry using a chart recorder) and secondly by recording photocurrents as images at one particular potential using a confocal scanning laser microscope. The information obtained from the photocurrent image was then verified and further explored using other imaging techniques. The other techniques were: confocal optical imaging, again using the scanning laser microscope; optical imaging using a light microscope; element concentration imaging; and scanning electron imaging. The latter two imaging techniques were carried out using an electron probe x-ray microanalyser.

2.1 ELECTRODE PREPARATION

The working electrode consisted of a small piece of sample material (in the form of wire, foil etc) inserted into a small plastic cup shaped container (1 cm height and diameter), with a hole in it at the bottom. This sample material was then either attached to a conductive brass button placed at the bottom of the cup using silver conductive paint , GaIn eutectic or alternately made to go straight through the bottom of the cup where it was attached to a conductive pieces of wire using silver conductive paint. Then

the remaining empty space in the cup was filled with epoxy resin up to the top of the cup and left to dry.

An electrode preparation technique was devised to give reliably a good electrical contact, avoiding wastage of material and time (this has been written in detail in the Appendix D).

In order to obtain a good contact, prior to mounting the electrode it was cleaned with ultra-pure water followed by acetone, in an ultrasonic bath. In the case of silicon it was etched by placing a drop of 30% HF on the back side of the sample for 60s and then rinsed immediately with plenty of water. It was also important to allow at least 12 hours for the silver conductive paint to dry properly (when used) before placing the glue in the cup.

Great care was taken to avoid leaks around the working electrode when sealing the working electrode material into the cup. This was done by careful handling of the resin so that bubbles were not formed, and in addition by using a primer for epoxy resin around samples such as stainless steel, in order to prevent crevice corrosion.

Care was taken in choosing the mounting and sealing materials to ensure they were inert. The epoxy resin used in the earlier experiments was Araldite® and in the later experiments was Epokwick®. This change in the resin type was due to the later resin being much more suitable for use than the earlier one. The Epokwick resin was a clear resin which set much harder than the Araldite. It was not affected by organic solvents such as acetone or ethanol whereas the Araldite dissolved in these if they were used for electrode cleaning purposes. With Epokwick it was found that if it was mixed up and used in the correct manner there was very little chance of forming bubbles. It existed as a very thin liquid when first mixed and could easily be syringed into the cup. Then placing the cup in an oven at 45°C eliminated any remaining bubbles. The cup, that the electrode sits in, was made of Kel-F. This material, like PTFE, will not react with most chemicals but has the added advantage of being able to stick to epoxy resin whereas PTFE will not.

Once the glue had dried the electrode was polished down using successively finer grades of abrasive papers (silicon carbide or aluminium oxide) and /or diamond polishing pastes down to between 1 and ¼ μm grain size.

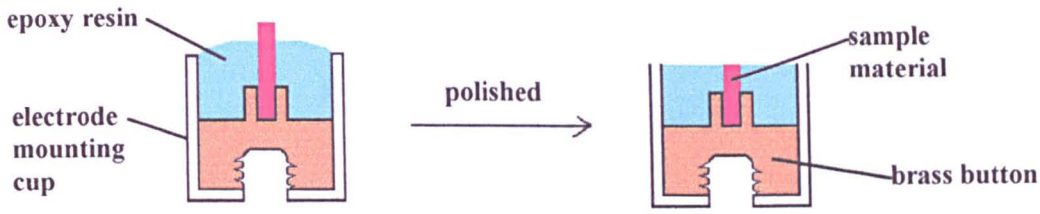

figure 2.1

Great care was taken not to contaminate the sample with the polishing materials. Using an appropriate solvent the sample was cleaned by first rinsing the electrode and then sonicating it in an ultra sonic bath followed by a further rinse. The cleaning solvent used was pure water, unless diamond polishing paste was being used with an oil based lubricant in which case AnalaR ethanol was used as the cleaning solvent.

2.2 SOLUTION PREPARATION

The solutions were all prepared using microselect grade (Fluka Biochemica) or AnalaR grade (BDH) chemicals. These chemicals are of a purity greater than 99%. The glassware used was cleaned prior to use in 50:50 mixture of distilled water and nitric acid, by soaking in this for at least 2-3 hours. Then the glassware was rinsed in single distilled water, then ultra pure water and then with AnalaR acetone and dried for immediate use if required using a clean gas (nitrogen or argon).

The solutions were all prepared in either triply distilled water or later on in the work using 'Milli-Q plus' water. Special care was required in water purification, since organic contaminants in the tap water were found to pass through the system and could affect the results (see chapter 4 , poisoning of a gold disc). Full details of the water purification system which eliminates these problems are given in Appendix F.

2.3 EXPERIMENTAL SETUP

- for electrochemical experiments

The Cell

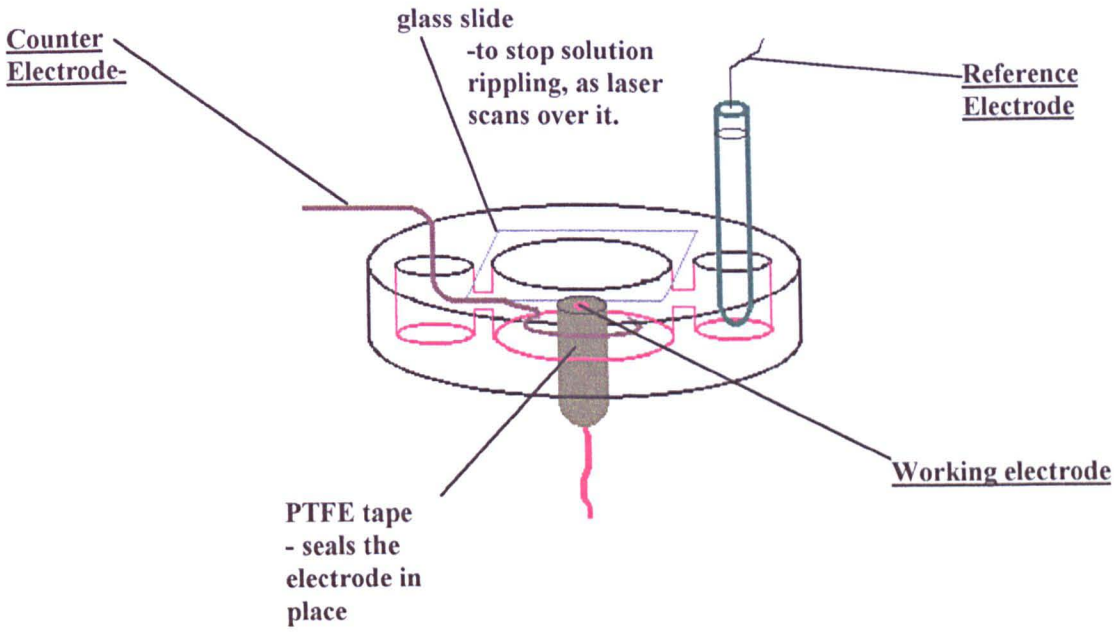

figure 2.2

There were three cavities in the top surface of the plastic container (made of PTFE) making up the cell. These cavities were linked to one another within the cell compartment. The central larger cavity was where the working electrode sat. The working electrode consisted of the material being studied (gold, silicon or stainless steel) mounted in its plastic container using epoxy resin after it had been finely polished down using a polishing material of at least 1μm grit size. (See Appendix D for details of how to prepare and polish the working electrode.) The working electrode was sealed in place using PTFE tape so that the cell was leak proof to any solution it may hold. The counter electrode (e.g. platinum wire) was then placed into one of the cavities in the cell. All three cavities were filled with the required electrolyte solution. A supporting electrolyte was used to increase the conductivity of the solution and therefore to reduce resistance between the working and counter electrode. Last of all, the reference electrode was placed in the third cavity, and a glass microscope slide or cover slip was placed over the central cavity.

This cell had many problems which included the following:

1. PTFE tape was wrapped around the working electrode and its holder and then this was jammed hard into the cell. Sometimes however the weight of the cabling hanging off the bottom resulted in the working electrode slowly slipping out causing a leak of the solution. In addition, tapping the working electrode into place time after time resulted in the slight widening of the cell making it even harder to keep the working electrode in place.

2.The counter electrode needed to be removed for cleaning (by heating in the flame of a Bunsen burner) and separate cleaning of the cell (soaking in concentrated acid). The removal and replacement of the counter electrode involved straightening and bending it on a regular basis, which resulted in it frequently breaking.

3. It was difficult to get the height of the electrode the same each time as this depended on how much PTFE tape had been wrapped around it, and therefore how much pressure had been applied in pushing it into the main body of the cell.

4. The reference electrode sat in an almost upright position in the cell. This resulted in it standing between sets of objectives on the microscope. So the objectives could not be moved around without the removal of the reference electrode, which could not be done without switching off the potentiostat it was attached to, and therefore stopping the electrochemical experiment.

5. The depth of the well, and therefore the depth of the solution the reference electrode was sitting in, was very small and it was easy for the reference electrode to drop out mid experiment.

A new cell was therefore designed with these problems in mind, together with a mini-Faraday cage specifically built to fit around the new cell.

Design of a new cell

The problems with the original cell were addressed as follows:

1. The working electrode holder, a PTFE rod with a brass rod thorough the centre, was made so that it had a screw fitting into the cell so it was more secure. O-rings sealed the teflon rod with the cell body and the PTFE rod with the working electrode cup. In addition the end of the rod was made into the shape of a phono-connector.

2. The counter electrode was made from a platinum wire curled around into an open ring shape and bent around a teflon plug with a groove in it. For easy removal the plug could simply be pulled out (using a screw) with the platinum wire.

3. As long as the electrode cup height is constant we could be certain of the height of the electrode and additional rings were available to put below the cell and above the working electrode holding rod to increase the depth if required.

4. The reference electrode was made to sit at an angle. This allows the objectives to be rotated without removing the reference electrode and switching off the electrochemical apparatus.

5. The depth of the wells were increased a little allowing the reference electrode to sit more comfortably.

6. Instead of crocodile clips, close fitting connectors were used.

7. A mini-Faraday cage was designed to fit around this cell.

THE NEW CELL

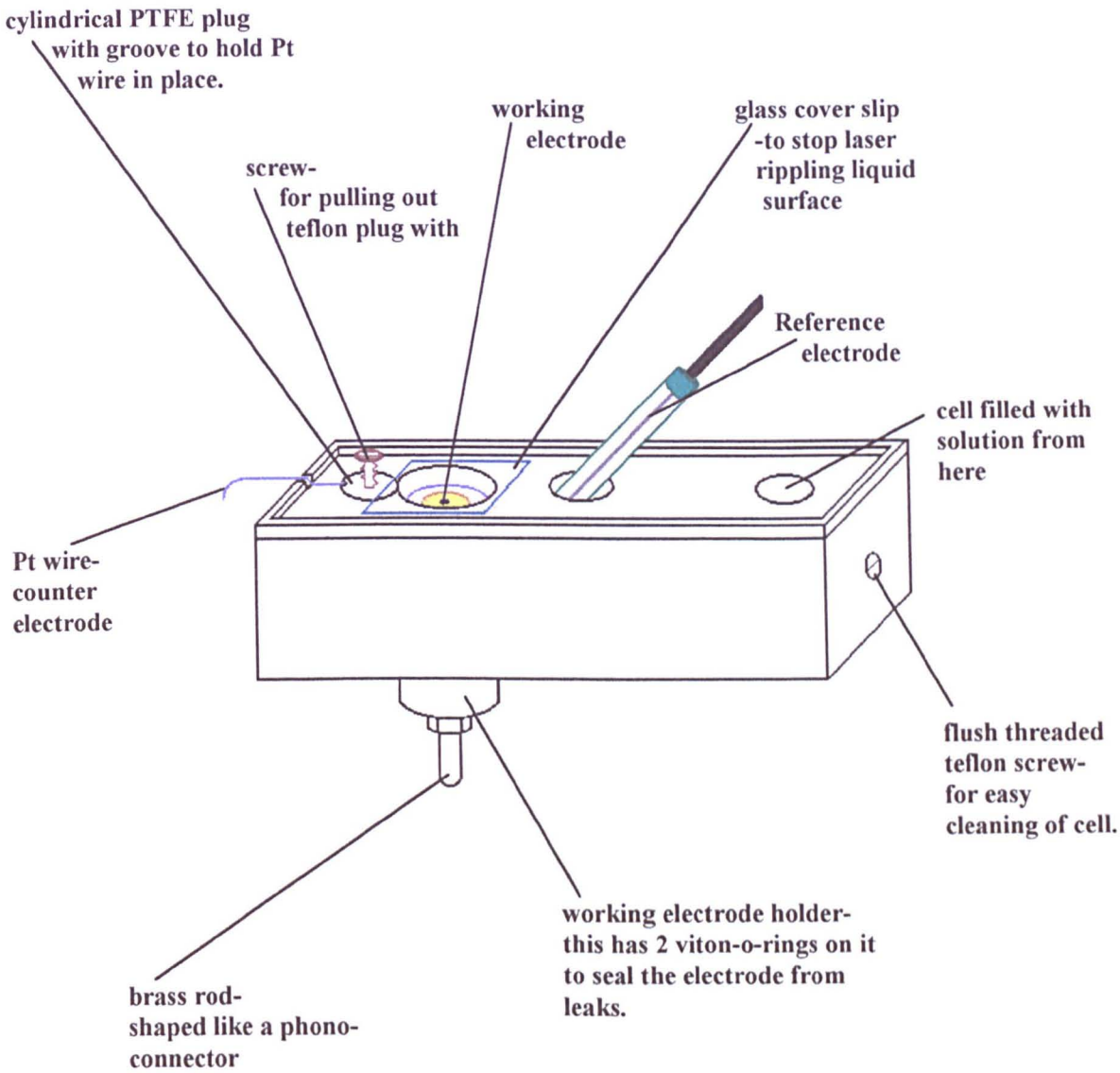

Note: The size of the rectangular cell body is: length = 12.0 cm, width = 2.7 cm, depth = 2.2 cm. Viton-o-rings were used as they are more resistant to temperature and chemicals than ordinary o-ring. Photographs of the various components of the cell are given in figure 2.4 and the mini-Faraday cage (which surrounds it) are given in figure 2.10. Further details can be found in Appendix C.

figure 2.3

A mini-Faraday cage was constructed to fit around this cell. This was constructed with aluminium 3mm thick, and lined with Mu-metal sheeting on the inside, and a RFI / EMI shielding paint on the outside. This was made with easy hatches to access the electrodes (see sub-section on noise reduction).

The reference electrode

The reference electrode used was a saturated calomel electrode (SCE): Hg/Hg_2Cl_2 in saturated KCl solution, or in cases where Cl^- contamination had to be kept to an absolute minimum, a mercury / mercurous sulphate electrode (SSE) was used : Hg/Hg_2SO_4 in saturated K_2SO_4 solution.

The electrodes can be related to one another using the following formulae:

$$SCE = NHE - 241.2\ mV \quad (2.1)$$

$$SSE = NHE - 640\ mV \quad (2.2)$$

$$SCE = SSE + 399\ mV \quad (2.3)$$

Cleaning the cell

It was important to keep the cells clean and free from contamination, avoiding incorrect results, particularly between different experiments. Ways of cleaning included soaking in acid (concentrated HCl) and then rinsing with distilled water and then tripled distilled water and then AnalaR acetone and then leaving to dry. The cell was dried with a clean gas (e.g. argon) if it was required quickly. The new cell, which had been constructed, was used in the study of stainless steel in very dilute controlled amounts of Cl^- or with no Cl^- present at all. In order to avoid chloride contamination this cell was not cleaned with HCl in the usual way but with HNO_3 AnalaR grade, and then rinsed with and subsequently boiled in ultra pure water (Milli-Q plus).

The counter electrode was a platinum wire in all the experiments carried out. This was cleaned by rinsing in purified water and then in AnalaR acetone and on occasion heating in the blue flame of a Bunsen burner. The reference electrode was cleaned by rinsing in our ultra pure (Milli-Q plus) water or triply distilled water prior to use and tapping dry on a medical wipe prior to use.

The working electrode was usually cleaned with pure water and AnalaR ethanol and tapped dry on a clean tissue, prior to use as well.

PHOTOGRAPHS OF THE ELECTRODES USED IN THE CELL

a.

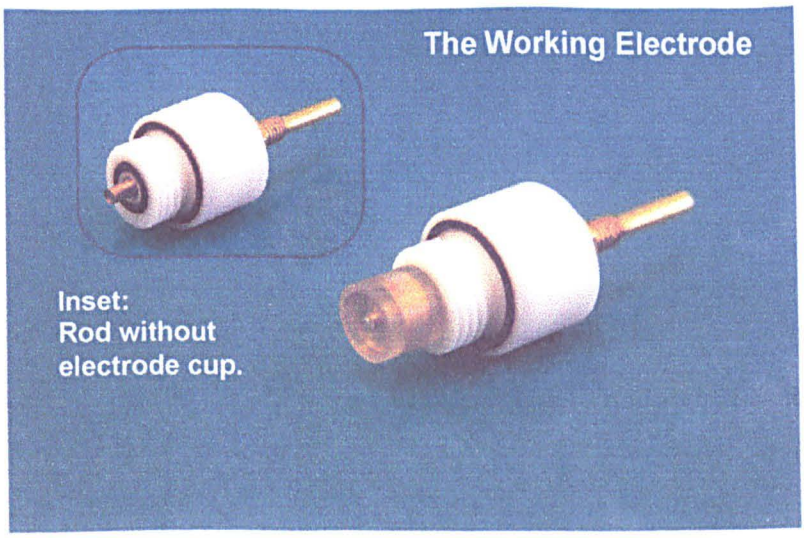

b.

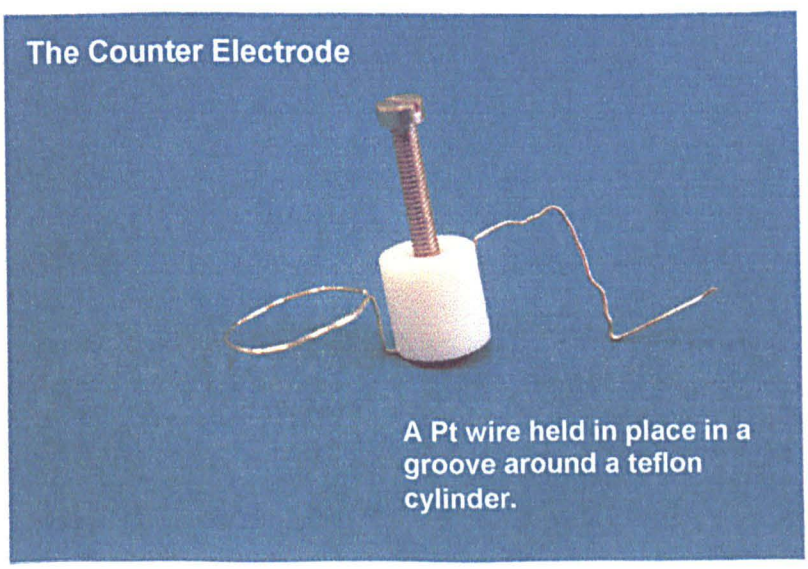

c.

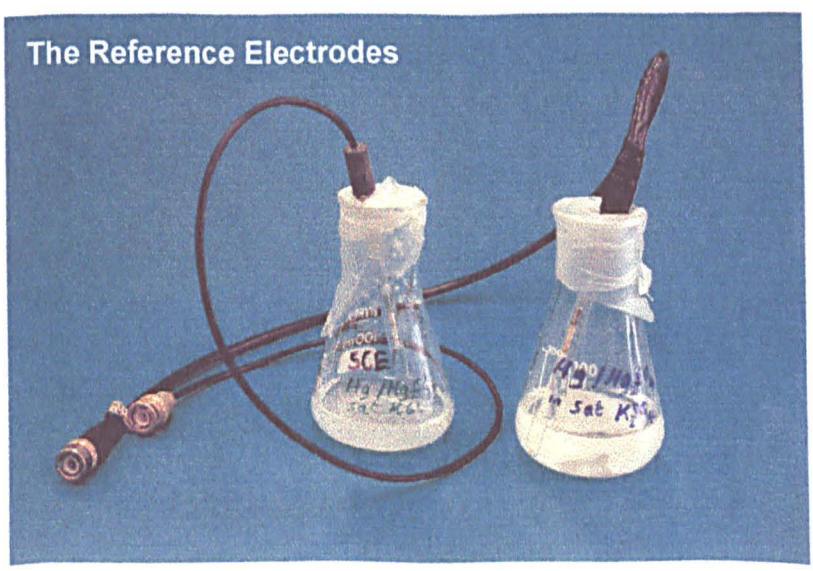

figure 2.4

Electrochemical Measurements

In electrochemical experiments the cell is attached to a device called a potentiostat. This connects the components in a cell (the working electrode, counter electrode and reference electrode) together forming a complete circuit. This can then be used to apply a fixed or moving potential at a known sweep rate ($V\ s^{-1}$). The potentiostat then records the current generated by electrochemical reaction in the cell. The way the output current is recorded varies depending on the conditions being applied and what properties we wish to study. Three different methods of recording the electrochemical signal have been used in this work. The change in current was recorded against sweeping voltage (this technique is called cyclic voltammetry). The change in current which occurred on contact of the laser on the working electrode surface (the photocurrent) was also recorded. The third technique involved the total current being measured with time (the whole current transient measurement) and this was found to be useful when it was simultaneously recorded in experiments where the effect of time on the was photocurrent image was being monitored. These techniques have been discussed in more detail in the work that follows.

A PHOTOGRAPH SHOWING HOW THE POTENTIOSTAT WAS ATTACHED TO THE CELL

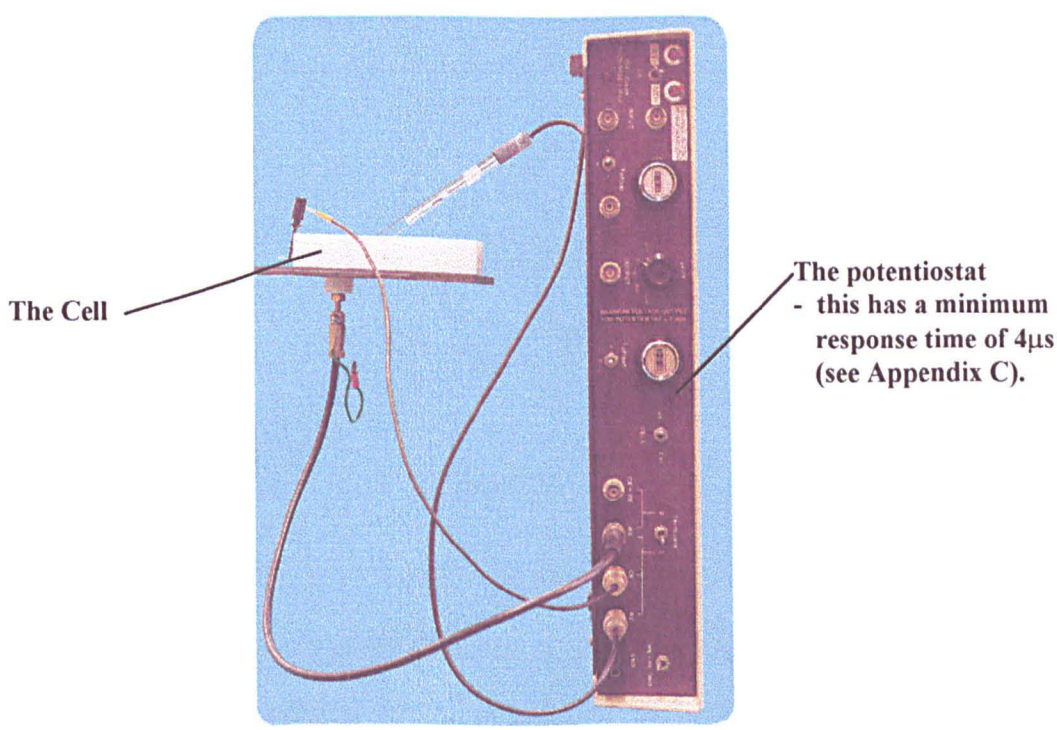

figure 2.5

Cyclic Voltammetry

In this process the cell had a range of potentials applied to it at various scan rates and the variation of currents produced was recorded. This information was then used to characterise a newly polished / made electrode surface.

In order to do this the cell was attached to a potentiostat which was then in turn attached to a waveform generator, which supplies the potential, and a chart recorder which records the current output at the working electrode.

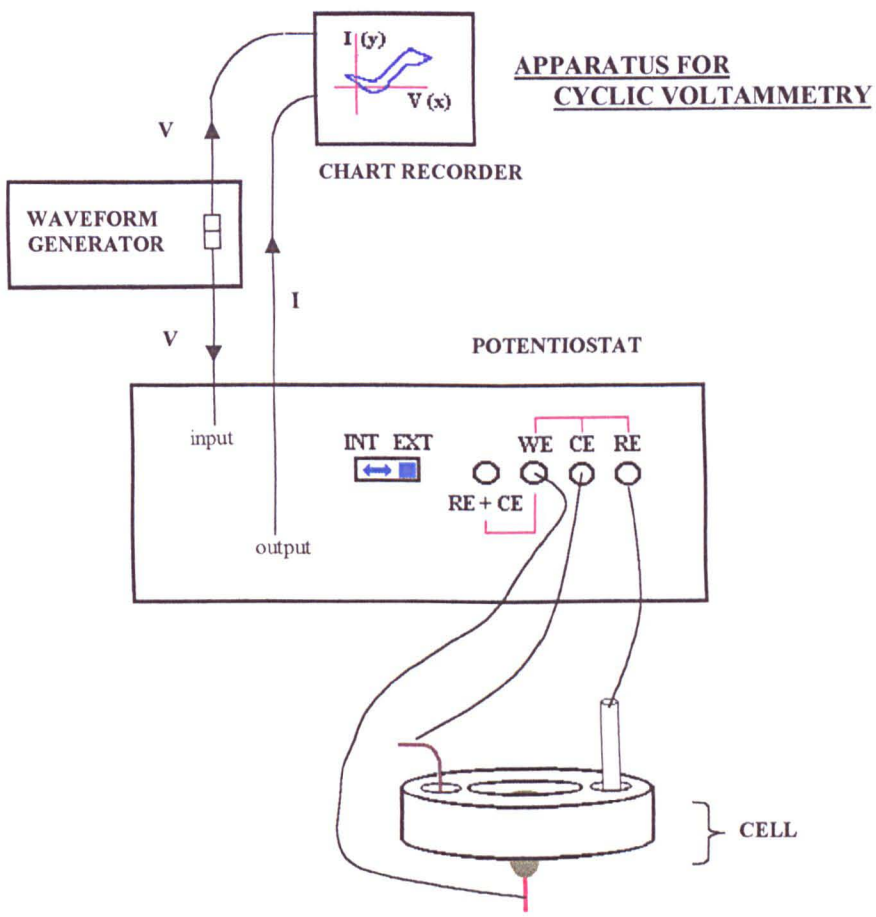

figure 2.6

The electrodes of the cell were attached to the potentiostat using coaxial cables. Each of these cables have 2 wires running through them, the black wire in each goes around the central signal wire giving shielding from external currents. The waveform generator

was used to supply the potential to the potentiostat which in turn applied it to the cell when switched to EXTERNAL (or the internal resistor of the potentiostat when set on INTERNAL). The resulting current output was measured by the potentiostat and sent to the y axis of the chart recorder, where it was recorded as a function of the applied potential, from the waveform generator.

An Outline of the Laser Spot Scanning Technique

Once the cyclic voltammogram had been recorded, the microscope was finely focussed over the cell in order to see the surface of the working electrode clearly and an optical image recorded. The optical image can be clarified by adjusting the gain and black level (contrast and brightness).

The software / electronics which run the laser can recognise the optical image on one channel and the photocurrent image on a second channel. In order to record a photocurrent image the lead taking the output from the potentiostat to the chart recorder (in the cyclic voltammetry experiment) can simply be removed from the chart recorder and attached to a series of electronics leading to the computer which is attached to the microscope.

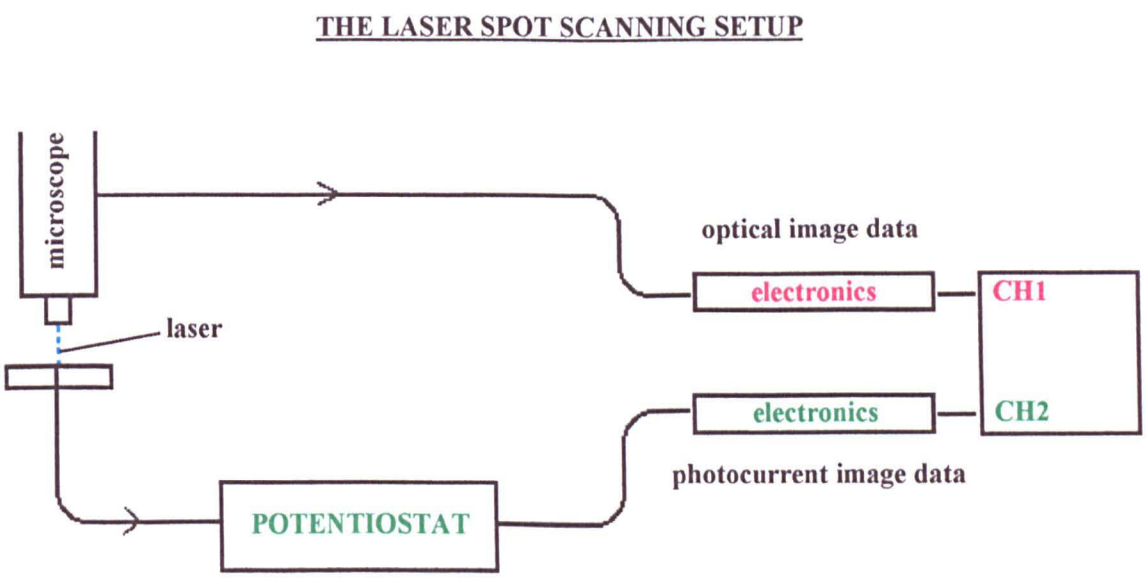

figure 2.7

With the potentiostat switched on to the external cell and the 2nd channel selected, laser spot scanning was used to produce and record an image of how the current changes at each point across the surface of the electrode at particular known values of: laser scan speed (line scan time); a particular applied potential; known objective lens magnification (N.A.); electronic zoom (line length); laser intensity (power); overall electrode surface area; temperature; and time if the reaction being studied is time dependent.

Experimental variables effecting the photocurrent image contrast:

Variables	Control or Recording of Variable by :
laser scan speed	line length, line scan time, pixel dwell time
potential	originates from waveform generator applied to cell via potentiostat
magnification	electronic zoom, objective lens magnification and numerical aperture
laser intensity	neutral density filters, alignment of laser at source and through microscope
electrode surface area	mechanically cutting a small enough area or coating area over with clear nail varnish
temperature	digital thermometer, fan, heater
time	accurate digital clock, computer controlled data logger.

How the variables which effect the photocurrent image contrast are controlled and measured is explained in detail in the sections which follow (in particular section 2.4, scanning laser imaging).

As well as recording images individually both the photocurrent image and optical image may be recorded simultaneously by selecting both the channels, for detecting the photocurrent and reflective signals, at once when recording the images.

Total Current Versus Time Data Logging

This was set up in the very last part of the work done (studying the corrosion of stainless steel), in order to monitor the total current being produced at any particular time. This was set up to collect data simultaneously as the images were being collected with time. The total current could be read off for any corresponding photocurrent image recorded. Data was recorded using an external 12 bit data logging device (Picotech ADC100), which connected to the parallel port of a computer separate from that recording the image data.

A clock (hr: min: sec) was used to synchronise the computer recording the images (the time the laser stops scanning is recorded on each image, which is not the same as the time the image data is saved to computer disc) and the computer recording the total current. Then this clock was also used to make note of any other important times such as when instrumental settings were changed or when particular observations were made.

The data logger had two channels, one of which was attached to the potentiostat output, and the other to a hand held event marker which could be pressed in order to give out a 1½ volt spike to record an event mark in terms of observations or the time as spoken into a dictaphone. The data logging device was made to record signals at ½ to 1 second intervals and it was found that the noise was reduced by a significant amount by signal averaging (total sampling time = 2220 μs for 100 readings signal averaged to give one data point) for each value recorded.

To limit the number of monitors being used to a minimum (and incidentally saving space as well) and hence keep the electrical noise generated by them to a minimum, a monitor switch was used, allowing both the imaging computer and the data logger computer to be attached to one monitor.

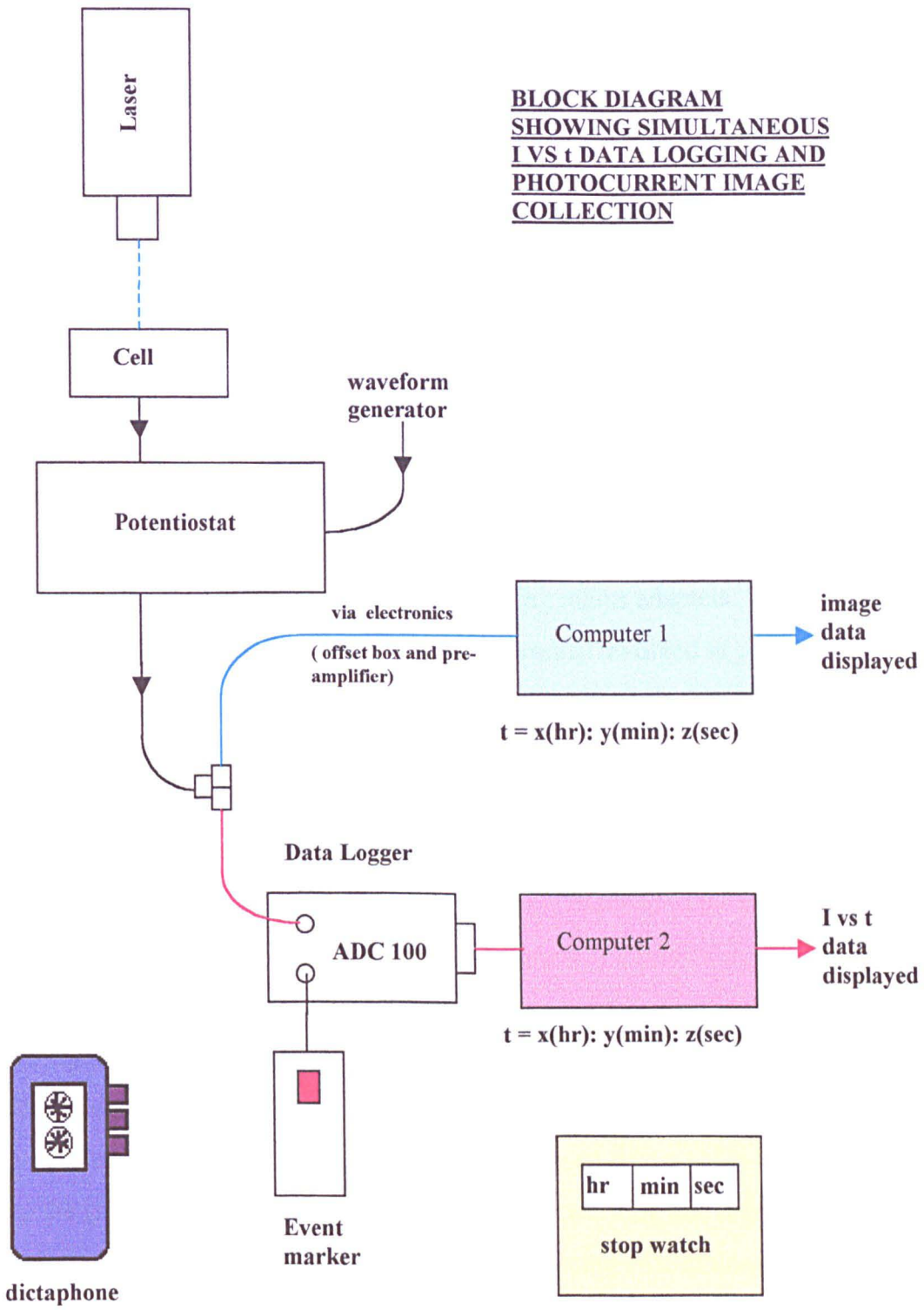

figure 2.8

Signal Optimisation and Noise Reduction

Any electrical noise picked up by the apparatus was kept to a minimum by carrying out many small improvements. Many improvements were required due to the location of

the laboratory, which being in central London and near the Birkbeck Chemistry Department Nuclear Magnetic Resonance facility, together with a poor electric mains supply meant that there were problems, of electromagnetic and radio frequency interference.

The noise picked up by the apparatus was reduced initially by placing the whole microscope, cell and the potentiostat in an earthed metal box (Faraday cage 1.) lined with Mu-metal (see figure 2.9). Reducing the length of the coaxial wire attached to the reference electrode also helped. All the other wires connecting instrument to instrument were also coaxial and kept short. It also helped to run custom made apparatus from rechargeable batteries, instead of the mains. Where it was not possible to use batteries as in the case of some commercial instruments and the computers, these were all plugged into EMI / RFI and surge and spike filtering mains adapters. As it was found that noise was still being picked up the other electronics involved in photocurrent imaging (pre-amplifier and offset box) were also placed in a thick aluminium cupboard (Faraday cage 2.), directly adjacent to the microscope shield.

Further problems were then identified by using a resistor (one end connected to the 'RE + CE' position and the other end to the WE position) attached to the potentiostat as a dummy cell. The output of the potentiostat was then connected to an oscilloscope in order to monitor any noise reduction. In this noise reducing experiment it was found that switching off the computer reduced the noise, but booting up the computer created the most amount of noise. It was found that earthing the preamplifier by having an earth wire from the Faraday cage around it to a screw on its case also helped. It helped to keep the length of unscreened wire attached to the working and reference electrodes as small as possible. In addition it was found that placing an aluminium foil bag over the resistors making sure it was connected to the earthing material within the coaxial cable also helped. In order for this to work at its best the potentiostat had to be switched to the GND (ground) position. The GND switch provides optional grounding of screening on the leads to the working and reference electrodes. This connects the screening of all the leads coming to and from the potentiostat together. However leaving the ground switch off and connecting directly to the main earth cable to the aluminium bag did not help.

Restricting the band width also helped reduce the noise. Moving from 30 kHz to a 10 kHz filter halved the noise and moving to the next setting of 3 kHz also halved the noise again. The band width was restricted carefully by viewing the photocurrent image and if parts of it disappeared or there was loss of contrast the frequency had to be raised back up to the next position. After all this there was still a some unaccounted for noise.

DIAGRAM OF THE EXPERIMENTAL SETUP,
SHOWING THE MEASURES TAKEN FOR NOISE REDUCTION

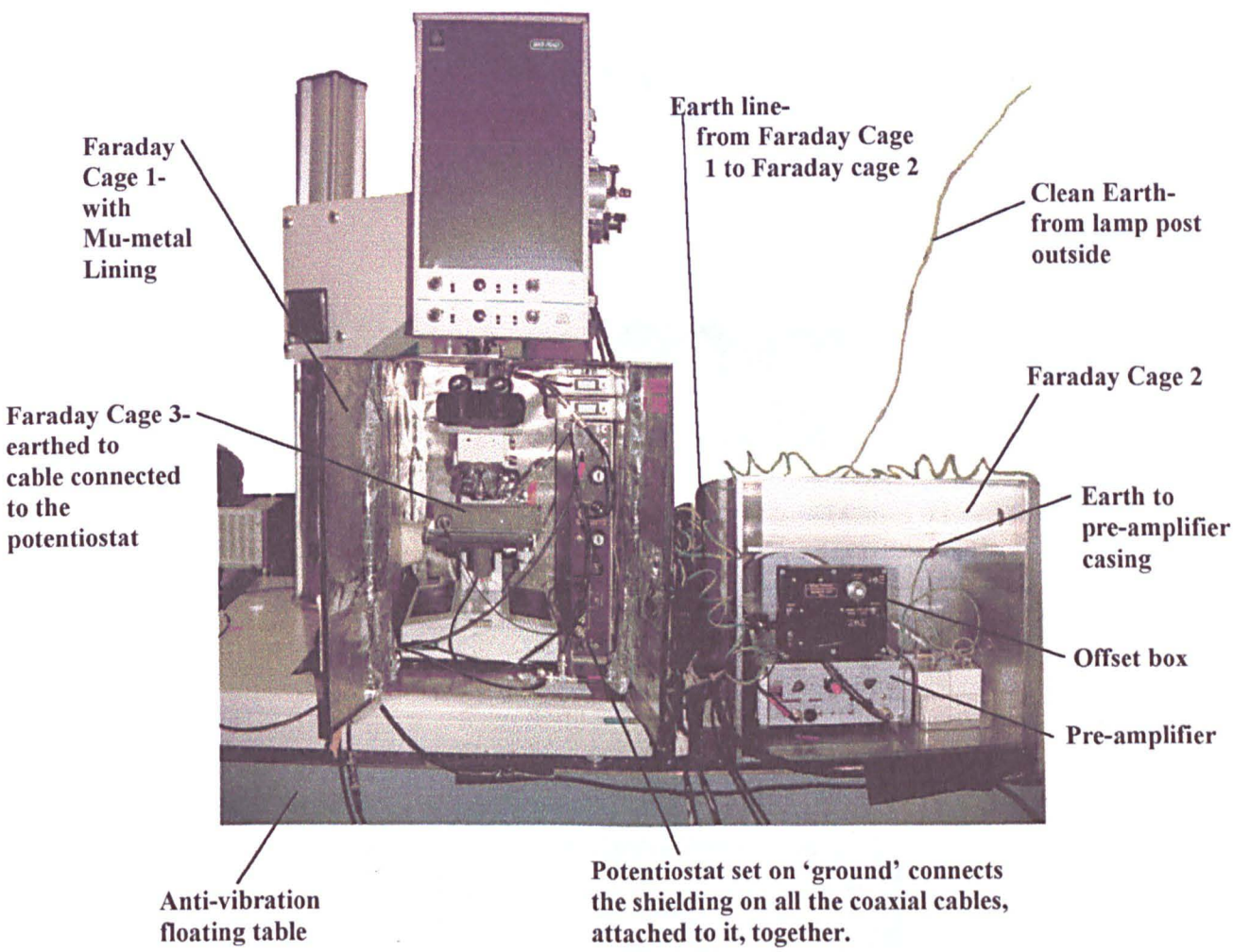

figure 2.9

For the work on stainless steels when the noise was required to be reduced even further, a mini-Faraday cage (Faraday cage 3) was custom made to fit around the new cell (type 2). The mini-Faraday cage was made of aluminium and lined with 'Mu-metal' sheeting and coated on the outside with an EMI / RFI shielding paint (see figure 2.10).

DIAGRAMS SHOWING THE MINI-FARADAY CAGE AROUND THE CELL

a) Side View

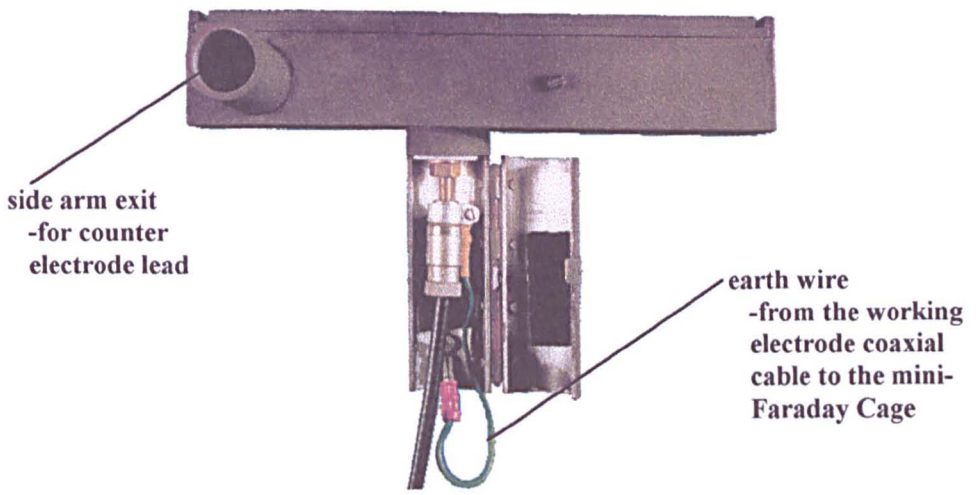

b) Top View

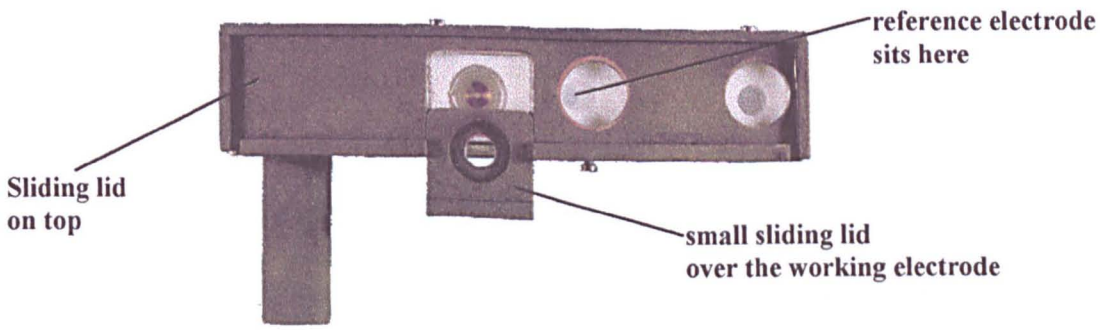

c) Inside the Faraday Cage
Top View, showing the cell positioning

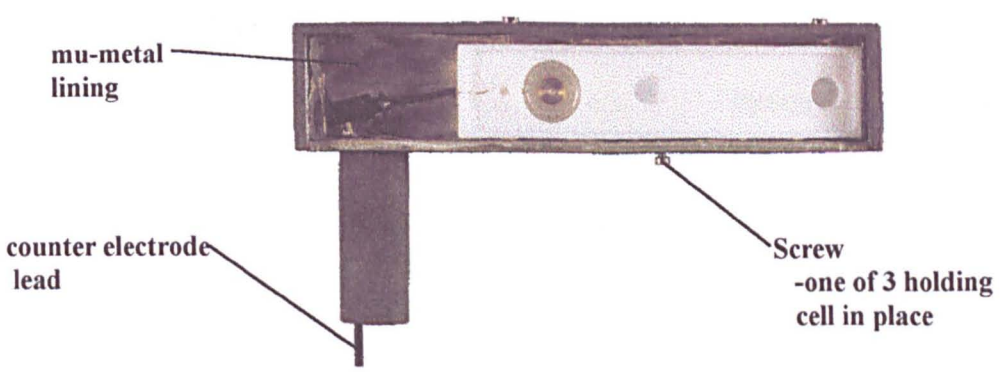

Notes: Further information on the construction of the items shown here can be found in Appendix C (part 5-The cell, part 2-The mini-Faraday cage).

figure 2.10

During the experiment

As well as practical precautions which can be carried out prior to the experiment, noise reduction can also be carried out during the experiment. One such method is by signal averaging. This allows for the removal of randomly occurring noise. In addition. the images could be improved by having long dwell times on each pixel when recording, and by adjusting the blacklevel (offset) and gain controls which results in the brightness and contrast of the image being adjusted in order to give a clearer image. The low / high frequency filtering devices on the pre-amplifier may be operated during the photocurrent imaging experiment. In addition the photocurrent can be kept as large as possible by good laser alignment, because the photocurrent reflects the change in current due to the area of the laser beam, compared to the area of the whole surface. The signal can be further optimised by using small sized samples for mounting or by covering over the surface of the electrode with a clear nail varnish, leaving only a small exposed area.

After the experiment

After the experiment Fourier transformation, using a scientific image processing software package, can also be done with caution in order to remove further noise not in the same frequency region as the image. Further details on this final image processing procedure are given in the next section.

2.4 SCANNING LASER IMAGING

- recording and analysis

This section shows in more detail the method and principles involved in carrying out the photoelectrochemical experiment, that is, in recording and analysing the images. As well as a photoelectrochemical image a confocal optical image may be recorded for comparison and then the images can be stored for analysis at a later time.

Optical / Reflective Imaging

In order for the optical image to be recorded, the light intensity reflected off the surface was detected by the photomultiplier tube which sent a signal to the framestore of the computer. The framestore holds information on what value the pixel is (one of 256 possible values from 0-255).

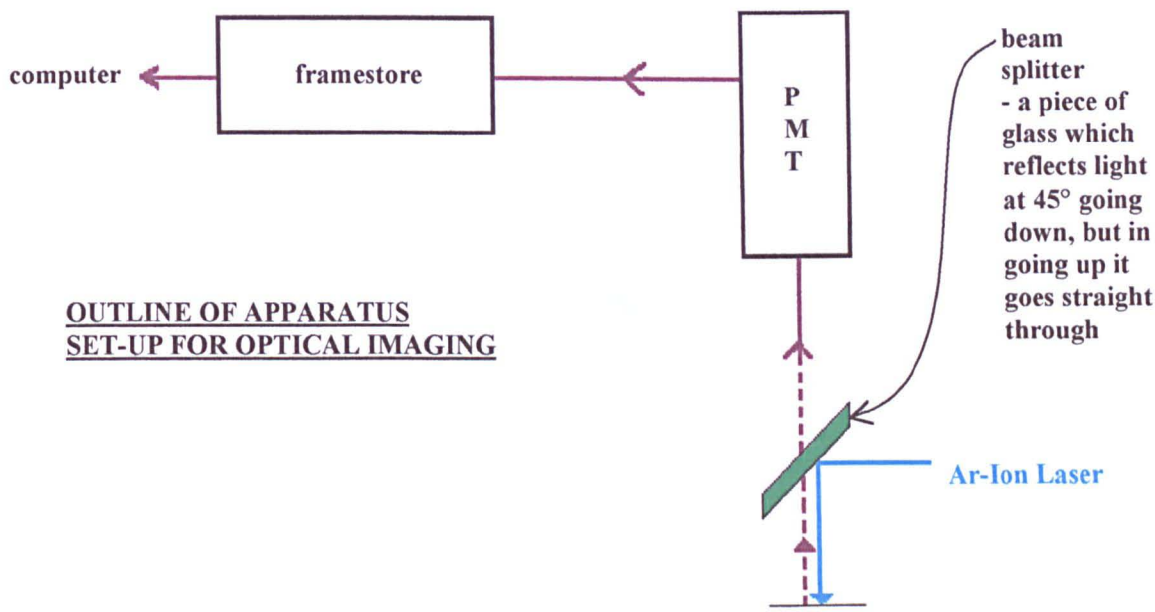

figure 2.11

The focused optical image was optimised further still to give a clearer image using the gain and black level knobs on the scanning head of the microscope.

The signal picked up by the photomultiplier tube was high or low depending on the extent of reflectivity. The signal required was between the two extremes of very high and very low. The black level knob on the microscope was used to move the signal up and down in order to reach the desired position.

figure 2.12

The gain was then used to maximise the amplitude of variations on the signal.

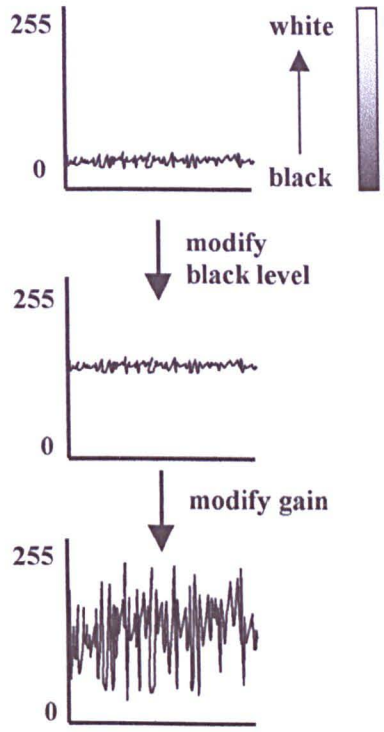

figure 2.13

Photocurrent Imaging

The photocurrent imaging was carried out in a remarkably similar fashion to the optical imaging. In this process instead of the reflectivity being analysed and recorded in terms of pixel intensity the currents generated at the working electrode were recorded instead.

The current output from the cell had to be adjusted to between 0 and 1 volt in order that the computer would recognise it and convert it to a digital signal. This was done using a black level (offset) box. The dial on this box can move the signal up and down. Changing the black level does not effect the current changes, as we are looking at the change in current relative to the background current.

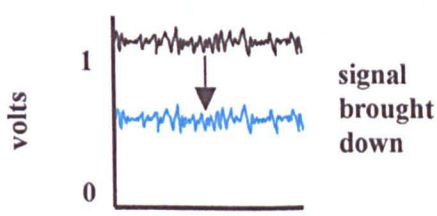

figure 2.14

Then the current was suitably amplified to give a large as possible signal between 0 and 1 volt.

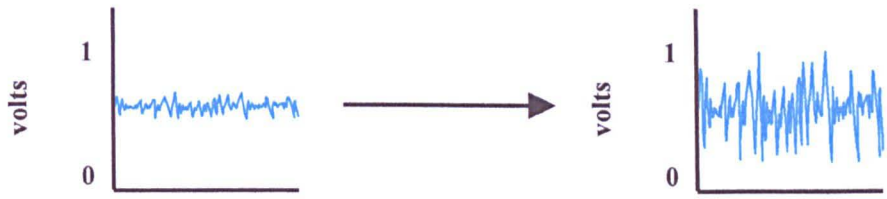

figure 2.15

The signal and how it changes when the black level and amplification were adjusted, was observed directly using an oscilloscope screen (figure 2.16).

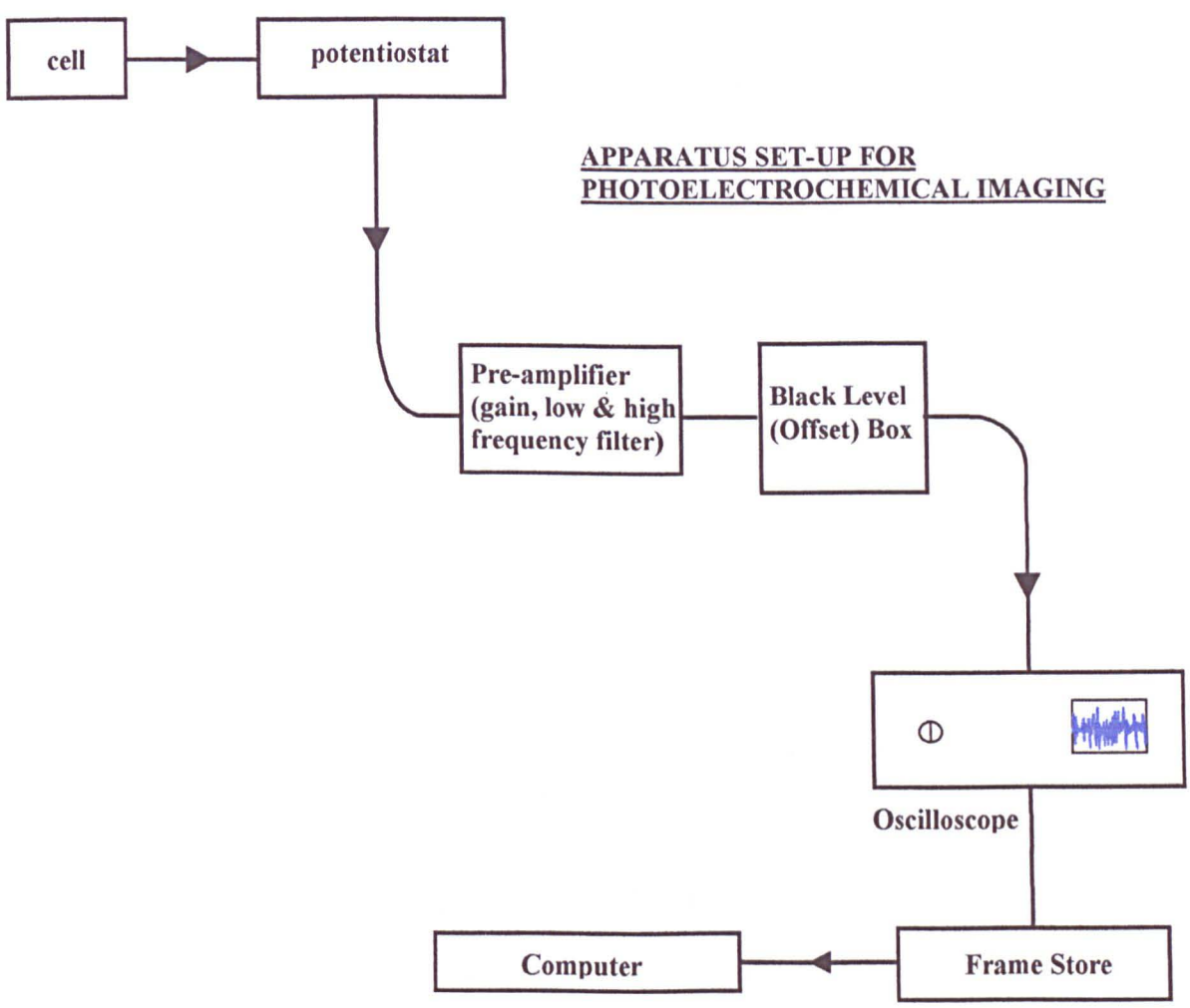

figure 2.16

The current output can therefore be recognised by the computer and shown as a grey scale image consisting of light (white) and dark (black) regions on the computer screen.

The bright areas on the image are of a high pixel value and these correspond to high photocurrent generation on this region of the electrode and darker areas on the image are of low pixel intensity and these correspond to low / no photocurrents being produced.

The image is normally recorded so that the highest pixel intensity is white in colour and the lowest is black in colour.

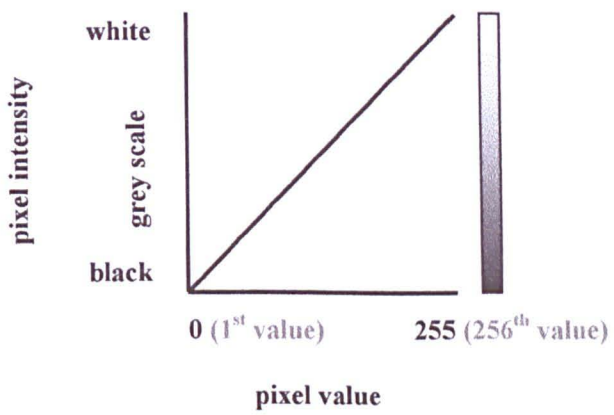

figure 2.17

The image however can be artificially coloured so that different colours can represent different pixel intensities. This is done by different proportions of red, green and blue to represent each pixel intensity value and then applying the map drawn to any black and white image.

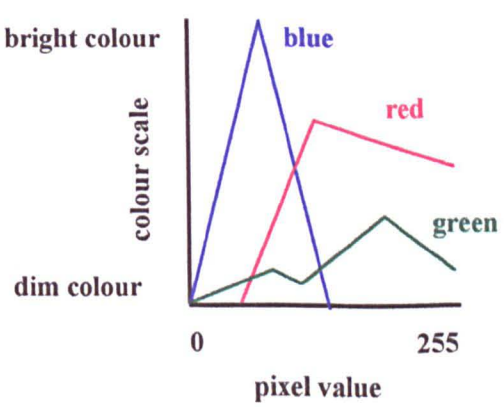

figure 2.18

The images can be recorded using different collection filter commands, within the menu of the computer program operating the laser. If the direct filter command is used the signal is recorded direct from the object being observed and each successive image is overwritten by a new image until the laser is stopped from scanning. The Kalman filter is another useful filter. This is used for signal averaging. This is useful in eliminating / reducing any electrical noise which may be picked up from the surroundings. For example if 5 scans are asked for 5 frames are recorded summed together and divided by 5. In this method previous images are added to and not overwritten. However if required the laser may be stopped at any frame before the final one asked for. This is useful if there is no further improvement in the image, which can be observed after each successive frame has been collected and averaged with respect to the previous frame.

Image Storage

After the image had been recorded it was then stored as a file on a 486 DX computer. After storing a series of images on the computer hard disc during an experiment these were then removed to rewritable magneto optical discs (capacity 128 MB) using an optical disc drive. This was used because the images were very detailed so they required a large amount of hard disc space, and it was found that recording the data for a couple of long experiments was enough to fill the hard disc to almost its maximum capacity.

Image Analysis

Once the images have been stored they can easily be analysed to find out the level of pixel intensity at any place in the image. An area may be selected to give the average pixel intensity for that area.

$$I_{photo} = I, \text{centre} - I, \text{background area prior to electrode} \qquad (2.4)$$

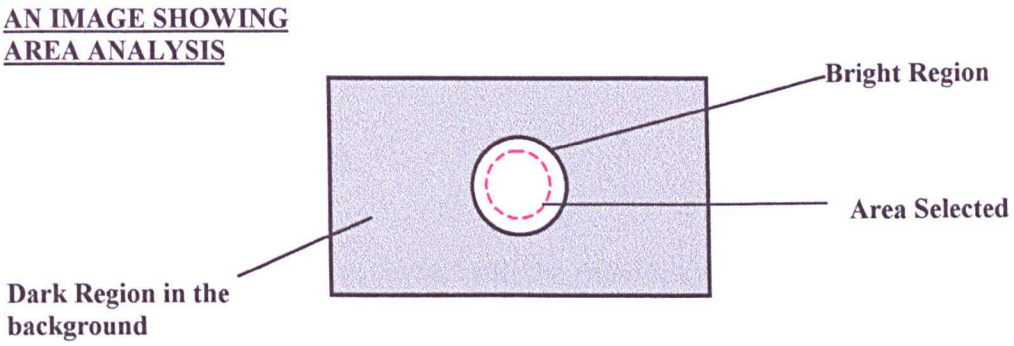

figure 2.19

Another method is by analysis of how the pixel intensity changes across a selected line anywhere on the image.

$$I_{photo} = I, \text{ at peak in line} - I, \text{ background at start of line} \quad (2.5)$$

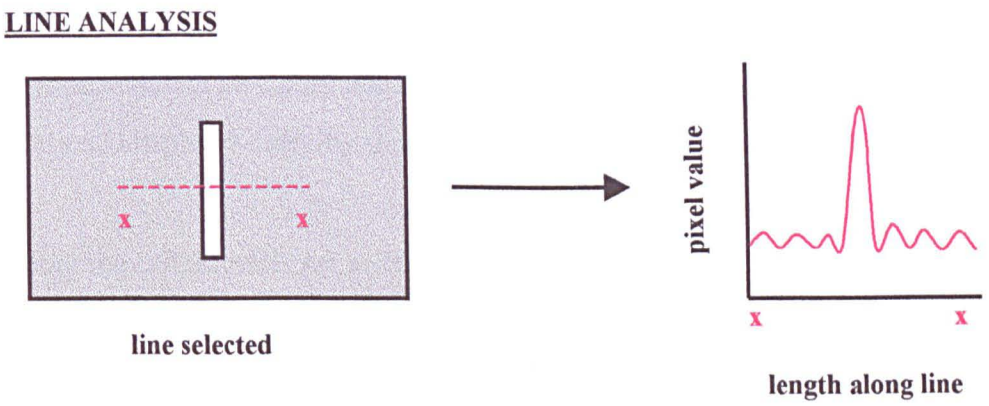

figure 2.20

In later work a third more reliable method of determining photocurrent data was obtained. This was done by taking a photocurrent image with the laser light on the surface of the electrode and then taking a dark image immediately after this, with the same experimental settings. This was simply done by placing a dark board in front of the laser beam source and prior to its entry into the microscope. The scanning head was then made to scan as usual, as the computer did not know the laser beam was not there, and a uniform grey image reflecting the setting on the offset (blacklevel) box was obtained. Analysing the average pixel intensity of this dark image and subtracting from

the pixel intensity on the area of interest on the light image, gave the required photocurrent.

$$I_{photo} = I_{light} - I_{dark} \tag{2.6}$$

This method was better as it was found with the previous method of subtracting the background prior to the electrode, as this only worked with a low zoom and magnification. However if the electrode filled a large part of the total image area, there were problems in that there was not enough background area surrounding the electrode to analyse. In addition if we could not analyse sufficiently far away enough from the electrode slightly incorrect results were obtained for the background pixel intensity reading. This is since the area surrounding the electrode also showed subtle changes in photocurrent when leading up to the electrode area.

Calculation of the laser induced photocurrents as given by the image

Conversion of the pixel values from the images (shown by the colour or shade of grey), to values of current can be easily done using the values selected for use on the potentiostat and amplifier carrying the signal from the cell to the computer screen.

e.g. Using the potentiostat set at 10 μA volt $^{-1}$ and the pre-amplifier gain at x50 .

$$\frac{10\,\mu A}{1\,volt} = \frac{10000\,nA}{1\,volt}$$

$$\downarrow \div 50 \text{ (gain)}$$

$$200\ nA\ volt^{-1} \tag{2.7}$$

$$\frac{200}{1\,volt} = 256 \text{ pixel value}$$

$$\frac{200}{256}\,nA = 1 \text{ pixel}$$

For example if the electrode region on a photocurrent image has a value of 219 pixels with the light on, and 151 pixels with the light on a 0-255 grey scale where 0 = the 1st pixel intensity value and 255 = the 256th pixel intensity value,

then the current is the n^{th} pixel value out of a possible 256 the following calculation will gives the value of the photocurrent:

I (light-on) = (219 +1)/256 x 200 = 171.88 nA
I (light-off) = (151+1)/256 x 200 = 118.75 nA

$\therefore$ Using equation 2.6 gives:

$$I_{photo} = (219 - 151) \times \frac{200}{256} = 53.1\,nA$$

Final Image Processing

Removal of noise

Further removal of noise was carried out by FFT if required using a scientific image processing package (NIH image on the Machintosh platform or the same package on the PC called ImagePC). This was done by first converting the raw data image file saved in the 'Bio-Rad pic' format to the 'tiff' format using an scientific image conversion utility (X-image for Windows). Then the image saved as a tiff image was imported to the image processing package. Here a square can be selected for Fourier transform analysis. This uses a real 2D Fast Hartley Transform (FHT) routine. This gives a map of the frequencies in four quadrants.

FFT IMAGE (Power Spectrum)

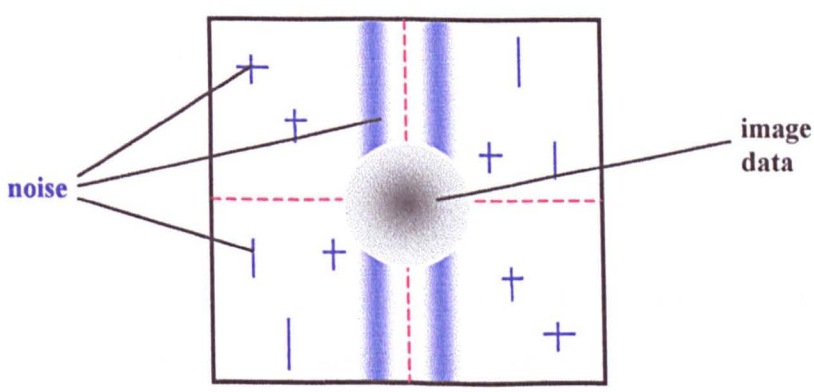

figure 2.21

The 2 diagonal quadrants always contained matched but mirrored patterns which were noise. (Looking at the non-electrode i.e. resin area on its own confirms this.) These were eliminated by simply selecting and cutting out the not required patterns, which were noise and then doing inverse FFT to this map which gave the picture back but with reduced noise.

Scaling Images

The scanning laser imaging system distorted the image such that the scale on the x-axis did not match that on the y-axis and further more the scale depended on the lens and magnification settings (see Appendix E, part 3., for the calibration) Image processing allowed the scale of the x axis can be made to match that on the y axis. So allowing the rectangular pixels which are recorded on the slow scan speeds for both optical and photocurrent images to be converted to exact squares giving the correct sense of proportion when viewing these images.

e.g. if 1 pixel = 1 μm on the y axis and 1 pixel = 0.90 μm on the x axis
the x axis can be stretched by 10% to make it equal 1 μm as well.

In addition if the optical image had been recorded using a high numerical aperture, and low zoom to give the best optical image and the photocurrent image at a low numerical aperture and high zoom to give the best photocurrent image, the optical image can be resized exactly so that the x and y pixel lengths are the same as that on the photocurrent image for easy comparison.

Experimental Parameters

1. Laser power

The microscope used is a 25 mW argon ion air cooled laser which has several wavelengths emitted simultaneously. The two principal lines are at 488 nm (blue) and 514 (green) which are both approximately 10 mW each.

Under normal circumstances the laser power was kept at its optimum intensity by careful alignment of the laser first at the source and then through a series of mirrors directing the laser into and then through the microscope (details of the laser alignment procedure has been given in appendix G). This was required as the higher the laser intensity, the lower the noise to signal ratio is. This is since the laser intensity increases but the noise stays the same. So the resulting effect is that images are very much clearer for small sized electrodes, and if the laser intensity is increased photocurrent images can be seen for larger electrodes which could not be seen at lower light intensities.

It was also found that the laser power at source varied with room temperature. So it was found that it was best to do the alignment at a known temperature (25°C) and then to keep the beam power constant by keeping the temperature at 25°C ± 1°C at all times in the laser room (a sectioned off part of the laboratory with no air vents so allowing easy heating of the room). This was easy to do by using a thermostat controlled heater in the winter and a fan or by leaving the doors open in the summer. The temperature was monitored at all times during an experiment using a large digital thermometer and the heating or fan switched on or off as necessary. This was found particularly important for time dependent experiments with stainless steel carried out over very long periods of time (many hours). Comparison of the images could therefore be carried out at constant laser room temperature and therefore laser power.

The laser power and therefore laser light intensity could be reduced by known amounts by the use of neutral density filters. When no filter is present the percentage transmission is roughly 100%, as some may be lost along the pathway due to incorrect alignment and deflection by dust.

2. Laser beam spot size

The laser beam spot size can also be calculated (Ref. B2-3). This is done using the numerical aperture on the lens.

The dimensions of the intensity pattern of the laser beam can be given by the distance of the first node of the diffraction pattern (r).

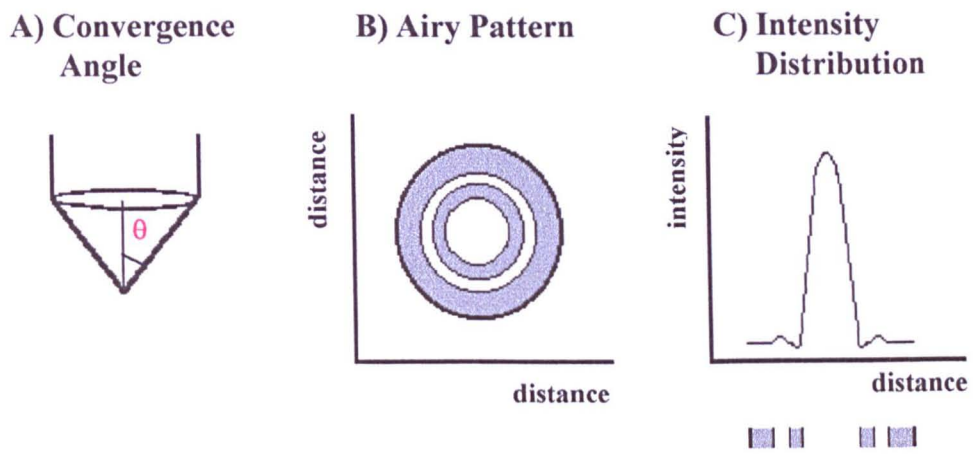

figure 2.22

$$r = 0.61\frac{\lambda_o}{n \sin \theta} \tag{2.8}$$

and

$$n \sin \theta = N_A \tag{2.9}$$

Where λ_0 = vacuum wavelength of the focused light, 0.61 = numerical prefactor (for coherent light = 0.77), n = refractive index (this varies in different mediums), θ = half the angle of the converging cone of light, and N_A = numerical aperture (N.A.).

The full width at half the maximum of the central spot is close to the same value, so equation (2.8) is often approximated to

minimum spot size, $$2r \approx \frac{\lambda_o}{2N_A} \tag{2.10}$$

A variety of lens were available for use with the microscope. The original lenses which came with the microscope were of high numerical aperture at each given magnification. This meant that, the higher the magnification the closer the lens came to the sample surface. This made it impossible to use such lenses with an electrochemical cell in

operation as the lens would be so close to the sample surface it would end up in the reaction solution. To allow some space between the objective lens and solution, the cell and mini-faraday cage around it, long working distance lenses were purchased. However the other lenses were still found to be useful with the lower magnification lens having just enough space to be used for electrochemical experiments and the higher magnification (N.A.) lens being used for accurate optical imaging prior to and after the experiment. A list of the lenses which were available, together with the laser beam diameters produced by these lenses has been listed in Appendix E.

The formula for calculating the minimum spot size is only approximate as it is known that if the beam is travelling just through liquid instead of a gas the spot size should be smaller still. In our case the beam is travelling through air, then a thin glass cover slip and then the reaction solution.

With the use of other lenses not provided with the microscope system with very different numerical apertures the image magnification was very different. This required the recalibration of the software using a reflective scale bar cut in to a microscope slide. The calibrations are given in Appendix E (part 3).

The best optical images were taken with the highest magnification objective lens and the highest zoom possible. The best images of each sort gave the greatest signal and hence the greatest detail of the electrode and its edges, and they could be used for direct comparison with one another.

The optical images taken were clearer using a high magnification objective lens and as low as possible electronic zoom as this gave better resolution. The topographic effect, whereby the edges of the sample were lost in the image because the sample tapers down very slightly towards the resin surrounding it, were not so great with this lens configuration. This tapering occurred particularly if the sample was considerably harder than the resin. The problem was limited to an extent by using a 'hard' polishing material such as diamond polishing paste.

The photocurrent images were clearer with a low magnification objective lens (large as possible laser beam diameter). The pixel size was usually smaller than the beam

diameter so meaning that the laser beam was slowly moved through a length equal to its beam size.

3. Image parameters

In addition to the recalibration of the software provided, due to the long distance working lenses having different numerical apertures to that of the provided lenses of the same magnification, it was found that changing the speed from the normal to slow setting resulted in the x-axis being 'squashed' in comparison to the y-axis. In other words the pixels were of rectangular shape. This meant that the x and y axis had to be calibrated separately for each magnification lens.

Calibration of an objective lens gave an objective factor which could be manually fed into the microscope software to give the correct size on the image. A table listing the calibration factor required to calculate the image size for each available lens and hence the pixel size used has been listed in Appendix E.

4. Line scan time

The line scan time was one experimental parameter which resulted in the photocurrent image being changed.

The size of the images collected were 768 x 512 pixels (x,y). The line length being 786 pixels long.

There were two principal types of scan speed available these were the faster and slower speeds. Each set was controlled by a separate lead going to and from the microscope and computer framestore (i.e. there are 2 leads going to the computer marked scan speed and slow scan speed).

<u>The Faster Scan Times</u> :

There were three standard faster times available defined as 'normal', 'fast' and 'very fast'. All these line scan times had a precise pixel dwell scan time of 2.5μs. However for the normal setting every line was sampled (512 lines), for the fast speed every other line was sampled (½ of 512 = 256 lines) and for the very fast speed every fourth line

was sampled (¼ of 512 =128 lines). These have frame scan times of roughly 1 s, ½ s and ¼ s (from the Bio-Rad MRC-600 manual). These values are only approximate and in addition depend on the magnification and zoom as the time it takes to jump from the end of one line to the beginning of the next will depend on these parameters.

The frame scan time may be calculated roughly from the known pixel dwell time and the number of pixels in an image.

$$\text{Frame Scan Time} = \text{No. pixels in a frame} \times \text{pixel dwell time} \quad (2.11)$$
$$= (\text{No. of pixels in a line} \times \text{No. of lines}) \times \text{pixel dwell time}$$

For the normal line scan time:

Frame scan time = $(768 \times 512) \times 2.5 \times 10^{-6} = 0.98$ s

For the fast line scan time:

Frame scan time = $(768 \times 256) \times 2.5 \times 10^{-6} = 0.49$ s

For the very fast line scan time:

Frame scan time = $(768 \times 128) \times 2.5 \times 10^{-6} = 0.25$ s

This shows the approximate frame scan times given in the manual have not taken account of the time to jump from one line to the next.

The Slower Scan Times :

There was one standard slow scan time available on the software provided. This had a precise pixel dwell time of 10 μs per pixel. (The approximate frame scan time is given as 3s in the Bio-Rad manual, this is an error and should read 4s).

For the standard slow line scan time:

Frame scan time = $(768 \times 512) \times 10.0 \times 10^{-6} = 3.93$s

In addition to the standard slow setting, the slow setting could be changed to a user defined slow setting using a special made program custom made for us by the

microscope company. The custom made program allowed the slow line scan time to be selected as any value in 'ms/line' units (where one line contains 768 pixels).

so $$\text{pixel dwell time} = \frac{\text{line scan time}}{768} \qquad (2.12)$$

A table showing the pixel dwell time for the line scan time selected:

Setting	Dwell Time per Pixel / μs	No of lines per frame	line scan time / ms line^{-1}	Approx. Frame Time
very fast	2.5	¼ of 512 = 125	1.92	¼ s
fast	2.5	½ of 512 = 256	1.92	½ s
normal	2.5	512	1.92	1 s
slow	10	512	7.68	4 s
selectable slow	t_{line} / 768	512	t	512 x t

5. Pseudo-velocity of the laser beam, v_p

$$v_p = \frac{\text{line length}}{\text{line scan time}} \qquad (2.13)$$

The pseudo-velocity of the laser beam , v_p is in fact not a true velocity as the laser has a dwell time on each pixel so it may be dwelling on a point and then jumping to the next point and then dwelling at this point and then jumping to the next and so on. A question to ask is , does the dwell time on each pixel meant that the laser is moving continuously over the pixel length in the pixel dwell time or stays in the middle of the pixel length? The movement of the laser spot (beam) is controlled by the scanning mirrors. The movement of the mirrors is controlled by a smoothly increasing and the decreasing voltage causing the mirrors to rotate. Even if the mirrors are moving smoothly the data will still be collected in 1 pixel packages and an average of the information picked up in one unit of pixel dwell time will be displayed as one item.

The effect of zooming in electronically onto a selected region, the use of a lower magnification lens during the experiment gave rise to the same effects as slowing the

laser scan time. In these two cases the line length is reduced but the number of pixels collected is still 768 x 512 pixels. Both these changes give rise to a smaller pixel size. However it should be noted that electronically zooming in whilst recording an image was not the same as zooming in electronically after the image has already been acquired as the time to scan a line is not slowed further and not as much detail can be seen as there are fewer pixels in the zoomed in region. What all these factors giving and slowing the line scan time have in common, is the decrease in the ratio v_p.

6. The laser beam irradiation time, τ

This gives the characteristic time scale of the perturbation which occurs when the laser makes contact with the electrode surface. Knowing the size of the laser beam diameter (2r) and $2r \sim \lambda \div 2N_A$, where λ= wavelength, N_A = numerical aperture of objective lens, the time to scan the horizontal length of the image equal to the beam diameter (τ) can be calculated.

$$\tau = \frac{\text{line scan time}}{\text{line distance}} 2r \qquad (2.14)$$

or

$$\tau = \frac{1}{v_p} 2r \qquad (2.15)$$

This is an important parameter as the photocurrent generated depends on the laser beam inducing a current where it interacts with the electrode and it has time dependent effects which can be captured as laser scans very fast.

In a typical electrochemical experiment the image parameters used were ;
x 4 lens (N.A.=0.13), zoom x 5.0, with a standard slow setting of 10 μs per pixel,
beam diameter = 2 μm, image size = 758 x 512 pixels = 632 x 390 μm and
line length time = 10 μs x 768 pixels = 7680 μs = 7.68 ms.

If 7680 μs is the time for the laser beam to travel 632 μm, where τ = 2 μm then,

$$\tau = \frac{2 \times 7680}{632} = 24.30\,\mu s$$

INSTRUMENTATION FOR LASER SCANNING MICROSCOPY

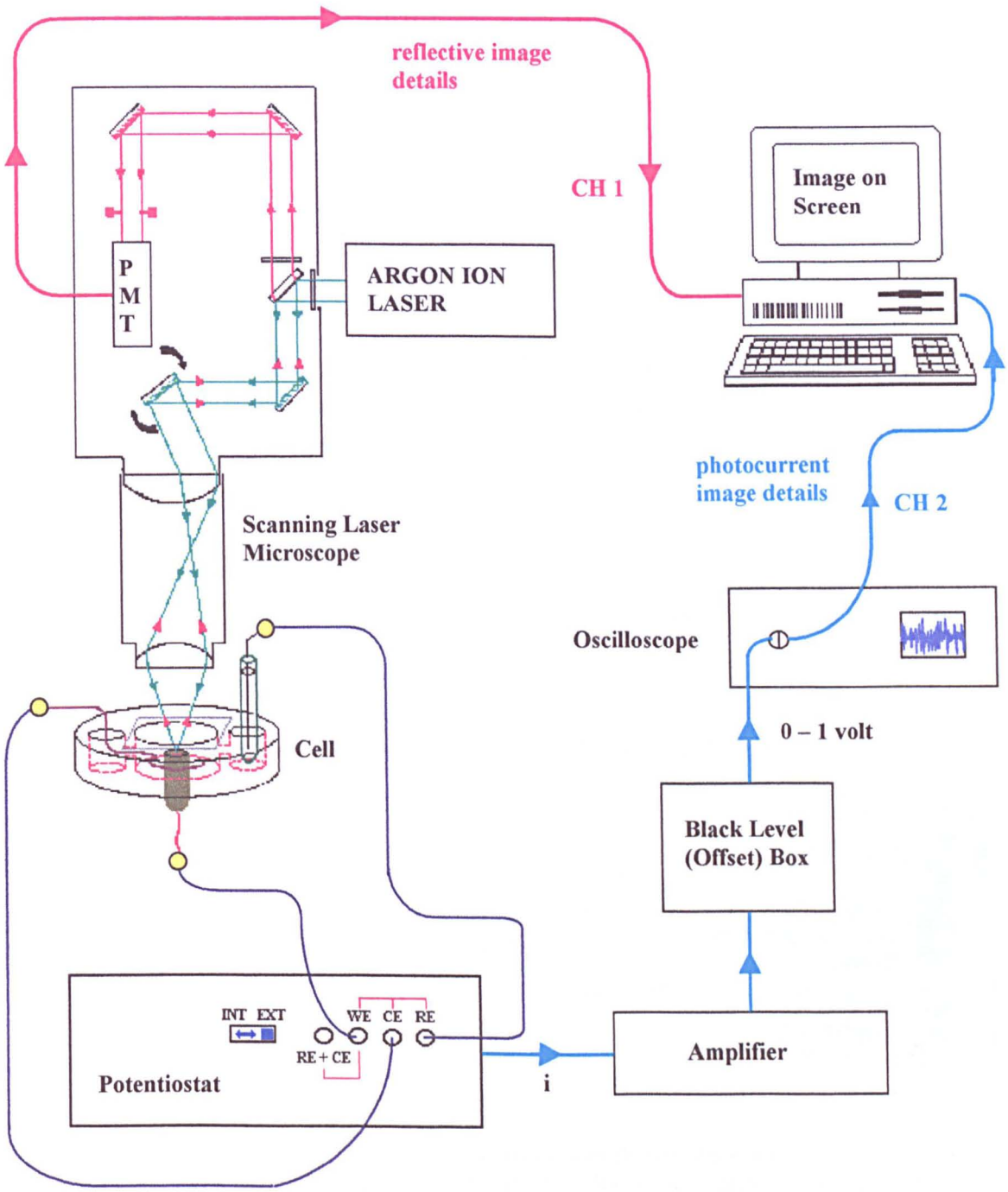

Notes: This diagram shows how the Bio-Rad MRC-600 confocal scanning laser microscope was adapted to use for photocurrent imaging, as well as for confocal reflective imaging. See Appendix G (figure G-2) for a more detailed 3D cross-sectional diagram of the Bio-Rad MRC-600 microscope system's scanning head.

figure 2.23

2.5 TRUE COLOUR OPTICAL IMAGING

As well as confocal optical imaging carried out with the scanning laser microscope, ordinary optical images were also recorded using a regular light microscope (model- Jenalab, manufacturer- Carlzeiss). This was used as confocal images have restricted depth of focus and the images recorded have a false grey scale or colour scale related to the reflectivity of the sample as opposed to a true colour image.

In some cases ordinary light imaging may be required to see the true different colours of the different areas of the sample and therefore areas of different composition. In addition ordinary optical images can also be used to see topographic effects / depth more quickly and clearly. In some cases areas of like reflectivity but different colours may for example be picked up more clearly on an ordinary optical image.

The optical microscope was attached to a colour video camera (JVC, CCD colour video camera, TK-1085E) and this in turn to a colour video printer (Sony, UP-2200P) and a monitor.

APPARATUS SETUP FOR ORDINARY OPTICAL IMAGING

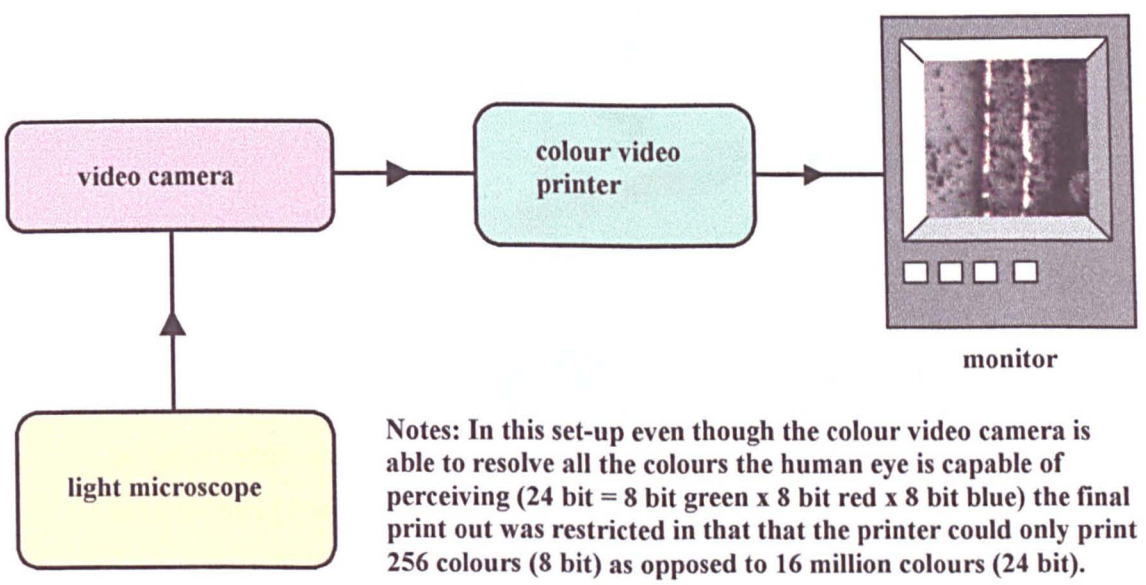

Notes: In this set-up even though the colour video camera is able to resolve all the colours the human eye is capable of perceiving (24 bit = 8 bit green x 8 bit red x 8 bit blue) the final print out was restricted in that that the printer could only print 256 colours (8 bit) as opposed to 16 million colours (24 bit).

figure 2.24

This microscope was calibrated for each magnification used with a standard 100 μm graticule with 1μm divisions.

2.6 MICROPROBE X-RAY ANALYSIS IMAGING

- element concentration microprobe maps and SEM

General Outline

An electron probe microanalyser (Jeol JXA-8600) was used to determine the chemical structure of electrodes used in the photocurrent imaging experiments. This was of particular interest in areas which showed greatest difference from the surroundings or the greatest amount of change with time on the photocurrent image. The two imaging techniques used with this instrument were the recording of microprobe elemental maps and scanning electron microscopy (SEM). SEM was primarily used to select the region of interest for microprobe analysis. This could easily be compared with the confocal optical image which in turn could be compared with the photocurrent image.

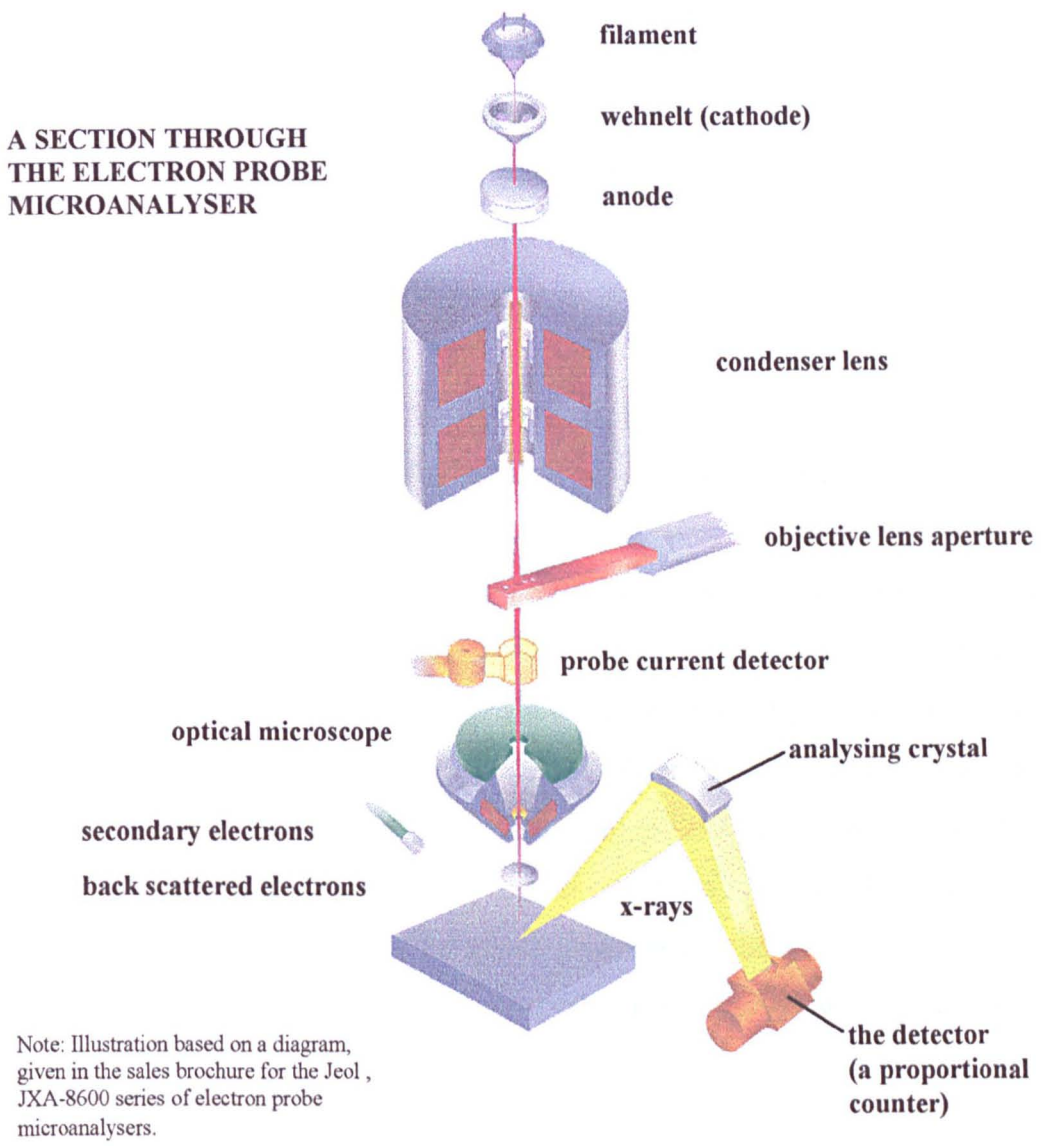

figure 2.25

Calibration

The instrument was calibrated using standards with known percentages of elements and the best wavelength was found specifically for each element at a particular time, and the number of counts to give 100.000% calculated. This calibration with standard elements was carried out prior to starting each session of microprobe work. If the filament broke then the instrument had to be recalibrated all over again using standards.

Procedure

The sample (working electrode cup) for use was carbon coated and then placed on a metal sample holding tray using a conductive carbon tab. Then silver conductive paint was applied in a thin line from the top edge of the sample down the side and touching the conductive carbon tab it was sitting on to improve the contact. The tray holding one or more samples was then placed in the microprobe under vacuum. The sample was then roughly focussed by eye using the optical microscope part of the instrumentation. Then the current and acceleration voltage were chosen and the SEM image switched on.

At the start of the microprobe work, for any sample, an SEM image of the whole sample was recorded after further focussing. The electrode area was then zoomed in onto an area of interest and fine focussing carried out. An appropriate wavelength and detecting crystal was then selected to give the best counts for a chosen element and to distinguish it from the other elements. Then a map was recorded by moving the stage in a rastered fashion collecting data uni-directionally (left to right, left to right again and so on) at known values of beam voltage and current and selected image parameters including image size (No. of pixels in the x and y direction), pixel size and dwell time on each pixel (i.e. how slow the scan is). The noise to signal ratio decreased and the number of counts increased with dwell time per pixel. The image collected in this way showed how the element concentration varied across the surface (i.e. how it is spatially distributed).

Then another SEM image depicting the region given in the element concentration maps was recorded if the region shown on the microprobe maps was, of a more zoomed in region and, not the whole electrode region as recorded in the preliminary SEM image at the start of the work.

With the elemental map in front of us we could then verify whether the map seen was true or just due to topographic effects. This was done by carrying out compositional analysis showing the exact percentages (to three decimal places) present at any one spot. This was done by moving the beam to the spot of interest on the SEM image and then carrying out microprobe spot analysis.

As the microprobe spot analysis is a much more sensitive technique than SEM more can be seen on microprobe elemental maps. When this happens the SEM image shows little contrast, but the wavelength and crystal for a particular element can be selected manually and the electron beam, seen as a bright spot on the SEM image, can be moved on the SEM image roughly to the area the elemental map shows a high. Then by fine movements of the beam using a joy-stick, at a selected SEM image magnification, and watching the spectrophotometer for a high we can locate an area for microprobe spot analysis.

As well as recording percentages in unique areas of interest, usually several background readings were also recorded in areas of the electrode with uniform distribution of elements for comparison and general analysis of the material.

Then a low kV oxygen map was recorded if required. In addition combination element concentration images for oxygen and another element could be recorded at low kV. This involved recording both the oxygen and other element map simultaneously on two different channels. This was done only for larger % weight elements as the 2^{nd} channel did not have the same crystal the second best line had to be used.

Finally any special SEM pictures such as at high zooms of a particular inclusion, at low kV or yz modulated images were recorded. Where as a normal SEM image is obtained by modulating the brightness of the cathode ray tube by the detector signal, a

y-modulated image is obtained by modulating the CRT vertical scan by the detector signal. The yz-modulated image is then obtained by mixing the brightness modulated image with the y-modulated image. The effect is a contrast enhancement.

Experimental Parameters

The acceleration voltage (given in kV units), the current, and electronic magnification are user selectable together with detection crystal type and wavelength. The energy of an electron in the electron beam is directly related to the acceleration voltage as, energy in keV units = charge of an electron (1e) x acceleration voltage in kV units.

The four detection crystals which were available to use were; Pentaerythritol (PET), Lithium Fluoride (LIF), Thallium acid Phthalate (TAP), Lead Stearate (STE). The physical properties of these crystals are given in the Appendix E (part 4).

The crystal and wavelength required for a particular element could be selected from standard tables of data when doing elemental maps, or preferably by selection of much more precise values by calibration of the instrument using known standard elements or alloys. This method of standardisation was particularly important for microprobe spot analysis giving the percentage of any element present, where at any spot the sum of the percentages of all the elements is 100%.

Summary of the Experimental Settings used:

	Experimental image type	Acceleration Voltage/ kV	Current / A	typical dwell time
1.	microprobe spot analysis	25	5×10^{-8}	20s
2.	microprobe elemental maps	25	1.3×10^{-7}	100 ms
3.	standard SEM pictures	25	5×10^{-8}	———
4.	special oxygen maps	12	1.3×10^{-7}	100 ms
5.	oxgyen and another element combination map	12	1.3×10^{-7}	100 ms
6.	low kV SEM picture	12	5×10^{-8}	———

1. Microprobe spot analysis: A current of 5×10^{-8} A was used compared to a current of 1.3×10^{-7} A, which was used to record microprobe elemental maps. A lower current was used in the spot analysis technique in order to prevent the counts going off scale at the slower dwell times involved.

2. Microprobe elemental maps: More current was used for this than for spot analysis as the dwell time per pixel was much smaller, ranging between 75 to 300 ms (typically 100 ms), compared to at least 20 s dwell time in the spot analysis. This allowed the count to be high enough for measurement. The faster dwell times were required due to time restraints. This problem arises due to many pixels in the area being sampled with the selection of the smallest as possible pixel size (1 μm = 1 pixel) in order to get an accurate high resolution image capable of showing small features on the surface.

3. SEM: 5×10^{-8} A was used, and not 1.3×10^{-7} A, as the optical beam size and SEM picture deteriorate at the higher current.

4. Special low kV oxygen maps: A low kV was used to record oxygen maps as the, higher the kV the deeper and wider the sampling is and, the oxygen is located very much at the surface.

5. For oxygen and another element combination maps: Only the elements present in higher concentrations could be used in this technique as a reduction in counts occurs due to the effect of using a lower kV and therefore a lower energy. An added complication was that most of the elements which were analysed required a higher acceleration voltage than 12 kV to be excited, to give a sufficient number of counts.

6. Low kV SEM picture: This allowed surface features to be seen more clearly as a lower acceleration voltage gives a shallower and narrower sampling region.

Additional notes: 25 kV and not 12 kV is generally used as many of the elements need at least this amount to be excited and give enough counts to work with. In addition spot analysis could not be carried out for Oxygen as the ZAF factor value is too high and the model for working out % weights does not work.

Image Storage

The images were stored to the computer hard disc. The computer system and operating environment were specific to the microprobe instrument, the computer being a multi-CPU (central processor unit) system allowing multi-job or multi-user operation. The host computer for total control and data processing is DEC's LSI-11/73 and the 2nd CPU is DEC's LSI-11/23, for equipment control and data acquisition. At intervals the data then may be moved to an optical disc for further storage.

Image Processing and Analysis

The data collected from the microprobe map analysis could be displayed on the screen in such a way as to see the features as best as possible, by use of appropriate user selectable image output properties as defined by the computer program which runs the microprobe. The properties which can be varied are discussed in the following section and they are important to select carefully or the output results may be useless and not show the features we are looking for.

The variables controlling the output image were as follows

1. No of images to display on screen
2. Image display size
3. Level selection (colour scale bar attributes)

1. Image selection

The data could be displayed as it is being collected or once the data had been collected and saved onto the hard disc it could be retrieved and displayed. The number of images which could be displayed on screen simultaneously were one or two.

2. Image display size

The image can be displayed as double size or normal size. Usually the image is displayed on screen in double sized mode as this gave all the details of features present on the image. Using normal size viewing of the image was not suitable as this seemed

to remove every other pixel in order to fit the image on to the display screen. This consequently resulted in loss of detail particularly with stainless steel as many of the inclusions were very small (1 μm width) and the smallest sampling pixel size 1μm. The single sized image was suitable to get a general idea of what is present. Sometimes the area analysed was larger than the double display size allowed (225 x 230 pixels). In this case co-ordinates for various areas can be given for the parts of the whole area analysed and photos taken and re-matched together like a jigsaw. Alternatively the most interesting region was viewed and photographed after first looking at the whole image on the normal sized display.

3. Level selection

a) Colours- There were a maximum of 14 fixed colours to choose from spanning the whole visible spectrum. However as colour 13 was very light pink and colour 14 white these were similar and could easily be confused. So only a 13 colour scale was used.

b)Widths of colours- The colours could be banded in increasing widths or in equal widths from the average measured. Increasing widths around the average was generally used to display the information. How the levels increased were generally chosen automatically by the software but sometimes it was found to be preferable to select our own level width. The level width is the size of the 1st level (colour) around the average counts and further levels above and below the average increase in increasing multiples of the number chosen.

Choosing your own level width within the increasing widths from average command also allows some sort of comparison to be made between images for different experimental samples by giving similar level widths for the number of counts seen. However it must be remembered that the total number of counts observed does depend on the dwell time per pixel as well. Another advantage in picking your own level widths for the image seen was that the bands of colours could be made more sensitive for small increases around the average. Making the 1st level width as a small number, allowed small changes to be picked up across 2 different shades of colour instead of a change occurring within one band of colour.

Even though the amount of resin being scanned was kept to a minimum in an analysis it was however still scanned as I wished to see features on the edge of the electrode. As the amount of resin varied from one analysis to another the average count for an element could also depend on the resin, especially if there was a fair amount of resin in the area analysed, therefore giving another good reason to select your own level widths.

4. Image analysis

Once the images were displayed in the best possible way they could then be compared with the photocurrent images recorded in order to see if any of the element concentration maps showed features resembling any of the features seen on the photocurrent images.

A PHOTOGRAPH OF THE MICROPROBE APPARATUS

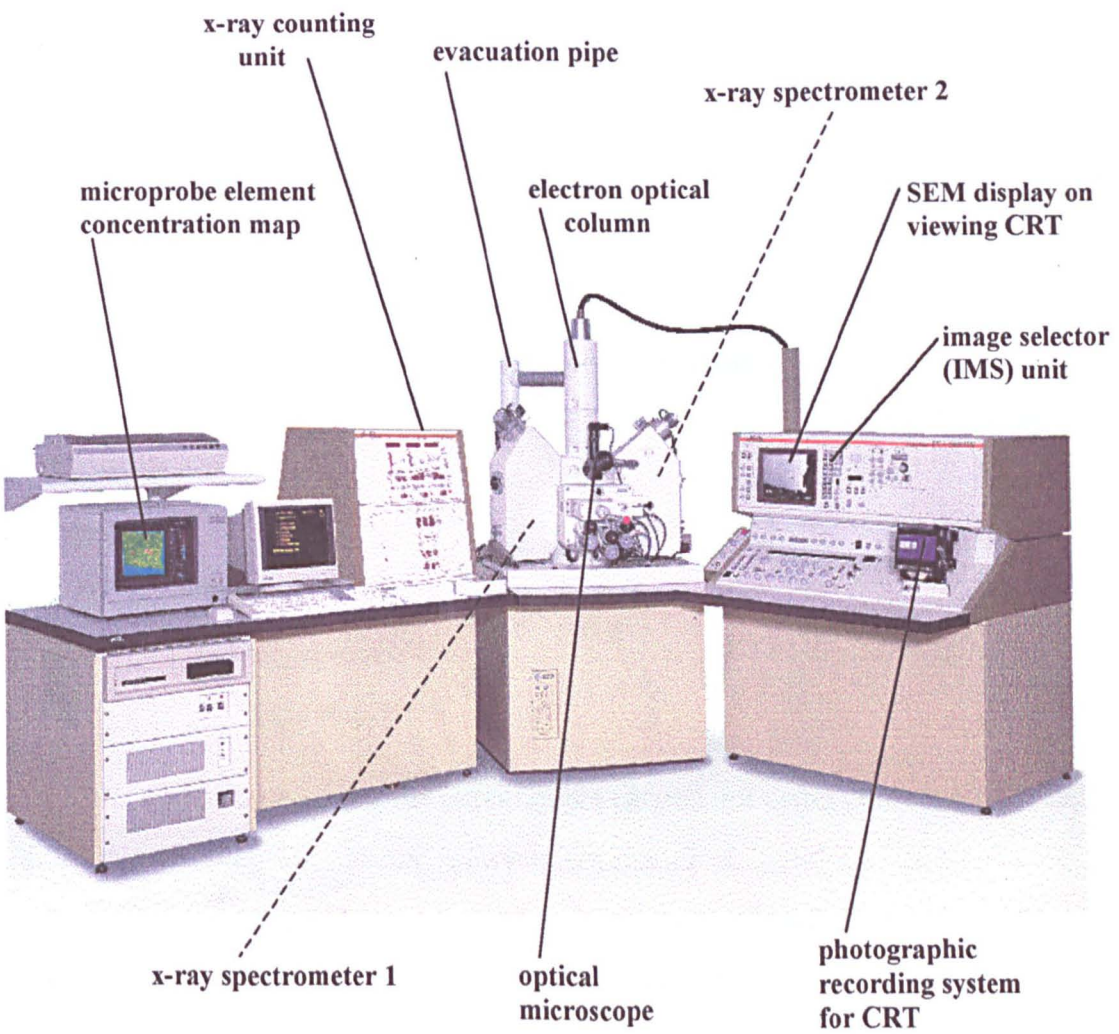

figure 2.26

In the results which follow the name of the analysing crystal and spectrometer position have been noted for each microprobe elemental concentration map shown. The spectrometer position (L) has been given in 'mm' units. This shows the distance from the x-ray source to the analysing crystal, and it represents the wavelength detecting position of any JEOL spectrometers. The spectrometer position may be related to the wavelength using the following equation:

$$L = \frac{2R}{2d} \cdot N_{th}\lambda \qquad (2.16)$$

Where : 2R = The diameter of the Rowland circle (in millimetres)

2d = Spacing between the atomic layers in the crystal (in Angstroms)

λ = Wavelength (in Angstroms)

N_{th} = Order of reflection

For the work given in this thesis $N_{th} = 1$ and R = 140 mm (the value of R is the same for all JEOL microprobe spectrometers), so equation 2.16 can be simplified to:

$$\lambda = \frac{2d}{280} \cdot L \qquad (2.17)$$

Substituting the value of d into equation 2.17 shows the wavelength of the line selected in the microprobe work.

Calculation of the wavelength in the for each analysing crystal:

Analysing Crystal	Crystal Spacing, 2d / Å	Equation Relating the L-value (mm) to the λ (Å)
Pentaerythritol (PET)	8.742	$\lambda = 0.0312 \times L$
Lithium Fluoride (LIF)	4.0267	$\lambda = 0.0144 \times L$
Thallium Acid Phthalate (TAP)	25.757	$\lambda = 0.0920 \times L$
Lead Stearate (STE)	100.4	$\lambda = 0.3586 \times L$

The results and discussion for the experiments carried out using photocurrent imaging with a laser scanning microscope follow in chapters 3, 4, 5 and 6. The results are classified here by electrode / device type and they give an outline of the experimental method together with any alterations to the general experimental method used as well as a discussion of the observations made.

3. INFLUENCE OF LASER INTENSITY ON THE PHOTOCURRENT IMAGING OF SILICON AND SEMICONDUCTOR DEVICES

3. INFLUENCE OF LASER INTENSITY ON THE PHOTOCURRENT IMAGING OF SILICON AND SEMICONDUCTOR DEVICES

3.1 AN INTRODUCTION TO SEMICONDUCTOR ELECTRODES

As this chapter involves the photocurrent imaging of semiconductors, some basic concepts of semiconductor chemistry, as well as the effects of electrolyte contact with semiconductors are given in this section.

Semiconductors are composed energetically of a series of closely spaced low lying mainly filled orbitals known as a valence band separated from a 2^{nd} series of closely spaced high energy mainly vacant orbitals known as the conductance band by a forbidden gap. The optical characteristics of a semiconductor depend depends on the amount of energy required to promote electrons across the band gap from the valence band to the conductance band. An explanation of how the band gap arises as well, as the comparison of semiconductor structure; with metals, insulators, and semi-metals has previously been given in Chapter 1 (section 1.1).

Types of Semiconductors

Semiconductors can be **intrinsic** (pure)semiconductors or extrinsic (impure) semiconductors, where impurity atoms have been added by a process known as doping, to improve electrical conductivity. There are two types of doped semiconductors; **n-type** with an excess of negative charge carriers, and **p-type** with an excess of positive charge carriers. In addition semiconductors may also exist as **compound** semiconductors where n and p-type semiconductors have been joined together. A discussion of these four types of semiconductors follows.

a) Intrinsic Semiconductors

In an intrinsic semiconductor the Fermi-level (the energy level below which all the electron states are occupied, and above which all the states are unoccupied at absolute zero) is nearly always in between the valence and conductance bands.

$$E_{F,i} \approx \frac{E_{bg}}{2} \tag{3.1}$$

A perfect (pure) semiconductor is a non-conductor (insulator) at 0 K because it's valence band is totally full and it's conductance band totally empty. In order to get electrical conduction, charge carriers (i.e. free holes / electrons) must be generated by thermally exciting the electrons present from their normal positions to other higher empty energy levels, where they can move laterally along any adjacent empty levels. So at room temperature there is no clear energy level separating filled from empty states. In an intrinsic (pure) semiconductor there is a 1:1 correspondence between holes and electrons so $E_{F,i}$ remains ~ $E_{bg}/2$.

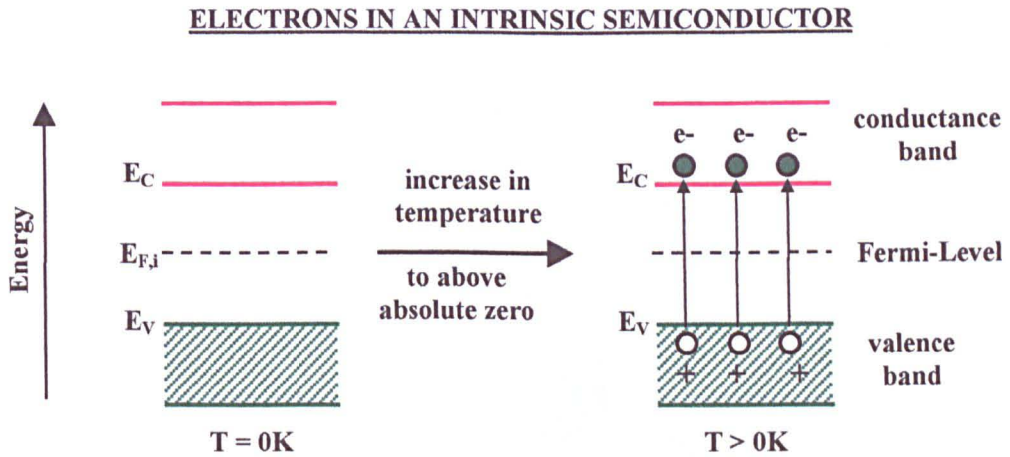

figure 3.1

As there is interaction between atoms in a solid the valence electrons can be thought of as shared by the solid as a whole and not localised on specific atoms. There is constant interchange of valence electrons between atoms so the holes they leave also appear to move.

The concentration of the negative electrons, [n], and positive holes, [p], depends on the absolute temperature and the band gap energy and is given by the following equation:

$$[n]\times[p]= N_c N_v \exp\left(\frac{-E_{bg}}{kT}\right) \qquad (3.2)$$

Where: N_c = the effective density of energy levels at the conductance band edge, N_v = the effective density of energy levels at the valence band edge, N_v and N_c are ~ 10^{19} cm^{-3} at room temperature (25 °C) . For an intrinsic semiconductor [n] = [p] and at room temperature kT = 0.0257 eV.

Breaking of covalent bonds, and therefore conductivity, of silicon is low. Even at fairly high temperatures very few bonds are broken to produce free carriers. The concentration of free carriers increases exponentially with increasing temperature. Another way of increasing the concentration of electrons in the concentration of electrons in the conductance band or holes in the valence band, which is more useful is by the **doping** of **semiconductors**.

b) n-type semiconductors

A semiconductor containing impurity atoms which are electron donors, is called an **n-type semiconductor**. For example when intrinsic silicon is doped with a group V element such as phosphorous, an n-type silicon is formed (figure 3.2).

ATOMIC STRUCTURE OF n-TYPE SILICON

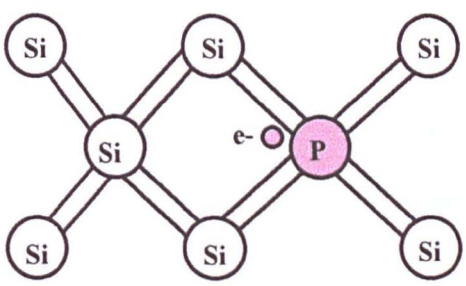

Notes: Each phosphorus atom occupies a position the silicon atom would normally occupy. Only four of the five valence electrons are used to form covalent bonds with the adjacent Si atoms. This leave one electron in excess weakly bound to its P parent atom. This electron is easily freed, i.e. exited to the conductance band where it becomes a conduction electron.

figure 3.2

The donor electrons can be found at an energy level just below the conductance band. At zero Kelvin (absolute temperature) all the donor levels are occupied but at even low temperatures above 0 Kelvin most of the electrons are excited to the conduction band. This increases the free electron concentration therefore the conductivity of the material.

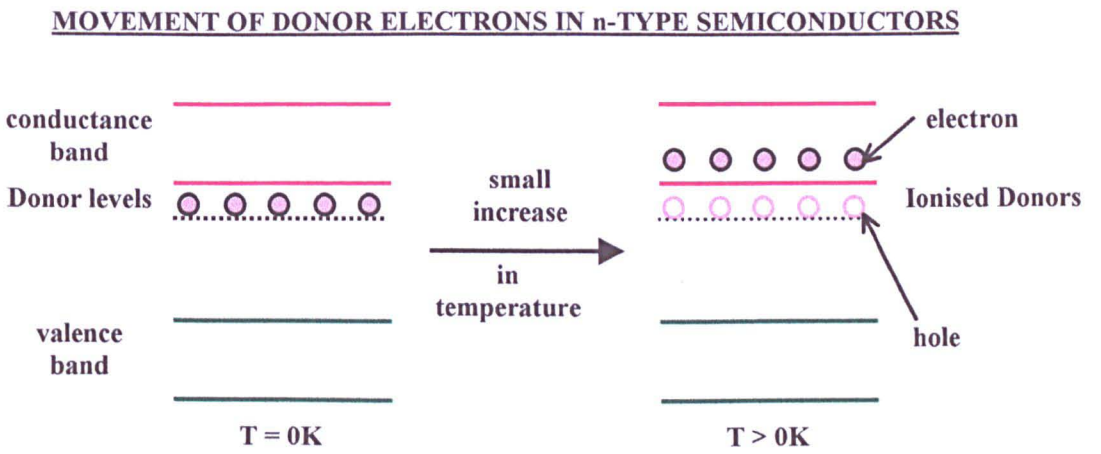

figure 3.3

As a result in an n-type semiconductor there are more free electrons present than there are more free electrons present (originating from both the semiconductor and donor atoms) than there are holes formed by excitation of electrons from the valence band (figure 3.4).

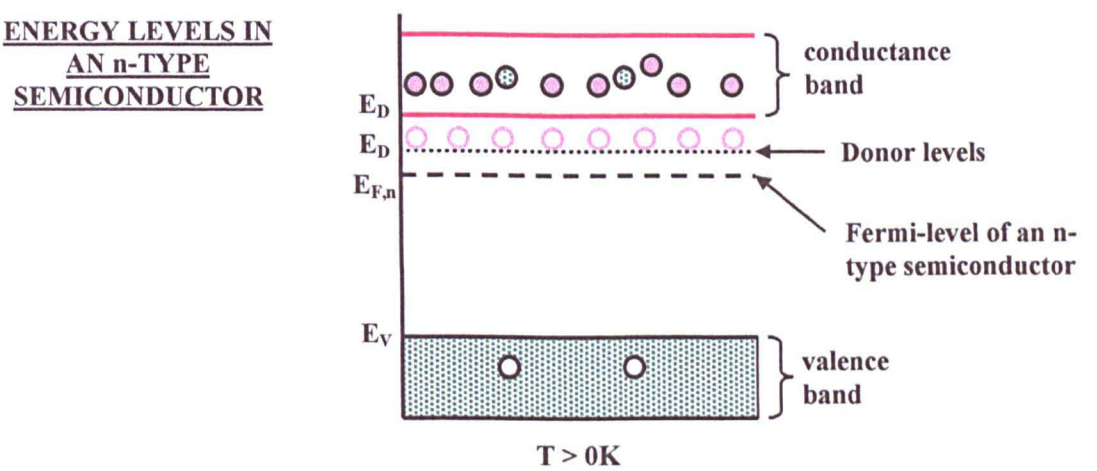

Here the: **majority charge carriers are -VE electrons,**
minority charge carriers are +VE holes

figure 3.4

The **Fermi-level** of the n-type semiconductor (containing donor atoms) is found to be closer to the conductance band as opposed to in between the conductance and valence bonds. The position of the Fermi-level is related to the concentration of the charge carriers and hence the doping level by :

$$[n] = N_c \exp\left[\frac{-(E_C - E_F)}{kT}\right] \qquad (3.3)$$

c) p-type semiconductors

A semiconductor which contains impurity atoms which are electron acceptors is know as a p-type semiconductor. For example, silicon can be doped with a trivalent impurity such as Boron, to form p-type silicon.

ATOMIC STRUCTURE OF p-TYPE SILICON

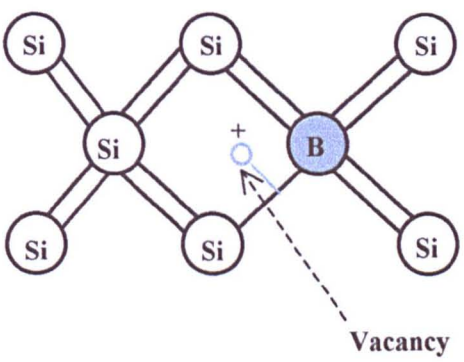

Notes: Here the B impurity atoms occupy sites normally occupied by Si. However B does not have enough electrons to bond to all four Si atoms as it is trivalent. This leaves a vacancy bound to the impurity atom.

figure 3.5

At temperatures above zero Kelvin an electron from the valence band moves up to impurity atom energy level. The impurity atom then is able to accept an electron from the silicon. The impurity atom is therefore called an acceptor atom.

MOVEMENT OF ELECTRONS IN p-TYPE SEMICONDUCTORS

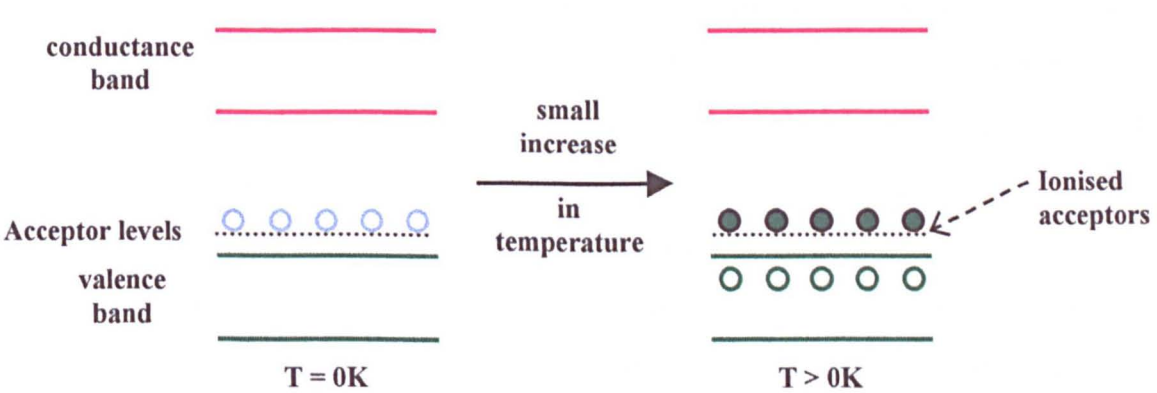

figure 3.6

In a **p-type semiconductor** the conduction of current is mainly due to positive charges known as holes, as more holes are created by ionising the donor atoms than electron holes pairs of the silicon itself.

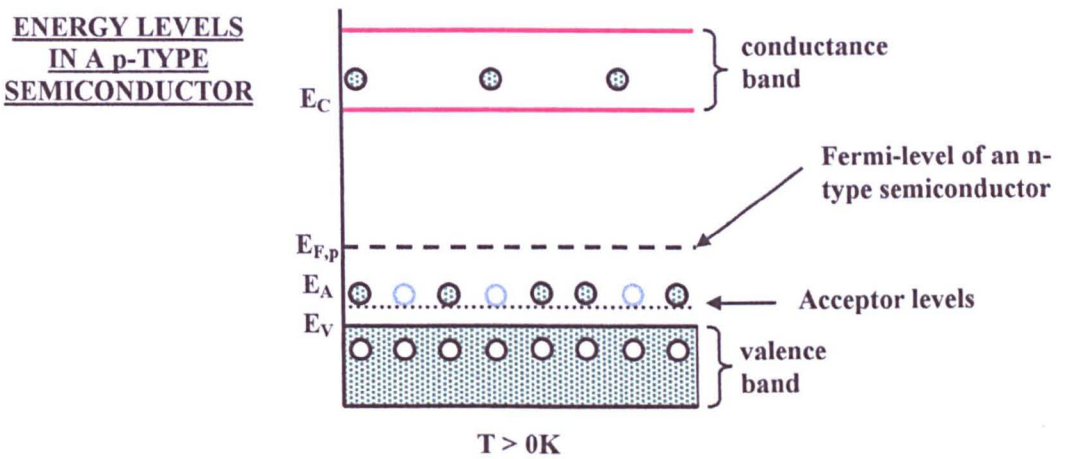

So here the: **majority charge carriers are +VE holes,**
minority charge carriers are -VE electrons.

figure 3.7

The Fermi-level of a p-type semiconductor (containing acceptor impurities) is found to be closer to the valence band this time. The position of the Fermi-level is related to the concentration of the charge carriers and hence the doping level by :

$$[p] = N_V \exp\left[\frac{-(E_F - E_V)}{kT}\right] \qquad (3.4)$$

To summarise adding a small quantity of donor atoms can increase the number of holes by adding electron acceptor atoms, or the number of electrons by adding electron donor atoms. This technique is especially helpful in semiconductors which have a large band gap between the valence and conductance bands. When the doping atom donates electrons (in an n-type semiconductor) the energy level of the donor electrons is close to the valence band, so these electrons can easily be promoted to the conductance band by thermal excitation, where they are mobile. Similarly when the doping atom accepts electrons (in a p-type semiconductor) the energy level of the acceptor atom is close to the valence band so electrons are captured by the acceptor atoms forming an excess of

holes which are the mobile positive charge carriers in the valence band. So doping can allow electrical conductance in semiconductors with a band gap as large as 3.5 eV.

d) Compound semiconductors

As well as single element semiconductors, compound semiconductors with higher electron mobility, made of two or more elements joined together, also exist. Examples of compound semiconductors made of one or more elements include; GaAs (gallium arsnide), GaInAs (gallium indium arsnide) and SiN (silicon nitride). The compound semiconductors can also be doped, for example if GaAs, a group III-IV semiconductor is doped with a group II impurity atom such as zinc p-type GaAs is created and similarly addition of group IV impurity such as tellurium gives n-type GaAs.

Another combination of semiconductors involves combining a p-type semiconductor with an n-type semiconductor, forming a p-n junction as shown in figure 3.8.

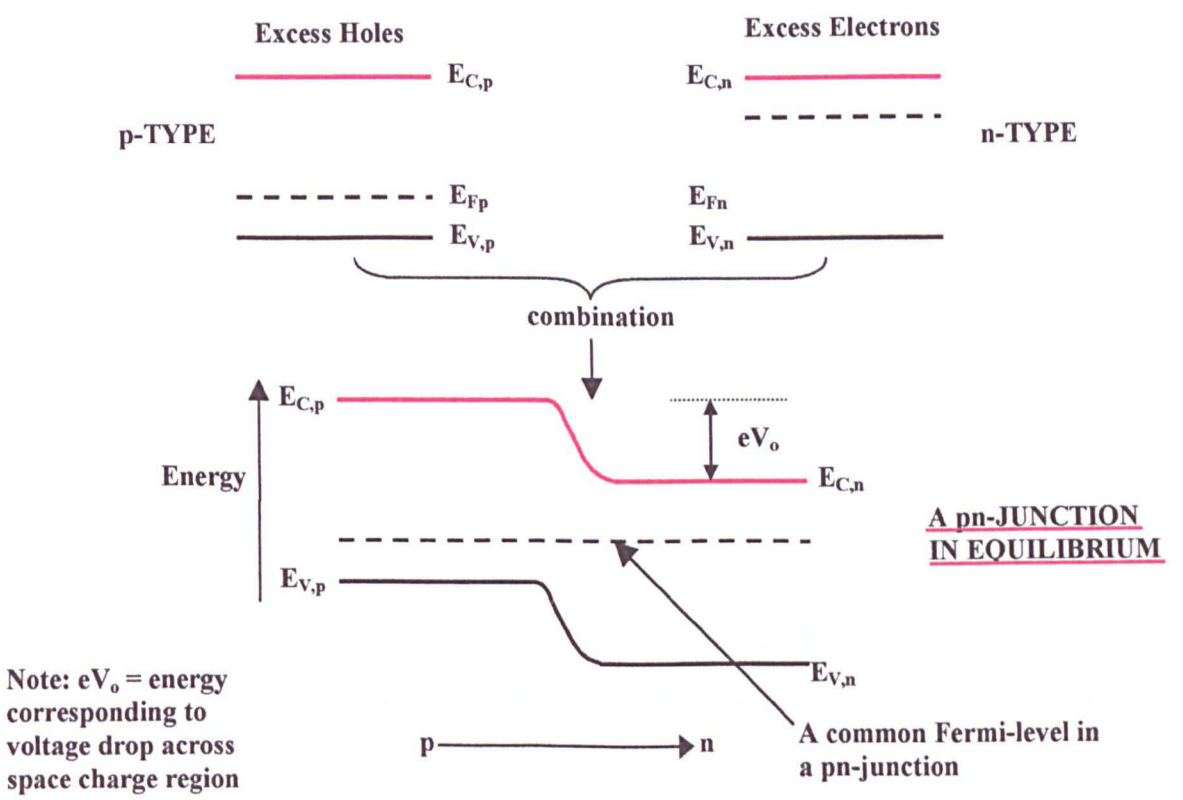

figure 3.8

On making contact electrons diffuse from the n-region to the p-region due to the concentration gradient which has been established and similarly holes diffuse from the p to the n-region.

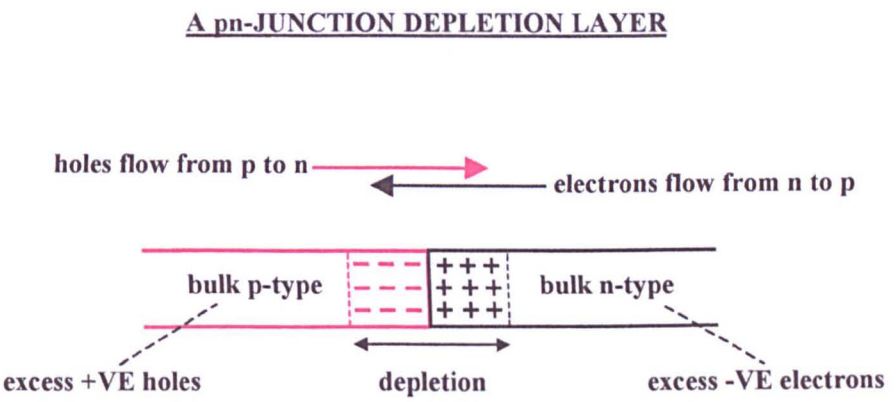

figure 3.9

This movement of electrons and holes leaves a depletion of the majority charge carrier in each type of semiconductor at the pn-junction.

Photoelectrochemistry at a Semiconductor

If a field is applied electrical conductivity is contributed by; 1. **free electrons** in the conductance band, 2. **holes** in the valence band.

Contact with an electrolyte and band bending

When a semiconductor is in contact with an electrolyte band bending can occur at the surface of the semiconductor. The semiconductor bands bend so as to equalise the Fermi-levels of the semiconductor and the electrolyte (e.g. a redox couple).
Looking at the overall picture of the semiconductor electrode in an electrolyte solution three distinct layers can be seen at the semiconductor-electrolyte interface;

1. **Space-charge**-double layer,
2. **Helmholtz** between semiconductor and outer Helmholtz plane.
3. **Gouy region**-in solution near semiconductor in which an excess of ions, of one sign exists.(See figure 3.10)

BAND BENDING AT THE SEMICONDUCTOR -ELECTROLYTE INTERFACE

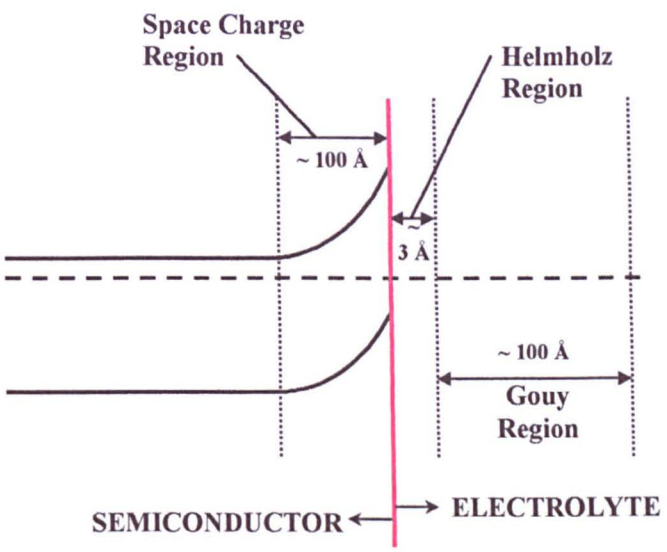

figure 3.10

The energy bands in a semiconductor in contact with the electrolyte may bend either upwards or downwards. The size of the band bending and which way it occurs can be predicted knowing the size of the applied potential with respect to the potential at which the band edges do not bend. This potential is known as the flat band potential (V_{fb}). The flat band potential is a **unique potential** which exists for any given semiconductor and electrolyte there exists a for which the **potential drop between the surface and the bulk of the electrode is zero** (i.e. there is no space charge layer).

This allows the determination of whether a semiconductor can be used to reduce or oxidise a sample in solution. This reasoning allows the selection of an appropriate potential which can be applied in order to carry out the required reaction.

$$E_{C,S} = E_{V,S} = q\,(V_{app} - V_{fb}) \qquad (3.5)$$

Where, $E_{C,S}$ = energy of the conductance band at the surface, where it is in contact with the electrolyte, $E_{V,S}$ = energy of the valence band at the surface, q = electronic charge, V_{app} = applied potential and V_{fb} = flat band potential.

How to find the flat band potential for a semiconductor-electrolyte couple

1. One method of finding the flat band potential is by following how capacitance varies with the applied potential. Here an alternating current (AC) is applied to the electrode.

As $$C = \frac{Q}{V} \qquad (3.6)$$

and substituting for Q = it, $$C = \frac{it}{V} \qquad (3.7)$$

so monitoring how $\frac{i}{V}$ changes with time allows capacitance to be calculated.

Where; C = capacitance, Q= charge, V= voltage applied, i = current and t = time.

How the capacitance varies for a semiconductor surface under depleted majority carrier conditions in the absence of surface states is given by the Mott-Scottky equation (ref. A-4):

$$C_{sc}^{-2} = \frac{2}{qN_d\varepsilon\varepsilon_o}\left(V_{app} - V_{fb} - \frac{kT}{q}\right) \qquad (3.8)$$

Where : C_{sc} = capacitance of space charge layer, ε = dielectric constant normal to electrode surface, q = electron charge, ε_o = permittivity of free space , V_{fb} = flat band potential, d = doping density, V_{app} = the applied potential, k = Boltzmann's constant, T = temperature.

Using this equation, C^{-2} is plotted against the applied potential in order to give a straight line graph. This is known as a Mott-Scottky graph (see figure 3.11).

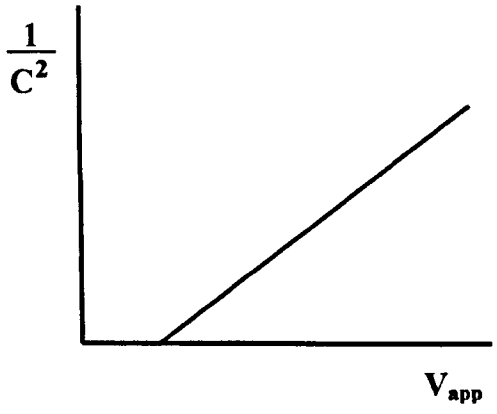

figure 3.11

The flat band potential is found from the intercept of the V_{app} axis, where the $\frac{kT}{q}$ term is often ignored unless the measurement is known to be extremely accurate. The Mott-Scottky equation may be only used provided the following conditions apply; 1. carrier inversion has not occurred, 2. the Fermi-level is at least 2kT (0.05 eV) away from the nearest band edge, 3. all the donor or acceptor levels are ionised and 4. the donor atoms are uniformly distributed in the semiconductor and are immobile

Another way to find the flat band potential is by measurement of the photocurrent. A plot of the square of the photocurrent versus the potential applied gives a straight line graph with the intercept at V_{fb} using equation 3.9.

$$i^2_{photo} = \left(\frac{2q\varepsilon\varepsilon_o I_o{}^2 \alpha^2}{N_d} \right) \left(V_{app} - V_{fb} \right) \qquad (3.9)$$

Where, i_{photo} = photocurrent density and α = absorption coefficient for the solid involved and I_o = the incident light intensity (for other symbols see equation 3.8).

This method allows the prediction of the flat band potential, V_{fb} from potential at which the semiconductor is no longer zero. The photocurrent onset potential V_{on} is typically higher (more +VE) than V_{fb} for the n-type electrode and lower (more -VE) than V_{fb} for the p-type electrode.

If the majority carriers are drawn to the surface region by an electric field then an accumulation region is formed. If the majority carriers are withdrawn away from the surface region then a depletion region is formed. If however the majority carriers are

withdrawn away in very great numbers resulting in the very depleted region ending up with more minority carriers than the majority carriers the resulting region is known as an inversion region. The inversion region tends to occur in small band gap semiconductors whereas another extreme depletion situation arises in large band gap semiconductors (band gap > 2eV) where even though the minority carriers move away from the surface there are not many minority carriers present either, so there is a lack of both majority and minority carriers, this is known as deep depletion.

For example for a **n-type material** (donator atoms = excess electrons, E_F near E_C). If the work function of the electrolyte is greater than the semiconductor ($V_{app} > V_{fb}$) electrons flow from the semiconductor to the electrolyte until in equilibrium. As the Fermi-level is continuous across the junction, the electrons leave the semiconductor from near the junction and enter the electrolyte. This creates a depletion layer in the semiconductor near the surface as a positive space charge is left on the ionised donors. This leaves a depletion of the free majority charge carriers (electrons) and therefore a negative charge on the electrolyte next to the semiconductor. The electron transfer continues until the electric field set up by the dipole layer is strong enough to stop further electron movement. As the electrons in the conduction band move towards the negative charge just outside the surface, their energy rises, results in an upward bending of energy the band edges (figure 3.12c).

If the electrolyte has a smaller work function ($V_{app} < V_{fb}$) than the n-type semiconductor, electrons will move more readily from the electrolyte to the semiconductor. This will result in an electron accumulation layer building up near the junction. The accumulation of the majority charge carriers (electrons) results in the formation of a positive charge in the electrolyte next to the semiconductor until the Fermi-level becomes continuous in equilibrium. This results in a downward bending of the energy band edge in the semiconductor (figure 3.12a).

The opposite situation arises in a p-type semiconductor (figure 3.13) with accumulation of the major charge carrier at the surface resulting in upward bending of the energy bands at the semiconductor electrolyte interface, and depletion of the majority carrier giving rise to downward bending of the energy bands.

BAND BENDING IN n-TYPE SILICON

These diagrams show what happens to the majority carrier (= -VE electrons) under various circumstances.

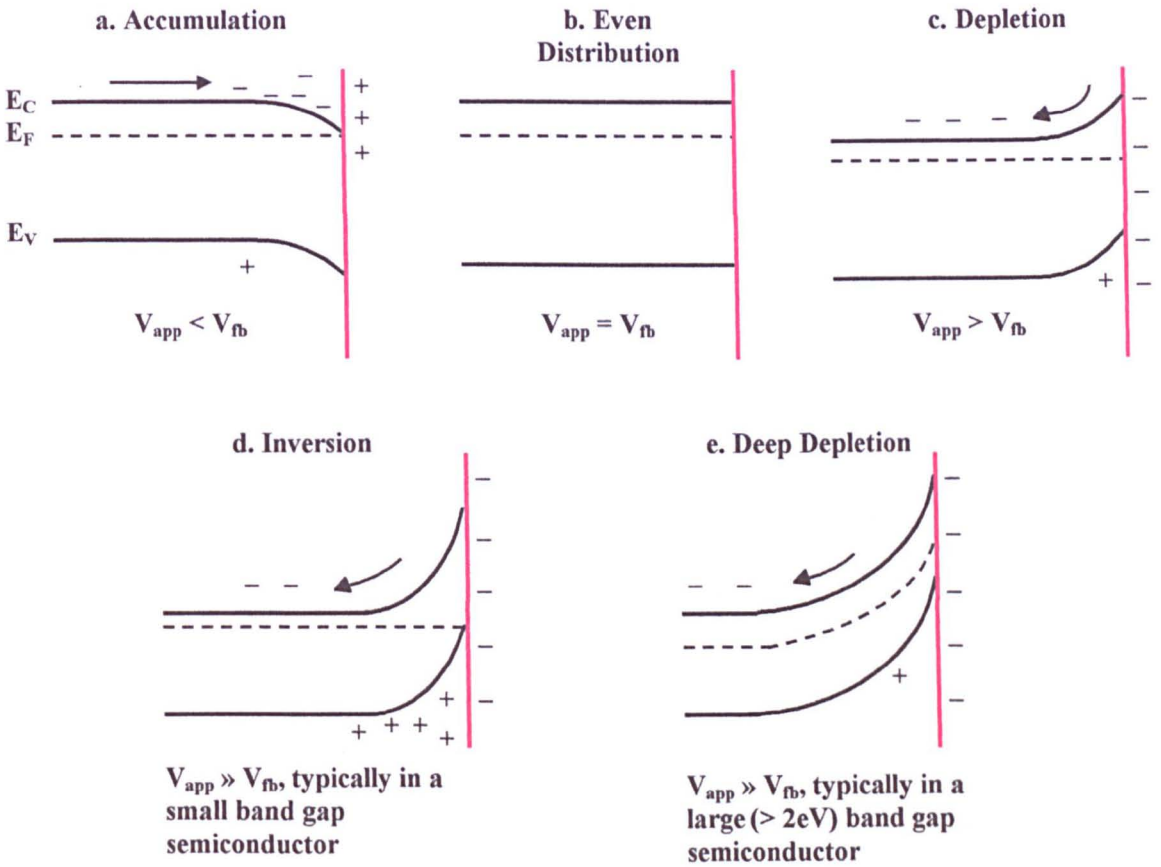

Surface conditions in the semiconductor:

a. Accumulation in a n-type semiconductor- here the electrons move towards the surface.

b. Depletion in an n-type semiconductor- here the electrons move away from the surface.

c. An even distribution of charges at the surface- here the potential drop between the surface and the bulk of the semiconductor difference is zero, so no band bending occurs. V_{fb} = the flat band potential, at which no band bending.

d. Inversion in an n-type semiconductor- many electrons move away from the surface. resulting in more holes than electrons being present.

e. Deep depletion in a semiconductor- here there is an lack of both electrons and holes.

figure 3.12

BAND BENDING IN p-TYPE SILICON

These diagrams show what happens to the majority carrier (= +VE holes) under various circumstances.

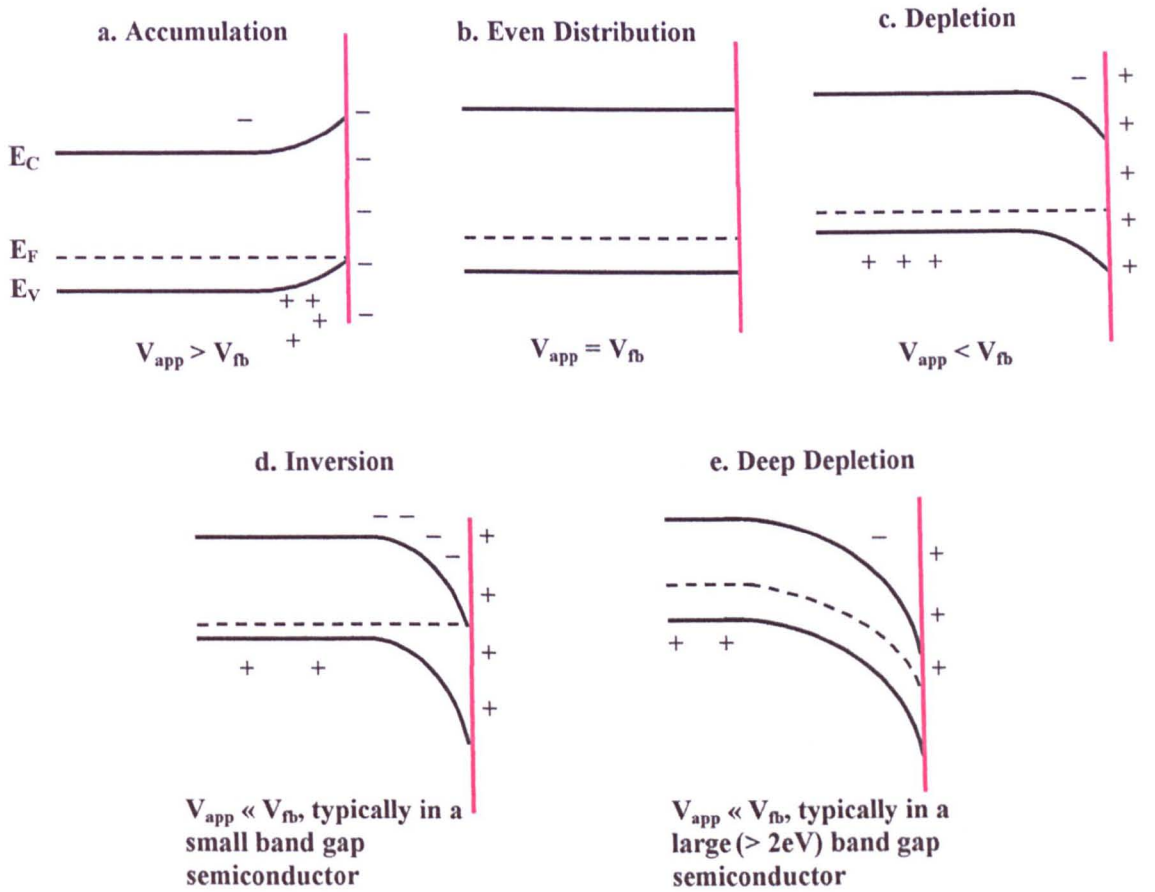

Surface conditions in the semiconductor:

a. **Accumulation in a p-type semiconductor - here the holes move towards the surface.**

b. **Depletion in an p-type semiconductor - here the holes move away from the surface.**

c. **An even distribution of charges at the surface - here the potential drop between the surface and the bulk of the semiconductor difference is zero, so no band bending occurs. V_{fb} = the flat band potential, at which no band bending.**

d. **Inversion in an n-type semiconductor - many holes move away from the surface resulting in more electrons than holes being present.**

e. **Deep depletion in a semiconductor - here there are very few holes or electrons.**

figure 3.13

A reaction at the surface of a semiconductor-electrolyte interface

The energy levels of a reacting species and the semiconductor can be considered individually. The energy level diagram of the semiconductor can be given by the how the energy levels change with distance into the semiconductor from the surface (figure 3.14a) and the energy diagram of the electrolyte can be given by the energy vs density of states (the number of energy levels per unit energy, this is not uniform as some energies are packed more closely together than others) diagram (figure 3.14b).

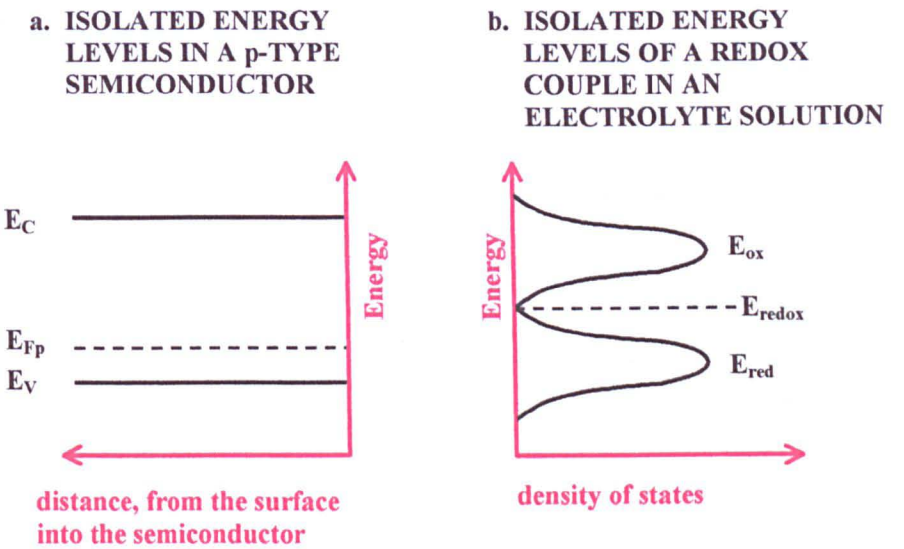

figure 3.14

When the semiconductor electrode is in contact with the electrolyte an equilibrium is set up by band bending as previously mentioned. The desired type of band bending which is required to study the photoelectrochemical properties of a system is the sort that accompanies the formation of a depletion layer. With the formation of a depletion layer at the surface of the semiconductor, the majority charge carriers move away from the surface. The depletion layer is said to have a blocking effect on the electrochemical reaction, this results in low dark currents. This is since as long as the Fermi-level does not approach, the valence (n-type) or the conductance(p-type) band, the surface concentration of the minority carriers remains very low. So in the dark electron change with redox couples is kinetically hindered and remains low by the lack of electrons and holes at the surface.

However if accumulation occurs movement towards the surface of majority carriers occurs with either the valence (p-type) or conductance (n-type) band approaching or overlapping with the Fermi-level. So the number of majority carriers is high and may be easily transferred to a redox couple in the dark. This is not required as we wish to study the effects of light on a reaction, and already having a current in the dark will result in a very small current change on application of the light, as a large current is already flowing in the dark.

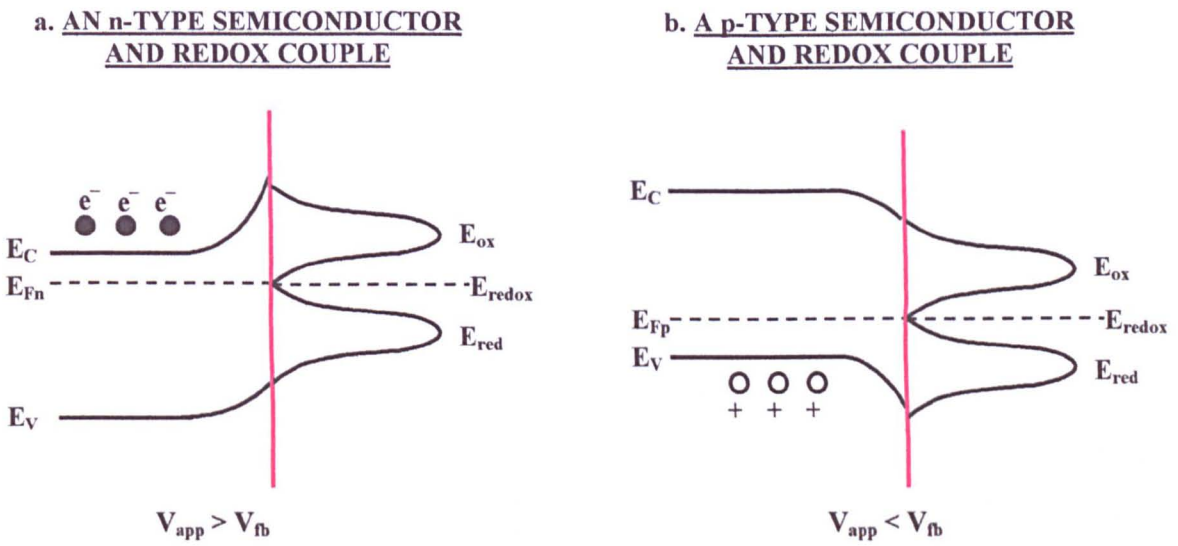

figure 3.15

Under depletion conditions, when the semiconductor is illuminated with light of a greater energy than the band gap energy a sudden increase in minority carriers at the surface occurs. This results as light absorption generates an electron-hole pair in the depletion layer and the electric field which is present then separates the two charge carriers with the minority charge carrier moving into the solution.

In an n-type semiconductor (major charge carrier = -VE electrons) the electrons near the surface move into the bulk of the semiconductor whilst the holes leave the surface to oxidise the redox couple. Similarly in a p-type semiconductor (major carrier = +VE holes) the holes move into the bulk of the semiconductor and the electrons enter the solution to reduce the redox couple. For both the p-type and n-type semiconductors the minority carrier moves into the surrounding solution to take part in the reaction.

EFFECT OF LIGHT ON A SEMICONDUCTOR - REDOX COUPLE INTERFACE

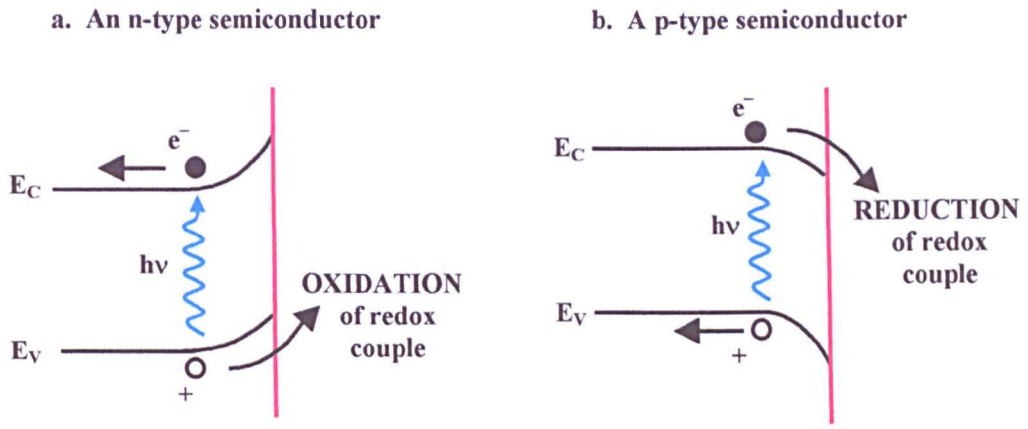

figure 3.16

What the minority carrier does in solution, shows whether the current generated is positive or negative. By convention **adding electrons** (reduction, as exhibited by the p-type semiconductor) gives a **negative (cathodic) current** and the **removal of electrons** (oxidation, as exhibited by the n-type semiconductor) gives rise to a **positive (anodic) current**.

PHOTOCURRENT GENERATION IN AN
n-TYPE SEMICONDUCTOR

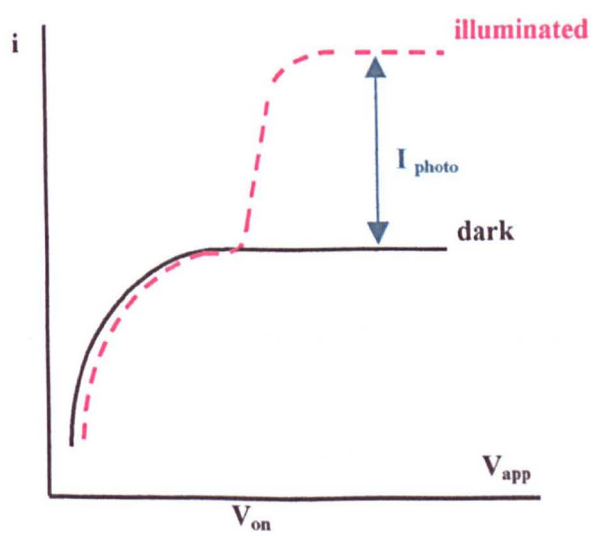

figure 3.17

Analysing Photoeffects at the Semiconductor-Electrolyte Interface

When light is applied to a doped semiconductor the resulting absorption of light generates excited electrons and holes. This process changes the overall concentration of the majority carrier very little (p-type, majority carrier = holes, n-type, majority carrier = electrons). However the **minority carrier concentration is greatly enhanced** (p-type, minority carrier = electrons, n-type, minority carrier = holes).

The photo-generated minority carriers move towards the electrode surface, i.e. towards the electrode-electrolyte interface. The behaviour of the minority carrier affects the photocurrent and photo-potential. How the photocurrent behaves at any particular excitation wavelength of the applied light gives information about the band gap energy. As the light increases above the threshold wavelength, λ_{bg} ,the electrode will become insensitive to light.

$$\lambda_{bg} \propto \frac{1}{E_{bg}} \tag{3.10}$$

The wavelength of the light has to remain below the threshold wavelength in order for the electron to separate from a hole and overcome the band gap in order to reach the conductance band. Recombination is also important to the photoeffect. This is when an electron and hole meet and combine, which results in them annihilating one another and they disappear. The behaviour of the minority charge carriers is reflected in the Gärtner equation (ref. A-4).

$$i_{photo} = qI_{s,abs}\frac{1-e^{-\alpha W}}{1+\alpha L_{min}} \tag{3.11}$$

i_{photo} = photocurrent density

$I_{s,abs}$ = amount of light entering the semiconductor after it has been corrected for reflection

W = the width of the depletion layer, his is the length across which the energy band bends

L_{min} = the diffusion length for the minority carriers, this is the average length they must move before they are annihilated

q = charge on an electron = 1.60219×10^{-19} C

α = absorption coefficient

The width of the space-charge region is given by $W = \left(\frac{2 \Delta \emptyset \varepsilon \varepsilon_0}{qN} \right)^{1/2}$ where ε = the relative permitivity of the semiconductor, N = the donor or acceptor density, $\Delta\emptyset$ = potential difference = $V_{app} - V_{fb}$.

Using the above equation, a graph of $-\ln \frac{1 - i_{photo}}{I_{s,abs}}$ vs $V-V_{fb}$ should be linear with the slope = α and the intercept = L_{min}.

For example if the photocurrent versus the applied potential can be noted for an electrode - electrolyte system (figure 3.17). The results obtained can be used to characterise an electrode - electrolyte system. If for example L is found to be small then the electron or hole will not make it to the surface, therefore a smaller current would be produced. It can also be used to measure light intensity. When photocurrent imaging is being considered and the photocurrent is recorded in terms of a video image reflecting spatial distribution across the surface questions such as, 'is the photocurrent uniform across the surface ?' can be asked. The results can be examined looking at the factors involved in the Gärtner equation, to see which of these reflect the amount of photocurrent generated at each point of the surface.

Deviation from Expected Photoelectrochemical Behaviour

The behaviour is not always as predicted due to the presence of STATES or ENERGY LEVELS at the SURFACE of the semiconductor which can trap charge there, causing band bending even in the absence of any other material (electrolyte) being in contact with it. Surface states can arise from absorbed impurity atoms onto the surface, oxide layers and physical defects on the surface. Surface states can behave as either **Electron Traps** or **Hole Traps**

Both p and n-type electrodes under go surface oxide formation either by an external oxidant such as air or in electric field such as in an electrochemical cell. The surface

oxide is not required as this passivates the surface so inhibiting any electrochemical reaction which we may wish to study at the semiconductor-electrolyte interface.

This problem can easily be remedied as the oxide can be removed prior to an electrochemical experiment. This process leaves a very thin layer having been formed after etching and before the experiment. The etching is achieved by oxidation from SiO_2 to SiO_y where y is less than 2 followed by a further reaction of this with a component of the etchant to form a soluble oxide which is easily removed by rinsing in water.

The most common etching treatment is 48% HF (aqueous) for times between 10-60 s at room temperature which results in the production of a water soluble fluorosilicate. Washing this off with water is supposed to leave a hydrogen terminated surface free of both oxide and fluoride. Other etchants which employ various mixtures of HF and HNO_3 have also been used. Majority of etchants work well on Si(111) face but not as well on the (100) orientation. So if an etchant which has a preference to the (111) face is used on a sample containing both (111) and (100) orientated planes results in the formation of pyramidal topography (ref. F1-1).

3.2 AIMS

The aims of the work shown in this chapter were; to investigate the effect of the laser intensity on the photocurrent image, and in addition to demonstrate the effectiveness of the photocurrent imaging technique, and the spatial resolution achievable.

Two different semiconductor systems were studied in order to investigate the above aims :

1) a silicon memory chip (a solid state system),
2) a p-type silicon electrode in an 1M HCl solution (an electrochemical system).

3.3 INFLUENCE OF LIGHT INTENSITY ON THE PHOTOCURRENT IMAGE OF A SILICON MEMORY CHIP

Introductory Notes on the Type of Silicon Memory Chip Used

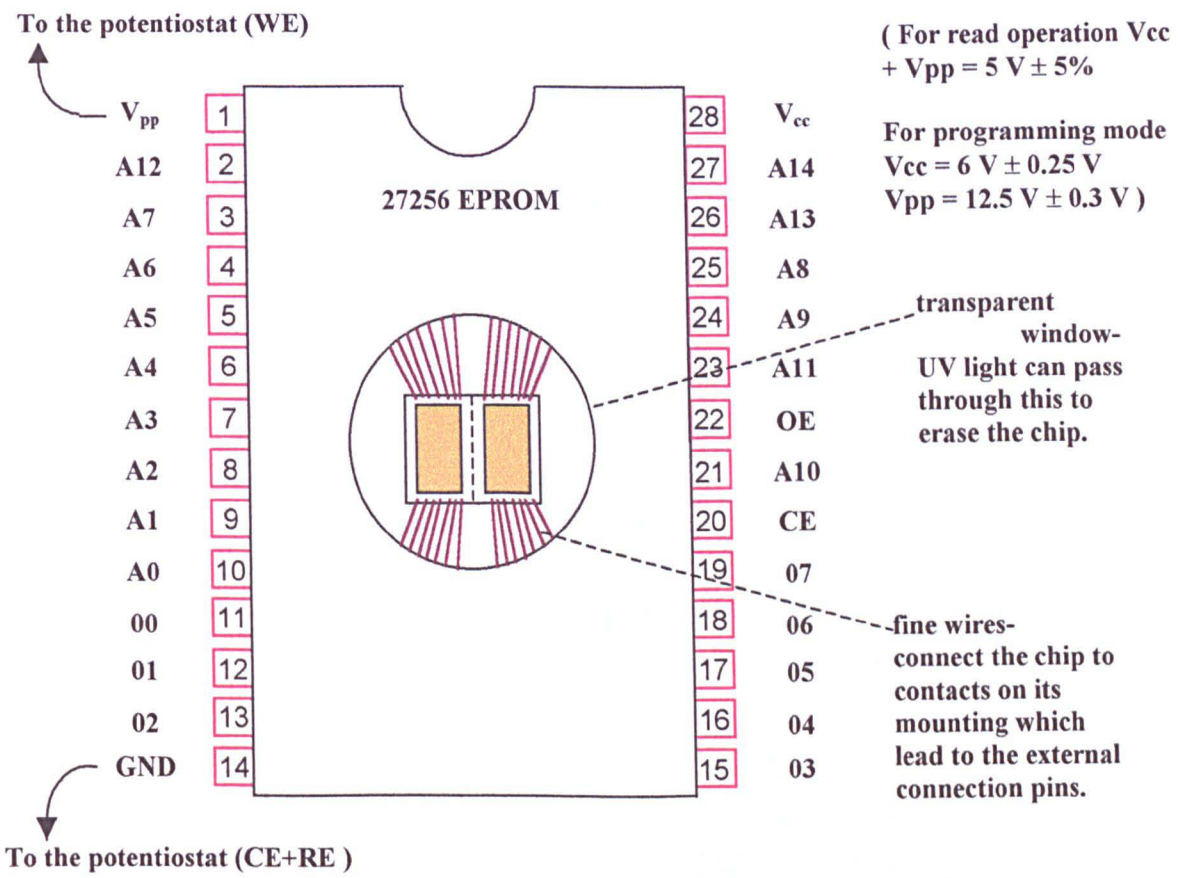

figure 3.18

A 256 K erasable programmable read only memory chip was used in this experiment. This chip has a transparent window on top of the integrated circuit allowing the bit pattern to be erased by exposure to ultra-violet light at 253.7 nm with incident energy of 12 mW cm^{-2}. With the device positioned 2.5 cm from a suitable source with no intervening filter or glass, the bit pattern will be completely erased in about 20 minutes. This feature, of the existence of the transparent window, is why this chip was chosen for our experiment.

Experimental

In this experiment a silicon microchip (256K EPROM) was used instead of the usual electrochemical cell, as described in the general experimental method. The experiment was carried out with the potentiostat connected for two electrode control (figure 3.19).

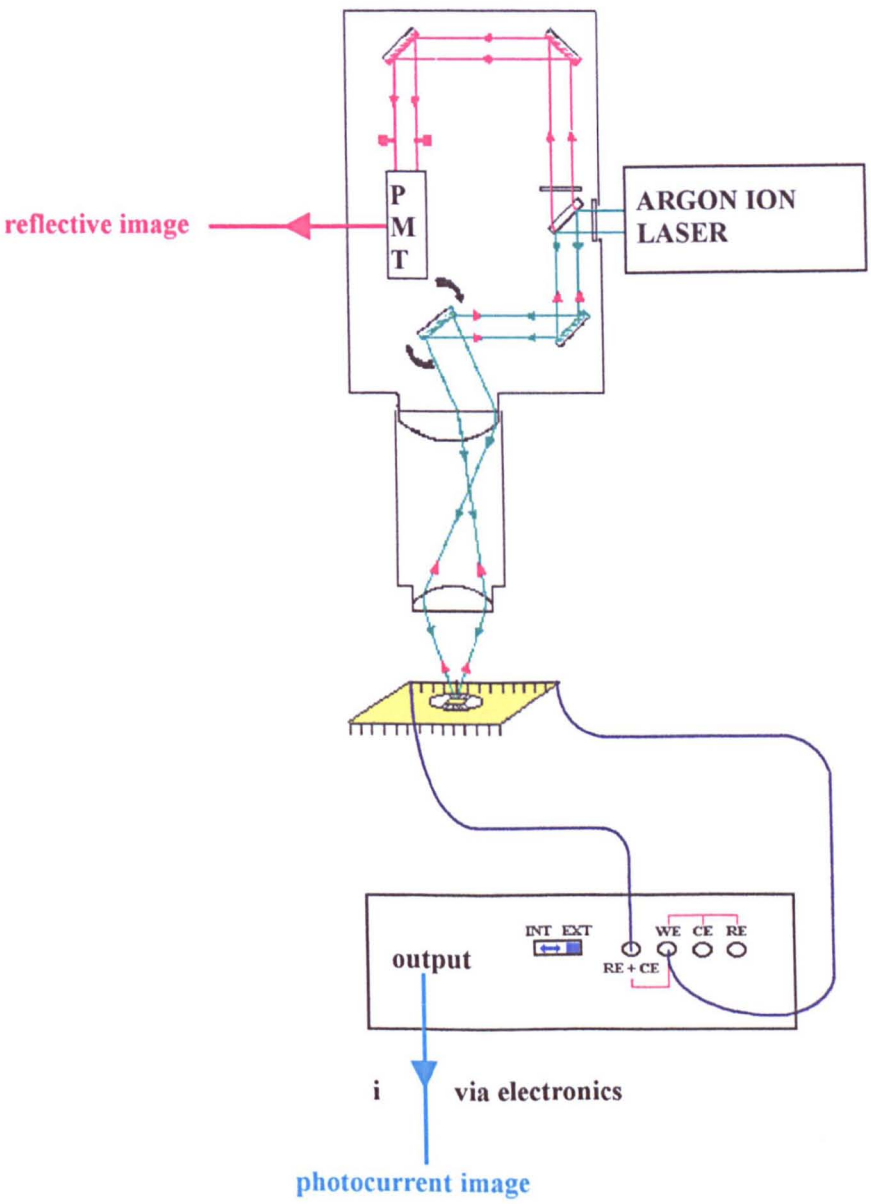

figure 3.19

A reflective (confocal optical) image was recorded by focusing the microscope over a small interesting looking region on the silicon chip containing a diverse range of visible features.

Photocurrent images were also recorded. In this case a potential was not applied via an external waveform generator as described in the general experimental method, but the internal bias of the potentiostat was simply set to zero volts. A neutral density filter was selected and placed in the path of the laser beam, and then the laser was used to scan across the integrated circuitry via the clear window over the chip. This resulted in the light from the laser being picked up by the silicon patterns on the chip to generate electron / hole pairs, which may be separated by the internal electric fields associated with the junctions. The current was relayed via a black level box, amplifier and oscilloscope to the frame store which converted the resulting 0-1V signal to byte values to give a photocurrent image which can be displayed on the computer screen. In this experiment the preamplifier was set to analyse AC variations only, with the low frequency filter set at 0.03 Hz and the high frequency filter at 30 kHz.

This experiment was repeated using different neutral density filters which allowed different percentages of incident light to be transmitted, as this was found to give different photocurrent images.

The reflective images were optimised using the black level and gain controls on the microscope and similarly the photocurrent images were optimised using a black level (offset box) and an amplifier attached to the potentiostat. Optimised reflective and photocurrent images were then recorded side by side and the signals averaged over 40 frames using a fixed line scan time (the standard slow time was used = 10 μs per pixel, with 768 pixels in a line).

The light intensities given in this experiment have been noted as values relative to I_o, where I_o is the unfiltered light intensity from the laser source operating at its maximum power output (25 mW) and a wavelength of ~500 nm.

Further details of the experimental settings and image parameters for the photocurrent and confocal optical images shown in this chapter are given in Appendix J (part 1).

Results

On the reflective images as silicon had a smaller reflectivity, this was shown as darker regions and other metal areas had greater reflectivity which were shown as brighter regions. On the photocurrent images the brighter areas this time represented greater photocurrents and not reflectivity.

General observations show at lower light intensities the reflective image was dimmer as could be expected, but the image could be adjusted to about the same sort of optimum clarity by judgement of eye using the gain and blacklevel controls on the microscope scanning head each time. The features on the reflective images were found to remain the same regardless of the light intensity (see right hand side of figure 3.20).

However using different neutral density filters did change the features on the photocurrent image (left hand side of figure 3.20). The photocurrent images obtained of a silicon memory chip show that good resolution can be achieved as illustrated by the left hand side of figure 3.20. As the images recorded are very complicated with a vast number of features, two prominent features labelled A and B have been zoomed into and shown in more detail in figure 3.21.

At location A, a kidney shaped structure can be seen at 100% I_o light intensity. Reducing the light intensity to 10% I_o made this structure change shape. Reducing further to 3% I_o resulted in this structure being reduced in size. Further reduction of the light intensity to 1% left the image unchanged with only the photocurrent diminished.

At location B, a large rectangular gridded area can be seen at 100% I_o light intensity. Reducing to 10% I_o light intensity changed the feature into smaller rectangular areas embossed with a picket fence structure across them. Reducing the light intensity to 3% I_o resulted in these smaller rectangular shapes vanishing leaving larger 'picket fence' structures. Reducing the light intensity even further to 1% I_o did not change the image much but just reduced the photocurrent generated.

SIMULTANEOUSLY RECORDED OPTICAL AND PHOTOCURRENT IMAGES OF A SELECTED AREA OF A SILICON MEMORY CHIP AT DIFFERENT INCIDENT LASER BEAM INTENSITIES

a.

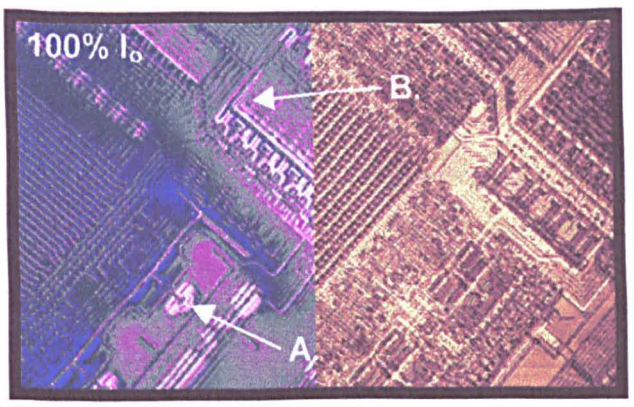

b.

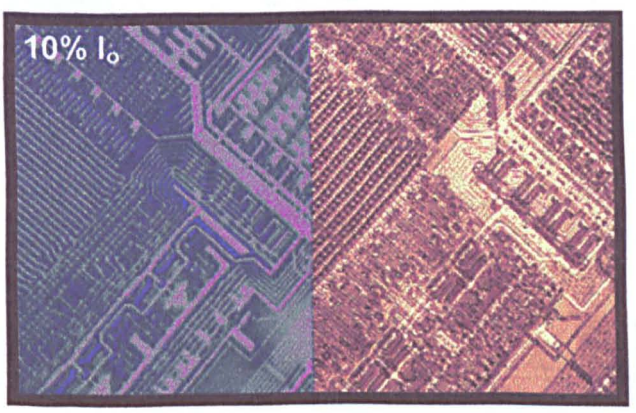

c.

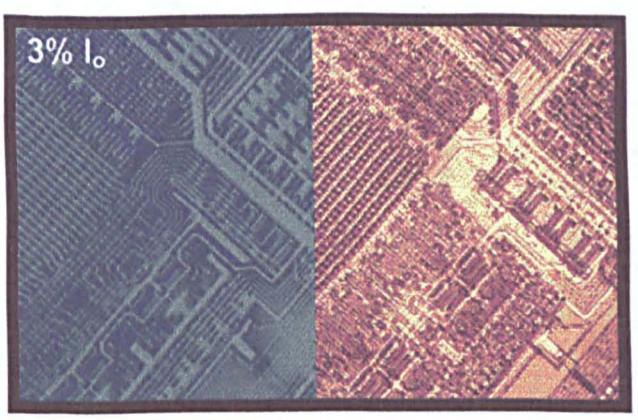

d.

The left hand side:
photocurrent image

dI / nA

(note * = 100 nA for image d.)

The right hand side :
reflective optical image

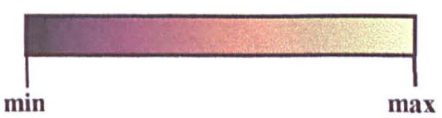

reflectivity

400 μm

length scale

Notes: Lens mag. = x10 (N.A. = 0.25), calculated laser spot diameter (2r) = 1μm, pixel dwell time = 10 μs , line length = 1132 μm, total area sampled in the experiment = 1132 x 695 μm (768 x 512 pixels), laser beam irradiation time (τ) = 7 μs. No solution present, potential applied = 0 mV (internal bias of potentiostat).

figure 3.20

HOW TWO PROMINENT FEATURES CHANGE WITH LIGHT INTENSITY

Observations showing how a couple of prominent features on the image change with the amount of light which was shone on them has been given in the following table .

location A = bottom left of photocurrent images (fig 3.20)
location B = top right of photocurrent images (fig 3.20)

scale
100 μm

Neutral Density Filter	Incident Light % I_o	Location A on Image	Location B on image
0	100% I_o	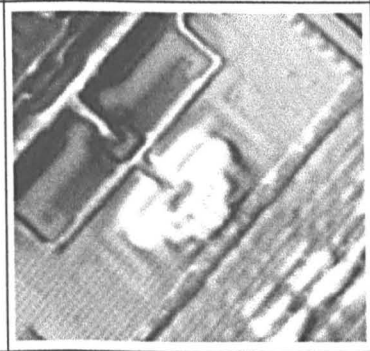	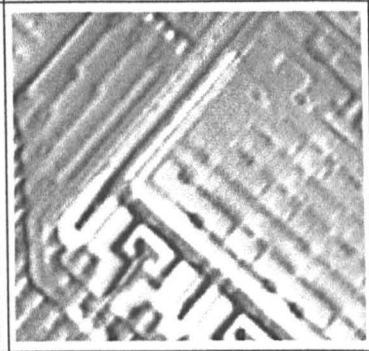
1	10% I_o	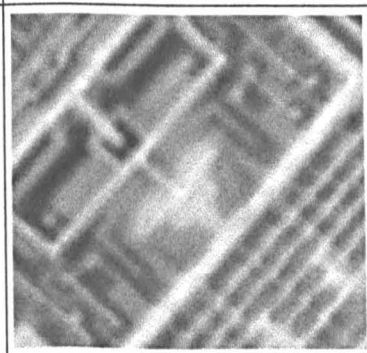	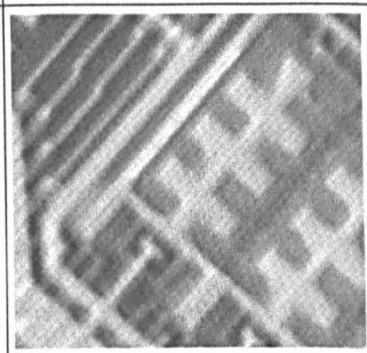
1.5	3% I_o	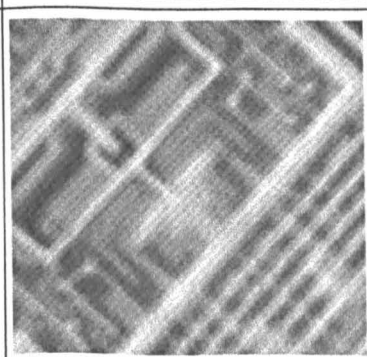	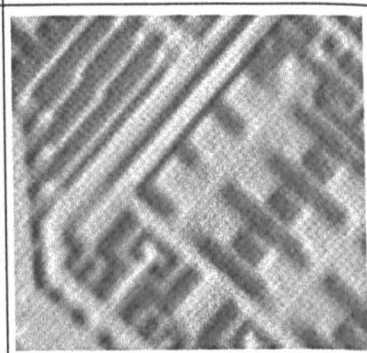
2	1% I_o	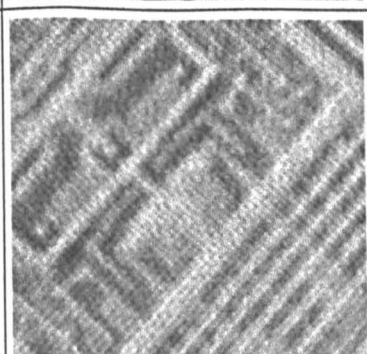	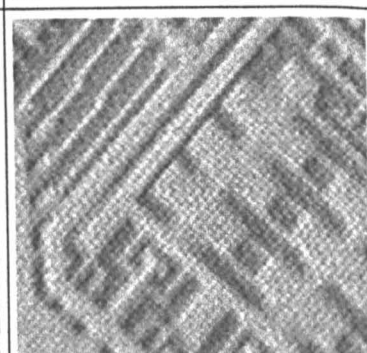

note: photocurrent range, as in figure 3.20

figure 3.21

Discussion

In the silicon memory chip there are many solid-solid junctions between the semiconductors making up the memory chip. The photocurrent is generated by photoexcitation which occurs as the laser strikes the surface of the device. If the incident light has an energy greater than the semiconductor band gap then the electron-hole pair will be created. If there is an electric field then these will be separated and a current will be observed in the external circuit.

Therefore the photocurrent image showed where the light was absorbed and where there was an electric field between the solid-solid junctions (between different semiconductors and p-n junctions) within it.

One possible explanation for the differences in the photocurrent images as the light intensity is changed is due to the light beam of higher intensity being absorbed to a greater depth.

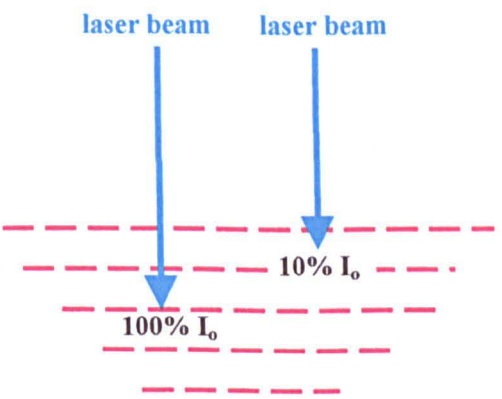

figure 3.22

This reasoning can be explained using the Beer-Lambert relationship for the absorption of light.

$$I_f = I_s e^{-\alpha x} \qquad (3.12)$$

Where; I_o = the laser beam intensity from the laser source operating at its maximum power output. I_s = intensity of light incident on the sample after travelling through the neutral density filter. I_f = intensity of light after having travelled a distance 'x' into the

sample. The light entering the silicon device (I_s) was one of I_o, 0.10 I_o, 0.03 I_o or 0.01 I_o depending on the neutral density filter that was used.

For the case where the light incident on the silicon device was I_o with no neutral density filter being present and 100% transmission occurred, equation 3.12 can be written as

$$I_f = I_o e^{-\alpha x} \tag{3.13}$$

Values given at Si, 2.4 eV incident light, n (refractive index) = 4.215 and k (complex absorption coefficient) = 0.06. The absorption coefficient α can then be calculated using the Einstein Relationship:

$$\alpha = \frac{4\pi\nu k}{c} = \frac{4\pi k}{\lambda} \tag{3.14}$$

$$\alpha = 1.467 \times 10^6 \text{ m}^{-1}$$

If a $\frac{1}{e}$ drop in light intensity is assumed, substituting for $I_f = \frac{1}{e} I_o$ in equation 3.13 gives, x = 0.68 μm at $\frac{1}{e}$ drop in light intensity.

Now we can start the development of an interpretation of the result by calculating the penetration depth for an arbitrary final intensity (I_f) relative to the unfiltered laser intensity (I_o). For example if we wish to work out the distance (x) travelled through the silicon device when the original intensity diminishes to 10^{-3} I_o light intensity. Taking natural logs of equation 3.12 gives ,

$$x = -\frac{1}{\alpha} \ln\left(\frac{I_f}{I_s}\right)$$

When $I_s = I_o$ is the unfiltered light intensity,

$$x = -\frac{1}{\alpha} \ln\left(\frac{10^{-3} I_o}{I_o}\right)$$

$$= -\frac{1}{\alpha} \ln\left(10^{-3}\right)$$

$$= 4.71 \text{ μm} \tag{3.15}$$

Like calculations can be done for the other various incident light intensities (I_s).

Penetration depth, by the laser, for various light intensities:

The incident light intensity , I_s	Distance travelled / μm		
	when $I_f = 10^{-3}\ I_o$	when $I_f = 10^{-5}\ I_o$	when $I_f = 10^{-8}\ I_o$
1.00 I_o	4.71	7.85	12.56
0.10 I_o	3.14	6.28	10.99
0.03 I_o	2.32	5.46	10.17
0.01 I_o	1.57	4.71	9.42

So different photocurrent images must be of different depths into the silicon memory chip and therefore show different structures present at each of these depths.

When we examine these findings more carefully the effect due to the light intensity on the surface of a semiconductor is not simple as it first seems. I have stated that following the Beer-Lambert Law the higher the light intensity the further into the sample the light travels so that different structures are observed at different depths. However we have to consider why the outside (very top layer of the surface) structure does not dominate at any light intensity, therefore resulting in the same image being seen at all the light intensities. If the photocurrent decreases with distance in the same way as light intensity (figure 3.23), and if the photocurrent is proportional to light intensity, then the outside will always dominate regardless of the incident light intensity.

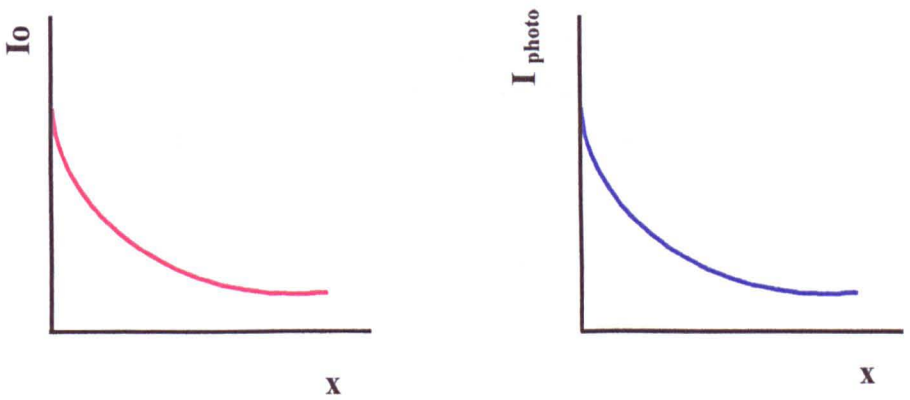

figure 3.23

So for a structure consisting of the top three layers A, B and C (figure 3.24), we would expect, the total signal = A + B + C , where A » B » C ∴ total signal ~ A.

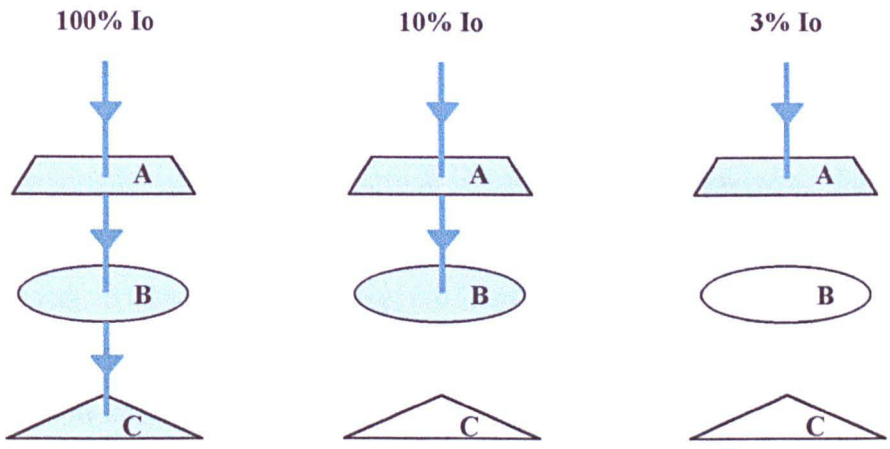

figure 3.24

Therefore in order to explain why photocurrent information from the lower layers, is obtained on application of a high light intensity, some sort of saturation effect (figure 3.25) must be postulated for the photocurrent signal at higher light intensities, allowing the signal from the lower layers (B, C) to become more significant.

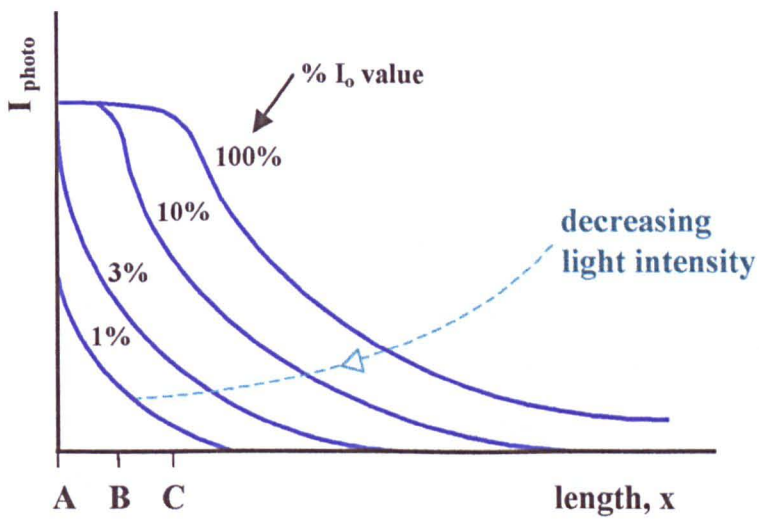

Notes: At 100% I_o , $I_p \propto$ A+B+C and at 10% I_o , $I_p \propto$ A+B and at 3% I_o as well as 1% I_o , $I_p \propto$ A

figure 3.25

If the signal limits in the way as described above, variation of image contrast with light intensity can be explained as a result of variation with depth in the structures present. Even though much previous work has been carried out using the laser spot scanning technique to image properties such as photocurrent of solid state devices (ref. section C2) very little work has been carried out profiling electroactive areas at different depths.

There has been one article published by H. Bergner and coworkers (ref. C2-7, 1989), which involved photocurrent imaging, using the laser spot scanning technique. This technique however did not use varying light intensity, but various different lasers of different wavelengths were used to examine integrated circuits, knowing that red light has a greater penetration depth than blue light in silicon. However the laser power was small (argon ion : 0.025 mW and He-Ne: 0.031 mW) and the resulting differences seen in the different depth images were small and not drastically different, as those shown in the experiment in this chapter.

However no other work has been documented in the use of photocurrent imaging in depth profiling, by the simple technique of altering the laser intensity by the use of neutral density filters, as shown here.

One other laser spot scanning technique by U. Bernini and coworkers (ref. E4-7, 1995) was used to image layered microcircuits. These authors however did not use photocurrent imaging but employed photoacoustic imaging, which monitors sound given out by a material when light is absorbed. The samples examined consisted of gold or aluminium printed layers on silicon. Two types of cell were used. One type of cell contained a piezoelectric transducer that detects the signal generated from coupling of thermal waves propagating in the sample with its elastic vibration modes. An alternative cell used consisted of a gas microphone acoustic cell. In this work an intensity modulated Ar^+ ion laser (488 nm, 20 mW) was scanned across the sample. It was reported that changing the laser frequency changed the thermal diffusion length of the heat waves in the sample allowing profiling of different layers beneath the sample. This work gave fairly high resolution images with the calculated laser beam diameter (2r) being given as 2.4 μm. The results from this work showed that it was possible to show the layers present below the opaque top layer of a semiconductor device using this technique, in that first layers, circuit tracts and conductive connections between the layers were detected. It was therefore concluded that the scanning photoacoustic microscopy can be used to detect sub-surface defects and therefore the function of the microcircuit. However images were not given for the same area at different depths as was shown in the work given here.

3.4 EFFECT OF LIGHT INTENSITY ON p-TYPE SILICON IN 1M HCl

Introductory Notes on Hydrogen Photoevolution at the p-Si Surface in HCl

Here a p-type semiconductor (silicon) was used. For a p-type sample the majority carriers are positive holes and the minority carriers are electrons. Under depletion conditions the majority carrier is depleted from the surface

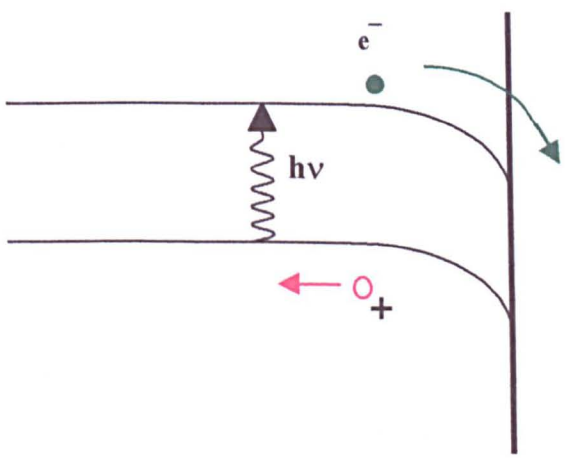

$$e^- + H_2O \longrightarrow H_2 + \tfrac{1}{2}O_2$$

figure 3.26

Capture of the minority carriers (electrons) by water results in a negative photocurrent accompanied by hydrogen evolution.

With p-type silicon in 1M HCl the more negative the potential the greater the quantity of hydrogen is produced so the photocurrent generated should be more negative (cathodic) as the potential is decreased.

Experimental

The general experimental setup was used (as shown in Chapter 2). A three electrode cell was used with the p-type silicon as the working electrode, after it had been etched (30s in 30% HF) and cycled in HCl between 0 and –800 mV for 5 minutes. The etching and application of negative potentials was used as it was found to substantially increase the photocurrents. A saturated calomel electrode was used as the reference electrode and a platinum wire ring as the counter electrode. These were placed in the cell and immersed in 1 M HCl solution. The area over the working electrode was covered in a glass coverslip to stop movement of the electrolyte (HCl) as the laser scans over it. Photocurrent images were then collected at a fixed potential with selected neutral density filter present. The pre-amplifier was set to collect AC photocurrent signals which were low and high pass filtered at 0.3 Hz and 30 kHz.

The photocurrent images were found to change with the amount of etching (hence the amount of defects), so a note has been made on the figures which follow, as to the amount of etching. The first etching, which took place prior to applying the GaIn Eutectic, consisted of 60s in 30 % HF. Then the electrode was etched again prior to any experiment for 30s on any one day. The first etch prior to an experiment (i.e. 60s +30 s) has been labelled as 'etch condition A' and the second time the sample was etched prior to an experiment as 'etch condition B' and so on with successive letters of the alphabet.

The Effect of Light Intensity on the Photocurrent Image

The following images (figure 3.27) show the effect of the light intensity on the image.

The origin of the photocurrent is firstly due to internal photoexcitation which results from the laser exciting the electron from the valence to the conductance band from where it moves from one part of the electrode, the silicon, to another part of the electrode, the silicon oxide, and then it moves from here into the solution where it reacts with the species present (figure 3.26).

EFFECT OF LIGHT INTENSITY ON p-TYPE SILICON IN 1M HCl

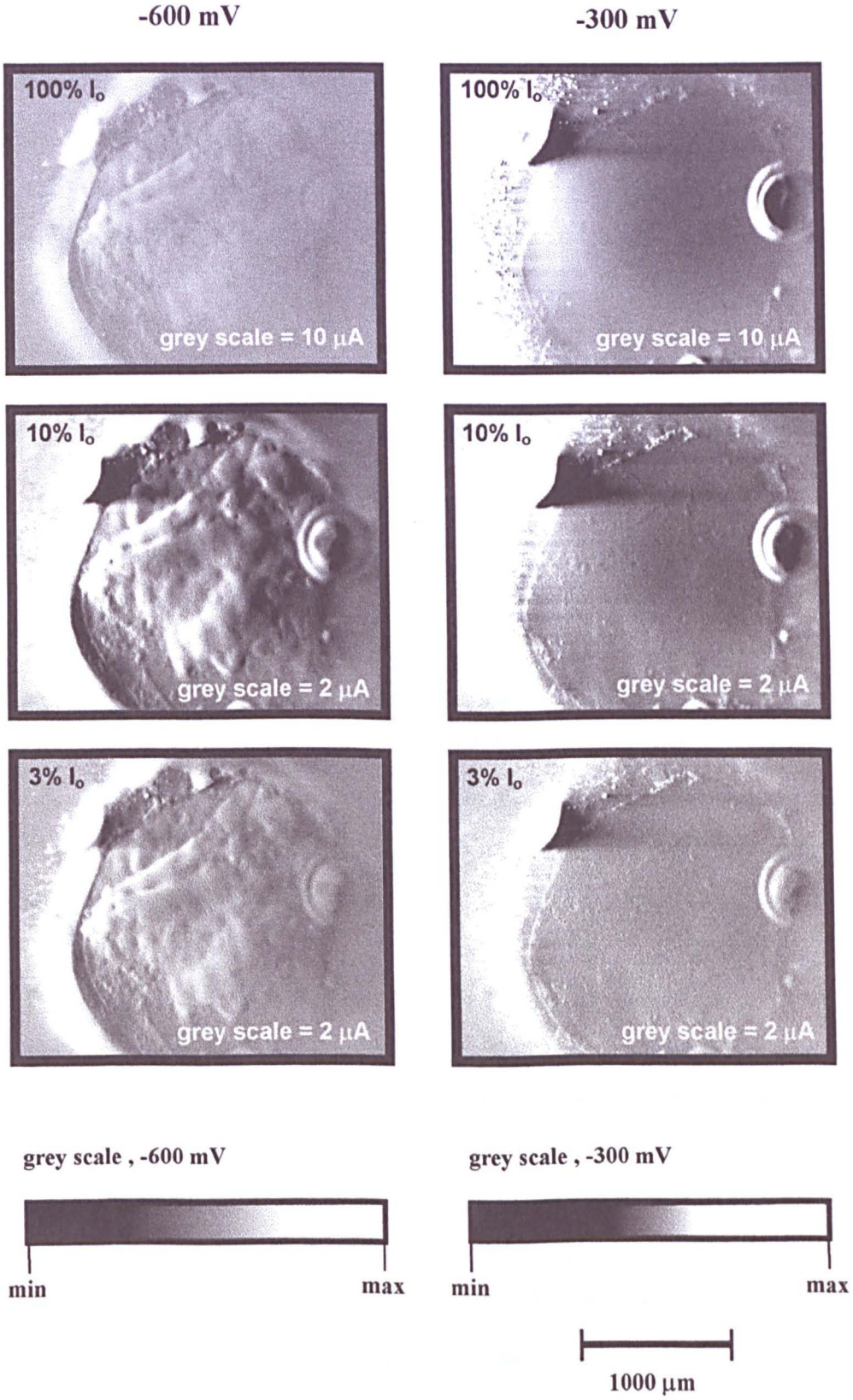

Notes: Lens magnification = x4 (N.A. = 0.12), laser spot diameter = 2 μm, pixel dwell time = 10 μs, τ = 5 μs, line length = 3080 μm, total area sampled in the experiment = 3080 x 1903 μm (= 768 x 512 pixels), etch condition B.

figure 3.27

As observed with the silicon memory chip, the image was found to vary with the laser intensity. Decreasing the incident laser light allowed more detail to be seen on the images. For example at –300 mV (figure 3.27) surface structure can be seen at 10% I_o and 3% I_o but the image looks totally plain at 100% I_o. This can again be attributed to photocurrent saturation at high light intensities as seen in the previous experiment with the silicon memory chip. The image contrast was found to depend on the potential as well as the light intensity. The greatest currents were found on the most negative potentials as expected.

Effect of Light Intensity on the Pulsed Laser Cyclic Voltammogram

The effect of laser intensity was also looked at using pulsed laser cyclic voltammetry by scanning the focussed beam over the electrode whilst chopping the light on and off.

This showed that the total current over the whole electrode stayed negative and became more negative with the laser switched on (figure 3.28). In addition it could be seen that the ratio of the current with laser on / current with laser off, decreased with decreasing laser intensity. The total background (laser-off) current over the electrode remained the same but the average photocurrent increased with increasing intensity as expected.

A smooth line was recorded on the cyclic voltammogram if a fixed (not scanning) laser beam defocused over the whole surface was used. However the results in figure 3.28 were obtained by scanning with a focussed laser beam, as it was in the photocurrent imaging experiment. Thus the observed total photocurrent showed a repeating semi-circular pattern of rise and fall. This resulted because the electrode was circular in shape and the data was recorded in bands for the top, the middle, and the bottom area of the electrode respectively as the laser scanned. This effect is shown in the pulsed photocurrent image with the chopper blocking the laser beam on and off (figure 3.29). Hence the current recorded on the chart recorder varied with the total illuminated area as well as with the detailed image contrast within each illuminated zone.

PULSED LASER CYCLIC VOLTAMMOGRAMS AT VARIOUS LIGHT INTENSITIES

Focussed Scanning Laser Spot, ~1Hz Pulsed (chopped) beam
Cyclic Voltammetry Sweep Rate (ν) = 20 mV s^{-1}, sweep from -800 mV to 0 mV

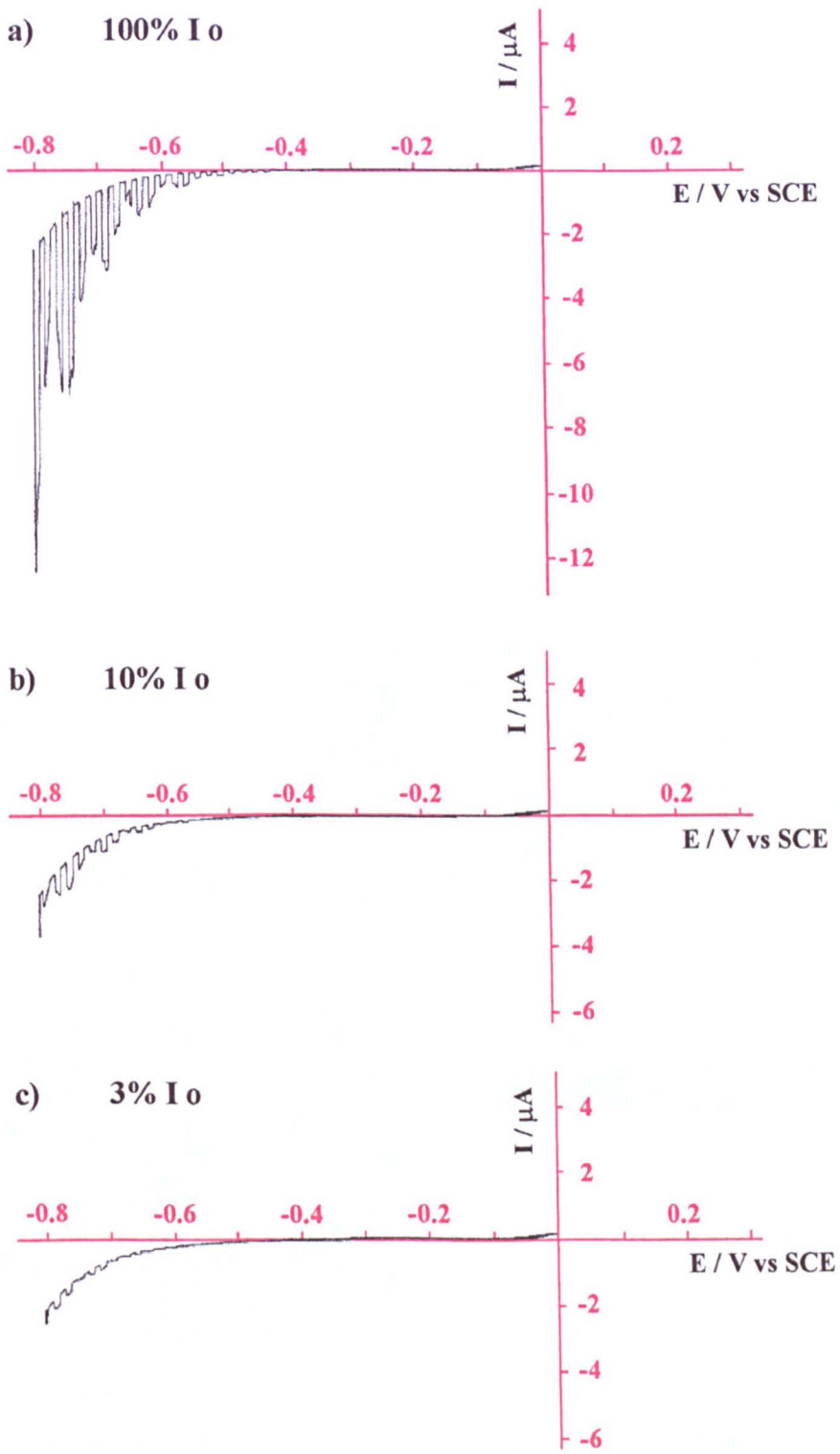

Notes: Sample = p-type Si, solution = 1M HCl, etch condition E, lens magnification = x4 (N.A. 0.12), pixel dwell time = 10 µs, total area sampled in the experiment = 3080 x 1903 µm (768 x 512 pixels), τ = 5 µs. The scanned confocal optical image showed 4 'light on' bands for this experiment.

figure 3.28

The cyclic voltammetry looked normal in shape and behaviour compared to the literature for p-Si in 1M HCl after HF etching, in that it became increasingly negative the more negative the potential. However this is not true for the same electrode under the same conditions for the photocurrent images collected. So the average photocurrent seen on an image, at a known potential, was not the same as the average total current measured by cyclic voltammetry, with the laser light on. This difference probably arises because cyclic voltammetry shows the average current signal over the whole electrode surface but in the photocurrent imaging technique one point at a time is being examined on the surface.

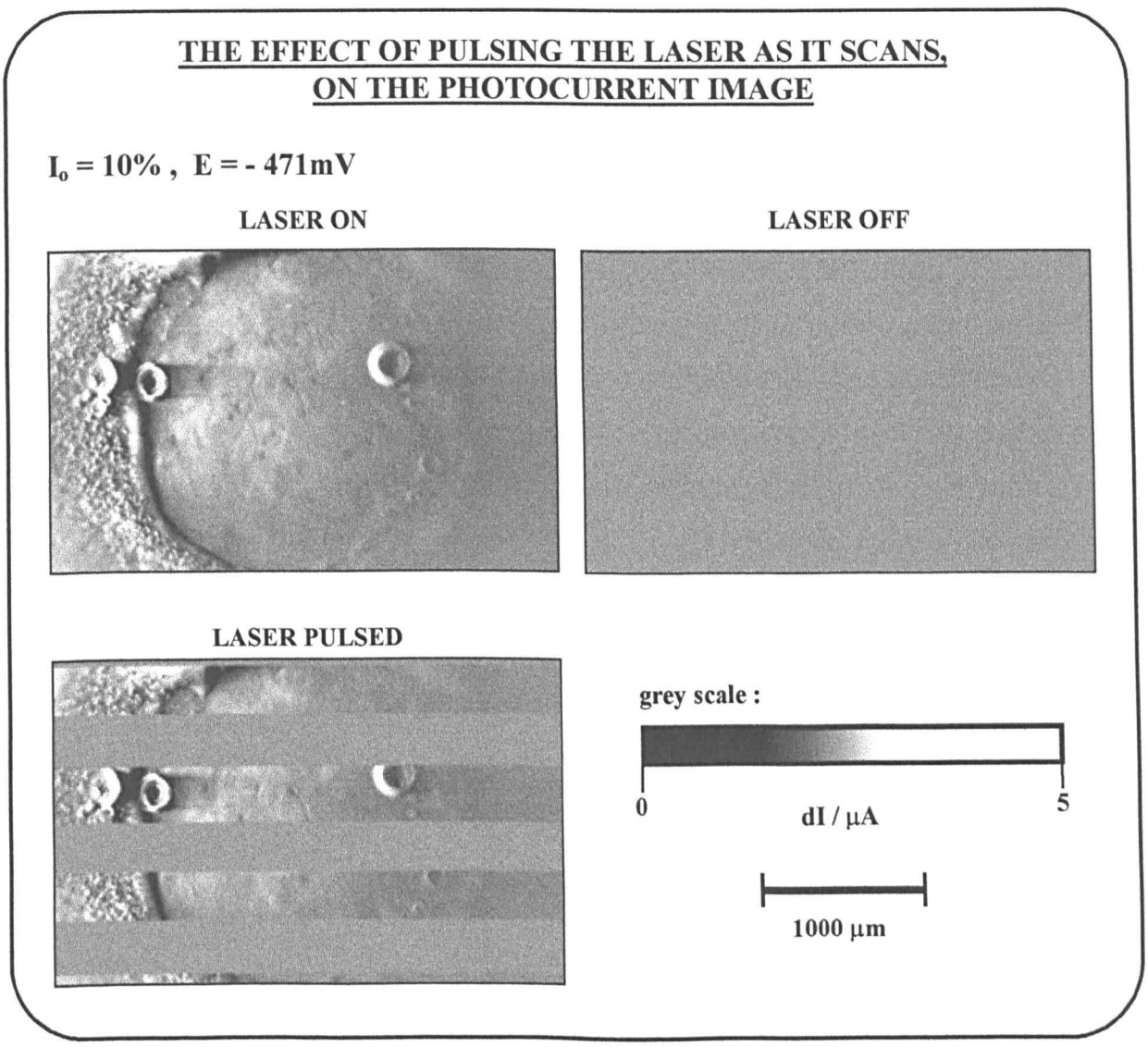

Notes: Sample = p-type Si, solution = 1M HCl, etch condition E, lens magnification = x4 (N.A. 0.12), laser spot diameter = 2 μm, total area sampled in the experiment = 3080 x 1903 μm (768 x 512 pixels), pixel dwell time = 10 μs, τ = 5 μs (time to scan laser beam diameter length). The pulsed laser photocurrent image shows 3.2 'light on' bands.

figure 3.29

A More Detailed Study of the Effect of Potential as Well as Light Intensity on the Photocurrent Image

As the potential was found to effect the image contrast further images were taken over a wide range of potentials, from –700 mV to +300 mV vs SCE at each of three different light intensities. An example of the images obtained when the potential was varied for a fixed light intensity is given in figure 3.30.

From these images the photocurrent was obtained by subtracting the background (mid-grey) value from the pixel intensity obtained for the central region of the electrode, and then a graph of photocurrent vs potential plotted (figure 3.31).

Figure 3.31, shows that the more negative the potential became, the more negative the photocurrent became but then at potentials more negative than (–300 mV) the trend in photocurrent turned upwards becoming more positive. The minimum on the photocurrent vs potential curve occurred roughly where the photocurrent onset potential is. Further experiments repeated at the same laser intensities and range of potentials (without further etching) showed extremely good reproducibility. At potentials more negative than –300 mV the photocurrents were unevenly distributed across the surface. This effect disappeared when the potential was taken back to a value more positive of –300 mV.

At lower light intensities the image contrast was found to change more drastically with potential. For example comparing the experiments for 10% I_o and 3% I_o shown here, the dip in the curve at –300 mV gets deeper with lower light intensities.

EFFECT OF POTENTIAL ON THE PHOTOCURRENT IMAGE

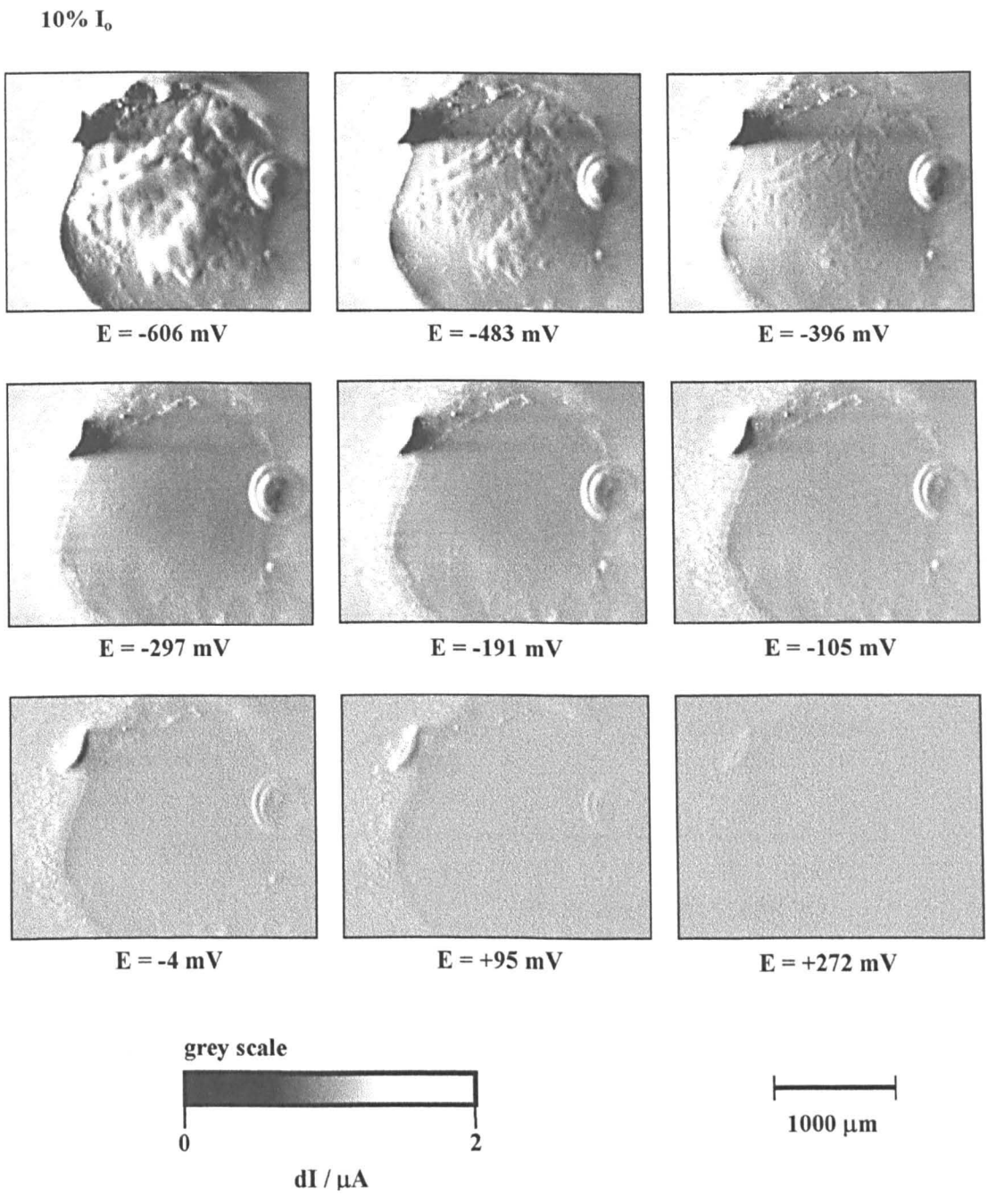

Notes: Sample = p-type Si, solution = 1M HCl, etch condition B, lens magnification = x4 (NA 0.12), laser spot diameter = 2 μm, line length = 3080 μm, total area sampled in the experiment = 3080 x 1903 μm (= 768 x 512 pixels), pixel dwell time = 10 μm, τ = 5 μs .

figure 3.30

PHOTOCURRENT CHANGES WITH POTENTIAL AT VARIOUS LIGHT INTENSITIES

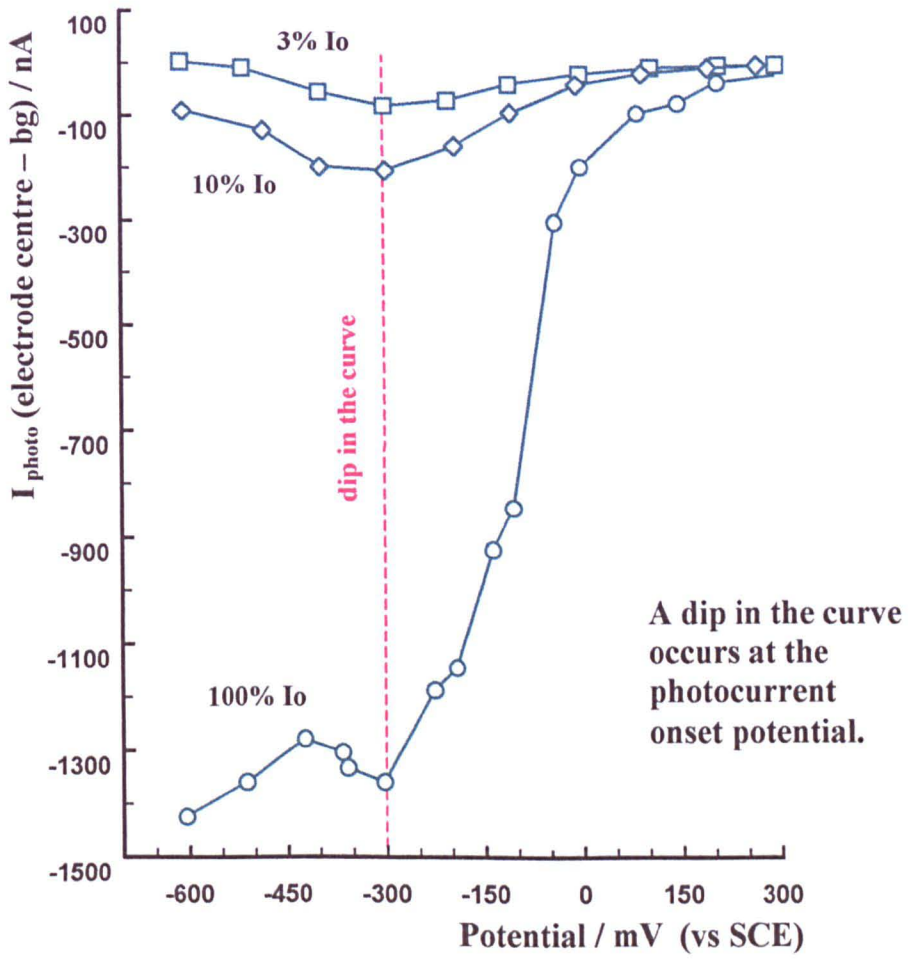

Notes: Sample = p-type Si, solution = 1M HCl, etch condition B, lens magnification = x4 (NA 0.12), laser spot diameter = 2 μm, line length = 3080 μm, total area sampled in the experiment = 3080 x 1903 μm (= 768 x 512 pixels) , pixel dwell time = 10 μs , τ = 5 μs

figure 3.31

The scanning laser imaging experiment is a dynamic experiment recording changes in current in the form of AC variations as the beam scans the surface (figure 3.31). In this it is fundamentally different from a DC experiment (figure 3.28) in which the total current of the whole surface is recorded with the use of a chart recorder (ref. C1-21, D.E. Williams et al., 1992). As a result the way that the photocurrent generated (figure 3.31), varied with potential on the photocurrent images was not the same as that on the pulsed laser cyclic voltammogram (figure 3.28), for the same electrode under the same conditions.

The variation in the trend in photocurrent with potential seen on the images (figure 3.30) can be explained by a change in capacitance at the electrode-electrolyte interface. A maximum in the apparent capacitance corresponds to the dip in the curve where the photocurrent generated is lower (more cathodic) than expected. C^{-2} is known to go through a minimum at the flat band potential. In most cases the flat band potential is known to occur at the photocurrent onset potential. So the simplest explanation would be that the minimum in the photocurrent curve occurs at the flat band potential.

Work done by Nakato et al. (refs. F3-1, 1987 and F3-2, 1992) with p-Si in 1M HCl was found to give cyclic voltammetry results as shown in the work in this chapter (figure 3.29). However it was stated here and in other work (ref. F2-1, J.A. Bardwell and coworkers, 1996) flat band potential does not occur near the onset potential for this system but more negative to it. This suggests that the hydrogen photo-evolution reaction, in 1 M HCl, on p-type silicon has a high activation energy. So occurrence of the apparent maximum in capacitance, on figure 3.31, may actually be due to surface states.

An equivalent (model) AC circuit which will give the same properties with potential as the cell can be represented by the circuit in figure 3.32.

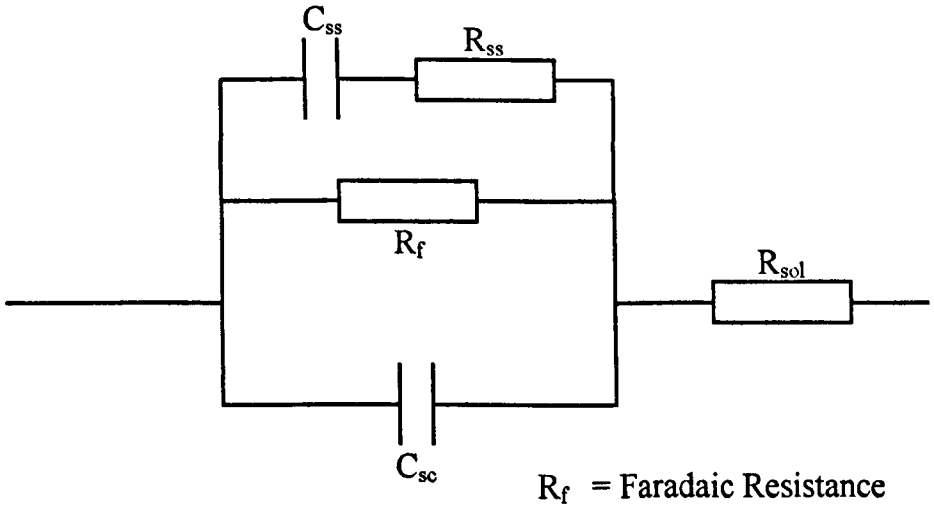

R_f = Faradaic Resistance
R_{ss} = resistance due to surface states
R_{sol} = solution resistance
C_{sc} = space charge layer capacitance
C_{ss} = capacitance due to surface states

figure 3.32

Only the apparent capacitance (which depends on the Faradaic resistance) is known. We know that the space charge layer capacitance is a maximum at the flat band potential, but there is also a smaller capacitance due to surface states of which we have no information. One of C_{ss} or R_{ss} will have to vary with potential, which will therefore result in the apparent capacitance varying with potential allowing a maximum to occur.

The photocurrent imaging experiment reveals different elements of behaviour due to the effect of light, as the cyclic voltammetry is not sensitive to the capacitors in the system whereas the imaging system is. The experiment with the chart recorder does not pick up the effect of capacitance as it is much slower, with a sampling time in the region of a tenth of a second compared to the signal collected by the laser scanning system which has a sampling time of microseconds.

Further work by Y. Nakato and coworkers (ref. F3-1, F3-2) showed that depositing Pt-islands gave good rectification in the dark with the photocurrent onset voltage occurring near the flat band potential. More recent work carried out by Nakato and coworkers (ref. F3-3, 1994; ref. F3-4, 1997; ref. F3-5,1998) using other metal particles (Cu, Ag, Au) instead of platinum also moved the onset potential to one that was more positive than for a naked p-Si in 1.0M HCl (pH 2.0). A brief study of the effect of potential on the photocurrent image was also carried out, by myself, in the presence of platinum islands deposited on p-Si. Preliminary results from this indicated that the average photocurrent, from the image decreased (became more cathodic) in a smooth curve with decreasing potential. The minimum at -300 mV (figure 3.31) was eliminated in the presence of Pt particles.

Added Complications Resulting from Surface Defects

If the sample had been left for a few days an oxide layer grew on it reducing the photocurrents observed significantly so the sample had to be etched again. However an added complication arose with this procedure. Each time the electrode was further etched the many holes and scratches present on a very poor thin sample became much

worse. Repeatedly etching the same electrode in successive experiments changed the photocurrent image.

This was most evident at the most negative potential applied (-600 mV or lower). Here the currents on the electrode became more and more positive with each successive experiment and each successive etch. The image at 100% I_o was affected the most followed by that at 10% I_o then 1% I_o so resulting in an inversion (etch conditionE), compared to the curves seen on figure 3.31 (etch condition B), at potentials below –300 mV. However even though the photocurrent on the images became positive the overall current on the cyclic voltammetry remained the same with the current generated becoming more negative with the decreasing potential.

Etching further after this resulted in the photocurrents over the electrode surface staying positive but diminishing (etch condition I / J). The photocurrents observed on the pulsed laser cyclic voltammetry decreased in size as well, but were still negative at the negative potentials.

The positive signal on the image may be due to internal photoemission from the silicon to silicon oxide becoming much more dominant than photoelectrochemical excitation of the electrons from the electrode to the solution as the surface grew rougher. One other possibility was that there may have be a lot of fluoride left on the surface layer and more surface states due to fluoride could have caused the effect seen.

One other effect that was considered but ruled out, was that the effect may have been due to the excessive etching of the very thin defect ridden sample down to its base (possibly a p-n layer) on which it is grown. This can not be so, as even though the signal changed from negative to positive on the photocurrent image, the cyclic voltammetry remained the same. If the silicon type had changed this would have resulted in the cyclic voltammogram changing as well.

Other Features Noticed

It was noticed that the area following the electrode is darker, i.e. the photocurrents were more negative than the region before. This effect was due to an undershoot of the photocurrent signal after the beam had passed off the electrode due to the slow relaxation of the current change which occurs on laser irradiation of this system.

At very negative potentials such as below -600 mV hydrogen bubbles could be readily detected on the photocurrent image (figure 3.34), where outside the bubble and inside the bubble the photocurrent was the same, but at the edge of the bubble the photocurrents observed were more positive than the rest of the electrode in general, and were detected as white in colour on a grey scale image.

At the edge of the bubble H_2 can be oxidised to H^+ and then an anodic (positive i.e. white in colour on a grey scale) photocurrent would be generated. In this process the hydrogen evolved has to capture the holes.

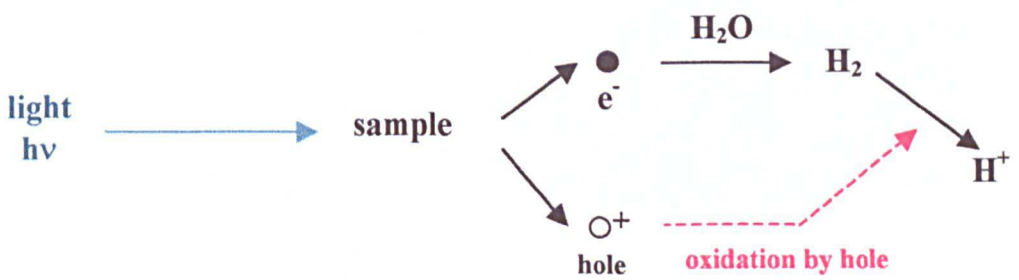

figure 3.33

A PHOTOCURRENT IMAGE SHOWING THE OCCURRENCE OF H_2 BUBBLES ON THE P-SI SURFACE

Io = 100% , E = -742 mV

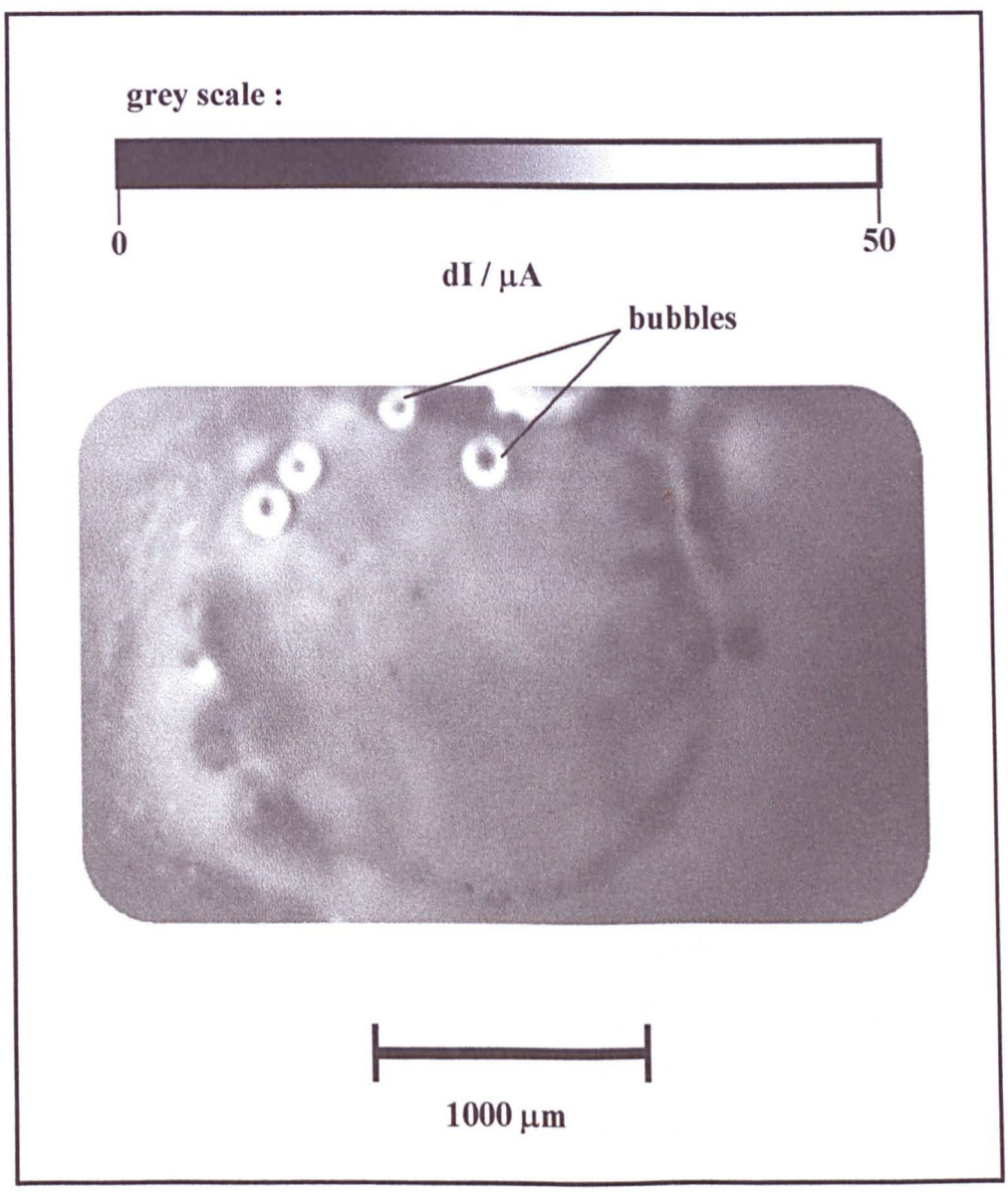

Notes: Sample = p-type Si, solution = 1 M HCl, etch condition D, lens magnification = x4 (N.A. = 0.12), laser spot diameter = 2 μm , line length = 3080 μm, total area sampled in experiment = 3080 x 1903 μm (768 x 512 pixels), pixel dwell time = 10 μs, τ = 5 μs.

figure 3.34

3.5 CONCLUSION

These experiments show that as well as recording optical images the confocal scanning laser microscope could be used to collect photocurrent images. This technique shows function (photocurrent images) as well as topography (confocal optical images) so it could be used for example to check that semiconductor devices actually work, in the computer industry. In addition this method was also found to give results for an electrochemical system where the electrode is immersed in a solution so allowing a quick method of directly observing reactions as they happen between the electrode surface and surrounding electrolyte, using the laser as a source of energy to promote a reaction. This will allow any increase in current to be observed as the laser scans over the liquid-solid interface and was done so for the p-type silicon electrode in 1M HCl seen here. Further work in this area could involve looking at metal islands e.g. platinum deposited on the electrode to speed up the reaction, one use for such a system being in a solar cell. An improvement to the work using the p-type silicon would be to use a cleaner sample with fewer defects that is a little thicker (e.g. 0.5 mm).

Photocurrents at different depths were observed for both the silicon memory chip and p-type silicon. This is useful as it allows semiconductor devices to be characterised in three dimensions.

It was also shown that good resolution can be achieved in the photocurrent imaging of semiconductor devices. For semiconductors in particular the photocurrents generated are relatively high and the signal to noise ratio is very high, so that fairly clear images were seen without additional noise removal / suppression methods such as a large amount of signal averaging, use of a faraday cage around the cell, or FFT to remove further noise. These techniques were required in later work in which the electrode samples were not semiconductors.

4. PHOTOTHERMAL IMAGING OF GOLD IN FERROCYANIDE

4. PHOTOTHERMAL IMAGING OF GOLD IN FERROCYANIDE

4.1 INTRODUCTION

The Ferrocyanide Oxidation Reaction

The overall ferrocyanide oxidation reaction at a gold electrode reaction can be described by:

$$Fe^{2+} \longrightarrow Fe^{3+} + 1e^{-} \qquad (4.1)$$

The electrode reaction can be split up into more basic steps:

$$Fe^{2+}_{solution} \xrightarrow[\text{mass transfer}]{\text{diffusion (1)}} Fe^{2+}_{electrode} \xrightarrow[\text{transfer}]{\text{electron}} Fe^{3+}_{electrode} \xrightarrow{\text{diffusion (2)}} Fe^{3+}_{solution} \qquad (4.2)$$

Where :-

If the diffusion step (1) is slow = then the reaction is mass transport controlled.

If the diffusion (1) step is fast = then the reaction is kinetically controlled.

followed by slow e^- transfer

R.B Lowry (refs.G-5, G-6, 1991-1993) discussed the mechanism of the $Fe(CN)_6^{4-/3-}$ adsorption onto gold found from results of Raman spectroscopic studies. The attachment of the ferricyanide (hexanocyanate ferrate (III)) ion was thought to be due to 2 cyanide ligands in contact with the electrode surface. It was also found that the $Fe^{II}(CN)_6^{4-}$ was not as strongly absorbed as $Fe^{III}(CN)_6^{3-}$. In addition the $Fe^{III}(CN)_6^{3-}$ was shown to be considerably distorted. From infra-red studies it is thought that electron donation from the π^* orbital of the cyanide group of the C≡N bond lying

parallel to the surface occurs. Lowry (ref G-6) also showed by using Rahman spectroscopy that the attachment of the of the $Fe^{III}(CN)_6^{3-}$ ion to the gold was sufficiently strong that it was able to withstand removal from the solution in order to permit exposure to air, or be placed in a base electrolyte. So this work showed that the heterogeneous electron transfer that occurs at the gold electrode must be mediated by a chemisorbed layer of $Fe^{III}(CN)_6^{3-}$ ions which result in the electrode surface being effectively modified

A POSSIBLE MECHANISM FOR $Fe(CN)_6^{4-/3-}$ ATTACHMENT TO GOLD

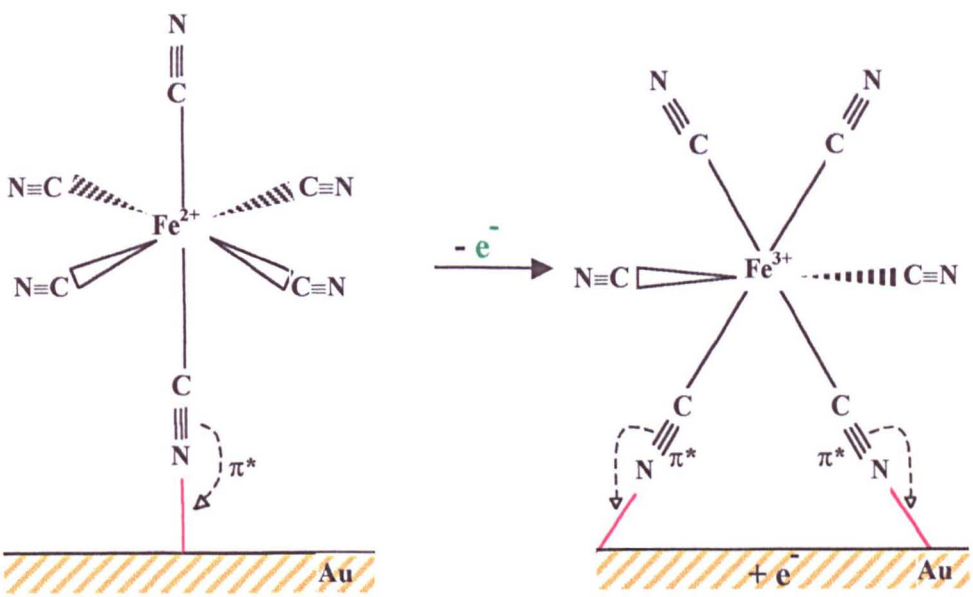

figure 4.1

Experimental Work Showing the Effect of a Temperature Rise on ΔS^o

The current(i) vs potential(E) curve moves on application of heat to a different position. The direction it moves in depends on the sign of the standard entropy change, ΔS^o, for the electrode reaction. The entropy for a reaction is given by:

$$\Delta S^o = nF\left(\frac{\delta E^o}{\delta T}\right)_p \qquad (4.3)$$

where; δE^o = a small change in the standard electrode potential and δT is a small change in the temperature.

From equation 4.3 it may be seen that, if ΔS° is negative ($\Delta S^\circ < 0$) then the standard electrode potential E° shifts to a negative direction when there is a rise in temperature. Similarly if the ΔS° is positive ($\Delta S^\circ > 0$) then the standard electrode potential E° shifts to a positive direction when there is a rise in temperature. Subtracting the amount i vs E curve obtained for the raised temperature (T + ΔT) from that obtained for the original temperature (T), shows the amount of current generated by the laser induced temperature rise at each potential (see figures 4.2 and 4.3).

For -VE value of ΔS° :

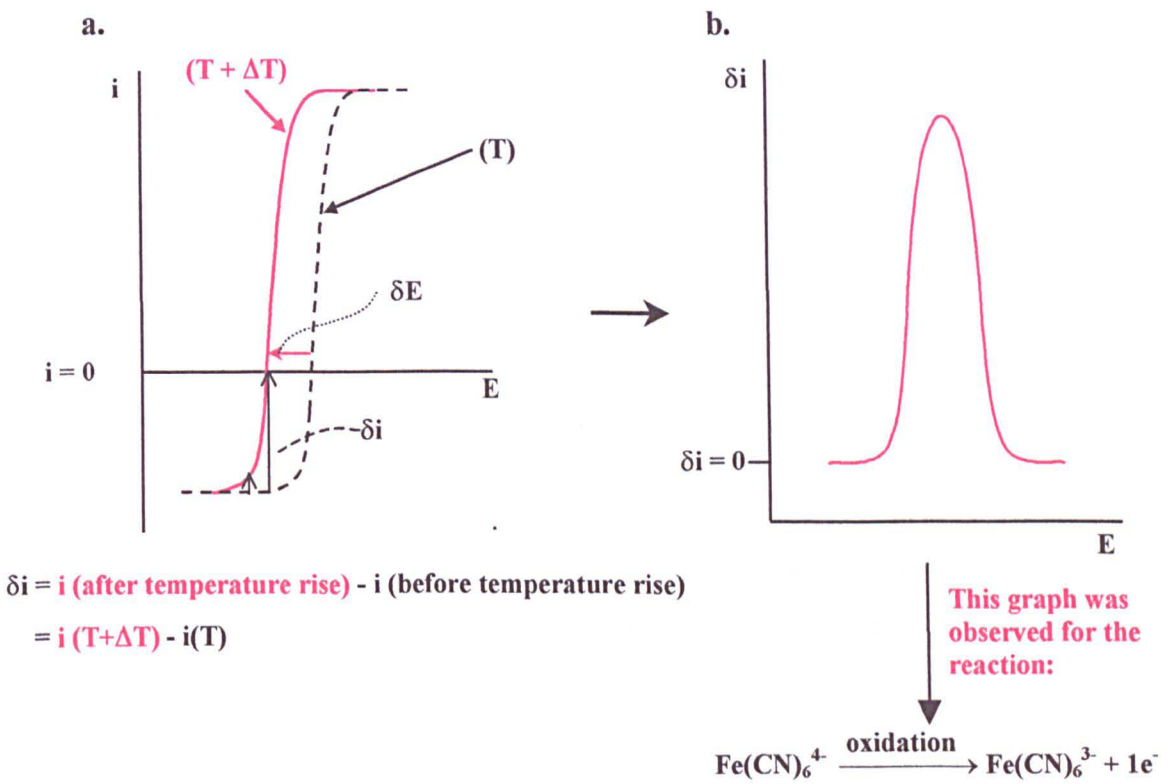

figure 4.2

From the previous work it was shown that a solution containing $Fe(CN)_6^{4-}$ exhibited the behaviour shown in figure 4.2b with a peak at $E_{½}$ (δI was found to be maximum at, 0.2V by cyclic voltammetry by Hinue et al. (ref. I-8) ,and at 0.2V by photocurrent imaging by R. Hutton et al. (ref. D2) .

So when ΔS° is negative the electron transfer process of the oxidation reaction is increased by a rise in temperature.

For a +VE value of ΔS^{o} :

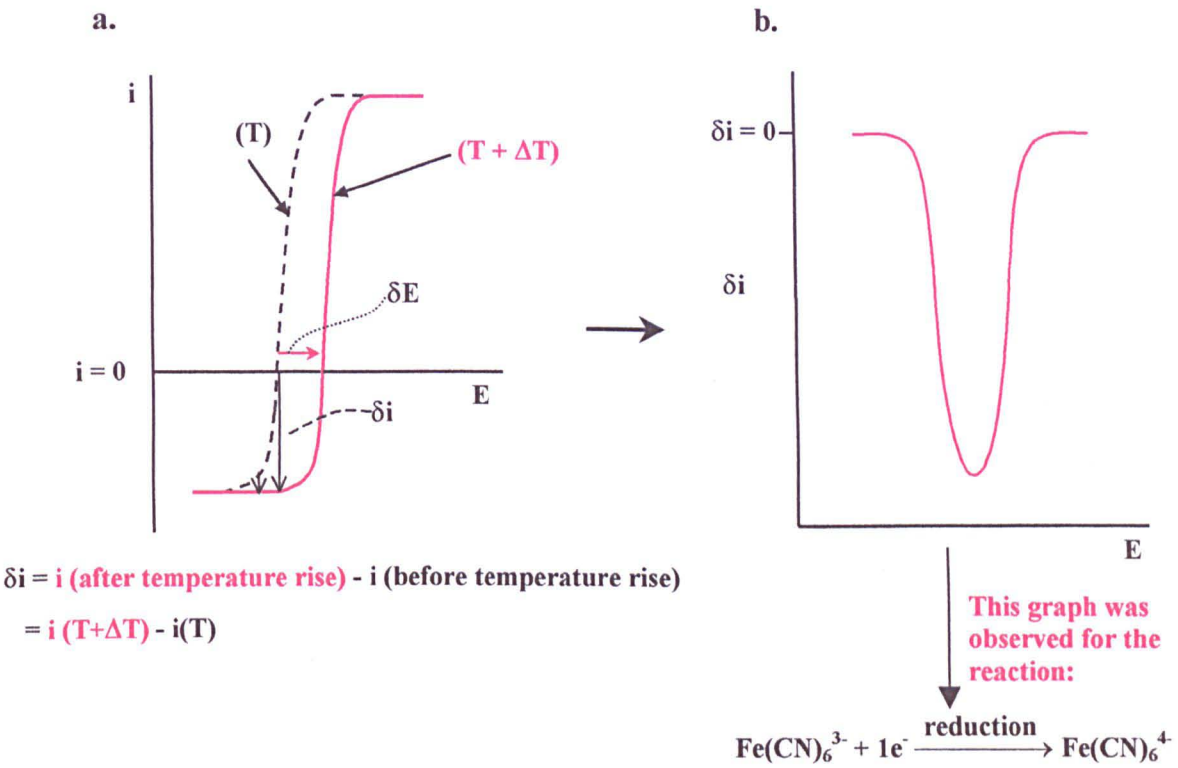

figure 4.3

From the previous work (ref. I-8) it was shown that a solution containing $Fe(CN)_6^{3-}$ showed the behaviour depicted in figure 4.3b,with a trough (negative peak) occurring at 0.23V.

This shows for a positive value of ΔS^{o} the electron transfer reaction is suppressed by the increase in temperature

Theory of How a Temperature Rise Will Effect an Electrochemical Reaction

The effect the rise on temperature has on the current generated depends on the extent of reversibility / irreversibility of the reaction. The terms reversible and irreversible refer to limiting cases according to whether the electrode kinetics are fast (reversible) or slow

(irreversible) compared to the mass transport conditions of the electrode of interest. The reaction in each case is controlled by the slowest transport mechanism involved.

The electrode kinetics define the movement of the electrons to or from the electrode to the species in the solution whereas mass transport is the process of the movement of ions in the solution. Mass transport is contributed to by three processes; diffusion, convection and migration. Diffusion is a process which occurs due to uneven concentration distribution. Here the entropy is maximised by smoothing out inhomogenities of composition within any system. Convection is a movement of ions due to a mechanical force acting on the solution. The convection can be due to natural sources such as thermal gradients, or density differences within the solutions or due to forced convection by external forces such as pumping, stirring or bubbling gas. Migration is caused by an external electric field at the electrode solution interface as a result of the change in electrical potential from the metal to solution phase. This results in an electrostatic force being created on the charged species at the interface helping to move the ions to or from the electrode.

Where the reaction is reversible the system appears to be in equilibrium at the surface. With a surface process in equilibrium the surface concentration can be calculated using thermodynamic arguments i.e. by using the Nernst Equation. In comparison if the reaction involved is irreversible the surface concentrations have to be estimated using kinetic equations.

Examples for the theory on the two limiting cases i.e. for a mass transfer controlled and kinetically controlled reaction follow.

1. Effect of a temperature rise on a mass-transfer-controlled reaction

The effect of changing temperature results in a change in the reversible (equilibrium) electrode potential (E_r) as shown in figure 4.2. For a stirred solution when $\Delta S^\circ < 0$, the effect of temperature on a mass transfer controlled reaction may be calculated:

$$E^\circ = -\frac{\Delta G^\circ}{nF} \qquad (4.4)$$

where $\Delta_r G^\circ = \Delta_r H^\circ - T\Delta_r S^\circ$

$$E^\circ = \frac{-\Delta H^\circ}{nF} + \frac{T\Delta S^\circ}{nF} \tag{4.5}$$

Where $\Delta_r H^\circ$ and $\Delta_r S^\circ$ are assumed invariant with temperature for a small change.

$$\delta E^\circ = \frac{\Delta S^\circ}{nF}\delta T \tag{4.6}$$

Where: E° = standard electrode potential applied, E_r = reversible (equilibrium) electrode potential, ΔH° = change in the standard enthalpy for a reaction, ΔS° = standard entropy change for a reaction, ΔG° = Gibb's free energy, n = number of electrons transferred in reaction, F = Faraday Constant.

Consequently the temperature variation of E° for the observed current can be calculated. For a reversible process it is assumed that the reaction kinetics are so fast that local equilibrium prevails so the Nernst equation (equation 4.8) can be used to relate the local surface concentration to E_r.

$$R \xrightarrow{\text{oxidation}} O + ne^- \tag{4.7}$$

$$E_r = E^\circ - \frac{RT}{nF}\ln\frac{c_R{}^s}{c_O{}^s} \tag{4.8}$$

Where: $c_R{}^s$ = concentration of reduced species at the surface, $c_O{}^s$ = concentration of oxidised species at the surface and R = the gas constant.

Here, all activity coefficients have been assumed unity (dilute solution approximation). The Nernst diffusion layer approximation can be used to derive the relationship between surface concentration and current, and hence between current and electrode potential.

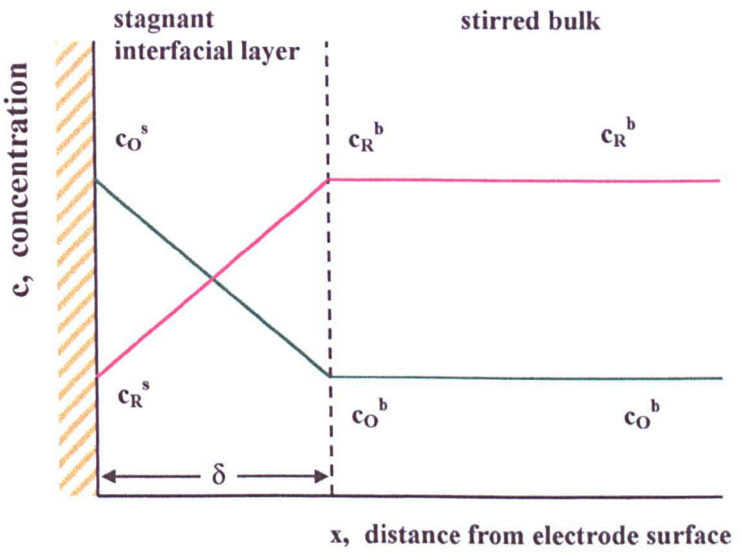

Where:

δ	= the Nernst diffusion layer thickness
c_O^s	= concentration of oxidised species, at the surface of the electrode
c_O^b	= concentration of oxidised species in the stirred bulk of the solution
c_R^s	= concentration of the reduced species at the surface of the electrode
c_R^b	= concentration of the reduced species in the bulk of the solution

figure 4.4

Assuming $D_O = D_R = D$ where D = the diffusion coefficient

then the diffusion limited current density, $$i_{lim} = D\frac{c_R}{\delta} \qquad (4.9)$$

If $i < i_{lim}$, and $[c_R^b - c_R^s]$ and $[c_O^s - c_O^b]$ are the differences in concentration between the bulk and surface concentration gradients of the reduced and oxidised species respectively.

$$\begin{aligned} i &= -\frac{D}{\delta}\left[c_R^b - c_R^s\right] \\ &= -\frac{D}{\delta}\left[c_O^s - c_O^b\right] \end{aligned} \qquad (4.10)$$

Hence the relation between current density and potential (using equation 4.6) is:

$$E_r - E^o = -\frac{RT}{nF}\ln\left[\frac{{c_R}^b}{{c_O}^b}\cdot\frac{(1-i/i_{lim})}{1+\frac{{c_R}^b}{{c_O}^b}i/i_{lim}}\right] \tag{4.11}$$

Now,
$$\left(\frac{\delta E^o}{\delta T}\right)_p = \frac{\Delta_r S^o}{nF} \tag{4.12}$$

so the variation of current with small changes of temperature, at a constant applied potential (E), ignoring the variation of i_{lim} with T (caused by variation of D with T), can now be derived:

$$\left(\frac{\delta i}{\delta T}\right)_E = \left(\frac{\delta i}{\delta E^o}\right)\left(\frac{\delta E^o}{\delta T}\right) \tag{4.13}$$

The expression for current in terms of potential is given as,

$$i = \frac{\left[\exp\left(nF\frac{E_r - E^o}{RT}\right)c_O i_{lim}\right] - c_R i_{lim}}{\left[\exp\left(nF\frac{E_r - E^o}{RT}\right)c_R\right] + c_R} \tag{4.14}$$

The derivative of current with respect to E ° is,

$$\frac{\delta i}{\delta E^o} = -nF\exp\left[-nF\frac{E_r - E^o}{RT}\right]\times\frac{i_{lim}}{c_R}\times\frac{c_O + c_R}{\left[\exp\left(-nF\frac{E_r - E^o}{RT}+1\right)\right]^2 RT} \tag{4.15}$$

The expression for change of current caused by temperature perturbation is,

$$\frac{\delta i}{\delta T} = -nF\exp\left[-nF\frac{E_r - E^o}{RT}\right]\times\frac{i_{lim}}{c_R}\times\frac{c_O + c_R}{\left[\exp\left(-nF\frac{E_r - E^o}{RT}+1\right)\right]^2 RT}\times\frac{\Delta S}{nF}\cdot\delta T \tag{4.16}$$

When the current change is maximum, can now be found by differentiating this expression with respect to E_r and setting it equal to zero:

$$0 = nF \cdot i_{lim} \cdot (c_O + c_R) \cdot \Delta S \cdot \delta T \cdot \frac{\exp\left[-2nF\left(\frac{E_r - E^o}{RT}\right)\right] - \left[\exp\left(-nF\frac{E_r - E^o}{RT}\right)\right]}{c_R\left(\exp\left[\left(-nF \times \frac{E_r - E^o}{RT}\right) + 1\right]\right)^3 (R)^2 (T)^2} \quad (4.17)$$

The maximum current occurs when $E^o = E_r$. This gives the value of the maximum current as,

$$\delta i_{max} = -\frac{1}{4} \times \frac{i_{lim}}{c_R} \times \left(\frac{c_O + c_R}{RT}\right) \times \Delta S \cdot \delta T \quad (4.18)$$

If $c_O{}^b = c_R{}^b$ then,

$$\delta i_{max} = -\frac{1}{2} \times \frac{i_{lim}}{RT} \Delta S^o \quad (4.19)$$

2. Effect of a temperature rise on an electrode-kinetics-controlled-reaction

For an kinetically controlled (irreversible) reaction E_a ,the effect of a temperature change results in the change of the kinetics of the electrode reaction.

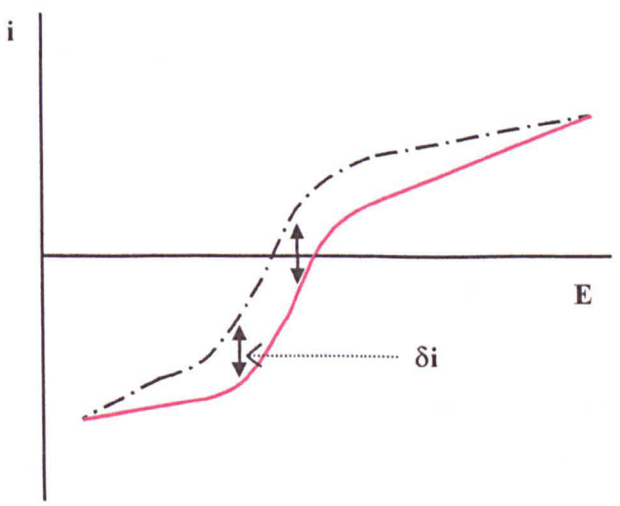

figure 4.5

The equation describing kinetic control is,

$$i = i_o \exp\left(\frac{-E_a}{RT}\right) \cdot \exp\left(\frac{\alpha n F \eta}{RT}\right) \tag{4.20}$$

Where E_a is the activation energy for the reaction, $\eta = E - E_r$ (the deviation of the potential from the equilibrium value) is the overpotential for the reaction and α is the transfer coefficient

The effect of temperature variation is given by:

$$\delta i \approx i \frac{E_a}{RT^2} \cdot \delta T \tag{4.21}$$

The effect of temperature change on E^o can be ignored for a large enough value of η.

Photocurrent Generation by a Laser Beam Induced Temperature Rise

When a laser beam makes contact with the surface of a metal electrode in an electrolyte solution. The metal electrode is heated and this heat is rapidly passed into the surrounding solution providing a means of excitation to the reaction occurring at the electrode-electrolyte interface. This results in a photocurrent being produced due to the effects of the laser induced temperature jump at the electrode surface.

Previous work using the laser-induced-temperature-jump method included effects produced at a mercury drop electrode in various solutions (including, NaF, KCl, LiCl, CsCl,) by V.A. Bederskii et al., (1982-1984, ref. I1-1 to I1-5). In addition more recent work by Benderskii and coworkers (1991, ref. I1-6) has included use of solid metal electrodes (including; Zn, Pb, Al, Ni, Ti, Ta) with various electrolytes (including; H_2SO_4, $CuSO_4$, NaOH). In this work (ref. I1-6) effects of laser heating was shown to cause plastic deformations in the metal subsurface layer which resulted in the activation of; metal dissolution, hydrogen evolution and plating in the exposed area. Other work involving a temerature jump has been carried out using a glass electrode (R.K. Jaworski ref. I1-6), a gold electrode (Smally et al., ref. I1-7), and on platinum (T.Hinue

et al., ref. I1-8). These systems however use a pulsed (chopped) laser beam and not a continuous one as in this thesis, and in addition just a point or line of points were examined not many lines making a 2D-image as in our work.

A equation giving the temperature rise for a pulsed laser beam on a electrode-electrolyte system was derived by Benderskii et al. This related the temperature to the physical and thermal properties of the metal and the surrounding solution as well as the shape of the pulse. For the maximum change in temperature (ΔT_{max}) this equation simplified to on describing just the properties of the metal and electrolyte-solution as shown in equation 4.22 (1982-1983, refs. I1-1, I1-2).

$$\Delta T_{max} = \frac{I_{o,abs}}{\sqrt{\pi \cdot y_{metal}}} \cdot \frac{1}{1+\sqrt{(y_{sol}/y_{metal})}} \cdot \sqrt{t_o} \qquad (4.22)$$

Where $I_{o,abs}$ = intensity of light absorbed = I_o (1-R), and y = is a constant relating to the physical and thermal properties of the metal and solution given by: '$y = K c_p \rho$' , c_p = specific heat capacity, ρ = density, K = thermal conductivity, I_o = incident light intensity = P ÷ laser spot area = P ÷ πr^2, R = reflectivity, and t_o = time of laser pulse duration.

This equation only applied provided the following conditions were met.

1. Each data (image) point collected is illuminated by a pulse.
2. The temperature is allowed to relax between points.
3. The size of the electrode is much greater than the illuminated area.

In this work the time dependence of the temperature jump was given by $\frac{\Delta T}{\Delta T_{max}} \approx \sqrt{\frac{t_o}{t}}$ where $t \gg t_o$, where to = pulse duration and t = time after the pulse duration. for the case where the thickness of the layer of metal heated is given by (ref. I1-2) $\ell \approx \left(K_{metal} / c_{p,metal}\rho_{metal}\right)^{1/2}$ and the thickness of the layer of solution heated is given by $\ell \approx \left(K_{sol} / c_{p,sol}\rho_{sol}\right)^{1/2}$.

In later work (1984, refs. I1-3, I1-4) an equation was given for the amplitude of periodic change temperature change (see equation 4.23), where ω_{mod} = the frequency of modulation of the amplification of the heating signal, and the length of the heat propagation in the metal was given as; $\ell = \left(K_{metal} / 2c_{p,metal} \cdot \rho_{metal} \cdot \omega_{mod}\right)$.

$$\Delta T_{max}\omega_{mod} = \frac{I_{o,abs}}{2\sqrt{y_{metal}\omega_{mod}}}\left[1+\sqrt{(y_{sol}/y_{metal})}\right] \qquad (4.23)$$

In the more recent work still (1991, ref. I1-5) using the solid metal electrodes the temperature change was given simply as :

$$\Delta T_{max} = \frac{I_{o,abs}\,2\cdot\exp\left(-r^2/r_o{}^2\right)\cdot\sqrt{t_o}}{\sqrt{y_{metal}}} \qquad (4.24)$$

Where r = the laser spot radius

(Note: the term relating to the electrolyte solution, as given in equation 4.22, was probably omitted as calculations show that; $1 \div \left[1+\sqrt{y_{sol}/y_{metal}}\right] \approx 1$ in many cases, eg for solution = water and metal = gold : see Appendix D for thermal and physical properties of gold and water.)

Previous Photocurrent Imaging work at Gold Electrodes

Previous work carried out by R.S. Hutton and D.E. Williams (refs. D-2, D-3) involved the study of the ferrocyanide reaction at a gold disc electrode. Work was also carried out by the same people on a gold microelectrode array (ref. D-5) which consisted of a group of many 10μm diameter gold wires bundled in to a disc shape. Here the value of the expected temperature rise was calculated by substituting a calculated value of i_{lim} from equation describing the behaviour at a microelectrode into equation 4.18, this gave a value of ~ 1K. In addition work was also carried out at high potential (E > +800 mV vs SCE). This showed unusual effects which occurred at high values of E, showing loss

of photocurrent due to photo-deactivation in the region the laser scanned in on the electrode surface.

In the work with the gold disc electrodes in ferrocyanide it was noticed in some cases the contrast at the edge of the electrode and hence the photocurrent was higher than in the middle of the electrode. This was explained due to the fact that at the electrode edge faster radial diffusion is dominant (see figure 4.6). As a result the contrast at the edge of a gold disc arises because i_{lim} is different there. An explanation can be given by faster rate of diffusion at the edge.

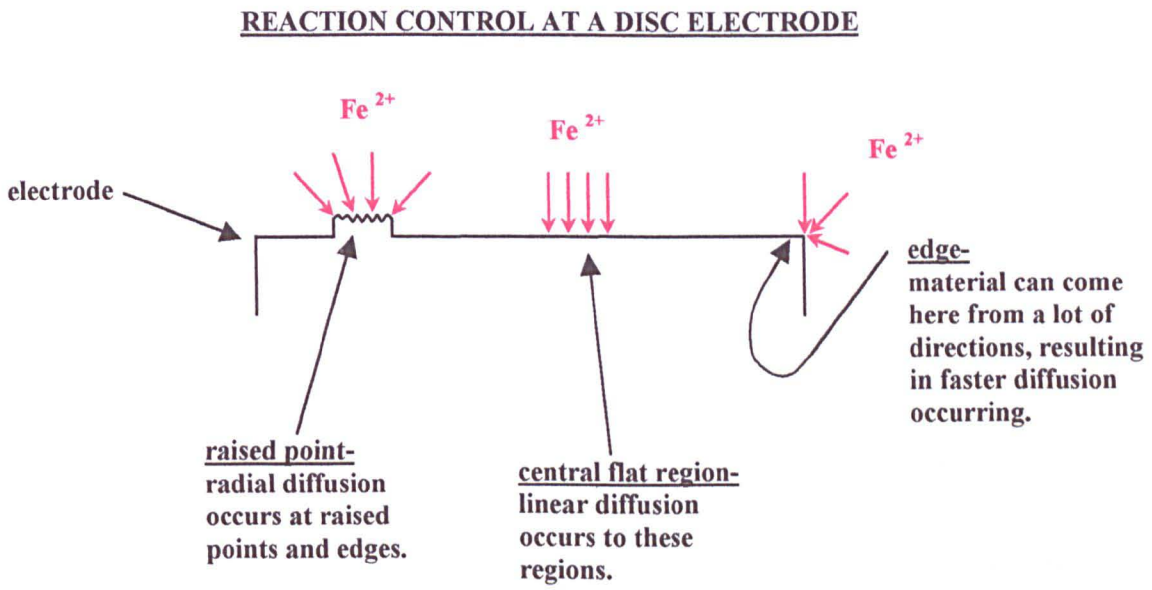

figure 4.6

There are three types of region allowing different rates of diffusion. Therefore at a disc electrode for a quasi-reversible reaction below the limiting current, the theory given above shows that contrast could develop as a consequence of the spatial variation of the limiting current density.

From previous work the electro-oxidation of ferrocyanide at a gold disc electrode under the influence of a laser beam has been found to be principally due to thermally induced change in the rate of electron transfer kinetics, as the maximum photocurrent was found to occur at the half wave potential where the electrode kinetics provide the rate determining step of the reaction. So the equation describing the kinetically controlled reaction (equation 21) was used to estimate the change in current for a known

temperature rise. If 'a' is the area of the focussed laser beam spot equation 4.25 can be adapted to give the variation in total current which gives rise to the image:

$$\delta I \approx i\frac{aE_a}{RT^2}\cdot\delta T \qquad (4.25)$$

Where δI is the small change in current produced by the rise in temperature. If only the thermal effects produced by electrode kinetics contribute to the overall change in current when the laser contacts the electrode surface then $\delta I = I_{photo}$, the overall photocurrent generated.

For a electrode-kinetics controlled reaction

$$I_{photo} \approx ia\frac{E_a}{RT^2}\cdot\delta T \qquad (4.26)$$

Hence the temperature change can be given by the change in dark current i and the activation energy, E_a.

In addition it was found that with a gold disc experiment two effects due to time lapsed (transient effects) were observed. These included; 1) blurring of the image at a faster line scan times i.e. as the scan velocity increases and 2) a shadowing effect showing a current below the average following a hot spot. After a hot spot there was always a dark area (lowering of the photocurrent observed). The interpretation given was that the perturbation concentration of Fe^{2+} near the surface of the gold electrode had not had time to recover.

Whereas previous work involved a disc electrode in this chapter microband electrodes have been studied. Where microband electrodes are concerned it is like imaging an electrode which is 'all edge' with no middle due to its small dimensions.

Microelectrodes tend to have very thin diffusion layers and the concentration gradients induced across them will be correspondingly high, so the mass transport to them will be much faster than for a macroelectrode. So the electrode kinetics might be the controlling factor in this reaction, more so than in the macrodisc electrode.

4.2 AIMS

An understanding of the image contrast of simple model systems is necessary to understand and interpret images from complex electrochemical systems. Here we have studied the thermally induced image contrast on gold band and disc electrodes, with Fe $(CN)_6^{3-}$ / Fe $(CN)_6^{4-}$ as the redox couple present in the solution. The reason for studying the band electrodes was to aid the modelling of images featuring electrochemically active lines in an electrochemically inert matrix.

The aims of the present work were:

1) To explore further the limits to image resolution in this method.
2) To develop further understanding of the image contrast in electrochemistry due to the photothermal effect.
3) To investigate the effect of electrode geometry on the image contrast.
4) To compare images of electrochemically reversible and irreversible systems.

4.3 EXPERIMENTAL

Three types of gold microband electrode and a gold disc electrode were investigated. The gold electrodes used were prepared as follows:

1. Pure gold microband electrode- This was a homemade electrode prepared by clamping a gold foil between two glass slides, the contacting surface of which had been sputter-coated with gold. This was then mounted in an electrode holding cup and polished to reveal the gold band (more specific details about the preparation of this electrode has been given in appendix D). This homemade gold band was of 5 mm long and ~ 20 μm wide.

2. Screen printed single gold microband electrode- This was fabricated commercially by printing and firing commercial gold ink on to an high alumina ceramic tile and then, over-printing this with an ceramic insulator (a dielectric material used for thick-film

capacitor manufacture, which was found to be comparable to light flint in structure from the microprobe analysis carried out). The tile was cut across the gold strip and the assembly was mounted in epoxy resin and polished to show the gold band.

3. Screen printed double gold microband electrode- This was prepared commercially by successive printing of gold and dielectric as shown above but this time an extra layer of the gold ink and insulating material was present. In the commercial double gold double microband electrode each gold band had a width of ~ 10 μm and the two bands were spaced 50 μm apart. This was also set in epoxy resin .

4. Gold disc electrode- This was constructed from a pure gold (diameter 500 μm) wire mounted in epoxy resin and polished down to show the cross sectional disc shape of the wire.

All the electrodes were polished with successively finer grades of aluminium oxide paper and diamond polishing pastes down to 1μm. In addition, after polishing with each grade of polishing material the surface was cleaned using an ultrasonic bath.

Solutions were prepared from triply distilled water (first distillation from alkaline $KMnO_4$ solution) and AnalaR grade chemicals were used without further purification. The solutions contained $K_4 Fe^{II}(CN)_6$ (5×10^{-3} mol dm^{-3}), K_2HPO_4 (0.1 mol dm^{-3}), and KH_2PO_4 (0.1 mol dm^{-3}), pH 6.8. The confocal scanning laser microscope (BioRad MRC-600 system : Ar^+ laser , main lines, 488 nm and 514 nm, 25 mW total output) electronics and electrochemical cell arrangement have been described previously in chapter 2. A conventional 3 electrode electrochemical cell was used consisting of the gold band (working electrode), a saturated calomel (reference) electrode and a platinum open ring wire (counter) electrode all in the electrolyte solution. The continuous-scan, direct-detection mode of operation was used. The signal was amplified, offset and high (0.03 Hz) and low pass filtered (10 kHz : printed electrodes, 3 kHz : pure gold electrode). Experimental settings for specific experiments are given in more detail in Appendix K. When in use a thin glass slide (cover slip) was placed over the cell in order to stop the liquid from rippling as the laser spot moved over the surface. The gap between electrode and coverslip covering the cell was 0.5 cm. Spatially resolved

photocurrents were recorded as videographic images consisting of a maximum of 768 x 512 data points. No neutral density filter was used in the path of the laser beam, so the intensity of the laser beam at the sample (I_s)was the same as that at the source (I_o).

Firstly a series of experiments showing the effect of changing the potential on geometry have been given in this chapter. This work was carried out on flat microband gold electrodes; 1. of pure homemade quality, 2. of commercially available screen printed (not so pure quality) electrodes. The behaviour of these bands were then in turn compared with the behaviour of a gold disc electrode.

Secondly the effect of irreversibility on the photocurrent image, which was studied, is given in this chapter. This effect was studied on the screen printed double band electrode as it was found by chance that the screen printed bands changed in nature with time due to their composition leaving the system progressively poisoned with time. Materials formulated for screen printing contain a variety of additives to promote adhesion to the substrate and cohesion of the gold layer. The presence of these additives caused a progressive drift in the electrochemical behaviour of the Fe $(CN)_6^{3-}$ / Fe $(CN)_6^{4-}$ couple, from reversible to irreversible, over a period of several hours of use. This trend could be partly reversed by ultrasonic cleaning in acetone as well as by polishing on previously un-used polishing pads. This became progressively more difficult to do with increased use of the electrode. In addition irreversible reaction behaviour was also investigated on the macrodisc electrode due to the adventitious contamination of the water. In addition the composition of the electrodes was examined by optical microscopy and x-ray analysis (using the electron probe microanalyser instrument). The extent of reversibility of the reaction has been classified by the letters A, B, C and D (see figure 14.23a, page 197), where 'A' is a very reversible reaction system and 'D' a very irreversible one. The extent of reversibility has been noted on the figures which follow.

Finally an experiment to see how changing the laser scan velocity effects the resulting image for a gold microband electrode is discussed.

The photocurrent images obtained in the electrochemical experiments were analysed both qualitatively by visually examining any spatial features and quantitatively by

analysing the magnitude of the photocurrent generated in the electrode containing region. The microband electrodes were analysed quantitatively in the calculation of the photocurrent for any given pixel on the electrode region, by subtracting the pixel value from the average pixel value on the electrode mounting prior to the electrode (bg) in the direction of the laser scan on the same scan line. The disc electrodes were analysed by subtracting the average pixel intensity in the centre of the electrode area on the image from the background region prior to the electrode.

The diameter of the focused spot was calculated from the numerical aperture of the lens to be approximately 2μm. The resultant local temperature rise (R.S. Hutton, D.E. Williams, ref. D-5) was approximately 1K. The movement of the focused spot across the electrode can be considered as a perturbation with a laser beam irradiation time (characteristic time scale) $\tau = 2r / v_p$ where r denotes the laser spot radius and v_p the laser scan pseudo-velocity. In this work, τ was varied over the range 1 - 100μs. The theory for the thermal response for the scanning Gaussian laser beam has been developed here.

Appendix J (part 2) may be consulted for further details of experimental setting and image parameters for the photocurrent images given in this chapter.

4.4 COMPOSITION OF THE MATERIALS

The microband electrodes were analysed to determine the composition and surface structure and hence the physical properties of the materials used in the electrode. This was especially important for the commercially screen printed gold band electrodes as they did not behave as expected for pure gold after being used for a period of time. This was due to the presence of other elemental contaminants in the gold bands present as a consequence of the manufacturing process.

Optical Imaging of the Different Types of Gold Microband Electrodes

Light microscope images of the different gold bands are given in figure 4.7.

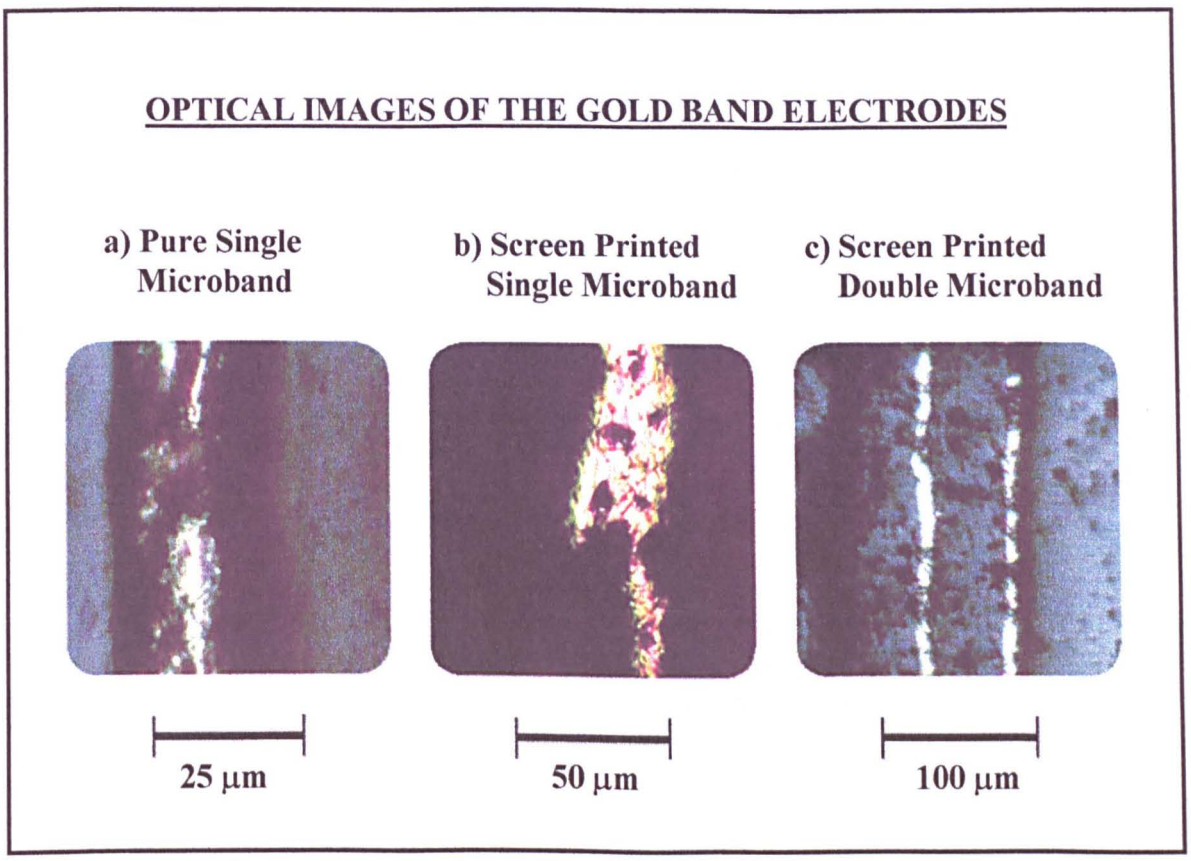

Notes: The structure of the electrodes given in figure 4.1 is as follows; a) a pure single gold microband electrode- consisting of a thin pure gold foil sandwiched between two glass slides, b)a screen printed single microband electrode- consisting of a gold band with a serrated edge which is formed between an insulator ($BaTiO_3$ dispersed in a lead silicate glass, which is comparable to light flint in composition) and a ceramic tile, c) A screen printed double gold microband electrode- from left to right shows, epoxy resin - insulator - gold - insulator - gold - insulator, where the insulator and ceramic tile were made of the same materials as the single screen printed band

figure 4.7

Microprobe Analysis of the Screen Printed Microband Electrodes

Analysis of the screen printed microband electrodes was carried out using the microprobe in order provide at high resolution scanning electron images, elemental concentration maps, and quantitative analysis of the principal elements present.

SEM images (such as that in figure 4.8) showed the porous nature of the insulator material. There were also a few small holes in the ceramic but not as many as in the insulator. It was found that when the pores on the insulator occurred next to the gold band, dips in the gold band resulted as a bit of the gold next to the hole can easily be polished away. However these dips in the gold were very shallow and were not noticeable by any means except confocal optical means and the photocurrent generated along the length was usually seen as uniform along the length with the dips in it.

SECONDARY ELECTRON IMAGE OF THE SCREEN PRINTED DOUBLE GOLD MICROBAND ELECTRODE

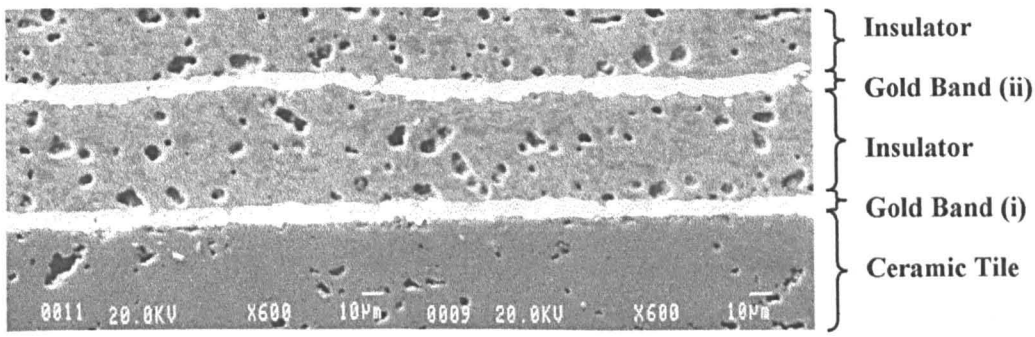

Note : This image was recorded using the electron probe microanalyser.

figure 4.8

The insulator- Microprobe analysis (figure 4.9) showed that the insulator contains mainly Si and Pb as well as Ca and clumps of Ti and Ba. The quantitative analysis showed that the insulator contained 12% lead, 18% silicon and 3% calcium (by % weight ,where the % weight of all the elements present at one spot adds to 100%). It is known that these elements will be present as an oxide where Pb will be as PbO (= 12% + 1% = 13%) and Si will be as SiO_2 (18% + 26% = 36%). So the insulator can be described as a dispersion of $BaTiO_3$ in a lead silicate glass (PbO : 13%, SiO_2 : 38%). The physical and mechanical properties of light flint were used as a guide to the properties of the insulator material. (Flints are materials composed of primarily SiO_2 and PbO where light flint contains less than 40% PbO, ordinary flint between 40-50% PbO and heavy flint more than 50% PbO and very heavy flint more than 70% PbO.)

MICROPROBE ELEMENTAL MAPS OF THE SCREEN PRINTED DOUBLE BAND ELECTRODE : Principal Elements in the Insulator

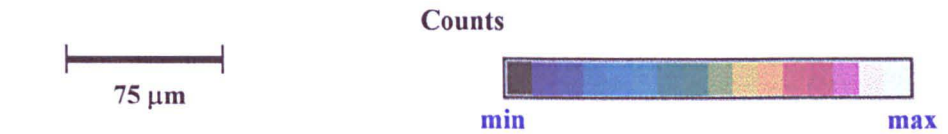

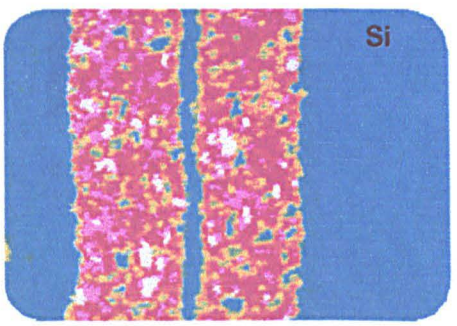

Crystal- Thallium Acid Phthalate
77.465 mm (x-ray line Kα)

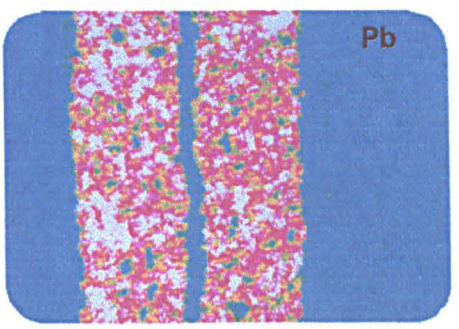

Crystal- Pentaethyritol
169.095 mm (x-ray line Mα)

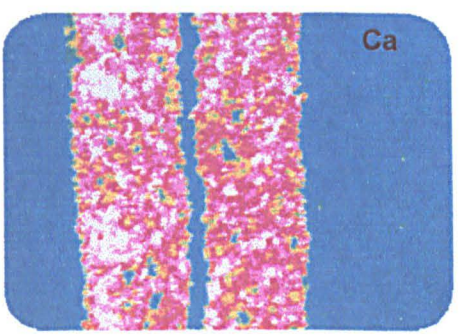

Crystal- Pentaerythritol
107.540 mm (x-ray line Kα)

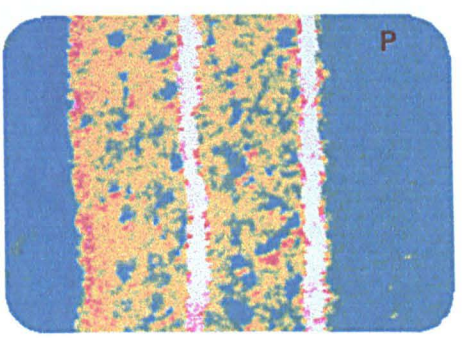

Crystal- Thallium Acid Phthalate
66.935 mm (x-ray line Kα)

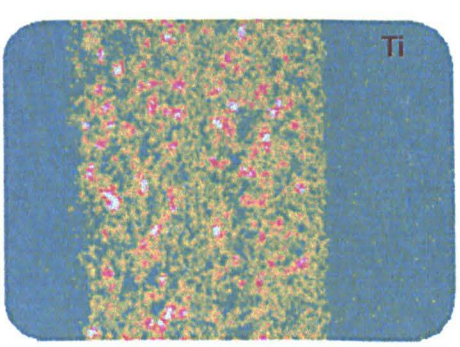

Crystal- Lithium Fluoride
191.135 mm (x-ray line Kα)

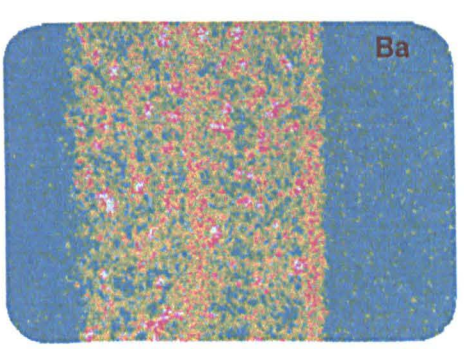

Crystal- Lithium Fluoride
192.795 mm (x-ray line Lα)

Notes: Sample = screen printed double gold microband electrode, scan type = unidirectional, movement type = stage, total area sampled in experiment = 250 x 250 μm (250 x 250 pixels), pixel dwell time = 125 ms. The spectrometer position (mm) has been noted for each crystal used as well as the x-ray line it corresponds to.

figure 4.9

The ceramic tile- This was the base material on to which the gold and then the insulator was printed on to. This was known to be an high alumina ceramic (96% Al_2O_3). Microprobe elemental map analysis (see figure 4.10.) also showed clumps of Mg probably present as MgO.

MICROPROBE ELEMENTAL MAPS OF THE SCREEN PRINTED DOUBLE BAND ELECTRODE : Principal Elements in the Ceramic Tile

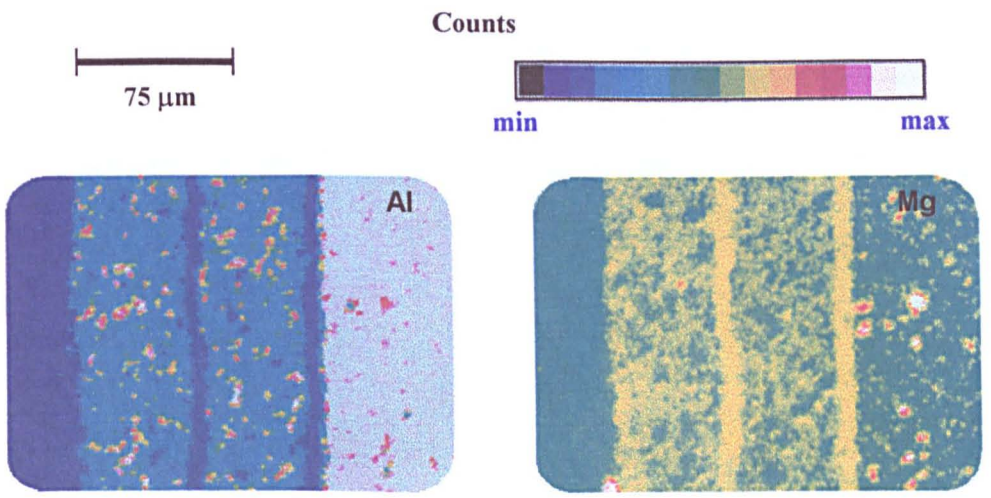

Crystal- Thallium Acid Phthalate 90.665 mm (x-ray line Kα)

Crystal- Thallium Acid Phthalate 107.515 mm (x-ray line Kα)

Notes: sample = Screen printed double gold microband electrode, scan type = unidirectional, movement type = stage, total area sampled in experiment = 250 x 250 μm (250 x 250 pixels), pixel dwell time = 125 ms. The spectrometer position (mm) has been noted for each crystal used as well as the x-ray line it corresponds to.

figure 4.10

The gold microbands- These contained mainly gold as the name would suggest but electron microprobe analysis (Joel Superprobe JXA-8600) of the screen printed electrode (figure 4.11.) revealed the presence of Cd (0.05 %), Cu (0.12%) , Zn (0.010%), Si (0.2%), Ca(0.05%) as well as Ti, Ba and P throughout the gold. It was found that the width occupied by the Cd was wider than the width occupied by the gold on its own. The Cd segregated to the interfaces between gold and insulator and gold and ceramic tile and diffused into the insulator (found to be slightly porous) during the firing process. As a result cadmium was found in much higher concentration on the very edge of the gold band (0.20-0.35%). Hence the detailed composition of the two screen printed gold bands in the double microband electrodes was different one of the

bands being between insulator on both sides and the other between insulator and ceramic.

MICROPROBE ELEMENTAL MAPS OF THE SCREEN PRINTED DOUBLE BAND ELECTRODE : Principal Elements in the Microbands

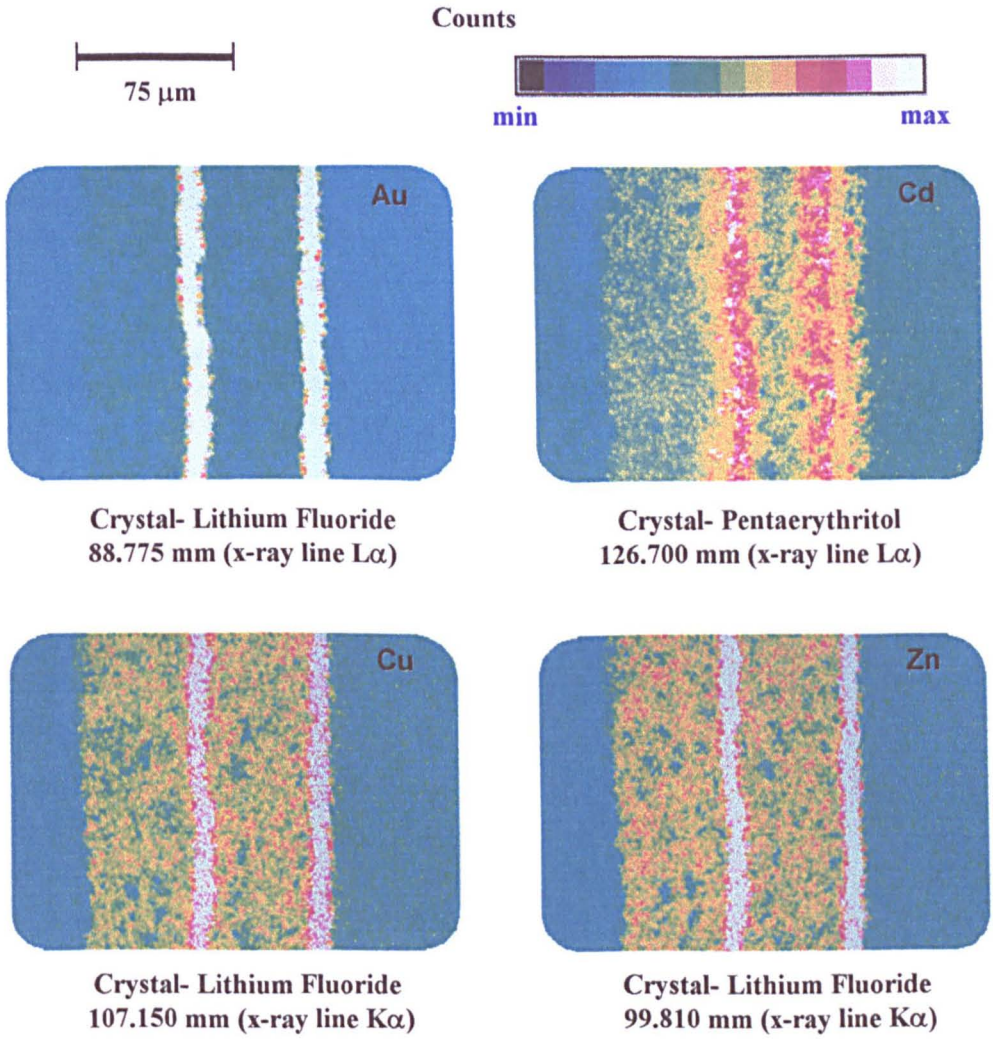

Notes: Sample = screen printed double gold microband electrode, scan type = unidirectional, movement type = stage, total area sampled in experiment = 250 x 250 µm (250 x 250 pixels), pixel dwell time = 125 ms. The spectrometer position (mm) has been noted for each crystal used as well as the x-ray line it corresponds to.

figure 4.11

The Physical and Mechanical Properties of the Electrode Materials

Physical properties for the various materials used in this work:

material	c_p / J g^{-1} K^{-1}	ρ / g cm^{-3}	K / W cm^{-1} K^{-1}	D / cm^2 s^{-1}	λ_T / s
gold	0.129	19.3	3.17	1.273	7.85×10^{-9}
water	4.181	1.00	6.0×10^{-3}	1.435×10^{-3}	6.88×10^{-6}
ceramic 95% Al_2O_3	0.774	3.8	0.23	7.820×10^{-3}	1.27×10^{-7}
insulator (light flint)	0.67	3.26	7.95×10^{-3}	3.640×10^{-3}	2.75×10^{-7}
glass (pyrex)	0.85	2.23	11.30×10^{-3}	5.961×10^{-3}	1.68×10^{-6}

Note: The above values were taken directly or calculated from the following literature sources: A) CRC hand book 73rd edition (1992-1993), B) Macmillan's Chemical and physical data book (1992), C) Nuffield Book of Data (1986)

Where:

c_p = specific heat capacity,

ρ = density , K = thermal conductivity

2r = minimum spot size,

D = thermal diffusivity,

λ_T = time scale for thermal diffusion,

and $$2r \sim \frac{\lambda}{2N_A} = \frac{500 \times 10^{-9}\,m}{0.24} = 2 \times 10^{-6}\,m,\ r^2 = 1 \times 10^{-8}\,cm^2,$$

$$D = \frac{K}{c_p \rho},$$

$$\lambda_T = \frac{r^2 c_p \rho}{K} = r^2 x \frac{1}{D}.$$

4.5 Cyclic Voltammetry

Cyclic voltammetry was carried out using the pure gold disc electrode over a wide potential range from -2 volts to +2 volts in order to show the various reactions which occur between the gold and $Fe^{II}(CN)_6^{4-}$ solution. The results found follow (figure 4.12).

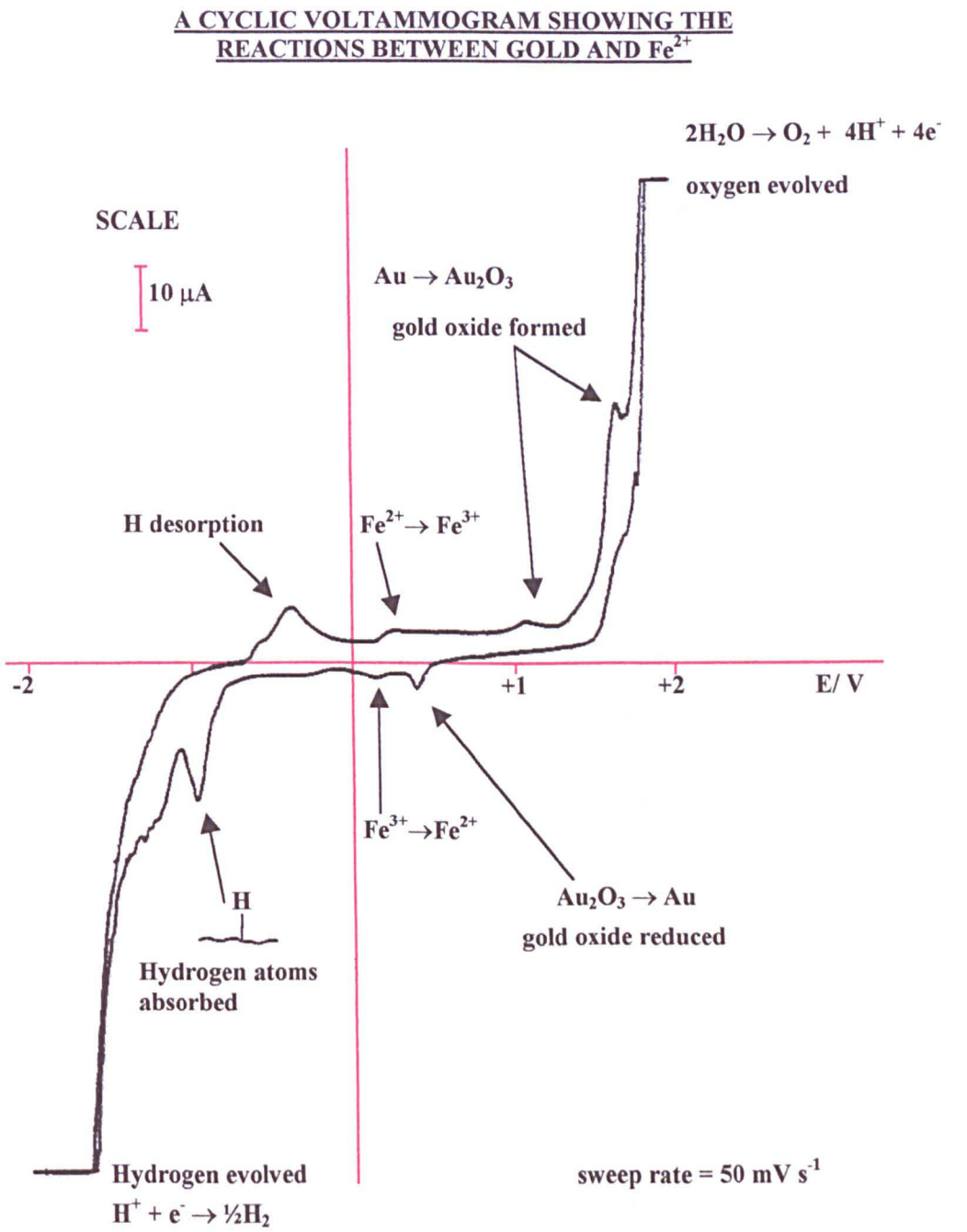

Notes: Sample = gold macro disc (500 μm diameter), solution = $K_4Fe^{II}(CN)_6$ (5 mM), K_2HPO_4 (0.1 M) and KH_2PO_4 (0.1 M). Reversibility = A.

figure 4.12

EFFECT OF SWEEP RATE ON THE CYCLIC VOLTAMMETRY FOR THE $Fe(CN)_6^{3-}$ / $Fe(CN)_6^{4-}$ REDOX COUPLE ON A GOLD ELECTRODE

a) Cyclic Voltammetry

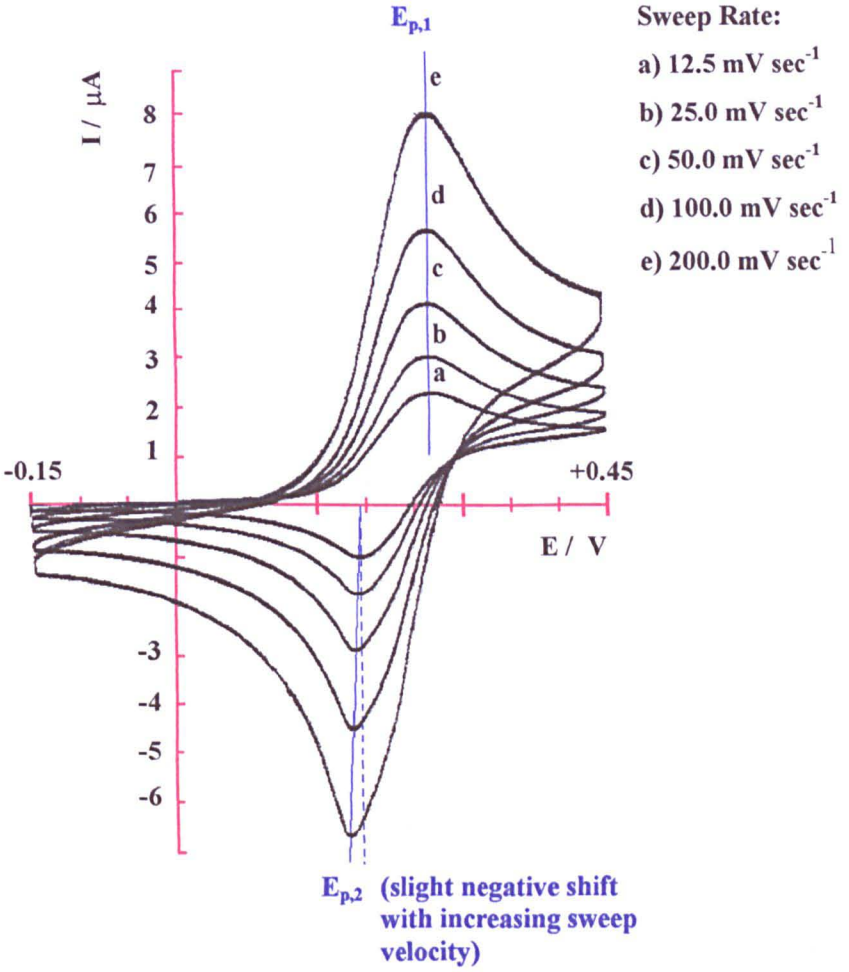

b) Variation of the Current with the Square Root of the Sweep Rate

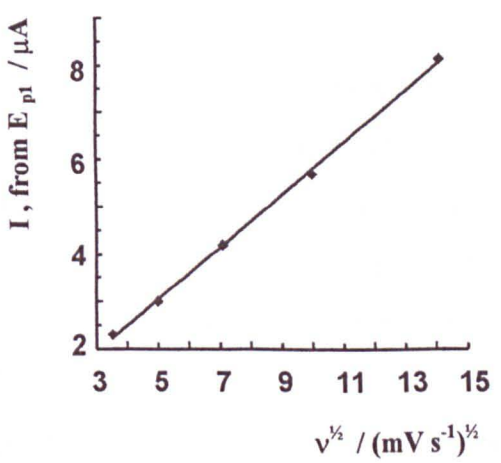

Notes: Sample = gold macro disc (500 µm diameter), solution = $K_4Fe^{II}(CN)_6$ (5 mM), K_2HPO_4 (0.1 M) and KH_2PO_4 (0.1 M). Reversibility = A.

figure 4.13

Pretty good reversibility of the reaction on such a gold electrode was shown by cycling over a smaller potential range between -150 to +450 mV at different scan rates (figure 4.13a). The characteristics found on the cyclic voltammograms confirm the presence of mild quasi-reversible characteristics. These characteristics include the fact that ΔE_p is greater than [59/n] mV and increases with increasing sweep rate, but it must be noted that ΔE_p is quite close to [59/n] mV at the slowest speed used here. Another feature indicative of quasi-reversible behaviour is that E_p^c shifts negatively with increasing potential sweep rate. In addition a graph of current versus the square root of the sweep rate (figure 4.13b) was plotted, from the data on the cyclic voltammograms, and this looked fairly linear in nature. As a straight line on this type of graph is indicative of the reversibility this shows that the system is near reversible.

4.6 Effect of Electrode Geometry

General Features on the Photocurrent Image

It has been shown previously (D.E. Williams and coworkers, refs. C1-21, C1-22, D-2, D-3, D-5) that the photothermally - induced current change should be maximum at the half-wave potential for the redox reaction as given by a conventional technique (cyclic voltammetry). The theory has been given in section 4.1. Typical photocurrent images are shown in figure 4.14, together with the corresponding optical images for comparison. These images show that only the electroactive structures can be seen on the photocurrent images whereas all the structures present can be seen on the confocal optical images. Figure 4.14 also illustrates a negative current perturbation following the image of the band: this 'shadow' means that, after the spot passed over the band, the current momentarily diminished below the steady state level. The magnitude and width of this minimum tracked that of the maximum as the potential changed. Such an effect at the edge of a disc has been interpreted previously (ref. D-2) as due to the relaxation of concentration within the boundary layer after the heating stopped.

EXAMPLES OF PHOTOCURRENT IMAGES

a) Pure- Single Gold Microband Electrode

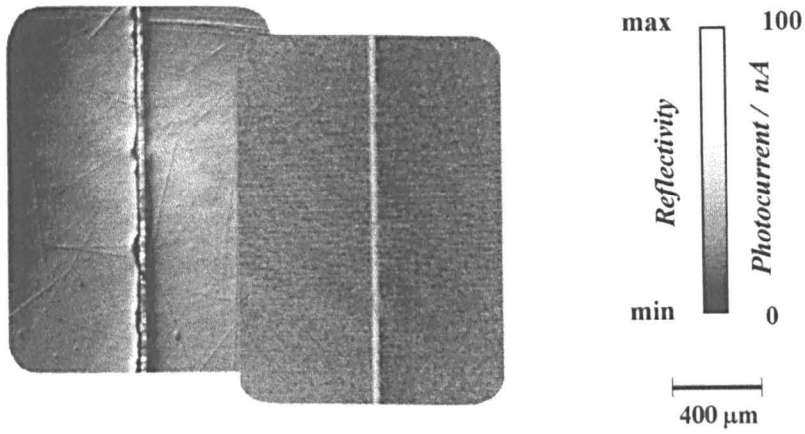

b) Screen Printed- Single Gold Microband Electrode

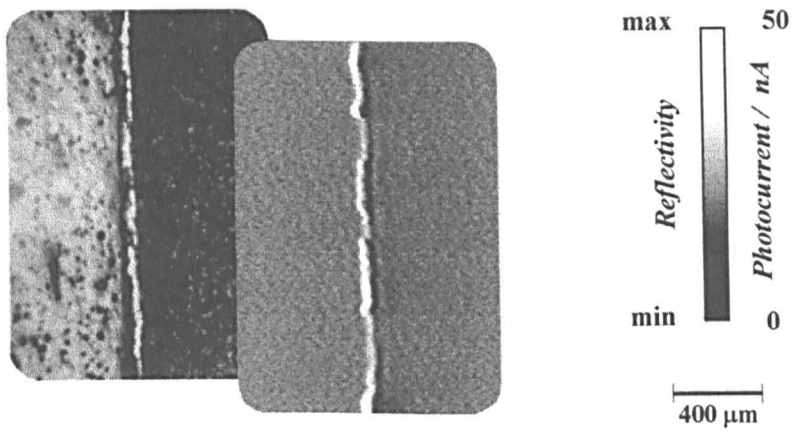

c) Screen Printed- Double Gold Microband Electrode

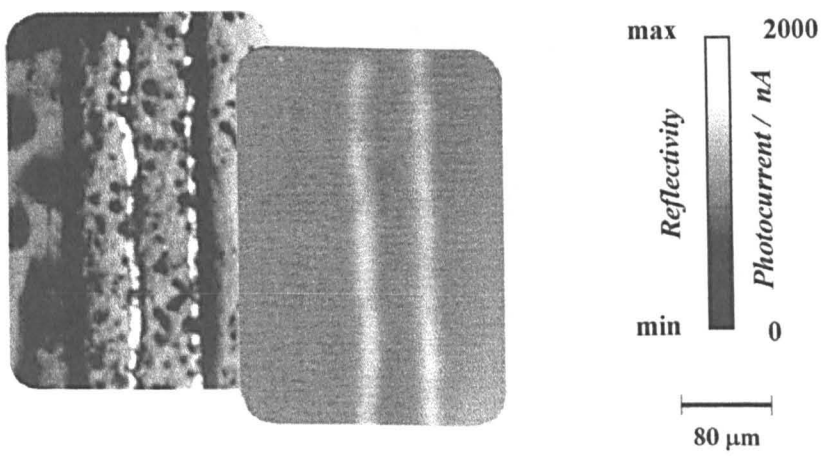

Notes: LHS = confocal optical reflectivity images , RHS =Photocurrent images taken in a solution containing $K_4Fe^{II}(CN)_6$ (5 mM) , K_2HPO_4 (0.1 M) and KH_2PO_4 (0.1 M). Lens = x4 (N.A. = 0.12), (a) E= –100 mV, v_p = 12.32 cm s^{-1} , τ = 16.3 μs, reversibility = A. (b) E= +200 mV, v_p = 13.39 cm s^{-1}, τ =14.93 μs, reversibility = A. (c) E= +400 mV, v_p = 8.53 cm s^{-1}, τ = 23.45 μs, reversibility = C .

figure 4.14

Differences between the pure gold band electrode and the screen printed electrode included the fact that the trailing dark shadow on the pure gold single band electrode was much more subtle than that on the screen printed electrodes. It was much harder to track down the minima of the dark shadow compared to the bright band, as the bright band has a very sharp peak on the pure gold but the image intensity of the dark shadow in this case dips down very slowly and in addition it goes back very slowly to the background intensity. Hence, where the dark shadow ended could not be found and therefore the dark shadow width could not be noted. The shadow for the screen printed band however was much clearer.

GOOD RESOLUTION IS POSSIBLE IN PHOTOTHERMAL IMAGING

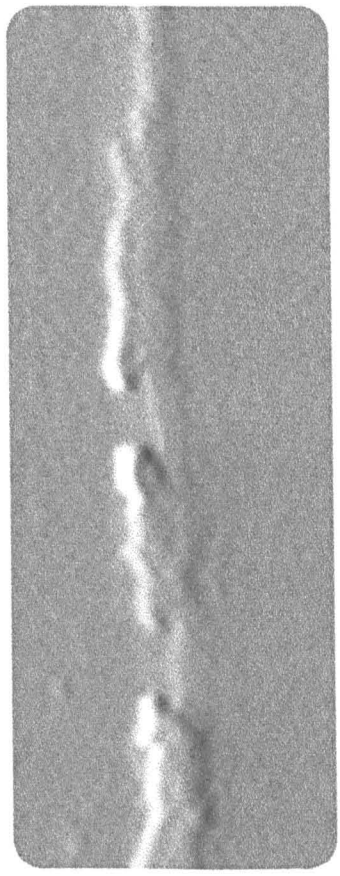

150 μm

Notes: The mesh markings from the manufacture process can clearly be seen. Grey scale = 20 nA . Solution = $K_4Fe^{II}(CN)_6$ (5 mM), K_2HPO_4 (0.1M) and KH_2PO_4 (0.1 M). Sample = screen printed single gold band, poisoned state (reversibility = B), v_p = 2.05 cm s^{-1}, τ = 29.94 μs, E = + 200 mV, this image is composed of two images which were taken one below the other during the experiment.

figure 4.15

The printed gold single band electrodes were irregular in width as a consequence of a variation in the printing procedure. They showed mesh markings ; a common artefact in which the gold does not spread evenly over the surface, so retaining a profile reflecting the mesh through which it is printed (figure 4.15). The alternate thick and thin areas showed up clearly in the photocurrent imaging. There was an enhancement of the photocurrent at the very edge of the thick part of the electrode, figure 4.15. This image demonstrates clearly resolution on a micrometer scale of spatial variations in electrochemical activity.

Effect of Potential on the Photocurrent Image

Effect of potential on the photocurrent image of a gold disc

Using the gold disc electrode again a cyclic voltammogram was recorded using a solution containing $5x10^{-3}$ mol dm^{-3} $K_4 Fe^{III}(CN)_6$ as well as $K_4Fe^{II}(CN)_6$ and then a photocurrent imaging experiment was carried out using the confocal scanning laser microscope. Then photocurrent images were recorded at various potentials between -300 and +300 mV. The images recorded were found to change colour (represented by the pixel value) as the potential was changed. The potential at which maximum current change occurs could easily be identified visually to be in the region of +200 mV as shown in figure 4.16. The photocurrent image data was analysed and the average photocurrent recorded over the electrode region on was noted for each potential. From this data a graph of photocurrent vs potential was plotted (figure 4.17a). Summarising the observations made in changing the potential has on the photocurrent images obtained for the gold disc, we can see that with increasing potential there is a sharp peak in the pixel intensity recorded in the + 200 mV region. Similar results were found in previous work done for just $[Fe^{II}(CN)_6]^{4-}$ (see section 4.1 - Introduction).

EFFECT OF POTENTIAL ON A GOLD MACRODISC

a) Effect on the Photocurrent Image at Various Potentials

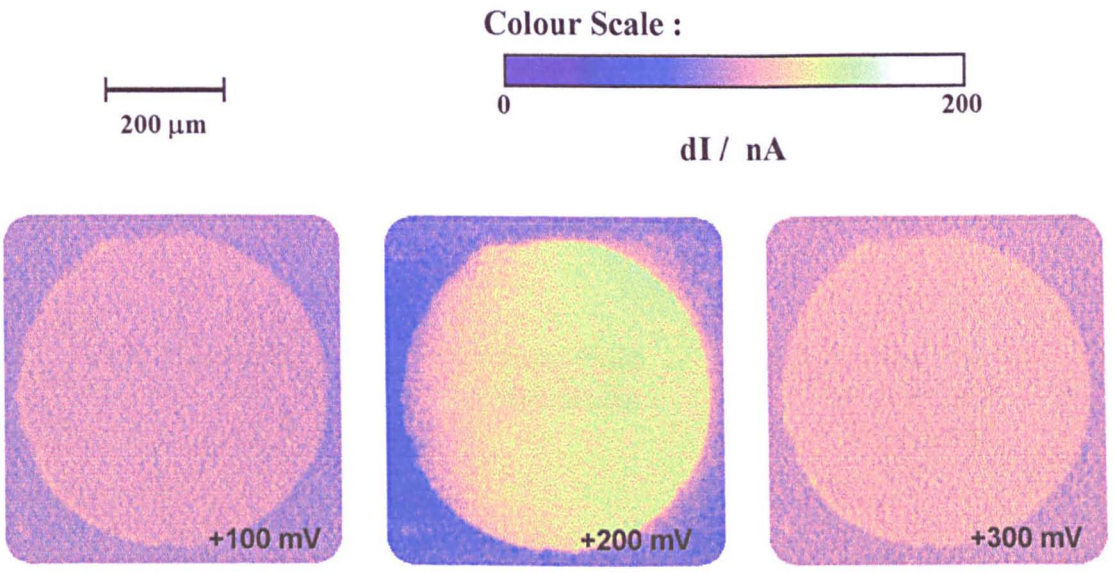

b) Cyclic Voltammetry for the Gold Disc Shown in the Above Images

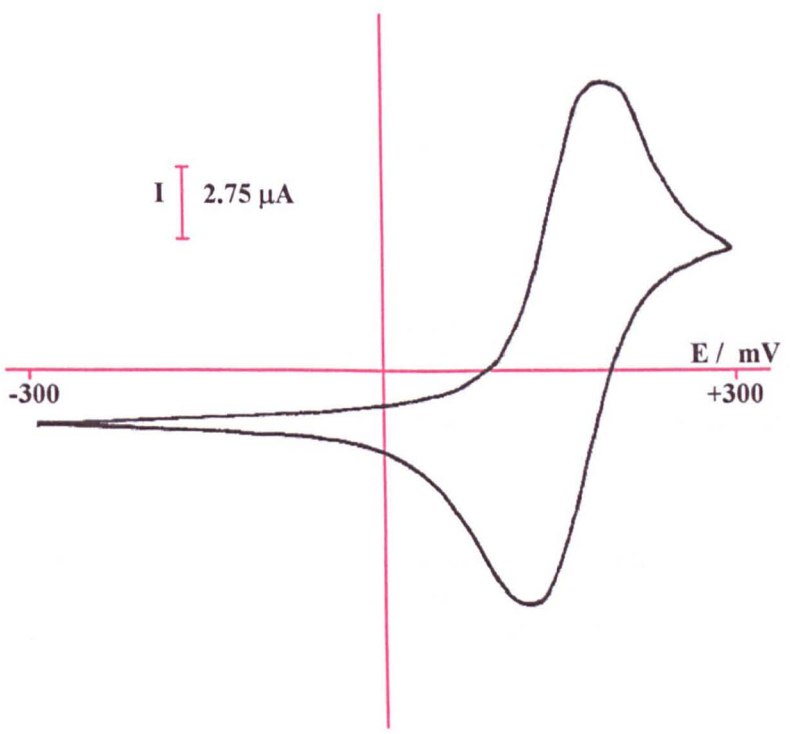

Notes: Sample = gold macro disc (500 μm diameter), solution = $K_4Fe^{II}(CN)_6$ (5 mM), $K_3Fe^{III}(CN)_6$ (5 mM) K_2HPO_4 (0.1 M) and KH_2PO_4 (0.1 M). a) Examples of photocurrent images, v_p = 4.98 cm s^{-1}, τ = 20 μs laser spot diameter = 1 μm, lens x10 (N.A) = 0.25. b) Cyclic voltammetry with a sweep rate (υ) = 0.5 V sec^{-1}.

figure 4.16

Comparison with the photocurrents observed on band electrodes

Similarly the effect of potential on the photocurrent image for the pure gold home-made microband electrode (figure 4.14b) and the screen printed double gold microband electrode (figure 4.14c) was recorded and the images analysed to give the photocurrent generated on the electrode region.

THE EFFECT OF CHANGING POTENTIAL ON THE PHOTOCURRENT

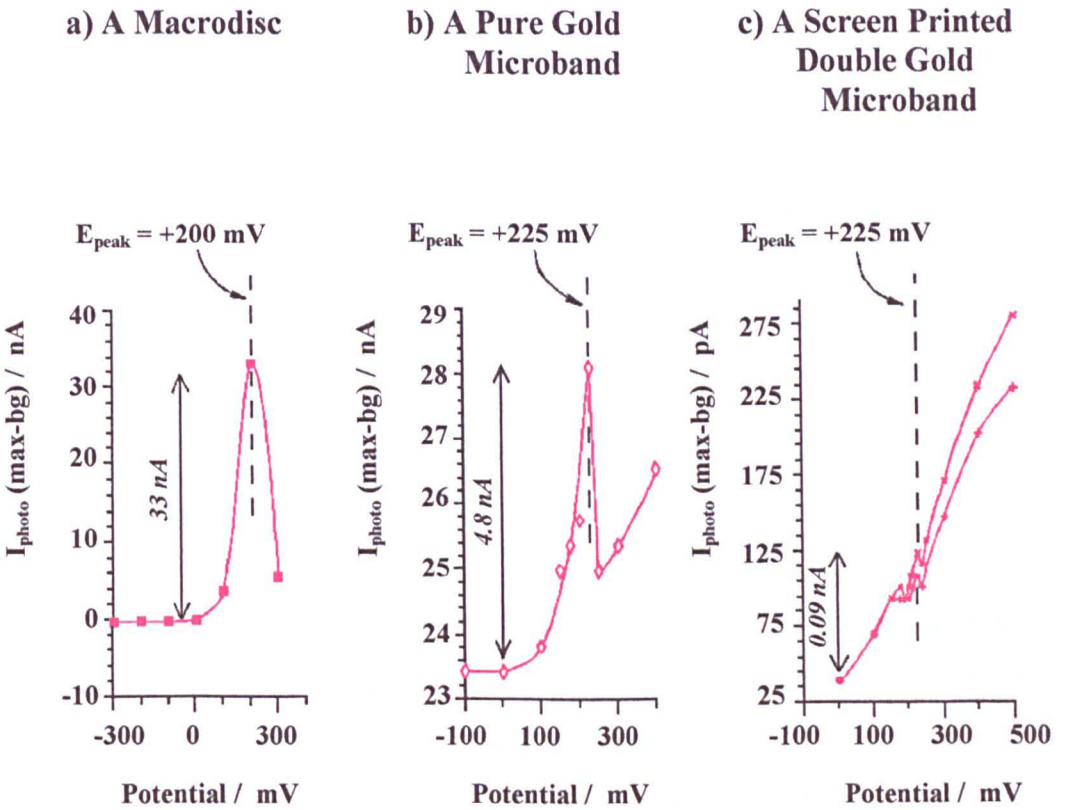

Notes: Photocurrent variation with potential for the various gold electrodes, reversibility =A : (a) v_p = 4.98 cm s^{-1}, τ = 20 μs). (b) v_p = 12.32 cm s^{-1}, τ = 16.3 μs. (c) v_p = 8.53 cm s^{-1}, τ = 23.45 μs, where (i) is the inner band adjacent to ceramic tile and (ii) is the outer band).

figure 4.17

The images themselves did not show much of a change at $E_{½}$ by direct observation, as the change was much more subtle but the graphs plotted of photocurrent vs potential from these images did show a change. Graphs plotted of photocurrent vs potential are given in figures 4.17b (pure gold single microband) and 4.17c (screen printed double

gold microband). From cyclic voltammetry the limiting current density for ferrocyanide oxidation (5×10^{-3} mol dm^{-3}) on the printed double gold band electrodes (10 μm width spaced 50 μm apart) was identical to that on the pure gold single band electrode (20 μm).

It can be seen from the comparison of the graphs plotted (figure 4.17) the photocurrent observed for an apparently reversible system was very different for the different types of electrode used. However a peak in the photocurrent was found to at occur at $E_{½}$ for all the electrodes.

For the homemade band, as the potential was increased there was a general rise in the pixel intensity (and hence the induced photocurrents) in the bright band on the photoelectrochemical image with a peak superimposed on the rising curve in the +200 mV region. Similarly for the screen printed band, the line, on the pixel intensity versus potential graph, showed a slight rise in the intensity with potential (figure 4.14).

Effect of potential on the width of the band observed in the photocurrent image
With a good, reversible, microband system the width of the photocurrent image of the pure gold band was found to change subtly with potential.

Under steady-state heating conditions at a potential equal to $E_{½}$ the photocurrent image was slightly wider than the optical image. With steady state heating, the potentials above and below $E_{½}$ were found to decrease back down to the optical width. Figure 4.18 shows a graph of how the width on the photocurrent image changes with potential. However the bright band on the photocurrent image was not as wide even at $E_{½}$, wide as it would be under instantaneous heating conditions (as shown with faster laser scan times, in section 4.8).

WIDTH OF THE BAND ON THE PHOTOCURRENT IMAGE AT VARIOUS POTENTIALS

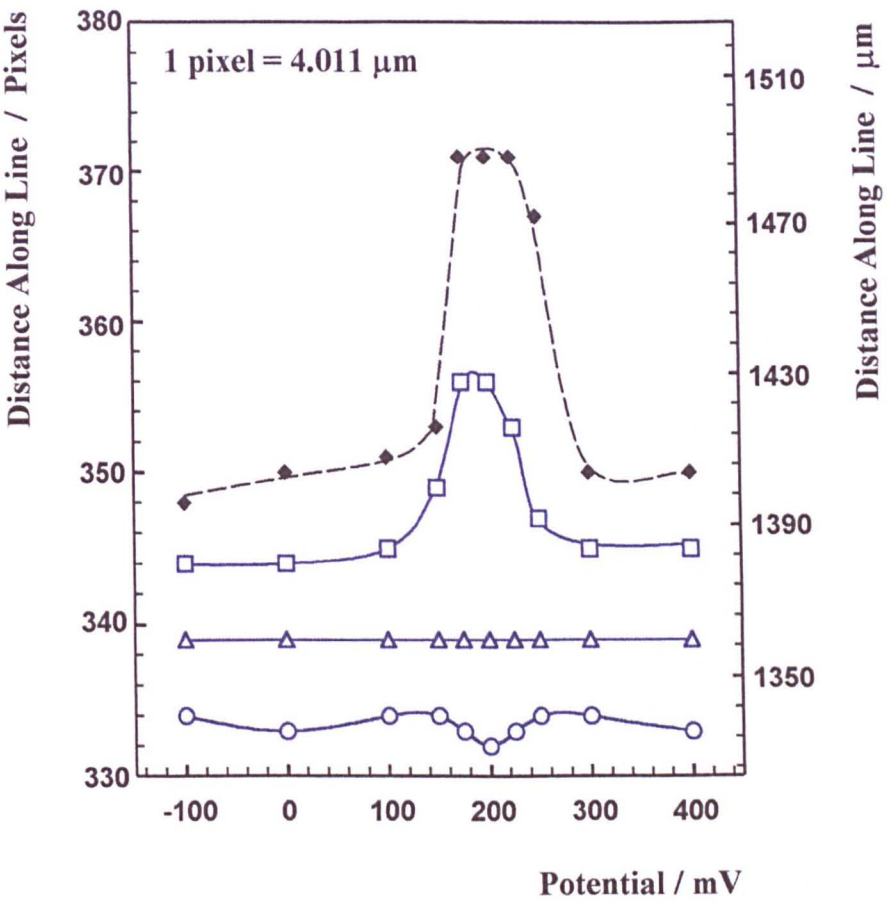

Photocurrent Image Features : -

- ○ start of bright band
- △ maximum photocurrent of bright band
- □ end of bright band / beginning of dark band
- ◆ minimum photocurrent of dark band

Notes: Sample = pure gold microband, solution = $K_4Fe^{II}(CN)_6$ (5 mM), K_2HPO_4 (0.1 M) and KH_2PO_4 (0.1 M), v_p = 12.32 cm s^{-1} , τ = 16.3 μs, total area sampled in the experiment = 3080 x 1903 μm (768 x 512 pixels), x4 lens (N.A. = 0.12), 2r = 2 μm, reversibility = A.

figure 4.18

Conclusions drawn on the effect of potential on the photocurrent images observed
The most remarkable effect observed here has been the strong dependence of the photocurrent signal on the geometry of the electrode.

The explanation for the difference in signal magnitude between disc and line electrodes, that the temperature change was greater on the disc electrode, is not justifiable, since for the line electrode the heated zone was confined on two sides by material (alumina substrate, ceramic insulator or glass) whose thermal diffusivity was lower than that of gold so the heat would not be withdrawn from the gold efficiently into these materials implying that the temperature rise on the gold should have been greater.

In a section 4.1 an expression for the photothermal current change for a reversible electrode reaction at a microdisc electrode has been developed (ref. D-5). This development assumed that the whole electrode was heated, thus greatly simplifying the calculation : the boundary conditions are that the ratio of concentration of oxidised and reduced species at the electrode surface is given by the Nernst equation and that sufficiently far from the electrode the concentrations are those of the bulk solution ; the current is determined by the flux of material to the surface. When only a small part of the surface is heated, however, the circumstance is one of a perturbation of the diffusion field around the electrode : one can imagine an axially symmetric diffusion field around the perturbed area, in a volume where the initial and boundary conditions are not that the concentration of species is uniform, but that the concentration is spatially varying in a fashion determined by the geometry of the whole electrode.

The important difference between the geometries investigated here is now plain : on the disc electrode, in the plane of the electrode, in both directions the electrode is much larger than the perturbed spot, whereas on the line electrode in one dimension the electrode is comparable in size to the perturbed zone. Furthermore, the band electrodes have one dimension comparable to the concentration boundary layer thickness.

On the double band electrode the concentration boundary layers for the two bands overlapped. This can be explained as two isolated 10μm bands (with 2 x 4 edges) would be expected to have a greater limiting current density than one 20μm wide band (with 4 edges) as there are more edges present for the two electrode case than the one,

and it is known that greater currents are produced at the edges than the electrode centre. Hence microbands are said to have a strong edge effect (ref. H-7). The diffusion layer at a microband electrode can be considered to be a semi-cylinder. If band electrodes are sufficiently close together an overlap of the diffusion layers can occur. The resulting behaviour of the diffusion limiting current would then be as if there are only the number of edges equivalent to the single band electrode, so the resulting diffusion limiting current will be smaller than that expected for two isolated electrode.

THE BEHAVIOUR OF DIFFUSION LAYERS AT A DOUBLE MICROBAND ELECTRODE

a. **No overlap of diffusion layers**

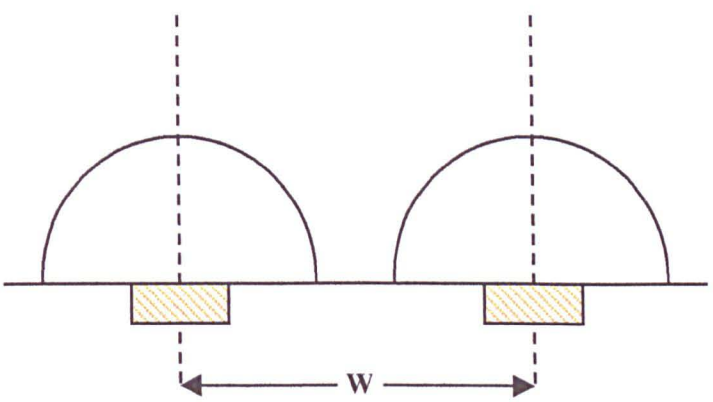

$$\delta < \frac{W}{2}$$

(The current is the sum of current expected for each single electrode)

b. **Overlap of diffusion layers**

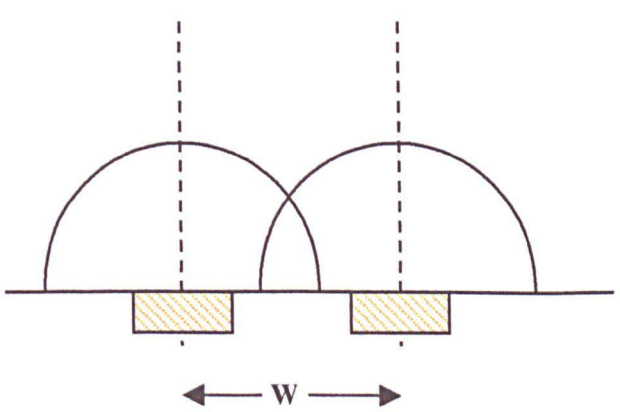

$$\delta > \frac{W}{2}$$

(The current is lower than the sum of current expected for each single electrode)

Notes: W = the central distance between two adjacent electrodes and δ = the diffusion layer thickness.

figure 4.19

Work carried out by J. Huangaxian and coworkers (1992, ref. H-7) showed that when an array of microband electrodes were electrolysed for a sufficiently long enough time the diffusion layers at each band partially overlapped and the total current was smaller than the sum of the currents at all the single microbands individually. This effect is known as the shielding effect (see figure 4.19).

In addition on the double band electrodes the perturbation effected only one band at a time. Theoretical treatment of this problem is not straight forward. Figure 4.17 shows that the image of the gold band apparently extended beyond the geometrical confines of the gold with a maximum width at the half-wave potential. We attribute this to an effect of heat transfer from the insulating boundary to the electrode as the spot moves towards and away from the electrode.

The images of the microband electrodes are also notable because they show a photocurrent at low potentials, increasing steadily with increasing potential. In part this effect was observable because the background current was small. The photothermal effects on the ferrocyanide oxidation reaction were also small, so observation could be made on a sensitive current scale. Photoelectric effects in anodic gold oxides are only observable at potentials greater than about +800 mV. Therefore if one postulates that the effects arise as a consequence of photoelectric effects in a surface film, the question arises as to what the film might be. Three other possibilities exist. One is photo-hole emission, the second is a thermal effect on the value of the double layer capacitance, causing a transient charging current; the third is a thermally-induced desorption of ions from the surface (T. Hinue et al., 1995, ref. I1-8).

4.7 EFFECT OF LASER VELOCITY

Effect of Line Scan Time on the Photocurrent Image

The effect of the laser pseudo-velocity (v_p) was studied by recording the photocurrent image generated at various line scan times using a fixed lens size and electronic magnification.

Where $$v_p = \frac{\text{line distance}}{\text{line scan time}} \tag{4.27}$$

The line scan time (t_{line}) is related to the parameter ,τ , the laser beam irradiation time. This is the time it takes for the laser beam to travel a length equal to its own beam diameter.

$$\tau = \frac{1}{v} 2r \quad \text{or} \quad \tau = \frac{t_{line}}{d_{line}} 2r \quad \text{or} \quad \tau = \frac{\text{pixel dwell time}}{\text{pixel length}} 2r \tag{4.28}$$

Where 2r = laser beam diameter = 2 μm, calculated using $2r \sim \lambda \div 2N_A$.

The images recorded at each line scan time were comparable as they were all recorded at a fixed potential of +200 mV vs SCE and a fixed laser intensity (T = 100%) and at fixed high and low frequency filters of 0.1 Hz and 10 kHz.

The images recorded (figure 4.20) showed the image was blurry and wide at the very fast scan times ($\tau < 7$ μs). At around $\tau = 7$ μs the bright band on the photocurrent image was brightest and had decreased in width to approximately the size of the optical image. At very slow scan times ($\tau > 7$ μs) the line on the image was very much dimmer and close in size to the optical image.

EFFECT OF LASER SCAN VELOCITY ON PHOTOTHERMAL IMAGING

E = +200 mV,
2r = laser beam diameter = 2 μm
τ = laser beam irradiation time (the time to scan a distance equal to 2r)

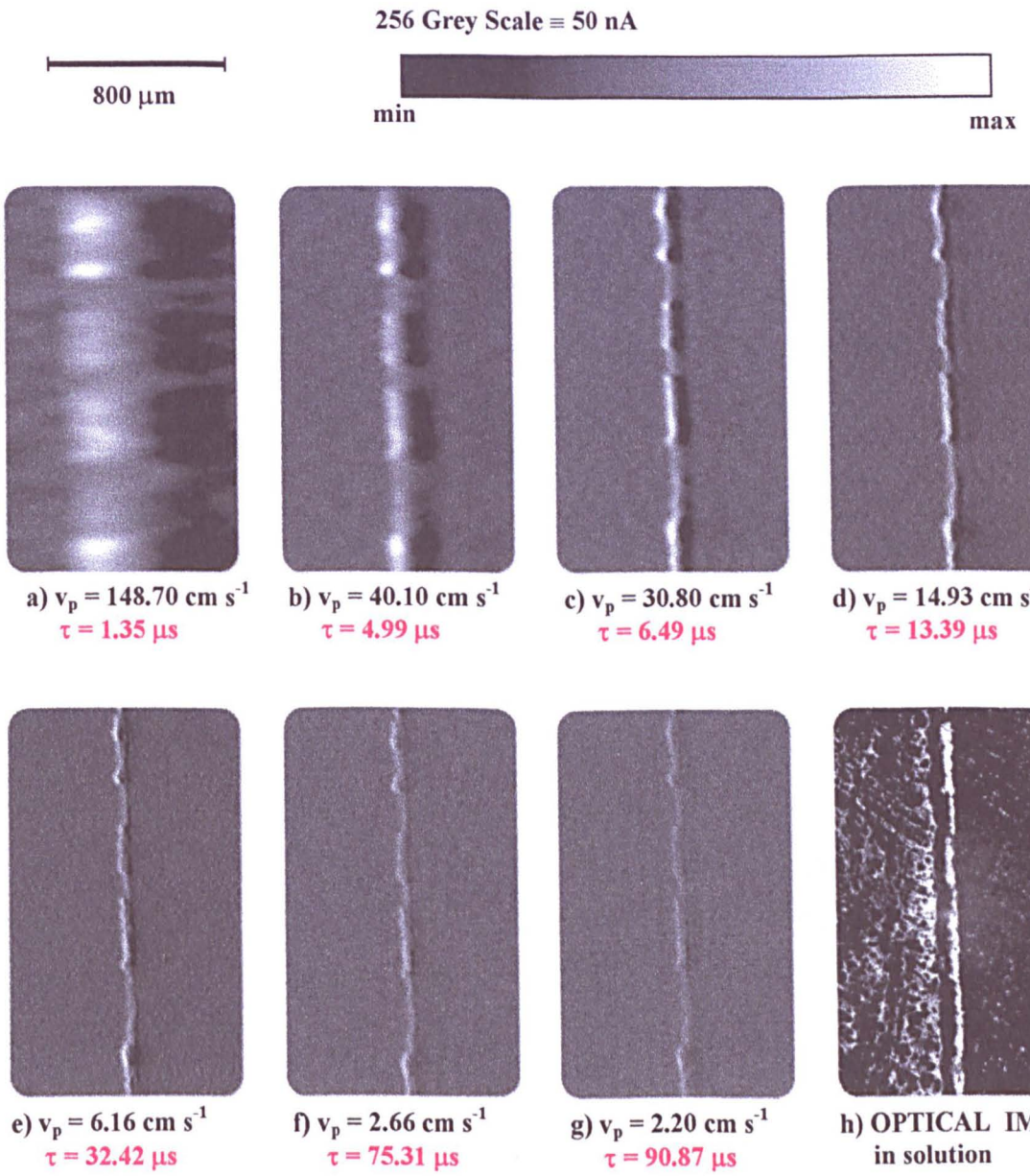

Notes: Sample = screen printed single gold microband electrode, solution = $K_4Fe^{II}(CN)_6$ (5 mM), K_2HPO_4 (0.1 M) and KH_2PO_4 (0.1M), lens magnification = x4 (N.A. = 0.12), 2r = beam diameter = 2 μm, I_s = 100% I_o, Extent of Reversibility = A.

figure 4.20

Table of observations from figure 4.20:

Velocity	Pixel Intensity (α photocurrent)	Clarity of Image	Width of Bright Band
very fast $\tau < 7$ μs	medium = bright	slightly fuzzy / blurry	wider than optical (reflective) band width
fast, $\tau = 7$ μs	high = very bright	less blurry	near optical width
slow, $\tau > 7$ μs	low = very dim	clearer detail	near optical width

It was found that zooming in electronically during the experiment produced the same effect as slowing down the laser, as the line scan time stayed the same but the line length decreased so changing the laser pseudo-velocity in the same way as if the line scan time is slowed directly at fixed magnification.

Effect on the Width of the Photocurrent Band

Line analysis was carried out on the 2nd thick band (brighter area) down from the top of the image. A line was averaged over 20 points (pixels) above and below the line going through the middle of the second bright area along the line. The data from the line analysed across each photocurrent image was used to find the width of the leading bright band and the width of the trailing dark band and the maximum and minimum photocurrent observed.

Graphs plotted (figures 4.21a and 4.21b) of the width of the bright band (+VE photocurrent area) and the width of the dark band (-VE photocurrent area) showed a marked change in the gradient at the laser beam irradiation time $\tau = 15$ - 16 μs. This just happens to be the limiting response time of the instrument (τ_{inst}) in this case. The characteristic limiting time of the instrument is due to the preamplifier was , $\tau_{inst} = 15.9$ μs (as a high frequency filter of 10 kHz was used i.e. $\tau_{inst} = 1 \div 2\pi f$, where f = 10 kHz).

EFFECT OF THE LASER SCAN VELOCITY ON THE PHOTOCURRENT BAND WIDTH

a) Width of the Bright Band on the Photocurrent Image

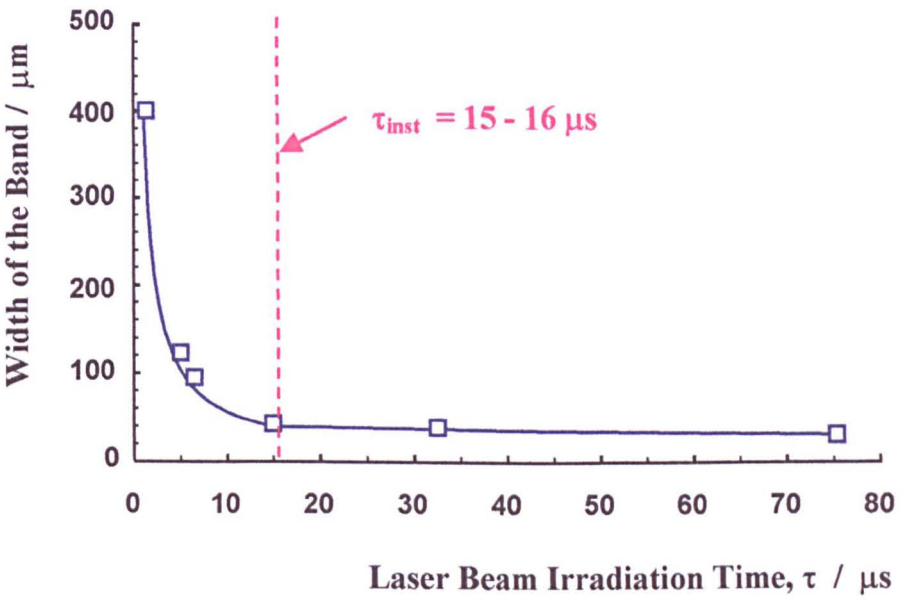

b) Width of the Dark Band on the Photocurrent Image

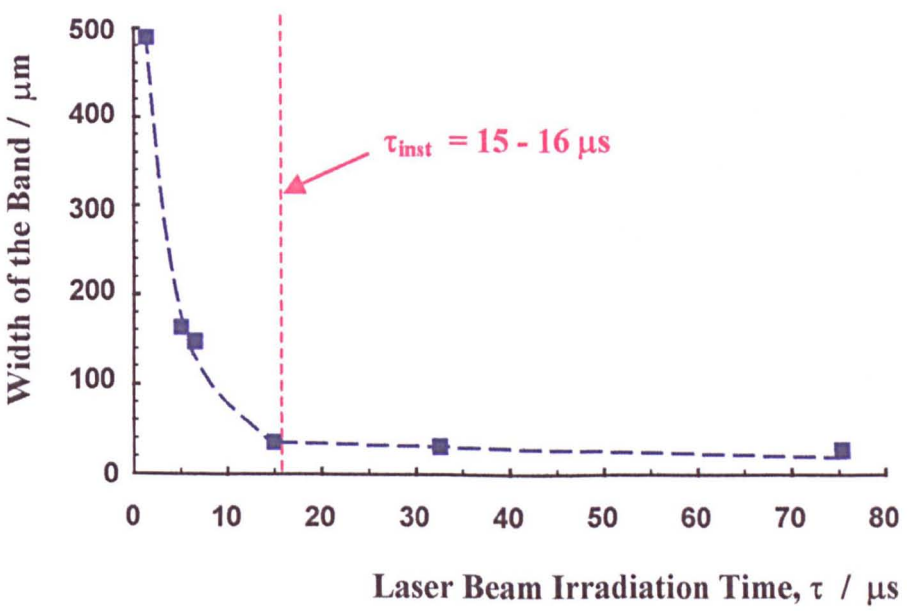

Notes: Sample = screen printed single gold microband electrode, Notes : solution = $K_4Fe^{II}(CN)_6$ (5 mM), K_2HPO_4 (0.1 M) and KH_2PO_4 (0.01 M), lens magnification = x4 (N.A. = 0.12), laser spot diameter = 2 µm, E = +200 mV, I_s = 100% I_o. Reversibility = A. Data taken from images shown in figure 4.8 .

figure 4.21

Effect on the Magnitude of the Photocurrent Generated

On the graph plotted of photocurrent vs laser beam irradiation time (figure 4.23), the maximum photocurrent on the bright band on the photocurrent image and the minimum photocurrent value on the following dark band occurred at 6-7 μs. This corresponds to, or is coincidentally the same as the time scale for thermal diffusion in the solution $\lambda_{T,\ water} = 6.9$ μs. On the electrode area the photocurrent was found to increase up to $\tau =$ 7 μs then at $\tau > 7$ μs was found to decrease again. In addition it may be argued that there is a very slight change in the curve at 15-16 μs showing a very slightly lower positive photocurrent on the electrode area. The characteristic time scale for the experiment can be defined as the laser beam irradiation time at which the greatest amount of photocurrent is generated for an experimental system, and this was found to occur at 7 μs for the system studied here.

So this showed that the transfer function determining the photocurrent generation depends on the characteristics of both the apparatus and the electrochemical cell. The fact that we are able to see the change in the trend at $\tau \approx 7$ μs is because the instrument does not actually cut-off dead at $\tau_{inst} = \frac{1}{2\pi f}$ as it is still able to pick up the signal at time scales shorter than τ_{inst} (i.e. at higher frequency values). However the response does drop drastically below this value. So there are two relaxations: one associated with $\lambda_{T,\ water}$ (shown by a marked increase in the photocurrent) and the other associated with τ_{inst} (shown by a subtle decrease in the photocurrent).

EFFECT OF THE LASER SCAN VELOCITY ON THE PHOTOCURRENT GENERATED

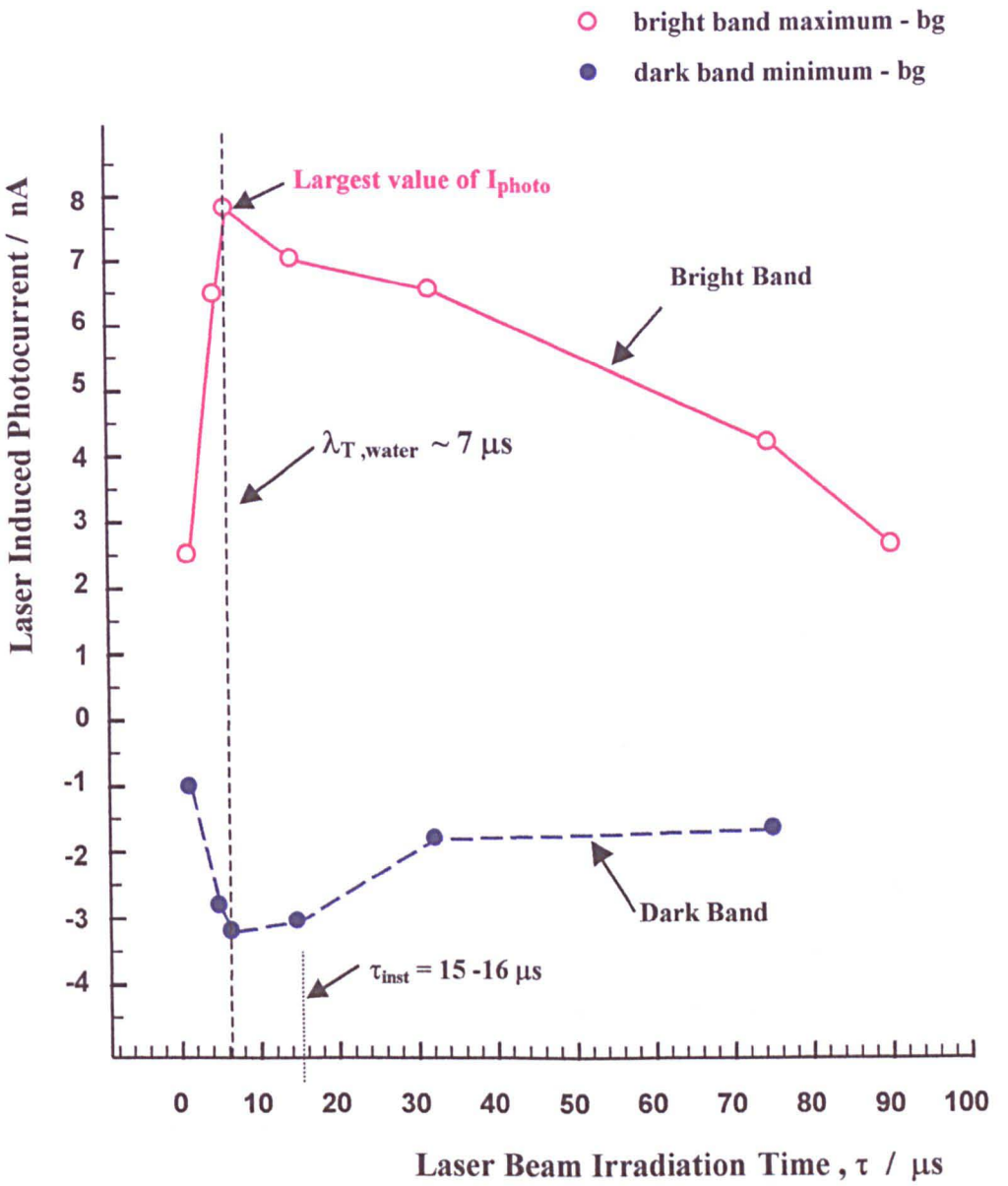

Notes: Sample = screen printed single gold microband electrode, solution = $K_4Fe^{II}(CN)_6$ (5 mM), K_2HPO_4 (0.1M) and KH_2PO_4 (0.1 M), lens magnification = x4 (N.A. = 0.12), laser spot diameter = 2 µm, E = +200 mV, I_s = 100% I_o. Reversibility = A. Data taken from images shown in figure 4.8.

figure 4.22

Theoretical Aspects of Thermally Induced Photocurrent Generation

The first question to discuss is the thermal perturbation induced by the scanning laser technique (refs. I2-5, I2-11). The thermal response for a scanning Gaussian laser beam is characterised by the ratios, γ (a geometrical factor) and ν^{-1} (a time factor).

$$\gamma = \frac{\text{beam radius } (r)}{\text{absorption depth } (\alpha^{-1})} \tag{4.29}$$

$$\nu^{-1} = \frac{\text{irradiation time } (\tau)}{\text{time scale for thermal diffusion } (\lambda_T)} \tag{4.30}$$

Where the minimum spot size is $2r \approx \frac{\lambda}{2N}$, the time to scan over the beam diameter is $\tau = \frac{1}{v} \cdot 2r$ and the time scale for diffusion $\lambda_T = \frac{r^2 \rho c_p}{K}$.

With λ the wavelength of the laser (cm), N the numerical aperture of the lens, α^{-1} the absorption depth (cm), v the laser scan velocity (cm s^{-1}), ρ the density (g cm^{-3}), c_p the specific heat capacity (J K^{-1} g^{-1}), K the thermal conductivity (W cm^{-1} K^{-1}).

Two limiting conditions can arise.

1. ***Steady state solution:*** For this limiting condition, the rate of energy delivered by the beam is balanced by the rate of conduction in the solid ($\nu^{-1} = \infty$). This is approached if the beam is scanned slowly compared to the rate of thermal diffusion, as $\nu^{-1} \rightarrow \infty$.

If $\tau > \lambda_T$, i.e. $\nu^{-1} \gg 1$:quasi-steady state conditions result

Here the temperature rise only depends on the geometrical factor. The largest temperature rise occurs when $\gamma \rightarrow \infty$ i.e. the absorption depth $\alpha^{-1} \rightarrow 0$.

2. ***Energy Density Solution:*** Another limiting solution is when the beam is scanned faster than the rate of thermal diffusion. This occurs as $\nu^{-1} \rightarrow 0$.

If $\tau < \lambda$, i.e. $\nu^{-1} \ll 1$: instantaneous heating occurs

Here the temperature rise is proportional to energy input divided by heat capacity, C. Where heat capacity = specific heat capacity x area at surface x absorption depth x density. $C = c_p \cdot \pi r^2 \cdot \alpha^{-1} \cdot \rho$.

Here $\lambda_{T,Au} = 8 \times 10^{-9}$ s $\lambda_{T,water} = 7 \times 10^{-6}$ s **$\lambda_{T,expt} = 7 \times 10^{-6}$ s.**

The characteristic time scale found experimentally, is same as that calculated for water. This shows the laser heats the gold which heats the adjacent solution. The gold cools quickly but the solution stays hot. Therefore the amount of photocurrent generated is determined by the heat transfer in the aqueous phase. The greatest amount of photocurrent is therefore generated as instantaneous heating conditions arise and the laser heats up the gold at the same rate as the solution surrounding the gold removes the heat.

Image blurring (showed by the width of the area over the gold band electrode on the photocurrent image being much greater than that on the optical image) associated with the subsequent temperature relaxation should accompany the transition from steady state to instantaneous heating with increasing laser scan velocity. Such blurring did not occur at $\tau = 7$ μs as expected, where the induced temperature rise may go through a maximum. Instead the image blurred for $\tau = 15$-16 μs, because unfortunately, the instrumentation was limited by the need to high pass filter the signal at 10 kHz for noise reduction, and this a gave a time constant ~ 15-16 μs.

4.8 POISONING OF THE GOLD ELECTRODES

The Poisoning of a Screen Printed Double Gold Microband Electrode

The characteristics of the screen printed microband electrodes changed with time of operation: cyclic voltammetry showed that the ferrocyanide oxidation to became progressively more irreversible (figure 4.23a). The magnitude of the photothermal current response was rather sensitive to this change (figure 4.23b): the small peak at a potential in the region of the half wave potential for this reaction, in the photocurrent vs potential curve, disappeared as the electrode reaction became irreversible. As the irreversibility became extreme the photocurrent response at higher potentials also changed (figure 4.24) with other peaks appearing.

The effect of poisoning on cyclic voltammogram with time

Carrying out cyclic voltammetry on a commercial double gold band electrode showed that the cyclic voltammograms looked extremely similar if not the same in shape as for the home made band. However with time the cyclic voltammogram (figure 4.23a) was found to change shape with time as other parasitic reactions occurring due to the presence of impurities began to take effect and dominate over the situation. It was found that increasing the scan speed for the cyclic voltammogram made the cyclic voltammogram worse. Cleaning the surface using such processes as polishing with a diamond polishing paste or even better still cleaning the surface in a sonic bath with a very small amount of acetone for a few seconds were found to reverse this process a little (a polar solvent will help to draw off CuO, a possible impurity attached to a surface). It was found that as more time and the more the electrode was used it got progressively harder to clean the electrode back to a better state.

POISONING OF THE SCREEN PRINTED DOUBLE MICROBAND ELECTRODE WITH TIME

a) Dark Currents

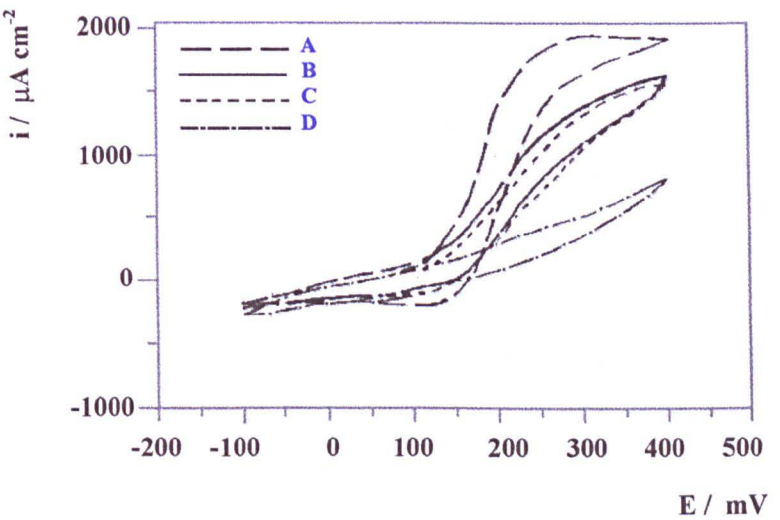

b) Photocurrents

Key to symbols :- ◆ **the inner band (i),** □ **the outer band (ii).**

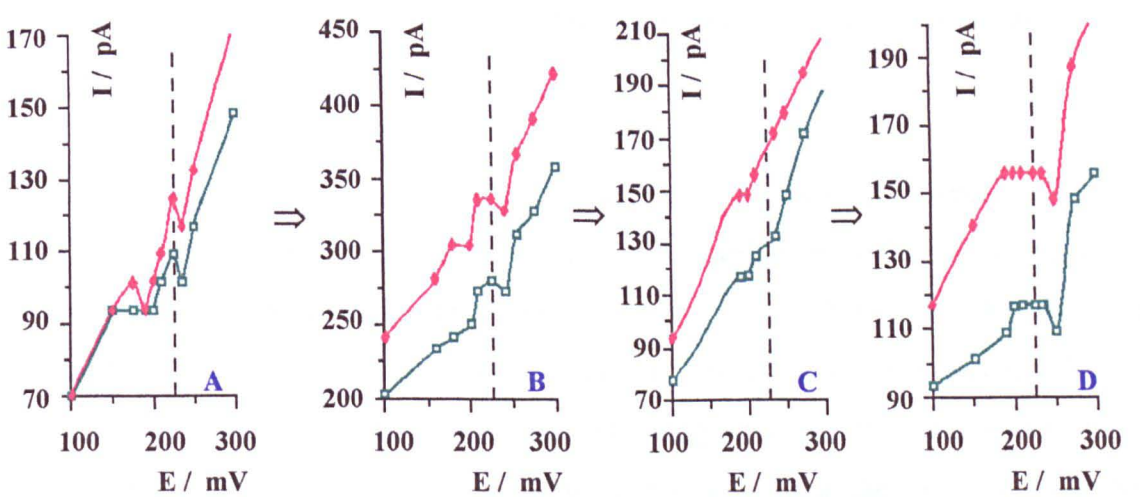

poisoning

time of exposure

Notes: Progressive poisoning (A → D) with continued cycling of printed microbands; 5 mM $Fe(CN)_6^{4-}$, phosphate buffer: (a) cyclic voltammetry (scan rate υ = 10 mV sec^{-1}), (b) photocurrent variation with potential. v_p = 8.53 cm s^{-1}, τ= 23.5 µs, x4 lens (N.A. = 0.12), 2r = 2 µm.

figure 4.23

The effect of poisoning on the photocurrent vs potential graph

Photocurrent images were recorded for different degrees of poisoning and therefore behaviour; A) Good, B) Intermediate, C) Bad, and D) Very bad. In each experiment the photocurrent images were recorded at a large variety of potentials between -200 and +825 mV. Prior to carrying out the photocurrent imaging experiment the length of the gold band was narrowed down using clear nail varnish to approximately 1 mm. In addition a cyclic voltammogram was also recorded. The cyclic voltammogram was used to define the type of behaviour / degree of poisoning. The reduction of the surface area was carried out in order to reduce the overall surface current (background) so making it easier to pick out the very small current change associated with the gold band. The images showed that there was a general increase in current with potential. Again the photocurrent images followed the reflective images closely.

The data from this imaging experiment was analysed as before by taking a line across the image in order to see how the pixel intensity changed across this line. In the +100 to +300 mV region one can see that the peak representing the Fe^{2+} / Fe^{3+} reaction was present at +225 mV superimposed on a overall rising current curve and this peak was found to decrease in sharpness: that is it flattened out with increased poisoning (prolonged use) of the electrode.

Summarising the observations: the shape of the cyclic voltammogram was found to change as it was poisoned progressively with use. Cleaning the surface using such processes as polishing with a diamond polishing paste or even better still cleaning in an ultra sonic bath with a very small amount of acetone for a few seconds followed by further polishing, were found to reverse the poisoning process a little. From any one stage (A, B, C, or D) it was found it was possible to go back at the most one and a half stages using the cleaning techniques mentioned but with progressive use even this became harder to do. With the investigation of the induced photocurrents the peak present at +225 mV on the induced photocurrent versus potential graph was found to flatten out in shape with increased poisoning (prolonged use) of the electrode.

THE DOUBLE BAND ELECTRODE IN A VERY POISONED STATE

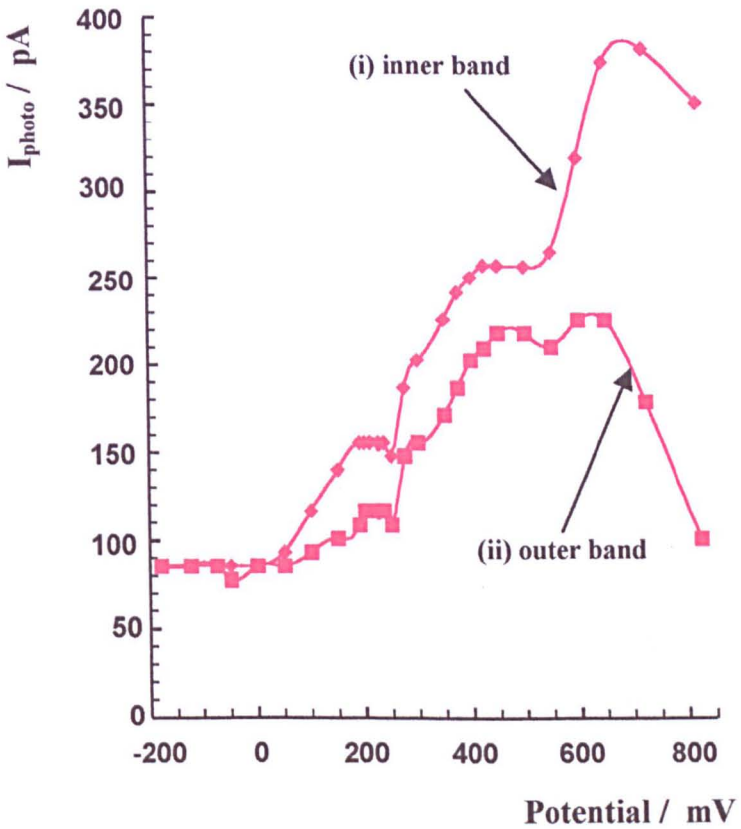

Notes: Photocurrent variation with potential over an extended range, for a severely poisoned double microband electrode : (i) inner, (ii) outer band. I_s = 100% I_o , x4 lens (N.A. = 0.12), 2r = 2 μm, v_p = 8.53 cm s^{-1}, τ= 23.45 μs, reversibility = D. Solution = $K_4Fe^{II}(CN)_6$ (5 mM), K_2HPO_4 (0.1M) and KH_2PO_4 (0.1M).

figure 4.24

In section 4.1 the photothermal effect on a reversible electrochemical process (refs. D-5, I1-8) as a thermal effect on the standard potential for the electrode reaction. For an irreversible reaction, (refs. D-2, D-3, C1-21) an alternative treatment relating the magnitude of the current change, on heating by the laser spot, to the dark current and activation energy for the electrode process: $\delta I \approx (ia)\frac{E_a}{RT^2}\delta T$ where i denotes the dark current density, a the illuminated area and E_a the activation energy for the reaction. With $i = 10^{-3}$ A cm^{-2}, $a = 3 \times 10^{-8}$ cm^2, T = 300K, $\delta T \approx$ 1K and $E_a \approx$ 57 kJ mol^{-1} (E_a = 56.8 ± 1.5 kJ mol^{-1} : from experimental work, or Ea = 30 ± 10 kJ mol^{-1} : from theoretical calculations on quantum mechanics or 50 ± 10 kJ mol^{-1} : from theoretical calculations on parabolic energy dependence, Halley et al., 1991, ref.G-3), then $\delta I \approx 2$

pA. Most importantly this shows that the expected signal is much smaller than the magnitude of current perturbation expected for a reversible electrochemical reaction, which induces a photothermal change of the order of nA (e.g. figure 4.17), the theoretical calculation of which has been given previously (ref. D-2). The present work has indeed confirmed (figure 4.23) that the variation of photocurrent image contrast with potential was much more sensitive to irreversibility in the electrode reaction than was cyclic voltammetry. The images also showed that, in this case, the irreversibility was induced uniformly over the electrodes.

The Poisoning of a Gold Macrodisc Electrode

A dramatic demonstration of the effect on the photothermally-induced current image of the poisoning of a electrode reaction was obtained when the distilled water became contaminated with some unknown compounds originating, we believe, in the feed water to the still. In this case cyclic voltammetry at a gold disc showed that ferrocyanide oxidation became irreversible. The photothermal current response fell markedly. The resultant image is shown in figure 4.25.

When a gold disc electrode was contaminated by impurities in the solution, the image showed circular shaped regions (figure 4.25). The electrochemical behaviour resembled that of a line electrode rather than that of a macroscopic disc.

The adventitious contamination of the water therefore resulted in the photocurrent imaging of the non-uniform poisoning of a gold disc. As the electrode progressively poisoned, the peak-to-peak separation in cyclic voltammetry first increased. Later, the voltammetry resembled that of a microband and later still that of a poisoned microband. With $\Delta E_{peak} = 75$ mV, the photocurrent image was uniform over the disc, but with $\Delta E_{peak} = 100$ mV the image (figure 4.25) displayed directly that the developing poisoning comprised a set of patches such that the active electrode area could be considered as a network of microbands. The result was consistent with the study of bands in that the development of this texture was associated with a marked decrease in

the photocurrent image signal, to a value consistent with that calculated above for an irreversible reaction.

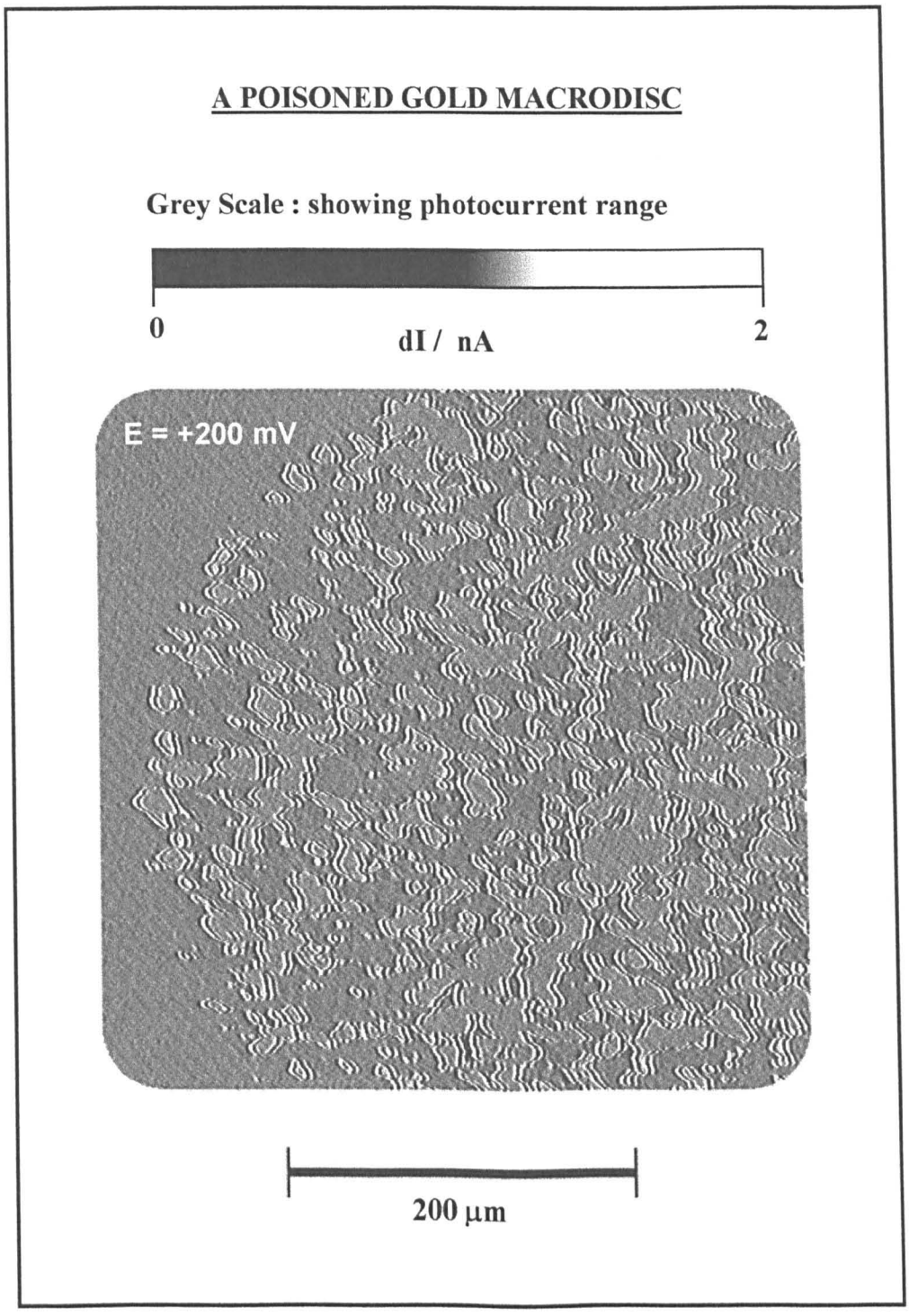

Notes: A gold disc electrode poisoned by adventitious contamination of the water. Solution = $K_4Fe^{II}(CN)_6$ (5 mM), K_2HPO_4 (0.1 M) and KH_2PO_4 (0.1 M). E = +200 mV, I_s = 100% I_o, x4 lens (N.A. = 0.12), 2r = 2 μm, v_p = 8.91 cm s^{-1}, τ= 22.45 μs.

figure 4.25

4.9 OTHER ANOMALIES

Light and Dark Regions on the Photocurrent Images of Screen Printed-Electrodes

For the screen printed band electrodes when the image was bright enough it was just possible to see the presence of light and dark regions giving a striated effect (figure 4.20). This effect was not found to correspond with any structural topographical features observed on the reflective image (e.g. shallow holes/pits in the gold which can only be seen by confocal imaging means).

The striated effect in photocurrents observed for screen printed microband electrodes, was unexpected. The single screen printed bands had a great variation in width, with thick and thin regions differing by as much as 15 μm. The pixel intensity and hence the photocurrents generated varied greatly from the thick to the thin regions. With the double band electrodes the thickness difference between thick and thin regions was only 1 - 2 μm so the photocurrent variation was much more subtle and could only be just picked up and observed at higher potentials when the signal was large. If the material behaved uniformly then photocurrents observed should be the same on thicker and thinner regions of the bands. If the bright edge to the image was a consequence of a transient effect as the spot came onto the electrode, then a bright edge (figure 4.15) should have been observed on both thick and thin parts of the electrode. This element of photocurrent contrast increased steadily with increasing potential. Hence it could not be associated with local variations in the reversibility of the electrochemical reaction. The photocurrent variation could have been a consequence of the firing process in the manufacture of these bands, which resulted in the cadmium additive moving out of the gold and collecting at the edge of the band. The movement of the Cd was probably helped by the porous insulator into which it seeps. According to this interpretation the signal should have correlated with Cd concentration at the edge and in the middle of each part of the electrode. Unfortunately, we were unable to obtain sufficient resolution in electron probe analysis to confirm this hypothesis.

OTHER ANOMALIES SEEN ON THE PHOTOCURRENT IMAGE

a) A Dark Spot on the Photocurrent Image

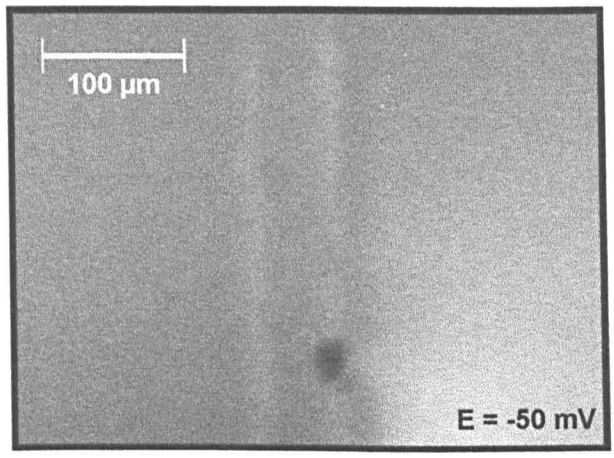

b) Bright Areas on the Band

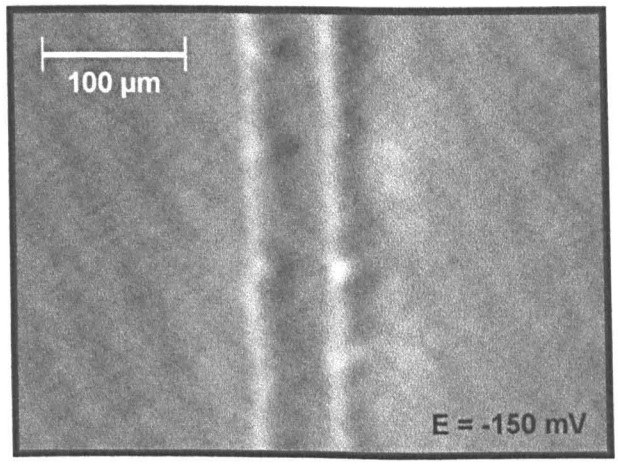

c) A Bright Region Following the bands

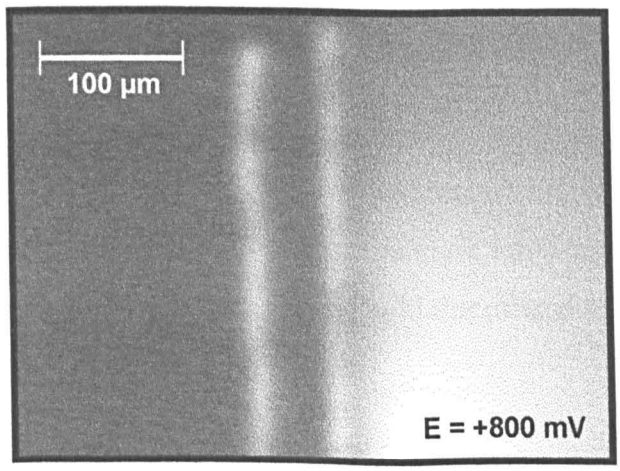

Notes: Experiments were carried out in 5 mM $K_4Fe^{II}(CN)_6$, 0.1 M K_2HPO_4, 0.1 M KH_2PO_4, 256 grey scale = 2 nA, v_p = 8.53 cm s^{-1}, τ= 23.45 µs, x4 lens (N.A. = 0.12), 2r = 2 µm. a) E = -50 mV, reversibility = C. b) E = -150 mV, reversibility = A. c) E = +800 mV, reversibility = C.

figure 4.26

An alternative explanation is that the contrast arose either from a variation in absorption of the light caused by surface texture or from a thermal perturbation of mass transport to the line (ref. D-2), with the perturbation largest at the electrode edge and becoming smaller as the electrode became thinner. In the absence of a detailed interpretation of the origin of the smoothly rising component of the photocurrent, we can do no more than note the existence of these subtle effects.

Unusual Points of Photocurrent on the Images

Other small anomalies noticed included a 'black spot' i.e. a photoelectrochemical dark area which appeared in one experiment (figure 4.26a) as the potential was decreased to below 100 mV and disappeared when the potential was increased again, and points of higher than the average photocurrent were also observed on occasion (figure 4.26b). On very poisoned electrodes at high potentials greater than 500 mV an area of higher than normal photocurrent was seen following the two bands (figure 4.26c). It was not possible to correlate these effects with any measurable chemical or topographical effects.

4.10 CONCLUSION

Geometrical effects on image contrast in photoelectrochemical microscopy, where the image is developed as a consequence of the temperature transient induced by a rapidly scanned, focused laser spot, was explored using gold microband and disc electrodes and the Fe $(CN)_6^{3-}$ / Fe $(CN)_6^{4-}$ redox couple.

The photocurrent signal obtained on a line electrode was much less than that on a disc. Image contrast due to the photothermal effect is, on a microelectrode, sensitive to the electrode geometry. For the experiments carried out with the gold microbands as the potential increased, there is a rising induced photocurrent with a peak super-imposed on the curve in the +200 mV region. The general increase with photocurrent showed that

some other effect such as the photoelectric effect was contributing to the photocurrents generated on the microband. In comparison the disc showed virtually no general rise in current with potential, but just a peak at +200 mV. Changing from a macrodisc to a microband resulted in a decrease in the peak at +200 mV in terms of induced photocurrent. Another phenomenon found was that the width of the band on the photocurrent image appeared to increase to a maximum also at +200 mV. In addition the microband electrodes showed a rise in the background current with potential.

The signal was also very sensitive to poisoning of the surface causing the electrode reaction to become irreversible. The signal resulting from the occurrence of an electrochemically reversible reaction is much larger than that resulting from an irreversible reaction. As a consequence of these two effects, both the photothermal signal and the image contrast are very sensitive to electrode poisoning. Other elements are present in the gold in the form of impurities in the commercial gold band electrode. This was found from the microprobe analysis. Elements found in the gold band which might have influenced and caused the poisoning behaviour with time included copper, cadmium and zinc. Large amounts of lead were also found in the surrounding insulator which may have leaked into the gold causing further problems.

Rapid electrochemical imaging at micrometer resolution was also demonstrated.

A summary of the findings are as follows;

1. Contrast is determined by heating in the aqueous phase.
2. The width of a microband photocurrent image was greatest at a potential equal to $E_{½}$.
3. The signal due to the reversible process was greater than the irreversible process.
4. The element of contrast is very sensitive to the poisoning of the electrode.
5. It is possible to see contrast on the photothermal images which relates to function.
6. It is possible to resolve down to a micrometer scale in imaging photoelectrochemistry.

5. PHOTOELECTROCHEMICAL IMAGE CONTRAST OF STAINLESS STEEL

5. PHOTOELECTROCHEMICAL IMAGE CONTRAST OF STAINLESS STEEL

5.1 AN INTRODUCTION TO STAINLESS STEELS

What are stainless steels?

Stainless steels are iron containing alloys containing chromium to at least 11% of the total weight of the alloy. This level of chromium prevents the formation of rust (iron oxide-hydroxide) in unpolluted atmospheres. Having at least 11% chromium present, enables the chromium to form a very thin layer of chromium oxide (Cr_2O_3), known as a passive film. This is invisible to the human eye, and protects stainless steel from corrosion. If this layer is damaged a new one forms immediately in a variety of environments due to the oxygen content of air, so it is self healing and does not need any action to maintain it. Further raising the chromium content can improve the protection. Other alloying elements such as Mo (ref. K2-2) are also added for this purpose. Stainless steel also contains nickel but this is used to make the steel ductile and not for corrosion resistance purposes.

The Introduction of Impurities in the Manufacturing Process

Stainless steel is usually made from raw steel, steel scraps and of alloying additions. The steel itself is an iron carbon alloy made from iron ore and coal. In the manufacture of stainless steel the steel scrap and further alloying elements are heated in an electric furnace to form molten stainless steel, which is then cast into moulds typically to form ingots. The stainless steel is sold in a wide variety shapes including rods, pipes, sheets and discs. The shapes are typically produced at the steel mills by rolling or forming heated ingots into the required shape. The basic process of working steel is known as hot rolling. A cast ingot is first heated to bright-red heat in a furnace called a soaking pit and then passed between a series of metal rollers that squeeze it into shape and size.

The distance between rollers gets smaller for each successive pair as the steel is elongated and reduced in thickness.

Impurities are introduced into stainless steel at various stages of the manufacturing process. These impurities tend to be present as oxides or sulphides. The occurrence of sulphide inclusions in particular is a problem as they are known to be the starting point of pitting and crevice corrosion. If the sulphur is present as an impurity unintentionally it tends to be of a very low concentration of less than 0.03%, but in some cases sulphur is added on purpose to improve machinability of the stainless steel. The sulphide inclusions are known to be predominantly MnS but these MnS inclusions also contain chromium, iron and other elements and may be physically associated with oxides.

Mn may also occur as a MnO impurity as Mn is introduced as an impurity in the scrap steel, which is used to make stainless steel. The Mn content can be lowered using less scrap metal and more Ni but this is not usually done as it would be more costly.

Another way of minimising the impurity content is by the use of a process known as electroslag remelting. This involves reheating and remaking the stainless steel from the previously made stainless steel. This type of stainless steel is said to be of super-clean quality and is used for applications where great purity is required such as for surgical repairs inside the human body.

Types of Stainless Steels

Stainless steels can be classified firstly by the metallograpic structure the atoms present in it take up and secondly by the element composition specific to it.

a) Metallograpic structure of stainless steels

Stainless steels can be broadly divided up into groups depending on the type of packing the atoms present tend to take up within the structure.

A table showing the structural positions of atoms in stainless steel:

Predominant Structure Type Present	**Name of group of stainless steels**
Face-centred cubic	Austenitic Stainless Steels
Body centred cubic	Ferritic Stainless Steels
Body centred tetragonal, or cubic	Martensitic Stainless Steels
Equal amounts of austenitic and ferrite structures	Duplex stainless Steels

The structural type of a particular stainless steel can be determined from the respective amounts of Ni (which favours the austenitic form) and Cr (which favours the ferrite form) present in a sample. Other elements present can also be classified as behaving as austenite formers like Ni or ferrite formers like Cr.

A SCHAEFFLER DIAGRAM

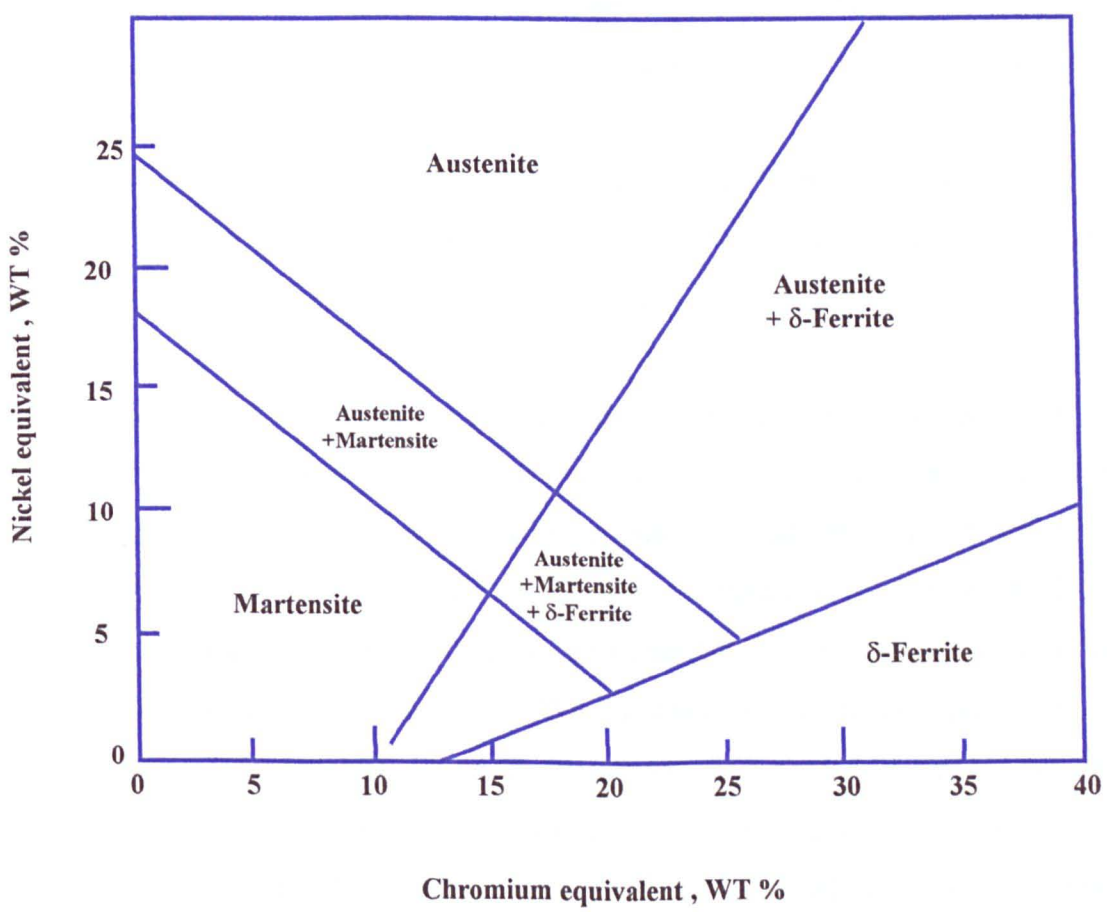

figure 5.1

The nickel equivalent and chromium equivalent percentages can be calculated using equations 5.1 and 5.2 and from this the structural type may be found from a diagram known as the Schaeffler diagram (figure 5.1)

$$\%\ \text{Ni equivalent} = \%\ \text{Ni} + \%\text{Co} + 30\,(\%\text{C}) + 25(\%\text{Ni}) + 0.5(\%\text{Mn}) + 0.3(\%\text{Cu}) \quad (5.1)$$

$$\%\ \text{Cr equivalent} = \%\ \text{Cr} + 1.5(\%\text{Mo}) + 5\,(\%\text{V}) + 5.5(\%\text{Al}) + 1.75(\%\ \text{Nb}) + 1.5\,(\%\text{Ti}) + 0.75(\%\text{W}) \quad (5.2)$$

b) Classification names by element composition

Stainless steels of a particular elemental composition are identified by the American Iron and Steel Institute (AISI) numbering system. Other methods of identification include the unified numbering system (UNS) and by manufacturers trade names and reference numbers. In this work the AISI method of stainless steel classification has been used. In this method of identification each type of stainless steel is given a three digit number to represent the amount of the main constituents in stainless steel present. In addition changes to the general composition are represented by suffix, after the three digit number, consisting of one or more letters representing small changes by addition of further elements or reduction of the amount the principle elements present.

All the stainless steel types designated AISI identification numbers from 300 to 399 are said to belong to the 300 series of stainless steels, which are the most common stainless steels. These contain Ni as well as Cr and structurally are austenitic stainless steels. In comparison the 200 series, though being austenitic in structure and containing both Cr and Ni, differs in that all the stainless steels in this series contain a high amount of Mn (> 2%). The 400 series of stainless steels do not contain nickel and structurally are classified as martensitic or ferritic stainless steels. However duplex stainless steels and higher alloy (i.e. Fe < 50%) containing stainless steels do not have a AISI designation and tend only to be known by the UNS number (a letter followed by five numbers) or the manufacturer's trade name.

The most common stainless steel is 304 (AISI) which contains 16-18% Cr and 8-10 % Ni. The next most common is 316 (AISI) stainless steel which contains 2-3% Mo as well for increased pitting resistance.

Further variations in the 304 and 316 stainless steels are made by addition of new elements or partial removal of the elements present. These changes are donated by one or more capital letter following the three digit name (e.g. 304, 316). The suffix gives the grade of stainless steel.

A table of stainless steel grading letters:

Grade (suffix to AISI N^{o})	Composition	Properties / Use
L	low carbon C ~ 0.03 %	Used in welding to minimise the carbide precipitation in heated areas of welds as this can result in intergranular corrosion in certain surroundings.
H	high carbon > 0.08%	Used in solution annealing to give high creep rupture strengths at high temperatures.
N	addition of nitrogen N = 0.10 to 0.16%	Used to increase strength.
(Hi)N	extra high nitrogen N = 0.16 -0.30%	Further increases strength.
LN	low carbon and high nitrogen C = 0.03% N = 0.10 to 0.16%	Loss in strength due to low C replaced by use of N.
F	high sulphur S » 0.03% typically 0.1%	Used for improved machinability.
M	contains high levels of molybdenum Mo = 4 to 5%	Used for greater resistance to pitting and crevice corrosion.

Typical compositions for various grades of 304 and 316 stainless steels:

	AISI	% Weight Composition (balance = % Fe)								
	name	Cr	Ni	C	Mn	Si	P	S	Mo	N
	304	18-20	8-10	0.08	2.0	1.0	0.045	0.030	--------	----------
	304L	18-20	8-12	0.03	2.0	1.0	0.045	0.030	--------	----------
	304N	18-20	8-10.5	0.08	2.0	1.0	0.045	0.030	--------	0.1-0.16
	304LN	18-20	8-12	0.03	2.0	1.0	0.045	0.030	--------	0.1-0.16
	316	16-18	10-14	0.08	2.0	1.0	0.045	0.030	2-3	----------
	316F	16-18	10-14	0.08	2.0	1.0	0.20	0.10 *	~2	----------
	316L	16-18	10-14	0.03	2.0	1.0	0.045	0.030	2-3	----------
	316N	16-18	10-14	0.08	2.0	1.0	0.045	0.030	2-3	0.1-0.16
	316LN	16-18	10-14	0.03	2.0	1.0	0.045	0.030	2-3	0.1-0.16

* this is a typical value, and it can be different to this.

Notes: The % weight of elements present for the various stainless steel classifications are from the book 'Corrosion of Stainless Steels' by- A.John Sedriks, 2nd edition 1996, John Wiley & Sons (ref K1-4).

Uses of Stainless Steels

The most common reasons for using stainless steel are: it does not corrode easily; it is easy to clean; and it is durable and attractive. Stainless steels are used for the pipes and tanks of petroleum refineries, space capsules, aeroplanes, surgical equipment and in surgery to patch and replace broken bones. Stainless steel is also used widely for domestic purposes such as in kitchens where much of the food handling and cutting equipment is made of stainless steels as it can be easily cleaned. Stainless steel is also the most common material used in the manufacture of mechanical tools. In this case stainless steels with extra molybdenum and tungsten are used to give extra strength and hardness.

Structure of Stainless Steel Passive Films

Even though the structure of the passive film on stainless steel has still to be fully determined. Previous work investigating the film (ref. sec. J-2) has shown it to be an iron-chromium oxide containing substance.

Some analytical studies were carried out on stainless steel by G. Lorang and coworkers (refs. J2-1, J2-2, J2-3) by quantitative auger analysis. This work showed that the stainless steel passive film consisted of two layers. An inner layer of chromium oxide, of a few atomic layers was found to be directly in contact with the metal, and an outer layer was made of iron hydroxides and oxides.

THE STRUCTURE OF THE STAINLESS STEEL PASSIVE FILM

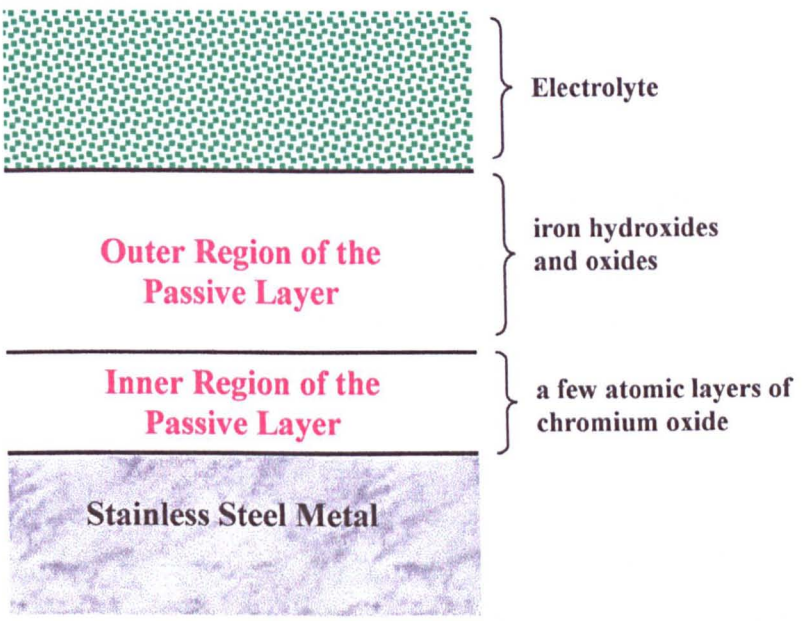

figure 5.2

The presence of an outer iron oxide rich layer and an inner chromium rich layer has also been confirmed using XPS studies by Kosaka and coworkers (ref. J2-4, 1996). The outer most part of the passive film is similar to that found on iron. The difference being that in the iron (ref. sec. J-5) the n-type semiconducting properties reported were associated with the outer γ Fe_2O_3 part of the film where the inner Fe_3O_4 region was assumed to be a metallic conductor. In the case of stainless steel the effects of the chromium need to be considered as well when examining the behaviour of the passive film on stainless steel, as it is known to be important in the corrosion resistance behaviour (see ref. sec. J-6 and also ref. K2-1).

The Electrochemical Behaviour of the Passive Films on Stainless Steels

Earlier work carried out on stainless steel showed that the passive films on stainless steel depicted the characteristics of a highly doped amorphous or highly disordered n-type semiconductor (ref. sec. J3). Recent work (T.B. Du et al., 1996, ref. J3-11 and N.E. Hakiki et al.,1995, ref. J3-9) however has shown that the passive films on stainless steels are characterised with p-type or n-type semiconductor behaviour in different potential regions. The p-type behaviour was seen by going down to much lower potentials than was previously used. p-Type behaviour was found at potentials below -900 mV vs SSE (SSE = Hg / Hg_2SO_4, sat K_2SO_4, where -900 mV vs SSE = -500 mV vs SCE) and n-type behaviour was found at potentials above -900mV vs SSE (ref. J3-9). It was noted however that the capacitance studies lower than -900 mV may be questionable as the passive film is unstable especially the iron oxide outer layer, but it was assumed that the layer would not change much in the 10 s required to make a capacitance measurement. Plots of $1/C^2$ which were given (ref J3-9) are shown in figure 5.3.

It was found that polarising the electrode prior to the experiment at increasingly negative (cathodic) potentials reduced the $1/C^2$ values obtained. If polarised for a few minutes at very low potentials, ~ -1.9 V vs SSE, this reduced the p-type behaviour peak seen on the $1/C^2$ vs potential curve considerably more than the n-type behaviour peak. It was noted that iron oxide is probably reduced at -1.9V and is instantly developed in the passive potential range above -900 mV. In addition it was shown that the p-type behaviour below -900mV was affected by a change in the %Cr in the stainless steel sample but the n-type behaviour above -900 mV was not (see figure 5.4). From this work we can therefore deduce that the electrochemical behaviour of the stainless steel passive film is very similar to the passive film on iron.

GRAPHS SHOWING THE EFFECT OF POTENTIAL ON CAPACITANCE FOR STAINLESS STEEL AND IRON

a) 304-TYPE STAINLESS STEEL

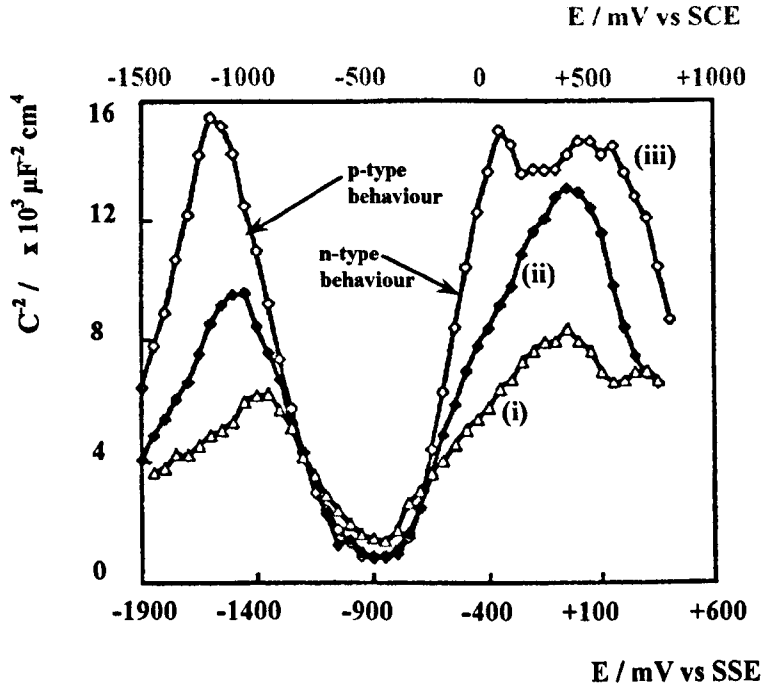

b) IRON

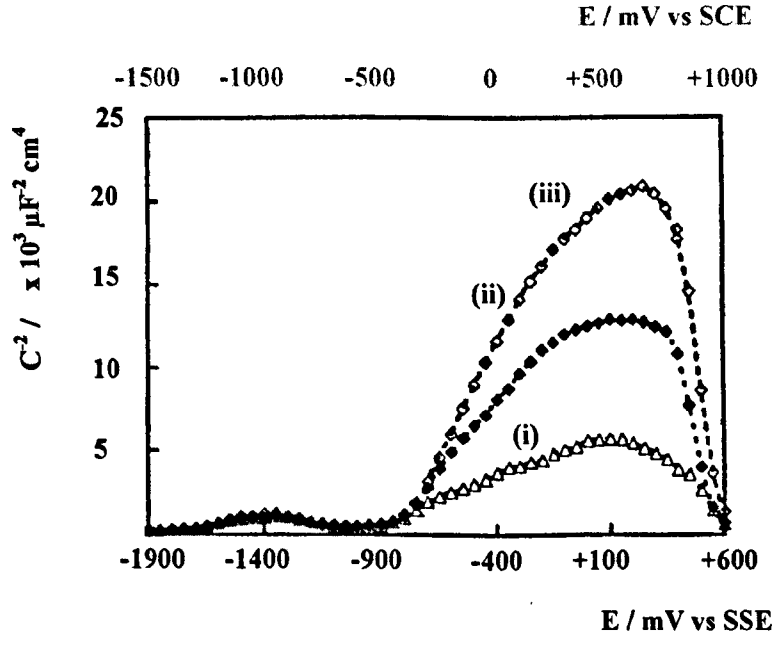

Notes: The above work was carried out by N. E. Hakiki and coworkers (ref. J3-9). The experiment was conducted in an electrolyte buffer solution containing 0.05M H_3BO_3, 0.075M $Na_2B_4O_7$. Prior to the experiment the sample was cathodically pre-polarised for 5 minutes to give ≈ 5mA cm^{-2}) and the left to polarise at the film forming potential for 2 hours prior to carrying out the experiment. The film forming potentials used were; (i) -700 mV, (ii) -100 mV, (iii) +400 mV vs SSE. It should be noted that the reference electrode used was actually SCE but these values have been converted here to that for Hg/Hg_2SO_4, sat K_2SO_4 (SSE) in order to allow easy comparison with the work given in this chapter of this thesis.

figure 5.3

HOW THE %CHROMIUM IN A Fe-Cr ALLOY EFFECTS THE CAPACITANCE

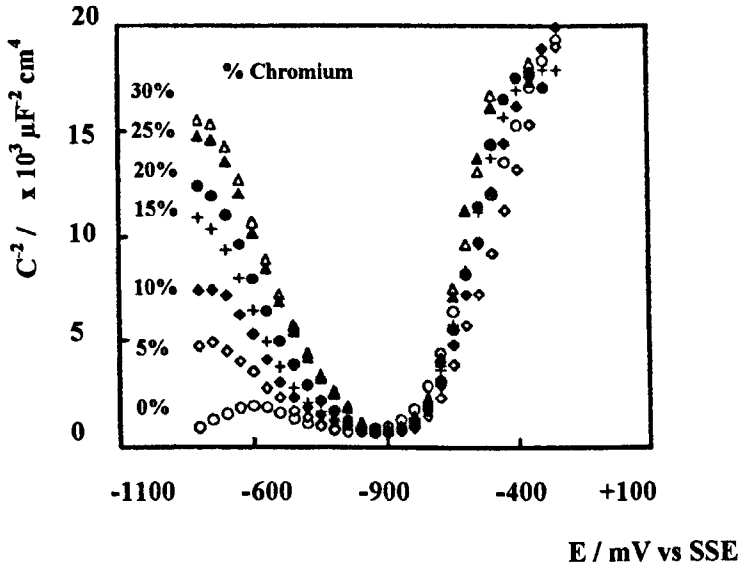

Notes: Work by N.E. Hakiki and coworkers (ref. J3-19). Values of $1/C^2$ vs E for passive films formed at +400 mV.

figure 5.4

5.2 AIMS

The aims of the work in this chapter were to investigate the origins of image contrast on stainless steel using photoelectrochemical microscopy. The work in this chapter was carried out as preliminary work to the investigation of the corrosion of stainless steel (chapter 7) in order to show the effects of various parameters on the image when the steel is not corroding. Variation of the potential, laser intensity and laser velocity, as well as examination of how various impurity inclusions effect the photocurrent image contrast under non-corroding conditions, were explored.

5.3 EXPERIMENTAL

The general experimental setup as shown in Chapter 2 was used with a few changes. The working electrodes were either 304L or 316F stainless steel. These were prepared as follows. They were first cut to size and cleaned in purified water and acetone. The 316F sample in addition was cleaned in acetic acid prior to this as it was a very old sample. The sample was then attached to a brass button using silver conductive paint in an electrode cup. When the paint was dry an epoxy resin primer solution (Permabond SIP ®) was poured into the electrode cup, surrounding the stainless steel, where it was left to sit for at least half an hour, then removed. When electrode was dry the epoxy resin (Epo-kwick®) was placed into the cup (see appendix D for further details of the electrode preparation procedure). The epoxy resin primer was used in the preparation of stainless steel electrodes to form a good seal between the resin and the electrode via the primer in order to minimise the chance of crevice corrosion occurring. Another precaution used in the preparation of the stainless steel electrodes, to minimise the chance of crevice corrosion, was to place the electrode cup in an oven at 45°C to allow any bubbles present in the very thin liquid epoxy resin, after it had been syringed into the electrode cup, to rise up and out to the surface. The working electrodes made were polished using successive grades of diamond polishing pastes down to ¼ μm. This differed from the previous work on gold and p-type silicon where only polishing down to 1 μm was required. The higher degree of polishing was required here as many of the inclusions we wished to observe in the stainless steel were only about 1 μm in size themselves, so could not be clearly viewed on the optical images without this level of polishing.

The newly designed cell (see Appendix C for technical diagrams, and Chapter 2-figure 2.9 for photographs also of this apparatus) was used with a miniature faraday cage around it in order to reduce the noise, allowing the images to be collected at lower potentials, where they would not normally have been seen due to a low signal to noise ratio. In addition, increasing the signal to noise ratio in this way allowed image data to be collected more quickly without signal averaging. The cell used was boil washed in the Milli-Q plus water after regular cleaning in order to get rid of any chloride present prior to any experimental work.

A three electrode cell was used with either 304L or 316F stainless steel as the working electrode, an open ring platinum wire as the counter electrode and Hg/Hg_2SO_4 in a saturated K_2SO_4 solution as the reference electrode. A saturated calomel electrode (Hg/Hg_2Cl_2 ,sat KCl) was not used as initial experiments carried out showed that leakage of Cl^- from this it to easily triggered the corrosion of the 316F stainless steel samples. The values of the potential applied vs Hg/Hg_2SO_4, sat K_2SO_4 (SSE) given for the work shown here may be related to other work given in terms of a saturated calomel (SCE) or hydrogen (NHE) electrode by the following equation:

$$\text{SCE value in mV} = \text{SSE} + 399 \text{ mV} \quad (5.3)$$

$$\text{NHE value in mV} = \text{SSE} + 640 \text{ mV} \quad (5.4)$$

e.g. -640 mV vs Hg/Hg_2SO_4, sat K_2SO_4

$\equiv$ -241 mV vs SCE

$\equiv$ 0 mV vs NHE

The solution used in this experiment was $NaClO_4$ (0.3M unless otherwise stated). Experiments conducted included looking at the variation of potential between -900 and + 800 mV vs Hg/Hg_2SO_4, sat K_2SO_4 on both the cyclic voltammetry and photocurrent image. Photocurrent images were also recorded under conditions of varying laser intensity and velocity. The laser intensity was varied between 100% I_o and 1% I_o with the use of the ND filters. The laser velocity was varied by keeping the length across the image the same in each case but varying the line scan time. The variation of the laser line scan time resulted in the laser beam irradiation time, τ, (the time to scan over a distance equal to the laser spot diameter) was varied from 29 μs to 152 μs (v_p = 6.86 cm s^{-1} to v_p = 1.32 cm s^{-1}). The limiting time of the detection apparatus was 16 μs. This was determined by the preamplifier high frequency filter setting. The photocurrent signal detected was band pass filtered so that the out coming signal would have a low frequency cut-off of 0.03 Hz and a high frequency cut-off of 10 kHz. The response time of the apparatus was given by the frequency of the high frequency filter ($\tau_{inst} = 1 \div 2\pi f$ = 16 μs). In comparison the response time of the potentiostat was 4 μs (see Appendix C-section 1, for how the response time of the potentiostat was calculated). One difference in the instrumental settings used for the work with stainless steel was that the incoming

signal for the pre-amplifier was set to DC and not AC coupling. This was possible because the DC current was very small, and had the advantage of greatly diminishing the settling time of the pre-amplifier. However a low frequency filter of 0.03 Hz was still applied to the outgoing signal so an AC current is still seen on the photocurrent image.

In all the experiments the potentiostat was switched on with the potential to be applied to the electrochemical cell set at -900 mV vs SSE and then the potential raised from this value to the desired one.

Further details on the experimental settings and image parameters of the photocurrent and optical images shown in this chapter have been given in Appendix J (Part. 3).

5.4 ELECTRODE COMPOSITION

Quantitative Microprobe Spot Analysis of the 304L and 316F Samples

The 304L sample used in the work was a 250 μm diameter annealed wire purchased from Advent Research Materials Ltd, UK.

The 316F sample used was a wrought austenitic stainless steel in the form of a disc (3.8 cm diameter x 1.9 cm depth). The sample used was a very old one available in our lab (circa 1960), however it is still available today from the same company in exactly the same form with exactly the same constituents. The 316 sample came from the Bureau of Analysed Samples Ltd, Cleveland, England. The trade name for this sample is 'BCS/SS-CRM 466/1', where the letters BCS/SS-CRM stands for 'British Chemical Standard and Spectroscopic Standard, Certified Reference Material'.

Both the 304L and 316F samples used in the experiments in this and the following chapter were analysed, using many samples, to show the amounts of elements present in the non-inclusion areas. These findings were compared to the manufacturer values

showing the average amount of any element present in both the inclusion and non-inclusion areas. These finding have been summarised in the two tables which follow.

A table showing the % weights of elements present in the 316F stainless steel :

Element	316F (BAS) manufacturers values, average of inclusion and non- inclusion areas	316F (Bureau of Analysed Samples Ltd) microprobe analysis values in non-inclusion areas only, Readings taken at many points in many samples Dwell time per element reading = 20s		
		%	S.D. for 31 points	notes
Fe		69.391	1.270	
Cr	17.65	17.891	0.243	
Ni	8.61	8.330	0.279	
Mo	2.19	2.022	0.058	
Al	0.101	>0.0001 *		is high in some inclusions
Si	0.505	>0.0001 *		is high in some inclusions
Cu		0.010 var	0.010	
Ti		0.002	0.002	
Mn	0.698	0.702	0.0534	
As	0.017	>0.0001*		
S	0.160	0.051	0.009	
P	0.020	0.032	0.016	
Co	0.035	0.083	0.012	
Sn	0.0050	0.003 var	0.013	
V		0.023 var	0.007	
Sr	3.551			
Pb	0.0014			
Nb	0.029			
B	0.0024			
Ba				
C	0.062			

Notes: The main line of Sr is close to second line of Cr on of the main elements, so was not investigated.* = in non inclusion areas 0.0001> % weight > 0.0000 , however this element was found present in high quantities in some inclusions, by the microprobe spot analysis method.

A table showing the % weights of elements present in the 304L stainless steel:

Element	304L (Advent) manufacturers values (average of inclusion and non inclusion areas)	304L (Advent Research Materials Ltd.) microprobe analysis in non-inclusion areas as seen on SEM , at many points in many samples Dwell Time per element reading - 20s		
		%	S.D. for 8 points	notes
Fe		66.849	1.937	
Cr	17-20	18.597	0.279	
Ni	8-11	9.256	0.245	
Mo		0.236	0.021	
Al		>0.0001		is high in some inclusions
Si	< 2	0.188	0.112	high in some inclusions
Cu		0.132	0.070	
Ti		0.003	0.003	very variable
Mn		1.126	0.089	
As		0.012	0.029	very variable
S		0.010	0.007	
P		0.026	0.007	
Co		0.151	0.062	
Sn		0.007	0.007	very variable
V		0.065	0.005	
Sr				
Pb				
Nb				
B				
Ba				
C				

Notes: Main line of Sr is close to second line of Cr on of the main elements, so can not be investigated. * = in non inclusion areas 0.0001> % weight > 0.0000 , however this element was found present in high quantities in some inclusions (by the microprobe spot analysis method).

Types of Impurity Inclusions Present in the 304L and 316F Samples

In the 304L stainless steel, inclusions containing Mn + S were rarely present as the amount of sulphur present was low (0.01%). Inclusions typically present were found to contain Si as well as Al and Ti on occasion, in greater levels than was present in the non-inclusion areas. The distribution of Cr and Ni tended to be uniform in this sample and the Mn and S were fairly evenly distributed.

The 316F stainless steel was found to contain a variety of different inclusions. Inclusions enriched in S + Mn or Mn + O, or mixed inclusions with both, tended to occur in lines across the metal, in bands which contained lower amounts of Ni. It was found that Ni and Cr were slightly unevenly distributed in bands with the areas with a slightly lower amount of Ni being higher in Cr and visa-versa. Although the Mn + S in the MnS containing inclusion were higher than the bulk matrix of the stainless steel, they were not pure MnS inclusions but contained the other bulk materials making up the stainless steel i.e. Fe, Cr, Ni, Mo.

Where mixed inclusions were present containing oxides as well as sulphides these existed as two separate phases which could easily be easily on high resolution confocal microscopy or true colour video microscopy or SEM images. These typically existed as an eye-like shape or resembled peas in a pod. Here the central spherical oxide containing region was seen as a lighter colour on the SEM image than the surrounding oblong sulphur containing area which appeared black in colour. This was also true on the confocal optical image where the oxide containing centre was lighter than the sulphide containing outer region which appeared black. On the true colour optical micrographs the centre appeared a mid-grey colour and the outer-shell a very dark grey/pink colour. In very rare occasions the mixed inclusion was seen to exist as two separate halves with the sulphide occupying one half the oxide the other half of the inclusion. The oxides containing regions were not just Mn + O though quite often these elements were the major constituents. The oxide regions usually contained other impurity elements in lesser amounts: mainly Si, Al, Ti, and quite often were also a little enriched in sulphur.

Other inclusions present in the 316F stainless steel which were not associated with higher amounts of Mn or S included inclusions containing enrichments in Si, Ti, Al separately or in combination as well as O. Other inclusions enriched in elements such as V were also present but less frequently.

5.5 EFFECT OF POTENTIAL

Cyclic Voltammetry for 304L and 316F Stainless Steels

The cyclic voltammetry was carried out after the electrode had been polarised for 1 hour as this helped to minimise the occurrence of corrosion during the scan to high potentials and back. The cyclic voltammetry was carried out from -900 to +800 mV vs SSE and back again for both the 304L and 316F samples. Typical cyclic voltammograms recorded are given in figure 5.5. There were 3 main differences and one similarity in the peaks seen on the cyclic voltammetry for the two types of stainless steel. These observations have been summarised on the table below.

Observations made from the cyclic voltammetry:

Area on figure 5.5	304L	316F
Area 1., -300 to -600 mV	flat area (i.e. I = constant)	broad peak
Area 2., 0 to +400 mV	broad peak centring around +200 mV	broad peak centring around +200 mV
Area 3., +400 to +800 mV	smooth broad peak	uneven variations superimposed on a broad peak
Area 4., approaching +800 mV	curve turns up sharply, i.e. a sharp increase in current	current does not increase very much

Chromium oxidation occurs in area 3 on the cyclic voltammogram. The uneven variations on the cyclic voltammogram between +400 and +800mV, for 316F stainless steel sample, occurred due to the dissolution of sulphide inclusions. Transpassive dissolution of MnS was observed by Keller et al. (ref. K5-2), in the potential range around +800 mV vs SSE. In this work the dissolution of the MnS was found to occur prior to the dissolution of the steel itself.

EFFECT OF POTENTIAL ON THE CYCLIC VOLTAMMETRY

a) 304L Stainless Steel

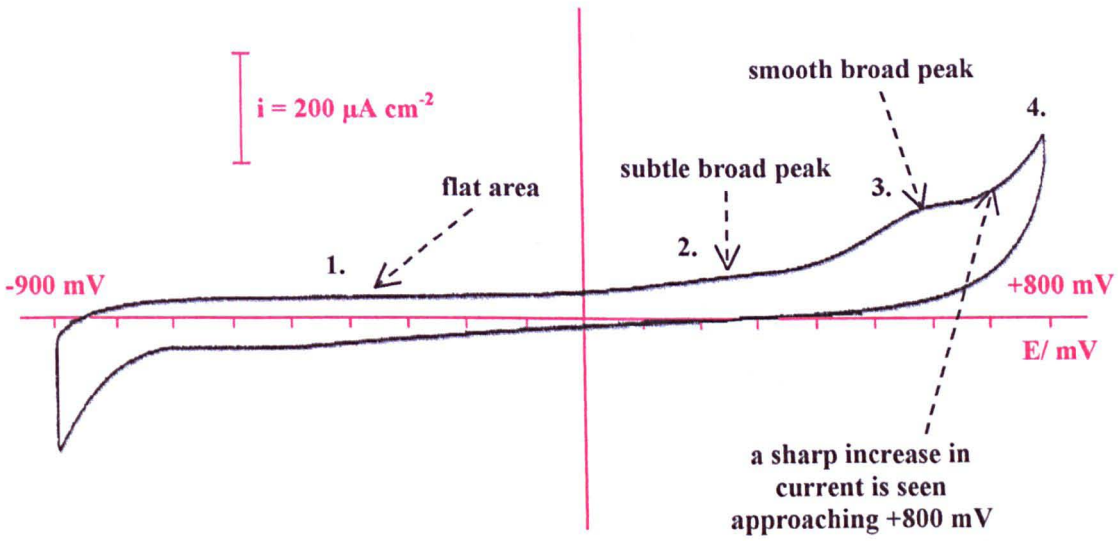

b) 316F Stainless Steel

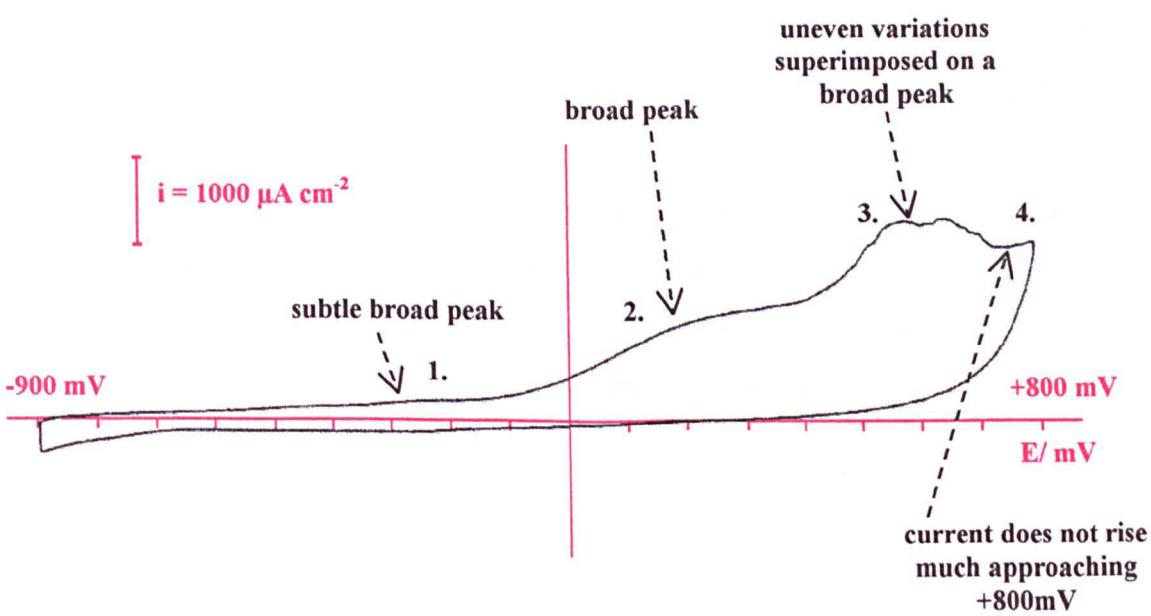

Notes : Potential vs Hg/Hg_2SO_4 , K_2SO_4 is shown in the above cyclic voltammetry. Sweep rate = 0.2 V sec^{-1}, solution = 0.3M $NaClO_4$

figure 5.5

Effect of Potential on the Photoelectrochemical Image Contrast

Photocurrent images were recorded for both 304L (figure 5.6) and 316F (figure 5.7) over the same range of potentials as in the cyclic voltammetry. On the odd occasion inclusions on the 316F sample were found to give activity and dissolved away at the higher potentials despite the precautions taken when studying the effect of potential on the photocurrent image (see figure 5.6, white region formation seen due to anodic photocurrent generation). A graph of the photocurrent generated at the electrode centre on the photocurrent image at each potential was plotted for each sample used (figures 5.8a, 5.8b). The value of the photocurrent was obtained by the subtraction of the average pixel intensity value on an image collected with no laser-light on the electrode, from that on a large rectangular area in the centre of the electrode (~ 40% of the total electrode area was analysed to exclude the overshoot and undershoot) with the laser-light on. Graphs of photocurrent at the electrode centre versus potential for both types of stainless steel gave a broad peak which started to rise drastically with potential around -530 mV and then subsided again around +700 mV. From the many experiments carried out it was seen that the 304L photocurrent peak maximum was between +150 and +200 mV. For the experiments carried out with the 316F the photocurrent peak maximum varied between +150 and +300 mV but the top of this peak was not clean cut and fairly unsymmetrical compared to that seen for the 304L stainless steel. Further examples of this behaviour may be seen in figure 5.9. On the photocurrent graph for the 316F sample it looked as if there was an overlap of 2 peaks. The peak maximum of the double peak tended to be close to +300 mV for the high sulphur containing stainless steel, but on occasion when there were not as many active inclusions present it would occur between + 150 and +200 mV as was seen for the 304L stainless steel.

It should be noted that what appeared to be a dim 'echo' of the image could be seen to some extent on some of the images exhibiting the higher photocurrents (figure 5.6 and figure 5.7). These artefacts may have been due to the potentiostat 'ringing', so we have to be careful to distinguish these effects from the chemistry.

EFFECT OF POTENTIAL ON THE PHOTOCURRENT IMAGE OF 304L STAINLESS STEEL IN 0.3M NaCl

The images show the value of the applied potential vs Hg/Hg_2SO_4, sat. K_2SO_4

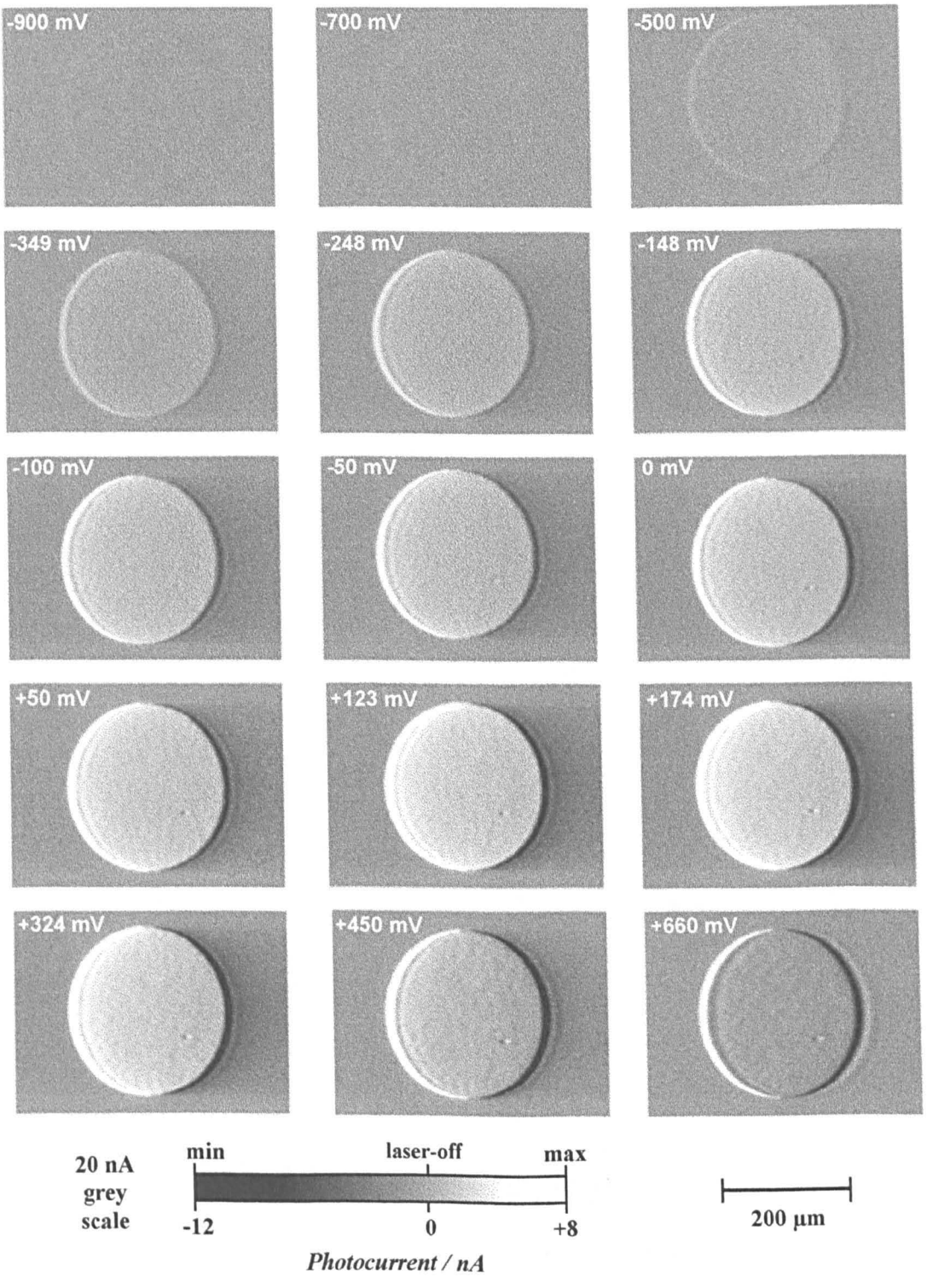

Notes : Lens magnification = x 4 (N.A. = 0.13), laser spot diameter = 2 µm, laser intensity = 10% I_o, total area sampled in experiment = 527 x 325 µm (768 x 512 pixels), selection of image shown here = 303 x 221 µm, pixel dwell time = 10 µs, τ = 29 µs, $v_p = 6.68$ cm s^{-1}, electrode area = 4.9×10^{-4} cm^{-2}.

figure 5.6

EFFECT OF POTENTIAL ON THE PHOTOCURRENT IMAGE OF 316F STAINLESS STEEL IN 0.3M NaCl

The images show the value of the applied potential vs Hg/Hg_2SO_4, sat. K_2SO_4

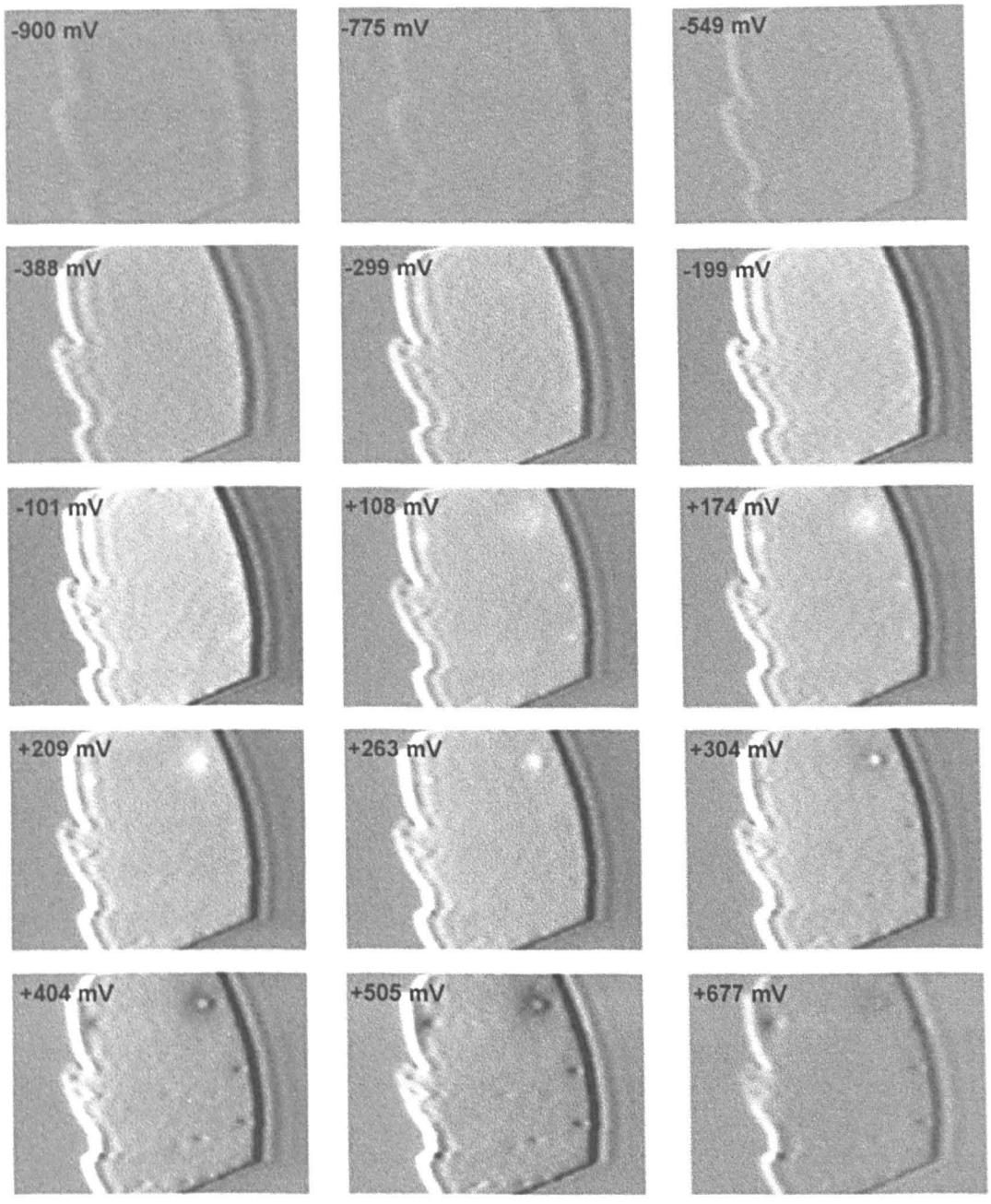

Grey scale for the images shown above
50 nA (-12 to +8 nA) for -900 to +108 mV,
20 nA (-30 to +20 nA) for +174 to +505 mV,
10 nA (-60 to +40) for +677 mV

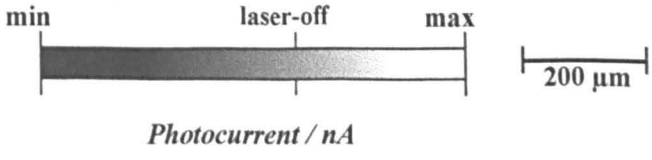

Photocurrent / nA

Notes : Lens magnification = x 4 (N.A. = 0.13), laser spot diameter = 2 µm, laser intensity = 100% I_o, total area sampled in experiment = 633 x 390 µm (768 x 512 pixels), selection of image shown here = 364 x 265 µm, pixel dwell time = 10 µs, τ = 24 µs, v_p = 8.24 cm s^{-1}, electrode area = 7.2 x 10^{-4} cm^{-2}.

figure 5.7

EFFECT OF POTENTIAL ON THE PHOTOCURRENT GENERATED AT THE ELECTRODE CENTRE

a) 304L stainless steel

This graph shows the data for the images seen in figure 5.6

$\tau = 29\ \mu s$, $v_p = 6.68\ cm\ s^{-1}$

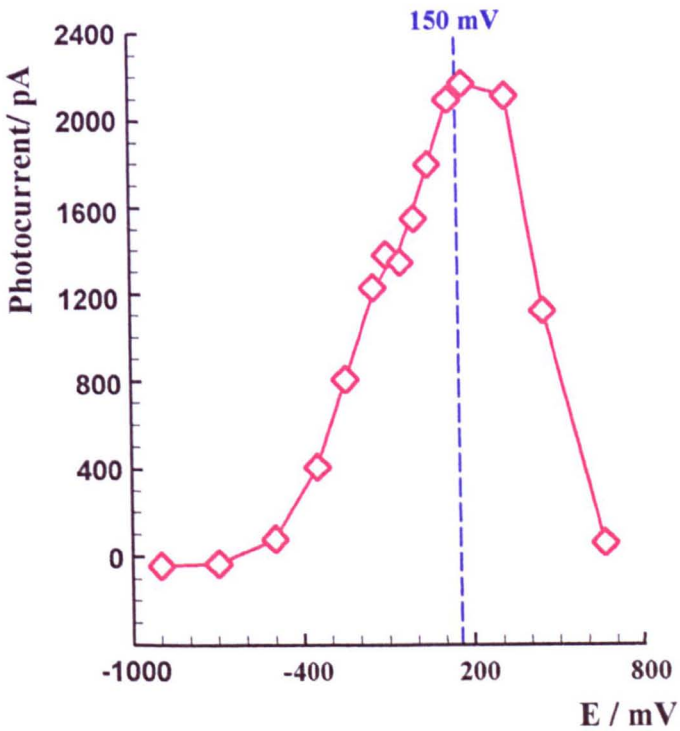

b) 316F stainless steel

This graph shows the data for the images seen in figure 5.7

$\tau = 24\ \mu s$, $v_p = 8.24\ cm\ s^{-1}$

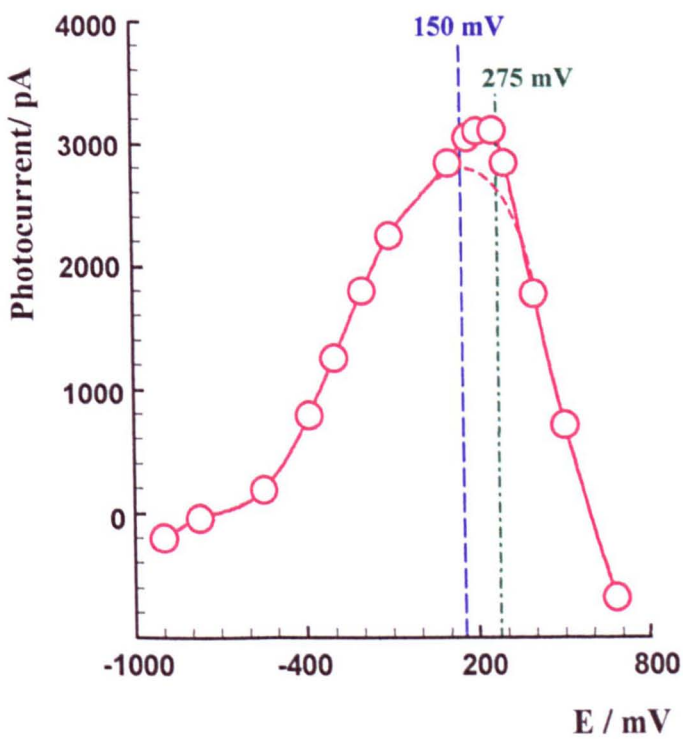

Notes : Solution = 0.3M $NaClO_4$, potential vs Hg/Hg_2SO_4-sat K_2SO_4, lens magnification = x 4 (N.A. = 0.13), laser spot diameter = 2 µm. a) Light intensity = 10% I_o. b) Light intensity = 100% I_o. See figure 5.6 for further examples, showing the effect of potential on the photocurrent generated.

figure 5.8

FURTHER EXAMPLES OF PHOTOCURRENT VS POTENTIAL GRAPHS ACQUIRED FROM PHOTOCURRENT IMAGING EXPERIMENTS

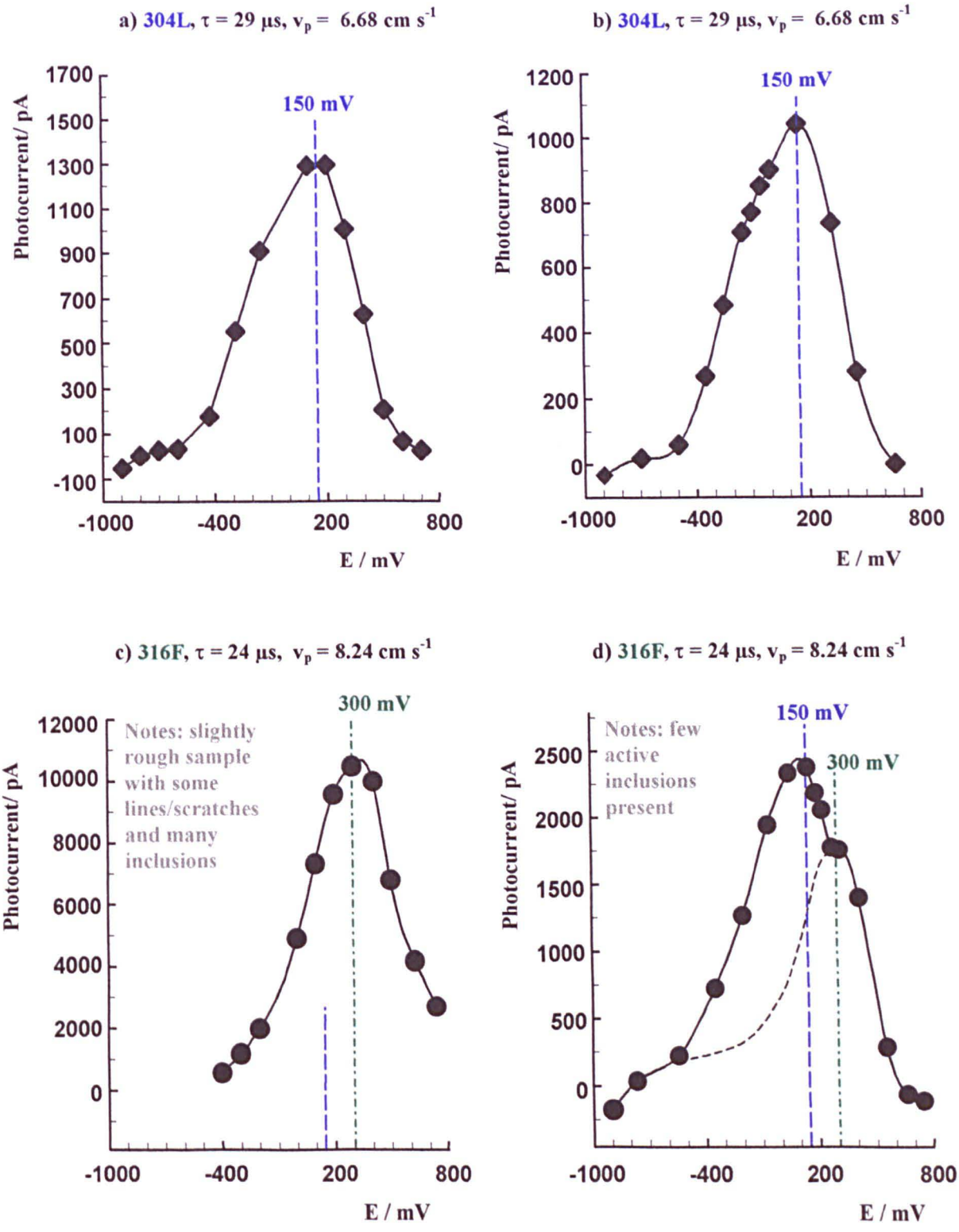

Notes : Solution = 0.3M $NaClO_4$, potential vs Hg/Hg_2SO_4 in sat. K_2SO_4, lens magnification = x 4 (N.A. = 0.13), laser spot diameter = 2 μm. Graphs a) and b) have the same experimental settings as figure 5.8a. Graphs c) and d) have the same experimental settings as figure 5.8 b.

figure 5.9

Further Analysis of Photocurrent Image Data by Line Analysis

The photocurrent images recorded show a bright leading edge and a dark trailing edge encompassing the electrode area. The effect seen on the photocurrent image showing a high in the photocurrent at the start of the electrode followed by a lower photocurrent through the middle and an even lower negative photocurrent after the electrode, resulted due to the fact that the effect of the laser perturbation on a point on the electrode was longer that the time the laser spent on the point. So the effect on the overall photocurrent observed was still being felt when the following point and similarly further points still were being stimulated. So the resulting signal at any point will contain a sum of signals from previous points which are still being felt at that time after perturbation. There are two effects: an overshoot and relaxation of the photocurrent as the laser passes on to the steel, and an undershoot and relaxation as it passes off the steel. This is the same form of photocurrent transient that is found on Fe (ref. C1-22).

The photocurrent versus potential graphs do not show how these bright and dark areas changed with potential as only the electrode centre region was analysed. So further analysis of the photocurrent images was carried out to investigate this effect, using the line analysis technique. Here a line was taken across the image averaging 20 pixels (i.e. 10 pixel above and 10 pixels below the line chosen). From the line data a graph of photocurrent versus the length across the image was plotted for each potential. Examples of some of these graphs are given in figure 5.10.

The line graphs showed that :

1. At very low potentials (e.g. -900 mV, see figure 5.10a) both the electrode centre and edges (leading bright edge and trailing dark edge) had low photocurrents of near zero.
2. At the peak potential (e.g. +174 mV, see figure 5.10d) both the edges and the centre had fairly high photocurrents.
3. At the very high potentials (e.g. +600 mV, see figure 5.10f), even though the leading and trailing edges still exhibit a fairly high photocurrent the photocurrent at the centre was near zero.

EXAMPLES OF LINE DATA ANALYSIS CARRIED OUT ON THE PHOTOCURRENT IMAGES FOR THE 304L STAINLESS STEEL

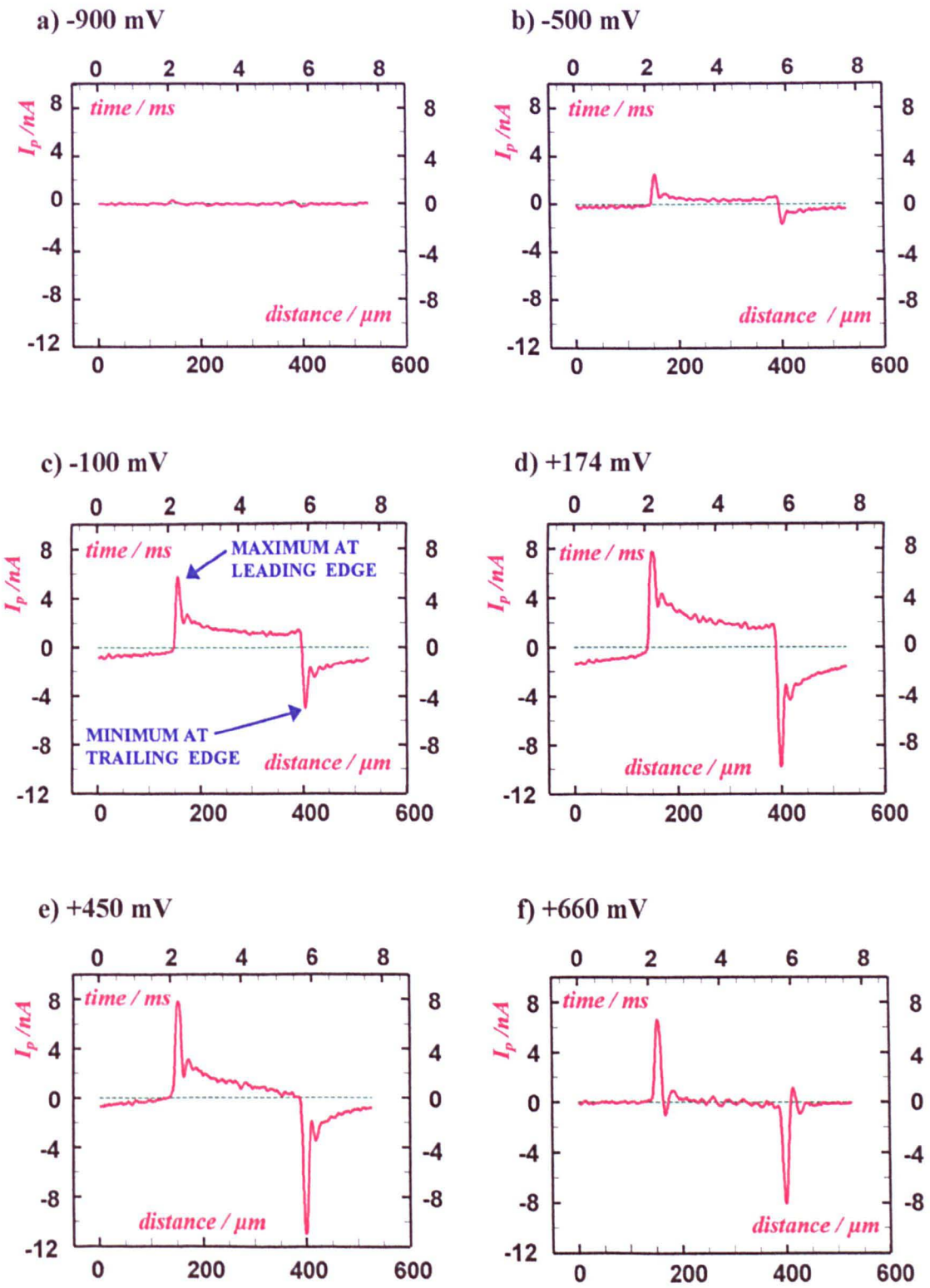

Notes : Solution = 0.3M $NaClO_4$, potential vs Hg/Hg_2SO_4 in sat. K_2SO_4, laser intensity = 10% I_o, total, pixel dwell time = 10 μs, τ = 29 μs, v_p = 6.68 cm s^{-1}. This data was taken from the images shown in figure 5.6 .

figure 5.10

It was surprising to see that, even though the photocurrent at the centre of the electrode region at the very high potentials resembled that at the very low potentials, the positive photocurrent at the leading bright edge and the negative photocurrent at the trailing dark edge did not: the photocurrent signal for both the edges and the electrode centre increased at the low potentials in a similar manner but then with increasing potential the photocurrent at the centre decreased to near zero but the photocurrent at the edges did not. This suggest the occurrence of two types of reaction with two different relaxation times: a fast one and a slow one.

This effect was further investigated by extracting the information showing magnitude of the maximum photocurrent at the leading edge and the minimum photocurrent at the trailing edge at each potential. From this information graphs showing how the positive photocurrent on the bright leading edge varies with potential (figure 5.11a) and how the negative photocurrent on the dark trailing edge varies potential (figure 5.11b) were plotted. These graphs show an almost mirror like relation to one another. However comparing the maximum photocurrent seen at the leading edge, with the photocurrent seen on the centre of the electrode clearly showed that two processes were occurring: for both, where the response at the low potentials was similar, but at the higher potentials, one process stayed fairly constant in amplitude with increasing potential whilst the other diminished.

In addition it was noticed that if any lines or scratches were present in the sample, due to insufficient polishing, the photocurrent magnitude at the electrode centre were found to be similar that seen at the leading edge of the electrode. So good polishing was essential, not only to see the inclusions better on the confocal optical images, but to keep the photocurrents at the centre fairly low so that any change due to the dissolution of any inclusions could be easily observed and not swamped by the large photocurrent signal due to the surrounding bulk of the electrode.

VARIATION IN THE MAXIMUM AND MINIMUM PHOTOCURRENT EXTRACTED FROM THE LINE DATA

a) Maximum at the leading edge

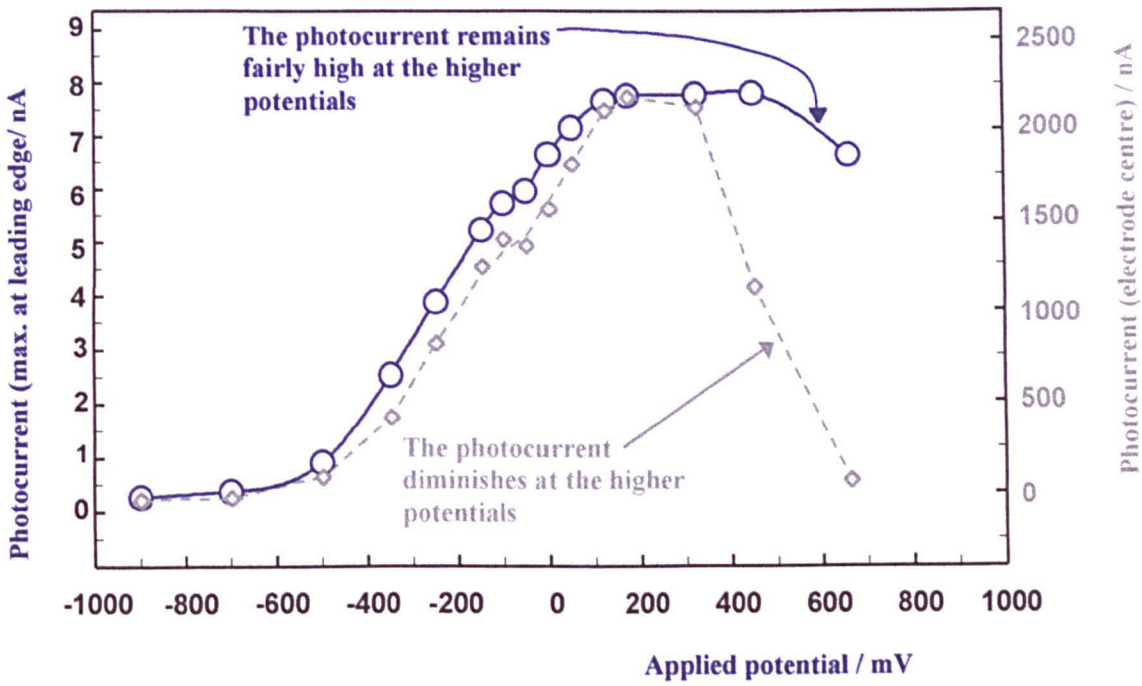

b) Minimum at the trailing edge

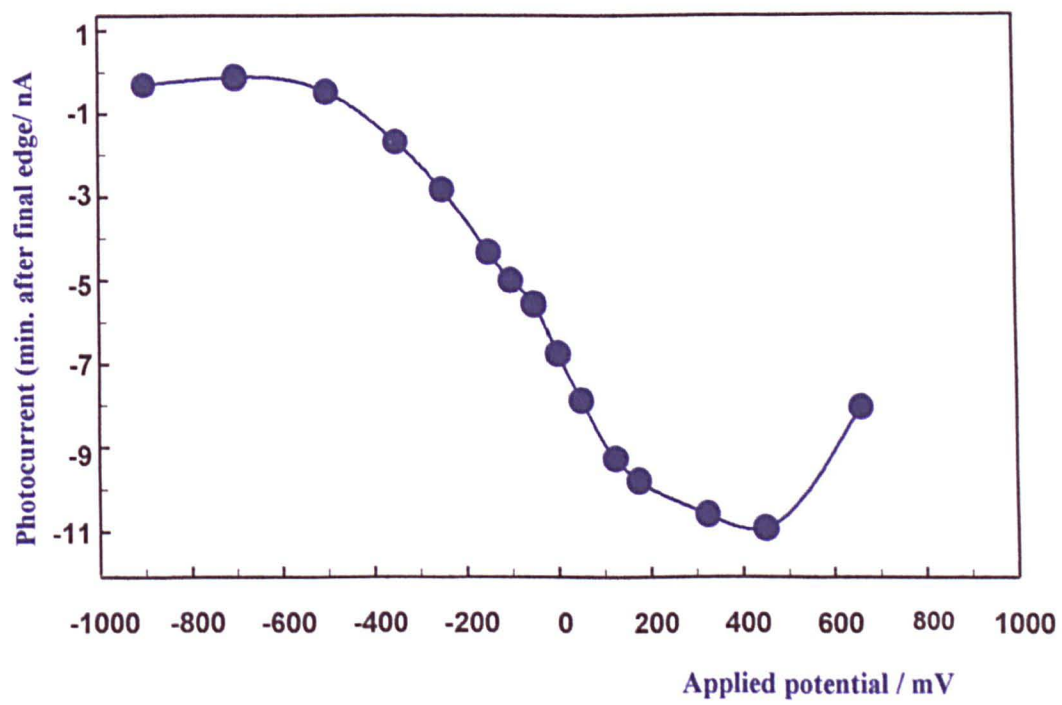

Notes : Solution = 0.3M $NaClO_4$, potential vs Hg/Hg_2SO_4 in sat. K_2SO_4, laser intensity = 10% I_o, total, pixel dwell time = 10 μs, τ = 29 μs, v_p = 6.68 cms^{-1}. The data was taken from the images shown in figure 5.6 .

figure 5.11

A Discussion of the Effects of Potential

The reason for the occurrence of two overlapping photocurrent peaks (see figures 5.8, 5.9) in the stainless steel containing sulphide inclusions may be due to the fact that the first peak is associated with the behaviour of the stainless steel itself and the second peak is associated with the sulphide containing inclusions. This implies the photocurrent density on the inclusions is greater than on the stainless steels.

In this work the measurements were carried out starting at a potential of -900mV vs SSE, and increased in a positive direction. The passive films on stainless steels are known to exhibit n-type behaviour above this potential (-900 mV) as previously explained in section 5.1. From previous electrochemical work on stainless steel films (see ref. sec. J3), in this potential region, C^{-2} vs E graphs showed a similar broad curve pattern (figure 5.3a) to the I_{photo} vs potential curves seen in the work shown here. This would suggest a relationship between the amount of photocurrent generated an the capacitance at the electrochemical interface. This suggests as the capacitance decreases the photocurrent increases.

As previous work showed that stainless steel (ref. sec. J3) and iron (ref. sec. J5) gave similar results when C^{-2} vs E were plotted for potential above -900 mV SSE (see figure 5.3) this would suggest that the behaviour of the passive film above -990 mV SSE depicts the behaviour of the iron content of the film. This was confirmed using not just previous work involving capacitance measurements but work involving photocurrent measurements as well. Previous work by D.E. Williams and coworkers showed the occurrence of a similar the broad peak in photocurrent versus potential behaviour in the study of iron (ref. C1-22, 1993).

From this work it may be deduced that this behaviour occurs due to the presence iron containing anodic oxides/ hydroxides on stainless steel. Capacitance at the interface may change due to surface states which are higher oxidation states of iron. This would lead to an increase in the photocurrent. Then trapping states may be generated at the surface which trap the charge carriers, or the iron may dissolve out of the passive film

as the potential is increased past the peak value (~150 mV, SSE) leading to the reduction of the photocurrent magnitude.

5.6 EFFECT OF LASER INTENSITY

Effect of laser Intensity on the Magnitude of Photocurrent Seen on the Image

The effect of laser intensity was first studied using a 316 sample with the neutral density filters present on the filter wheel supplied with the microscope system. These allowed through 100% (no neutral density filter), 10%, 3% and 1% transmission of the original light intensity (I_o). Photocurrent images were recorded (figure 5.12) and the images analysed to show how the photocurrent varied with light intensity. This suggested the occurrence of a non-linear relationship (figure 5.13a) between the applied light intensity and the photocurrent generated. Even though there was an increase in the photocurrent with light intensity at the higher light intensities a photocurrent lower than expected from that seen at the lower photocurrents was produced. This behaviour was later confirmed using a 304L sample with the use of a further two neutral density filters (55.6% I_o, 27.3% I_o) . The transmission of the Ar^+ laser light through the new filters was determined by means of absorbance readings taken over the appropriate wavelengths using a UV/visible spectrophotometer (see Appendix E-section 3). The photocurrent versus intensity curves plotted for this (figure 5.13b) again showed a non-linear relationship.

A straight line graph would be expected if a 1:1 relationship exists between the number of photons absorbed and the number of separated electron-hole pairs generated. However here, as the laser intensity was increased, the generation efficiency (photocurrent per photon) was found to decrease. This could be due to the occurrence of a saturation effect, with only a limited number of centres being capable of the generation of separated electron-hole pairs.

EFFECT OF LIGHT INTENSITY ON THE PHOTOCURRENT IMAGE

Sample - 316F stainless steel, Solution = 0.3M $NaClO_4$, Potential = +317 mV

a) 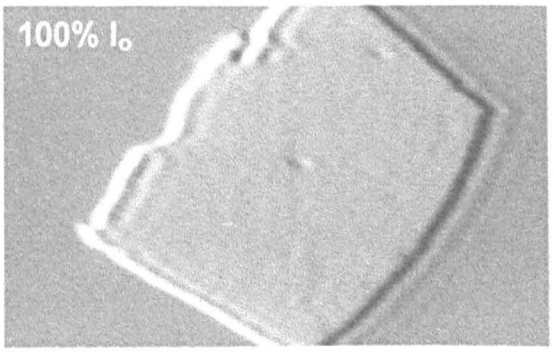

Grey scale = 100 nA,

Photocurrent range = -60nA to +40 nA from black to white on the grey scale

b) 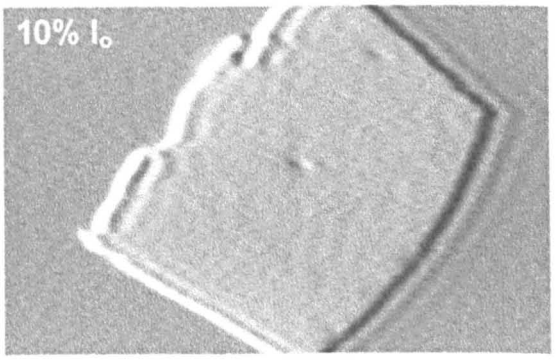

Grey scale = 20 nA,

Photocurrent range = -12nA to +8 nA from black to white on the grey scale

c) 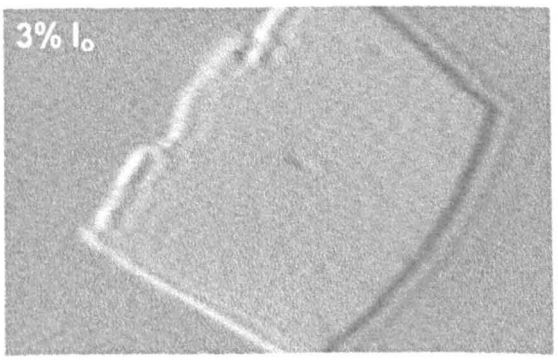

Grey scale = 20 nA,

Photocurrent range = -12nA to +8 nA from black to white on the grey scale

d) 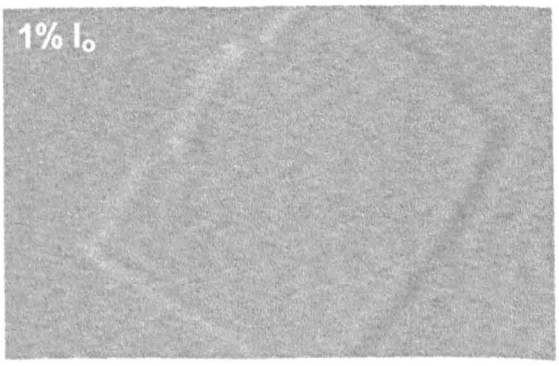

Grey scale = 20 nA,

Photocurrent range = -12nA to +8 nA from black to white on the grey scale

Notes : Lens magnification = x 4 (N.A. = 0.13), laser spot diameter = 2 μm, laser intensity = 100% I_o, pixel dwell time = 10 μs, τ = 24 μs, 'laser-off value' = 153/256 pixels.

figure 5.12

EFFECT OF LASER INTENSITY ON THE PHOTOCURRENT GENERATED

a) 316F stainless steel, E = 0 mV

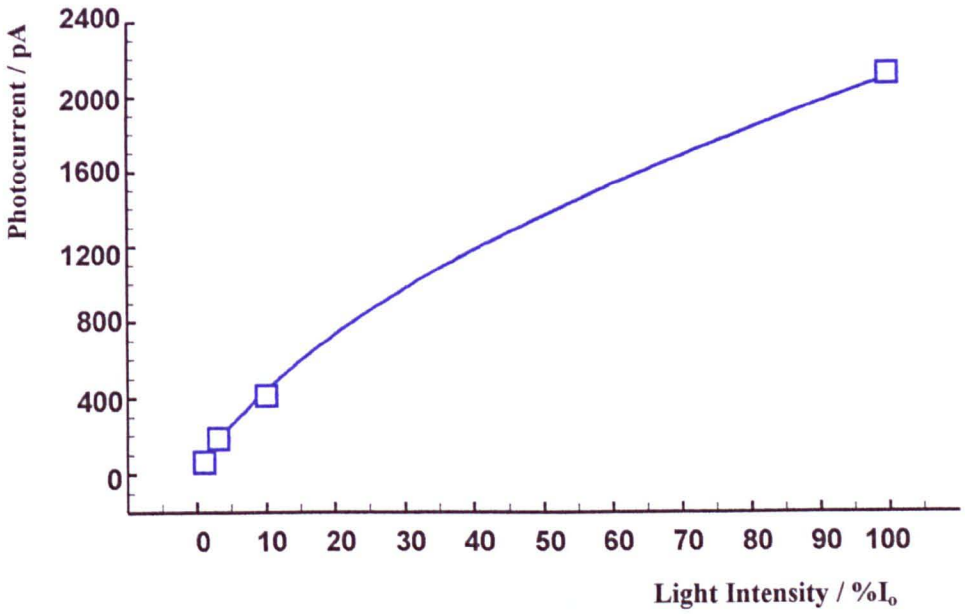

b) 304L stainless steel, E = +448 mV

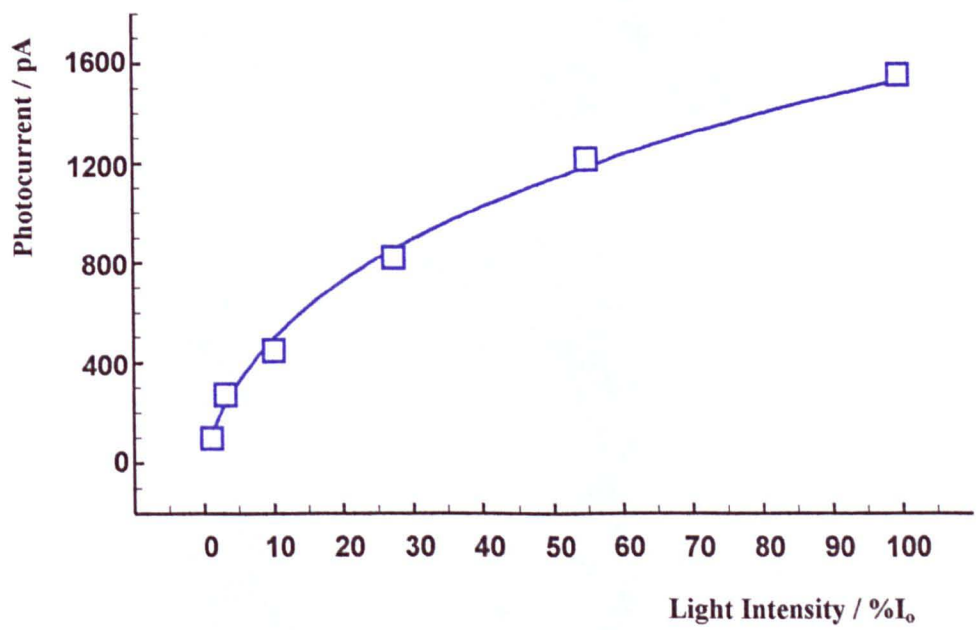

Notes : Solution = 0.3M $NaClO_4$, lens magnification = x 4 (N.A. = 0.13), laser spot diameter = 2 µm. a) Pixel dwell time = 10 µs, τ = 24 µs, v_p = 8.24 cm s^{-1}, see images in figure 5.9. b) Pixel dwell time = 10 µs, τ = 29µs, v_p = 6.68 cm s^{-1}, see images in figure 5.11.

figure 5.13

Effect of Laser Intensity on the Spatial Variations Seen on the Image

The apparent shape of the inclusions revealed on the photocurrent image changes with decreasing light intensity. Figures 5.14 and 5.15 illustrate the effect for a particular inclusion containing a high concentration of Si and Al. The image was found to change shape from a 'crescent shape' at high light intensity to a 'rectangular' shape at low light intensity and back again if the intensity was made high again (figure 5.15). From the comparison with the topography with the high resolution confocal optical or SEM images it can be seen that the low photocurrent image resembled the topographical shape (figure 5.14) the most.

THE SHAPE OF AN INCLUSION ON A 304L STAINLESS STEEL SAMPLE GIVEN BY TOPOGRAPHICAL IMAGING

a) A Confocal Optical Image

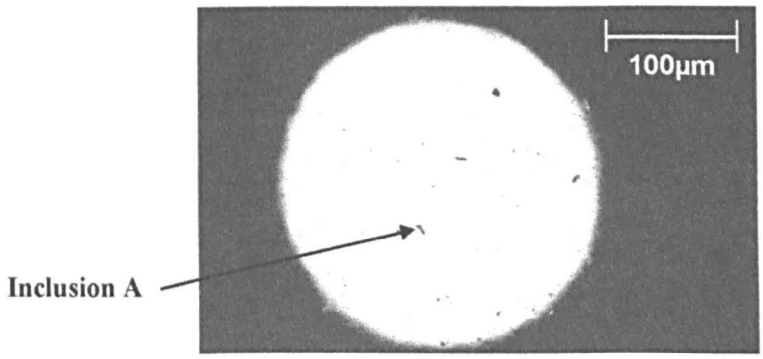

b) An SEM Image

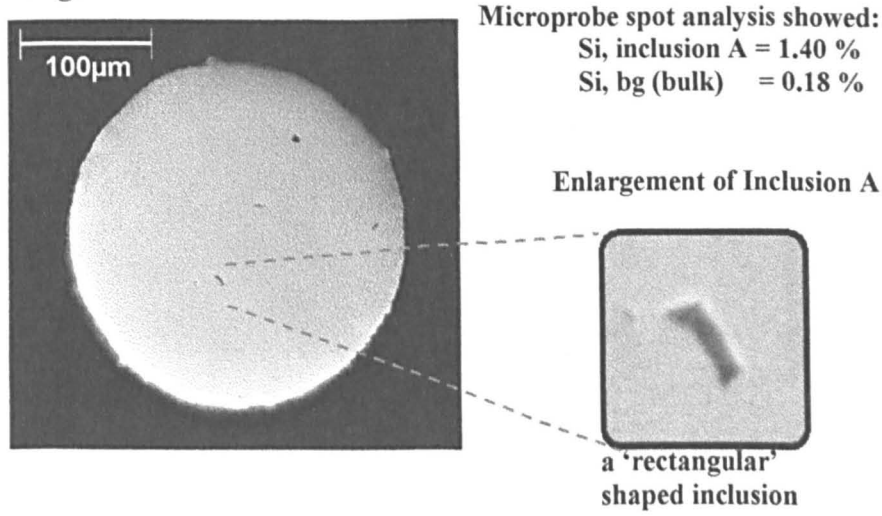

Notes : a) Lens magnification = x 40 (N.A. = 0.40), laser spot diameter = 0.6 µm, total area sampled in experiment = 421 x 251 µm (768 x 512 pixels), pixel dwell time = 10 µs, τ = 11 µs. b) Acceleration voltage = 25 kV.

figure 5.14

EFFECT OF LIGHT INTENSITY ON THE SHAPE PRODUCED IN THE REGION OF AN INCLUSION ON 304L STAINLESS STEEL SAMPLE

a) **A Photocurrent Image of the Whole Electrode at 100% I_o**

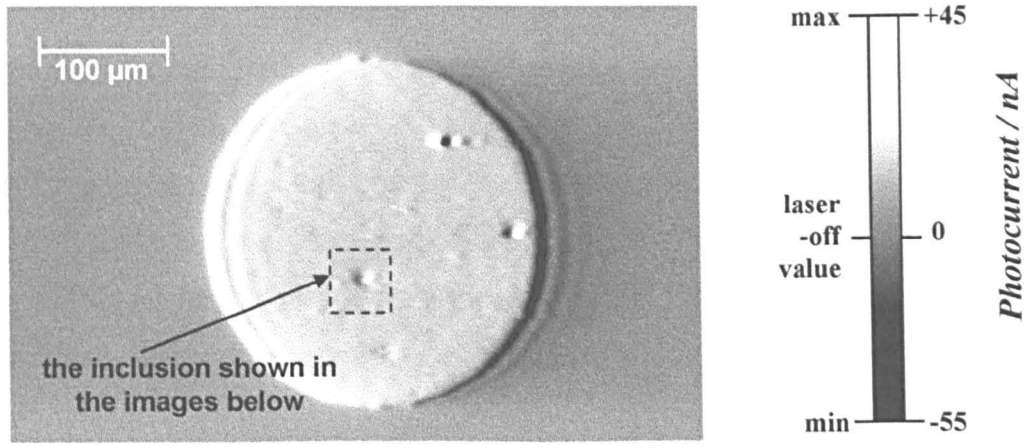

b) **An enlarged Selection of the Image Data Showing How the Photocurrent Variation over an Inclusion Changes with Light Intensity**

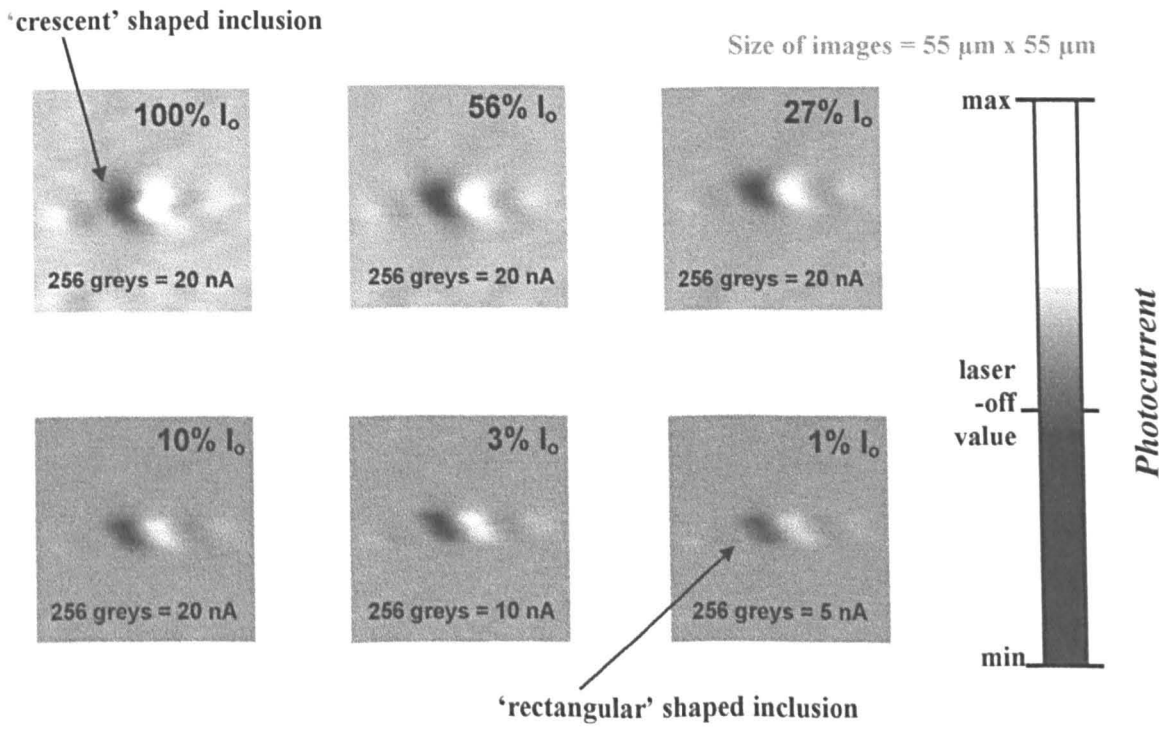

Notes : Sample - Solution = 0.3M $NaClO_4$, potential = +0 mV, lens magnification = x 4 (N.A. = 0.13), laser spot diameter = 2 µm, laser intensity = 100% I_o, total area sampled in experiment = 527 x 325 µm (768 x 512 pixels), pixel dwell time = 10 µs, τ = 29µs. laser-off value = 141/256 pixels.

figure 5.15

5.7 EFFECT OF LASER VELOCITY

The effect of slowing down the line scan time and hence the laser beam irradiation time (τ) resulted in the photocurrent average over the entire electrode decreasing (figure 5.16). In addition the bright leading edge narrowed in width and became dimmer, whilst similarly the dark trailing band became brighter and decreased in length. The ringing (see the 1st image in figure 5.16) also decreased. This simply showed that when the laser was moving fast the early part of the photocurrent versus time signal, which was a high photocurrent, was dominant. However at the very slow scanning times the photocurrent signal derived mostly from the later part of the photocurrent versus time transient where a low photocurrent was dominant.

5.8 INCLUSION COMPOSITION AND PHOTOCURRENT GENERATION

304L Stainless Steel

The inclusions contained in 304L stainless steel were enriched in Si. These also quite often contained some other materials typically Al and/or Ti in higher than expected amounts. These inclusions were found to produce a more negative photocurrent than the background area of the bulk stainless steel containing no inclusions. Over a range of photocurrents from -900 mV to +800 mV the photocurrent became progressively more negative over these inclusions.

EFFECT OF LASER SCAN VELOCITY ON THE PHOTOCURRENT IMAGE

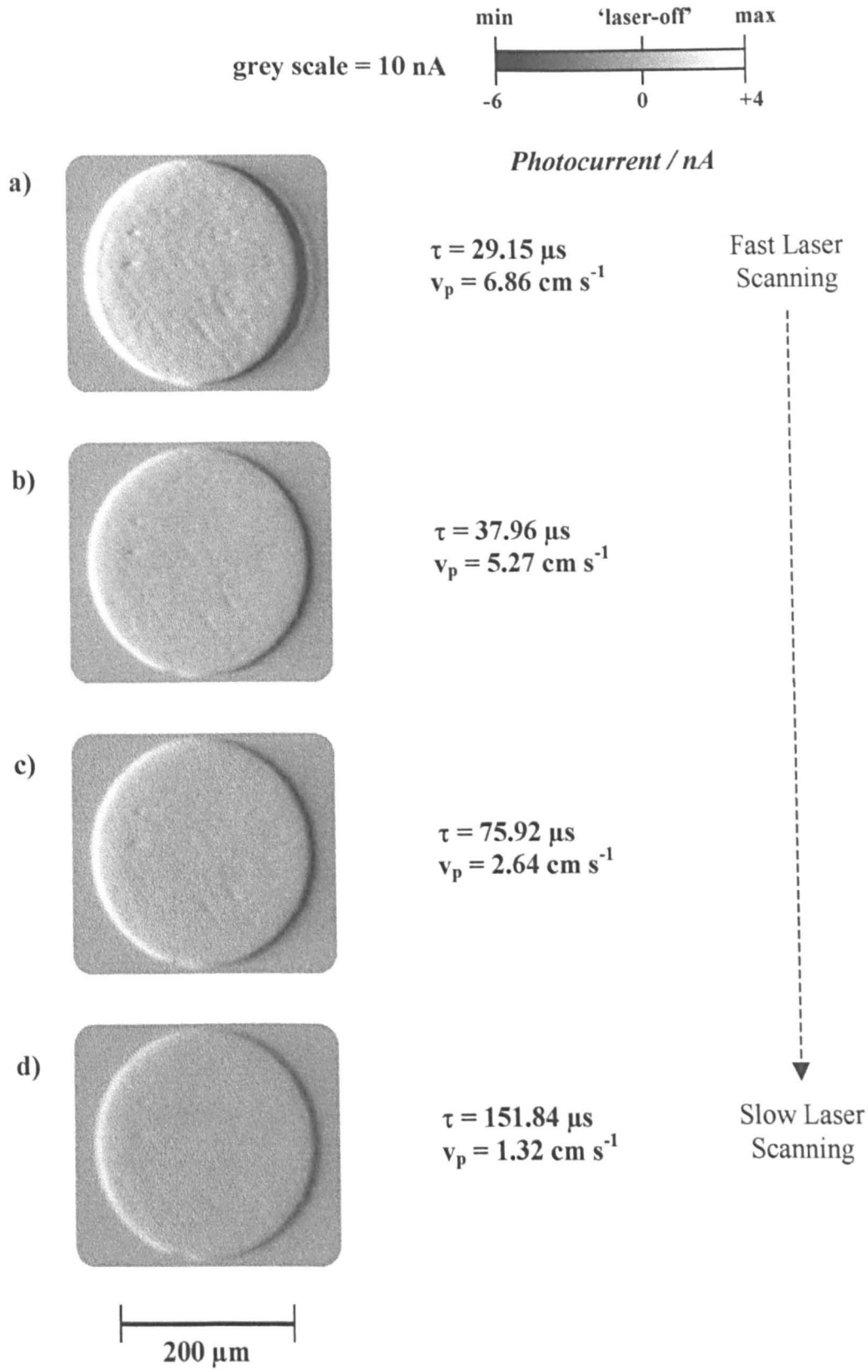

Notes : Solution = 0.1M $NaClO_4$, E= +488 mV vs Hg/Hg_2SO_4-sat K_2SO_4, lens magnification = x 4 (N.A. = 0.13), laser spot diameter = 2μm, laser intensity = 100% I_o, total area sampled in experiment = 527 x 325 μm (768 x 512 pixels), pixel dwell time = 10 μs, laser-off value = 150/256 pixel values.

figure 5.16

316F Stainless Steel

The majority of the inclusions contained in 316F stainless steel were enriched in Mn + S or Mn + O or a mixture of both. These inclusions did not show up on the photocurrent image unless they were very large or they were undergoing dissolution. At lower potential, and if large enough, these inclusions were seen as an area that was slightly darker than the surrounding background area of the stainless steel. The inclusions containing Si / Al / Ti were also present but in much smaller sizes than that found for the 304L stainless steel. These typically did not show up on the photocurrent image.

5.9 CONCLUSION

The general photocurrent vs potential trends observed are probably due to the behaviour of the iron in the outermost layer of the passive film on stainless steel. A broad peak was seen in the photocurrent (average over the electrode area from the image) versus potential range from -900 mV to +800 mV vs SSE. The rise in the photocurrent with potential may have occurred due to the increasing oxidation state of iron in the outer part of the passive layer. As the potential was increased further still (above ~ +150 mV) a reduction in the photocurrent occurred which may have resulted due to the iron dissolving out of the passive layer.

A maximum in the photocurrent occurred between +100 and +300 mV for the stainless steels examined, with the tendency for the 304L peak to be near +150 mV and the 316F peak to be near +300 mV. There did however in the case of, the sulphur rich, 316F samples seem to be a second overlapping peak, the maximum of which also occurred at ~ +150 mV. The difference between these two samples was that 316F contains molybdenum and sulphur to higher levels than the 304L sample. A peak in the total current did occur around +200 mV on the total current cyclic voltammogram but it was very subtle compared to the very pronounced peak seen on the photocurrent, from the photocurrent images.

Transient effects observed in the photocurrent suggested the occurrence of at least two separate reactions one with a faster relaxation time than the other. This was suggested by the fact that the photocurrent vs potential behaviour at potentials higher than the peak potential was different at the edges of the electrode, to that at the centre of the electrode.

Decreasing the laser intensity was found to decreased the photocurrent but not linearly, due to the occurrence of a saturation effect and resulted in a change of the image contrast seen. This is consistent with the results found with varying light intensity for a silicon memory chip (Chapter 3). As this showed the photocurrents decreased with decreasing light intensity, and that the lowest light intensity image most resembled the optical image.

Increasing the laser beam irradiation time, from $\tau = 29$ μs to $\tau = 152$ μs, slightly decreased the photocurrent.

Many different types of inclusion were found present in the two samples. The difference in the composition resulted in different sign of photocurrent over the inclusion compared to the surrounding steel not containing inclusions. The difference depended on the specific composition and the size of the inclusion.

As work carried out in these experiments showed that 316F was more susceptible to corrosion even in $NaClO_4$ alone at high potentials, this sample was chosen to study, the corrosion of stainless steel, in the chapter which follows.

6. A STUDY OF THE INITIATION OF LOCALISED CORROSION IN STAINLESS STEEL

6. A STUDY OF THE INITIATION OF LOCALISED CORROSION IN STAINLESS STEEL

6.1 AN INTRODUCTION TO THE CORROSION OF STAINLESS STEELS

The work in this chapter investigated the effect of sulphide inclusions, primarily in pitting corrosion, and secondly in crevice corrosion. This section (6.1) explains what corrosion is, the different types of corrosion which can occur, and reviews the previous work carried out involving sulphide initiated corrosion.

What is Corrosion?

Corrosion is the degradation of a metal by an electrochemical reaction with its environment. Most metals have an inherent tendency to corrode. This is because the metal exists at a higher energy state than the associated corrosion products so they are preferred. In order for the metal atoms to corrode enough activation energy must be provided to surmount the energy barrier from reactant to products. The Gibb's free energy shows the tendency of a metal to corrode. Most metals used in every day life have already corroded to an extent. That is they have layers of oxides, known as passive layers, on their surfaces which renders them less likely to corrode.

Corrosion can be studied using an electrochemical cell. Corrosion will occur in an electrochemical cell if there is a net release of free energy across the metal - electrolyte interface if the nature of the metals changes when exposed to the electrolyte. This energy difference manifests itself as an electrical potential.

Corrosion of a metal: $M \longrightarrow M^{2+} + 2e^{-}$ (6.1)

Two forms of corrosion can result directly from changes in composition within an electrolyte. These are:

1. Crevice corrosion - this occurs at the edge of a metal at its junction with another substance
2. Pitting corrosion - this occurs centrally in a metal surface often at the site of an impurity inclusion in the sample

Much of the work carried out on pitting and crevice corrosion has suggested that the initiation process for pitting and crevice corrosion may differ from one another but that the latter part of the corrosion process is the same for both.

Corrosion in Stainless Steels

Stainless steel has excellent corrosion resistant properties but even so corrosion can readily occur under some conditions such as sea-water (this is high in Cl^-). In the corrosion process hydrogen ions are usually produced, leading to an acidic local environment within the confined region of a pit or crevice (equation 6.2) which results in the metal degrading in this region.

Production of acid: $$M^+ + H_2O \longrightarrow MOH + H^+ \qquad (6.2)$$

Stainless steel is made up of many metals (see Chapter 5, section 5.1) the principle elements being Fe, Cr and Ni. The corrosion of Fe not is thought to be the most damaging process but the dissolution of chromium (6.3) subsequently followed by its hydrolysis is thought to lead to the greatest drop in pH.

$$Cr^{3+} + 3H_2O \longrightarrow Cr(OH)_3 + 3H^+ \qquad (6.3)$$

It is thought that disturbances of the oxide film such as those due to grain boundaries, flaws and inclusions could provide preferential sites for the adsorption of Cl^- ions causing the cracking of the passive oxide film covering the stainless steel. In

comparison, pitting in very pure iron occurs at random on the surface with no preference for a particular site.

Pitting Corrosion

Environmental variables which are known to effect the pitting behaviour of stainless steels are the temperature, the cathodic reactants (O_2, H^+, M^{n+}), chloride ions (Cl^-), and sulphur compounds such as: sulphate (SO_4^{2-}), thiosulphate ($S_2O_3^{2-}$), and sulphide (HS^- or H_2S) or sulphite (SO_3^{2-}). The sulphur compounds originate from sulphide inclusions present in the stainless steel. Pitting corrosion develops in stages known as: initiation / nucleation followed by metastable growth of the pit and then finally stable growth of the pit. These three stages of pitting corrosion have been discussed in detail in the work which follows.

a) Initiation of pitting corrosion

The importance of the role of sulphide inclusions in the occurrence of pitting corrosion has been known for some time (ref. K3-2, G. Wraglen, 1974). Wraglen said that chloride would preferentially be absorbed onto sulphide inclusions, typically MnS, and this would occur due to the fact that sulphide inclusions have a higher electrical conductivity than the surrounding film on the bulk stainless steel. This results in the formation of strong electrostatic forces helping to attract and then hold the Cl^- ions to the inclusion surface. It has been since shown that MnS inclusions do not contain just Mn and S alone (ref. K1-4) but that they may also contain chromium and iron and as well as other elements which may be physically associated with the oxides.

Wraglen (ref. K3-2) stated that the Cl^- ions helped to facilitate the anodic dissolution of MnS which he suggested would dissociate into elemental sulphur spheres on the MnS inclusion surface (equation 6.4). This reaction would then be balanced by a cathodic oxygen reduction reaction occurring on the adjacent stainless steel surface over the oxide film (equation 6.5).

INITIATION, STAGE 1. FORMATION OF ELEMENTAL SULPHUR

Anode reaction:

$$MnS \longrightarrow S + Mn^{2+} + 2e^- \quad (6.4)$$

Cathode reaction:

$$O_2 + 4H^+ + 4e^- \longrightarrow 2H_2O \quad (6.5)$$

Wraglen stated that the sulphur formed would then be electrochemically oxidised to sulphite which would provide a local acid environment which would initiate the corrosion of the stainless steel (equations 6.6 to 6.8).

INITIATION, STAGE 2. THE FORMATION OF SULPHIDE

Anode reactions:

$$S + 3H_2O \longrightarrow HSO_3^- + 5H^+ + 4e^-$$
$$\downarrow H_2O$$
$$SO_4^{2-} + 3H^+ + 2e^- \quad (6.6)$$

resulting dissolution of the MnS

$$MnS + 2H^+ \longrightarrow H_2S + Mn^{2+} \quad (6.7)$$

Local Cathode Reaction:

$$2H^+ + 2e^- \longrightarrow H_2 \quad (6.8)$$

The formation of sulphur spheres was shown experimentally by Eklund (ref. K5-1, 1974). It was shown that when a MnS electrode was polarised at +200 mV vs NHE in 0.1M NaCl solution, the formation of discrete sulphur spheres of around 1 μm radius occurred on the surface (the SEM image showed white coloured spheres compared to the darker surroundings). Eklund presented thermodynamic calculations which showed that MnS would be less stable compared to S in a Cl^- containing solution at potentials greater than -0.1V NHE. As the sulphur was deposited in perfect sphere shapes it was suggested that these particles had grown from the solution near the electrode. Eklund showed that the pH in equilibrium with the solid decreased to 5.8 over time and if the

sulphide preparation contained Fe and Cr as well, then the solution became even more acidic reaching a final value of around pH 4.

It was suggested by both Wraglen and Eklund that immediately after the dissociation of the MnS had begun the depth of the MnS inclusion would decrease forming a gap (pit) where the MnS was previously attached to the bulk stainless steel. This gap would contain bare stainless steel, without an oxide layer on it, which would then be easily attacked and dissolved by the acidic pit solution containing H_2S and HSO_3^-.

INITIATION, STAGE 3. BULK METAL DISSOLVES WHEN ATTACKED BY ACIDIC SUBSTANCES FROM THE PIT SOLUTION

Anodic dissolution of the iron:

$$Fe \longrightarrow Fe^{2+} + 2e^- \qquad (6.9)$$

Supporting cathodic reaction on the surrounding passive surface:

$$O_2 + 4H^+ + 4e^- \longrightarrow 2H_2O \qquad (6.7)$$

More recent work has shown the occurrence of areas enriched in sulphur on the stainless steel just outside the inclusion area after exposure to Cl^-. Castle and Ke (ref. K3-8, 1990) showed that a ring enriched in S appeared around certain oxide / sulphide inclusions. It was presumed that the S ring would act as a local cathode. Ke and Alkire (ref. K3-16, 1992) also reported that sulphur species were found to spread on to adjacent passive surface occupying an area of about 4 times in diameter compared to that of the inclusion. It was suggested that the subsequent dissolution of the metal then only occurred at inclusions of around 1 μm size or much larger. Ke and Alkire also said that the pitting corrosion is initiated from a microcavity formed in the inclusion in the surrounding sulphur enriched area as opposed to directly over the inclusion area.

Another idea suggested by Alkire and Ke (ref. K3-16, 1992) is that the presence of thiosulphate is necessary in the occurrence of pitting corrosion as this will induce pitting at low potentials. They suggested that MnS breaks down into thiosulphate in the first instant and not sulphur. This mechanism was also used by Alkire and Lott (refs. K4-5,

K4-6, K4-7, 1988 - 1989) to describe how it can lead to crevice corrosion initiation. This has been described further in the next sub-section which follows (on crevice corrosion) along with more recent work in this area which strongly suggests this theory to be incorrect (refs. K4-9, K4-12, K4-14, 1993-1998) based on the way the experiment was conducted as well as new experimental evidence.

Baker and Castle (ref. K3-18, 1993) showed that pitting corrosion started at the edge of an inclusion and that $MnCl_2$ was seen to be deposited around the edges of the corrosion site and in the resulting cavity. They proposed that the formation of the $MnCl_2$ helped to stabilise the pitting corrosion.

b) Metastable pit growth

Recent work by Hong and Nagumo (ref. K3-30, 1997) suggested that for a pit nucleated at a given potential there must be a certain chloride concentration above which the pit can be activated into metastable propagation once it has been initiated. It was shown that if the bulk electrolyte was below a critical minimum chloride concentration for a particular potential then there were an insufficient number of ions to sustain the metastable pit. Under these conditions the pit which may have already been initiated just dies out by repassivation at the nucleation stage. The critical concentration of Cl^- required at a given potential in order to force metastable pit propagation to start to occur was given by the equation:

$$E \text{ in mV, vs SCE} = -37 \log [Cl^-] - 212 \qquad (6.8)$$

All pits are known to grow by metastable growth at first. Metastable growth requires a perforated cover to be maintained over the pit mouth. In this state the pit grows at a constant mean current density which is maintained by periodic partial rupture of the cover. Metastable pit growth can be detected by an observation of small spikes in the total current. Wraglen (ref. K3-2) suggested that the porous crust was initially made of red rust (FeOOH) which then is reduced to black rust (Fe_3O_4). As the crust / cap is porous in nature it allows the Cl^- to go into the pit maintaining the concentration of the aggressive pit solution (containing H_2S , HCl and $FeCl_2$). The partial rupture of the pit cap was said to occur occasionally to let out the H_2 gas produced and to maintain the local environment. More recent experimental work by Newman et al. (1997-1998, refs.

K3-37, K3-38, K6-2) has shown the presence of a metal lace like cover (the SEM image showed a white coloured area with dark holes in it) over the pit and surrounding region.

c) Stable pit growth

After metastable pit growth stable growth of the pit occurs. This occurs when the pit loses its cover and it continues to grow in a destructive fashion. This can be monitored by a continuously rising total current.

Even though sulphide inclusions have been shown in the work mentioned here to be the main influence in the initiation of pitting corrosion there have been some schools of thought that have ignored the effect of sulphide inclusions totally and just developed ideas based on the effects of chloride on the passive film alone.

Crevice Corrosion

Like pitting corrosion crevice corrosion can be split into initiation (incubation) and propagation stages. Initiation refers to a change from passivity to the development of an aggressive local solution in the area of the crevice. Propagation is then concerned with the continued metal dissolution in the crevice area.

The majority of models for crevice formation have not considered the involvement of sulphides at all until fairly recently. The models not involving sulphides include the 'passive dissolution model' and 'IR drop model'. The more recent models for crevice initiation include the 'sulphide or thiosulphate entrapment model' and the 'metastable pitting model'. A discussion of these mechanisms follows.

a) Mechanisms for crevice corrosion not involving sulphur

The passive dissolution model

The passive dissolution model (ref. K4-3, K4-4) is the simplest and most widely used model used for crevice corrosion in stainless steels. This suggests that the passive dissolution of Cr^{3+} results to a drop in the pH and an increase in the chloride

concentration to maintain the neutral charge. The increase in the local acidity and Cl^- then result in the initiation of crevice corrosion.

The IR drop mechanism of crevice corrosion.

Work by Pickering and Frankenthal (refs. K4-1, K4-2) suggested that an IR drop (I = current, R = resistance) within a crevice initiated the corrosion in and around the crevice area. It was suggested that an anodic current would result due to the resistance between the crevice and the solution, and in the confines of the restricted crevice geometry it could force the local electrode potential to change from a passive value to a value that would initiate corrosion.

b) Mechanisms for crevice corrosion considering the role of sulphur

The problem with the two mechanisms mentioned is that the role of sulphur (a minor alloying element) in stainless steel is not considered. It is well known that crevice corrosion shows many similarities to pitting corrosion. Increasing properties such as potential, chloride concentration, and the percentage of sulphur in the stainless steel, result in the same effect on both pitting and crevice corrosion. So if sulphur compounds play an important role in pitting corrosion they would be expected to play an important role in crevice corrosion as well.

The sulphide (or thiosulphate) entrapment model.

Alkire and Lott (refs. K4-5, K4-6, K4-7, 1988-1989) developed a model of crevice corrosion on the basis of thiosulphate production which they said formed initially and then further dissolution of the MnS also occurred to produce sulphur (equations 6.9, 6.10).

$$2MnS + 3H_2O \longrightarrow S_2O_3^{2-} + 2Mn^{2+} + 6H^+ + 8e^- \qquad (6.9)$$

$$MnS + 2H^+ \longrightarrow Mn^{2+} + S + H_2 \qquad (6.10)$$

Lott and Alkire however did not measure the thiosulphate in the stainless steel crevices but instead measured an increase in the ultra-violet absorption of the solution, at 216 nm, during dissolution of a MnS powder electrode in a thin-film spectrometry cell. Lott and Alkire found there was an excess of Mn^{2+} compared to the amount of thiosulphate

produced (equation 6.9) this was attributed to the formation of elemental sulphur (equation 6.10).

Nash and Kelly (1993, ref. K4-9) found that studying the crevice solution removed during the incubation period showed that sulphide (HS^-) was the only sulphur species found during the incubation period and that thiosulphate was not found but they did not rule out its possible involvement as Lott and Alkire had previously detected it (refs. K4-5 to K4-7).

More recent work by Brossia and Kelly (refs. K4-12, K4-14, 1995-1998) involving the chemical analysis of the solution extracted from the crevices of 304L stainless steel showed that thiosulphate ($S_2O_3^{2-}$) was not present and the dominant species present was sulphide (HS^-) at the initiation stage of crevice corrosion. They ruled out the results previously obtained by Lott and Alkire (refs. K4-5 to K4-7) due to the fact that the crevice solution had not been directly removed and analysed and the fact that they had found no trace of thiosulphate in the crevice solution. Brossia and Kelly therefore concluded that thiosulphate did not play an important role in crevice corrosion initiation. In addition they found that sulphite (SO_3^{2-}) was only formed after long times as a result of homogenous oxidation during the crevice corrosion propagation stage. Brossia and Kelly were also able to show that the crevice solution chemistry was independent of the amount of sulphur present (i.e. the same constituents were present regardless of the %S present in the sample). However the percentage of sulphur in the stainless steel did affect the amount of time required to start corrosion propagation. They were also able to show that if 316-type stainless steel, with the same amount of sulphur as a 304-type stainless steel, was used that it took three times as long for the crevice corrosion propagation stage to be reached but the components analysed in the crevice solution remained the same. As the majority of the sulphur present occurs as MnS inclusions it can be concluded that these inclusions play an important part in crevice corrosion. In a recent publication by Newman, Laycock and Stewart (ref. K4-13, 1997) it was concluded that the 'thiosulphate entrapment model' as it was originally known should be renamed the 'sulphide entrapment model' in light more of recent developments.

A crevice corrosion model involving meta-stable pitting.

A few researchers have suggested that not only does sulphur play an important role in the initation of crevice corrosion but that pitting is a special case of crevice corrosion (ref. K3-1, I.L. Rosenfeild, I.S. Danilov, 1967). Stockkert and Boehni (ref. K4-8, 1989) suggested that crevice corrosion was a geometrically stabilised form of pitting. In pitting corrosion metastable pits are stabilised by a porous cover over the pit. This keeps the pit in an active state by maintaining the concentration of the local solution. The pits have to precipitate a salt film to survive the eventual collapse of the cover. However, it was suggested that if a pit formed within a crevice, then when its cover collapsed the resistive barrier of the crevice geometry is enough to stabilise the pit. So the crevice can be considered to be like a large pit. The area adjacent to the crevice would then be exposed to the pit solution resulting in a general breakdown of the stainless steel. The most favourable sites were thought to be where the opposing walls of a crevice were very close together such as areas of contact between adjacent walls in a crevice. More recent work by Newman et al. (ref. K4-11, 1994) showed that if iron oxide (rust) was already present on stainless steel this resulted in very aggressive crevice corrosion behaviour. They were able to show that crevice corrosion in rust covered samples occurred at the same potential as metastable pitting which occurred in the clean (rust-free) samples. So this work was said to support Stockert and Boehni's work (ref. K4-8) suggesting that crevice corrosion involves metastable pitting. In addition many authors, including some supporting the passive dissolution mechanism, have observed the presence of pits with in the crevice region (ref. K4-4, K4-10).

Experimental Modifications to Reduce Corrosion

The recognition that MnS inclusions play a crucial role in the initiation of stainless steel corrosion has lead to a search for ways of removing them, or modifying their composition or changing their morphology. Removal techniques have included immersion for half an hour in a 50°C solution of 50% nitric acid and 2% sodium dichromate. The surface holes left after the removal of the sulphides have to by very thoroughly rinsed in order to remove the acid, otherwise the acid itself results in the further pitting of the sample.

Another method of modification has included laser melting of the surface layers using a high power laser. Recent work by Pan et al. (ref. K6-1,1998) showed this method improved localised corrosion resistance.

In addition to modifying or removing the sulphide inclusions, work using the addition of inhibitors (ref. K4-13, K6-2) has also been carried out. Inhibitors such as sulphate (SO_4^{2-}), perchlorate (ClO_4^-) and nitrate (NO_3^-) have been used. Work conducted by Kelly and Brossia (ref. K4-14, 1998) showed that the addition of sulphate to the bulk solution resulted in an inhibiting action on the crevice corrosion. They stated that this occurred due to competitive migration and / or absorption between the SO_4^{2-}. However they found that nitrate was a far stronger inhibitor as it probably reacted with a mechanism to reduce the amount of acid present (equation 6.11) as opposed to just relying on competitive migration (i.e. the effect of being a supporting electrolyte) as the sulphate did.

$$NO_3^- + 10H^+ + 8e^- \longrightarrow 3H_2O + NH_4^+ \qquad (6.11)$$

The supporting electrolyte effect is an effect which occurs when a species such as ClO_4^- or SO_4^{2-} competes with the Cl^- present in migrating or absorbing on to the surface. This then prevents the increase of the chloride concentration in the pit. The concentration and mobility of such an inhibitor is extremely important as it can delay the movement of the Cl^- ions into the pit. Newman and Moayed (ref. K6-2, 1998) showed that addition of 0.5M Na_2SO_4 to 1M NaCl inhibited pitting on type 904L stainless steel. In the presence of the sulphate there were fewer pits but the main effect observed was the decrease in the growth rate of the pits. SEM imaging conducted by Newman and Moayed showed the presence of a lace like covering around the inclusion area. They found that the lacy cover formed in the solution containing sulphate (0.5M SO_4^{2-} + 1M Cl^-) was much less porous, being more denser and thicker, than that found on a sample without the sulphate present (1M Cl^- only). The SEM images showed that the hole present at the centre of the lacy cover in the Cl^-/SO_4^{2-} solution was found to be small on the image compared to the surrounding lacy area. However in the Cl^- solution alone the central hole was large with very little lacy surrounding. From this work it was suggested that the pits grew in a much more stable fashion with the sulphate present.

Experimental Techniques Used in Previous Work

Even though a considerable amount of work has been carried out investigating the corrosion of stainless steels, it has been by means of conventional electrochemical techniques which record an average signal for the whole electrode. After the experiment, the work was then substantiated by recording optical images, or SEM images. However this does not provide an indication of the electrochemical spatial behaviour during the experiment itself, in order to relate any changes seen on the surface topography to any electrochemical changes which may have occurred. The conventional techniques do not show exactly where corrosion might initiate, which areas act as local cathodes (producing negative currents), which areas act as anodes (producing positive currents), and how the electrochemical behaviour continues to change spatially with time. As a result much guess work has gone into determining the mechanisms for the reactions involved.

More recently a little work has been conducted looking at spatial effects by photocurrent imaging using the laser spot scanning technique (this has been discussed in Chapter 1, Section 1.4) but this has been mainly to do with the effects seen by the disruption of passive films by the use of very high potentials (refs. C1-18, C1-25) without the presence of Cl^-. Though the results seen have been a little contradictory as negative photocurrent were observed by some (C1-18), and positive photocurrent by others (C1-25).

Another imaging technique which has been used is scanning electrochemical microscopy (SECM). In this method the stainless steel is immersed in the electrolyte solution and an ultra-microelectrode is scanned across the surface to form an image of the electrochemical reaction observed on each point of the electrode area scanned. Recent work using this technique to examining pitting corrosion initiation has been conducted by Y.Y. Zhu (refs. K3-38, C1-39, 1997-1998). This work used an atomic force microscope system which had been adapted to record electrochemical images as well as AFM images. Similar work on pitting corrosion has also been conducted by Lin and coworkers (ref. K3-39, 1998). The SECM work (K3-38, C1-39, K3-39) showed the development of positive currents at various locations on the stainless steel.

6.2 AIMS

The aims of the work carried out in this chapter were;

1. To examine the changes occurring, on both the photocurrent and confocal optical images, prior to and after the establishment of pitting corrosion at sulphide enriched inclusions.

2. To determine which types of inclusion result in corrosion and which do not, and to determine how they vary in elemental composition from one another, in order to relate the composition to the likelihood of pitting corrosion.

3.To examine any products formed in the very early stages of the initiation of pitting corrosion by microprobe elemental analysis and by topographical means such as optical imaging (colour video imaging and confocal reflective imaging) and SEM.

4.To compare the work done with pitting corrosion to that seen for crevice / edge corrosion.

6.3 EXPERIMENTAL

The same technique was used here as in the previous chapter, but this time only the 316F type stainless steel was used. The corrosion of stainless steel samples, in solutions containing varying concentrations of $NaClO_4$ and NaCl, was investigated by monitoring the effect of time on the photocurrent image. Fixed conditions of light intensity and potential were used for each experiment.

The first experiment was carried out in $NaClO_4$ alone at a high potential. Subsequent experiments were then carried out using increasing amounts of NaCl present as well as $NaClO_4$ maintaining the ionic strength constant. The applied potential was also increased in subsequent experiments and the ionic strength decreased to speed up the

reaction occurring. Incidentally a few experiments in the many carried out also exhibited a more severe form, of crevice / edge corrosion at the junction of the resin and stainless steel despite the precautions taken, so this was also investigated. A summary of the experimental conditions used follows on the next page.

Another difference in the experimental method employed in this chapter from the last was the fact that in the later experiments the total current produced over the whole electrode was monitored as well as the spatial photocurrents. This was carried out by the use of a 12 bit data logging device (Picotech ADC 100), which allowed the total current and the photocurrent images to be recorded with time simultaneously. This method was used to determine whether any of the changes picked up on the imaging work corresponded to changes in the total current.

Microprobe x-ray spot analysis and elemental concentration maps, SEM and optical images were also examined to determine the structure and type of inclusions present in order to determine which type of inclusion gives rise to pitting corrosion and what products are produced on the initiation of pitting corrosion.

Effect of time was monitored using solutions containing varying amounts of NaCl and $NaClO_4$ at fixed potentials vs SSE (Hg/Hg_2SO_4, sat K_2SO_4) with a Pt wire open ring counter electrode. The maximum laser output (25 mW) was used without the use of any neutral density filers (i.e. Light intensity = 100% I_o). The time shown for each photocurrent image, in the work which follows, is the time that was recorded after the final data point for that image (including any signal averaging) had been collected. It should be noted that for the earlier experiments, the time t = 0 was the time at the end of the 1st photocurrent image to be recorded. In subsequent experiments where the data logger was simultaneously used, to record total current whilst the photocurrent images were being recorded, the time t = 0 was the time when the potentiostat was switched on to the external cell (from the previous internal cell setting, where it was monitoring a resistor in the potentiostat). It was found that the time between that recorded at the end of the 1st image (after making any required instrumental adjustments and signal averaging the image) and the time when the potentiostat was switched on to the external cell was 4-5 minutes.

A summary table of the experiments conducted:

Investigation	Expt. No.	Effect	Solution			Potential
			NaCl	$NaClO_4$	Ionic Strength	
Pitting Corrosion in $NaClO_4$	A	$NaClO_4$ alone at a high potential. Imaged at +173 mV then left at +675 mV (15 minutes), then imaged at +173 mV again.	0.1M	———	0.1M	+675 mV
Pitting Corrosion with a low concentration of NaCl present	B	With a low concentration of NaCl present.	0.0125M	0.2875M	0.3M	+175 mV
	C	A slightly higher concentration of NaCl present at a lower potential.	0.025M	0.275M	0.3M	-250 mV
	D	In the presence of NaCl with a lower ionic strength.	0.025M	0.075M	0.1M	0 mV
	E	Imaging in the presence of NaCl as well as simultaneous monitoring of the total current.	0.025M	0.075M	0.1M	0 mV
	F	Imaging in the presence of NaCl with a higher potential, and simultaneous monitoring of the total current.	0.025M	0.075M	0.1M	+108mV then later +176mV
The occurrence of pitting later followed by crevice corrosion in the presence of NaCl	G	Imaging in the presence of NaCl with a higher potential, and simultaneous monitoring of the total current.	0.025M	0.075M	0.1M	+173mV then later +252mV
The occurrence of crevice corrosion in the presence of NaCl	H	Crevice corrosion imaging in the solution. But electrode exposed to Cl^- (from HCl) prior to the experiment.	0.3M	———	0.3M	-100mV
	I	The occurrence of sudden crevice corrosion in the presence of a SCE reference electrode monitored by optical imaging.	0.1M	———	0.1M	-400mV vs SCE
	J	The occurrence of crevice corrosion in the NaCl containing solution even before turning on the potentiostat and applying a potential monitored by optical imaging.	0.025M	0.075M	0.1M	——— (no potential applied)

Notes: For further specific details on the photocurrent and confocal images shown in this chapter see Appendix J (part 4). In addition it should be noted that where colour optical micrographs have been given, the colour though fairly accurate, will not be exactly that which was seen as the video printer being used in the experimental work (Sony UP-2200P) could only print 8 bit images (256 colours) where as the human eye is capable of resolving 16 million shades of colour (≡ 24 bit).

6.4 EFFECT OF CORROSION AT INCLUSIONS USING ONLY $NaClO_4$ AT HIGH POTENTIALS

In this investigation (Experiment A, figures 6.1 - 6.6) a photocurrent image was recorded at +173 mV, then the potential was taken up to +676 mV and left at this potential for 15 minutes after this the potential was taken back down to +173 mV and then another photocurrent image was recorded (figure 6.1). Inclusions 1, 2 and 3 were found to change the most on the photocurrent and optical images, with a stain visible around inclusions 1 and 3 (figures 6.2, 6.3). These inclusions when analysed after the experiment (figure 6.6, page 267) were found to contain sulphur a little higher than the surrounding bulk (bg) area and Mn at about the same as the bulk value. However the surrounding stain which had formed around the inclusion contained considerably higher amounts of both Mn + S than in the inclusion. These three inclusions all showed the occurrence of a substantial negative photocurrent over the inclusion area. However one inclusion (inclusion 4) showed the development of positive photocurrents. All the inclusions (1, 2, 3, 4) which showed changes in the photocurrent activity were found to be enriched in Mn + S (figures 6.5, 6.6). So the composition was not a reason for the difference in the sign for the photocurrent seen at inclusion 4.

Later studies using NaCl as well as $NaClO_4$ showed that if the reaction was followed for some time, after the initial development of a white (+VE photocurrent) region on the grey scale photocurrent image, the inclusion area suddenly turned dark at which point a peak in the total current signal was seen indicating the formation of a pit at the inclusion centre. So it can simply be concluded that the effects observed at inclusion 4 were just due to the fact that the corrosion reaction was at an earlier stage of corrosion prior to that when the photocurrent signal became negative. The reason might have been that the surface area of inclusion 4 was smaller than any of the other inclusions (1, 2 or 3). Inclusion 4 despite being very small, still showed activity. It seemed that the occurrence of the reaction depended not only the surface area of the inclusion but also on its proximity to the edge of the electrode.

Microprobe analysis showed that a pit was probably present at inclusion 2, because high amounts of sulphur could only be found at the edges of the inclusion by peak seeking

for sulphur using the microprobe spot analysis technique (figure 6.4).

In this experiment one inclusion (inclusion 1) showed that a stain formed selectively around one side of the inclusion rather than the other. The area which formed the stain was darker in colour on both the optical micrograph (figure 6.3c) and on the SEM image (figure 6.4b). When analysed after the experiment the half of the inclusion with the stain was found to be considerably enriched in S and only a little in Mn.

The behaviour seen at the high potentials in $NaClO_4$ can be further confirmed by looking at the photoelectrochemical behaviour of the inclusions relative to the bulk stainless steel on the images recorded with potential in the last chapter (see figure 5.7). Previous work has showed that there was a critical potential for pitting to occur (ref. C1-25). This was said to be +400 mV vs SCE (+1 mV vs SSE), and due to Cr (III), Cr(IV) oxidation occurring at this potential. Looking at figure 5.7 it can be seen the photocurrent over the inclusions initially became positive relative to the bulk stainless steel after this critical potential and then with more time the photocurrents became considerably negative with respect to the bulk stainless steel area at any given potential. (When examining the images in figure 5.7, the fact that the images were recorded at various increasing potentials as well as with increasing time has to be considered. As the potential was changed, the ratio of the photocurrents on the inclusion compared to that on the bulk stainless steel has to be considered, as opposed to the change in magnitude of the photocurrents with time on the inclusion area alone as in the case of a fixed potential experiment.)

This work suggests that the early stages of pitting corrosion either with $Cl^- + ClO_4^-$ at a low potential, or ClO_4^- only at a high potential may both follow a similar path, as similar photoelectrochemical behaviour was seen in both cases, as well as the formation of a stain enriched in Mn + S in both cases. Either this could mean that the same mechanism is operating with or without the Cl^- present or that the photocurrent changes seen are similar but depict different mechanisms. Another alternative may be that Cl^- contamination from another source, such as the epoxy resin or may be even an ultra-trace amount of Cl^- from the stainless steel itself, could have been present in the experiment containing just ClO_4^- despite the precautions taken.

THE CHANGE IN THE PHOTOCURRENT IMAGE ON THE APPLICATION OF A HIGH POTENTIAL IN NaCl ALONE

Experiment- A
Sample -316F

Solution = 0.3M $NaClO_4$

a) A photocurrent image recorded at +173 mV vs Hg/Hg_2SO_4, sat. K_2SO_4

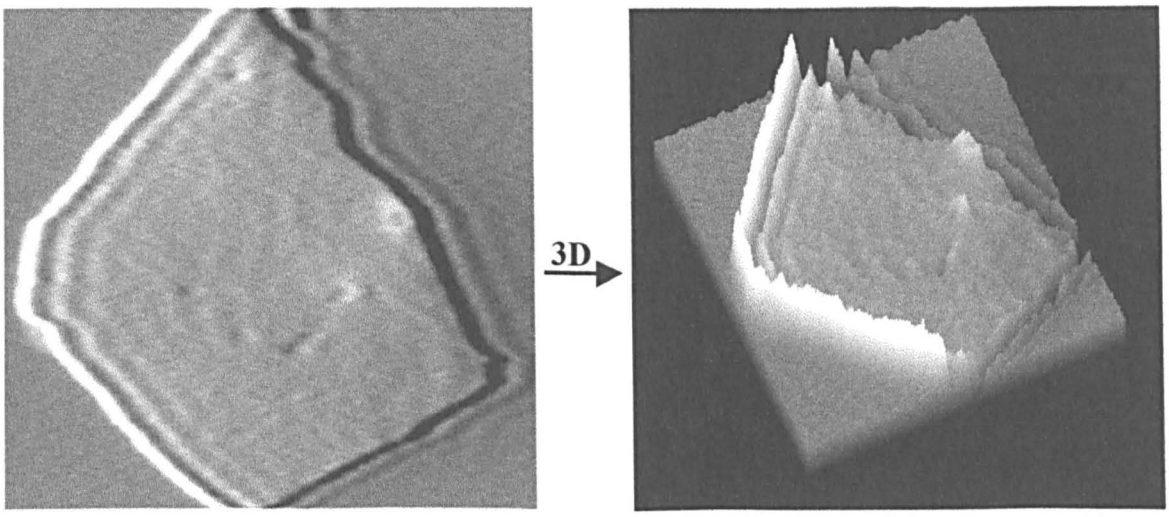

b) A photocurrent image recorded at +173 mV vs Hg/Hg_2SO_4, sat. K_2SO_4 after holding the potential at +676 mV for 15 minutes

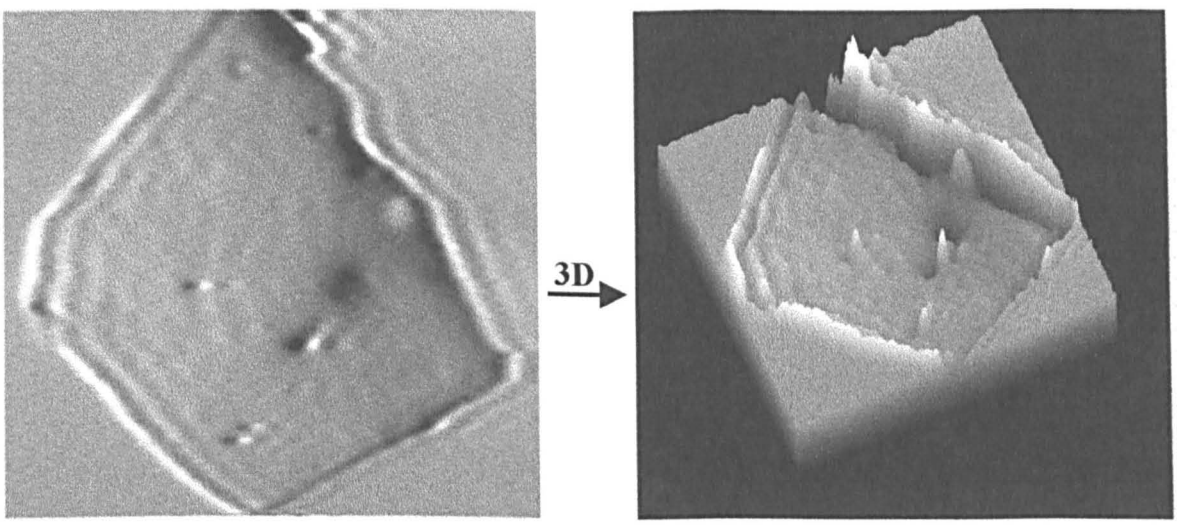

Image Parameters:

Image selection shown = 421 μm x 390 μm (x,y)
256 grey scale ≡ 50 nA
laser-light-off value = 154 out of 256 pixels (≡30 nA)
Photocurrent range = -30 nA to +20 nA

Notes: Lens magnification = x 4 (N.A. = 0.13), 2r = beam diameter = 2 μm, total area sampled in experiment = 633 x 390 μm (768 x 512 pixels), pixel dwell time = 10 μs, v_p= 8.24 cm s^{-1}, τ = time for laser bean to go over a distance equal to the laser beam diameter = 24.27 μs.

figure 6.1

HIGH RESOLUTION CONFOCAL OPTICAL IMAGES

Size of image shown here: 421μm x 390μm

Experiment- A
Sample- 316F

a) At the start of the experiment

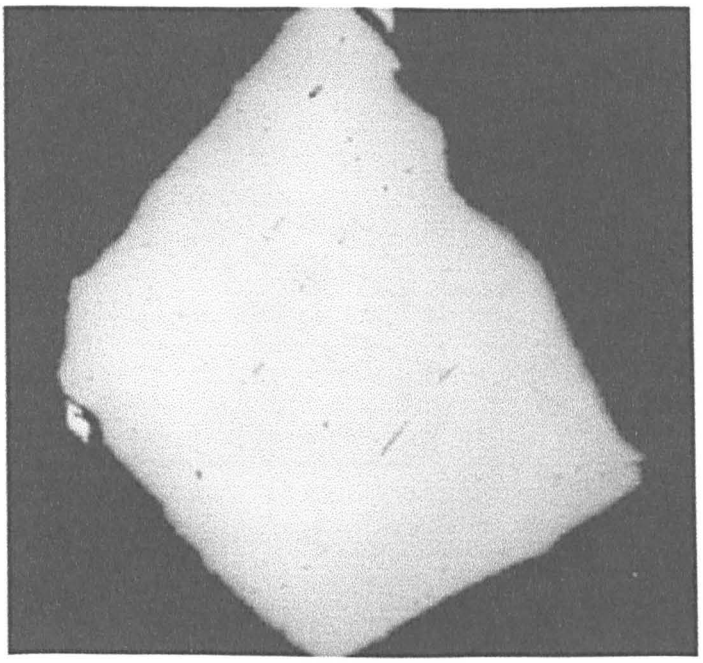

b) At the end of the experiment

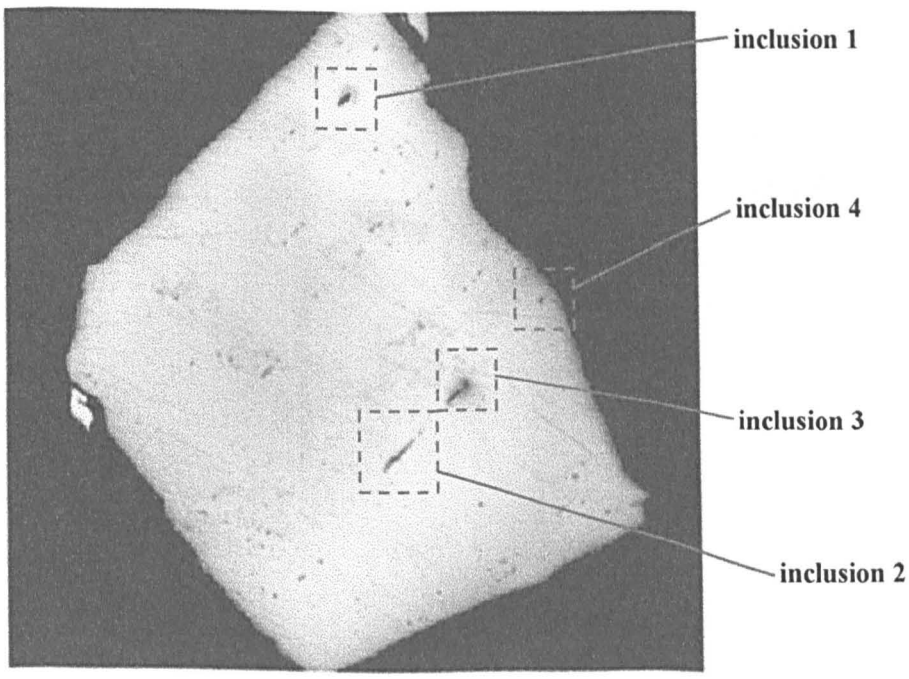

Notes: Lens magnification = x 20 (N.A. = 0.40), total area sampled in experiment = 818 x 497 μm (768 x 512 pixels), pixel dwell time = 10 μs, 2r = 0.6 μm, v_p= 10.65 cm s^{-1}, τ = 5.63 μs.

figure 6.2

OPTICAL MICROGRAPHS RECORDED AFTER THE EXPERIMENT

Experiment- A
Sample- 316F

a) Inclusions 2 and 3

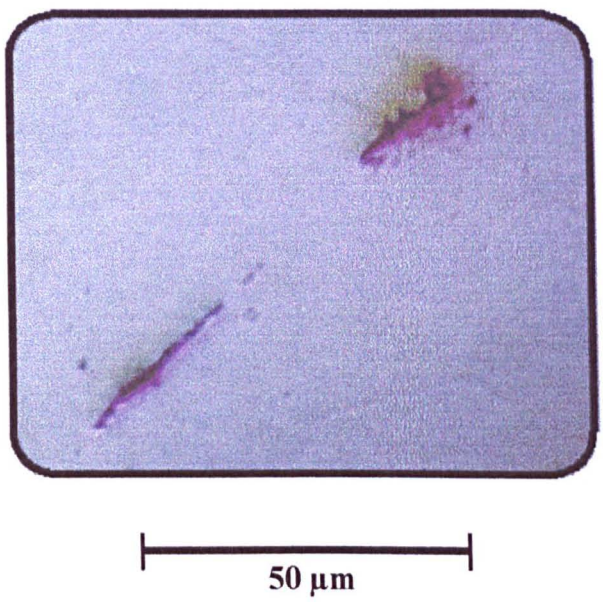

b) Inclusion 3

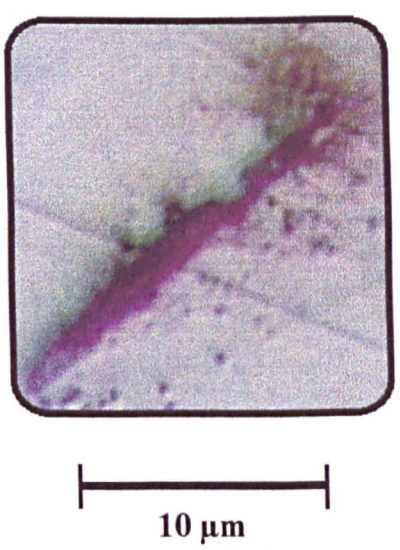

c) Inclusion 1

Notes: a) inclusions 1 and 2, lens magnification = x 10 (N.A. = 0.25), b) inclusion 3, lens magnification = x 50 (N.A. = 0.80), c) inclusion 1, lens magnification = x 50 (N.A. = 0.80).

figure 6.3

SEM IMAGES RECORDED AFTER THE EXPERIMENT

Experiment- A
Sample -316F

a) For the whole electrode

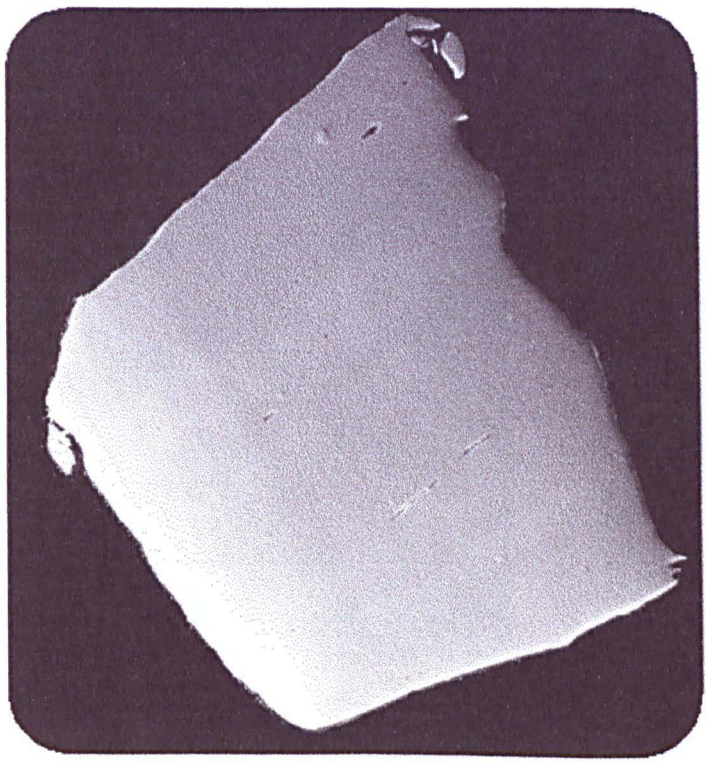

Magnification = x 230

100 µm

b) For inclusion 1

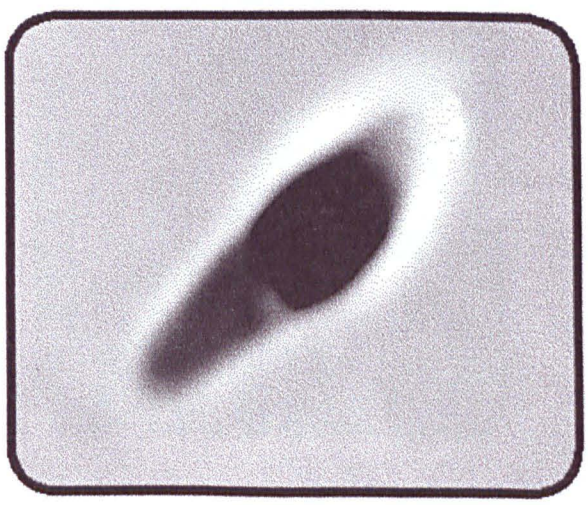

Magnification = x 3,700

10 µm

Notes: Acceleration voltage = 25 kV, current = $5x10^{-8}$A.

figure 6.4

MICROPROBE ELEMENT CONCENTRATION MAPS RECORDED AFTER THE EXPERIMENT

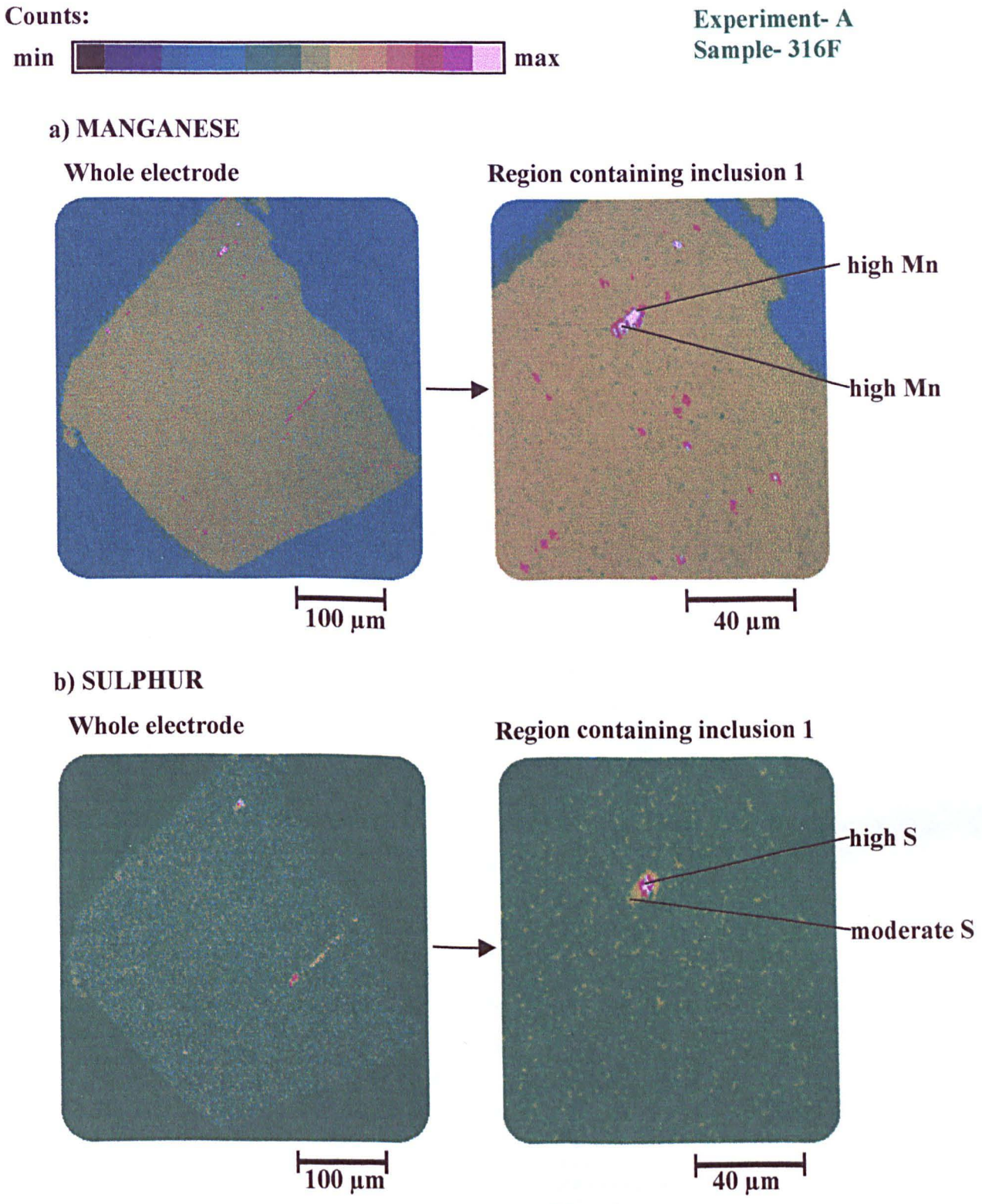

Notes: Acceleration voltage = 25 kV, current = 1.30 x 10^{-7}A, pixel dwell time = 60 ms, pixel size = 1 µm. a) Mn, X-ray line = Kα, crystal = lithium fluoride, spectrometer position = 145.875 mm. b) S, X-ray line = Kα, crystal = pentaerythritol, spectrometer position = 171.660 mm.

figure 6.5

A SUMMARY OF THE MICROPROBE SPOT ANALYSIS

Experiment- A
Sample- 316F

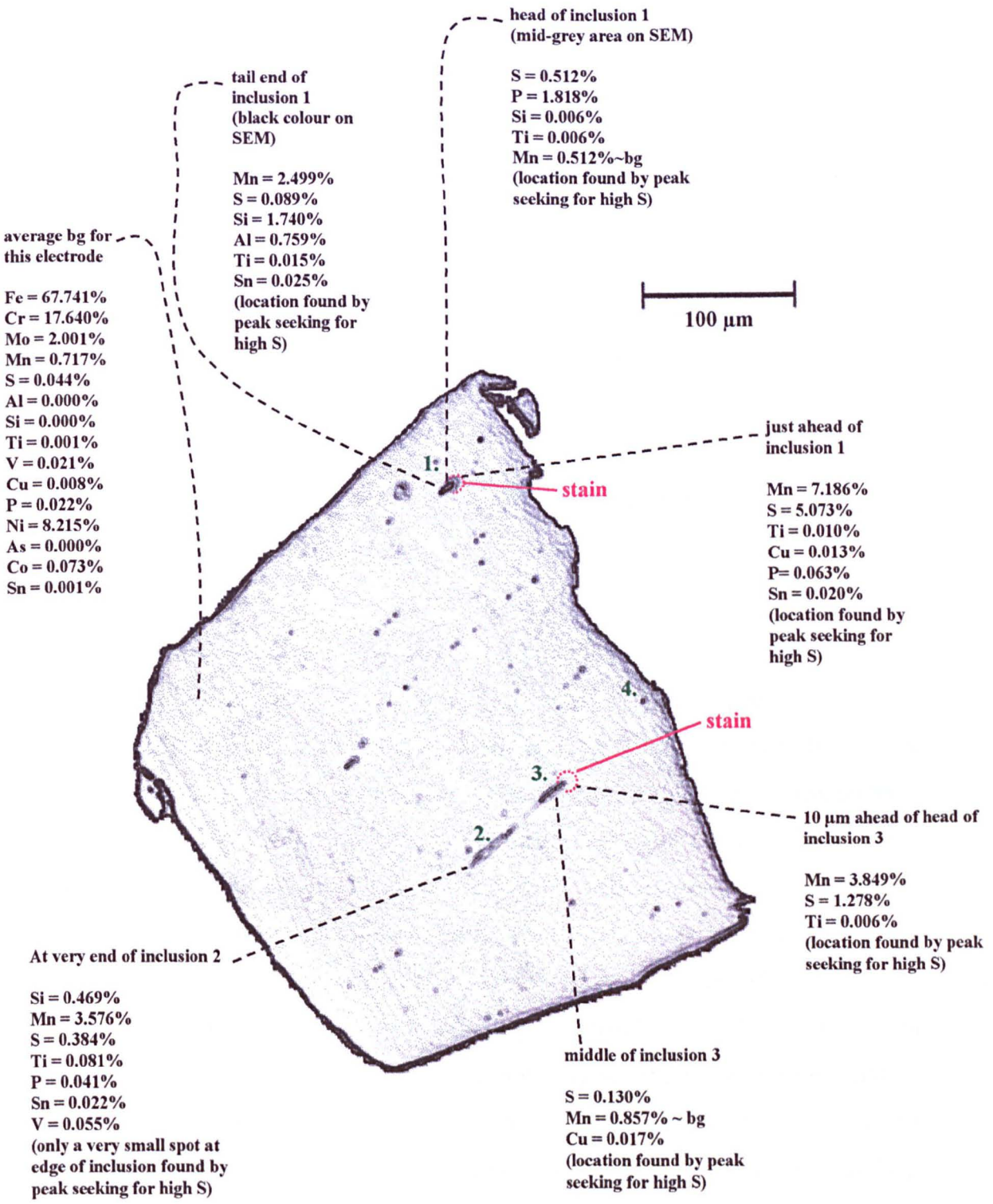

Notes: The % weight of Mn and S and any elements which increased significantly from the bg value are listed here. The bg value = bulk stainless steel, where there are no inclusions present. Acceleration voltage = 25 kV, current = 5 x 10^{-8} A, dwell time per element in the spot analysis =20 s.

figure 6.6

6.5 PRE-PITTING BEHAVIOUR AT INCLUSIONS (in dilute NaCl solutions)

Initial Observations of Small Fluctuations in the Photocurrent Image

Small fluctuations in the photocurrent signal were seen in the presence of a very low concentration of NaCl (experiment B, figure 6.7). The changes observed with time showed a subtle negative photocurrent area, which grew with time. Even in experiments with higher NaCl concentrations the subtle negative photocurrents generated over the inclusion areas could be noticed at the beginning of the experiment if the first image was captured fast enough (experiment D, figure 6.17a).

The Generation of Positive Photocurrents and Subsequent Stain Formation on the Optical Image

When the concentration of NaCl was increased a little further (Experiment C, figures 6.8 - 6.16) white regions were noticed on the photocurrent image (figures 6.8, 6.9). These corresponded to two fairly large inclusions as seen on the confocal optical image (figure 6.9). The upper inclusion (inclusion 1) changed the most on the photocurrent image. The photocurrents corresponding to the larger inclusion (inclusion 2) did not change very much, if at all. Examination of a high resolution optical micrograph (figure 6.10) shows that inclusion 1 was uniform and had a stain surrounding it. Inclusion 2 on the other hand showed two distinct areas, a central region which was different to the outermost region. Microprobe concentration maps (figures 6.13 - 6.15) showed that the inclusion 1 area was enriched in Mn and S but not oxygen, whereas inclusion 2 and another small inclusion close by (inclusion 3) were greatly enriched in Mn and oxygen. These findings were confirmed using microprobe spot analysis (figure 6.16). The larger oxide containing inclusion (2) was found to be largely enriched in Mn and slightly enriched in S, as well as many other impurities. This mixed oxide inclusion only contained a higher amount of sulphur in the thin outer layer surrounding the oxide centre.

EFFECT OF TIME ON THE PHOTOCURRENT IMAGE CONTRAST OF STAINLESS STEEL IN A VERY LOW NaCl CONCENTRATION

Experiment- B
Sample- 316F

Solution = 0.0125M NaCl, 0.2875M $NaClO_4$, I = 0.3M
E = +175 mV vs SSE

Image Parameters:

Size of 3D-surface plot = 191µm x 191µm (x,y)

256 grey scale (z-axis) ≡ 100 nA

a.

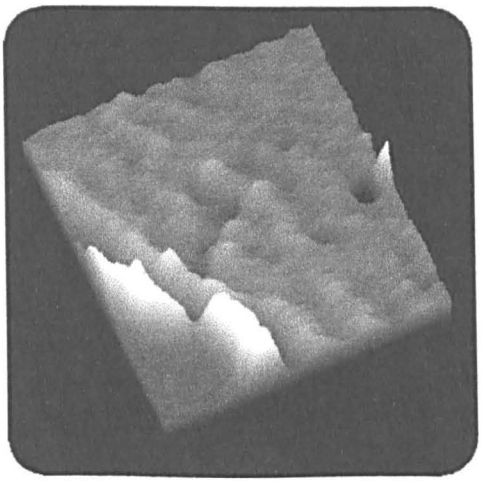

t = 0 min

b.

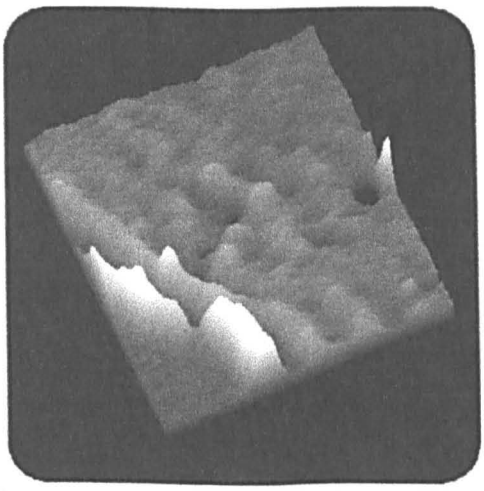

t = 4 min

c.

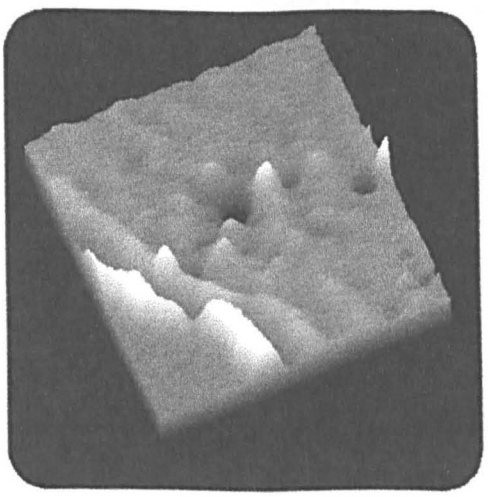

t = 1 hr 20 min

Notes: Lens magnification = x 4 (N.A. = 0.13), 2r = beam diameter = 2 µm, total area sampled in experiment = 633 x 390 µm (768 x 512 pixels), pixel dwell time = 10 µs, v_p= 8.24 cm s^{-1}, τ = 24.75 µm, Laser-light-off value = 154.5 out of 256 pixels (≡60.4 nA), photocurrent range = -60 nA to +40 nA. Where t = 0 minutes is the time recorded at the end of the 1st image.

figure 6.7

EFFECT OF TIME ON THE PHOTOCURRENT IMAGE CONTRAST OF STAINLESS STEEL IN A VERY LOW NaCl CONCENTRATION

Experiment- C
Sample- 316F

Solution = 0.025M NaCl, 0.275M $NaClO_4$, I = 0.3M
E = -250 mV vs SSE

a. 2D-photocurrent image, size of image shown = 421µm x 390µm

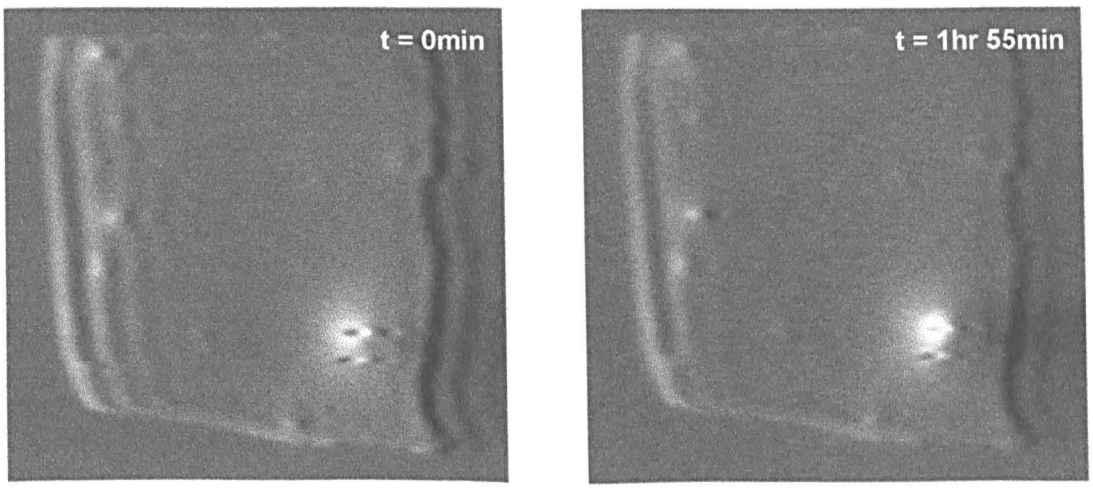

b. 3D-surface plot, size of selection shown = 195µm x 195µm

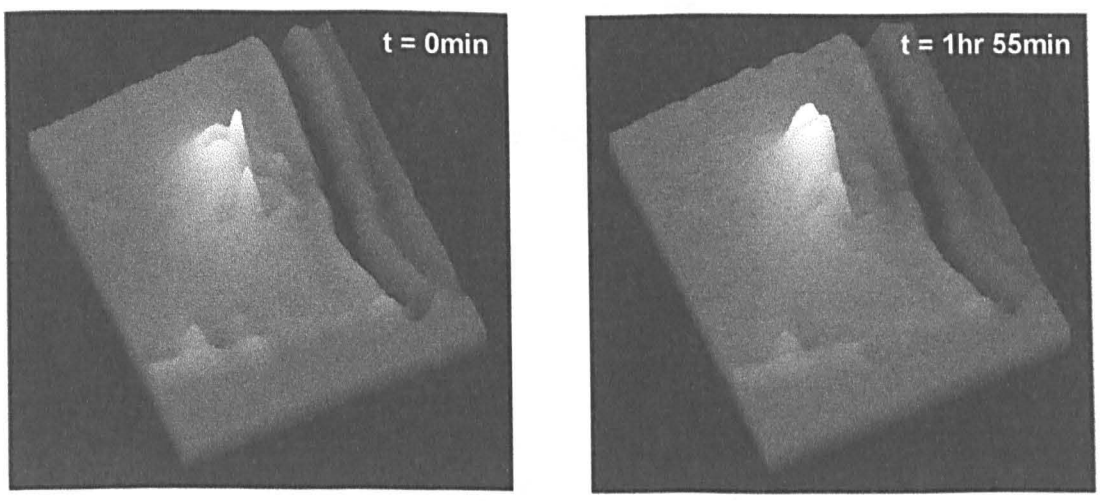

Image Parameters:

256 grey scale ≡ 50 nA (z-axis)
'Laser-off' value = 142.7/256 (≡ 27.9 nA)
Photocurrent range = -28 nA to +22 nA

Notes: Lens magnification = x 4 (N.A. = 0.13), 2r = beam diameter = 2 µm, total area sampled in experiment = 633 x 390 µm (768 x 512 pixels), pixel dwell time = 10 µs, v_p= 8.24 cm s^{-1}, τ = 24.75 µm. The time t = 0 min, is the time at the end of the 1st image to be recorded.

figure 6.8

HIGH RESOLUTION CONFOCAL OPTICAL IMAGES

Experiment- C
Sample- 316F

Size of image shown here: 421 μm x 390 μm

a)

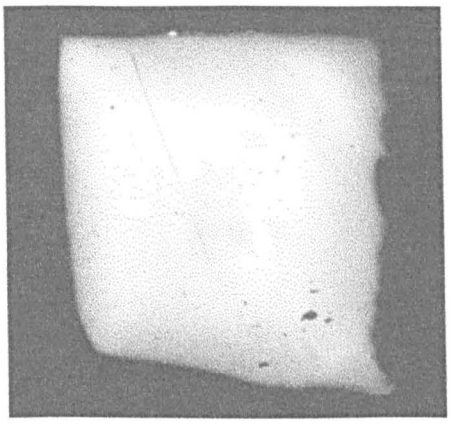

At the start of the experiment

b)

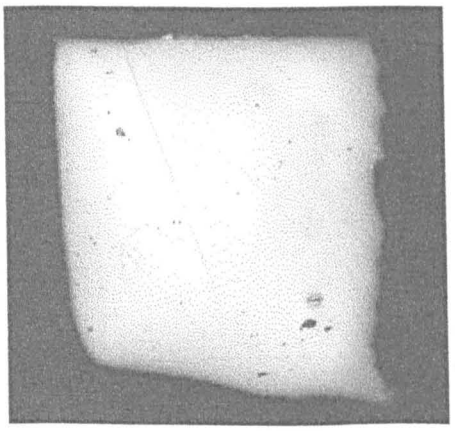

At the end of the experiment

c)

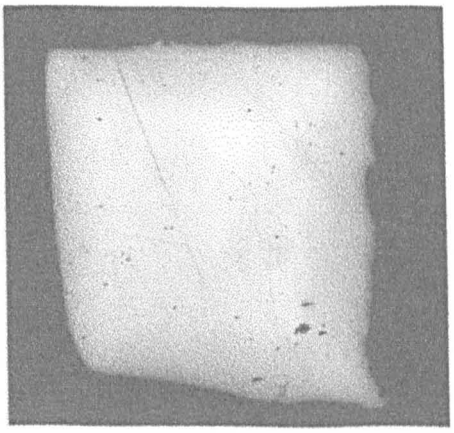

At the end of the experiment after further rinsing

150 μm

Notes: Lens magnification = x 20 (N.A. = 0.40), total area sampled in experiment = 818 x 497 μm (768 x 512 pixels), pixel dwell time = 10 μs, 2r = 0.6 μm, v_p= 10.65 cm s^{-1}, τ = 5.63 μs.

figure 6.9

VERY HIGH RESOLUTION CONFOCAL OPTICAL IMAGES

Experiment- C
Sample- 316F

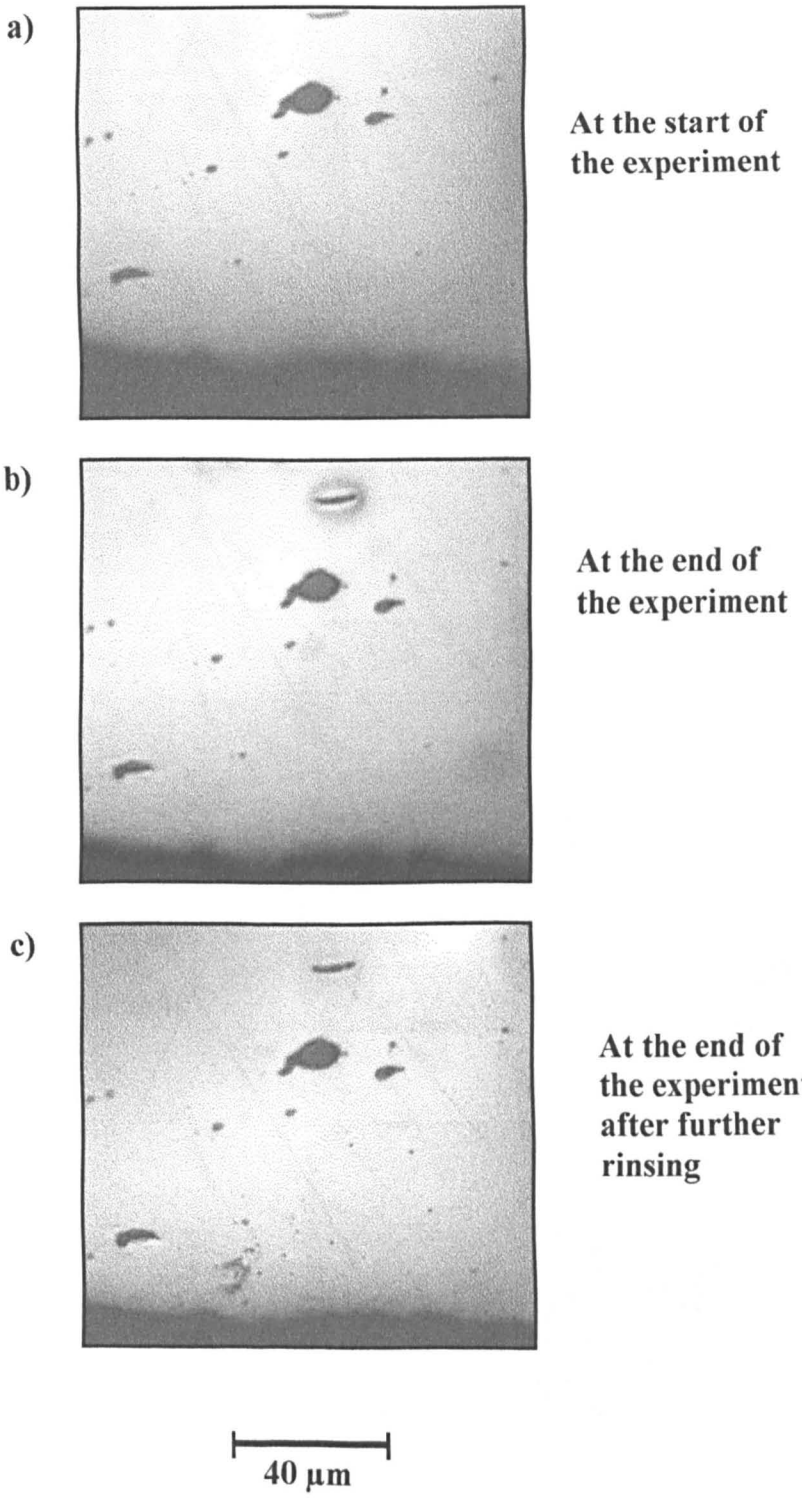

Notes: Lens magnification = x 40 (N.A. = 0.40), total area sampled in experiment = 175 x 107 µm (768 x 512 pixels), pixel dwell time = 10 µs, 2r = 0.6 µm, v_p= 2.28 cm s^{-1}, τ = 26.32 µs.

figure 6.10

OPTICAL MICROGRAPHS OF THE INCLUSION CONTAINING REGIONS

Experiment- C
Sample- 316F

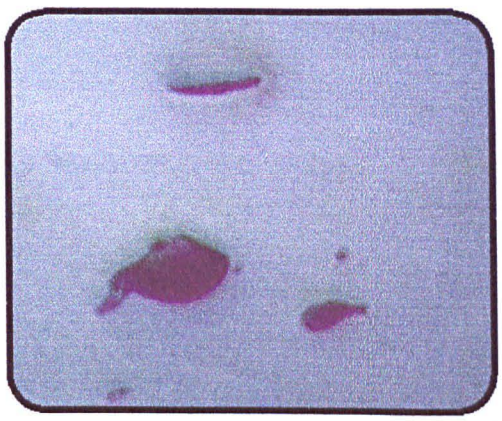

a) Inclusions 1, 2 and 3

25 µm

b) Inclusion 1

10 µm

c) Inclusion 2

10 µm

Notes: a) inclusions 1, 2 and 3, lens magnification = x 20 (N.A. = 0.40), b) inclusion 1, lens magnification = x 50 (N.A. = 0.80), c) inclusion 2, lens magnification = x 80 (N.A. = 0.80).

figure 6.11

AN SEM IMAGE RECORDED AFTER THE EXPERIMENT

Experiment- C
Sample- 316F

Acceleration Voltage = 25 kV
Current = 5 x 10^{-8} A

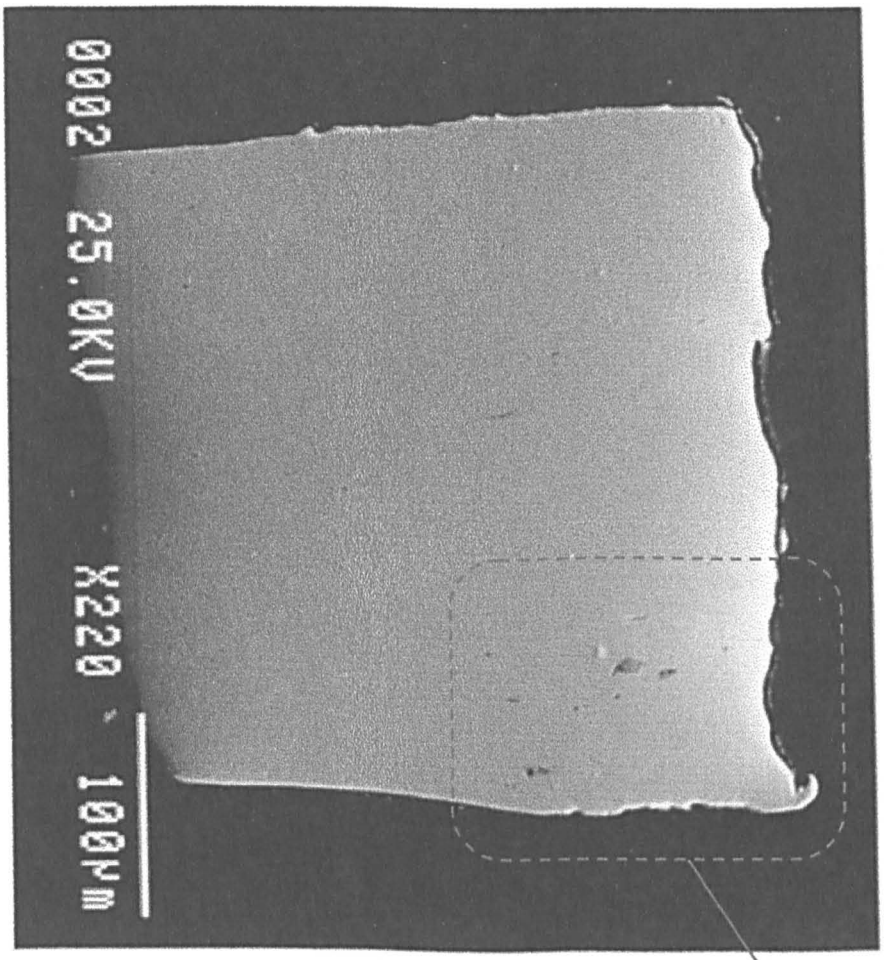

figure 6.12

MICROPROBE ELEMENT CONCENTRATION MAPS SHOWING SOME OF THE ELEMENTS PRESENT IN THE INCLUSIONS

Experiment- C
Sample- 316F

Counts:

min max

60 µm

Mn Crystal - LIF, 145.875 mm
(x-ray line = Kα)

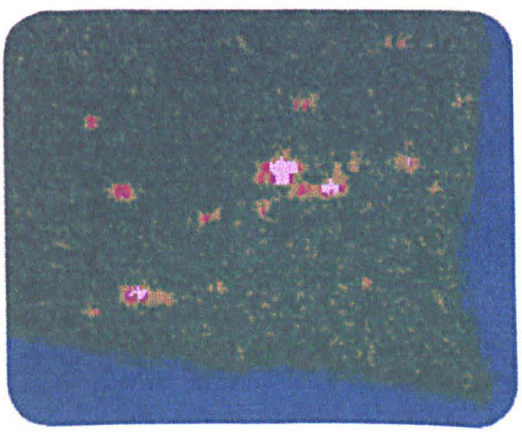

average in bulk = 0.657%
max. in inclusion = 21.801%

S Crystal - PET, 171.660 mm
(x-ray line = Kα)

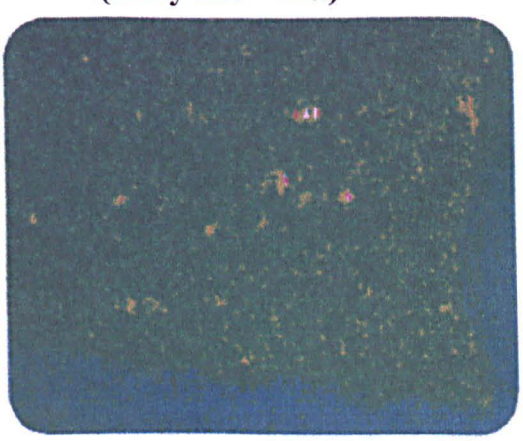

average in bulk = 0.051%
max. in inclusion = 1.287%

Ti Crystal - PET, 87.705 mm
(x-ray line = Kα)

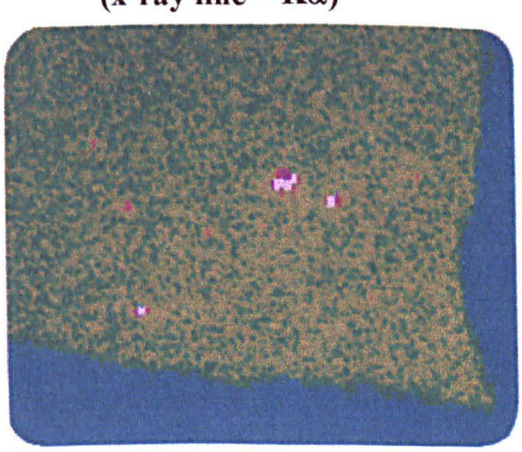

average in bulk = 0.003%
max. in inclusion = 0.856%

V Crystal - PET, 79.835 mm
(x-ray line = Kα)

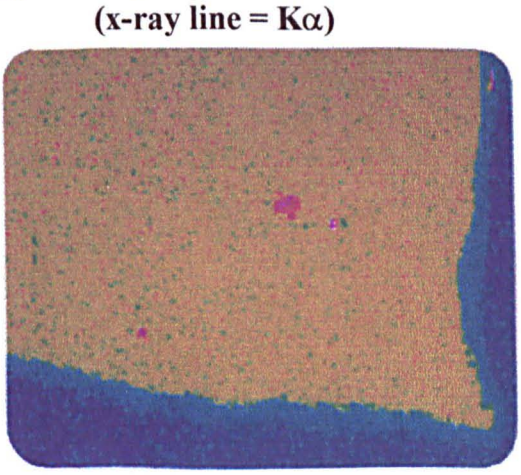

average in bulk = 0.025%
max. in inclusion = 0.254%

Notes: These images were recorded every pixel where 1 pixel = 1 µm , pixel dwell time = 100 ms, current = 1.3 x 10^{-7} A, acceleration voltage = 25.0 kV. The abbreviation for the crystals have been given as follows: LIF = lithium fluoride, PET = pentaerythritol. The crystal name is followed by the spectrometer position in 'mm' units.

figure 6.13

MICROPROBE ELEMENT CONCENTRATION MAPS OF THE PRINCIPAL ELEMENTS PRESENT IN 316 STAINLESS STEEL

Experiment- C
Sample- 316F

Counts:

min **max**

60 μm

Fe **Crystal - LIF, 134.450 mm**
(x-ray line = Kα)

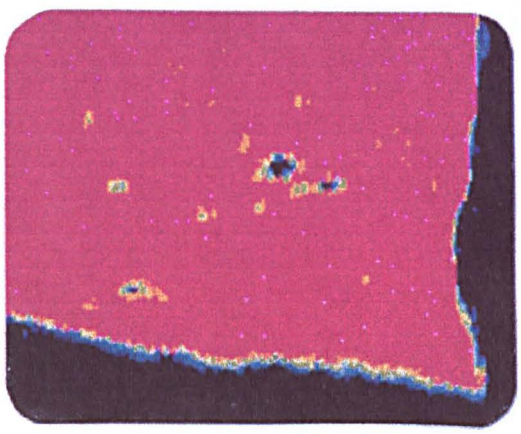

average in bulk = 68.592%
min. in inclusion = 3.206%

Cr **Crystal - LIF, 158.940 mm**
(x-ray line = Kα)

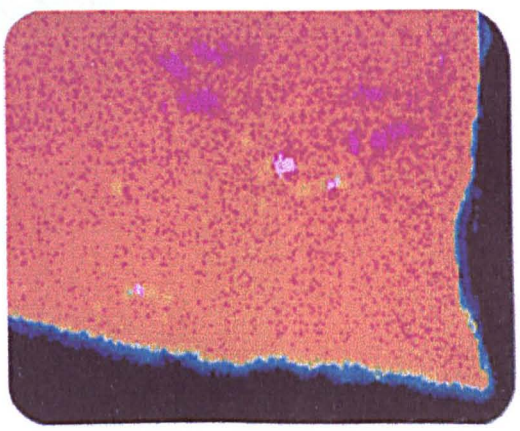

average in bulk = 17.731%
max. in inclusion = 29.575%

Ni **Crystal - LIF, 115.000 mm**
(x-ray line = Kα)

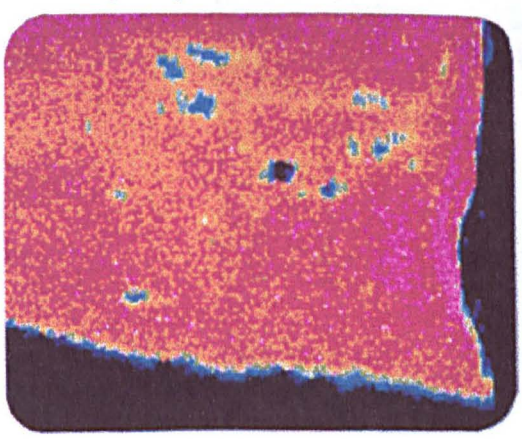

average in bulk = 8.354%
max. in inclusion = 0.258%

V **Crystal - PET, 172.700 mm**
(x-ray line = Lα)

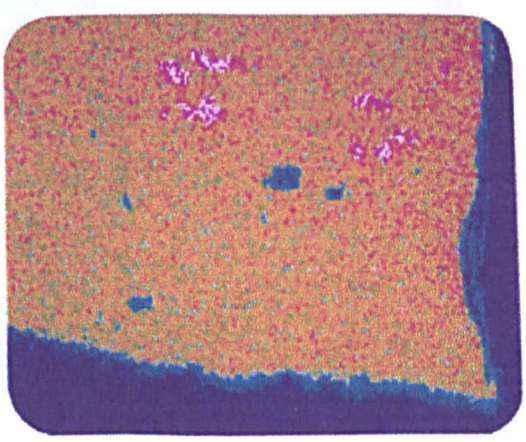

average in bulk = 2.044%
max. in inclusion = 0.104%

Notes: These images were recorded every pixel where 1 pixel = 1 μm , pixel dwell time = 100 ms, current = 1.3 x 10^{-7} A, acceleration voltage = 25.0 kV. The abbreviation for the crystals have been given as follows: LIF = lithium fluoride, PET = pentaerythritol. The crystal name is followed by the spectrometer position in 'mm' units.

figure 6.14

X-RAY MICROANALYSIS IMAGES RECORDED AT A LOW kV

Experiment- C
Sample-316F

Acceleration Voltage = 12 kV

a) An SEM Image

b) An Oxygen Concentration Map

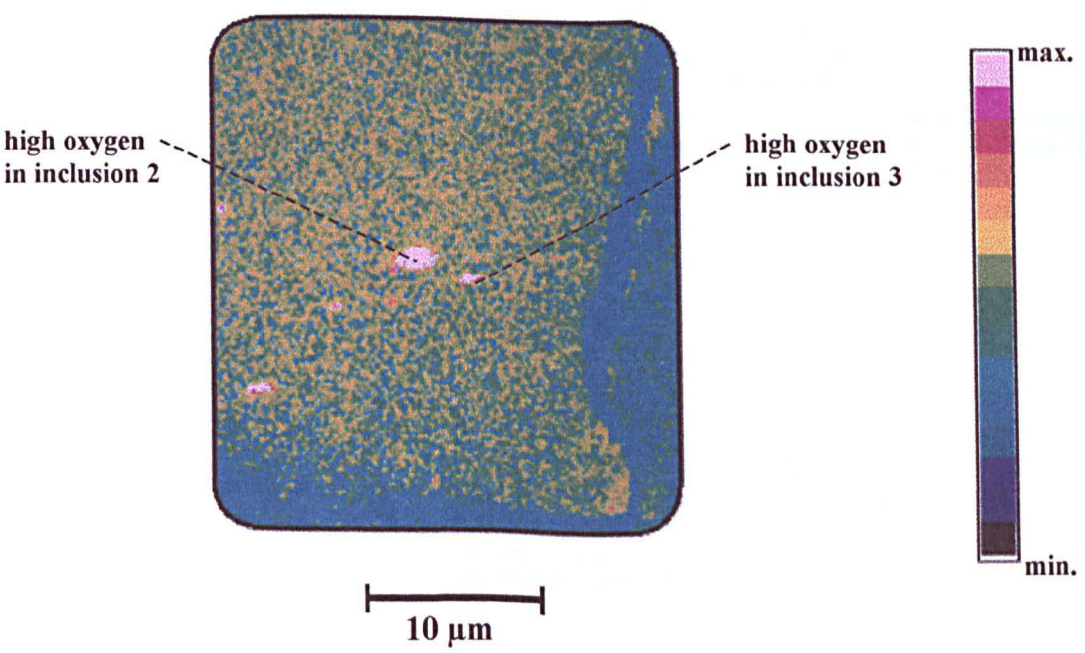

Notes: a) current = 5 x 10^{-8} A, b) current = 1.00 x 10^{-7} A , image data recorded every pixel, pixel dwell time = 75 ms.

figure 6.15

A SUMMARY OF THE MICROPROBE SPOT ANALYSIS

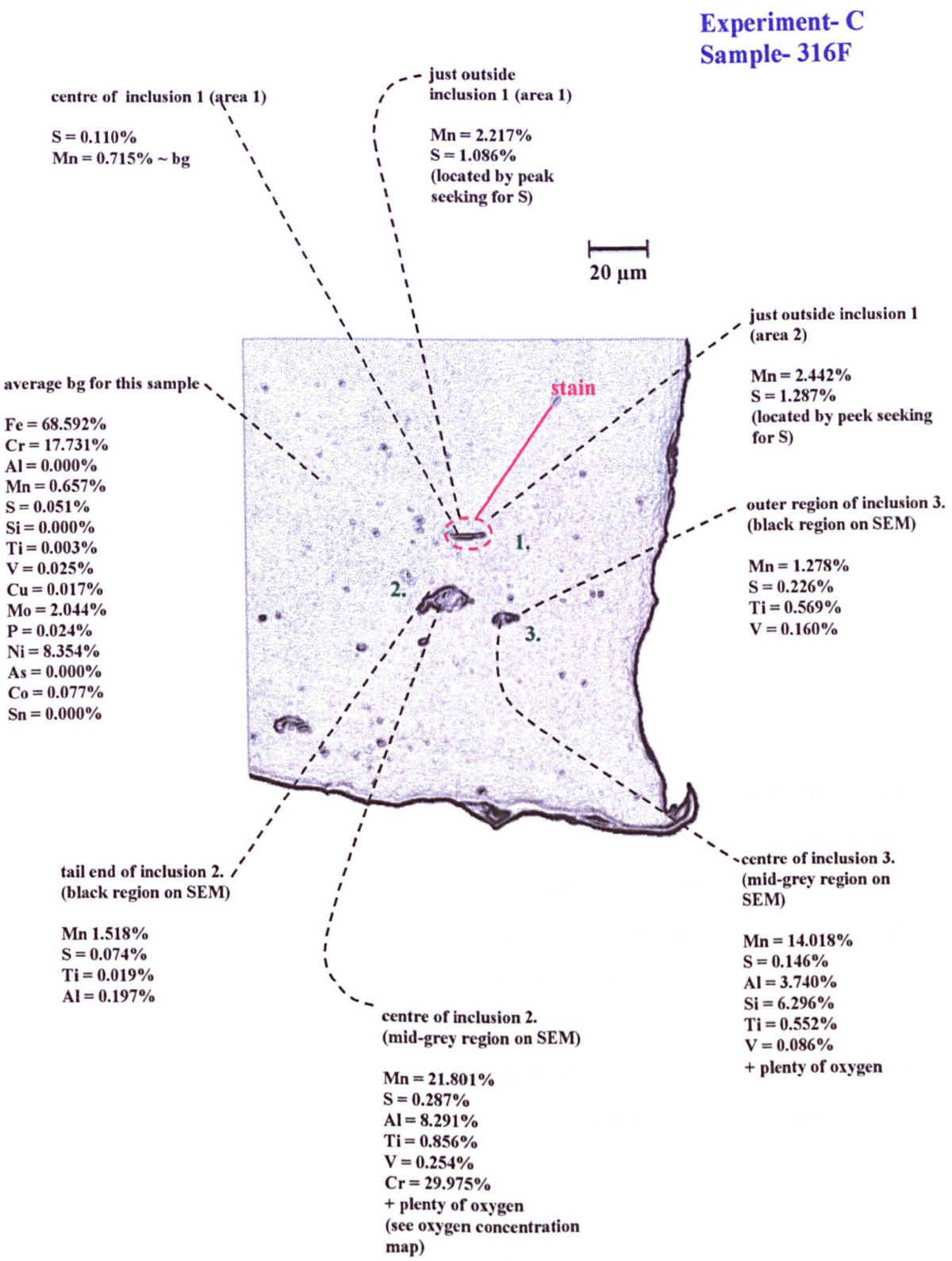

Notes: The % weight of Mn and S and any elements which increased significantly from the bg value are listed here. The bg value = bulk stainless steel, where there are no inclusions present. Acceleration voltage = 25 kV, current = 5 x 10^{-8} A, dwell time per element in the spot analysis = 20 s.

figure 6.16

In experiment D (figures 6.17 - 6.28) the conditions were made more extreme still by increasing the potential and decreasing the ionic strength. Much more accelerated behaviour could be seen at many inclusions (figure 6.17). Rings of positive photocurrent were found to form around some inclusions. Confocal optical images again showed changes, with the occurrence of stains surrounding the most active inclusions on the photoelectrochemical images (figure 6.18). This effect can be easily observed when the photocurrent and confocal images on a small zoomed in region of the electrode are compared (figure 6.19). It was noticed that some of the stain rings formed around the inclusion were like a 'halo' in that they did not touch the inclusion, but there was a gap between the inclusion and the stain which surrounded it. The stains were loosely attached and could be washed off easily. This has been shown on the very high resolution confocal optical images recorded before and after further rinsing with water (figures 6.21, 6.22). If a stain had been on the surface for a while, then dark spheres were seen to form in it (figure 6.21a, also seen in experiment F figure 6.40). If this denser sphere containing stain was then washed off small dents were revealed in the stainless steel surface (figures 6.21b, 6.21c).

Optical imaging and microprobe analysis showed that there were many types of inclusion present. The many small randomly arranged inclusions were found to be high in Si, Al, or Ti either individually or in combination with one another. These types of inclusions did not show changes on the photocurrent images with time. The Mn + S rich inclusions were generally all orientated in one particular direction. Some of the Mn + S enriched inclusions showed photoelectrochemical activity and some did not. Inclusions of interest have been marked on figure 6.20. Areas 1, 2, 3, 4, 5, 6, and 7 show Mn and S enriched inclusions which were photoelectrochemically active. Areas 8 and 9 show strings of inclusions which were inactive. The microprobe concentration maps (figures 6.25, 6.26, 6.27) recorded after the photocurrent imaging experiment showed oxygen was present as well as many other oxide forming elements, in the inactive inclusions. These results obtained from the microprobe elemental imaging were confirmed by the use of microprobe spot analysis (figure 6.28). The inclusions which showed the most activity during the experiment when analysed were found to be high in S but not Mn (the Mn was about the same as bg).

EFFECT OF TIME ON THE PHOTOCURRENT IMAGE CONTRAST AT A LOWER IONIC STRENGTH

Solution = 0.025M NaCl, 0.075M $NaClO_4$, I = 0.1M
E = 0 mV vs SSE

Experiment- D
Sample- 316F

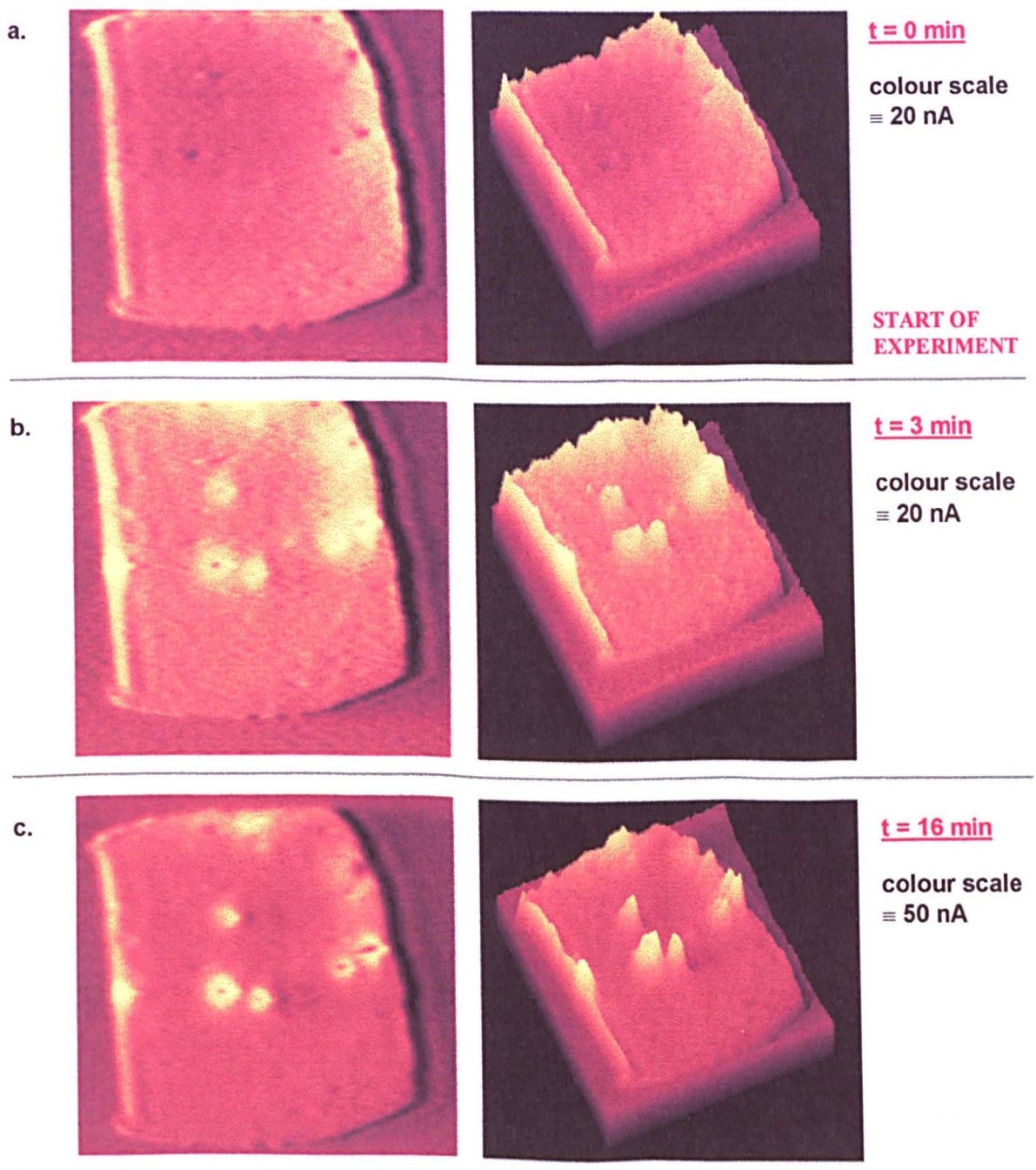

size of image shown = 458µm x 424µm (x,y)
'laser-off' value = 141.8/256 pixels

colour scale:
min — max

Notes: Lens magnification = x 4 (N.A. = 0.13), 2r = beam diameter = 2 µm, total area sampled in experiment = 688 x 424 µm (768 x 512 pixels), pixel dwell time = 10 µs, v_p= 8.96 cm s^{-1}, τ = 22.35 µm. The time t = 0 minutes, is the time at the end of the 1st image to be recorded.

figure 6.17: part 1

(continued on next page)

EFFECT OF TIME ON THE PHOTOCURRENT IMAGE CONTRAST AT A LOWER IONIC STRENGTH (continued)

Solution = 0.025M NaCl, 0.075M $NaClO_4$, I = 0.1M
E = 0 mV vs SSE

Experiment- D
Sample- 316F

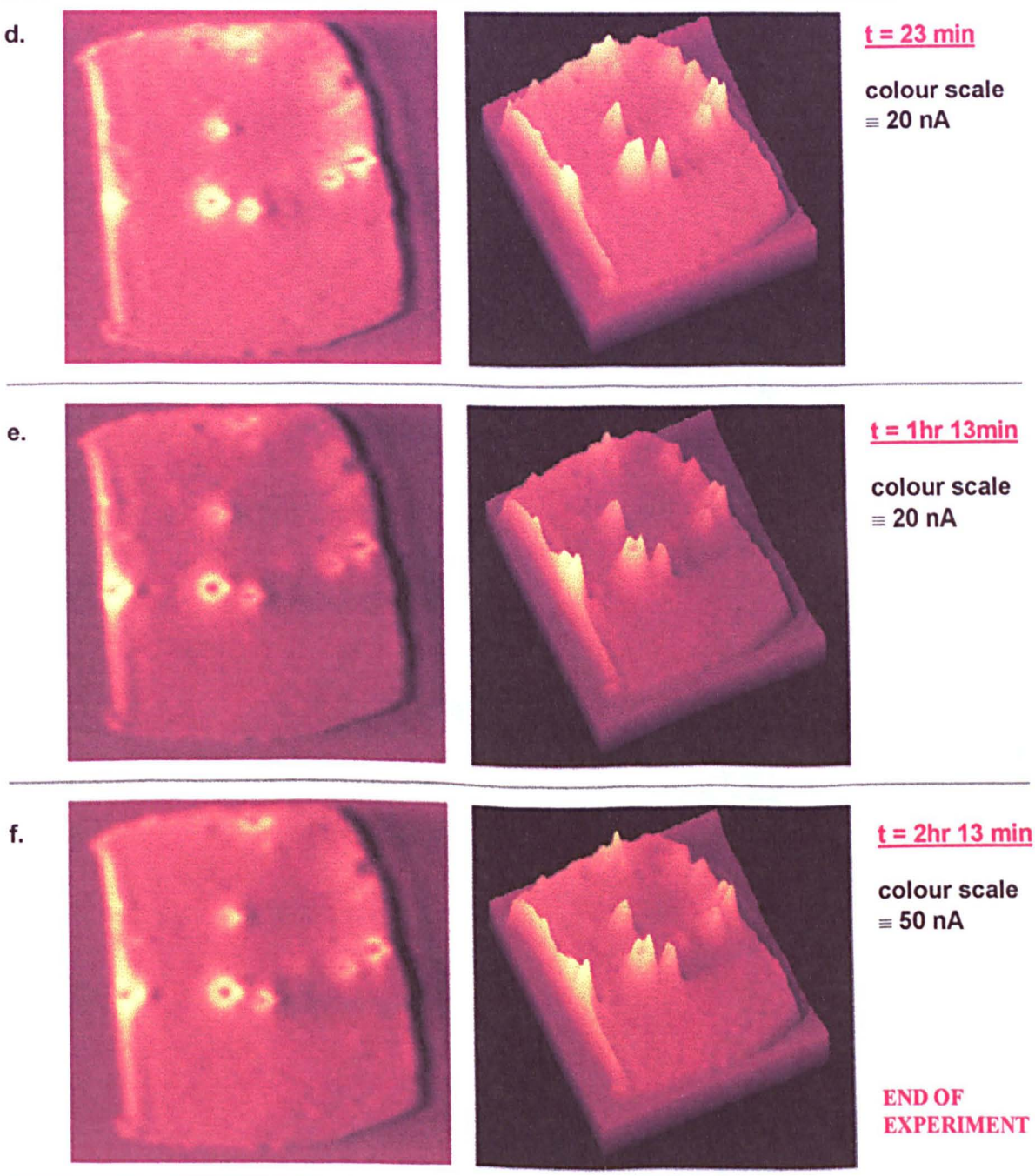

size of image shown = 458µm x 424µm (x,y)
'laser-off' value = 141.8/256 pixels

colour scale:
min max

Notes: Lens magnification = x 4 (N.A. = 0.13), 2r = beam diameter = 2 µm, total area sampled in experiment = 688 x 424 µm (768 x 512 pixels), pixel dwell time = 10 µs, v_p= 8.96 cm s^{-1}, τ = 22.35 µm. The time t = 0 minutes, is the time at the end of the 1st image to be recorded.

figure 6.17: part 2

HIGH RESOLUTION CONFOCAL OPTICAL IMAGES

Experiment- D
Sample- 316F

Size of image shown here: 458μm x 424μm (x,y)

a) At the start of the experiment

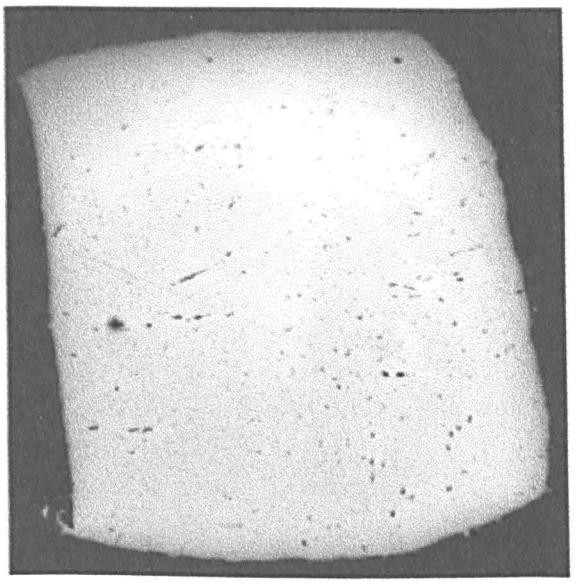

b) At the end of the experiment

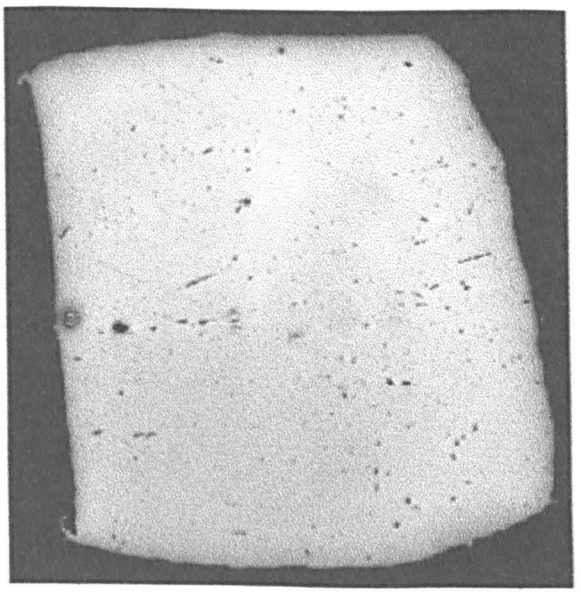

150 μm

Notes: Lens magnification = x 20 (N.A. = 0.40), total area sampled in experiment = 818 x 497 μm (768 x 512 pixels), pixel dwell time = 10 μs, 2r = 0.6 μm, v_p= 10.65 cm s^{-1}, τ = 5.63 μs.

figure 6.18

COMPARISON OF THE PHOTOCURRENT AND OPTICAL IMAGES SHOWN ON A ZOOMED IN SELECTION OF THE ELECTRODE

Experiment- D
Sample- 316F

PHOTOELECTROCHEMICAL IMAGES

a. START, t = 0 hr 0 min

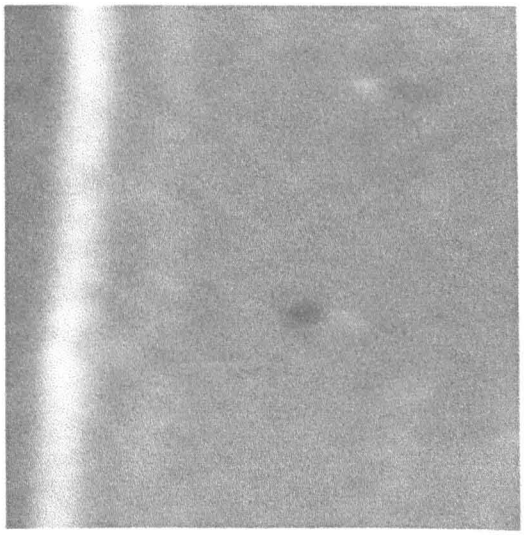

b. END, t = 2 hr 13 min

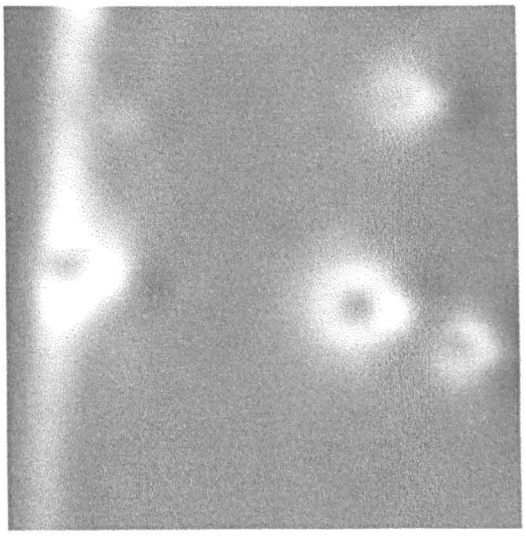

CONFOCAL OPTICAL IMAGES

c. START

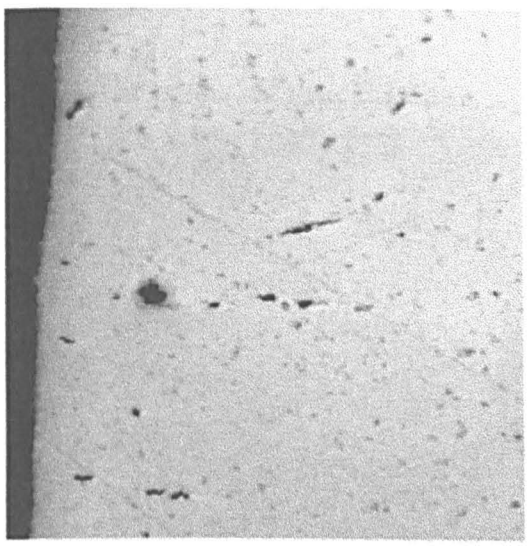

d. END

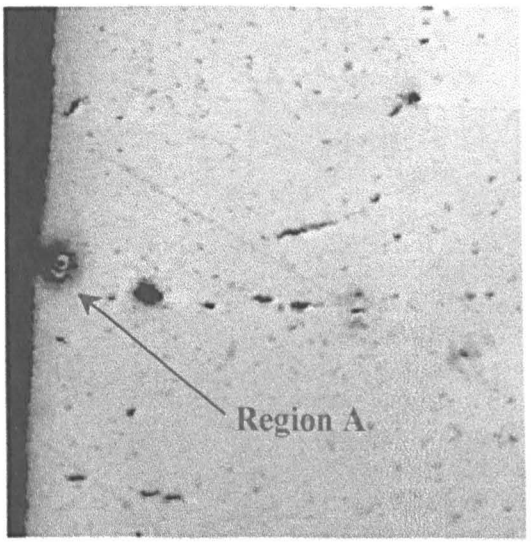

100 µm

Reflectivity (optical images)

min — max

0

Photocurrent generated (PEM images)

Notes : See figure 6.17 for the photocurrent image details for the images shown in figure 6.19 a and 6.19b. See figure 6.18 for the optical images details for the images shown in figure 6.19c and 6.19d.

figure 6.19

AREAS OF INTEREST SHOWN ON THE PHOTOCURRENT AND OPTICAL IMAGES RECORDED AT THE END OF THE EXPERIMENT

Experiment- D
Sample- 316F

150 μm

a) Photocurrent Image

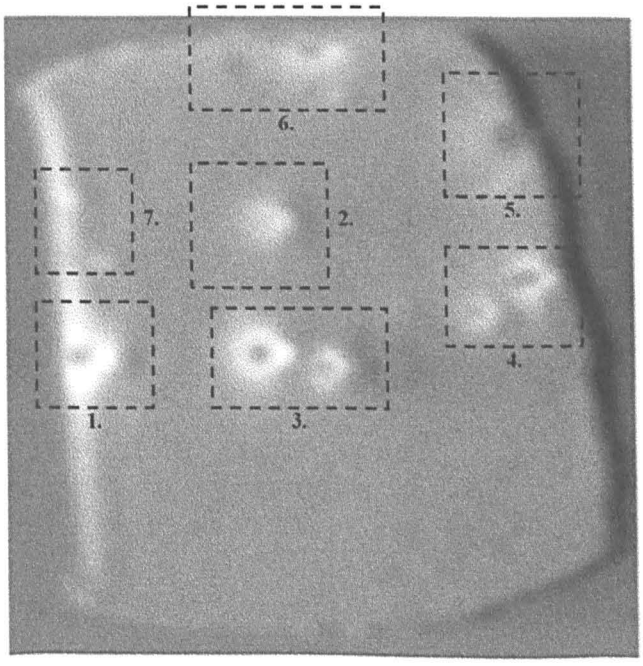

b) Confocal Optical Image

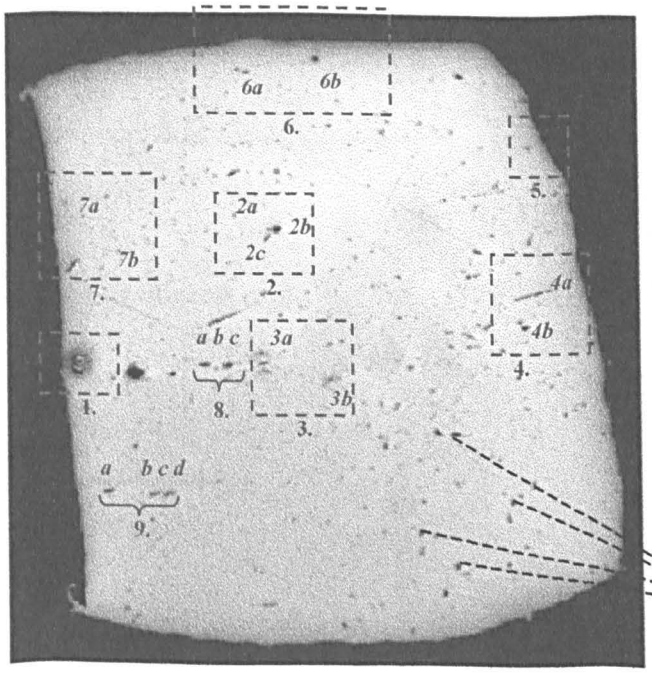

many Si enriched inclusions were found in this sample

Regions Enriched in Mn or S or Both

Areas 1,2,3,4,5,6,7 showed pre-pitting activity on the photocurrent image.

Areas 1,2,3 changed the most on the photocurrent image with time, and also showed stains on the optical image.

Area 1 changed the most optically with some tiny pits forming in the stain region.

Areas 8,9 contain very large amounts of Mn compared to S and a large amount of oxygen. These inclusions did not show any activity on the photocurrent image.

Notes : See figure 6.17 for the photocurrent image details for the image shown in figure 6.20a. See figure 6.18 for the optical images details for the image shown in figure 6.20b. (Also see figure 6.23 for the SEM image marked with the regions of interest.)

figure 6.20

VERY HIGH RESOLUTION OPTICAL IMAGES OF AREA 1, RECORDED AFTER THE EXPERIMENT

Experiment- D
Sample- 316F

a) OPTICAL IMAGE RECORDED AFTER THE EXPERIMENT

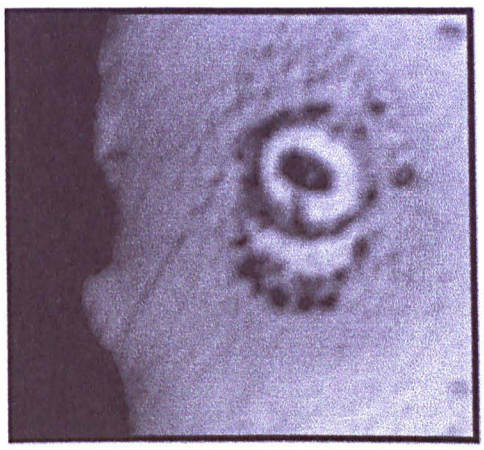

A confocal optical image

10 µm

b) EFFECT OF FURTHER RINSING

A confocal optical image

10 µm

An optical micrograph

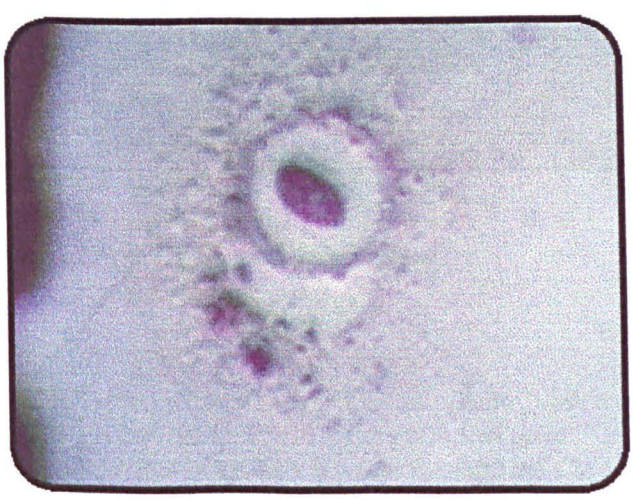

8 µm

Notes: The confocal optical images were recorded using a x40 lens (N.A. = 0.40) , zoom 10.0, using the Bio-Rad MRC 600 confocal scanning laser microscope system. The optical image was recorded using a x50 lens (N.A. = 0.80), using an ordinary light microscope.

figure 6.21

VERY HIGH RESOLUTION CONFOCAL OPTICAL IMAGES OF REGIONS 2 AND 3

Experiment- D
Sample- 316F

a) After the experiment

Inclusion Area 2

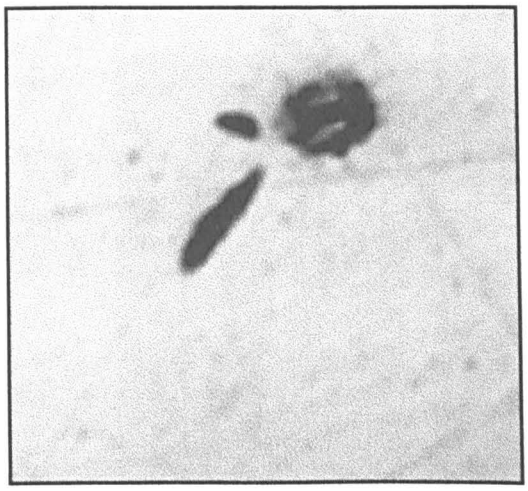

Inclusion Area 3

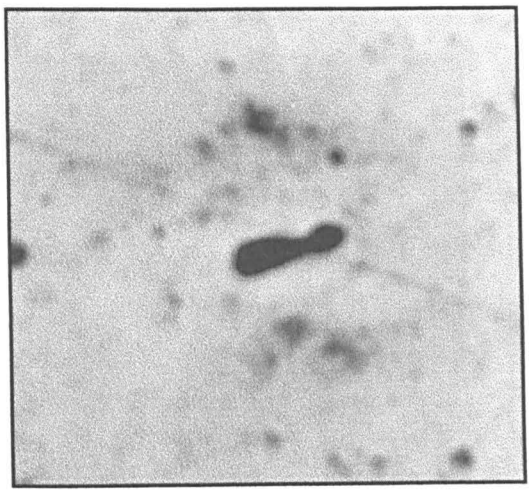

b) After further rinsing, after the experiment

Inclusion Area 2

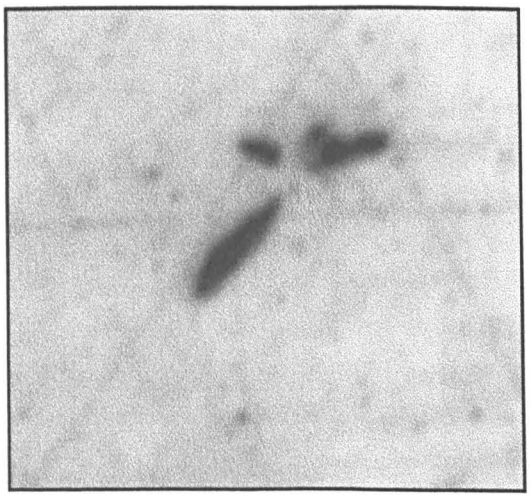

Inclusion Area 3

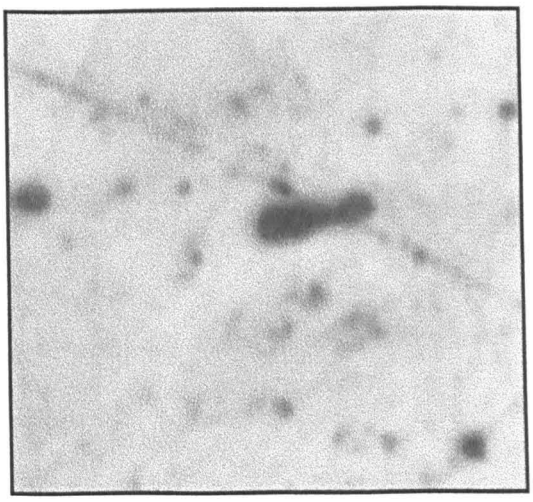

Scale for all images shown here:

10 μm

Notes: These confocal optical images were recorded using a x40 lens (N.A. = 0.40) , zoom 10.0, using the Bio-Rad MRC-600 confocal scanning laser microscope system. Total area sampled in experiment 42 x 26 μm (768 x 512 pixels, pixel dwell time = 10 μs, 2r = 0.6 μm, v_p= 0.55 cm s^{-1}, τ = 109.09 μs.

figure 6.22

AN SEM IMAGE FOR THE WHOLE ELECTRODE

Experiment- D
Sample- 316F

Acceleration Voltage = 25 kV
Current = 5 x 10^{-8} A

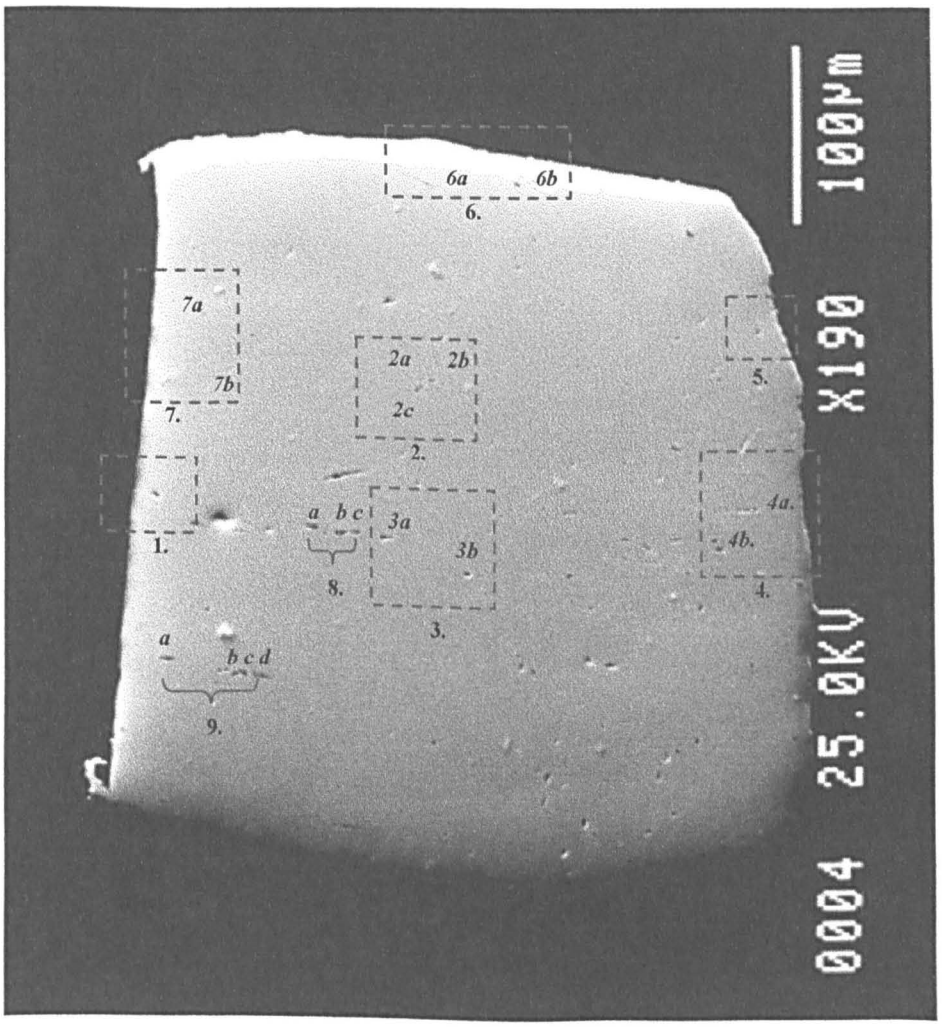

figure 6.23

AN SEM IMAGE FOR THE SELECTED REGION, SHOWN IN THE MICROPROBE MAPS WHICH FOLLOW

Experiment- D
Sample- 316F

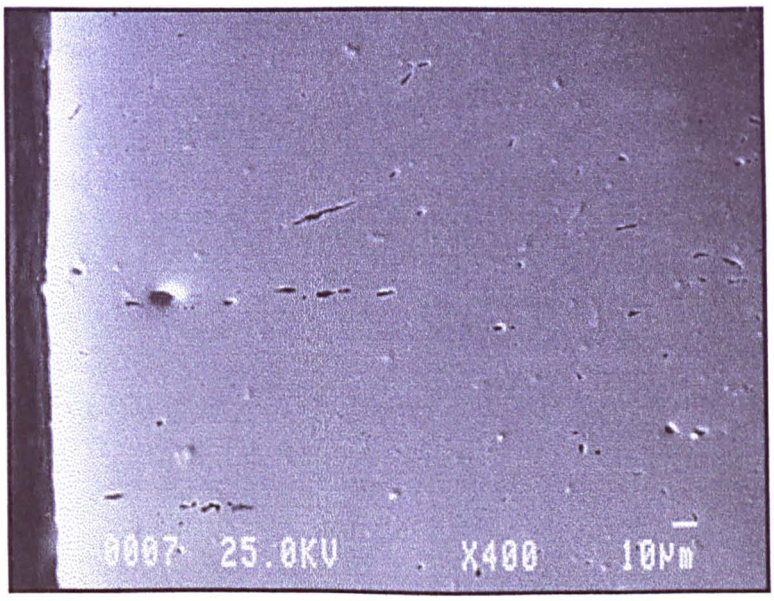

Notes: Acceleration voltage = 25.0 kV, current = 5 x 10^{-8} A

figure 6.24

A LOW kV OXYGEN CONCENTRATION MAP

Experiment- D
Sample- 316F

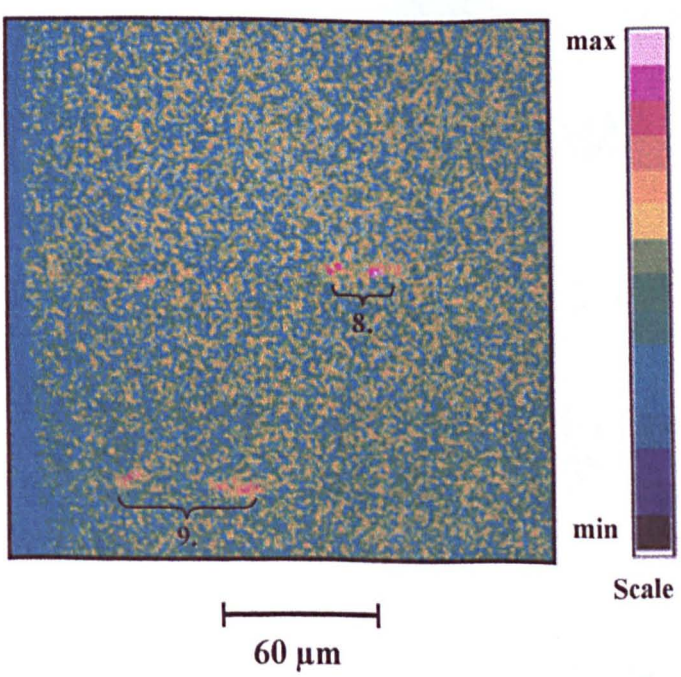

Notes: Acceleration voltage = 12 kV, Current = 1.00 x 10^{-7} A. Image data recorded every pixel where pixel dwell time = 100 ms.

figure 6.25

MICROPROBE ELEMENT CONCENTRATION MAPS OF A SELECTED REGION OF THE ELECTRODE, SHOWING SOME OF THE ELEMENTS PRESENT IN THE INCLUSIONS

S Crystal - PET, 171.665 mm (x-ray line = Kα)

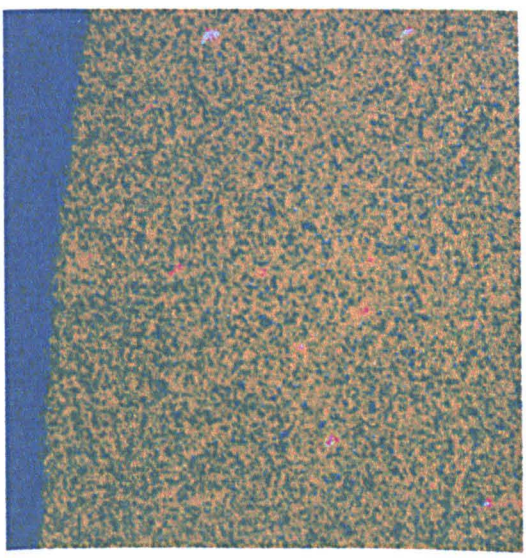

Mn Crystal - LIF, 145.875 mm (x-ray line = Kα)

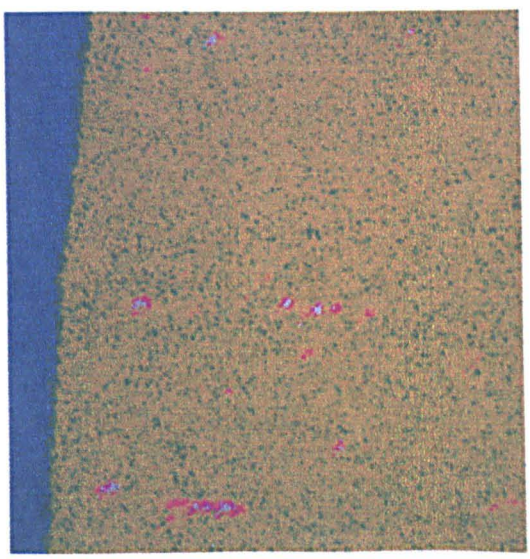

Si Crystal - TAP, 77.895 mm (x-ray line = Kα)

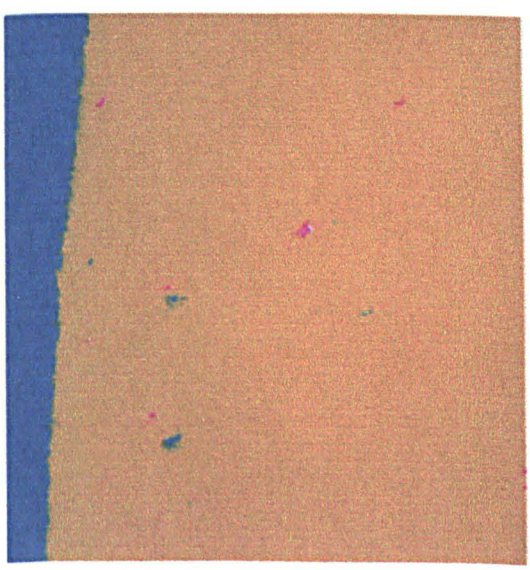

Ti Crystal - PET, 87.705 mm (x-ray line = Kα)

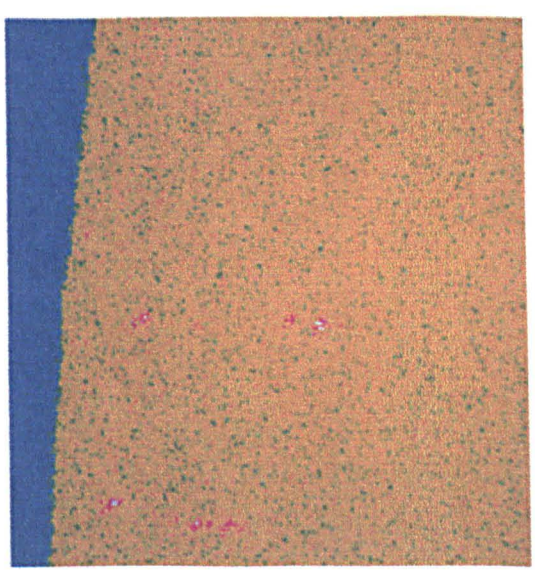

Notes: These images were recorded every pixel where 1 pixel = 1 µm , pixel dwell time = 60 ms, current = 1.3 x 10^{-7} A, acceleration voltage = 25.0 kV. The abbreviation for the crystals have been given as follows: LIF = lithium fluoride, PET = pentaerythritol, TAP = thallium acid phthalate. The crystal name is followed by the spectrometer position in 'mm' units. See figure 6.28 for the microprobe spot analysis giving % weights of the elements present for this region.

figure 6.26

MICROPROBE ELEMENT CONCENTRATION MAPS OF A SELECTED REGION OF THE ELECTRODE, SHOWING THE PRINCIPAL ELEMENTS PRESENT IN 316 STAINLESS STEEL

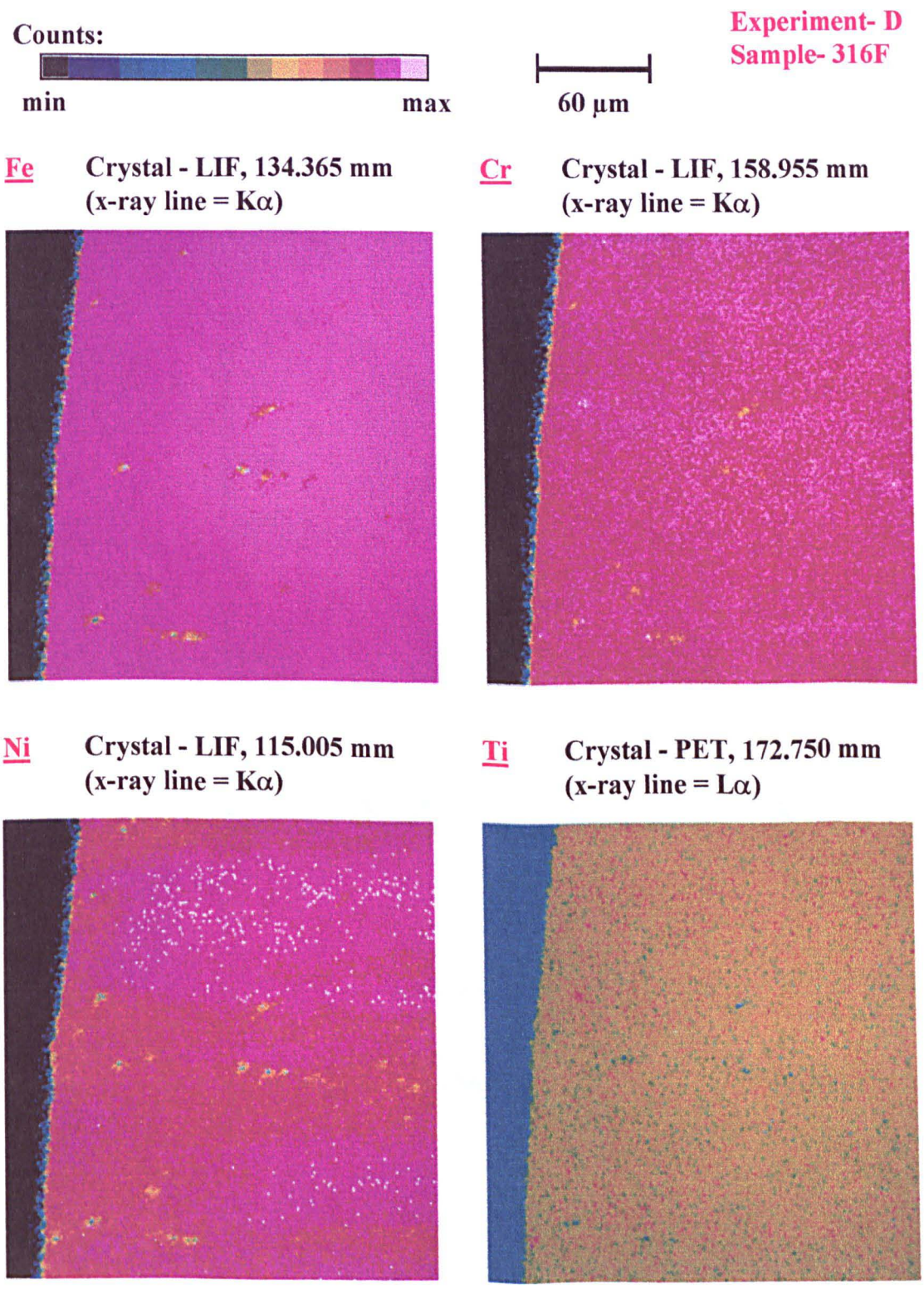

Notes: These images were recorded every pixel where 1 pixel = 1 µm , pixel dwell time = 60 ms, current = 1.3 x 10^{-7} A, acceleration voltage = 25.0 kV. The abbreviation for the crystals have been given as follows: LIF = lithium fluoride, PET = pentaerythritol, TAP = thallium acid phthalate. The crystal name is followed by the spectrometer position in 'mm' units. See figure 6.28 for the microprobe spot analysis giving % weights of the elements present for this region.

figure 6.27

A SUMMARY OF THE MICROPROBE SPOT ANALYSIS

Experiment- D
Sample- 316F

Rectangles mark the electroactive areas seen on the photocurrent image.

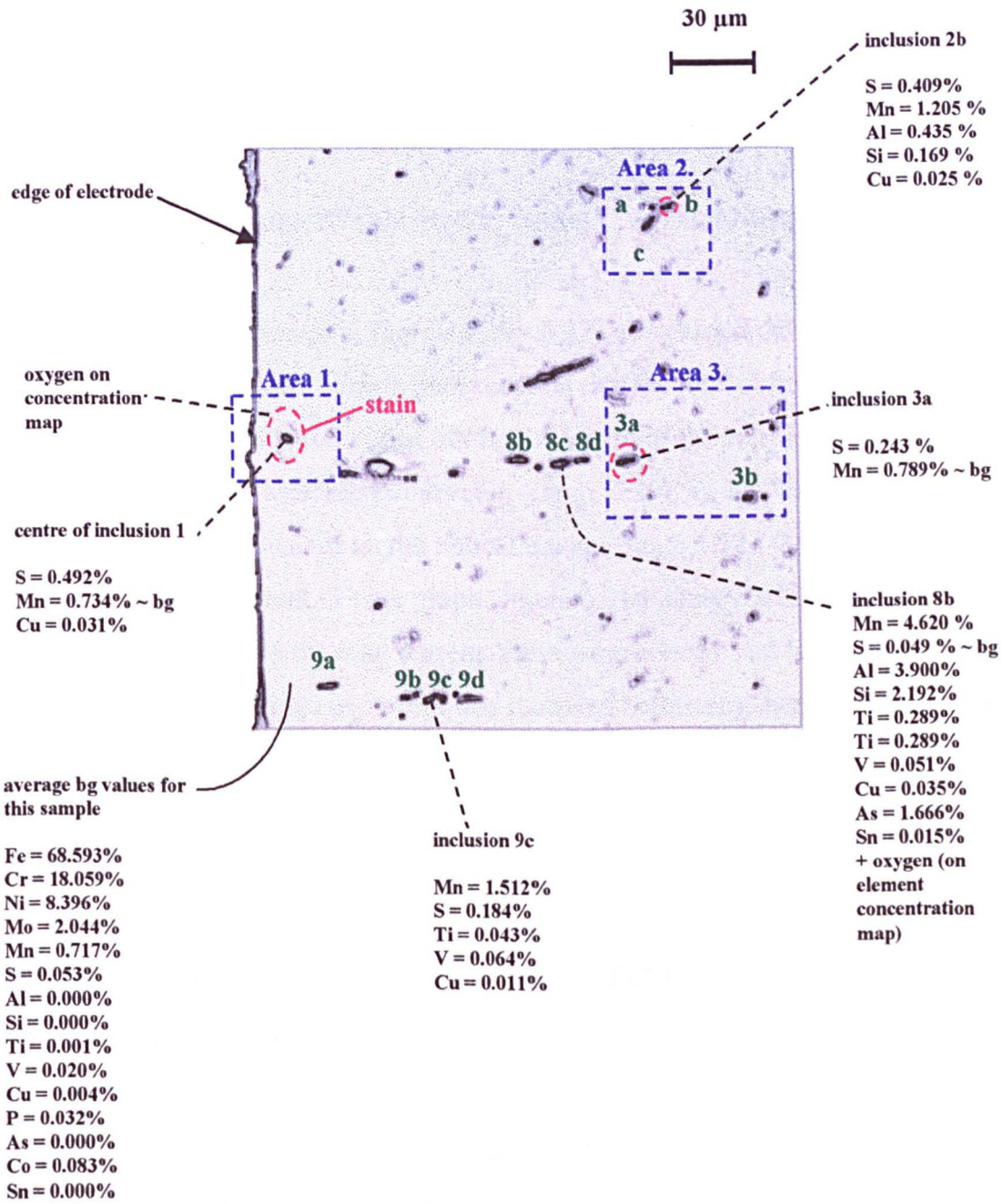

Notes: The % weight of Mn and S and any elements which increased significantly from the bg value are listed here. The bg value = bulk stainless steel, where there are no inclusions present. Acceleration voltage = 25 kV, current = 5 x 10^{-8} A, dwell time per element in the spot analysis = 20 s.

figure 6.28

6.6 PITTING BEHAVIOUR ON STAINLESS STEELS (in dilute NaCl solutions)

In order to track the pitting behaviour on the stainless steel the total current was monitored (using a 12 bit data logger) whilst recording photocurrent images with time in experiments E, F and G. It was found that the total current rapidly dropped to near zero after the potential was raised from a starting potential of -900 mV to the required potential.

Observation of a Small Peak in the Total Current Signal

This experiment (experiment E, figures 6.29 - 6.32) was carried out using the same conditions as in experiment D with the exception that the total current was being monitored as well. It was found that during the length of the experiment even though positive photocurrents were seen to develop (figure 6.29), as well as the occurrence of stains around some inclusions on the optical image (figure 6.30), there was very little activity on the total current vs time graph (figure 6.31). Only 2 small peaks were observed (figure 6.32) in the total current: these were about 10 nA in size and lasted for 2 seconds. The first change in current was recorded before any images were recorded, and the second change could not be correlated with the changes on the photocurrent image as it was very small in size and short lived.

Observation of a Slightly Bigger Peak in Total Current with a Change in Photocurrent Image Contrast

In experiment F (figures 6.35 - 6.44) the potential was slightly increased in order to further encourage pitting effects to occur at a faster rate. There was one inclusion (inclusion 1) in particular where in the early stages of the experiment, positive photocurrents developed, later followed by the development of a stain, visible on the in-situ confocal optical image (figure 6.34). The later stages of this experiment showed that the photocurrent over inclusion 1 changed from positive to negative (figure 6.35).

It was found that a 18 nA peak lasting for 4 s occurred in the total current signal (figures 6.36, 6.37). This peak occurred between the recording of two images (figure 6.38b and figure 6.38c). The image before the total current peak showed just a small amount of the positive photocurrent remaining on the photocurrent image and the image after the peak showed that the photocurrent had totally turned negative. This suggested that the peak in the total current, which is indicative of pitting, corresponded to a change in the sign of the photocurrent at the inclusion site.

Optical images (figures 6.39 , 6.40) showed that quite a large sized stain had formed around inclusion 1, and a smaller stain around a inclusion 2. The stain was seen to form selectively around the top half of the inclusion-1 indicating that the inclusion was only partially active. The top and bottom halves of the inclusion looked different on both the optical image recorded using the confocal scanning laser microscope and on the optical micrograph recorded using a traditional light microscope, the top half being darker than the bottom half. The stain present on inclusion-2 was dense enough to be seen on the SEM image but the larger stain around inclusion-1 could not be seen at 25 kV even at a high magnification (figure 6.41). However when low kV (12 kV) SEM images (figure 6.42) were recorded the stain was clearly visible. This shows the stain to be very thin, as at 12 kV the electron beam only travels a fraction of a micrometer into the surface of the sample (see Appendix E, figure E-4 for depth travelled by electron beam at various kV's). The yz-modulated SEM image (figure 6.42b), which is sensitive to small changes in topography, indicated that the formation of a pit had occurred at the inclusion centre.

The microprobe analysis carried out showed the presence of manganese and sulphur around inclusion 1 in a wider area than just where the inclusion occurred (figure 6.43). This was confirmed using microprobe spot analysis (figure 6.44), as well as showing the presence of some chloride in the stain.

EFFECT OF TIME ON THE PHOTOCURRENT IMAGE CONTRAST AT A LOW POTENTIAL SIMULTANEOUSLY MONITORED WITH THE TOTAL CURRENT SIGNAL

Experiment- E
Sample- 316F

Solution = 0.025M NaCl, 0.075M $NaClO_4$, I = 0.1M
E = 0 mV vs SSE

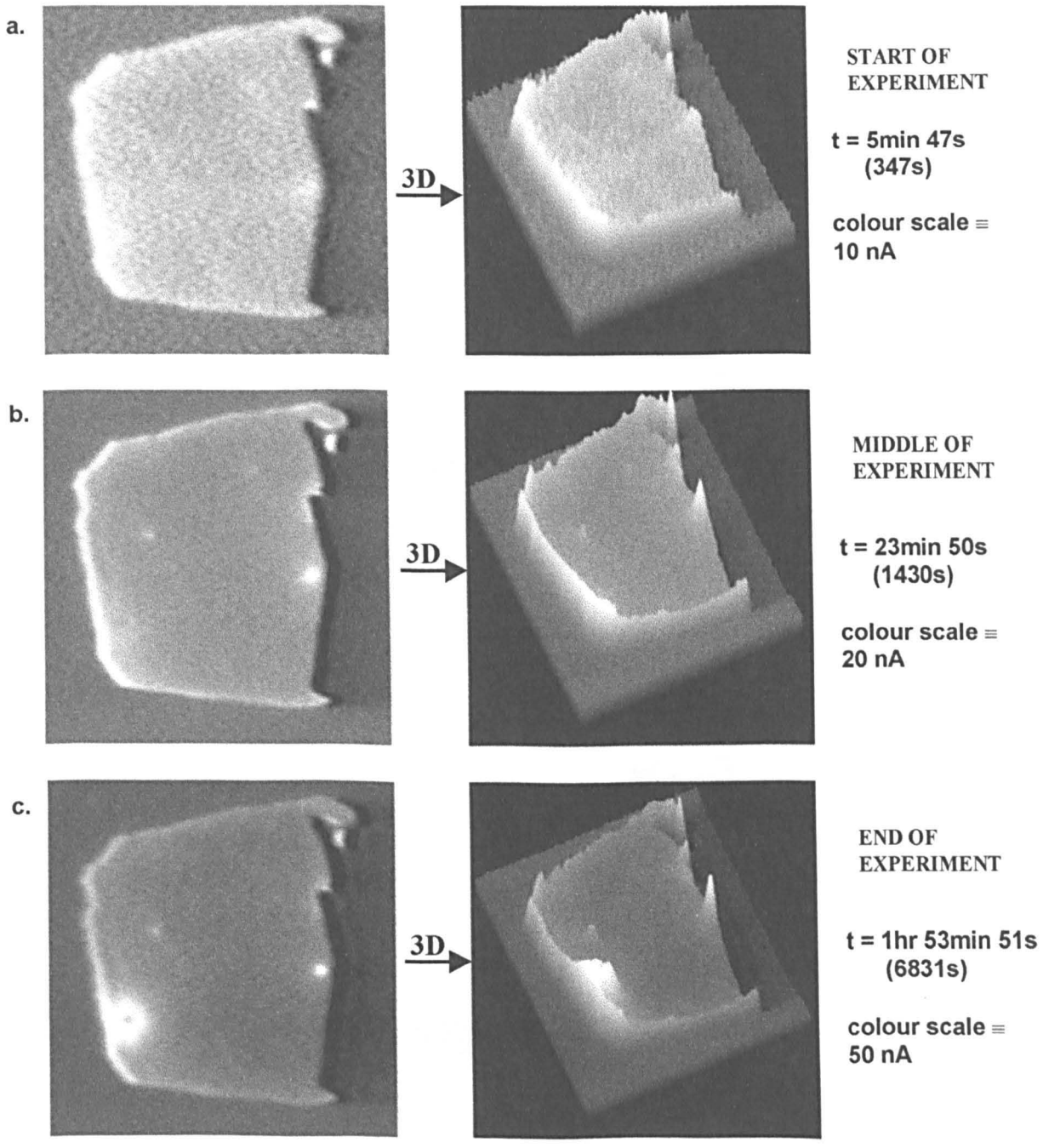

size of image shown = 390µm x 390µm (x,y), 'laser-off' value = 141.8/ 256 pixels

Notes: Lens magnification = x 4 (N.A. = 0.13), 2r = beam diameter = 2 µm, total area sampled in experiment = 633 x 390 µm (768 x 512 pixels), pixel dwell time = 10 µs, v_p= 8.24 cm s^{-1}, τ = 24.27 µm. The time t = 0 seconds, is the time when the potentiostat was switched on to the external cell at -900 mV. From t = 62 s to t = 130 s the potential was raised from -900 to 0 mV. The 1st image recorded after this is shown above in figure a).

figure 6.29

HIGH RESOLUTION CONFOCAL OPTICAL IMAGES

Experiment- E
Sample- 316F

Size of image shown here: 458µm x 424µm (x,y)

a) At the start of the experiment

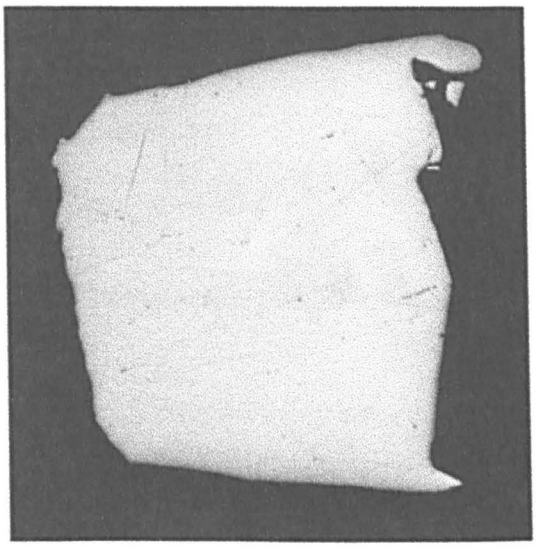

b) At the end of the experiment

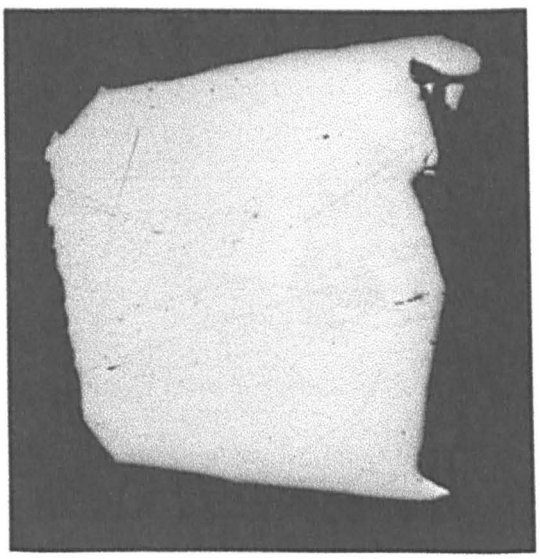

150 µm

Notes: Lens magnification = x 20 (N.A. = 0.40), total area sampled in experiment = 818 x 497 µm (768 x 512 pixels), pixel dwell time = 10 µs, 2r = 0.6 µm, v_p= 10.65 cm s^{-1}, τ = 5.63 µs.

figure 6.30

TOTAL CURRENT VS TIME GRAPH FOR THE WHOLE EXPERIMENT

Experiment- E
Sample- 316F

Solution = 0.025M NaCl, 0.075M $NaClO_4$, I = 0.1M
E = 0 mV vs SSE

This data was sampled every second.

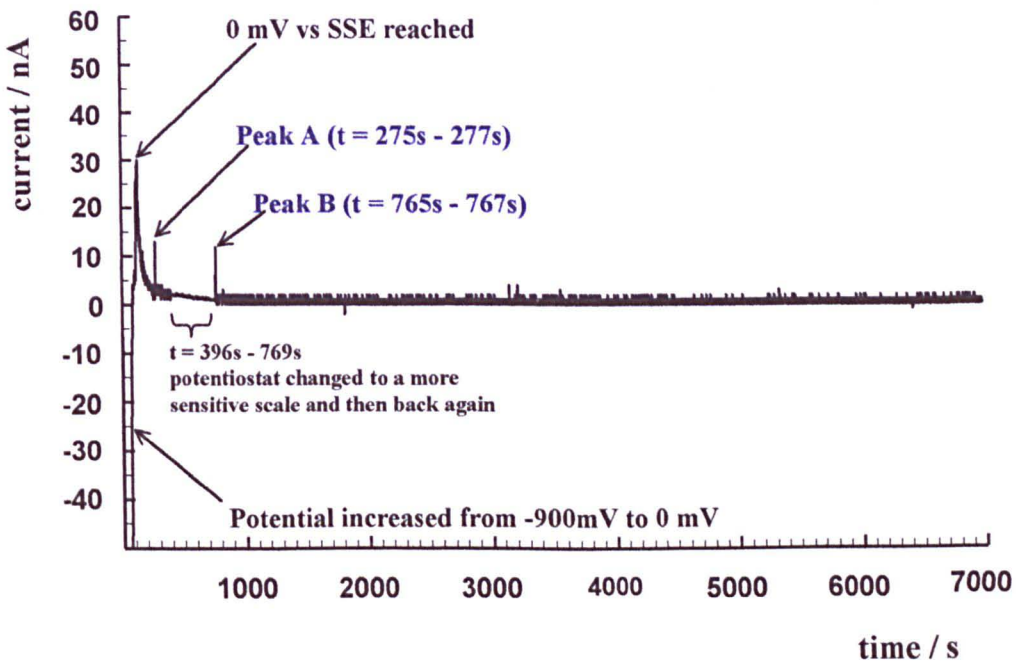

Summary of occurrences at various times for experiment E :

time		Information relating to the time
s	hr:min:sec	
<0	———	Data logger switched on and then the potentiostat was switched on to the internal cell at -900 mV
0	00:00:00	Potentiostat switched to external cell at -900 mV
62-130	00:01:02 00:02:10	Potentiostat raised from -900 mV to 0mV
275-277	00:04:35 00:04:37	Peak A on the total current vs time curve
347	00:05:47	Time recorded at the end of the 1st photocurrent image collected
396	00:06:36	Potentiostat switched from a 1 μA per volt setting to a more sensitive setting of 0.1 μA per volt setting
765-767	00:12:45 00:12:47	Peak B on the total current vs time curve
769	00:12:49	Potentiostat switched back to 1 μA per volt setting

Notes: One data point was recorded every 1 second on the current vs time graph using a 12 bit data logger. Each data point recorded involved 50 readings being collected and signal averaged at the beginning of each second. The signal averaging process took 1200 μs (1.2×10^{-3} s). See figure 6.32 for greater detail of the regions of the curve containing peak A and peak B.

figure 6.31

SELECTED REGIONS OF THE CURRENT VS TIME CURVE

Experiment- E
Sample- 316F

a) Current vs Time at Peak A

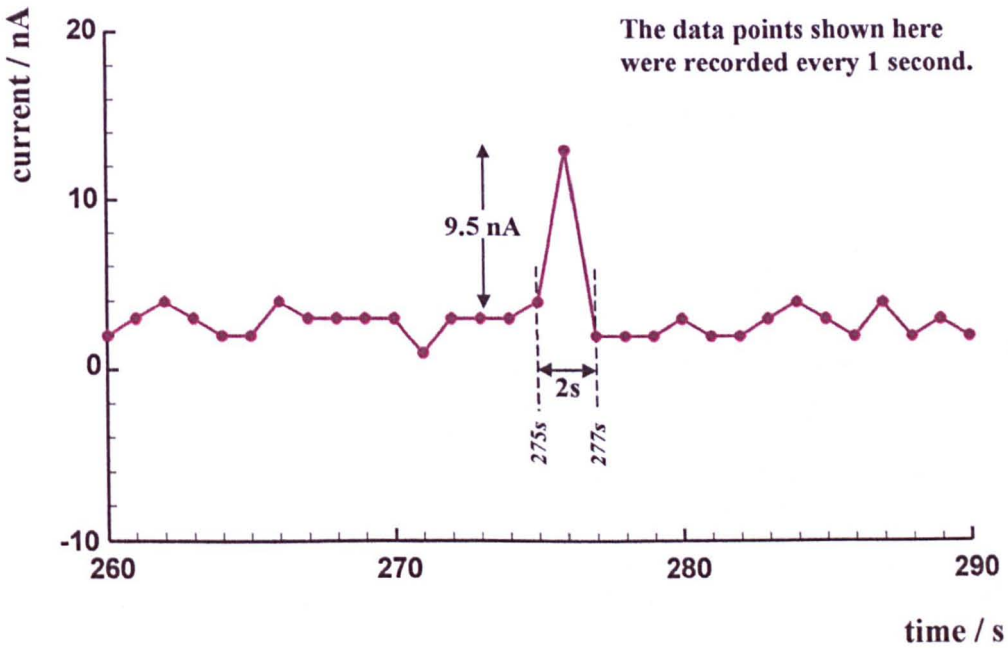

b) Current vs Time at Peak B

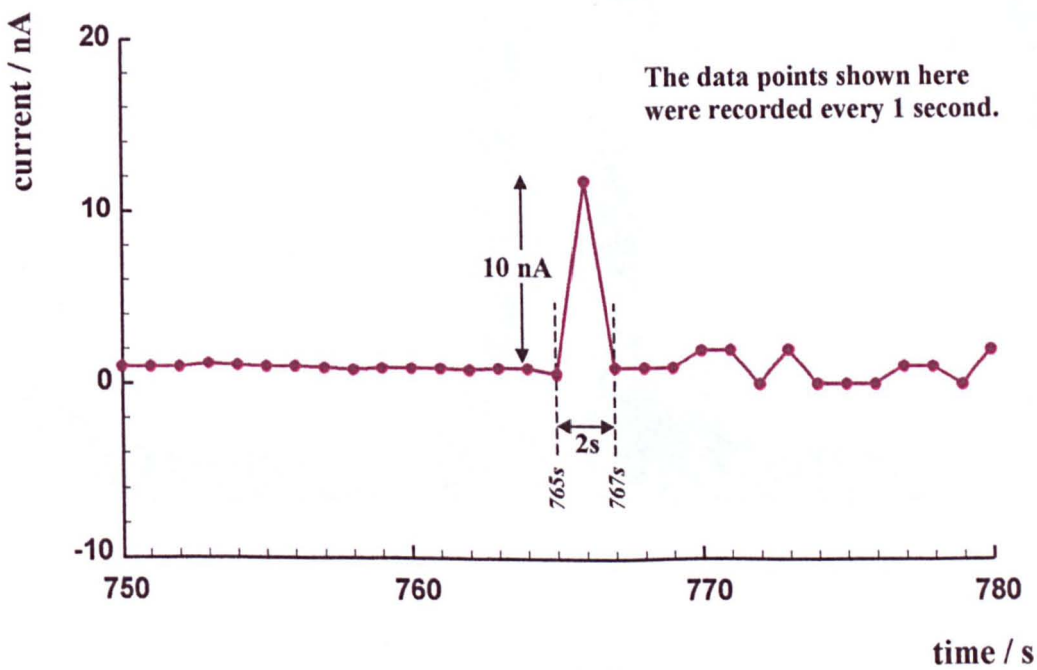

Notes: Each data point recorded involved 50 readings being collected and signal averaged at the beginning of each second. The signal averaging took 1200 μs (1.2×10^{-3} s).

figure 6.32

EFFECT OF TIME ON THE PHOTOCURRENT AND CONFOCAL OPTICAL IMAGES SIMULTANEOUSLY MONITORED WITH THE TOTAL CURRENT

Experiment- F
Sample- 316F

Solution = 0.025M NaCl, 0.075M $NaClO_4$, I = 0.1M

Photocurrent images

START

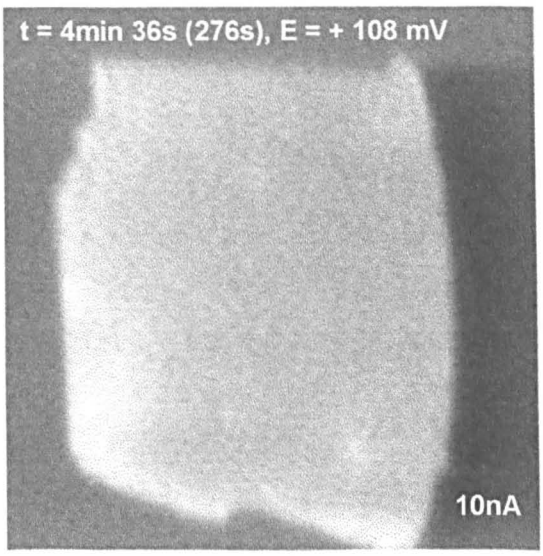

END

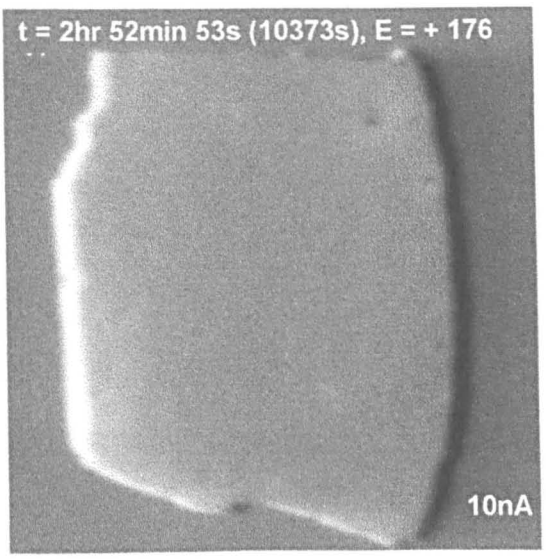

Confocal Optical Images

START

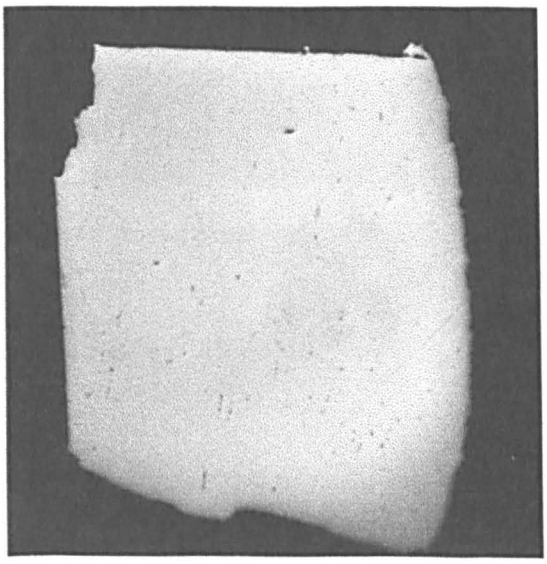

END

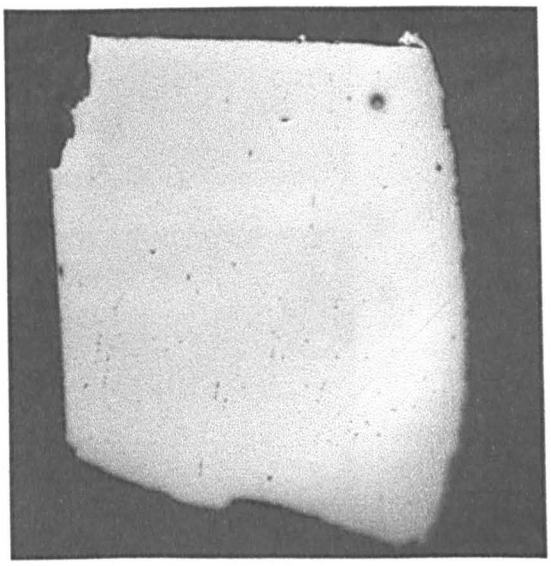

Size of images shown here: 454µm x 454µm

Notes: For the photocurrent images; lens magnification = x 4 (N.A. = 0.13), 2r = beam diameter = 2 µm, total area sampled in experiment = 763 x 454 µm (768 x 512 pixels), pixel dwell time = 10 µs, v_p= 9.93 cm s^{-1}, τ = 20.88 µm. The time t = 0 min, is the time the potentiostat was switched onto the external cell at -900 mV. The potential was then increased after this to +108 mV and the 1st image was recorded at t = 276 s (time recorded at the end of the image). For the optical images; lens = x20 (N.A. = 0.40), vp = 10.65 cm s^{-1}, τ = 5.63 µm.

figure 6.33

PHOTOCURRENT AND IN-SITU CONFOCAL OPTICAL IMAGES RECORDED IN THE EARLY PART OF THE EXPERIMENT

Experiment- F

Images Showing Stain Formation at an Inclusion:

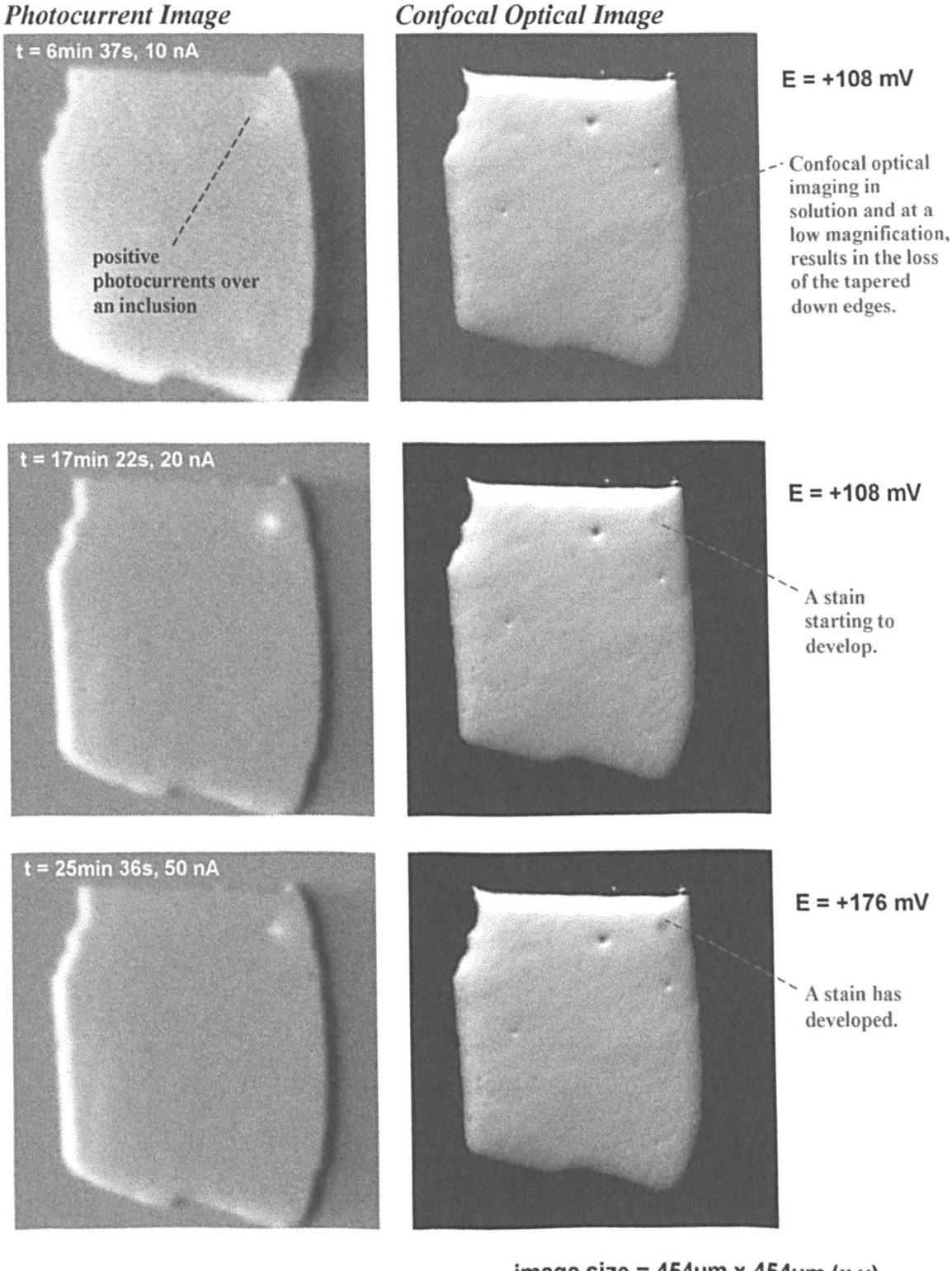

Notes: The following image parameters apply to both the photocurrent (R.H.S) and confocal optical images (L.H.S) shown. Lens magnification = x 4 (N.A. = 0.13), 2r = beam diameter = 2 µm, total area sampled in experiment = 763 x 454 µm (768 x 512 pixels), pixel dwell time = 10 µs, v_p= 9.93 cm s^{-1}, τ = 20.88 µm.

figure 3.34

EFFECT OF TIME ON THE PHOTOCURRENT IMAGES, RECORDED IN THE LATER PART OF THE EXPERIMENT

Experiment- F

Images Showing a Change in the Photocurrent Signal Over an Inclusion:

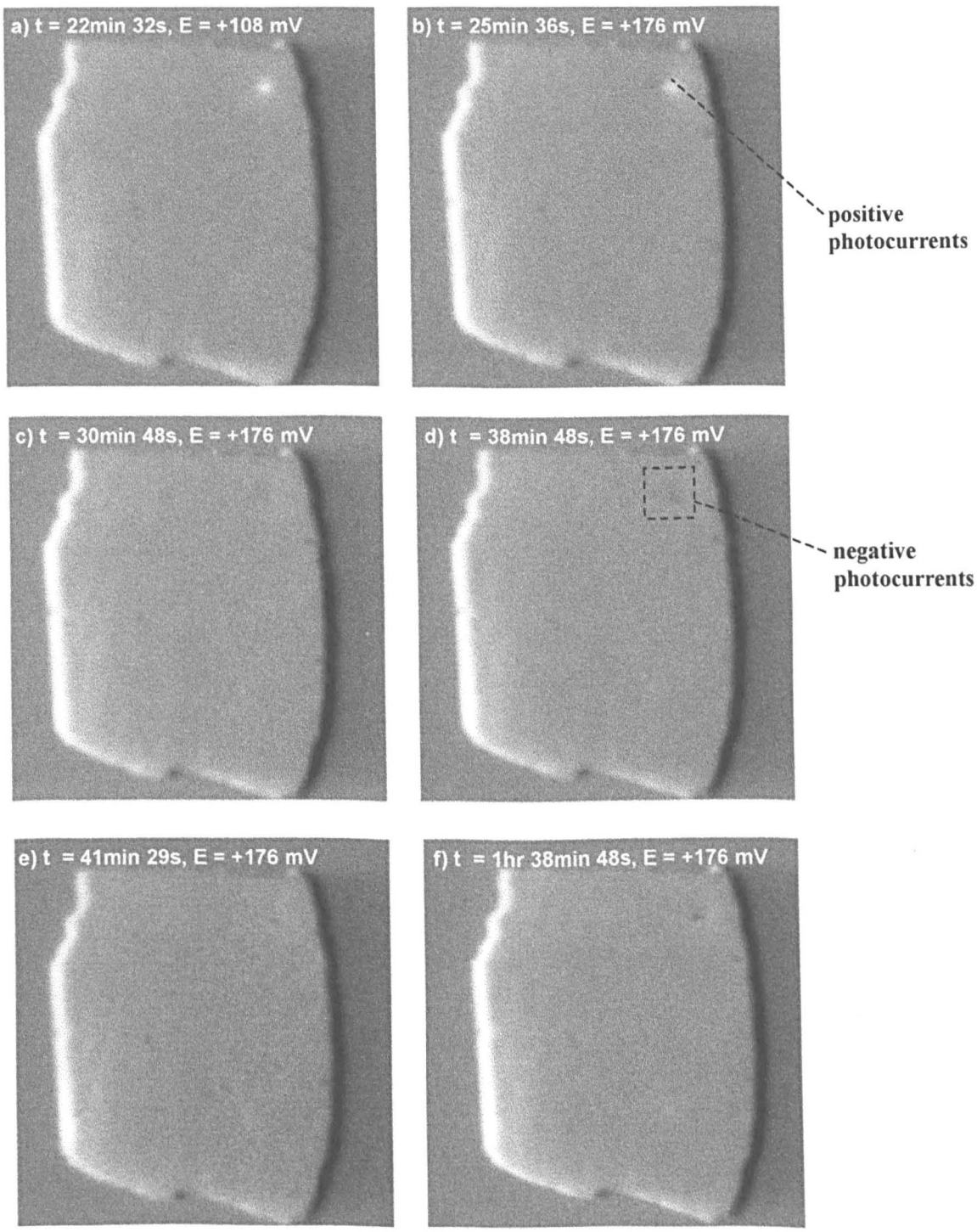

image size = 454 μm x 454 μm (x,y), 256 grey scale ≡ 50 nA

Notes: Lens magnification = x 4 (N.A. = 0.13), 2r = beam diameter = 2 μm, total area sampled in experiment = 763 x 454 μm (768 x 512 pixels), pixel dwell time = 10 μs, v_p= 9.93 cm s^{-1}, τ = 20.88 μm. A peak in the total current was seen after image c) and before image d).

figure 6.35

TOTAL CURRENT VS TIME GRAPH

Experiment- F
Sample- 316F

Solution = 0.025M NaCl, 0.075M $NaClO_4$, I = 0.3M
E = +108 mV / +176 mV vs SSE

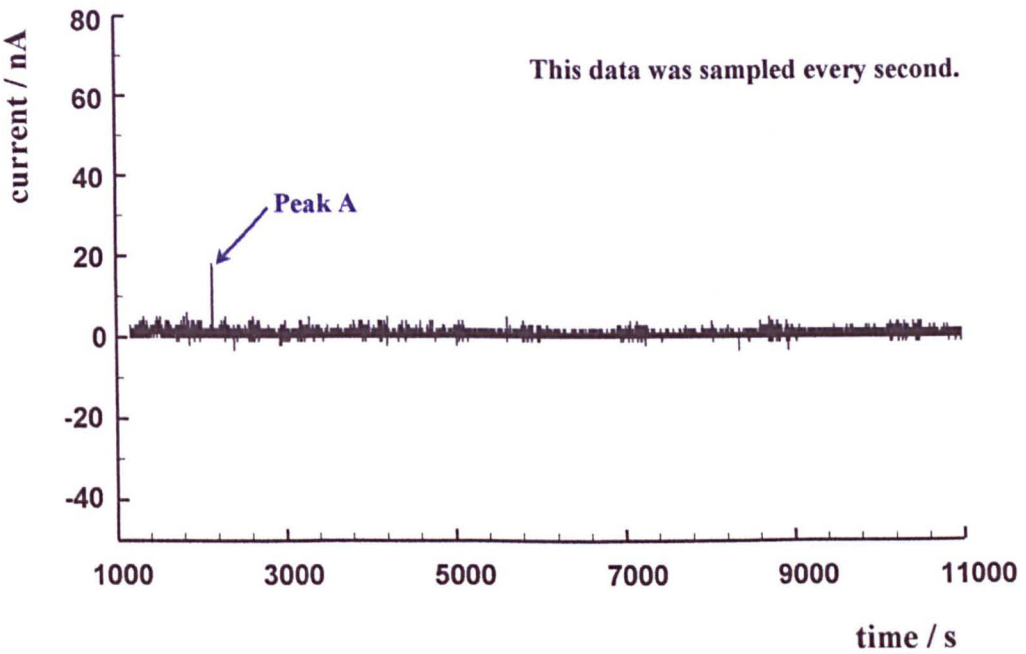

Summary of occurrences at various times for experiment F :

time		Information relating to the time
s	hr:min:sec	
0	00:00:00	Potentiostat switched on to external cell at -900 mV
> 0	————	Potentiostat raised from -900 mV to +108 mV
276	00:04:36	Time recorded at the end of the 1st photocurrent image
1163	00:19:23	Data logger switched on
1433	00:23:53	Potential increased to + 176 mV, from +108 mV, this value reached at this time
2138 - 2142	00:35:38 00:35:42	Peak A on the total current vs time graph

Notes: One data point was recorded every 1 second on the current vs time graph using a 12 bit data logger. Each data point recorded involved 100 readings being collected and signal averaged at the beginning of each second. This process took 2200 μs (2.2×10^{-3} s). See figure 6.37 for greater detail of the current vs time curve containing peak A.

figure 6.36

TOTAL CURRENT VS TIME AT PEAK A

Experiment- F
Sample- 316F

Solution = 0.025M NaCl, 0.075M $NaClO_4$, I = 0.1M
E = +176 mV vs SSE

This peak corresponded with change in the photocurrent image contrast from +VE to -VE in an area containing an inclusion. This effect can be seen in detail on the 3D-photocurrent surface plots shown in figure 6.38.

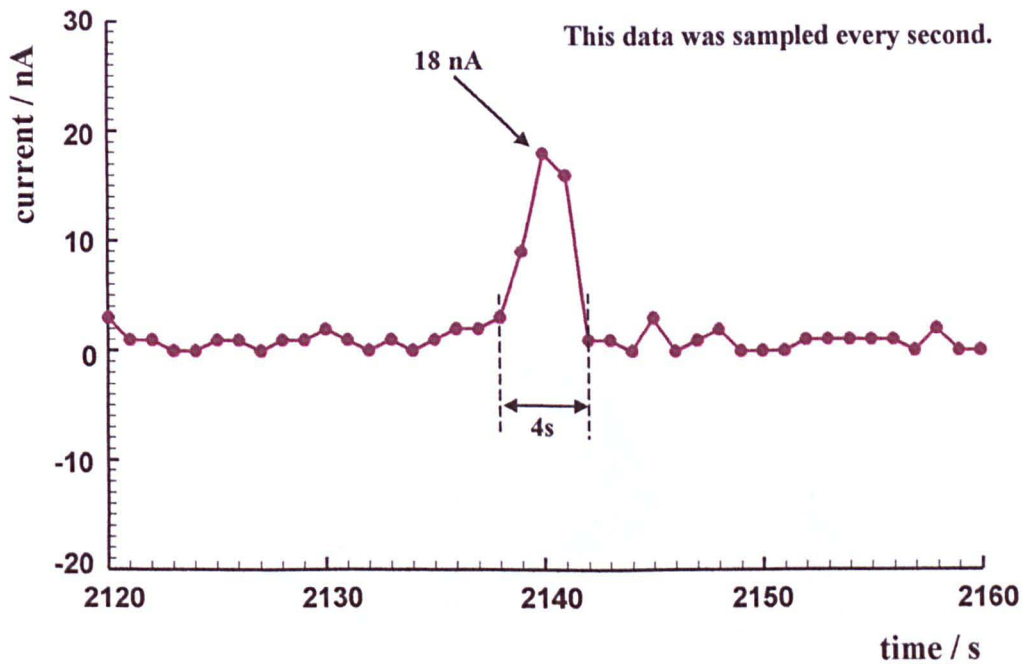

Notes: One data point was recorded every 1 second on the current vs time graph using a 12 bit data logger. Each data point recorded involved 100 readings being collected and signal averaged at the beginning of each second. This process took 2200 μs (2.2×10^{-3} s).

figure 6.37

3D-PHOTOCURRENT SURFACE PLOTS CORRESPONDING TO PEAK A IN THE TOTAL CURRENT SIGNAL

Solution = 0.025M NaCl, 0.075M $NaClO_4$, I = 0.1M
E = +176 mV vs SSE
Size of image shown here (x,y) = 228μm x 228μm, grey scale ≡ 50 nA

Experiment- F
Sample- 316F

a. t = 25min 36s (1536s)

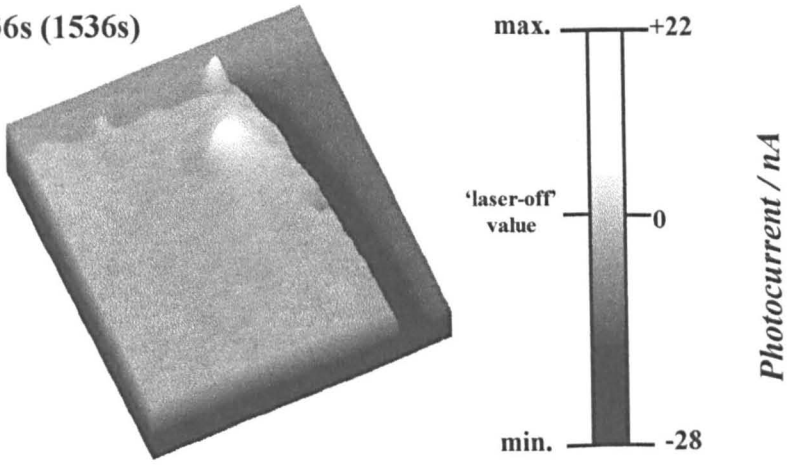

b. t = 30min 48s (1848s)

(Peak A on the total current vs time curve occurred after this image)

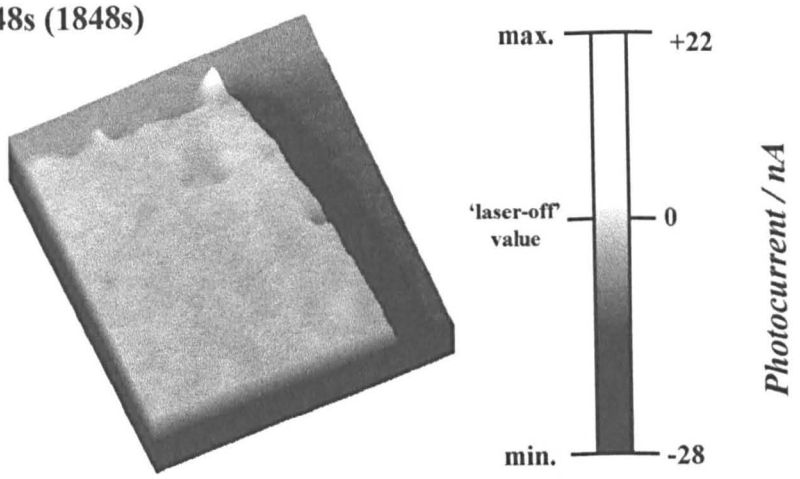

c. t = 38min 48s (2328s)

(Peak A on the total current vs time curve occurred before this image)

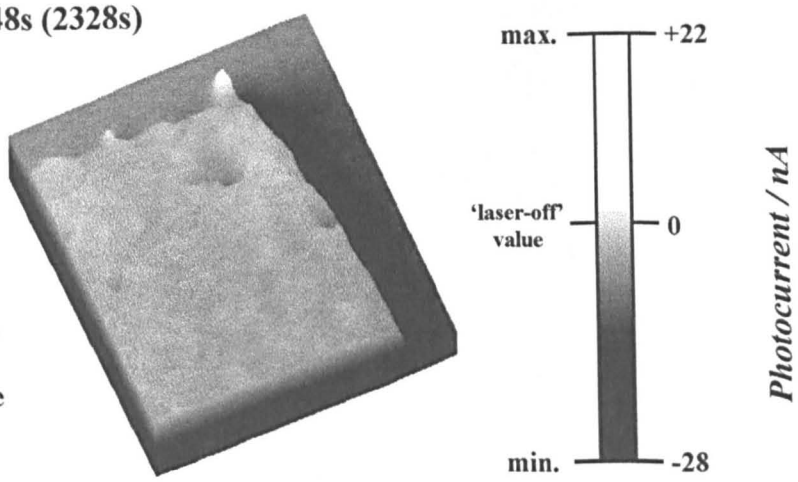

Notes: lens magnification = x 4 (N.A. = 0.13), 2r = beam diameter = 2 μm, total area sampled in experiment = 763 x 454 μm (768 x 512 pixels), pixel dwell time = 10 μs, v_p= 9.93 cm s^{-1}, τ = 20.88 μm. The time t = 0 s, is the time the potentiostat was switched onto the external cell.

figure 6.38

VERY HIGH RESOLUTION CONFOCAL OPTICAL IMAGES RECORDED AT THE END OF THE EXPERIMENT

Experiment- F
Sample- 316F

a)

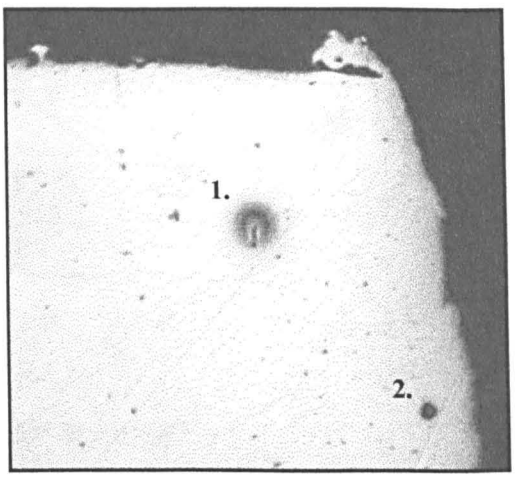

Areas 1 + 2

x 40 lens (N.A. = 0.40), zoom = x 1.9

size of image: 145µm x 135µm

b)

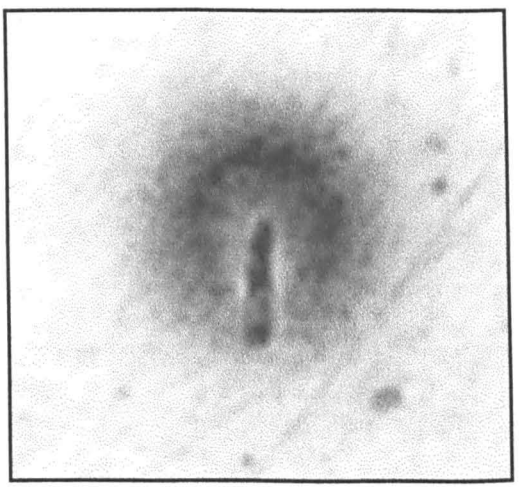

Area 1

x 40 lens (N.A. = 0.40), zoom = x 10.0

size of image: 28µm x 26µm

c)

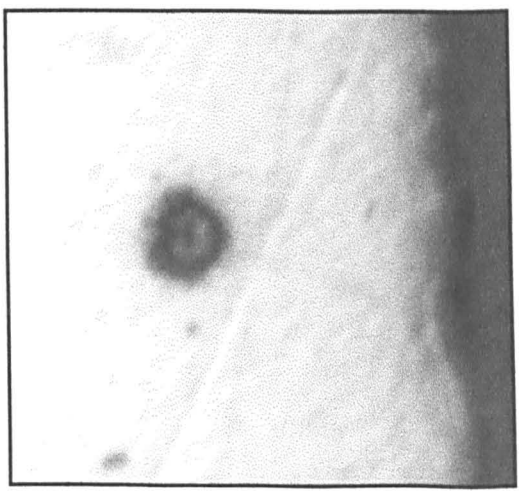

Area 2

x 40 lens (N.A. = 0.40), zoom = x 10.0

size of image: 28µm x 26µm

Notes : These images were recorded using the Bio-Rad MRC-600 confocal scanning laser microscope system. Image a): total area sampled in experiment = 222 x 135 µm (768 x 512 pixels), pixel dwell time = 10 µs, 2r = 0.6 µm, v_p= 2.29 cm s^{-1}, τ = 20.76 µs. Images b) and c): Total area sampled in experiment = 42 x 26 µm (768 x 512 pixels), pixel dwell time = 10 µs, 2r = 0.6 µm, v_p= 0.55 cm s^{-1}, τ = 109.09 µs.

figure 6.39

OPTICAL MICROGRAPHS RECORDED AT THE END OF THE EXPERIMENT

Experiment- F
Sample- 316F

Both images shown here were recorded using a x 50 objective lens = (N.A. = 0.80).

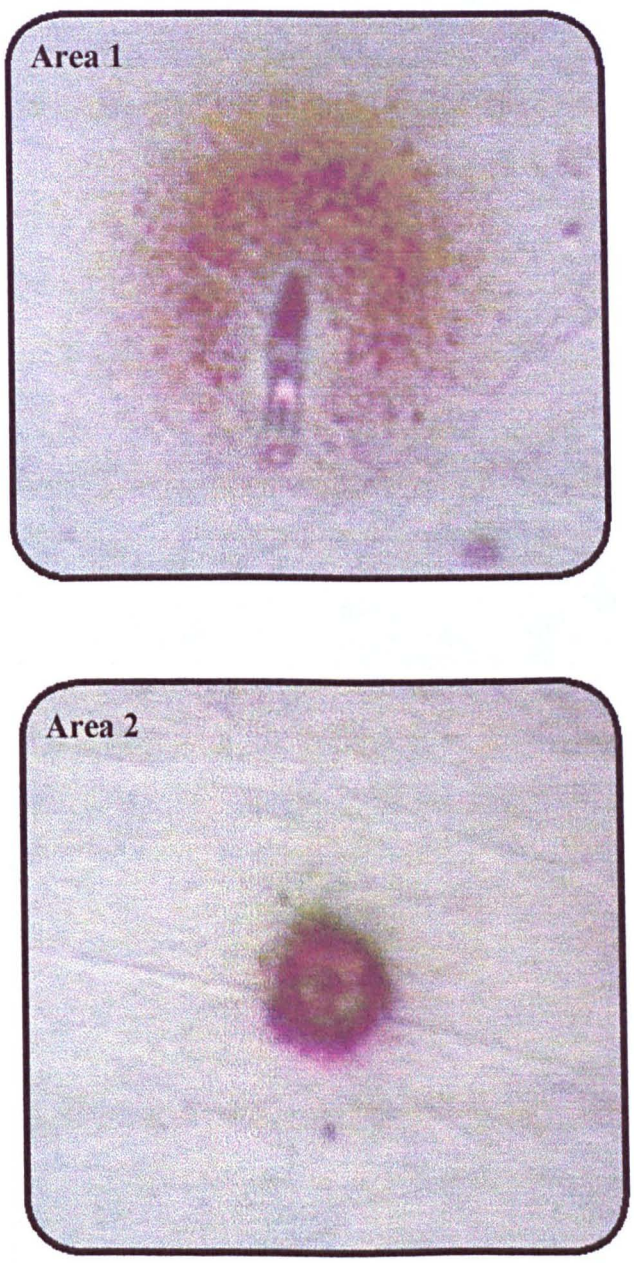

Notes: These images were recorded using a traditional light microscope.

figure 6.40

SEM IMAGES RECORDED AFTER THE EXPERIMENT

Acceleration Voltage = 25 kV
Current = 5 x 10^{-8} A

Experiment- F
Sample- 316F

a) The Whole Electrode

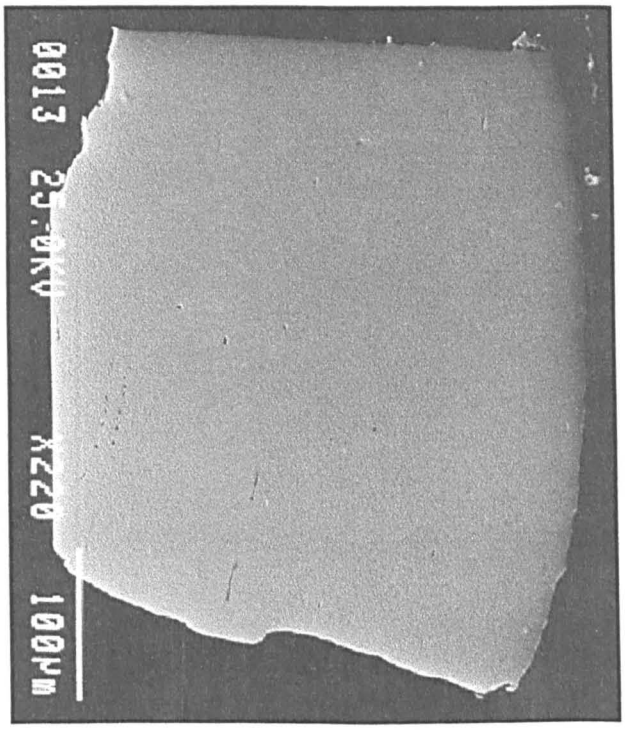

b) A Selection of the Electrode

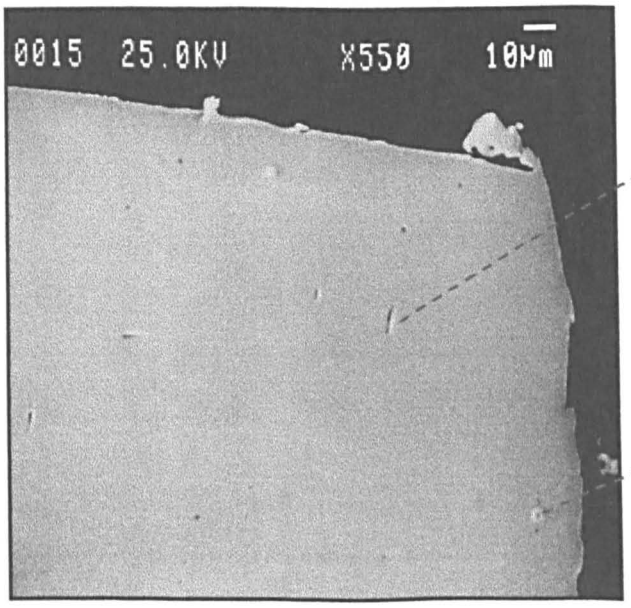

No evidence of the stain can be seen at this kV around inclusion 1.

A stain around inclusion 2.

Notes : Image b) shows the region examined by microprobe elemental analysis.

figure 6.41

LOW kV SEM IMAGES OF INCLUSION 1

Experiment- F
Sample- 316F

Acceleration Voltage = 12 kV
Current = 5 x 10^{-8} A

a) A Normal SEM Image

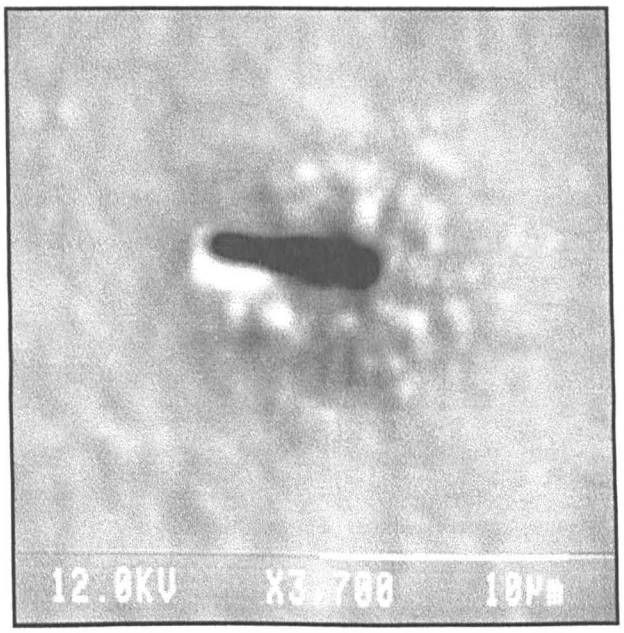

b) A yz-Modulated SEM Image

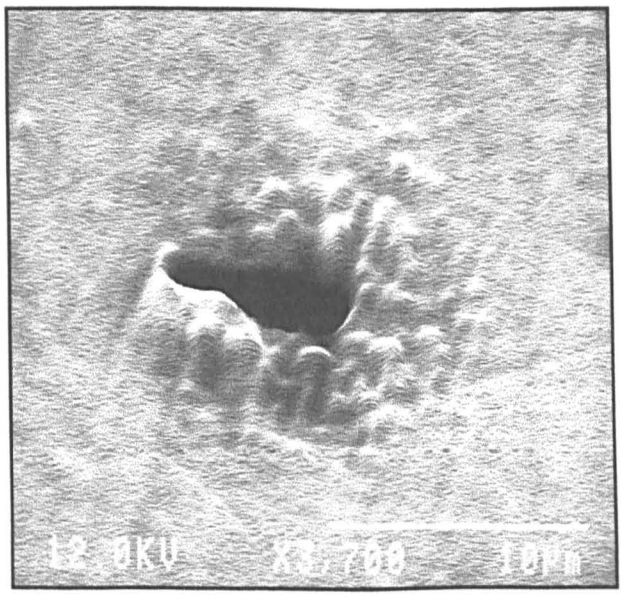

Notes : This image is rotated 90° clockwise from the position in which the image was recorded in the photocurrent images.

figure 6.42

MICROPROBE IMAGES RECORDED AFTER THE PHOTOCURRENT IMAGING EXPERIMENT

Experiment- F
Sample- 316F

Counts:

min **max**

60 μm

S Crystal - PET, 171.770 mm (x-ray line = Kα), 25 kV

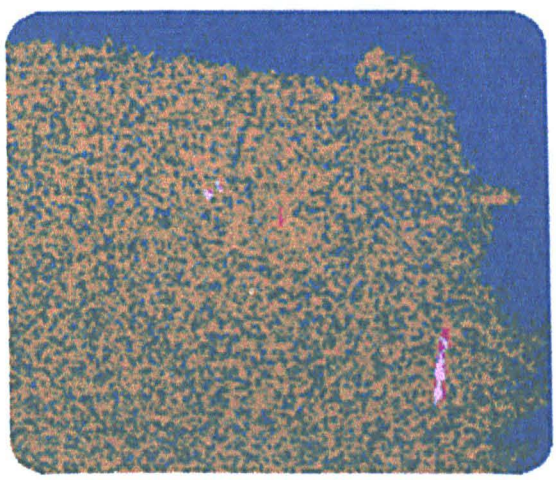

Mn Crystal - LIF, 145.885 mm (x-ray line = Kα), 25 kV

Ti Crystal - PET, 87.715 mm (x-ray line = Kα), 25 kV

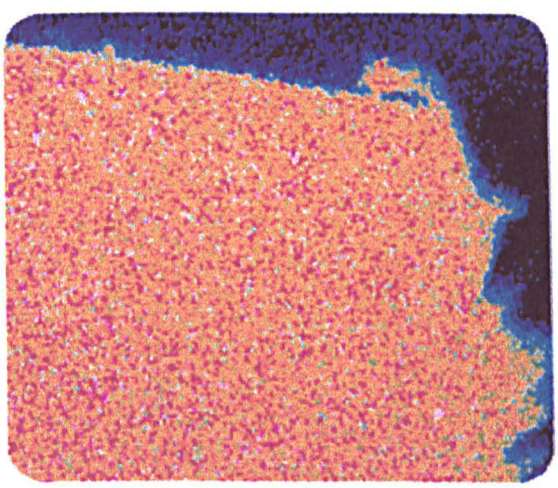

O Crystal - TAP, 256.770 mm (x-ray line = Kα), 12 kV

Notes: The images for [S], [Mn], [Ti] were recorded every pixel where 1 pixel = 1 μm , pixel dwell time = 100 ms, current = 1.3 x 10^{-7} A. The image shown for oxygen was recorded every pixel where 1 pixel = 1 μm and the pixel dwell time = 200 ms, current = 1.0 x 10^{-7} A. The abbreviation for the crystals have been given as follows: LIF = lithium fluoride, PET = pentaerythritol, TAP = thallium acid phthalate. The crystal name is followed by the spectrometer position in 'mm' units. See figure 6.44 for the microprobe spot analysis giving % weights of the elements present for this region.

figure 6.43

A SUMMARY OF THE MICROPROBE SPOT ANALYSIS

Experiment- F
Sample- 316F

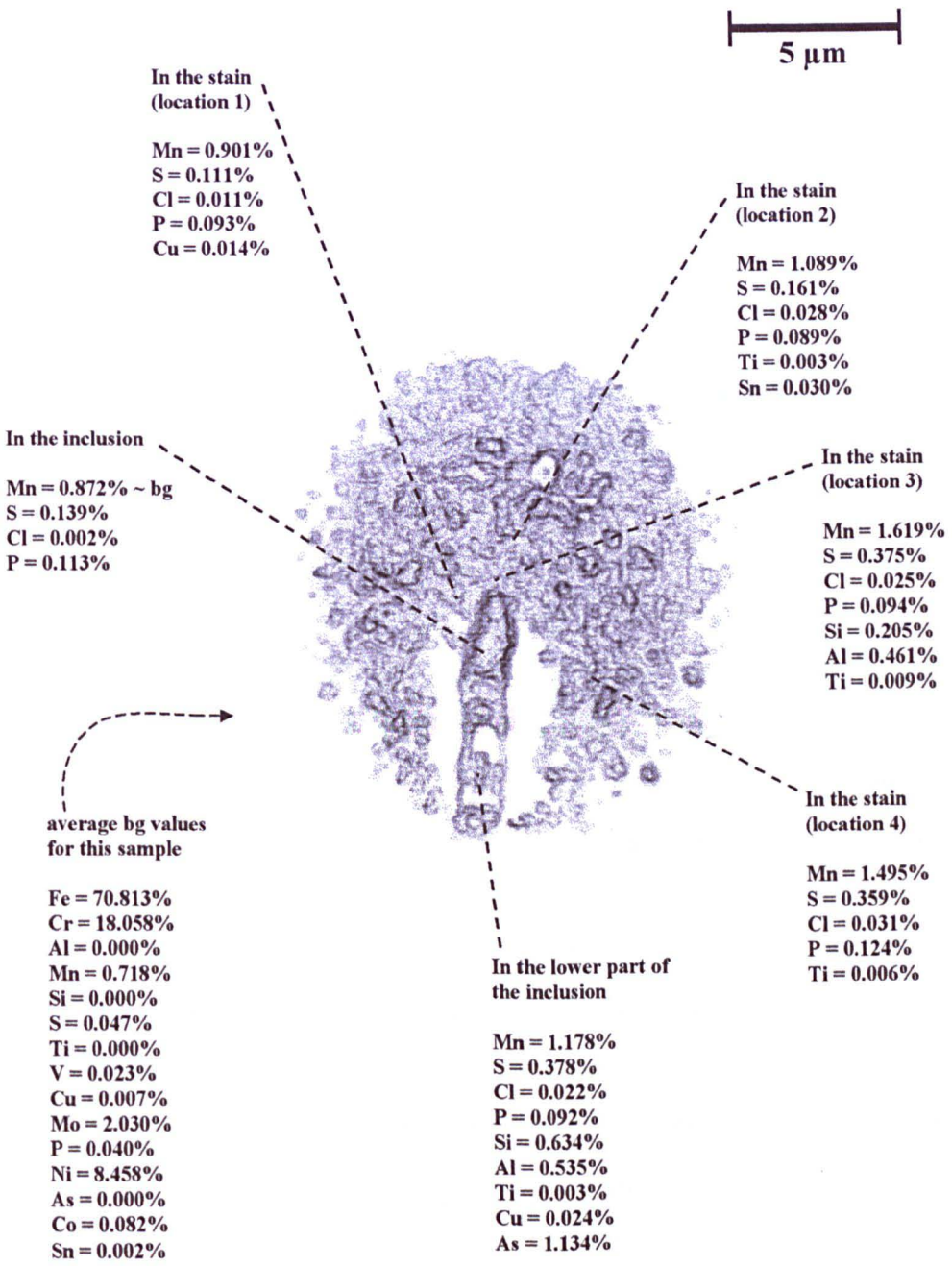

Notes: The % weight of Mn and S and any elements which increased significantly from the bg value are listed here. The bg value = bulk stainless steel, where there are no inclusions present. Acceleration voltage = 25 kV, current = 5 x 10^{-8} A, dwell time per element in the spot analysis = 20 s.

figure 6.44

Many Peaks in the Total Current Signal Correlating with Much Change in the Image Contrast

Experiment G (figures 6.45 - 6.52) was carried out at an even higher potential. An alternative procedure was to use just NaCl alone at a lower potential, but this reaction was found to be too fast to monitor. Positive photocurrents were found to occur at several inclusions which had turned into negative photocurrents by the end of the experiment (figure 6.45). Again some staining was seen on the optical image (figure 6.46)

The total current signal monitored with time for the whole experiment (figure 6.47) showed many more the peaks in the total current signal than in experiment F (previous sub-section) which lasted longer. The sections labelled region A and region B on the total current vs potential graph showed the were the first to show a significant change in the current. The first section (region A) lasted for 235 s with the change in the current reaching up to 97 nA. On closer examination this section of the graph (figure 6.48) seemed to exist of several peaks possibly overlapping one another. It may be possible that each peak corresponded to each inclusion which was undergoing a change. The photocurrent images which correspond to before, during, and after region A on the current vs time graph have been given in figure 6.49. From these photocurrent images, a change in the photocurrent signal from positive to negative can be seen on several inclusion areas. Region B (figure 6.50) lasted 213 s with total current reaching up to 19 nA. The photocurrent images taken before, during and after region B are given in figure 6.51. This figure shows the whole electrode slightly darkening (the photocurrents becoming more negative), in particular at the bottom edge of the electrode where crevice corrosion had started to occur. There were many other subsequent smaller peaks in total current, of about 10 nA magnitude. The photocurrent image recorded at the end of the experiment is given in figure 6.45b.

At the end of this experiment, height profiling (figure 6.52) was carried out using the confocal scanning laser microscope system. At the focussed position many inclusion regions could be seen as dark areas of reflectivity. However at a lower depth only some of the inclusion areas could be seen. These were the pitted areas. These areas

corresponded with those seen to have undergone a reversal of the photocurrent signal, which correlated in time with the occurrence of an increase in the total current signal.

PHOTOCURRENT IMAGES RECORDED AT EVEN HIGHER POTENTIALS WHILST SIMULTANEOUSLY RECORDING THE TOTAL CURRENT

Solution = 0.025M NaCl, 0.075M $NaClO_4$, I = 0.1M
Size of images shown = 454µm x 454µm

Experiment- G
Sample- 316F

150 µm

a) At the Start of the Experiment
t = 4min 13s (253s), E = +173 mV, grey scale = 20 nA

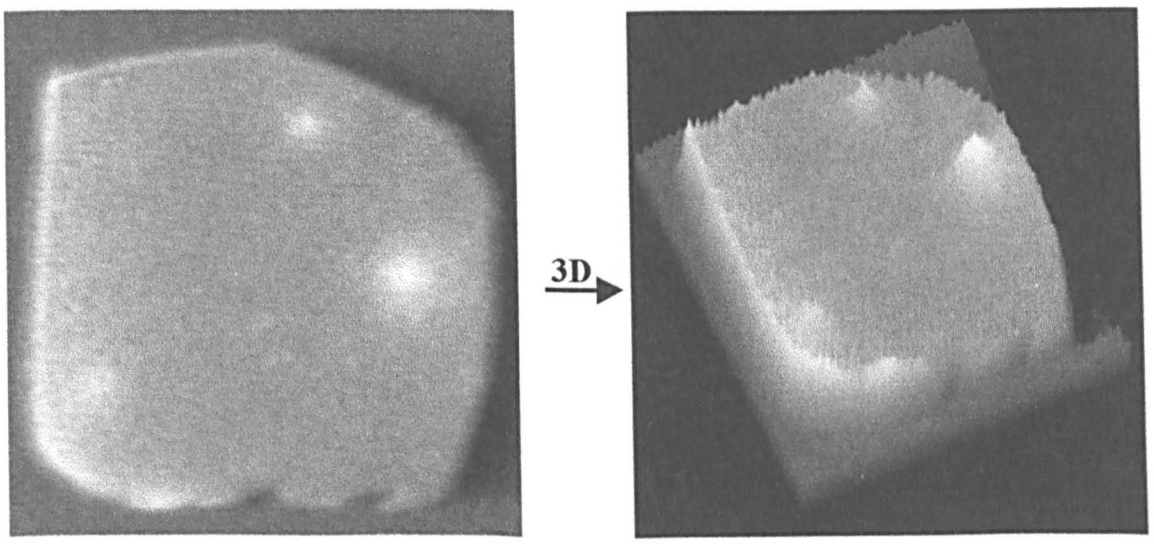

b) At the End of the Experiment
t = 1hr 52min 0s (6720s), E = +252 mV, grey scale = 50 nA

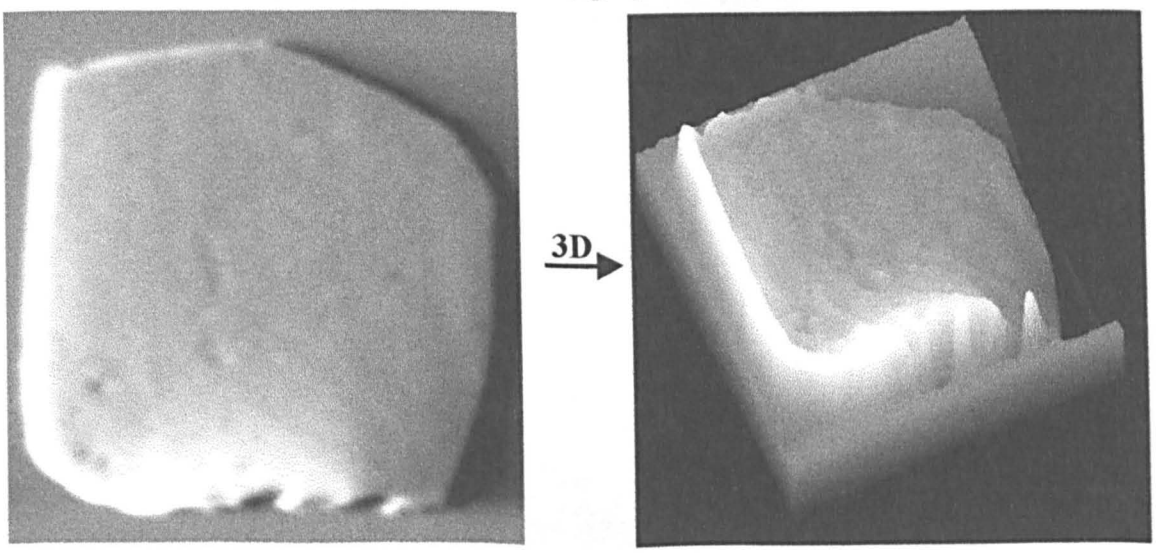

Notes: Lens magnification = x 4 (N.A. = 0.13), 2r = beam diameter = 2 µm, total area sampled in experiment = 763 x 454 µm (768 x 512 pixels), pixel dwell time = 10 µs, v_p= 9.93 cm s^{-1}, τ = 20.88 µm. The time t = 0 min, is the time the potentiostat was switched onto the external cell. The 'laser-off' value = 141.5 out of 256 possible pixel values.

figure 6.45

HIGH RESOLUTION CONFOCAL OPTICAL IMAGES

Experiment- G
Sample- 316F

Size of images shown here = 454μm x 454μm

a)

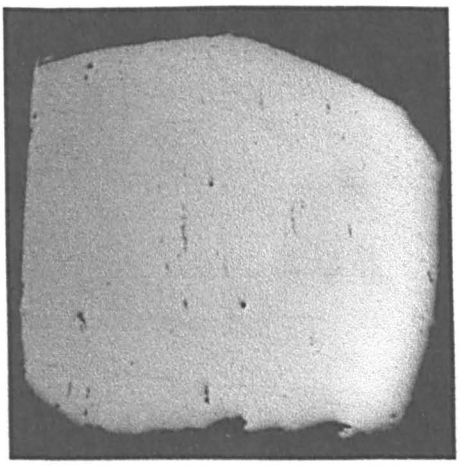

START OF EXPERIMENT

b)

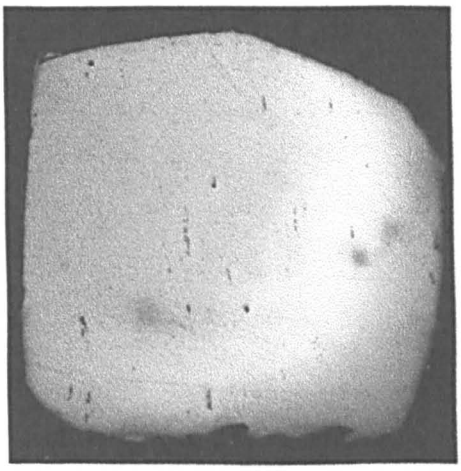

END OF EXPERIMENT

c)

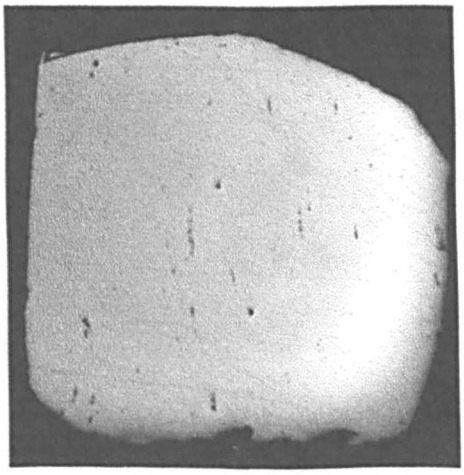

AFTER FURTHER RINSING

Notes: Lens magnification = x 20 (N.A. = 0.40), total area sampled in experiment = 818 x 497 μm (768 x 512 pixels), pixel dwell time = 10 μs, 2r = 0.6 μm, v_p= 10.65 cm s^{-1}, τ = 5.63 μs.

figure 6.46

TOTAL CURRENT VS TIME FOR THE LENGTH OF THE WHOLE EXPERIMENT

Experiment- G
Sample- 316F

Solution = 0.025M NaCl, 0.075M $NaClO_4$, I = 0.3M
E = +173 mV / +252 mV vs SSE

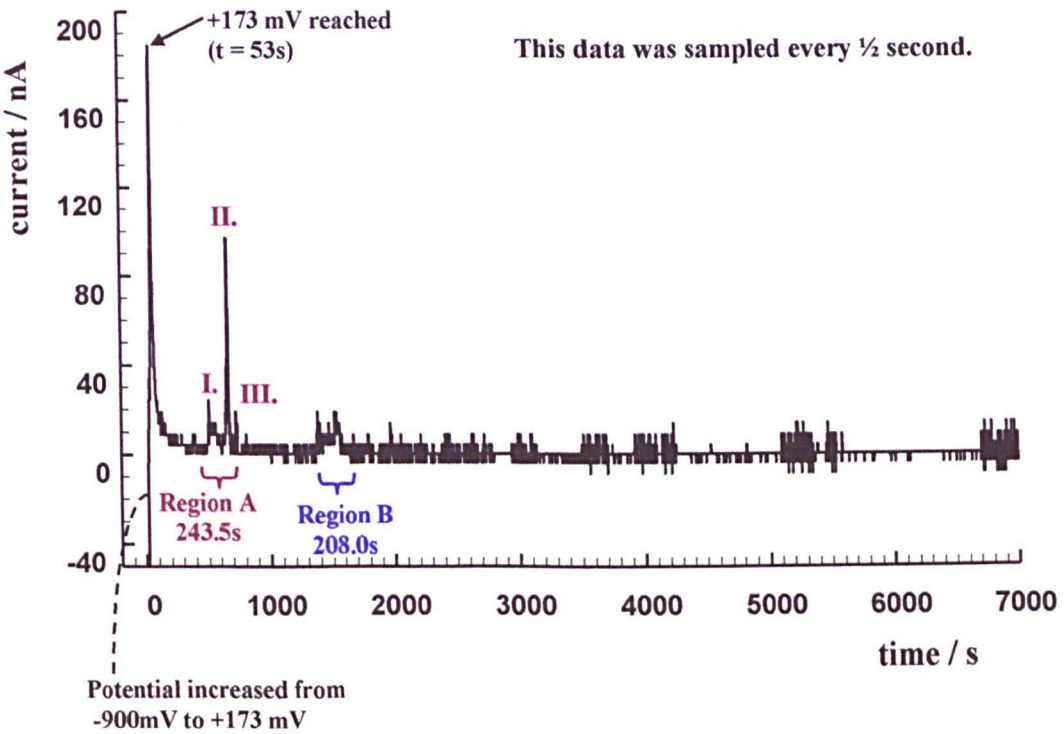

Summary of occurrences at various times for experiment G:

time		Information relating to the time
s	hr:min:sec	
<0	———	Data logger switched on and then the potentiostat was switched on to the internal cell at -900 mV
0	00:00:00	Potentiostat switched to external cell at -900 mV
6 - 53	00:00:06 00:00:53	Potential increased from -900 to +173 mV
117	00:01:57	Started to collect 1st image
253	00:04:13	Time at end of 1st image collection
502.5 - 737.0	00:08:23 00:12:17	Region A on the total current vs time graph
1369.0 - 1582.0	00:22:49 00:26:22	Region B on the total current vs potential curve
2350 - 2367	00:39:27 00:39:27	Potential increased from +173 to + 252 mV

Notes: One data point was recorded every ½ second on the current vs time graph using a 12 bit data logger. Each data point recorded involved 100 readings being collected and signal averaged at the beginning of each ½ second. This process took 2200 μs (2.2×10^{-3} s).

figure 6.47

TOTAL CURRENT VS TIME, REGION A

Experiment- G
Sample- 316F

Solution = 0.025M NaCl, 0.075M $NaClO_4$, I = 0.3M
E = +173 mV vs SSE

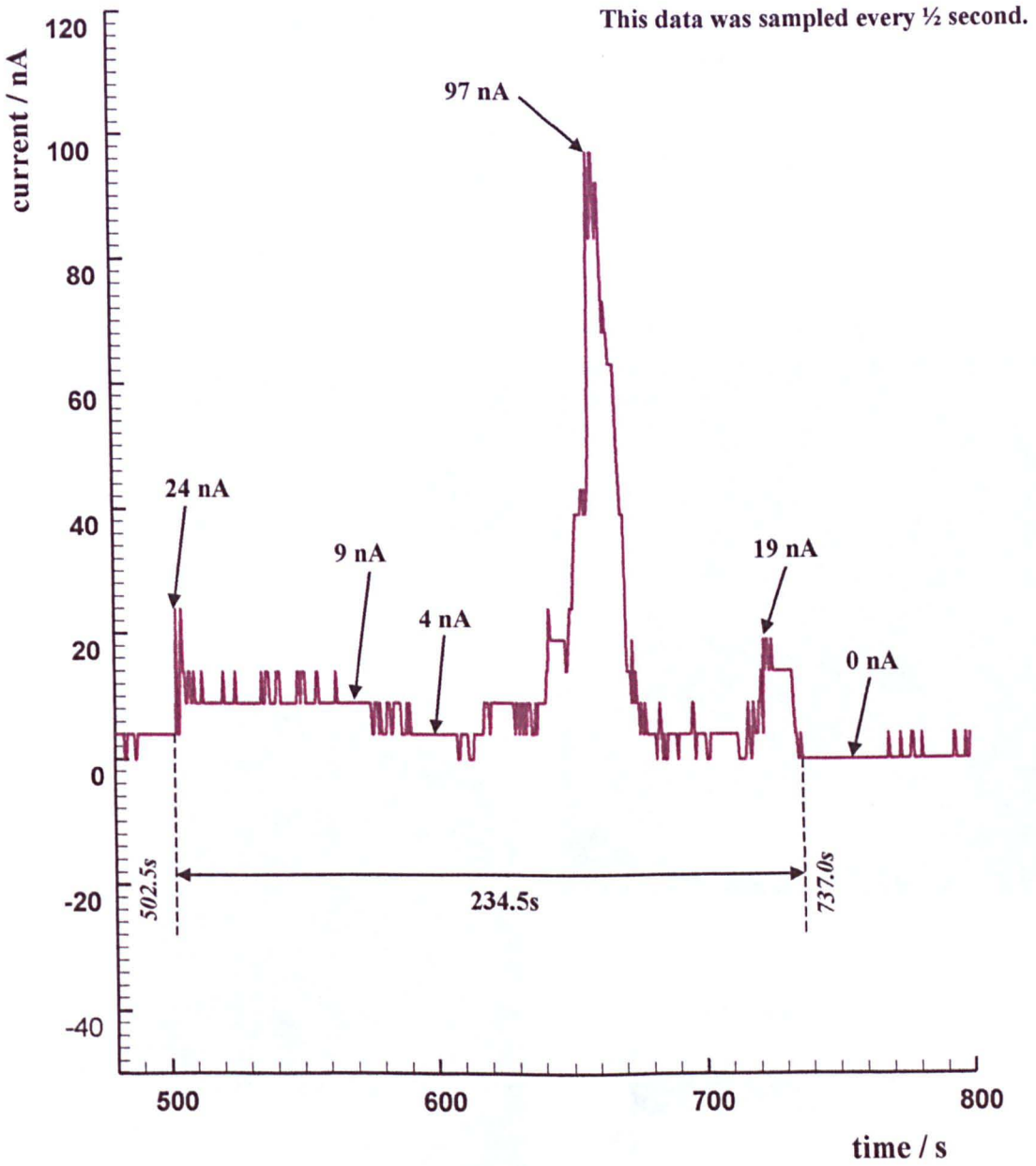

Notes: One data point was recorded every ½ second on the current vs time graph using a 12 bit data logger. Each data point recorded involved 100 readings being collected and signal averaged at the beginning of each ½ second. This process took 2200 μs (2.2×10^{-3} s). Photocurrent images corresponding to the time period shown in this graph can be found in figure 6.49.

figure 6.48

PHOTOCURRENT IMAGES CORRESPONDING TO REGION A ON THE TOTAL CURRENT VS TIME GRAPH

Solution = 0.025M NaCl, 0.075M $NaClO_4$, I = 0.1M
E = +173 mV vs SSE

Experiment- G
Sample- 316F

a) Before Region A

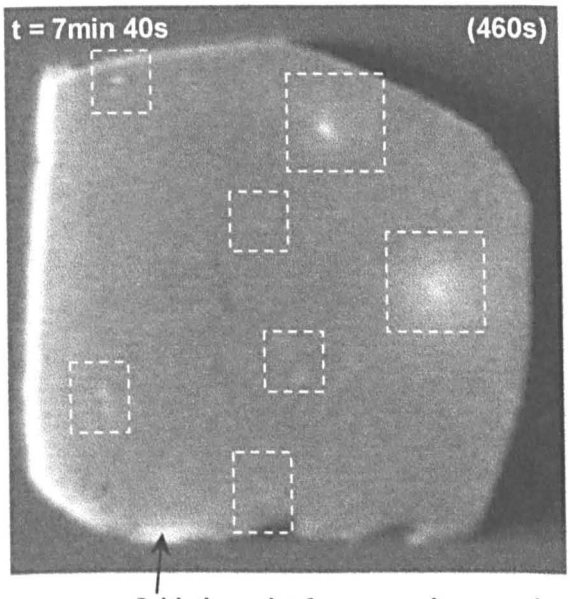

Initiation point for pre-crevice corrosion behaviour along the bottom edge.

During the time period shown here various regions on the image 'popped' changing from white to black i.e. from +VE to -VE photocurrents.

b) During Region A

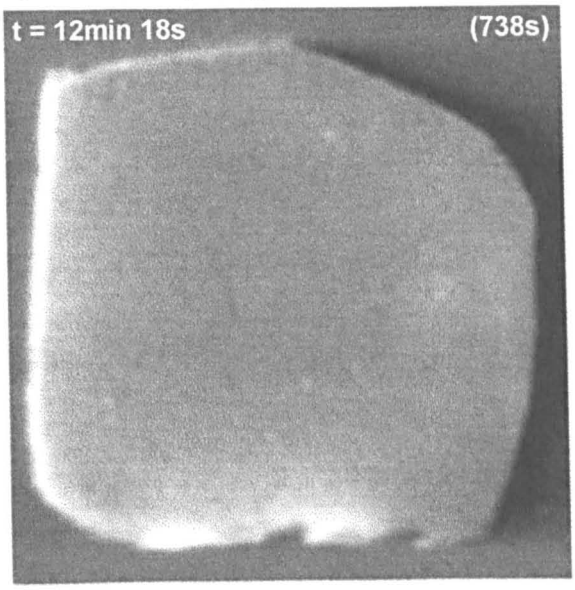

c) After Region A

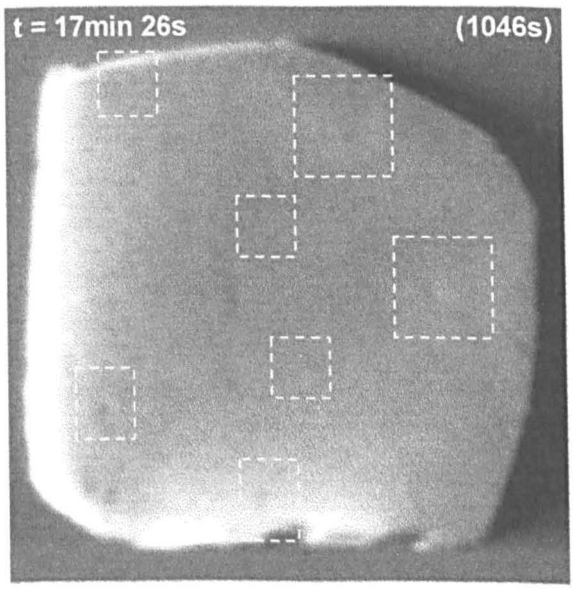

20 nA Grey Scale

min. **max.**

-11 **+9**

Photocurrent / nA

Notes: Lens magnification = x 4 (N.A. = 0.13), 2r = beam diameter = 2 μm, total area sampled in experiment = 763 x 454 μm (768 x 512 pixels), pixel dwell time = 10 μs, v_p= 9.93 cm s^{-1}, τ = 20.88 μm. The time t = 0 min, is the time the potentiostat was switched onto the external cell. The time noted on each image, is the time that was recorded at the end of the image on collection of the last data point (inclusive of any signal averaging).

figure 6.49

TOTAL CURRENT VS TIME, REGION B

Experiment- G
Sample- 316F

Solution = 0.025M NaCl, 0.075M $NaClO_4$, I = 0.3M
E = +173 mV vs SSE

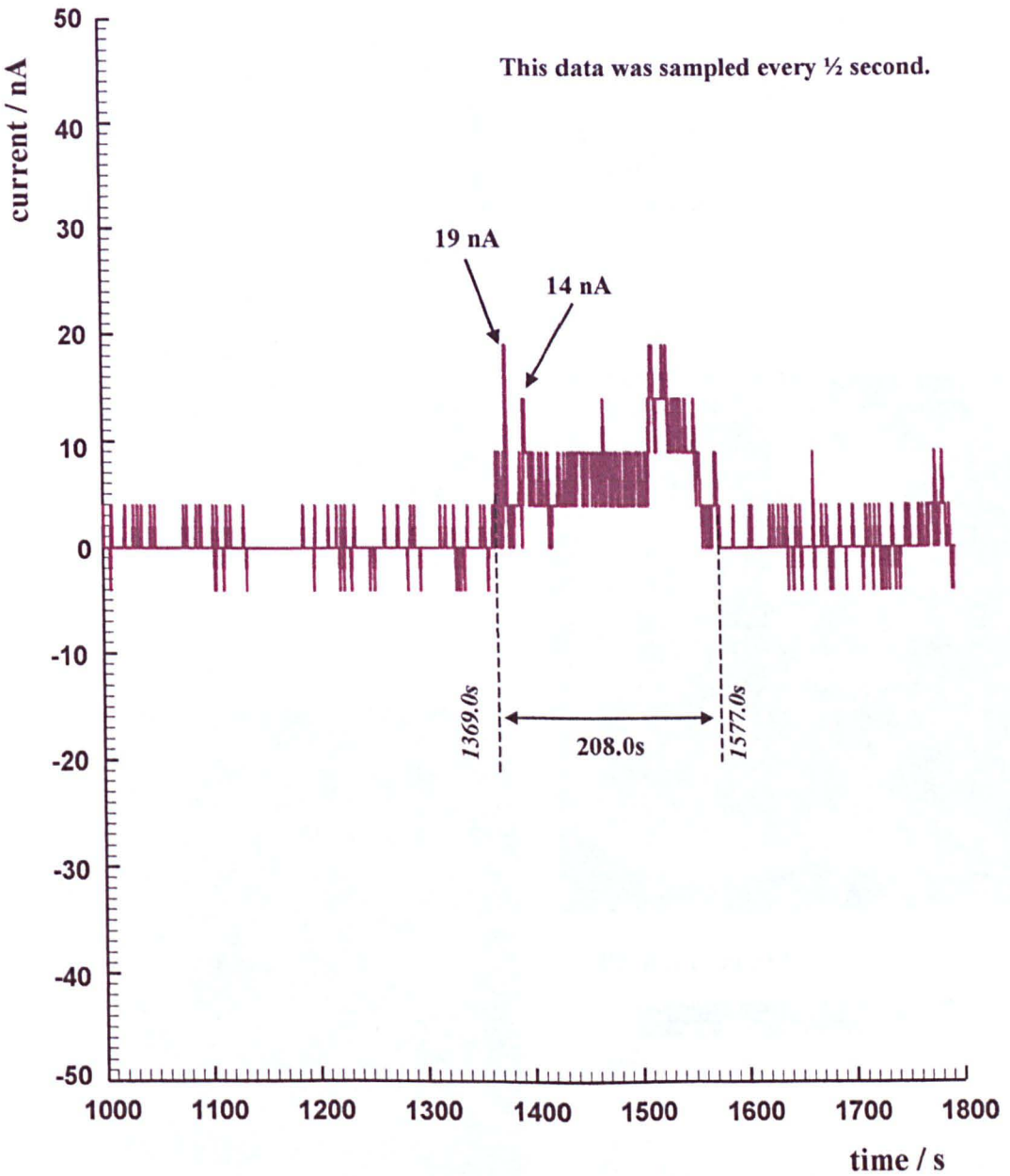

Notes: One data point was recorded every ½ second on the current vs time graph using a 12 bit data logger. Each data point recorded involved 100 readings being collected and signal averaged at the beginning of each ½ second. This process took 2200 μs (2.2×10^{-3} s). Photocurrent images corresponding to the time period shown in this graph can be found in figure 6.51.

figure 6.50

PHOTOCURRENT IMAGES CORRESPONDING TO REGION B ON THE TOTAL CURRENT VS TIME GRAPH

Solution = 0.025M NaCl, 0.075M $NaClO_4$, I = 0.1M
E = +173mV vs SSE

Experiment- G
Sample- 316F

a) Before Region B

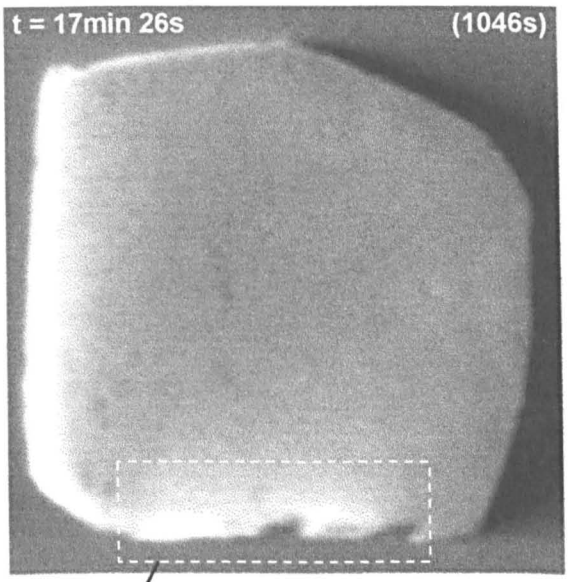

Pre-crevice corrosion behaviour

During the time period shown here image brightness over the whole electrode generally decreased compared to the resin area, this was especially evident in the region exhibiting pre-crevice corrosion behaviour.

b) During Region B

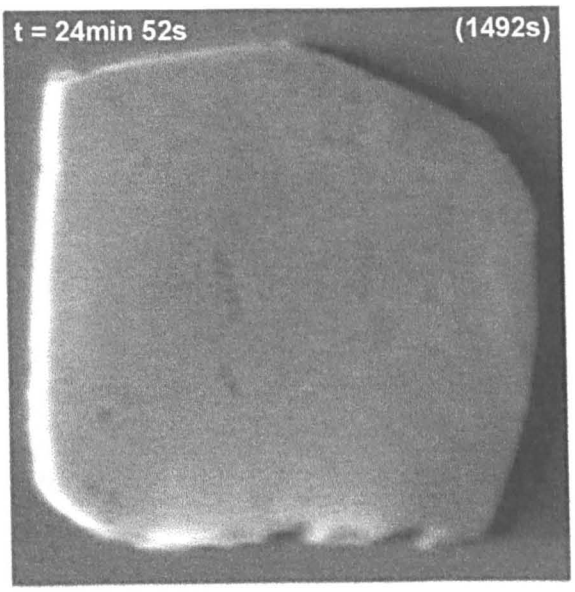

c) After Region B

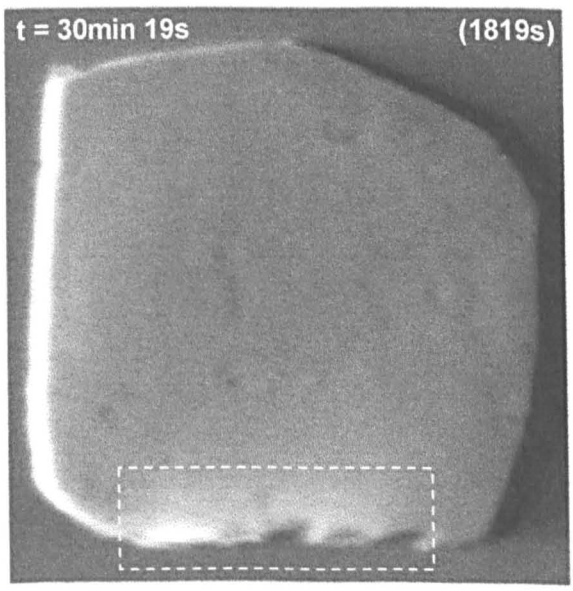

Photocurrent Scale

min. max.

I_{photo} :
for images a) + b) = -11nA to +9nA
for image c) = -28nA to +22nA

Notes: Lens magnification = x 4 (N.A. = 0.13), 2r = beam diameter = 2 μm, total area sampled in experiment = 763 x 454 μm (768 x 512 pixels), pixel dwell time = 10 μs, v_p= 9.93 cm s^{-1}, τ = 20.88 μm. The time t = 0 min, is the time the potentiostat was switched onto the external cell. The time noted on each image, is the time that was recorded at the end of the image on collection of the last data point (inclusive of any signal averaging).

figure 6.51

CONFOCAL OPTICAL IMAGE HEIGHT PROFILING AT THE END OF THE EXPERIMENT

Experiment- G
Sample- 316F

Size of images shown here = 454μm x 454μm

a) height = 0 μm

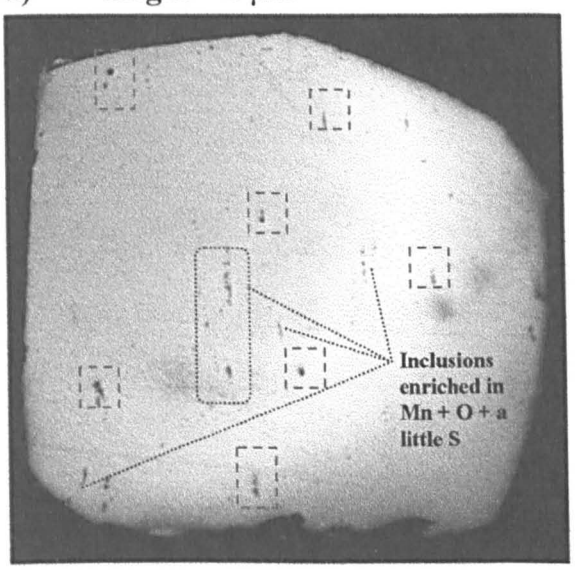

b) height = -5 μm

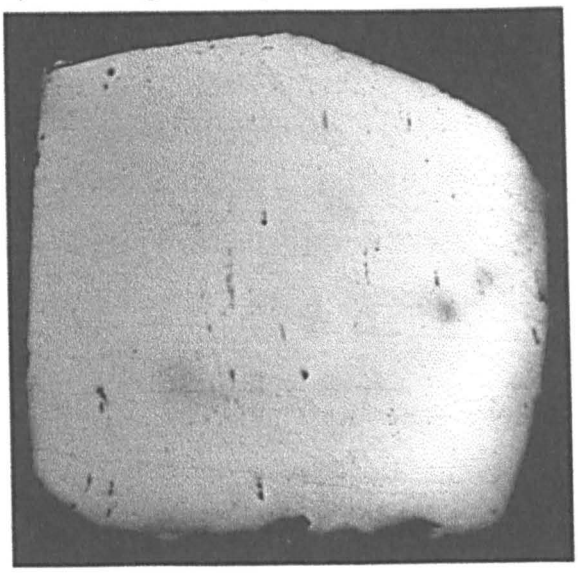

c) height = -30 μm

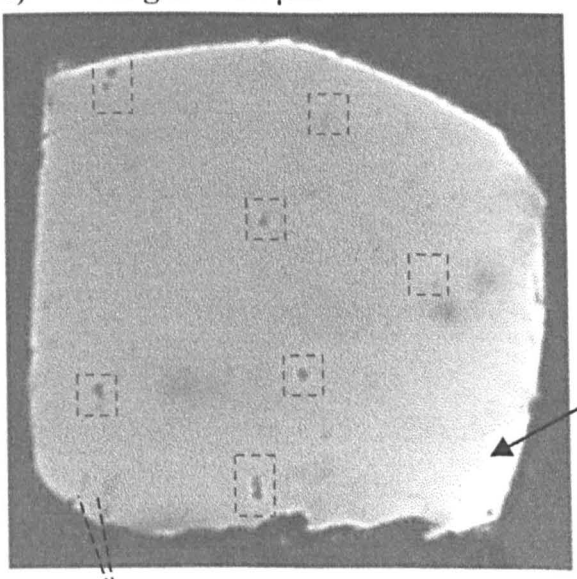

The dark (low reflectivity) areas correspond to changes seen on the photocurrent images seen when the peak (region A) in the total current occurred.

As these inclusions are at the edge where the electrode is tapered down, they are still visible here and therefore are not pits as in the case of the other low reflectivity areas.

Notes: Lens magnification = x 20 (N.A. = 0.40), total area sampled in experiment = 818 x 497 μm (768 x 512 pixels), pixel dwell time = 10 μs, 2r = 0.6 μm, v_p= 10.65 cm s^{-1}, τ = 5.63 μs.

figure 6.52

Microprobe concentration imaging for sulphur showed that the areas that had pitted (Experiment G) had lost there sulphur content. However there were some inclusions which had not pitted and therefore were still were sulphur enriched. Inclusions or parts of inclusions which were still sulphur enriched were found to be very enriched in oxygen and manganese as well. The amount of Mn present being considerably more greater than the amount of S present in these inclusions.

6.7 THE OCCURRENCE OF MORE EXTREME / CREVICE CORROSION

Some of the many experiments conducted to show pitting corrosion were found to exhibit crevice corrosion. Crevice / edge corrosion seemed to be triggered by Mn + S inclusions right on the edge of the electrode or within one or two micrometers of it. Experiment H (figures 6.53 - 6.55) showed crevice corrosion occurring along one side of a electrode which had been exposed to Cl^- from HCl. The photocurrent image showed the development of a wide semi-circular area of positive photocurrents (figure 6.53), followed by a widespread distribution of stain, as seen on the in-situ confocal optical images, in the same region as the occurrence of the positive photocurrents. This stain was very easily removed as seen in figure 6.54. The microprobe maps showed a collection of very small sulphur enriched areas along the corroded edge.

Experiment I (figures 6.56 - 6.57) showed the extensive crevice corrosion which occurred on the use of a saturated calomel electrode. This was the very first experiment conducted, prior to the use of the Hg/Hg_2SO_4, sat K_2SO_4 electrode. As it had for the pitting corrosion, the microprobe analysis again showed that the most corroded area had an increased amount of sulphur but that the Mn concentration was just slightly decreased from the bg level. In addition an increased amount of Cl^-, was present in the most corroded area.

PHOTOCURRENT AND CONFOCAL OPTICAL IMAGES SHOWING THE OCCURRENCE OF CREVICE CORROSION

Solution = 0.3M $NaClO_4$, I = 0.3M, E = -100 mV vs SSE

Experiment- H
Sample- 316F

Crevice corrosion occurred here due to contamination from Cl^- exposure from HCl prior to the experiment.

Photocurrent Image

Confocal Optical Image

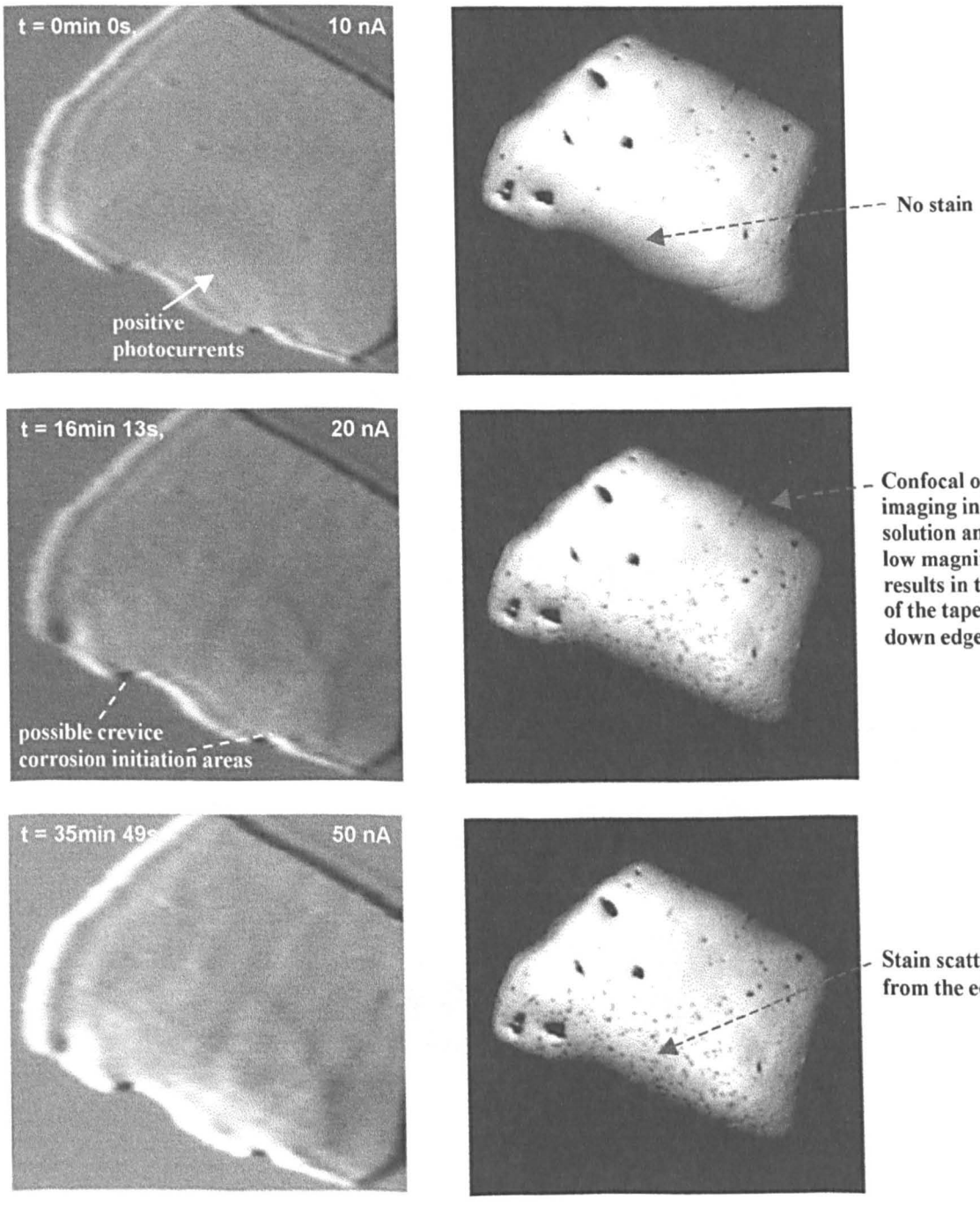

Size of images shown = 421µm x 390µm

Notes: Lens magnification = x 4 (N.A. = 0.13), 2r = beam diameter = 2 µm, total area sampled in experiment = 633 x 390 µm (768 x 512 pixels), pixel dwell time = 10 µs, v_p= 8.24 cm s^{-1}, τ = 24.27 µm. The time t = 0 min, is the time the time recorded at the end of the 1st image.

figure 6.53

HIGH RESOLUTION CONFOCAL OPTICAL IMAGES

Experiment- H
Sample- 316F

Size of images shown here = 454μm x 454μm

a) **Start of the Experiment**

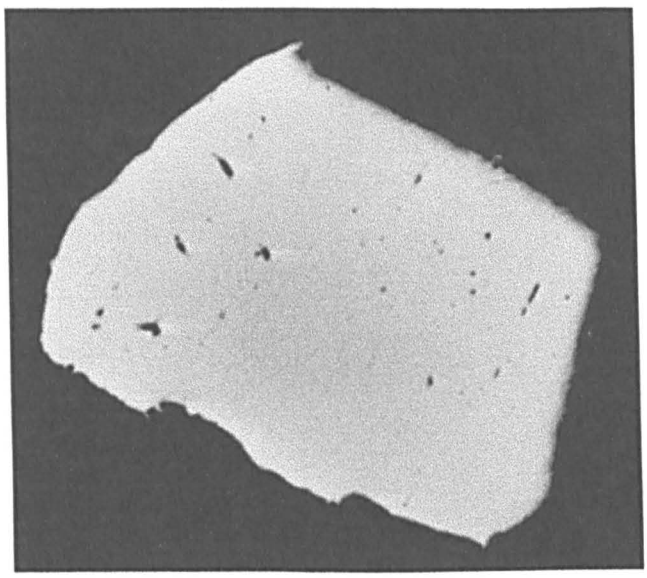

b) **End of the Experiment (after rinsing)**

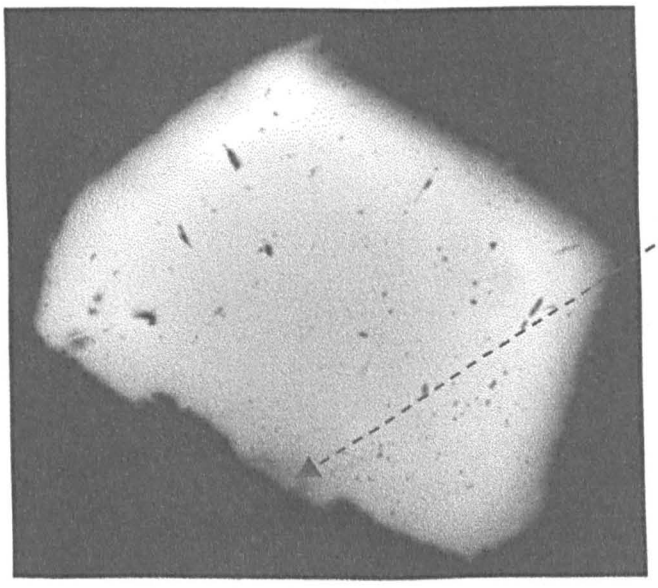

Notes: Lens magnification = x 20 (N.A. = 0.40), total area sampled in experiment = 818 x 497 μm (768 x 512 pixels), pixel dwell time = 10 μs, 2r = 0.6 μm, v_p= 10.65 cm s^{-1}, τ = 5.63 μs.

figure 6.54

MICROPROBE ELEMENT CONCENTRATION MAPS OF THE REGION DEPICTING CREVICE CORROSION

Experiment- H
Sample- 316F

Counts:

min **max**

S

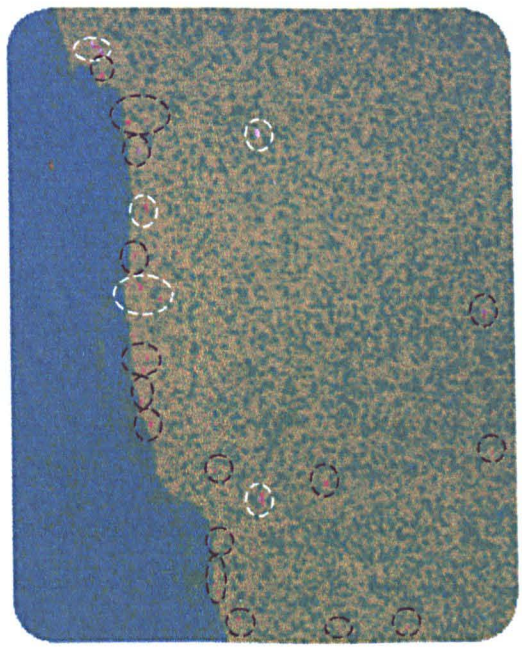

Crystal-PET, 171.640 mm (x-ray line =Kα), 25 kV, current = 1.3 x 10^{-7} A, data points recorded every pixel, 1 pixel - 1 µm, pixel dwell time = 75 ms.

Mn

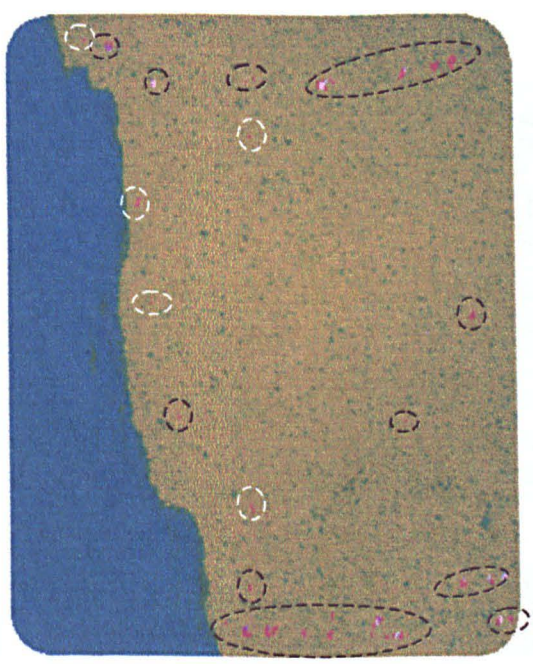

Crystal -LIF, 145.890 mm (x-ray line=Kα), 25kV, current = 1.3 x 10^{-7} A, data points recorded every pixel, 1 pixel - 1 µm, pixel dwell time = 75 ms.

In the above concentration maps regions containing higher than bg levels of S or Mn have been circled. White circles show regions which are high in both Mn and S.

figure 6.55

CONFOCAL OPTICAL IMAGING SHOWING THE OCCURRENCE OF SUDDEN CREVICE CORROSION IN THE PRESENCE OF A SATURATED CALOMEL ELECTRODE

Solution = 0.1M $NaClO_4$, I = 0.1M, E = -400 mV vs SCE

Experiment- I
Sample- 316F

Size of images shown here = 458μm x 283μm

a) Start of the Experiment

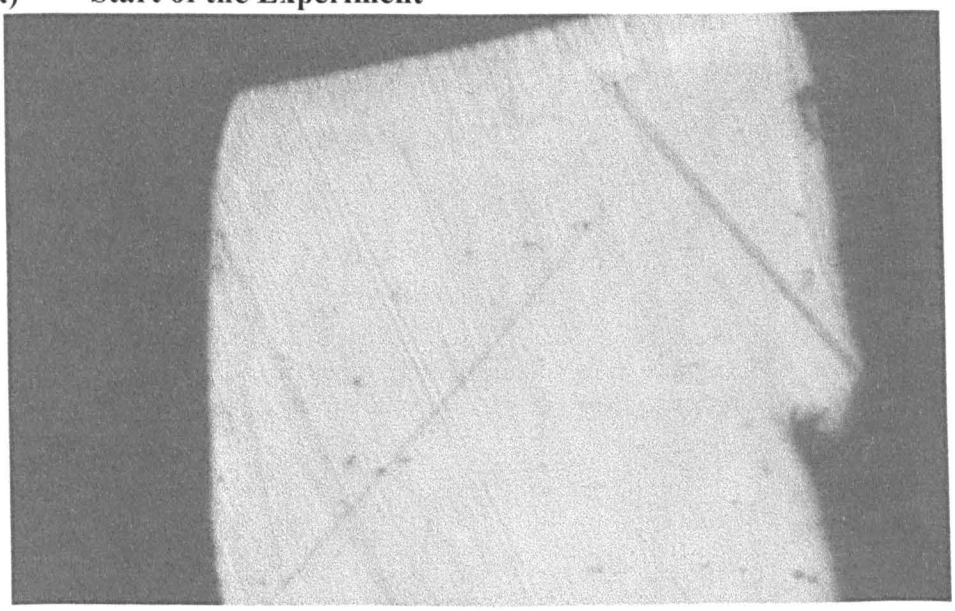

b) End of the Experiment (after rinsing)

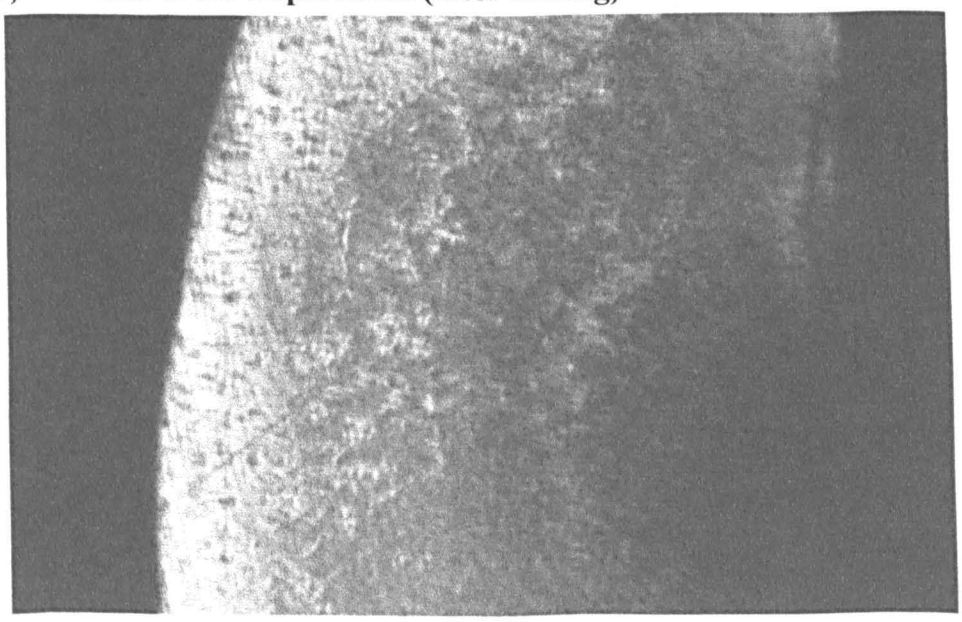

150 μm

Notes: Lens magnification = x 4 (N.A. = 0.13), total area sampled in experiment = 458 x 283 μm (768 x 512 pixels), pixel dwell time = 10 μs, 2r = 2 μm, v_p= 10.65 cm s^{-1}, τ = 33.50 μs. After 35 minutes of polarisation, at -400 mV vs SCE, the electrode shown above suddenly corroded.

figure 6.56

AN SEM IMAGE SHOWING CREVICE CORROSION

Experiment- I
Sample- 316F

Acceleration Voltage = 25 kV
Current = 5 x 10^{-8} A

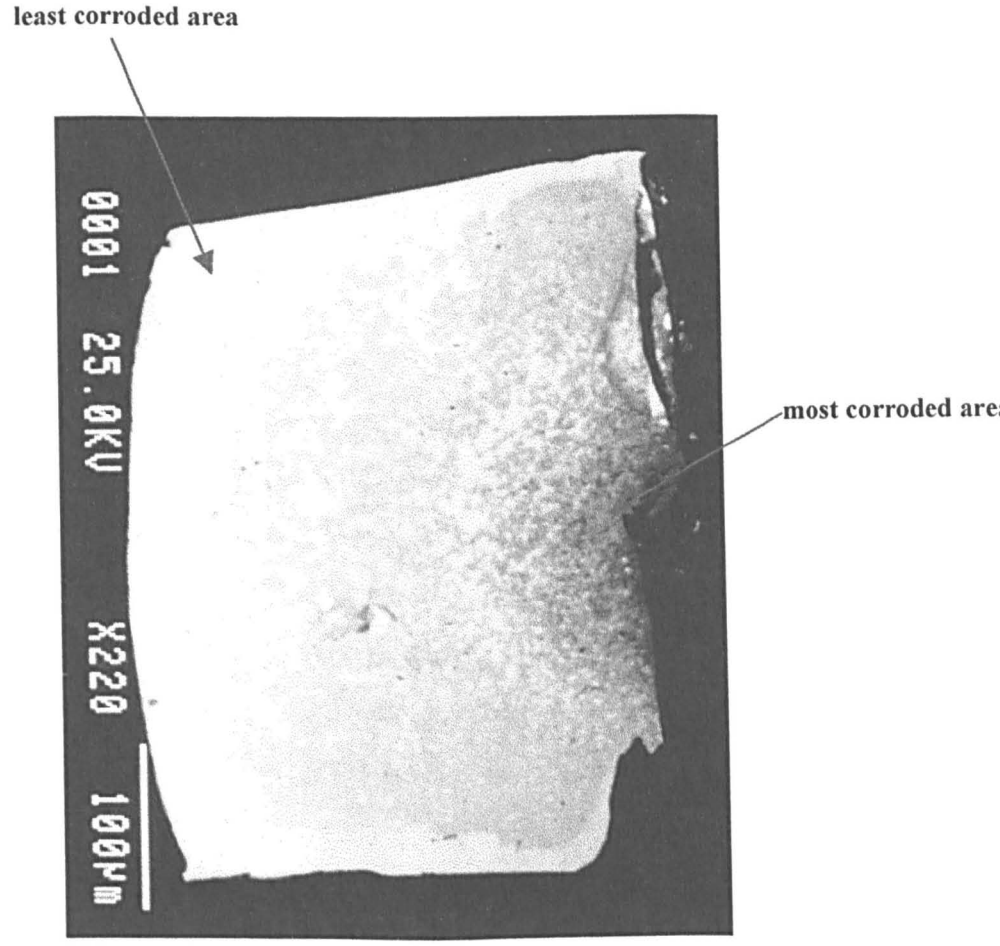

A summary of the microprobe spot analysis for the above sample:

Element	% Weight		
	Expected in a Clean Sample	In the Least Corroded Area	In the Most Corroded Area
Mn	0.70 ± 0.05	0.680	0.551
S	0.051 ± 0.009	0.053	0.221
Cl	———	0.009	0.041

figure 6.57

Experiment J (figures 6.58 - 6.65) showed the occurrence of edge / crevice corrosion spreading out in a semi-circular pattern starting at a dense stain ring starting some distance from what appeared to be a very small inclusion region on the very edge of the electrode. This reaction occurred in a Cl^- containing solution but without the potentiostat being switched on or a potential applied, unlike all of the previous experiments. The optical images (figures 6.58, 6.59) show several differently coloured product regions spreading out from the point of corrosion initiation. This is particularly evident on the colour optical micrograph (figure 6.59). The inner-most region consisted of a dark / dense well established stain region (ring A). From the microprobe concentration maps (figure 6.61 - 6.64) it was seen that ring A was enriched in S, Cl and O. Elemental maps of the principal elements in stainless steel (Fe, Cr, Ni) were simultaneously recorded with oxygen maps (figure 6.63). Combination maps produced of oxygen with each principle element showed that ring A contained significant amounts of Cr-O but not Fe-O or Ni-O (figure 6.64). The second region (ring B), was orange in colour on the colour optical micrograph. In ring B, the oxygen combination maps showed the presence of Fe-O in significant amounts. The amount of Fe-O seemed to alternate in rings, next highest being in ring D. Further out onto the electrode there was a wide scattering of very thin / new stain material in a broad semicircular pattern, as was seen in experiment H previously. Microprobe spot analysis (figure 6.65) showed that in going from the least corroded to the most corroded area there was an increase in S and Cl and a decrease in Mn.

The materials found in combination with oxygen in significant amounts could either be oxides or hydroxides. The circular patterns seen are due to the radial diffusion of various products out of the acidic pit solution, followed by segregated deposition, with the least soluble products precipitating out of the solution first.

HIGH RESOLUTION CONFOCAL OPTICAL IMAGES SHOWING CREVICE CORROSION IN A NaCl CONTAINING SOLUTION

Experiment- J
Solution = 0.025M NaCl, 0.075M $NaClO_4$, I = 0.1M **Sample- 316F**

This electrode rapidly corroded in the Cl^- containing solution, without switching the potentiostat on or, applying a potential.

150 µm

a) Start of Experiment

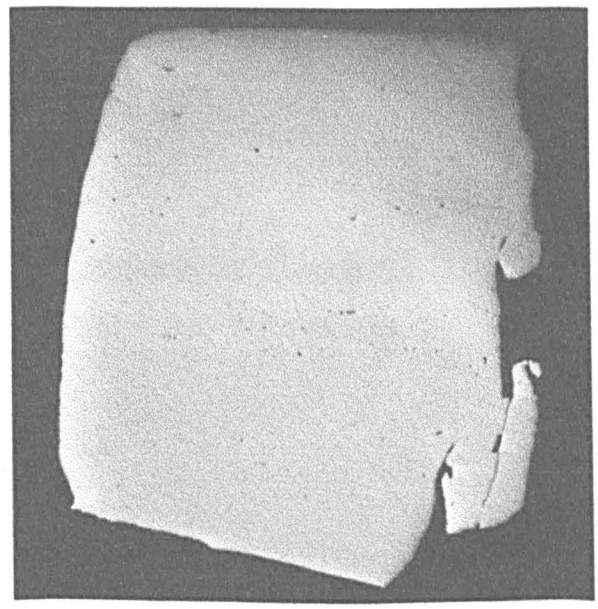

b) End of Experiment

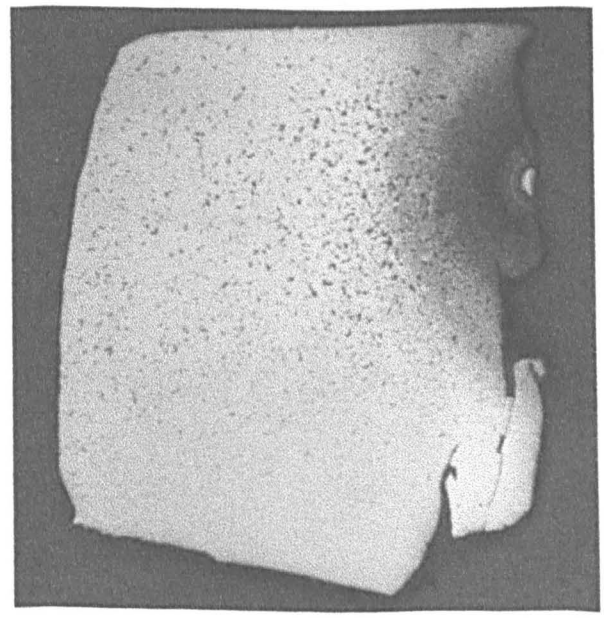

Notes: Lens magnification = x 20 (N.A. = 0.40), total area sampled in experiment = 818 x 497 µm (768 x 512 pixels), pixel dwell time = 10 µs, 2r = 0.6 µm, v_p= 10.65 cm s^{-1}, τ = 5.63 µs.

figure 6.58

COLOUR OPTICAL MICROGRAPHS

Experiment- J
Sample- 316F

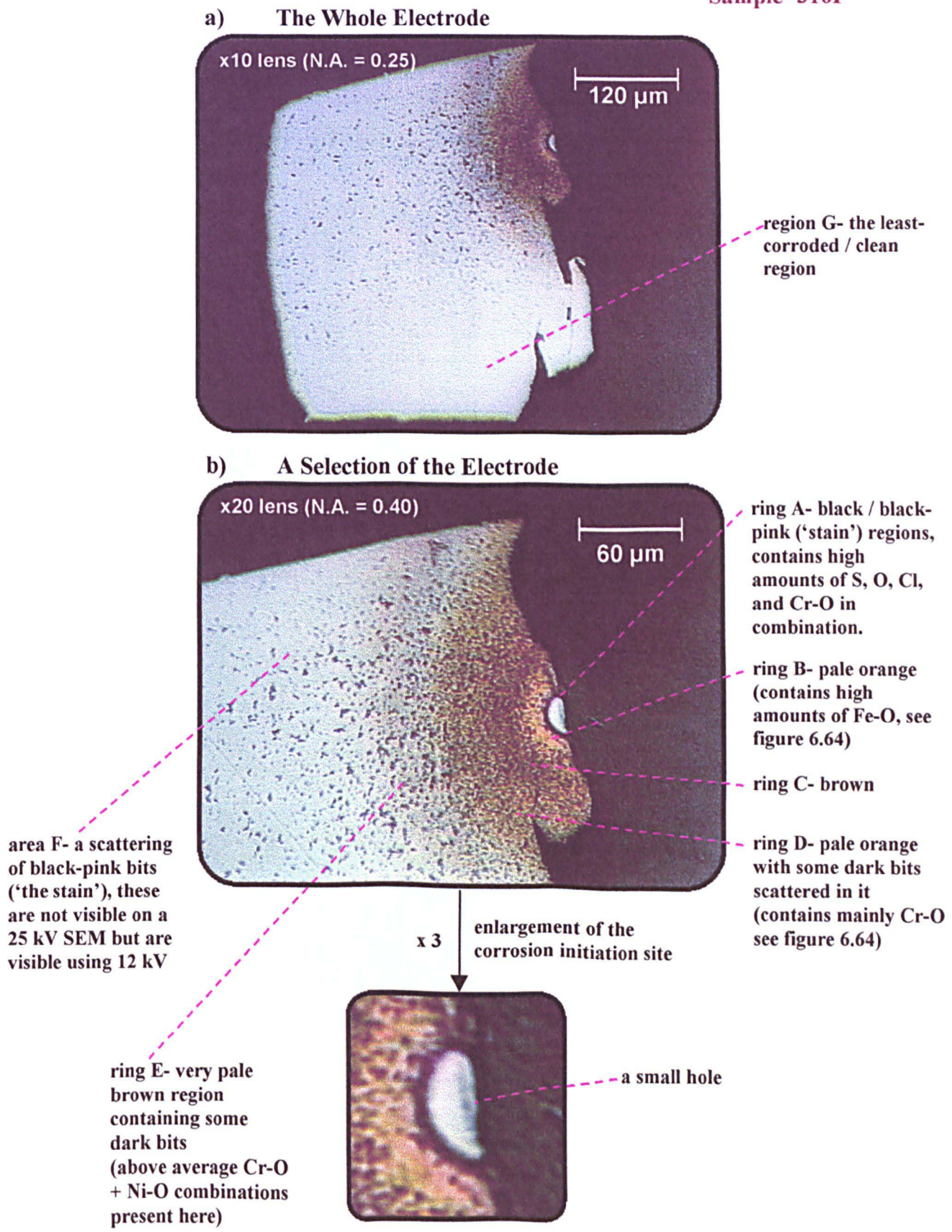

figure 6.59

SEM IMAGES OF THE CORRODED ELECTRODE

Experiment- J
Sample- 316F

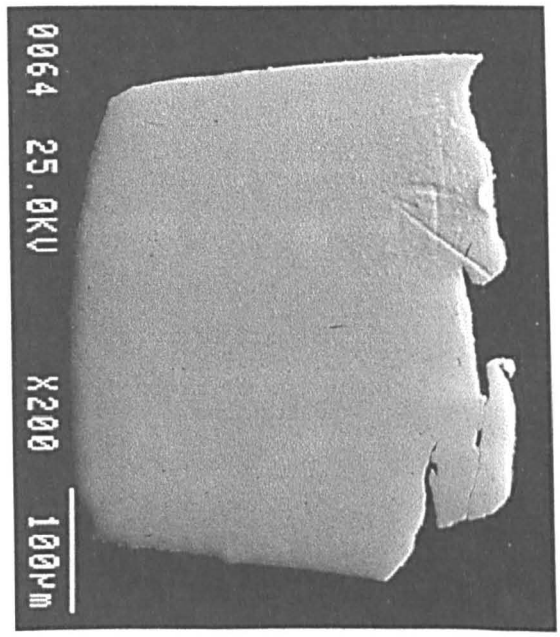

a) Whole Electrode

Acceleration Voltage = 25 kV
Current = 5 x 10^{-8} A

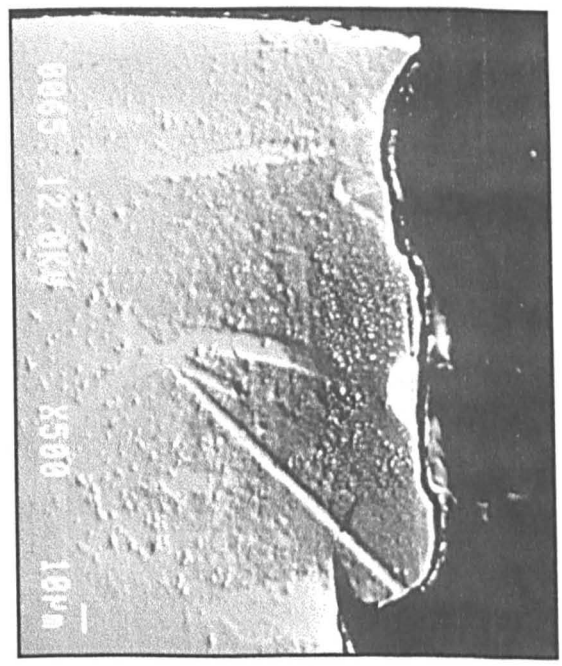

b) A Selected Region of the Electrode at a low kV

Acceleration Voltage = 12 kV
Current = 5 x 10^{-8} A

Notes : These SEM images were recorded using the Jeol JXA-8600 electron probe microanalyser.

figure 6.60

MICROPROBE ELEMENT CONCENTRATION MAPS OF SOME OF THE ELEMENTS PRESENT IN THE INCLUSION AREAS

Experiment- J
Sample- 316F

Counts:

min max

60 µm

S Crystal - PET, 171.640 mm (x-ray line = Kα)

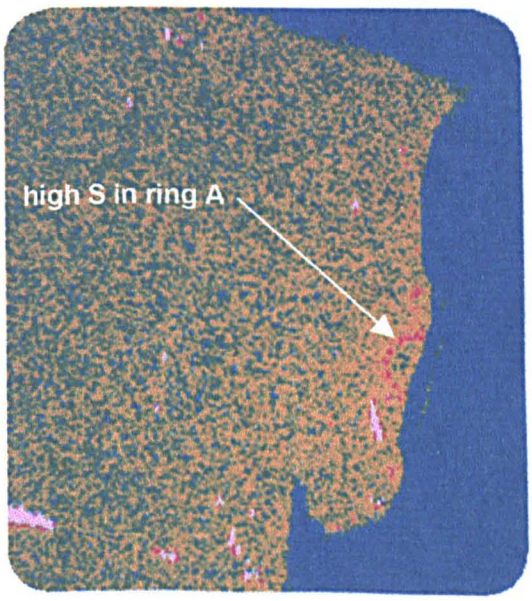

Mn Crystal - LIF, 145.890 mm (x-ray line = Kα)

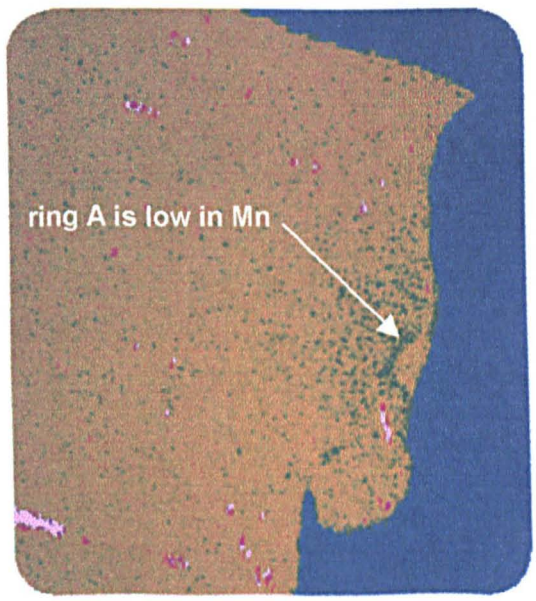

Cl Crystal - PET, 151.005 mm (x-ray line = Kα)

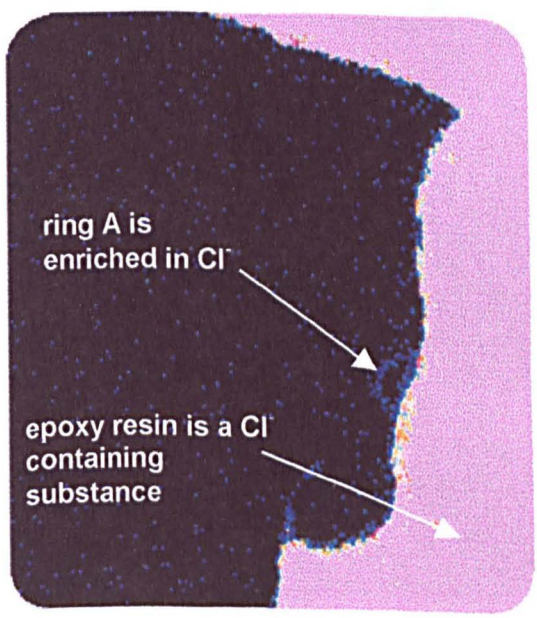

Ti Crystal - PET, 87.685 mm (x-ray line = Kα)

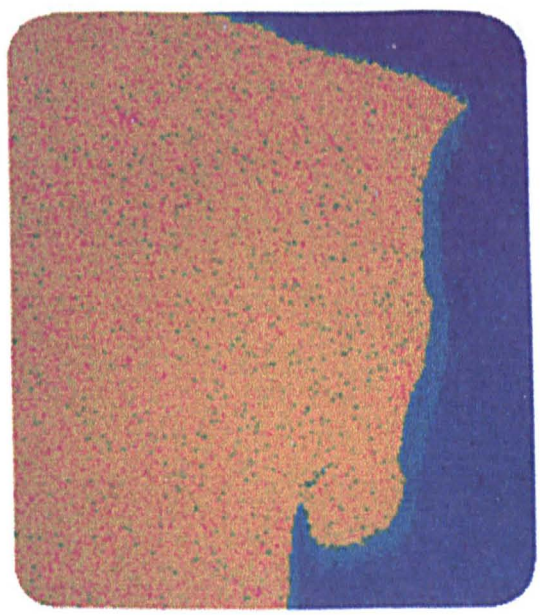

Notes: These images were recorded every pixel where 1 pixel = 1µm , pixel dwell time = 150 ms, acceleration voltage = 25 kV, current = 1.3 x 10^{-7} A. The crystals were as follows: LIF = lithium fluoride, PET = pentaerythritol.

figure 6.61

MICROPROBE ELEMENT CONCENTRATION MAPS FOR THE PRINCIPLE ELEMENTS IN 316 STAINLESS STEEL

Experiment- J
Sample- 316F

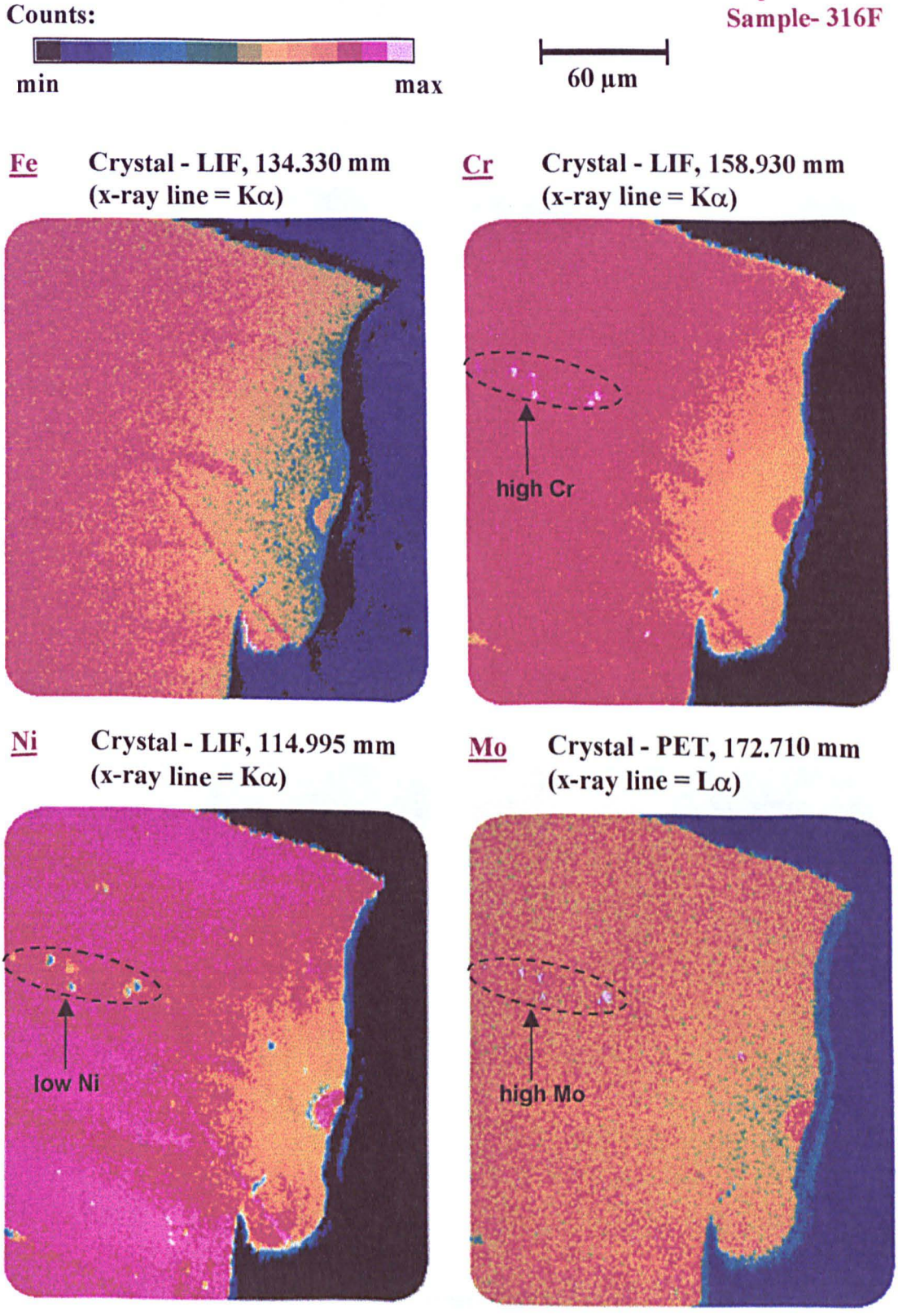

Notes: These images were recorded every pixel where 1 pixel = 1µm , pixel dwell time = 150 ms, acceleration voltage = 25 kV, current = 1.3 x 10^{-7} A. The crystals were as follows: LIF = lithium fluoride, PET = pentaerythritol.

figure 6.62

LOW kV MICROPROBE CONCENTRATION MAPS

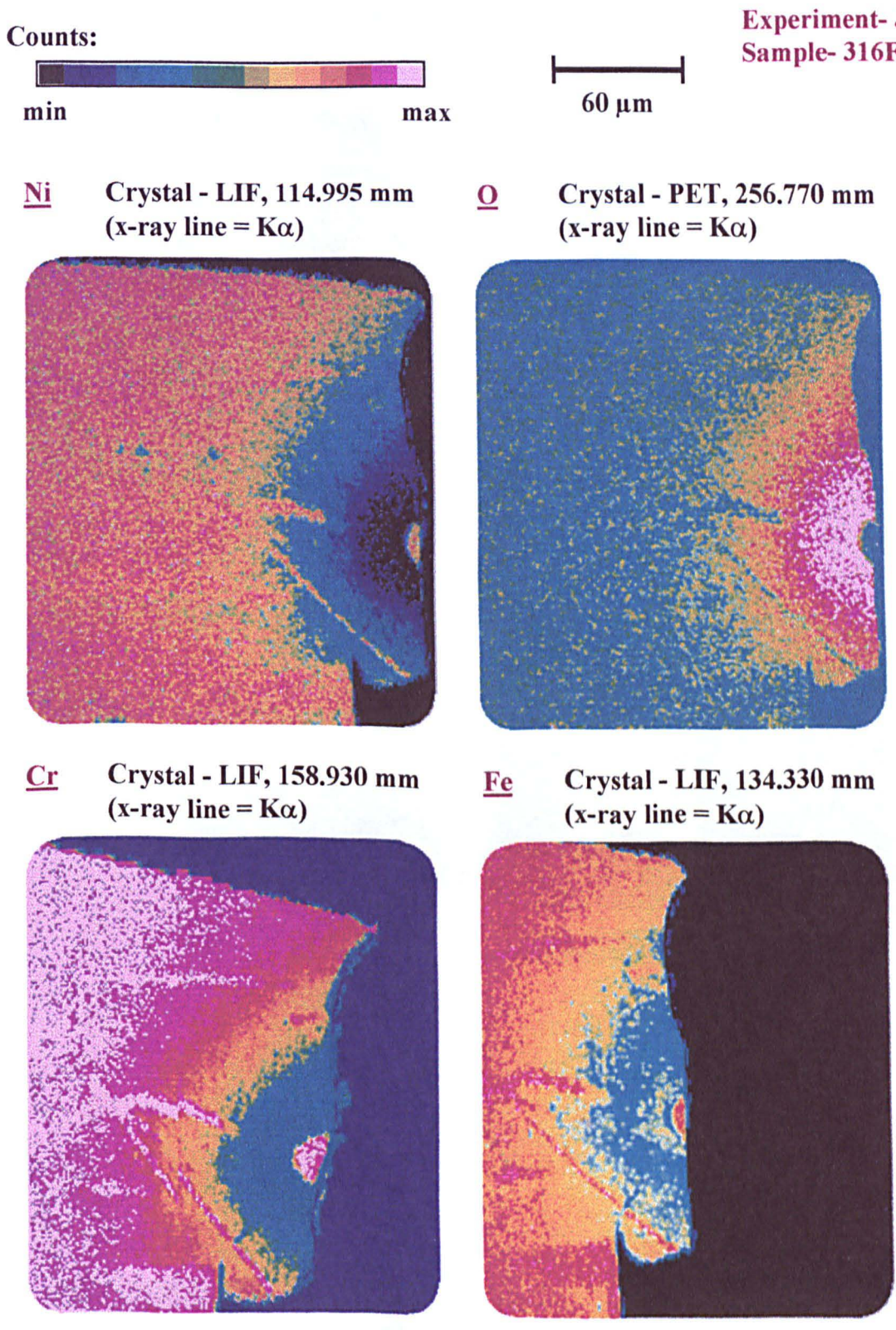

Notes: These images were recorded every pixel where 1 pixel = 1 µm , pixel dwell time = 150 ms, acceleration voltage = 12 kV (only the very surface is analysed: a fraction of a micron), current = 1.3×10^{-7} A. The crystals were as follows: LIF = lithium fluoride, PET = pentaerythritol, TAP = thallium acid phthalate. In this work each principle element present (Fe, Cr, Ni) was recorded as a map simultaneously with oxygen. Combination maps of each element with oxygen is given in figure 6.64.

figure 6.63

LOW kV COMBINATION MAPS OF OXYGEN WITH EACH PRINCIPLE ELEMENT PRESENT

Experiment- J
Sample- 316F

a) Nickel-Oxygen

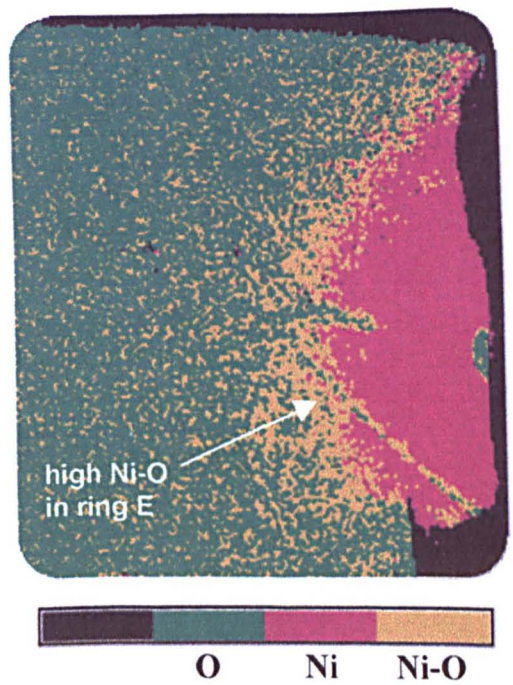

b) Iron-Oxygen

c) Chromium-Oxygen

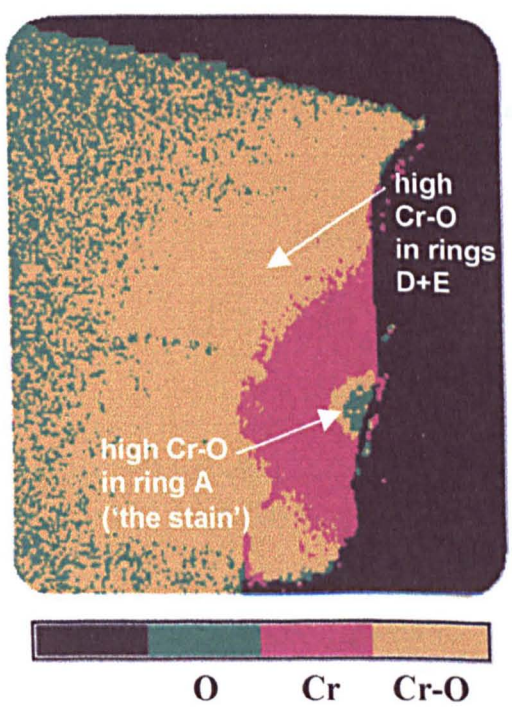

Notes: These images were recorded every pixel where 1 pixel = 1 µm , pixel dwell time = 150 ms, acceleration voltage = 12 kV, current = 1.3 x 10^{-7} A. See figure 6.63 for further information. These combination maps show the areas of above average occurrence of a principle element in the same position as oxygen

figure 6.64

A SUMMARY OF THE MICROPROBE SPOT ANALYSIS

Acceleration Voltage = 25.0 kV
Current = 5 x 10^{-8} A
Dwell time per element = 20 s

Experiment- J
Sample- 316F

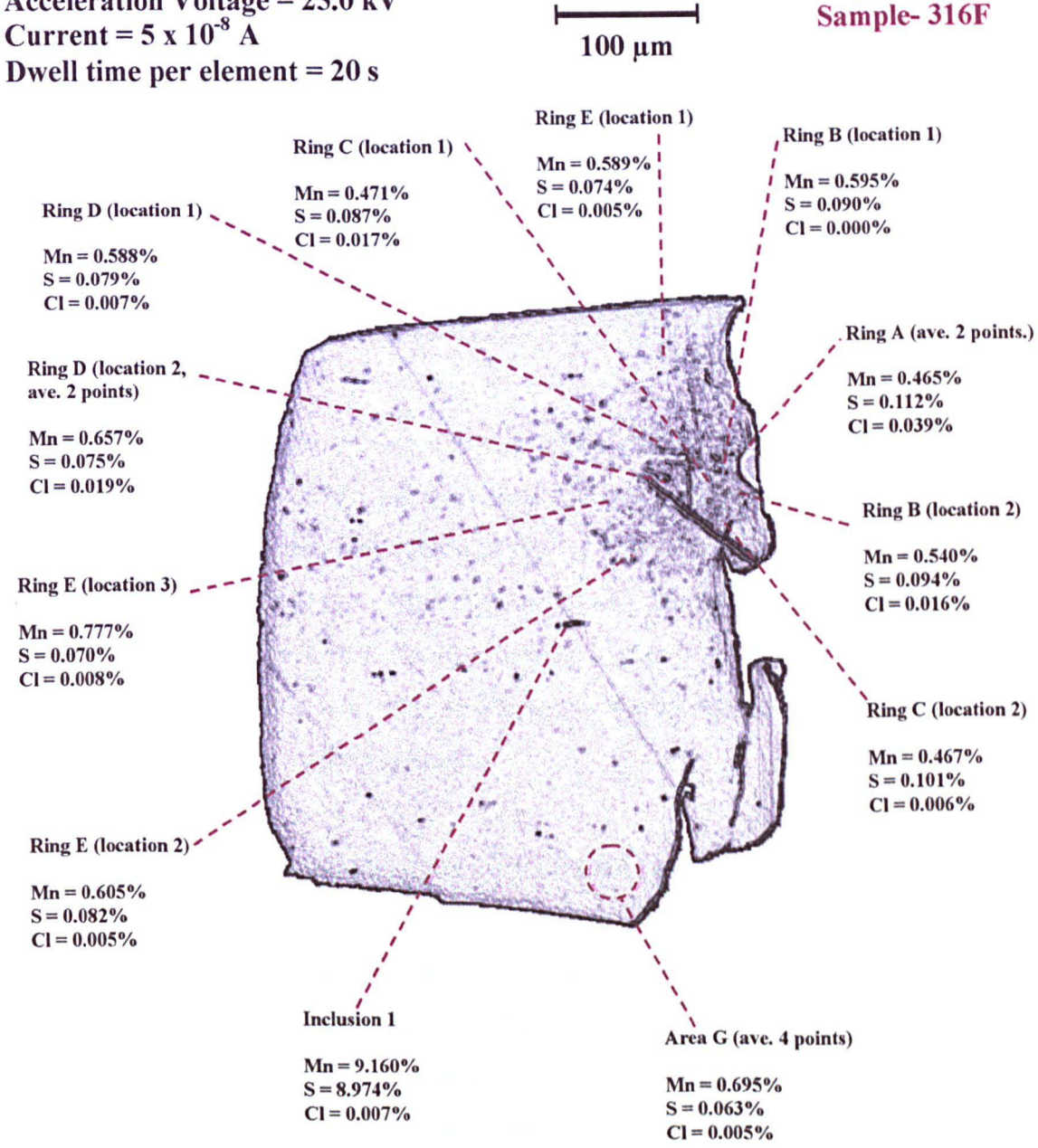

A summary of how the areas on the above electrode change from the most corroded to the least corroded area:

Element	% Weight at a given location (No. of points averaged)						
	Ring A (2 points)	Ring B (2 points)	Ring C (2 points)	Ring D (3 points)	Ring E (3 points)	Area G (4 points)	Expected value on non-corroded sample
Mn	0.465	0.548	0.469	0.634	0.657	0.695	0.702 ± 0.053
S	0.112	0.092	0.094	0.076	0.075	0.063	0.051 ± 0.009
Cl	0.039	0.008	0.012	0.014	0.006	0.005	———
O	high on concentration maps ——————→very low						———

figure 6.65

6.8 A SUMMARY OF THE EFFECTS SEEN ON THE PHOTOCURRENT AND OPTICAL IMAGES

1. Initially in a low NaCl concentration or just $NaClO_4$ alone, if the inclusion area was large enough a slightly dark area would be seen on the grey scale photocurrent image.

2. The dark area, if large enough to be seen, showed a subtle expansion becoming slightly more negative in a very low concentration of NaCl.

3. After subtle changes in the inclusion area, a white front develops on the grey scale photocurrent image, showing the occurrence of positive photocurrents, around the inclusion area. If the inclusion was large enough, i.e. at least a couple of micrometers in width, the positive photocurrents formed a ring shape around the inclusion area leaving a centre of negative photocurrents directly over the inclusion itself. However, if the dimensions of the inclusion were very small, then a white area still developed but without the more negative central region.

4. After the white (positive photocurrent) front started to develop and became bigger still, a 'stain' became visible on the optical image in the solution. The stain was found to form quite often like a 'halo' in that the stain appeared to be detached from the inclusion itself but a space was seen between the inclusion and the stain. Where the reaction was proceeding faster due to a higher potential or higher NaCl concentration the stain appeared to be closer to the inclusion. This was also true for very small inclusions, but it may also be that the gap between the stain and inclusion was relatively small compared to the inclusion size.

5. If the reaction was stopped at a stage just after the stain had been formed, it was found that the stain could be washed off leaving no traces of any pits / holes or any sort of activity having occurred. This showed that the stain material was very loosely attached. In addition it appeared to look totally flat with the highest resolution (high numerical aperture) lens on the confocal scanning laser microscope, when height profiling. This shows that the stain was very thin. The fact that no holes / dents could be seen when the under the stain area when the stain was rinsed away suggests that the

stain material originates from the surface of the inclusion where it diffuses out of as opposed to the stain material appearing by a tunnelling a hole out from a pit under a sulphur crust / cap in the region of the inclusion.

6. When the reaction was continued and the stain left alone, the stain built up and small dark spheres formed in it. Small holes were found to develop under this stain region (this was seen by washing off the stain). The stain also seemed to trigger further activity around itself.

7. Leaving the reaction to occur further still resulted in the white region on a grey scale photocurrent image 'popping' and turning black, showing a reversal of the sign of the photocurrent generated from positive to negative. This effect was found to coincide with a peak in the total current versus time. The peak in the total current did not occur until all the positive photocurrents over the inclusion region had diminished. Height profiling showed that this coincided with the occurrence of a pit at the inclusion centre itself. In addition the optical images showed dents in the stain if it was significantly present.

8. The reaction was found to occur faster for inclusions that had either a large surface area or were close to the edge. Inclusions right on the edge or within a one or two micrometers from the edge were found to cause a much more accelerated form of edge / crevice corrosion than was observed than for the more centrally located inclusions.

SUMMARY OF THE CHANGES OBSERVED ON THE PHOTOCURRENT IMAGES

1. Prior to any changes:

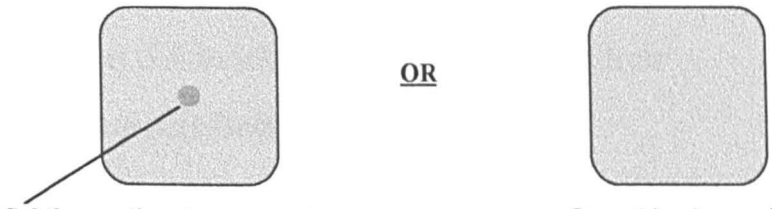

Subtle negative photocurrents are seen in the inclusion area, if the inclusion area is large enough

Or nothing is seen for very small inclusions (< 1 μm).

2. A subtle expansion of the negative photocurrents:

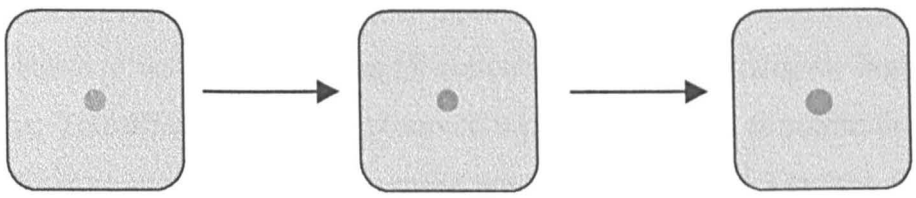

This can be seen provided the inclusion is large enough, and the initial images were recorded fast enough.

3. Positive photocurrents develop around the inclusion area:

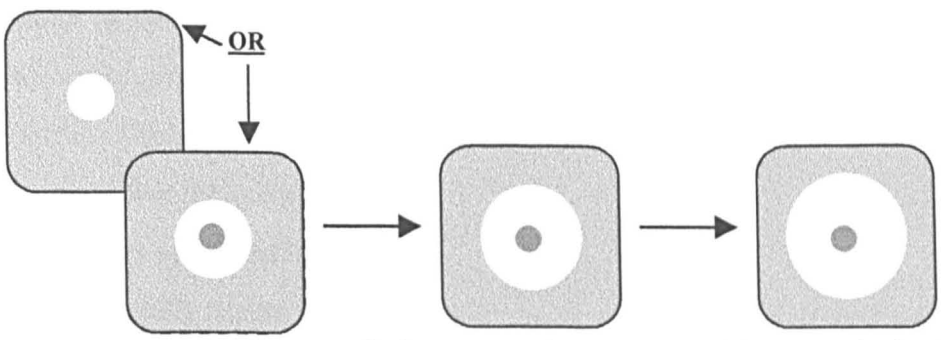

Stain seen around corresponding optical image, but it was not as large as the +VE photocurrent area.

Spheres seen in the stain region surrounding the optical image

4. The photocurrent changes sign from positive to negative over and immediately around the inclusion area:

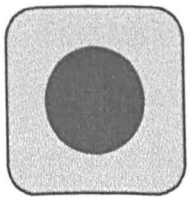

This change corresponded to a small peak in the total current. Further positive photocurrents were seen to develop further outside this region.

figure 6.66

6.9 OBSERVATIONS MADE FROM THE COMPOSITIONAL ANALYSIS

Types of Mn and S Enriched Inclusions and Their Photoelectrochemical Behaviour

Work carried out using microprobe element concentration analysis showed that samples which had not been experimented on contained inclusions with higher amounts of both Mn and S compared to the surrounding non-inclusion (bg) areas. The Mn and Sulphur enriched inclusions were found arranged in lines in a particular direction and occurred primarily in bands of very slightly lower Ni concentration and very slightly higher Cr concentration. This effect was clearly observed on the microprobe concentration maps. The inclusions were complex inclusions containing not just Mn and S but the other principal elements to be found in the stainless steel as well. On some occasions other 'slag' impurities resulting from the iron manufacture itself were present.

However some of these Mn-S enriched inclusions showed activity on the photocurrent images and some did not. Therefore these Mn and S enriched inclusions can be classified in terms of the photoelectrochemical and optical behaviour as:

a) Active inclusions
b) Non-active inclusions
c) Partially active inclusions

The type of inclusion was determined by electron-probe X-ray microanalysis (microprobe) work. It must be noted however when examining the results that if the inclusion was very small / shallow the electrode beam spread in the sample could be as such which will occupy a larger area than the inclusion so the signal analysed would come from the some of the bulk material surrounding the stainless steel as well. Nevertheless a good idea of the materials present in the stainless steel can be gained. Many inclusions were seen to be enriched in: 1) S + Mn, 2) Mn + O + a little S enriched, or 3) a combination of areas containing S + Mn and Mn + O enrichments.

a) Active Mn + S enriched inclusions

The difference found in the Mn + S enriched inclusions which did and did not corrode could easily be found by examination of the Oxygen map for the electrode concerned and comparing it with the maps for S and Mn. If the inclusion enriched in Mn + S was enriched in Oxygen as well then it did not show changes in the photocurrent image with time. However if the inclusion was enriched in both Mn and S but not Oxygen then it could be considered as an active inclusion. Even though enriched in both Mn and S the active inclusions were not pure MnS inclusions, as they stilled contained a substantial amount of the principle elements (Fe, Cr, Ni, Mo) present in the bulk stainless steel. After a stain had formed around the inclusion area the inclusion area was found to be enriched in only in S slightly (and no longer in Mn), with the surrounding stain being much enriched in both Mn + S (this material would have originated from the inclusion area).

b) Non-active Mn + S enriched inclusions

These oxide enriched inclusions tended to have a much higher amount of Mn than in the active inclusion and the ratio of [Mn]/[S] was high. This type of inclusion quite often contained one or more of other oxide forming impurities such as Al, Ti, Si, V, As, Sn and in addition frequently showed an extremely high concentration of Cr within itself. These inclusions appeared a mid-grey colour on the SEM images compared to the black colour for the non-oxide containing active inclusions. These oxide inclusions often tended to be surrounded in a very thin layer by the non-oxide enriched Mn + S containing material (black in colour on the SEM).

c) Partially active Mn + S enriched inclusions

Some inclusions were found to be partially active with the stain forming around only one half of the inclusion selectively. This occurred when half of the inclusion was oxide based and particularly high in Mn and the other half was not. (See experiment A inclusion 1, figures 6.2, 6.3, 6.4 and experiment F inclusion 1, figures 6.40, 6.41,6.43).

Composition of the Very Active Inclusions and the Surrounding Stain Material

Summary table of the % Wt. analysis of the inclusion centre after the experiment:

Experiment	Inclusion	Mn	S
In non-inclusion area		*0.702 ± 0.053*	*0.051 ± 0.009*
A (ClO_4^- only)	inclusion 1. (stained surrounded half)	0.512	0.512
	inclusion 3.	0.875	0.130
C	inclusion 1.	0.715	0.110
D	inclusion 1.	0.734	0.429
	inclusion 2b.	1.205	0.409
	inclusion 3a.	0.789	0.243
F	inclusion 1. (stain surrounded half)	0.872	0.139

Summary table of the % Wt analysis of the stain region formed:

Experiment	Inclusion	Mn	S	Cl	O	Extent of stain
A (ClO_4^- only)	inclusion 1.	7.186	5.073	____	_____	*
	inclusion 3.	3.849	1.278	____	_____	*
C	inclusion 1.	2.442	1.287	____	not visible on map	*
F	inclusion 1.	1.098	0.161	0.028	present on map to a small extent	***
J	ring A.	0.456	0.112	0.39	present on map	*****

The stains were usually too thin to analyse (the microprobe went through them) but when they could be analysed they were very enriched in the Mn at the very early stages.

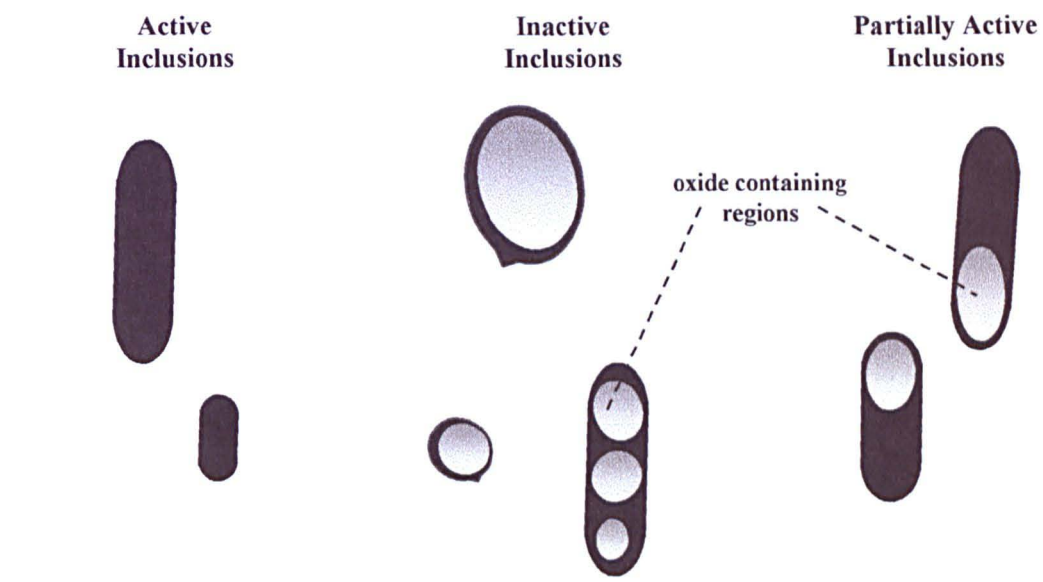

figure 6.67

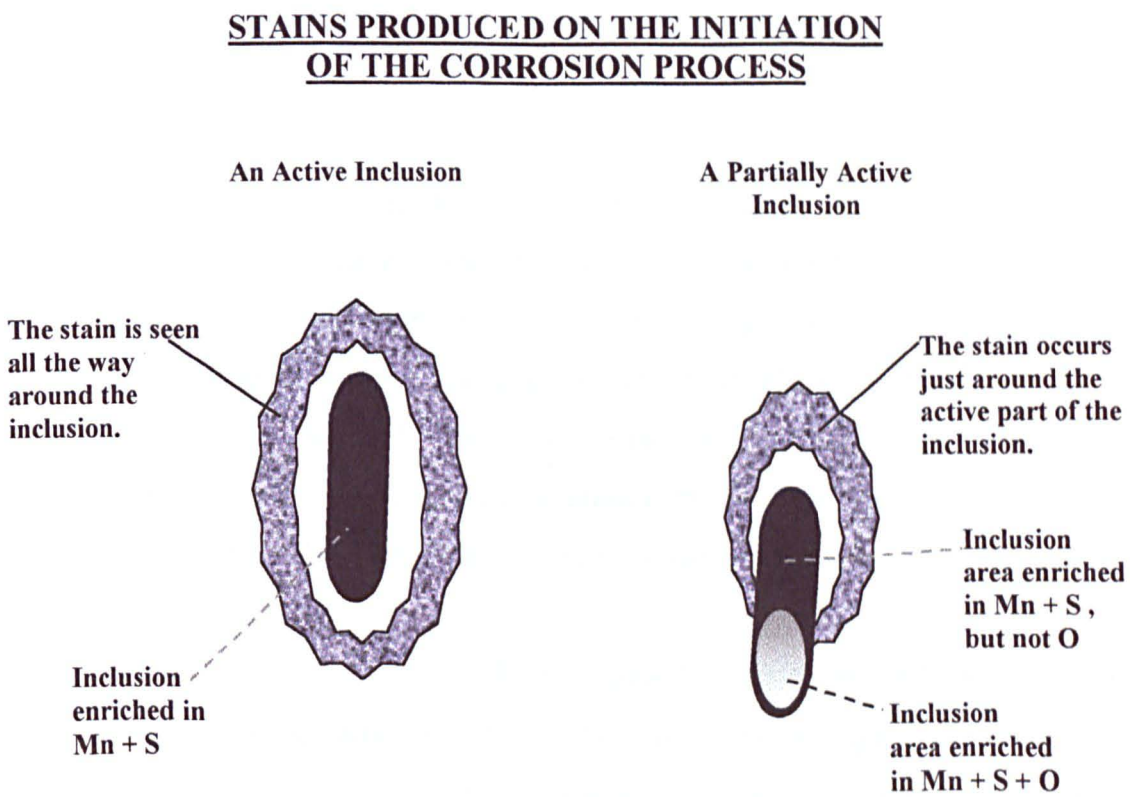

figure 6.68

How the Element Composition Varied at Different Stages of Corrosion and Element Movement

Active inclusions consisted of up to 15% Mn + S, the other 75% of the inclusion consisting of the other principle elements in stainless steel (Fe, Cr, Ni, Mo).

When the very active inclusion, which had rapidly resulted in the formation of a stain region, was analysed after a corrosion experiment it was found to be slightly enriched in sulphur (between 2 - 16 times greater than in the bulk stainless steel, $S_{bg} = 0.051 \pm 0.009\%$). In comparison the Mn in the inclusion region was found to be fairly similar to the bulk value ($Mg_{bg} = 0.702 \pm 0.053\%$). However it was found that the amounts of both the Mn and S in the surrounding stain were considerably higher, than in the inclusion itself. As the stain did not exist in this area at the start of the experiment, it may be assumed that the Mn + S content of the stain surrounding the inclusion resulted from the movement of the Mn and S from the inclusion region. The presence of the S enrichment alone at the inclusion centre, without the Mn being enriched more than the Mn bulk value, suggests that a sulphur crust (consisting of sulphur spheres) forms on the inclusion after most of the Mn and some of the S from the surface of the inclusion had moved out further out to form a stain.

With further reaction time, in the stain region the Mn concentration was found to drop to that of that in the bulk stainless steel or even slightly less, but the sulphur still remained a little enriched than the bg value (at least 2 x bg), the Mn and S having moved out to a further area still. This suggests that a S enriched crust formed on the stain area as most of the Mn and some of the S from the surface of the stain moved out to the surrounding region. With time as the concentration of the Mn decreased in the stain the concentration of the chloride was found to increase.

In a much corroded sample the stain which remained nearest to the inclusion was found to contain higher than bg values of S, Cl and O. Combination maps of this much corroded sample showed that oxygen was attached to Cr in above average amounts in the stain but not with Fe or Ni.

A SCHEMATIC DIAGRAM SHOWING HOW THE ELEMENT COMPOSITION VARIES WITH TIME IN AND AROUND THE SULPHIDE INCLUSION

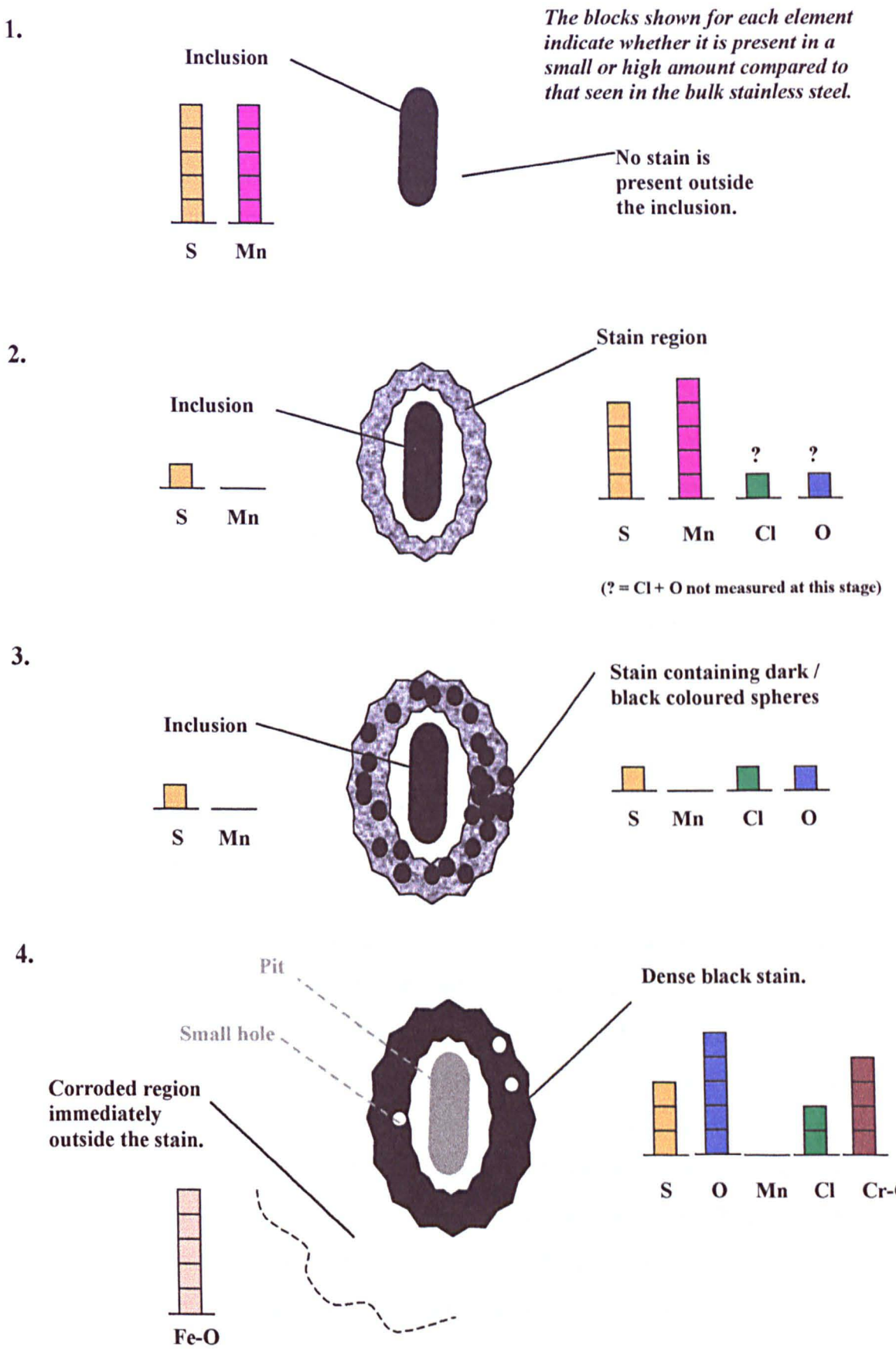

figure 6.69

6.10 A POSSIBLE MECHANISM FOR CORROSION INITIATION AT MnS ENRICHED INCLUSIONS

Pitting Corrosion

a) Breakdown of the passive film in the inclusion region

The photocurrent in the Mn + S enriched active inclusion was only slightly negative or roughly the same as the surrounding bulk stainless steel to start with. This would have been due to the fact that the inclusion area, though enriched in Mn + S, still contained mostly the same constituents in nearly the same magnitudes as present in the bulk stainless steel. This would suggest that the Fe / Cr oxide based passive layer which is present on the bulk stainless steel will exist over the inclusion region as well, but will be weaker as the amount of Fe and Cr is lower in the inclusion region than in the bulk stainless steel. As a result the passive film was easily broken by Cl^- attack using a Cl^- /ClO_4^- solution, or the use of high potentials in the case of ClO_4^- alone in the Mn + S enriched inclusion region. In the presence of the Cl^- ions it was found that the passive film could break down at much lower potentials than without Cl^- present. This may have resulted due to the electrostatic interactions between Mn-S and Cl^- causing a break down in the passive film. It may even be that the presence of the Cl^- over the inclusion surface helped to bring the MnS components in the inclusion to the surface causing the passive film to break.

The very first change observed on the photocurrent image, provided the inclusion was large enough was a subtle decrease in the photocurrent over the inclusion region which lasted for a very short time. This initial reaction was very fast, so it was difficult to observe. This suggests that a cathodic reaction occurs over the inclusion site itself in the very first instant. The application of the laser would probably have increased the magnitude of the cathodic current being generated over the inclusion area to a more negative current, and this change in the current would have been recorded as a negative photocurrent on the image. By convention addition of electrons result in the generation of a cathodic current. So the observation here may simply arise from the breakdown of the passive film as follows:

$$O_2 + 4H^+ + 4e^- \longrightarrow 2H_2O \qquad (6.12)$$

b) The formation of a surrounding stain region and a sulphur crust

After the subtle changes in the photocurrent, in the inclusion region, positive photocurrents were found to form around the inclusion region on the surrounding stainless steel, as well as a very slight increase in the photocurrent over the inclusion region. This was seen both with or without Cl^- and for both pitting and crevice corrosion. This area therefore acts as a local anode to balance the cathodic reaction which previously started in the inclusion area.

At first no changes could be seen on the optical images to correspond with the positive photocurrents observed.

However, later in time as the photocurrents increased becoming more positive still, a thin stain enriched in Mn + S was found to develop in the region where the positive photocurrents had previously been observed. At this point if the surface of the inclusion area was analysed it found to be enriched only slightly in S.

With more time still this stain then seemed to lose the Mn enrichment so just the S remained enriched above the background amounts and this was verified by the observance of sulphur spheres on the stain region. The occurrence of sulphur as perfect spheres suggests that the sulphur may have grown from the solution.

The most recent work analysing crevice solutions showed the presence of HS^- in the solution (refs. K4-9, K4-12, K4-14). The reaction involving S forming from HS^- is an anodic reaction, which should result in the formation of the positive photocurrents as were seen. If the same product (HS^-) results from pitting corrosion initiation as in crevice corrosion initiation, then a question that needs to be asked is; where does the HS^- come from? As the S in the stainless steel initially exists in the sulphide inclusion probably as MnS, the dissolution of the MnS and further reactions of any products will lead to the eventual formation of HS^- which will break down to elemental sulphur.

In the presence of Cl^- a possible mechanism for the Mn-S dissolution reaction may be:

$$MnS + 2Cl^- \longrightarrow MnCl_2 + S^{2-}$$
$$\downarrow + H^+$$
$$HS^-$$
$$\downarrow$$
$$S + H^+ + 2e^- \qquad (6.13)$$

This would result in the formation of a $MnCl_2$ stain as well as a sulphur crust over the inclusion. However this does not explain why the stain (an area enriched in Mn + S + Cl) produced initially contained considerably more Mn than Cl. It may be that the Mn also occurs as some other salt for example $MnSO_4.5\ H_2O$. Such Mn(II) salts are fairly water soluble which would explain why it could be easily rinsed-off with water. Another reason may be that the $MnCl_2^-$ very quickly decomposes on settling on the stainless steel around the inclusion.

Some Mn^{2+} salts which may be produced when the passive layer over the inclusion breaks could include: $MnSO_4$, $MnSO_4H_2O$, $MnSO_4 4H_2O$ and $MnSO_4 5H_2O$. These are a pinkish colour and all fairly soluble (amount to saturate $100cm^{-3}$ of $H_2O \sim 3 \times 10^{-1}$ to 6×10^{-1} mol, see Appendix I-part 3). In addition in the presence of Cl^- further salts including: $MnCl_2$, and $MnCl_2\ 4H_2O$ could be produced. These are also fairly soluble (amount to saturate 100 cm^{-3} of $H_2O \sim 5 \times 10^{-1}$ to 6×10^{-1} mol). In the first instant a pinkish (dark region on confocal image) colour was observed on the colour optical images in the region of the stain, then as it built up becoming more dense it looked more black in colour. It may be that both S and Cl containing salts are involved in the case of a solution containing Cl^- but only the S containing salts in a solution containing just ClO_4^- alone. What was certain was that the stain region produced in a Cl^- containing solution definitely contained Cl^- but it was present in a much smaller amount than the % of Mn present. However there was no real evidence that the Cl^- existed in the inclusion region, but this may be due to the fact that only solid products on the sample surface

were being analysed from this area and any liquid products such as HCl would therefore have been missed.

The stains seen close to the inclusion when just ClO_4^- was present (Experiment A, figures; 6.2, 6.3) where also found to be enriched in Mn and S but no Cl^- was present. So either a different Mn salt than MnCl must be present or even Mn-S itself may be thrown out of the inclusion area after the passive film bursts.

The work carried out here showed that the positive photocurrents moved further out from the initial stain region, the stain region was left enriched slightly in S and most of the Mn and some of the S present had moved away.

As well as MnS dissolution producing sulphide (HS^- / H_2S) other reactions in the pit under the sulphur crust could include:

$$Cr^{3+} + 3H_2O \longrightarrow Cr(OH)_3 + 3H^+ \quad (6.14)$$

$$Fe^{2+} + H_2O \longrightarrow FeOH^+ + H^+ \quad (6.15)$$

$$2H^+ + 2e^- \longrightarrow H_{2\ gas} \text{ (this will leave by bursting the crust occasionally)} \quad (6.16)$$

and in the presence of Cl^- the following reaction may also occur:

$$Cl^- + H^+ \longrightarrow HCl \quad (6.17)$$

c) The formation of dents in the stain region and pitting initiation

Dents were found to form in the stain region after the sulphur spheres had been there for some time. The acid formed as a by product of creating elemental sulphur may start to eat into the metal where the spheres are sitting once it has built up to a certain concentration. It may even combine with Cl^- to form HCl. When the acid has gone through the stain the metal will start to dissolve. This will result in holes in the stain region which will tunnel through the metal, connecting the stain region to the pit in the inclusion region which has been expanding horizontally under the stain. This would result in the formation of a lacy region containing holes as well as a central pit in the region of the inclusion as was observed by Newman and coworkers (refs. K3-37, K3-38, K6-2, 1997-1998). The SEM images observed of the lacy area showed a white region containing many dark gaps, compared to the dense stain seen in many of the

experiments shown in this work (depicted by a white area on the SEM image). It is likely that a lacy area such as that seen by Newman and coworkers would have developed if given more time by the holes in the stain region cutting right into the steel and meeting with the growing pit from the inclusion area. The differences seen in the density of the stain may also have been contributed to, by the fact that the samples that Newman and coworkers used were clearly rougher (as seen on the SEM images) containing many lines / scratches on the surface whereas the samples seen here were much more finely polished to allow for high resolution confocal imaging work.

A change was found to occur in the total current, at the same time as when the photocurrents around and in the in the inclusion region became negative, starting in the stain region and spreading right over the inclusion and remaining stain region. On examination of the areas which had undergone a reversal of the photocurrent sign, pits were found to have formed. Pits were formed in the inclusion region itself if there was not much stain present (Experiment A, Experiment G), and in the stain region if the stain was large (dips were visible in the surrounding stain without having to further rinse the electrode, see Experiment F). So the change in sign may simply reflect the collapse of the S crust either wholly or partially resulting in the formation of holes / pits in the stainless steel surface.

Previous work by Newman and Moayed (ref. K6-2, 1998) showed that having SO_4^- present as well as Cl_2^- produced a much wider lacy region than the size of the central pit over the inclusion itself, compared to when Cl^- was used alone. They suggested that having a Cl^- competitive inhibitor results in such an effect. However here it was found that having ClO_4^- (a Cl^- competitive inhibitor) could still result in the formation of a pit surrounded by very little stain material if the reaction was speeded up by any means such as increasing the potential (see most active inclusion areas for Experiment G, or with just ClO_4^- the most active inclusions for Experiment E). So it may be speeding up the reaction by any means. Increasing the Cl^- concentration, reducing the ionic strength or increasing the potential may have the same effect in reducing the amount / density of the stain around the inclusion area. This suggests that the formation of a stain probably depends strongly on the kinetics of the reaction with a faster reaction not having as much time to build up the stain, or alternatively the stain may be thrown out in a much thinner layer over a much larger region.

AN ILLUSTRATION OF A POSSIBLE MECHANISM INVOLVED IN PITTING CORROSION INITIATION

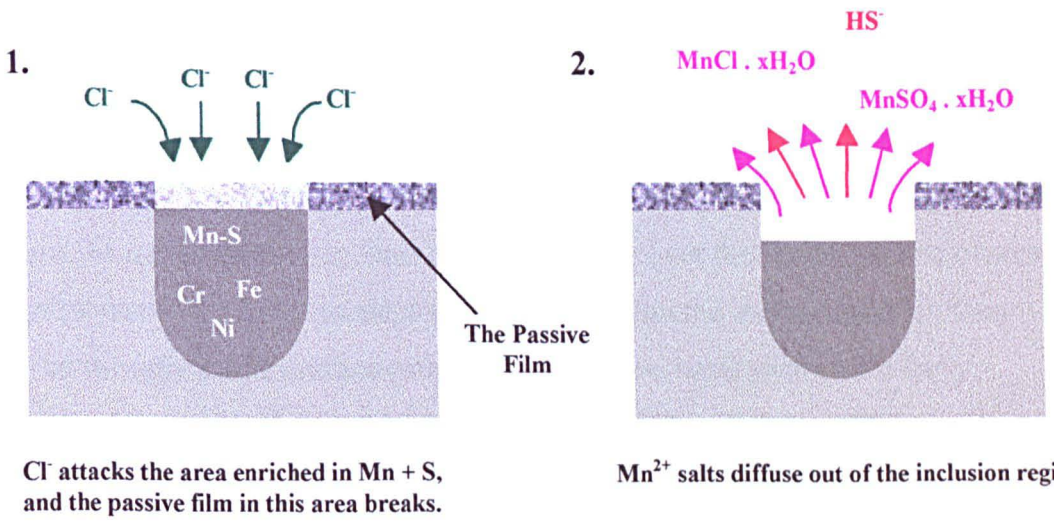

Cl^- attacks the area enriched in Mn + S, and the passive film in this area breaks.

Mn^{2+} salts diffuse out of the inclusion region.

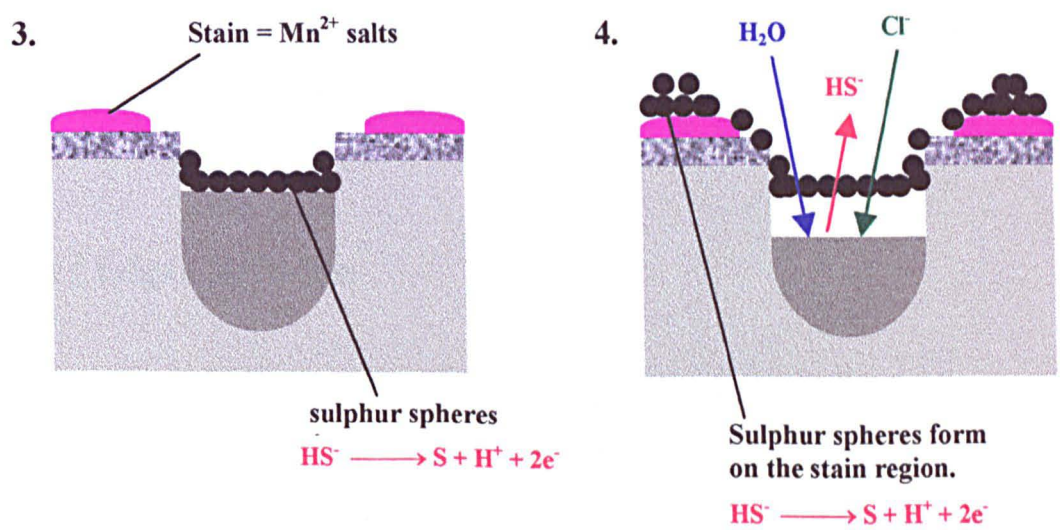

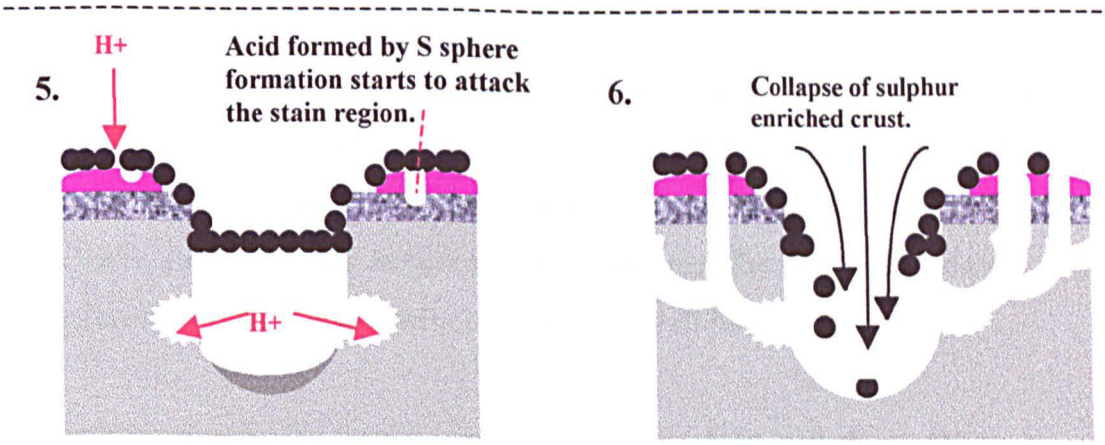

The acid formed by reactions in the pit (e.g. by MnS dissolution, Cr^{3+} hydrolysis, Fe^{2+} hydrolysis) starts to attack the surrounding bulk stainless steel metal.

The central pit in the inclusion area and the micro-pits under the stain region expand and combine to form a lace like region, containing holes where the S crust has collapsed.

figure 6.70

The Mn + S enrichment in the inclusion may have been important: firstly in providing weaker areas in the passive film which can easily breakdown, and secondly in providing the source of S to form a sulphur rich crust under which a strong acidic solution can develop in a locally restricted area. Active inclusions were not pure MnS but contained a substantial amount of the same material as was present in the bulk stainless steel as well. It may therefore be that even though the MnS serves to initiate the appropriate conditions for pitting corrosion, once the passive film over the inclusion area breaks, it is the hydrolysis of the bulk stainless steel metals within the inclusion which then creates the strongly acidic environment. This acid then starts to dissolve the surrounding stainless steel region leading to wide scale break down of the stainless steel material.

Even though there appeared to be a gap between the inclusion and the surrounding stain in many cases, the sulphur enriched crust may have been continuous over both the inclusion and stain regions, only being visible where it was the most dense.

Crevice / Edge Corrosion

The results found from the experiments which showed corrosion at the crevices / edges of the electrode were found to be very similar to those exhibiting pitting corrosion. The main difference being that when corrosion was seen to occur at the edge of the electrode it was extremely fast and the changes seen on the photocurrent and optical images were on a much wider scale. In pitting corrosion initiation it was seen that the pits found closer to the edge of the electrode were seen to corrode much faster than central inclusions. So it only follows that if there are one or more inclusions right on the edge of an electrode, either in a fine crevice or right in between the bulk stainless steel and the epoxy resin, then the reaction which occurs here will be much faster still.

The faster form of corrosion seen to occur at electrode edges, still showed the occurrence of a positive photocurrent region as well as stain formation but on a much wider scale than that which was observed for pitting corrosion.

The faster reaction for crevice corrosion allowed the study of the further development of the corrosion products seen in the region of the stain as well as other corrosion products which were deposited outside the stain region. The stain region when left to develop further (see Experiment J) was found to reduce in Mn but was still enriched S + Cl, in addition a build up of O and Cr-O in combination, was found to occur. However Fe-O in combination was not found in the stain region in a significant amount. The Cr-O may have been chromium hydroxide formed by Cr^{3+} hydrolysis as this is known to be fairly insoluble so it would have precipitated out first. Outside the initial stain ring Fe-O was seen in combination in an orange coloured area. Further out still various oxygen containing products were seen to occur in 'ring' shapes (semi-circular as it is at the electrode edge) due to the radial diffusion of the various acidic oxides and hydroxides out of the pit followed by the segregated precipitation of each product according to their solubility.

This work suggests that not only does the sulphur component of stainless steel have an important role to play in pitting corrosion initiation, but that it has an important role to play in crevice corrosion initiation as well.

Comparison with the Dissolution of Sulphide Minerals

The behaviour of sulphide minerals may also provide important information of the dissolution mechanism of the MnS present in the stainless steel inclusions.

The anodic dissolution of PbS (*galena*) in acetate buffer starts with the production of sulphur protrusions that are between 10 - 200 nm high (ref. K5-8). The mechanism proposed for this is chemical dissolution followed by electrochemical oxidation (equations 6.18, 6.19).

Chemical dissolution:

$$PbS \longrightarrow Pb^{2+} + S^{2-}$$
$$\downarrow H^+$$
$$HS^-$$
$$\downarrow H^+$$
$$H_2S \qquad (6.18)$$

Electrochemical oxidation:

$$nH_2S \longrightarrow S_n^{(0)} + 2nH^+ + 2ne^- \qquad (6.19)$$

FeS_2 (*pyrite*) has been found to have quite different behaviour (refs. K5-4, K5-11). FeS is unstable compared to FeS_2 or Fe_2O_3 at 0V NHE. So the electrochemistry of FeS_2 should predict the behaviour of FeS_2. The FeS_2 containing material is known to be of mixed composition containing just iron mixed in with it as well. In the case of FeS_2 water is essential for anodic dissolution to occur whereas it is not for PbS. One possible mechanism which has been suggested (ref. K5-11) is as follows:

Interaction with water and 3d states of the iron:

$$FeS_2 + H_2O + h^+ \longrightarrow Fe(OH)S_2 + H^+$$
$$\downarrow \text{rearrangement of OH groups so they are closer to the } S_2^{2-} \text{ sites in the pyrite lattice}$$
$$Fe\,S_2\,(OH)$$
$$\downarrow H_2O + h^+$$
$$Fe\,S_2\,(OH)_2 + H^+$$
$$\downarrow 2H^+$$
$$Fe^{2+} + 2S^{(0)} + 2H_2O \qquad (6.20)$$

The electro-dissolution of FeS_2 or the subsequent S formation is not Cl^- catalysed.

In comparison the chloride catalysis of $CuFeS_2$ (*chalopyrite*) and related metal enriched derivatives has been reported (ref. K5-7). In contradiction to this work Castle and Ke (ref. K3-8) claimed that if Cu was found within MnS enriched inclusions then they remained un-attacked. However in this work these claims were found to be untrue, as microprobe analysis clearly showed the presence of Cu in and around some of the active stain and inclusion regions (e.g. figure 6.28 - inclusion1, figure 6.28 -inclusion 2b). However there was a very small amount of Cu present through the whole electrode as well as in the oxide enriched inclusions. It may have been that the inclusions analysed by Castle and Ke even though enriched in Mn + S it were enriched in oxygen as well so the Cu was present as CuO. In any case it was repeatedly proved that with Cu present in small concentrations in the inclusions it certainly did not hinder the activity of the inclusion and may even have contributed to it in the same way as it is known to do in the Cl^- catalysis of $CuFeS_2$.

The chemistry of neither pure MnS or pure FeS_2 are appropriate models for the inclusion dissolution which results. Both FeS_2 and MnS are known to become passive in Cl^- after long exposure times (ref. K5-2). As the inclusion seen was not a pure MnS inclusion and contained other materials such as Cr as well, it must be concluded that this mixture of elements in an inclusion that helps to bring about corrosion initiation rather than just the presence of MnS itself.

6.11 CONCLUSION

It has been unequivocally shown that pitting corrosion is due to chemical changes in particular inclusions which are enriched in Mn and S but not enriched in oxygen.

Therefore the resulting photocurrents seen, are due to the photo-decomposition which occurs at the inclusion site.

The inclusion area initially either had slightly negative photocurrent or the same photocurrent as the surrounding bulk stainless steel. The initial change observed was a

subtle decrease in the photocurrents directly over the inclusion area as the passive film broke, provided that inclusion was sufficiently large enough and the reaction imaged fast enough. The next change noticed was the occurrence of positive photocurrents in a ring surrounding the inclusion followed by the subsequent deposition of a S and Mn enriched stain and then the formation of a sulphur enriched crust consisting of sulphur spheres. The third and perhaps most drastic change noticed was the change in sign of the photocurrent from positive to negative. This change was seen to sweep across the S enriched (stain and inclusion) region. This third change was found to correspond with a peak seen in the total current and the formation of a pit.

So in summary it can be said that the pit starts from inclusions enriched in Mn and S and the reaction is driven by the chemistry of the inclusion and the same thing appears to apply to the crevice.

7. FINAL CONCLUSIONS

7. FINAL CONCLUSIONS

This section deals with what the photocurrent imaging technique was found to be useful for, its limitations, and suggestions of further improvements to the apparatus and further work which could be carried out in the future. Specific conclusions and discussions to the experiments carried have been given previously at the end of each at the end results chapter (chapters 3,4,5 and 6).

7.1 THE USEFULNESS OF THE PHOTOCURRENT IMAGING TECHNIQUE

This technique proved to be very useful as a tool for studying electrochemistry as it provides spatial information about the electrochemical reactions which occur at the surface. In addition it can be used to study the solid state interactions at electroactive junctions. The work also showed that it was possible to record fairly high resolution photocurrent images in order to see variation of photocurrent at compositional changes at the surface.

The fact the laser scanning speed was fast allowed information on the kinetics of the reaction to be picked up, in changes which can be seen on the photocurrent image. This allowed more changes to be picked up, than would be possible with much slower conventional methods of recording data such as with cyclic voltammetry.

Where the photocurrent generated was large enough the beam intensity could be varied (by placing various neutral density filters in the laser beam path) allowing the photocurrent at different depths to be profiled.

In addition the effect of the potential on the image could be readily studied in order to discover at which potential a reaction may produce large photocurrents and therefore where it is most efficient. The work conducted also showed that the features present on

the photocurrent versus potential graphical data could be correlated with the features seen on cyclic voltammetry, known electrochemical information, and electrode geometry of a particular reaction. Continued work in this area will allow this apparatus to be developed into a diagnostic tool in order to see whether a reaction is occurring efficiently or to show the extent of reversibility or whether there may be faults or problems at specific points on the electrode surface.

This equipment was also found to be a useful tool in studying reactions with time at surfaces of varied elemental composition. This is since the technique allowed very fast direct gathering of image data with an instantaneous display on the computer monitor as the working electrode surface was scanned by the laser. This together with other imaging techniques such as confocal optical imaging and SEM imaging, to show topographical features, as well as electron probe x-ray microanalysis to show spatial concentration of the different elements present, and colour video microscopy imaging to show the different true colours of optical features (of products of various compositions), allowed the changes on the photocurrent images to be equated with the presence of particular elements and the reactions which occurred there.

It was found that the spatial changes in the photocurrent were particularly sensitive to the electrode edges and to composition within an electrode but they were not as sensitive to surface topography within an electrode made of the same pure material throughout, i.e. a few small scratches on the surface of a pure gold electrode due to rough polishing will not show up as lines on the photocurrent image but will contribute mainly to the general rise in photocurrents over the whole surface fairly evenly on the photocurrent image.

A summary of the specific observations and conclusions obtained when the photocurrent imaging technique was applied to various experimental systems has been given in sections 7.2 to 7.6 which follow.

7.2 THE USE OF PHOTOCURRENT IMAGING IN DEPTH PROFILING IN SEMICONDUCTOR DEVICES / ELECTRODES

It was found that photocurrent imaging of silicon in either solid-state physics or electrochemical systems could be used for depth profiling. This effect was easily produced by changing the light intensity by placing neutral density filters in the laser beam path. This effect can be explained using the Beer-Lambert Law which states that the higher the light intensity, the further the light would be able to travel into the sample.

This technique proved useful in height profiling in a semiconductor device (a silicon memory chip: namely a 256K EPROM). Reducing the laser intensity resulted in not only a drop in the photocurrent, but in the features seen on the photocurrent image varying considerably as well. In comparison the features seen on the confocal optical image remained the same as the light intensity was reduced. Similar results were found, in work carried out, using electrochemical systems which included the photocurrent imaging of p-type Silicon in 1M HCl as well as the photocurrent imaging of the oxide films (semiconductors) formed on stainless steel in $NaClO_4$ solutions. It was found that the features seen on the photocurrent image at the lowest light intensity most resembled the features seen on the optical image.

The effect of seeing different images at different light intensities is not as simple as it first seems, as it has to be considered why the features on the outside / uppermost layer do not dominate the signal at any light intensity as would be the case if the photocurrent is directly proportional to the light intensity. This effect can be explained by the occurrence of a saturation effect of the signal at the higher light intensities allowing signal from the deeper layers in the sample to be monitored. This effect was proved experimentally by plotting graphs for the average photocurrent generated at over the electrode area (for various types of stainless steel) versus the incident laser intensity. This work showed the graph curved over, as the light intensity was increased, and was not linear.

The magnitude of the photocurrents observed on the silicon memory chip and the p-type silicon were such that very little had to be done in terms of noise reduction and very few frames had to be signal averaged if any allowing the image to be very quickly captured. The fact the laser was continuously scanning at very fast speeds also contributed to this technique being very fast and efficient. The solid state work in particular was very easy to carry out and faster still to use, as a technique, as an electrochemical cell did not need to be set-up or solutions prepared. The work carried out on the stainless steel, which involved the photocurrents generated at the thin semiconducting film on its surface, resulted in smaller photocurrents therefore required the presence of extra shielding in the form of a miniature Faraday cage specifically designed to fit around the cell.

This technique of using photocurrent imaging would therefore be particularly useful in the for example the silicon chip manufacturing industry to check on the function by imaging for dead areas rather than just relying, on optical imaging which only shows features of the surface and further more can not show if the device is or is not functioning properly and therefore is faulty.

7.3 PHOTOCURRENT IMAGING OF p-Si IN 1M HCl

It was found that recording a photocurrent image showed much spatial variation which could not have been otherwise detected using a more conventional electrochemical technique such as cyclic voltammetry.

In addition the photocurrent versus potential curves for the average photocurrent obtained (from the electrode region) on the photocurrent image was found to be different to the photocurrent versus potential curve which was obtained from pulsed-laser cyclic voltammetry.

The I_{photo} vs E trend for the cyclic voltammetry was that as the potential increased the photocurrent decreased in a smooth curve. However in the I_{photo} vs E curve for the photocurrent image, the photocurrent decreased with decreasing potential until -300 mV

vs SCE was reached, but further decreasing the potential resulted in the photocurrent becoming more positive. The change in trend corresponded with the photocurrent onset potential as seen for this system. This work showed the scanning laser imaging experiment is fundamentally different to the cyclic voltammetry experiment. The main differences are given in the table below.

A summary of the differences:

Laser Imaging	Pulsed-laser Cyclic Voltammogram
Only one point at a time is examined.	The average current over the whole electrode is recorded.
This is a dynamic experiment recording changes in current in the form of A.C. variations.	This is a D.C. experiment where the total current is recorded using a chart recorder.
The data sampling time is microseconds.	The data sampling time is milliseconds.

The minimum in photocurrent (i.e. the most cathodic photocurrent)on the images is thought to occur at an apparent minimum in C^{-2}.

In many systems the flat band potential coincides with the photocurrent onset potential. As the capacitance is know to go through a maximum at the flat band potential the simplest explanation for this behaviour would be that the minimum (more cathodic) photocurrent on the images occurs at a potential which coincides with the flat band potential. However in previous work Nakato and coworkers (refs. F3-1, F3-2) had stated that the H-evolution reaction for p-Si in 1M HCl had a high activation energy, so the onset potential for this system is much more negative than the flat band potential. If this is so then the occurrence in the minimum in capacitance may have been due to surface states.

7.4 PHOTOCURRENT IMAGING OF PHOTOTHERMAL EFFECTS PRODUCED AT GOLD IN FERROCYANIDE SOLUTION

In this work the photocurrent images of gold in ferrocyanide were collected at various potentials. It was found that plotting a curve of the photocurrent observed on the image vs potential gave a peak at $E_{½}$ for any electrode geometry (microband, macrodisc). It was also found that the width of the microband on a photocurrent image was slightly wider than the optical image at $E_{½}$ with a fixed laser velocity and intensity.

However the width of the positive photocurrent band even at $E_{½}$ was not as wide as that given under instantaneous heating conditions when the laser velocity was scanning very fast. The effect of changing the laser velocity and hence the laser beam irradiation time (the time to scan over a length equal to the laser beam diameter), τ, showed that the photocurrent image had the greatest photocurrent magnitude at $\tau = 7$ μs. The calculated time scale of thermal diffusion, λ_T, for gold was found to be 0.008 μs and for water it was 7 μs. This showed that the ferrocyanide solution played a key role in the photocurrents which gave rise to the image contrast seen.

It was found that changing the electrode geometry from a disc electrode to a microband changed the photocurrent vs potential behaviour. In the case of the band electrodes there was a photocurrent observable at low potentials, which was not seen for the disc electrode (over the disc centre). In addition the peak at $E_{½}$ was superimposed over a generally rising photocurrent signal with potential. The photocurrents generated at a band electrode were found to be smaller than that for a disc electrode. The differences seen were attributed to the fact that, in the case of a disc the electrode the perturbed area is much smaller than the overall size of the electrode but in a band (line) electrode one dimension of the electrode is comparable to the size of the perturbed zone.

With this system it was also found that the photocurrent signal was very sensitive to poisoning of the surface causing the reaction to become irreversible. The poisoning could be achieved by using either an gold electrode containing impurities in the gold or

by contamination of the solution. In either case the photocurrent was found to be reduced significantly with a reduction in the $E_{½}$ peak seen on the photocurrent vs potential curve for the image. This showed that the photocurrent signal expected from an electrochemically reversible reaction is much larger than that for an electrochemically irreversible reaction.

7.5 PHOTOCURRENT IMAGING OF THE PASSIVE SEMICONDUCTOR FILMS ON STAINLESS IN $NaClO_4$

Photocurrent images were recorded for stainless steel at various potentials ranging from -900 mV vs SSE (~ -500 mV vs SCE) to +800 mV vs SSE. Broad curves were seen in the photocurrent vs potential curves. Similar broad curves were seen for C^{-2} vs potential measurements carried out in previous work for stainless steel and iron for potentials above -900 mV, SSE (refs. J3-7, J3-9, J3-11, J3-13). The electrochemical behaviour of the passive films on stainless steel and iron are known to differed from one another at potentials below -900 mV vs SSE (ref J3-9).

Previous work using structural analysis by Auger analysis (refs. J2-1, J2-2, J2-3) and XPS (ref. J2-4) showed that the passive film on stainless steel contained an outer layer that is very rich in iron oxides and a very thin inner layer that contains chromium oxides. So it can be concluded that the photoelectrochemical behaviour of the passive film seen by photocurrent imaging depends strongly on the on the iron-oxide enriched outer layer of the passive film.

At potentials above -900mV vs SSE the photocurrent was found to increase with potential, this may be due to the occurrence of higher oxidation states of iron which may give rise to an increase in the surface capacitance. When the potential was increased further still at values above ~ + 150 mV vs SSE (a peak in the photocurrent was observed at this value) a reduction in the photocurrent was observed, this may have resulted as the iron dissolves out of the passive film.

Examination of the changes in the photocurrent image with potential showed that at the centre of the electrode the photocurrent rose from approximately nothing to a peak value and then down to almost nothing again, when the potential was increased from -900 mV to +800 mV vs SSE. However at the electrode edge the photocurrents produced followed the same trend up to the peak potential but increasing the potential further still resulted in the photocurrents remaining fairly high and not returning back to zero as in the case of the electrode centre. This suggested the occurrence of two types of reaction with two different relaxation times: a fast one and a slow one.

A positive photocurrent was seen on the leading edge of the electrode as the photocurrent scans and a negative photocurrent was seen on the trailing edge. It was therefore found that the behaviour of the leading edge with potential produced an almost mirror like behaviour to the photocurrents observed at the trailing edge with potential. Similar behaviour was also seen with other electrochemical systems (e.g. gold in ferrocyanide) with the positive photocurrent at the leading edge being the greatest at the same conditions of potential, light intensity, laser velocity and solution concentration at which the negative photocurrents on the trailing edge of the electrode are the greatest. These effects seen are simply as a result of the how the photocurrent produced varies with time, in that the transient effects produced are still being monitored after the laser has moved off the point that was perturbed and on to the next point.

In addition it was found that changing the stainless steel sample from 304L (low sulphur content) to 316F (high sulphur content and molybdenum present) resulted in a change in the photocurrent vs potential behaviour seen for the photocurrent images. There was still a broad peak in the photocurrent vs potential curve but the peak was less symmetrical with a second overlapping peak occurring with a peak maximum of ~ +300 mV vs SSE. In this case the peak maximum for the unsymmetrical (double) peak varied between +150 mV and +300 mV the peak maximum tended to be near +150 mV if very few active inclusions were present or towards +300 mV if there were many active inclusions present.

Additional work on the stainless steel samples also showed decreasing the laser intensity decreased the photocurrents generated (this effect has been discussed in more detail in section 7.2).

Slowing down the laser from $\tau = 29.15$ μs ($v_p = 6.86$ cm s^{-1}) to $\tau = 151.84$ μs ($v_p = 1.32$ cm s^{-1}) also decreased the photocurrent being generated. The effect of the laser velocity showed that the signal derived from the early part of the photocurrent transient (a high photocurrent) was dominant at the faster speeds and at the slow scanning times the photocurrent derived from the later part of the photocurrent versus time transient (a lower photocurrent) was dominant.

7.6 PHOTOCURRENT IMAGING OF STAINLESS STEEL CORROSION IN DILUTE NaCl CONTAINING SOLUTIONS

In this work the changes in the photocurrent image of stainless steel in solutions containing various amounts of Cl^- and ClO_4^- were recorded with time. It was found that the photocurrent imaging technique could be used to capture the first stages of pit formation, and therefore corrosion initiation for stainless steels. Changes in the photocurrent image were observed, before any changes were seen on the optical image or the total current signal, both of which were being simultaneously monitored whilst conducting the photocurrent imaging experiment.

Changes were only seen on the photocurrent images at specific locations. These were found to correspond to inclusion sites as seen on the corresponding optical images. The inclusions were small areas consisting of a different elemental composition to that seen in the bulk stainless steel. However it was found that the changes on the photocurrent image only occurred at some of the inclusions and not others. In order to distinguish the type of inclusion which provides a site for corrosion initiation from one that does not, microprobe elemental maps were recorded to show the spatial distribution of each element, followed by microprobe spot analysis to give the percentage weight of each element present in the inclusions of interest. This work showed that there were many types of inclusion present in the stainless steel including those with higher concentrations of substances such as Si, Al, Ti, Mn and S, than in the bulk stainless steel. It was found

that inclusions enriched in Mn + S gave changes in the photocurrent images, that is they were active inclusions. However the inclusions which were enriched in oxygen as well as manganese and sulphur did not, that is they were inactive inclusions. It was noted that in the inactive inclusions the percentage weight of Mn present was much higher than the percentage weight of S present, the majority of the Mn being associated with the O as MnO. The inactive Mn and S enriched inclusions were quite often extremely high in Cr and other oxides of Ti, Si etc. In addition there were found to be some Mn and S enriched inclusions which were enriched in oxygen on one side but not the other, these inclusions were found to be partially active with only the non-oxide side showing activity.

Initially, prior to any changes occurring, the photocurrents seen at the Mn and S enriched inclusions were very slightly negative or about the same, as the photocurrents observed on the surrounding bulk stainless steel. In the presence of Cl^- and ClO_4^-, or ClO_4^- alone at a high potential, these initial observations were followed by three changes on the photocurrent image.

The very first change noticed on the photocurrent image was that the region of the inclusion became very slightly more negative. This behaviour lasted for a very short time and could only be recorded if the inclusion was large enough and the early photocurrent images were captured fast enough. This change was attributed to the break down of the passive film over the inclusion area in the first instant.

Very rapidly after the first changes had occurred, positive photocurrents were found to form around the inclusion area. After a while, as the positive photocurrents increased further still, a stain became visible on the optical image. When analysed the stain was found to be enriched in Mn, S, and Cl, however the percentage weight of Mn present was significantly higher than the percentage weight of Cl present. On production of the stain, analysis of the inclusion area showed that this region was no longer enriched in Mn and only very slightly enriched in S, with the Mn and S having been carried out to form the stain surrounding the inclusion. With further time still spheres of elemental sulphur could be seen in the stain region. This was followed by a decrease in the manganese and an increase in oxygen in the stain. The positive photocurrents were therefore attributed to the formation of firstly a stain, made of Mn^{2+} salts, around the inclusion and, then the

further development a sulphur enriched crust, which may have been continuous across both the stain and inclusion regions. The presence of the Cl^- lowered the potential at which positive photocurrents could be observed around the inclusion areas. The presence of Cl^- was important in speeding up the reaction.

The third and maybe the most important change observed in the photocurrent image was a change in the sign of the photocurrents from positive to negative right across the stain and inclusion region. This was found to correspond with a peak in the total current and the formation of a pit / hole in the sample.

As a Mn + S rich stain is produced around the inclusion, as well a S rich crust, and HS^- is known to be produced in the corrosion initiation stages (ref. K4-14), it can be concluded that the MnS is a necessary component of the active inclusion. However the active inclusions were not pure MnS inclusions as they contained a very large amount of the same material that was present in the bulk stainless steel (Fe, Cr, Ni, Mo). This suggests the passive film containing Fe and Cr oxides will therefore still be present on the inclusion in the first instant but weaker as the % Fe and %Cr present is lower. For this reason the passive film will break over the inclusion first even without the Cl^- ions present (i.e. in a solution containing just ClO_4^-). In addition it may be that a crucial amount of one of the elements present in the inclusion, such as Cr or Fe, is also required to produce the acidic conditions which will dissolve the stainless steel. When the passive film breaks the hydrolysis of ions such as Cr^{3+} and Fe^{2+} can lead to the production of hydroxides and acid as a by product. Cr^{3+} hydrolysis in particular can produce a considerable amount of acid.

In addition this work showed that similar behaviour to pitting corrosion was found to occur for crevice / edge corrosion at the electrode resin interface. The reactions in this case still produced similar changes on the photocurrent image, as well as S enriched stains which were observed on the optical and microprobe images. This suggests that sulphides have an important role to play in crevice corrosion initiation as well.

To summarise, this work therefore clearly showed that changes depicting the corrosion initiation could be monitored using the photocurrent imaging technique, it was found that

the pitting corrosion was initiated at inclusions enriched in S + Mn (but not oxygen) and the reaction is driven by the chemistry of the inclusion and the same conditions seem to apply to crevice corrosion initiation.

7.7 LIMITATIONS OF THE APPARATUS USED

The limitations of the apparatus used in recording the photocurrent images include difficulties in focussing on dark non-reflective substances. There is a need for a large photocurrent to noise ratio, though this problem could be solved by using the laser optimised to its maximum output and the use of a faraday cage around the electrochemical apparatus. An even better method would be to switch to a more powerful laser. Another limitation was the restriction to a small sample size. This was required as the change in current measured at an illuminated point has to be significantly larger than the background dark current over the whole electrode, again this situation can be improved by using a more powerful laser and therefore increasing the photocurrent signal.

7.8 FURTHER IMPROVEMENTS

More could still be done to reduce the electrical noise, this includes moving the computer a little further away, due to the restriction of space this was not possible here. The monitor could also be changed for a more modern lower noise model. An industrial monitor encased in an earthed metal case instead of plastic would also be better, another option would be the use of the new flat screen monitor which produce virtually no electrical interference. In addition it may be possible to place the whole apparatus in a room which is a walk in Faraday cage.

Changing the laser to a more powerful one such as a 100 mW laser instead of a 25 mW one would improve the signal to noise ratio. In addition having a second laser (a dual

laser system at the other end of the visible spectrum) where specific wavelengths can be picked out by the use of an appropriate filter can allow reactions to be studied spatially at different wavelengths.

Further improvements to the custom made apparatus would include having the pre-amplifier built into the potentiostat unit. The combined pre-amplifier and potentiostat unit should then be shielded using mu-metal around it. At the moment the pre-amplifier though run on batteries like the potentiostat, is in an aluminium faraday cage without any mu-metal around it. The potentiostat together with the microscope are in a mu-metal lined box but there are very large holes in this to allow the microscope in and out of it.

It was found quite often that one $\mu A\ volt^{-1}$ range selected on the potentiostat only just cut of the top of the signal but the next range was much to wide producing a very dim image so the grey scale has to be narrowed (contrast enhanced) by digital image processing after the image has been saved or a very high preamplifier gain had to be used and using a high gain resulted in the acquisition of background noise on the images. As the potentiostat has output potential monitoring ranges of 0.1, 1, 10, 1000 $\mu A\ volt^{-1}$, it therefore be improved if there were half way values to these as well, allowing a more closer range to be selected for the image to be seen allowing a higher resolution and the preamplifier gain to be kept to a minimum.

7.9 THE ADVANTAGES OF THIS TECHNIQUE OVER OTHERS

The advantages over this technique over other electrochemical methods include the fact that spatial features can be observed unlike in conventional techniques where only one average signal for the whole surface can be observed. Fast speed allows direct monitoring of images allowing imaging of time dependant reactions and the study of the kinetics of these reactions.

This technique is better than other probe techniques as we can scan into the non-electrode (non-conductive) area surrounding the mounted sample allowing the electrochemical behaviour right up to and at the very edge to be monitored, so allowing the electrode as a whole to be monitored. In addition this system allows monitoring of the optical images as well so making it easy to relate on changes in the surface composition to the photocurrents being observed directly.

8. REFERENCES

8. REFERENCES

This chapter lists the references related to the work in this thesis. The references have been listed firstly by subject matter and then secondly by year. Sections A-E cover the basics of photocurrent imaging and the laser spot scanning technique as used for photocurrent and other imaging techniques. Section F is related to the work on p-Si in HCl as given in Chapter 3. Sections G-I relate to the work on gold microbands in $Fe(CN)_6^{4-}$, as given in chapter 4, and include references to the chemistry of the reaction, the effect of the geometry on the electrochemistry and the theoretical aspects of the laser induced temperature rise. Sections J and K are concerned with the properties, types and corrosion of stainless steels as discussed in Chapters 5 and 6 of this thesis.

Journal article references have been listed in the form of :

Reference number. Author, *Journal*, Year, **Volume**, Page numbers, 'Title', Notes

and book references have been typically noted in the form of:

Reference number. Author, 'Book Name', *Publisher*, Year, Notes

The words in the title of the article and any notes on the contents have been written in British (International English) and not American English regardless of spellings in the article concerned.

A. BASICS OF PHOTOELECTROCHEMISTRY

These references include reviews and introductory articles to the concepts involved in photoelectrochemistry and photocurrent generation. In addition to the references listed here general text books in physical chemistry, electrochemistry and solid state physics were also found to be useful.

A-1. R. H. Wilson, *CRC Critical Reviews in Solid State Material Sciences.*, 1980, **10,** 1-41, 'Electron transfer processes at the semiconductor-electrolyte interface' (A Review)

A-2. H. Gerischer, *Surface Science,* 1980, **101,** 518-530, 'Photoassisted interfacial electron transfer' (A Review)

A-3. 'State of the Art Synoposium : Electrochemistry', 1983, **60,** 325-340, 'Photoelectrochemical Energy Conversion' Notes: A book containing a selection of articles reprinted from the journal of chemical education, including the following :-

a) H. O. Finklea, 325-327, 'Photoelectrochemistry: Introductory Concepts'

b) J. A. Turner, 327-329, 'Energetics of the Semiconductor-Electrolyte Interface',
c) M. T. Spitler, 330-332, 'Dye Photooxidation at Semiconductor electrodes : A Corollary to Spectral Sensitisation in Photography',
d) A. B. Ellis, 332-335, 'Excited-State Processes of Relevance to Photoelectrochemistry',
e) M. S. Writon, 335-337, 'Chemically Derivatized Semiconductor Photoelectrodes'

A-4. H.O. Finklea, 'Semiconductor electrodes: studies in physical and theoretical chemistry', Volume: **55**', Editor : H.O. Finklea, *Elsever,* 1988, This is a book containing a series of review articles and papers. See Chapter 1. 'Semiconductor concepts and terminology' pages 1-43.

A-5. N. S. Lewis, *Accounts of Chemical Research,* 1990, **23,** 176-177, 'Mechanistic studies of light-induced charge separation at semiconductor / liquid interfaces'

A-6. H. Gerisher, *Journal of Physical Chemistry,* 1990, **3,** 1677-1699, The impact of semiconductors on the concept of electrochemistry' (A Review Article.)

A-7. L. M. Peter, *Chemical Reviews,* 1990, **90,** 753-769, 'Dynamic aspects of semiconductor photoelectrochemistry'(A review Article.)

A-8. T. E. Mallouk, Nature, 1991, 353, 698-699, 'Bettering natures solar cells'

A-9. A. B. Bocarsly, *Chemistry and Industry,* 1992, **iss 21,** 813-818, 'Photoelectrochemistry : Converting light to electricity and chemicals'

A-10. C. A. Koval, J. N. Howard, *Chemical Reviews,* 1992, **92,** 411-433, 'Electron transfer at semiconductor electrode-liquid electrolyte interfaces'

A-11. H. Yoneyama, *Critical Reviews in Solid State and Material Sciences,* 1993, **18,** 69-111, 'Electrochemical aspects of light-induced heterogeneous reactions on semiconductors' (A Review)

A-12. A. Kumer, W. C. A. Wilisch, N. S. Lewis, *Critical Reviews in Solid State and Materials Sciences,* 1993, **18,** 327-353, 'The electrical properties of semiconductor - metal , semiconductor liquid , and semiconductor conducting polymer contacts'

A-13. M.X. Tan, P.E. Laibinis, S.T. Nguyen, J.M. Kesselman, C.E. Stanton, *Progress in Inorganic Chemistry,* 1994, **41,** 21-144, 'Principles and applications of semiconductor photoelectrochemistry'(A Review)

A-14. K.S.C. Babu, O.N. Srivastava, G.V.S. Rao, *Current Science,* 1994, **66,** 715-729, 'Photoelectrochemical solar-cells - Present status' (A Review)

A-15. S. Licht, *Solar Energy Materials and Solar Cells,* 1995, **38,** 305-319, 'Electrolyte modified photoelectrochemical solar -cells' (A Review)

A-16. A. J. Nozic, R. Memming, *Journal of Physical Chemistry,* 1996, **100,** 13061-13078, 'Physical chemistry of semiconductor-liquid interfaces' (A Review)

A-17. H. J. Lewrenze, *Chemical Society Reviews,* 1997, **26,** 239-246, 'Surface aspects in semiconductor electrochemistry' (A Review)

B. TECHNIQUES AND INSTRUMENTATION

The references in this section have been categorised as follows:

1. Electrochemistry
2. Microscopy
3. Microprobe Imaging
4. Computer Aided Imaging
5. General Instrumental Techniques

1. Electrochemistry

B1-1. J. N. Chazalviel, *Electrochimica Acta,* 1988, **33,** 461-476, 'Experimental techniques for the study of the semiconductor-electrolyte interface' (A Review Article)

B1-2. South Hampton Electrochemistry Group, University of South Hampton, 'Instrumental methods in electrochemistry', *Ellis Horwood,* 1993, (Book)

2. Microscopy

B2-1. T. Wilson, C.J.R. Sheppart, 'Theory and Practice of Scanning Laser Microscopy, *London Academic Press,* 1984, (Book)

B2-2. K. Carlsson, *Journal of Microscopy,* 1989, **157,** 21-27, 'Scanning and detection techniques used in a confocal scanning laser microscope'

B2-3. J. D. Harris, R. D. Grober, J. K. Truatman, E. Betzig, *Applied Spectroscopy,* 1994, **48,** 14A-21A, 'Super Resolution Imaging Spectroscopy', Notes: this includes how to calculate the laser beam spot size.

3. Microprobe Imaging

B3-1. V D. Scott, G. Love, S.J.B. Reed, 'Quantitative electron Probe micro analysis (2nd edition).', *Ellis Horwood Limited,* 1995, (Book)

B3-2. Grayham laws, 'Scanning Electron Microscopy and X- Ray Micro Analysis', *Wiley,* 1987, (Book)

4. Computer Aided Imaging

B4-1. Adrian Law, 'Introduction Computer Vision and Image Processing', *Mc-Graw Hill,* 1991, (Book)

B4-2. J. Russ, 'Computer Assisted Microscopy: Measurement and Analysis of images', *Chapman and Hall,* 1996, (Book)

B4-3. B.Jähn, 'Image Processing for Scientific Applications', *CRC Press,* 1997, (Book)

5. General Instrumental Techniques

B5-1. R.P. Wayne, 'Chemical Instrumentation', *Oxford University Press,* 1994, Notes: This book deals with signal collection, noise reduction and use of computers.

C. LASER SPOT SCANNING IN PHOTOCURRENT IMAGING, VIA PHOTOEXCITATION

The references in this section have been categorised as,

1. Electrochemical Systems (electrode-electrolyte)
2. Solid-State Physics Systems (electroactive electrode-electrode junctions)
3. Microbiological Systems (electrode-living micro-organism in an electrolyte solution)

1. Electrochemical Systems

C1-1. B. A. Parkinson, T. E. Furtak, D. Canfield, K. Kam, G. Kline, *Faraday Discussions,* 1980, **70,** 233-245, 'Evaluation and reduction of efficiency losses at tungsten diselenide photoanodes', Notes: System = n-WSe in 1M KI + 0.1M I_2, laser = pulsed He-Ne.

C1-2. T.E. Furtak, D.C. Canfield, B.A. Parkinson, *Journal of Applied Physics,* 1980, **51,** 6018-6021, 'Scanning light-spot analysis of the carrier collection in liquid-junction solar energy converters', Notes :System = n-WSe in 1M KI + 0.1 M I_2, laser = pulsed He-Ne.

C1-3. M. A. Butler, *Journal of the Electrochemical Society,* 1983, **130,** 2358-2362, 'Localised photoelectrochemical measurements of passive films on titanium', Notes: System = Ti/TiO_2 in Na_2SO_4, laser = pulsed Krypton.

C1-4. M. A. Butler, *Journal of the Electrochemical Society.*, 1984, **131,** 2185-2191, 'Photoelectrochemical imaging', Notes: Examples given = GaP in 0.1 M $HClO_4$ and Ti in Na_2SO_4 , laser = pulsed Krypton

C1-5. G. Vercrusse, W. Rigole, W.P. Gnomes, *Solar Energy Materials,* 1985, **12,** 157-167, 'Exploratory study of polycrystalline n-silicon photoelectrode by the scanning laser spot technique', Notes: System = n-Si in methanolic ferrocene, laser = pulsed Ne-He (0.76 mW, λ = 632.8 nm)

C1-6. A. Praet, G. Vercruysse, W.P. Gnomes, W. M. R. Divigalpititya, S.R. Morrison, *Solar Energy Materials,* 1986, **14,** 61-70, 'The effect of surface damage on photoelectrochemical and metal-insulator-semiconductor silicon solar cells', Notes: System = metal - insulator - semiconductor (MSI) and p-Si in 0.25M NH_4F + 0.1M $K_4Fe(CN)_6$ + 0.01M $K_3Fe(CN)_6$, laser = pulsed He-Ne.

C1-7. D. Shukla, T. Wines, U. Stimming, *Journal of the Electrochemical Society,* 1987, **134,** 2086-2087, 'Photoelectrochemical surface imaging of titanium corroding in 0.5M HBr', Notes : pulsed laser (does not mention laser type)

C1-8. M. R. Kozlowski, P. S. Tyler, W.H. Smyrl, R.T. Atanasoski, *Surface Science,* 1988, **194,** 505-530, 'Photoelectrochemical microscopy of oxide films on metals : Ti/TiO_2 interface', Notes: Ti/TiO_2 in 0.05M H_2SO_4 , laser = pulsed argon ion.

C1-9. P. Carlsson, B. Holmsrom, K. Uosaki, *Finnish Chemical Letters* , 1988, , 52-53, 'Laser spot scanning studies of the photoelectrochemical properties of InSe', Notes: system = InSe in 0.1M K_2SO_4 laser = He-Ne (λ = 632 nm) + optical fibre (diameter = 4μm).

C1-10. P. Carlsson, B. Holmstrom, K. Uosaki, H. Kita, *Applied Physics Letters,* 1988, **53,** 965-967, 'Fibre optical laser spot microscope : A new concept for photoelectrochemical characterisation of semiconductor electrodes', Notes: system = pt treated p-Si , laser = pulsed He-Ne (5mW).

C1-11. R. Peat, A. Riley, D.E. Williams, L. M. Peter, *Journal of the Electrochemical Society,* 1989, **136,** 3352-3355, 'In situ photocurrent imaging of surface heterogeneities during the photocorrosion of n-GaAs at the electrolyte interface', Notes: n-GaAs in 0.1 M KOH + 0.1 M Na_2S + 0.1 M S , laser = continuously scanning He-Cd (λ = 442nm) or He-Ne (λ = 633nm). Schematic diagram for scanning laser microscope system used included.

C1-12. M. Kozlowski, W.H. Smyrl, L. Atanasoska, R. Atanasoski, *Electrochimica Acta* , 1989, **34,** 1763-1768, 'Local film thickness and photoresponse of thin anodic TiO_2 films on polycrystalline titanium', Notes : Ti/TiO_2 in 0.05 M H_2SO_4 , laser λ = 351nm.

C1-13. M.R. Kozlowski, P. S. Tyler, W. H. Smyrl, R. T. Atanasoski, *Corrosion,* 1990, **46,** 505-509, 'photoelectrochemical microscopy on oxide covered metals', Notes: System = Ti/ TiO_2 in 0.05 M H_2SO_4, laser = pulsed Ar^+ .

C1-14. R. Peat, A. Kucernak, D.E. Williams, L.M. Peter, *Semiconductor Science Technology,* 1990, **5,** 914-917, 'Real-time imaging of photoinduced surface reactions using a scanning laser microscope', Notes: n-Si in 1M NH_4F , continuously scanning laser (λ = 632.8 nm).

C1-15. A. R. Kucernak, R. Peat, D. E. Williams, *Journal of the electrochemical Society* , 1991, **138,** 1645-1653, 'A primitive model for evaluating the contrast of photocurrent images obtained at the semiconductor-electrolyte interface', Notes: System = n-Si in 1M NH_4F , laser = continuously scanning (λ = 632.8nm).

C1-16. S. Eriksson, P. Carlsson, B. Holmstrom, K. Uosaki, *Journal of Applied Physics,* 1991, **69,** 2324-2327, 'Laser spot scanning in photoelectrochemical systems, relation between spot size and spatial resolution of the photocurrent', Notes: Mainly theoretical work.

C1-17. D. E. Williams, A. R. J. Kucernak, R. Peat, *Faraday Discussions,* 1992, **94,** , 'Photocurrent imaging of passive metals', Notes: Systems = photovoltage images of Cu electrodes in 0.1M NaCl (+ with and without bezotriazole and photocurrent images of Fe in 0.1M NaOH , laser = He-Ne (λ = 632.8nm, 3mW) or He-Cd (λ = 442nm, 10mW).

C1-18. A. R. J. Kucernak, R. Peat, D. E. Williams, *Journal of the Electrochemical Society,* 1992, **139,** 2337-2340, 'Dissolution and reaction of sulphide inclusions in stainless steel imaged using scanning laser photoelectrochemical microscopy', Notes: System = stainless steel in 0.1M $NaClO_4$, laser = continuously scanning or pulsed (λ = 442 nm).

C1-19. R. Peat, A. R. J. Kucernak, D. E. Williams, *Electrochimica Acta,* 1992, **37,** 933-942, 'Photoelectrochemical imaging of sub-monolayer lead deposits on n- GaAs', Notes: System = n-GaAs in 1M KNO_3 , laser = continuously scanning He-Cd (λ= 442 nm, 10mW) or He-Ne (λ= 633 nm, 3mW) or Ar^+ (λ= 488 nm, 30mW).

C1-20. R. Peat, A. R. J. Kucernak, D. E. Williams, *Faraday Discussions,* 1992, **94,** 369-385, 'Photocurrent distribution across the interfacial region of the n- GaAs / electrolyte junction', Notes: System = n-GaAs in 0.1M KOH + 0.01M Na_2S ,laser = continuous He-Ne (λ =632.8nm).

C1-21. D. E. Williams, A. R. J. Kucernak, R. Peat, *Electrochimica Acta,* 1993, **38,** 57-69, 'Photoelectrochemical imaging-part I. Background and theory', Notes: Step-scan lock in method and the continuous-scan direct detection method. In addition this includes some details on the photothermal imaging as the basis for imaging.

C1-22. D. E. Williams, A. R. J. Kucernak, R. Peat, *Electrochimica Acta*, 1993, **38**, 71-87, 'Photoelectrochemical imaging-part II. The passivating oxide film on iron', Notes: System = Fe/ Fe_3O_4 or αFe_2O_3 in 0.5M Na_2SO_4, laser = continuously scanning He-Cd (λ = 442 nm).

C1-23. R. Peat, A. Kucernak, D.E. Williams, P. M. Koenraad, M. Leys J.H. Wolter, *Electrochimica Acta*, 1994, **39**, 355-361, 'Photoelectrochemistry of silicon-delta-doped GaAs structures', Notes: System = Si-δ-doped GaAs in 1M NaOH + 1m NaS_2 , laser = continuously scanning He-Ne.

C1-24. R. S. Hutton, D. E. Williams, *Electrochimica Acta*, 1994, **39**, 701-709, 'Experimental investigation into the origin of contrast in photocurrent images at the semiconductor / electrolyte interface', Notes: System = n-GaAs in 0.1M KOH, laser = continuously scanning argon ion laser 25mW (of which 10mW at 488nm and 10mW at 514 nm)

C1-25. P. Schmuki, H. Bohni, *Journal of the Electrochemical Society*, 1994, **141**, 362-367, 'Large area photocurrent behaviour and laser spot scanning of passivated stainless steels' Notes: Various stainless steels in 1M Na_2SO_4 , laser = pulsed He-Cd (λ = 325 nm, P= 4mW, UV type).

C1-26. G. Razzini, S. Maffi, G. Mussati, L. P. Bicelli, *Corrosion Science*, 1995, **37**, 1131-1141, 'The scanning photoelectrochemical microscopy of diffusing hydrogen into metals' Notes: System = 304 stainless steel in 0.1M NaOH , laser = pulsed argon ion (λ = 488-515 nm, 25mW).

C1-27. S. Presser, U. Stimming, S. Tokunaga, *Journal of the Electrochemical Society*, 1995, **142**, 102-111, 'The wavelength and potential dependency of spatially resolved photoelectrochemical measurements on TiO_2', Notes: Laser = N_2/Dye laser varying dye varies the wavelength.

C1-28. Z. R. Xiao, Y.Lin, Y.Tang, X.G. Chen, J.K. You, *Applied Surface Science*, 1995, **90**, 321-324, 'Scanned laser spot photocurrent response studies of surface modifications of CdSe thin film electrodes', Notes: System = CdSe thin film in $Fe(CN)_6^{4-}$, laser = pulsed He-Ne (λ = 632.8nm).

C1-29. Y. Yang, X. G. Chen, X. G. Lin, *Electrochimica Acta*, 1996, **41**, 321-327, 'Distribution and laser induced behaviour of lead monooxide on lead electrodes in acid solution' Notes: System = Pb/PbO in 1M H_2SO_4, laser = pulsed Ar^+ (λ = 488nm).

C1-30. P. Salvador, A.M. Chaparro, A. Mir, *Journal of Electroanalytical Chemistry*, 1996, **100**, 760-768, 'Digital imaging of the effect of photoetching on the photoresponse of n-type tungsten diselenide single crystal electrodes', Notes: System = n- $MoSe_2$ and n-WSe_2 electrodes in 0.2M KI , laser = pulsed He-Ne.

C1-31. A.M. Chaparro, P. Salvador, A. Mir , *Journal of Electroanalytical Chemistry,* 1996, **411,** 79-85, 'The scanning microscope for semiconductor characterisation (SMSC): Comparative study on the influence of surface defects on the photoelectrochemical behaviour n-WSe_2 and n-$MoSe_2$ layered compounds', Notes: System = n-$MoSe_2$ and n-WSe_2 in 0.2M KI, laser = pulsed He-Ne.

C1-32. R.S. Hutton, S.N. Port, D.J. Schiffrin, D.E. Williams, *Journal of the Electrochemical Society,* 1996, **418,** 153-158, 'Photocurrent imaging and passivation of silicon in aqueous solutions in KOH', Notes: System = p-Si in 2M NaOH, laser = continuously scanning argon ion (25mW of which 10 mW = 488 nm and 10 mW = 514nm).

C1-33. P.James, N.Casillas, W.H. Smyrl, *Journal of the Electrochemical Society,* 1996, **143,** 3853-3865, 'Simultaneous scanning electrochemical and photoelectrochemical microscopy by use of a metallised optical fibre', Notes: System = Ti/TiO_2 in 1M KBr + 0.05M H_2SO_4, laser = pulsed focussed beam passed down an optical fibre.

C1-34. R.S. Hutton, D.E. Williams, *Journal of the Chemical Society-Faraday Transactions,* 1996, **92,** 4033-4040, 'The Influence of trace impurities on the passivity of iron revealed by photoelectrochemical microscopy' , Notes: System = Fe in 0.1M KOH, laser = continuously scanning argon ion (25mW of which 10 mW = 488 nm and 10 mW = 514nm).

C1-35. D.E. Williams, R.S. Hutton, *Bulletin of Electrochemistry,* 1996, **12,** 121-126, 'Photoelectrochemical imaging : What can you see and what does it mean ?', Notes : Review of various work done and photocurrent imaging via photoelectric and photothermal means.

C1-36. A.M. Chaparro, P. Salvador, A. Mir, *Journal of Electroanalytical Chemistry,* 1997, **422,** 35-44, 'Localised photoelectrochemical etching with micrometric lateral resolution on transition metal diselenide photoelectrodes', Notes: Real videoimages of photoresponce. System = n-$MoSe_2$ and n-WSe_2 + electrolyte.

C1-37. A.M. Chaparro, *Journal of Electroanalytical Chemistry,* 1997, **424,** 153-157, 'The scanning microscope for semiconductor characterisation: photocurrent, photovoltage and electrolyte electroreflectance imaging at the n-$MoSe_2$ / I^- interface'

C1-38. S. Kudelka, J. W. Schultze, *Electrochimica Acta,* 1997, **42,** 2817-2825, 'Photoelectrochemical imaging and microscopic reactivity of oxidised Ti', Note: Looking at Fe^{2+} oxidation and oxygen evolution.

C1-39. D. E. Williams, T. F. Mohiuddin, Y. Y. Zhu *The Journal of the Electrochemical Society,* 1998, **145,** 2264-2672, 'Elucidation of a trigger mechanism for pitting corrosion in stainless steels, using sub μm resolution and photoelectrochemical microscopy', Note: System = 316F stainless

steel (i.e. 316 stainless steel with extra sulphur) in NaCl + $NaClO_4$ solutions. Laser = continuous, scanning, argon ion (25 mW).

2. Solid-State Physics Systems

C2-1. G. Cheek, N. Inoue, S. Goodnick, A. Genis, C. Wilmsen, *Applied Physics Letters,* 1978, **33,** 643-645, 'Fabrication and characterisation of indium tin oxide (ITO) / polycrystalline silicon solar cells', Notes: System = indium tin oxide / polycrystalline silicon solar cells, laser = continuous, scanning He-Ne.

C2-2. C. H. Cheng, B.Merritt, C. W. Tu, K. A. Jones, *Solar Cells,* 1983, **10,** 287-294, 'Scanning light spot scan and electron-beam induced current studies of CdS/Cu_xS solar cells formed on rough and smooth single crystal substrates', Notes: System = CdS/Cu_xS solar cell, laser = He-Ne (λ = 632.8nm).

C2-3. M. Ogura, K. Sakaue, Y. Tokumara, *Japanese Journal of Applied Physics* , 1985, **24,** L616-L617, 'Scanning optical fibre microscope for high resolution laser beam induced current image observation of semiconductor defects', Notes: Systems = Si solar cell or GaAs, laser = Kr or Ar or Nd:YAG (pulsed beam).

C2-4. H. Bleichner, E. Nordlander, G. Fielder, P. A. Tove, *Solid State Electronics,* 1986, **29,** 779-786, 'Flying-spot scanning for the separate mapping of resistivity and minority- carrier lifetime', Note: System = n-Si/SiO_2 , laser = pulsed He-Ne.

C2-5. J. Bajaj, L. O. Bubulac, P. R. Newman, W. E. Tennant, P. M. Raaccah, *Journal of vacuum Science and Technology A.,* 1987, **5,** 3187-3189, 'Spatial mapping of electrically active defects in HgCdTe using a laser beam induced current', Notes: System = HgCdTe p-n junctions, laser = pulsed Ar^+ (λ = 514.5nm)or YAG (λ = 1060nm).

C2-6. J. Bajaj, W. E. Tennant, P.R. Newman, *Journal of vacuum Science and Technology A.,* 1988, **6,** 2757-2759, 'Laser beam induced imaging of surface non-uniformity at the HgCdTe / ZnS interface', Notes: System = HgCdTe / ZnS interface, laser = pulsed (λ = 339nm).

C2-7. H. Bergner, T. Damm, C. Koch, H. Seidel, *Journal of Modern Optics,* 1989, **36,** 1621-1629, 'Optical beam induced currents : investigations of integrated circuits using different excitation wavelengths', Notes: laser sources = a blue line from the argon ion laser (λ = 476 nm, P= 0.025mW), a red line from a He-Ne laser (λ = 633 nm, 0.031mW),a Nd: YAG laser (λ = 1064nm, 0.11mW).The red light has a greater penetration depth than the blue light in silicon. The blue light was used to look at the internal logical levels and the red and infra-red light to look at the depth and location of doped wells.

C2-8. J. Bajaj, W. E. Tennant, *Journal of Crystal Growth,* 1990, **103,** 170-178, 'Remote contact LBIC imaging of defects in semiconductors', Notes: System = p-n junctions of HgCdTe alloy semiconductor, laser system = YAG laser (λ = 1.06μm) via a non-confocal scanning laser microscope.

C2-9. J. Bajaj, W.E. Tennant, R. Zucca, S.J. C. Irvine, *Semiconductor Science and Technology,* 1993, **3,** 872-887, 'Spatially resolved characterisation of HgCdTe materials and devices by scanning laser microscopy', Notes: Review of work with HgCdTe materials and p-n junctions fabricated with these materials. Laser = He-Ne. Non-confocal scanning laser microscope system, real time imaging. with simultaneous reflected light display. Photocurrent, photoluminescence and infra-red imaging.

C2-10. A. C. Ribes, S. Damaskinos, H.F. Tiedje, A.E. Dixon, D.E. Brodie, *Solar Energy Materials and Solar Cells,* 1996, **44,** 439-450, 'Reflected light, photoluminescence and OBIC imaging of solar cells using a confocal scanning laser MACROscope / microscope', Notes: Samples = CdS / CuInSe thin film solar cells, lasers used = HeCd (λ = 442 nm), Ar-Kr (λ = 488, 568, 647 nm), He-Ne (λ = 633 nm) and IR He-Ne (λ = 1150 nm). Photocurrent, photoluminescence and reflected light optical images recorded using a confocal scanning laser microscope (CSLM) system.

3. Microbiological Systems

C3-1. M. Nakao, T. Yoshinubu, H. Iwasaki, *Sensors and Actuators B-Chemical,* 1994, **20,** 119-123, Scanning-laser-beam semiconductor pH imaging sensor' Notes : Calibration curves showing how the photocurrent varies with potential at a particular values of pH were drawn. Then the H^+ distribution of living yeast cells in a glucose containing solution was monitored using a Si- SiO_2-SiN_4 electrode. Yeast cells use glucose to produce lactic acid. A pulsed 10 mW He-Ne laser was used.

C3-2. M. Nakao, T. Yoshinubu, H. Iwasaki, *Japanese Journal of Applied Physics Part 2 - Letters,* 1994, **33,** L394-L397, 'Improvement of a laser-scanning pH imaging sensor' , Notes : Thickness and doping of the Si-wafer was optimised.

C3-3. M. Nakao, S. Inoue, R. Oishi, T. Yoshinubu, H. Iwasaki, *Journal of Fermentation and Bioengineering,* 1995, **79,** 163-166, 'Observation of micro-organisms colonies using a scanning-laser-beam pH sensing microscope', Notes: Yeast and E.coli colonies were examined.

C3-4. S. Inoue, M. Nakao, T. Yoshinubu, H. Iwasaki, *Sensors and Actuators B-Chemical,* 1996, **32,** 23-26, 'Chemical-imaging sensor using enzyme', Notes: an enzyme was immoblised on the sensing surface of the pH-sensor reported previously. A urea-imaging sensor was created using the enzyme urease.

C3-5. M. Nakao, S. Inoue, T. Yoshinubu, H. Iwasaki, *Sensors and Actuators B-Chemical,* 1996, **34,** 234-239, 'High-resolution pH imaging sensor for microscopic observations of micro-organisms', Notes: E.coli colonies examined.

C3-6. T. Yoshinubu, , H. Iwasaki, M. Nakao, S. Nomura, T. Nakanishi, S. Takamatsu, K. Tomita, *Japanese Journal of Applied Physics Part 2 - Letters,* 1998, **37,** L353-L355, Application of chemical imaging sensor to electro-generated pH distribution'

D. LASER SPOT SCANNING IN PHOTOCURRENT IMAGING, VIA PHOTOTHERMAL EFFECTS

See also, references C1-21 (D.E. Williams et al., 1993) and C1-35 (D.E. Williams et al.,1996)

D-1. S. Fujimoto, T. Shibata, T. Shono, *Corrosion Science,* 1991, **32,** 669-672, 'Scanning laser enhanced electrochemical microscopy for characterising localised corrosion', Notes: Focussed infra-red beam (λ = 830 nm, P = 40 mW). Acceleration of surface reactions by surface heating.

D-2. R. S. Hutton, D. E. Williams, *Journal of the Chemical Society. Faraday Transactions,* 1994, **90,** 345-347, 'Photothermal imaging of electrochemical reaction Dynamics', Notes: Continuously scanning Ar-ion laser, reaction = $Fe^{2+}(CN)_6^{4-}$ oxidation at a gold electrode.

D-3. R.S. Hutton, D.E. Williams, *Journal of the American Chemical Society,* 1994, **116,** 3453-3459, 'Photocurrent imaging of the layers formed during the electrooxidation of gold' Notes : Laser = continuous scanning Ag^+ (P = 25 mW). System = Gold electrode in 5mM $K_4Fe(CN)_6$ + 0.1M K_2HPO_4 + 0.1M KH_2PO_4.

D-4. R.S. Hutton, D.E. Williams, R.M. Allen, H.P. Bennetto, C. Meninghaus, *Journal of Electroanalytical Chemistry,* 1995, **391,** 203-205, 'Scanning laser photoelectrochemical microscopy of immobilised glucose oxidase' Notes: System = glucose oxidase on platinised carbon in 20mM glucose + 0.1M K_2HPO_4 + 0.1M KH_2PO_4 , laser = continuously scanning argon ion beam via a confocal scanning laser microscope'

D-5. R.S. Hutton, D.E. Williams, *Analytical Chemistry,* 1995, **67,** 280-282, 'Scanning laser photoelectrochemical microscopy of reaction dynamics at a microelectrode array' Notes: Laser = continuous scanning Ag^+ (P = 25 mW). System = Gold electrode in 5mM $K_4Fe(CN)_6$ + 0.1M K_2HPO_4 + 0.1M KH_2PO_4.

D-6. T.F. Mohiuddin, R.S. Hutton, D.E. Williams, *Electrochimica Acta,* 1996, **41,** 2025-2034, 'Effect of electrode geometry and poisoning on image contrast in photoelectrochemical microscopy'

Notes: Laser = continuous scanning Ag^+ (P = 25 mW). System = Gold electrode in 5mM $K_4Fe(CN)_6$ + 0.1M K_2HPO_4 + 0.1M KH_2PO_4.

E. LASER SPOT SCANNING AS USED IN OTHER (NON-PHOTOCURRENT) IMAGING TECHNIQUES

1. Photovoltage Imaging
2. Photoluminescence Imaging
3. Photoconductance imaging
4. Photoacoustic Imaging

1. Photovoltage Imaging

See also ref. C1-17 (D.E. Williams et al., 1992) and ref. C1-37 (A.M. Chaparro, 1997) for further work on photovoltage imaging.

E1-1. M. Nakao, T. Yoshinobu, H. Iwasaki, *Sensors and Actuators B,* 1994, **20,** 119-123, 'Scanning laser beam-pH imaging sensor', Notes: Photocurrent vs voltage behaviour correlation curves for various pH values. Electrolyte-insulator-semiconductor system with yeast colonies on the insulator-electrolyte interface being imaged by a He-Ne laser from the underneath of the cell across the semiconductor.

E1-2. H. Uchida, W. Y. Zhang, T. Katsube, *Sensors and Actuators B-Chemical,* 1996, **34,** 446-449, 'High speed chemical imaging sensor with digital LAPS system', Notes: 2D surface photovoltage (SPV) imaging using a scanning light spot.

E1-3. H. Uchida, W. Y. Zhang, H. Maekawa, T. Katsube, *Sensors and Materials,* 1997, **9,** 267-278, 'High resolution chemical imaging sensor using a high speed digital SPV measurement system' Notes : A scanning light beam is used to give a scanning photovoltage (SPV) image.

2. Photoluminescence Imaging

E2-1. A. T. Hunter , *Applied Physics Letters,* 1985, **47,** 715-719, 'Spatially resolved luminescence near dislocations in In-alloyed Czochralski-grown GaAs'

E2-2. H. J. Hovel, *IEEE Transactions on Electron Devices,* 1985, **ED-32,** 2331-2338, 'Correlations of photoluminescence with defect densities in semi-insulating gallium arsenide', Note: Kr-Ar laser.

E2-3. S. K. Krawczyk, M. Garrigues, H. Bouredoucen, *Journal of Applied Physics,* 1986, **60,** 392-395, 'Study of InP surface treatments by scanning photoluminescence microscopy', Notes: Argon ion laser.

E2-4. J. Marek, A. G. Elliot, V. Wilke, R. Geiss, *Applied Physics Letters*, 1986, **49**, 1732-1734, 'High resolution scanning photoluminescence characterisation of semi-insulating GaAs using a laser scanning microscope', Notes: A modified scanning laser microscope used. Laser λ = 752 nm, P = 250 mW.

E2-5. L. M. Do, K.J. Kim, T. Zyung, H.K. Shim, J.J. Kim, *Applied Physics Letters*, 1997, **70**, 3470-3472, 'In situ investigation of degradation in polymeric electroluminescent devices using time-resolved confocal laser scanning microscope', Notes: system = polymer layers on indium-tin-oxide electrodes

E2-6. H.L. Robins, D.K. Wickenden, *Applied Physics Letters*, 1997, **71**, 3841-3843, 'Spatially resolved luminescence studies of defects and stress in aluminium gallium nitride films' Notes: Cathodluminescence (CL) imaging and optical microscopy.

3. Photoconductance Imaging

E3-1. G. Mathian, M. Pasquinelli, S. Martinuzzi, *Physica*, 1985, **129B**, 229-233, 'Photoconductance laser spot scanning applied to the study of polysilicon defect passivation', Notes: He-Ne pulsed laser.

4. Photoacoustic Imaging

E4-1. M. Luukkala, A. Penttinen, *Electronics Letters*, 1979, **15**, 325-326, 'Photoacoustic microscope' Notes: Pulsed He-Ne laser (λ = 632.8 nm, P = 5mW).

E4-2. I. J. Cox, C. J. R. Sheppard, *Journal of the Acoustic Society of America*, 1984, **76**, 513-315, 'Imaging in a scanning photoacoustic microscope'

E4-3. R. S. Quimby, *Applied Physics Letters*, 1984, **45**, 1037-1039, 'Real-time photoacoustic microscopy'

E4-4. R. S. Quimby, Z.M. Liu, *Canadian Journal of Physics*, 1986, **64**, 1276-1280, 'Theory of real time photoacoustic microscopy'

E4-5. A. M. Ashurov, U. Madvaliev, V. V. Proklov, *Instruments and Experimental Techniques*, 1988, **31**, 439-442, 'Photoacoustic microscope with optical-scanning'

E4-6. R. Carey, D.F.L. Jenkins, D. M. Newman, B.W.J. Thomas, *Measurement Science and Technology*, 1993, **4**, 488-491, 'Full objective aperture laser scanning for application in an photoacoustic microscope'

E4-7. U. Bernini, P. Mormile, A. Novellino, P. Russo, *Journal of Materials Processing Technology,* 1995, **54,** 181-185, 'Photoacoustic imaging of layered microcircuits for non destructive evaluation of subsurface defects', Notes: Scanning photoacoustic microscopy using a focussed intensity modulated Ar+ laser (488nm, P = 20mW). It was found that changing the laser frequency changes the thermal diffusion length of the heat waves in the sample allowing probing of different layers beneath the sample.

E4-8. R.L. Thomas, L. D. Favro, *MRS Bulletin,* 1996, **21,** 47-52, 'From photoacoustic microscopy to thermal-wave imaging'

some associated papers on photoacoustic spectroscopy :

E4-9a. R. C. Gray, A. J. Bard, *American Chemical Society,* 1978, **50,** 1262-1265, 'Photoacoustic spectroscopy applied to photoinduced gas evolution or consumption'

E4-9b. H. Masuda, A. Fujishima, K. Honda, *Bulletin of the Chemical Society of Japan,* 1980, **53,** 1542-1546, 'In situ measurement of electrode surface change by photoacoustic spectroscopy.

E4-9c. J. K. Dohrmann, U. Sander, H. Streblow, *Zeitschrift für Physikalische Chemi Neue Folge,* 1983, **134,** 43-55, 'In situ studies of the electrode / solution interface by photoacoustic spectroscopy (PAS). PA spectrum and reflectivity of some clean and oxide- covered noble metal electrode', Note: electrode = Cu, Ag, Au or Pt .

F. ELECTROCHEMISTRY OF p-TYPE SILICON IN HCL AND RELATED ARTICLES

These references have been categorised as:

1. General Work on p-Si
2. p-Si in HCl
3. Comparison of p-Si in HCl with Metal-Particle-Coated p-Si in HCl

1. General Work on p-Si

F1-1. H. O. Finklae (editor), ' Semiconductor Electrodes : Studies in Physical and Theoretical Chemistry', *Published by Elsevier,* 1988, **55,** 241-275, Notes: A book containing a series of review articles and papers. See Chapter 5. 'Silicon (Si) and Germanium(Ge)' by N.S. Lewis and A.B. Bocarsly

F1-2. M.J. Madou, B.H. Loo, K.W. Frese, *Surface Science,* 1981, **1,** 135-152, 'Bulk and surface characterisation of the silicon electrode'

F1-3. E. Tomita, N. Matsuda, K. Itaya, *Journal of Vacuum Science and Technology A- Vacuum Surfaces and Films,* 1990, **8,** 534-538, 'Surface electronic-structure of semiconductor (p-Si and n-Si) electrodes in electrolyte solution'

F1-4. P. Demierry, D. Ballutaud, *Journal of the Electrochemical Society,* 1990, **137,** 2966-2973, 'Effect of surface preparations on electrical and chemical surface-properties of p-type silicon'

2. p-Si in HCl

F2-1. J. A. Bardwell, N. Drapper, P. Schmuki, *Journal of Applied Physics,* 1996, **79,** 8761-8769, 'Growth and Characterisation of anodic oxides on Si(100) formed in 0.1M hydrochloric-acid', Notes: Anodic oxidation at room temperature in 0.1M HCl with n-type and p-type substrates. The oxide thickness was found to be weekly dependent on the dopant level for p-type substrates (More doped = more negative/lower value of E_{FB} :0.3V-0.13V for N = 1.7 x 10^{15} - N = 2x10^{18} /cm^{-3} i.e. p-type - p^{+}. A shift in the flat band potential by -59.6 mV per pH unit was shown here.

3. Comparison of p-Si in HCl with Metal-Particle-Coated p-Si in HCl

F3-1. Y. Nakato, H. Yano, S. Nishiura, T. Ueda, H. Tsubmura, *Journal of Electroanalytical Chemistry,* 1987, **228,** 97-108, 'Hydrogen photoevolution at p-type silicon electrode coated with discontinuous metal layers', Notes: Includes work on p-Si in HCl.

F3-2. Y. Nakato, H. Tsubomura, *Electrochimica Acta,* 1992, **37,** 897-907, 'Silicon photoelectrodes modified with ultrafine metal Islands', Notes: Includes work on p-Si in HCl.

F3-3. R. Hinogami, T. Mori, S.J. Yae, Y. Nakato, *Chemistry Letters,* 1994, **Part No:9,** 1725-1728, 'Efficient photoelectrochemical reduction of carbon-dioxide on a p-type silicon (p-Si) electrode modified with very small copper particles', Notes: Here a comparison of particulate-Cu/p-Si to naked p-Si in 1M HCl shows the onset is much more positive in the presence of the Cu particles (V_{onset} with Cu-islands = 0.45V)

F3-4. R. Hinogami, Y. Nakamura, S. Yae, Y. Nakato, *Applied Surface Science,* 1997, **121,** 301-304, 'The modification of semiconductor surface with metal particles for efficient photoelectrochemical reduction of carbon dioxide'

F3-5. R. Hinogami, Y. Nakamura, S. Yae, Y. Nakato, *Journal of Physical Chemistry B,* 1998, **102,** 974-980, 'An approach to ideal semiconductor electrodes for efficient photoelectrochemical reduction of carbon dioxide by modification with small metal particles', Notes: Particles deposited on p-Si Cu, Ag and Au. The hydrogen photoevolution reaction showed the onset potential is much more positive than the naked p-Si on its own (V_{onset} for pure p-Si ~ -0.3Vin 1M HCl).

G. THE $Fe(CN)_6^{4-}$/ $Fe(CN)_6^{3-}$ REACTION ON GOLD

G-1. M.J. Weaver, *Journal of Physical Chemistry,* 1979, **83,** 1748, 'Activation parameters for simple electrode reactions. Application to the elucidation of ion-solvent interactions in the transition state for heterogeneous electron transfer.' Note: E_a = 40 kJ.

G-2. M. Fleischmann, P.R. Graves, J. Robinson, *Journal of Electroanalytical Chemistry and Interfacial Electrochemistry,* 1985, **182,** 87-98, 'The Raman-spectroscopy of the ferricyanide ferrocyanide system at gold, beta-palladium hydride and platinum-electrodes'

G-3. L.A. Curtiss, J.W. Halley, J. Hauatman, N.C. Hung, *Journal of the Electrochemical Society,* 1991, **138,** 2032-2041, 'Temperature-dependence of the heterogeneous ferrous-ferric electron-transfer reaction-rate comparison of experiment and theory', Notes: Ea = 56.8 ± 1.5 KJ from experimental work compared to 30 ± 10 kJ from quantum mechanics calculations or 50 ± 10 kJ from parabolic energy dependence calculations.

G-4. W. A. Badawy, N. H. Helal, *Bulletin de la Societe Cheimique de France,* 1991, **128,** 144-148, 'Kinetic-studies of the ferro-ferri hexacyanoferrate redox couple'

G-5. R. B. Lowry, *Journal of Raman Spectroscopy,* 1991, **22,** 805-809, 'SERS and Fourier-Transform SERS studies Hexacyanaferrate (III) hexacyanoferrate (II) couple on gold electrode surfaces'

G-6. R. B. Lowry, *Spectrochemica Acta :Part A-Molecular Spectroscopy,* 1993, **49,** 831-836, 'Fourier-Transform SERS studies of the chemisorption of ferricyanide'

G-7. J. F. Smally, L. Geng, S.W. Feldberg, *Journal of the Electrochemical Society,* 1993, **356,** 181-200, 'Evidence for adsorption of $Fe(CN)_6^{3-}$ on gold using the indirect laser - induced temperature-jump method'

H. MICROELECTRODES: EFFECTS DUE TO ELECTRODE GEOMETRY IN ELECTROCHEMISTRY

H-1. P. M. Kovach, W.L. Caudill, D.G. Peters, R.M. Rightman, *Journal of Electroanalytical Chemistry,* 1985, **185,** 285-295, 'Faradic electrochemistry at microcylinder, band and tubular electrodes'

H-2. C. A. Amatore, B. Fosset, *Journal of Electroanalytical Chemistry,* 1987, **225,** 33-49, 'Electrochemical kinetics at microelectrodes. Part III equivalency between band and hemicylinder electrodes'

H-3. R. B. Morris, D. J. Franta, H. S. White, *Journal of Physical Chemistry*, 1987, **91**, 3559-3564, 'Electrochemistry at Pt band electrodes of width approaching molecular dimensions. Break down of transport equations at very small electrodes'

H-4. M. Samuelsson, M. Armgarth, C. Nylander, *Analytical Chemistry*, 1991, **63**, 931-936, 'Microstep electrodes : Band ultramicroelectrodes fabricated by photolithography and reactive ion etching'

H-5. M.V. Mirkin, A.J. Bard, *Journal of Electroanalytical Chemistry*, 1992, **323**, 1-27, 'Multidimensional intergral equations. Part 1. A new approach to solving microelectrode diffusion problems'

H-6. M.V. Mirkin, A.J. Bard, *Journal of Electroanalytical Chemistry*, 1992, **323**, 29-51, 'Multidimensional integral equations : a new approach to solving microelectrode diffusion problems. Part 2. Applications to microband electrodes and the scanning electrochemical microscope'

H-7. J. Huangxian, C. Hongyuan, G. Hong, *Journal of Electroanalytical Chemistry*, 1992, **341**, 34-46, 'Investigation on microelectrodes Part XVI. Studying of the shielding effect at a microband - array electrode'

I. LASER INDUCED THERMAL EFFECTS

These references have been categorised as:

1. Electrochemical Work on the Laser Induced Temperature-Jump Method
2. Theoretical Aspects of Thermal Effects Produced at a Surface (by a Continuously Scanning Gaussian Laser Spot)

1. Electrochemical Work on the Laser Induced Temperature-Jump Method

I1-1. V.A. Benderskii, G.I. Velichko, *Journal of Electroanalytical Chemistry and Interfacial Chemistry*, 1982, **140**, 1-22, 'Temperature jump in electric double-layer study. 1.Method of measurements'

I1-2. G.I. Velichko, V.A. Benderskii, *Soviet Electrochemistry*, 1983, **19**, 553-526, 'Temperature-jump investigation of the electric double-layer'

I1-3. G.I. Velichko, V.A. Benderskii, *Soviet Electrochemistry*, 1984, **20**, 316-321, 'Investigation of the electrode solution interface by the temperature-jump method - dilute solutions'

I1-4. V.A. Benderskii, G.I. Velichko, *Journal of Electroanalytical Chemistry and Interfacial Chemistry,* 1984, **181,** 1-20, 'Temperature jump in electric double-layer study. 2. Excess entropy of EDL formation at the interface of mercury and electrolyte-solutions of various concentrations.'

I1-5. V.A. Benderskii, I.O. Efimov, A.G. Krivenko, *Journal of Electroanalytical Chemistry and Interfacial Chemistry,* 1991, **315,** 29-64, 'Short-pulse laser activation of metal electrodes'

I1-6. R. K. Jaworski, *Journal of the Electrochemical Society,* 1993, **140,** 1360-1365, 'Laser-induced transient currents on glassy-carbon electrodes-double-layer and ion adsorption effects'

I1-7. J. F. Smally, L. Geng, S.W. Feldberg, *Journal of the Electrochemical Society,* 1993, **356,** 181-200, 'Evidence for adsorption of $Fe(CN)_6^{3-}$ on gold using the indirect laser - induced temperature-jump method'

I1-8. T. Hinue, R. Harui, T. Izumi, I. Watanabe, H. Watarai, *Analytical Sciences,* 1995, **11,** 1-8, 'Laser induced detection technique in a flow system' Notes: Non-imaging work on the effect of the laser induced temperature rise. Sample = platinum, laser = pulsed Argon ion, solution = $K_4Fe(CN)_6$ + 1M KCl + 5mM KCN or $K_3Fe(CN)_6$ + 1M KCl + 5mM KCN .

2. Theoretical Aspects of Thermal Effects Produced at a Surface
(by a Continuously Scanning Gaussian Laser Spot)

I2-1. H.E. Cline, T.R. Anthony, *Journal of Applied Physics,* 1977, **48,** 3895-3900, 'Heat treating and melting material with a scanning laser or electron beam', Notes: Thermal analysis of a gaussian laser beam moving at a constant velocity.

I2-2. M. Lax, *Journal of Applied Physics,* 1977, **48,** 3919-3924, Temperature rise induced by a laser beam', Notes: Solution of the heat equation given here is further developed in a paper by D.J. Sanders (1984, ref I2-5).

I2-3. J. E. Moody, R. H. Hendel, *Journal of Applied Physics,* 1982, **53,** 4364-4365, 'Temperature profiles induced by a scanning cw laser beam', Note: Gives the equation 'laser intensity = power absorbed + laser spot area'

I2-4. I. Chen, S. Lee, *Journal of Applied Physics,* 1983, **54,** 106-1066, 'Transient temperature profiles in solids heated with a scanning laser'

I2-5. D.J. Sanders, *Applied Optics,* 1984, **23,** 30-35, 'Temperature distributions produced by a scanning gaussian laser beams', Notes: Gives 1. The general solution, 2. The scanning solution for a) the steady state situation and b) the energy density situation (where the scanning speed is

faster than the rate of thermal diffusion), 3. The pulsed solution (where the laser beam is pulsed and not continuous). The equation for thermal diffusivity '$D = K / c_p \rho$' is given here.

I2-6. E. Liarokapis, Y.S. Laptis, *Journal of Applied Physics*, 1985, **57**, 5123-5126, 'Temperature rise induced by a cw laser beam revisited'

I2-7. M.K. El-Adawi, E.F. Elshehawey, *Journal of Applied Physics*, 1986, **60**, 2250-2255, 'Heating a slab induced by a time-dependence laser irradiation – An exact solution'

I2-8. D.C. Skouby, K.F. Jensen, *Journal of Applied Physics*, 1988, **63**, 198-206, 'Modelling of pyrolytic laser-assisted chemical vapour decomposition : Mass transfer and kinetic effects', Note: Time scale for thermal diffusion equation : -'$\lambda_T = (r^2 c_p \rho) + K$' is given here.

I2-9. B.J. Bartholomeusz, *Journal of Applied Physics*, 1988, **64**, 3815-3819, 'Thermal response of a laser irradiated metal slab', Note: Pulsed static laser beam and scanning laser beam examined.

I2-10. T.T. Rantala, J. Levoska, *Journal of Applied Physics*, 1989, **65**, 4475-4479, 'A numerical simulation for the laser-induced temperature distribution'

I2-11. C. Garrido, B. Leon, M. Perez-Amour, *Journal of Applied Physics*, 1991, **69**, 1133-1140, 'A model to calculate the temperature induced by a laser', Note: Time scale for thermal diffusion equation, '$\lambda_T = (r^2 c_p \rho) + K$' , is given here.

I2-12. Y.F. Lu, *Journal of Applied Physics*, 1992, **71**, 3701-3712, 'Heat flow in substrates induced by a scanning laser beam', Notes: Heat flow induced by a scanning laser beam in a semi-infinite substance examined. The equation 'laser intensity = power absorbed + laser spot area' is given here.

I2-13. S.M. Zubair, M.A. Chaudhry, *International Communications in Heat and Mass Transfer*, 1994, **21**, 207-215, 'Temperature solutions due to steady, periodic-type, moving-point heat sources in an infinite medium'

I2-14. G.R.B.E. Romer, J. Meijer, *Optical and Quantum Electronics*, 1995, **27**, 1397-1406, 'Metal-surface temperature-induced by moving laser-beams', Notes: For a stationary beam where I_o = $P \div (\pi r^2)$ the maximum temperature at a metal surface = $T_{max} = I_o R \div \lambda$ is given. The definition of the temperature induced by a moving laser beam is also given.

I2-15. Z. Gertovsky, L. Kelmen, K. Piglmayer, *Applied Surface Science*, 1996, **106**, 422-428, 'Temperature distribution in multilayers covered by a liquid layer and processed by a focussed laser-beam', Notes: Sample = tungsten covered glass slide immersed in water. Laser = Argon-

ion laser. Effects of laser power,focus diameter and scanning speed examined. The greater the focal diameter the water plays an increasing role in the removal of heat from the surface heated. Temperatures calculated for a model focussed circular Gaussian laser beam. Absorbed intensity $I_{o,abs} = P(1-R) + \pi r^2$.

J. PASSIVE FILMS ON STAINLESS STEELS AND RELATED ARTICLES

The references in this section have been categorised as,

1. General Work on Passive Films
2. Structural Analysis of Passive Films on Stainless Steels
3. Electrochemical Analysis of Passive films on Stainless Steels
3. Effect of UV light on the Passive Film on Stainless Steel
4. Passive Films on Iron
5. Passive Films on Chromium

1. General Work on Passive Films

See also reference A-7 (L.M. Peter, 1990)

J1-1. R.C. Newman, H.S. Isaacs, 'Passivity of metals and semiconductors', Editor: M. Froment, *Elsevier, Amsterdam,*, 1983, pg 269

J1-2. L.M.Peter , J. Li, R. Peat, *Journal of Electroanalytical Chemistry and Interfacial Chemistry,* 1984, **165,** 29-40, Surface recombination at semiconductor electrodes 1. 'Transient and steady state photocurrents'

J1-3. U. Stimming, *Electrochimica Acta,* 1986, **31,** 415-429, 'Photoelectrochemical studies of passive films'

J1-4. L.M. Peter, *Berichte der Bunsen Gesellschaft für Phyikalische Chemie,* 1987, **91,** 419-426, 'Photocurrent characterisation of anodic films on metal electrodes'

J1-5. H. Gerischer, *Corrosion Science,* 1990, **31,** 81-88, 'On the interpretation of photoelectrochemical experiments with passive layers on metals'

J1-6. M. Buchler, P. Schmuki, H. Bohni, *Electrochimica Acta,* 1998, **43,** 635-637, 'A light reflectance technique for thickness measurements of passive films'. Note: studies carried out using iron.

2. Structural Analysis of Passive Films on Stainless Steels

J2-1. G. Lorang, M.D. Belo, J.P. Langerton, *Journal of Vacuum Science and Technology A-Vacuum Surfaces and Films,* 1987, **5,** 1213-1219, 'Sputter profiling of passive films in Fe-Cr alloys - A quantitative approach by auger-electron spectroscopy'

J2-2. G. Lorang, F. Basile, M.D. Belo, J.P. Langerton, *Surface and Interface Analysis,* 1988, **12,** 424-428, 'Quantitative auger analysis of passive films formed on stainless-steels'

J2-3. G. Lorang, M.D. Belo, A.M. P. Simoes, M.G.S. Ferreira, *Journal of the Electrochemical Society,* 1994, **141,** 3347-3356, 'Chemical-composition of passive films on AISI-304 stainless-steel', Notes: Effects of potential etc. studied by auger electron spectroscopy.

J2-4. T. Kosaka, S. Suzuki, H. Inoue, M. Saito, Y. Waseda, E. Matsubara, *Applied Surface Science,* 1996, **103,** 55-61, 'XPS/ GIXS Studies of thin oxide-films formed on Fe-Cr Alloys', Notes: This showed the presence of an iron rich oxide in the outer layer and a chromium rich oxide in inner layer.

3. Electrochemical Analysis of Passive Films on Stainless Steels

J3-1. A. Dipaola, F. Diquarto, C. Sunseri, *Corrosion Science,* 1986, **26,** 935-948, 'A photoelectrochemical characterization of passive films on stainless-steels'

J3-2. C. Sunseri, S. Piazza, A. Dipaola, F. Diquarto, *Journal of the Electrochemical Society,* 1987, **134,** 2410-2416, 'A photocurrent spectroscopic investigation of passive films on ferritic stainless-steels'

J3-3. A. Dipaola, *Electrochimica Acta,* 1989, **34,** 203-210, 'Semiconducting properties of passive films on stainless-steels'

J3-4. A.D. Paola, *Corrosion Science,* 1990, **31,** 739-744, 'Study of passive films on stainless-steels by photocurrent measurements'

J3-5. A.M.P. Simoes, M.G.S. Lorang, M.B. Belo, *Journal of the Electrochemical society,* 1990, **137,** 82-87,' Study of passive films formed on AISI 304 stainless-steel by impedance measurements and photoelectrochemistry'

J3-6. A. Dipaola, D. Shulka, U. Stimming, *Electrochimica Acta,* 1991, **36,** 345-351, 'Photoelectrochemical study of passive films on stainless-steel in neutral solutions'

J3-7. N.E. Hakiki, B. Rondot, M.D. Belo, *Comptes Rendus de l'Academie des Sciences Serie II ,* 1993, **317,** 457-462, 'Electronic-structure of passive films formed on austentic stainless steel Cr-17-Ni-8', Notes: Capacitance vs potential measurements. (See also J3-9).

J3-8. R. Babic, M. Metikoshukovic, *Journal of Electroanalytical Chemistry,* 1993, **358,** 143-160, 'Semiconducting properties of passive films on AISI-304 and AISI-316 stainless steels'. Note: studied in near neutral 0.5M NaCl solutions.

J3-9. N.E. Hakiki, S. Boudin, B. Rondot, M.D. Belo, *Corrosion Science,* 1995, **37,** 1809-1822, 'The electronic-structure of passive films formed on stainless-steels'

J3-10. P. Schmi, M. Buchler, S. Virtaten, H. Bohni, R. Muller, L.J. Gaukler, *Journal of the Electrochemical Society,* 1995, **142,** 3336-3342, 'Bulk-metal oxides as a model for the electronic-properties of passive films.' Note: looking at electronic properties of natural passive films on iron and chromium with sintered bulk metal oxides.

J3-11. T.B. Du, S.H. Chen, M.Z. Yang, L. Chen, *Journal of Materials Science and Technology,* 1996, **12,** 381-384, 'Photoelectrochemical study of passive films on sensitized stainless-steel'

J3-12. L.J. Oblongsky, M.P. Ryan, H.S. Isaccs, *Journal of the Electrochemical Society,* 1998, **145,** 1922-1932, 'In situ determination of surface films formed on Fe-Cr alloys'

J3-13. Q. LeXuan, B. Rondot, M.D. Belo, *Annales de Chime-Sciences des Materiaux,* 1998, **23,** 607-615, 'Relationship between the electronic structure of passive films and susceptibility to pitting corrosion of stainless steels', Notes: C^{-2} vs E curves given.

4. Effect of UV Light on the Passive Film on Stainless Steel

J4-1. C. B. Breslin, D. D. Macdonald, J. Sikora, E. Sikora, *Electrochimica Acta*, 1997, **42,** 127-136, 'Influence of UV light on the passive behaviour of SS316- effect prior illumination'

J4-2. C. B. Breslin, D. D. Macdonald, J. Sikora, E. Sikora, *Electrochimica Acta,* 1997, **42,** 137-144, 'Photo-inhibition of pitting corrosion on types 304 and 316 stainless steels in chloride containing solutions'

5. Passive Films on Iron

See also reference C1-22 (D.E. Williams et al., Electrochimica Acta, 1993)

J5-1. R. Peat, L.M. Peter, *Journal of Electroanalytical Chemistry and Interfacial Electrochemistry,* 1987, **228,** 351-364, 'A study of the passive film on iron by intensity modulated photocurrent spectroscopy'

J5-2. P.C. Searson, R.M. Latanison, U. Stimming, *Journal of the Electrochemical Society,* 1988, **135,** 1358-1363, 'Analysis of the photoelectrochemical response of the passive film on iron in neutral solutions,

J5-3. K. Azumi, T. Ohtsuka, N. Sato, *Corrosion Science,* 1990, **31,** 715-720, 'An analysis of transient photocurrents measured on passivated iron electrodes'

J5-4. P. Schumi, H. Bohni, *Electrochimica Acta,* 1995, **40,** 775-783, 'Illumination effects on the stability of the passive film on iron'

6. Passive Films on Chromium

J6-1. F. Diquarto, S. Piazza, C. Sunseri, *Corrosion Science,* 1990, **31,** 721-726, 'A photocurrent spectroscopic investigation of passive films on chromium'

J6-2. C. Sunseri, S. Piazza, F. Diquarto, *Journal of the Electrochemical Society,* 1990, **137,** 2411-2417, 'Photocurrent spectroscopic investigations of passive films on chromium'

K. STAINLESS STEEL AND CORROSION

The references in this section have been categorised as,

1. General Review Articles / Texts on Corrosion
2. Effects of Varying the Stainless Steel Composition
3. Pitting Corrosion at Sulphide Enriched Inclusions
4. Crevice Corrosion
5. Electrochemistry at Various Metal Sulphide Electrodes
6. Corrosion Resistance / Reduction Measures

1. General Review Articles/ Texts on Corrosion

K1-1. K. R. Tretheway, J. Chamberlain, 'Corrosion for Science and Engineering', *Longman,* 1995, Notes: This book has two relevant chapters , Chapter 4: 'Theory of aqueous corrosion', and Chapter 7 : 'Crevice and Pitting Corrosion'.

K1-2. C.S. Brossia, R.G. Kelly, , 'Critical factors in localised corrosion 2', Editors: P.M. Natisham, , R.G. Kelly, G.S. Frankel, R.C. Newman , *The Electrochemical Society, Pennington NJ, Proceedings,* vol 95-15, 1995

K1-3. G.H. Kelsall, Q.Yin, D.J. Vaughn, 'Int. Symp. on electrochemistry in mineral and materials processing IV' , Editors : R. Woods, P.E. Richardson, F.M. Doyle, *The Electrochemical Society, Pennington NJ, Proceedings,* vol 96-6, 1995, pages 131-142

K1-4. A.J. Sedriks, 'Corrosion of Stainless Steels' 2nd Edition, *John Wiley and Sons Inc.,* 1996, (Book)

2. Effects of Varying the Stainless Steel Composition

K2-1. Y. H. Yau, M.A. Streicher, *Corrosion,* 1991, **47,** 352-358, 'The effect of chromium content (0 to 35%) in Fe-Cr alloys on corrosion rates and mechanisms in 1.0N sulphuric acid'

K2-2. Y. M. Kolotyrkin, L.I. Freiman, I.I. Reformatskaya, E.A. Panshin, *Protection of Metals,* 1994, **30,** 391-400, 'The mechanism for increasing pitting resistance of stainless steels by the addition of molybdenum'

K2-3. M. Kraak, H. Boehni, W. Muster, J. Patscheider, *Surface and Coatings Technolology*, 1994, **68/69**, 541- 545, 'Influence of molybdenum on the corrosion properties of stainless steel films'

3. Pitting Corrosion at Sulphide Enriched Inclusions

See also references C1-18, C1-25, C1-39 and D-1 for work on photoelectrochemical imaging

K3-1. I.L. Rosenfeld, I.S. Danilov, *Corrosion Science*, 1967, **7**, 129-142, 'Electrochemical aspects of pitting corrosion', Notes: Here it was suggested that pitting was a special form of crevice corrosion.

K3-2. G. Wraglen, *Corrosion Science*, 1974, **14**, 331-349, 'Pitting and sulphide inclusions in stainless steel'

K3-3. R. C. Newman, H.S. Isaacs, B. Alman, *Corrosion*, 1982, **38**, 261-265, 'Effects of sulphur compounds on the pitting behaviour of type 304 stainless-steel in near neutral chloride solutions'

K3-4. D.E. Williams, C. Westcott, M. Fleischmann, *Journal of the Electroanalytical and Interfacial Electrochemistry*, 1984, **180**, 549-564, 'Initiation of pitting corrosion on stainless steels'

K3-5. D.E. Williams, C. Westcott, M. Fleischmann, *Journal of the Electrochemical Society*, 1985, **132**, 1796-1804, 'Stochastic-models of pitting corrosion of stainless-steels. 1. Modelling of the initiation and growth of pits at constant potential'

K3-6. D.E. Williams, C. Westcott, M. Fleischmann, *Journal of the Electrochemical Society*, 1985, **132**, 1804-1811, 'Stochastic-models of pitting corrosion of stainless-steels. 2. Measurement and interpretation of data at constant potential'

K3-7. R.C. Newman, W. P. Wong, H. Ezuber, A. Garner, *Corrosion*, 1989, **45**, 282-287, 'Pitting of stainless steels by thiosulphate ions'

K3-8. J.E. Castle, R. Ke, *Corrosion Science*, 1990, **30**, 409-438, 'Studies by auger spectroscopy of pit initiation at the sight of inclusions of stainless steel'

K3-9. A.M. Riley, D.B. Wells, D.E. Williams, *Corrosion Science*, 1991, **32**, 1307-1313, 'Initiation of events for the pitting corrosion of stainless steel'

K3-10. E.R. Schiapparelli, S.P. Cáceres, *Journal of Materials Science*, 1991, **26**, 1454-1458, 'Effect of the direction of inclusions on the tested surface on susceptibility to pitting and corrosion in stainless steel'

K3-11. R.D. Knutsen, A. Ball, *Corrosion*, 1991, **47**, 359-368, 'The influence of inclusions on the corrosion behaviour of a 12 Wt% chromium steel'

K3-12. J. Stewart, D.E. Williams, *Corrosion Science*, 1992, **33**, 457-474, 'The initiating of pitting corrosion on austenitic stainless steel : on the role and importance of sulphide inclusions'

K3-13. P. C. Pistorius, G.T. Burstein, *Philosophical Transactions Royal Society London (A)*, 1992, **341**, 531-559, 'Metastable pitting corrosion of stainless steel and the transition to stability' (A review)

K3-14. G.T. Burstein, S.P. Mattin, *Philosophical Magazine Letters*, 1992, **66**, 127-131, 'Nucleation of corrosion pits on stainless steel'

K3-15. P.C. Pistorius, G.T. Burstein, *Corrosion Science*, 1992, **33**, 1885-1897, 'Growth of corrosion pits on stainless steel in chloride solution containing dilute sulphate'

K3-16. R. Ke, R. Alkire, *Journal of the Electrochemical Society*, 1992, **139**, 1573-1580, 'Surface analysis of corrosion pits initiated at MnS inclusions in 304 stainless steel', Notes: This discusses the involvement of thiosulphate in pitting initiation. See also references K4-5, K4-6 and K4-7)

K3-17. A. U. Malik, P.C.M. Kutty, N.A. Siddiqi, I.N. Andijani, S. Ahamed, *Corrosion Science*, 1992, **33**, 1809-1827, 'The influence of pH and chloride concentration on the corrosion behaviour of AISI 316L steel in aqueous solutions', Notes: This work investigated pitting corrosion.

K3-18. M.A. Baker, J.E. Castle, *Corrosion Science*, 1993, **34**, 667-680, 'The initiating of pitting corrosion at MnS inclusions', Notes: This work showed that an MnCl stain developed around the edges of the corrosion site.

K3-19. G.T. Burstein, P.C. Pistorius, S.P. Mattin, *Corrosion Science*, 1993, **35**, 57-62, 'The nucleation and growth of corrosion pits on stainless steels'

K3-20. D.E. Williams, J. Stewart, P.H. Balkwill, *Corrosion Science*, 1994, **36**, 1213-1235, 'The nucleation, growth and stability of micropits in stainless steel'

K3-21. P.C. Pistorius, G.T. Burstein, *Corrosion Science*, 1994, **36**, 525-538, 'Aspects of the effects of the electrolyte composition on the occurrence of metastable pitting in stainless steel'

K3-22. R.M. Rynders, C.H. Paik, R. Ke, R.C. Alkire , *Journal of the Electrochemical society*, 1994, **141**, 1439-1445, 'The use of in-situ atomic-force microscopy to image corrosion at inclusions'

Notes: study of corrosion at sulphide inclusions in 0.6M NaCl. Deposits seen around the inclusion surface of a size up to 4 times that of the inclusion size'

K3-23. L. Ahuka-Shamba, Y. Roques, *Le Revue de Métallurgie CIT,* 1994, , 1826-1833, 'Statistical study of pitting corrosion on resulpurised AISI 303 stainless steel in NaCl solutions by digital image analysis'

K3-24. Y. Sugie, T. Motooka, S. Fujii, *Corrosion Science,* 1994, **50,** 513-515, 'Early growth of single pits in week acidic chloride media and anion effects on solubility of salt in the pit anolyte'

K3-25. D.O. Wipf, *Colloids and Surfaces,* 1994, **93,** 251-261, 'Initiation and study of localised corrosion by scanning electrochemical microscopy'

K3-26. E.A. Abd-EL-Meguid, V.K. Gouda, N.A. Mahmoud, *Materials Transactions,* 1994, **35,** 699-702, 'Pitting corrosion behaviour of type SUS904L and SUS316L stainless steels on chloride solutions'

K3-27. G.T. Burstein, P.C. Pistorius, *Corrosion Science,* 1995, **51,** 380-385, 'Surface roughness and the metastable pitting of stainless steel in chloride solutions'

K3-28. R. Ke, R. Alkire, *Journal of the Electrochemical Society,* 1995, **142,** 4056-4062, 'Initiation of corrosion pits at inclusions on 304 stainless steels'

K3-29. N. J. E. Dowling, C. Duret-Thual, G. Auclair, J.P. Audouard, P.Combrade, *Corrosion Science,* 1995, **51,** 343-355, 'Effects of complex inclusions on pit initiation in 18% chromium - 8% nickel stainless steel types 303, 304, and 321'

K3-30. T. Hong, M. Nagumo, *Corrosion Science,* 1997, **39,** 285-293, 'The effect of chloride concentration on the early stages of pitting for type 304 stainless steel'

K3-31. I. Annergren, D.Thierry, F. Zou, *Journal of the Electrochemical Society* , 1997, **144,** 1208-1215, 'Localised electrochemical impedance spectroscopy for studying pitting corrosion on stainless steels', Notes: Impedance spectra recorded at active and passive sites on the stainless steel simultaneously.

K3-32. T. Suter, H. Böhni, *Electrochimica Acta,* 1997, **42,** 3275-3280, 'A new microelectrochemical method to study pit initiation on stainless steels', Notes: Micro-capillaries were used as micro-cells. MnS inclusions were found to dissolve even in Cl^- free solutions but stable pit growth only occurred in the presence of Cl^-.

K3-33. J.O. Park, M. Verhoff, R. Alikire, *Electrochimica Acta*, 1997, **42**, 3281-3291, 'The effect of chloride concentration on early stages of pitting for type 304 stainless steel revealed by the AC impedance method', Notes: A relationship between the minimum chloride concentration at a particular potential required to metastable propagation has been given as E in mV vs SCE = -37 log[Cl^-] -212

K3-34. S. P. Mattin, G.T. Burstein, *Philosophical Magazine Letters*, 1997, **76**, 341-347, 'Detailed resolution of microscopic depassivation events on stainless steel in chloride solution leading to pitting', Notes: Nucleation of corrosion pits in chloride.

K3-35. C. Duret-Thual, D. Costa, W.P. Yang, P. Marcus, *Corrosion Science*, 1997, **39**, 913-933, 'The role of thiosulphates in the pitting corrosion of Fe-17Cr alloys in neutral chloride solution: Electrochemical an XPS study', Notes: Work was carried out in a 0.02M NaCl solution containing $S_2O_3^{2-}$, this showed that the thiosulphates are reduced on the metallic surface whereas they do not interact strongly with the passive film. Sulphide islands were formed at the bare alloy surface and prevent repassivation.

K3-36. Y.Y. Zhu, D.E. Williams, *Journal of the electrochemical society*, 1997, **144**, L43-L45, 'Scanning electrochemical microscopic observation of a precursor state to pitting corrosion of stainless steel'

K3-37. P. Ernst, N.J. Laycock, M.H. Moayed, R.C. Newman, *Corrosion Science*, 1997, **39**, 1133-1136, 'The mechanism of lacy cover formation in pitting'

K3-38. N.J. Laycock, S.P. White, J.S. Noh, P.T. Wilson, R.C. Newman, *Journal of the Electrochemical Society*, 1998, **145**, 1101-1108, 'Perforated covers for propagating pits'

K3-39. C.J. Lin, J. L. Luo, J.L Luo, X. D. Zhuo, Z. Y. Tian, *Corrosion*, 1998, **54**, 265-270, 'Scanning microelectrode studies of early pitting corrosion of 18/8 stainless steel'

4. Crevice Corrosion

K4-1. H.W. Pickering, R.P. Frakenthal, *Journal of the Electrochemical Society*, 1972, **119**, 1297, Notes: This gives the mechanism for the 'IR drop model' of crevice corrosion.

K4-2. H.W. Pickering, R.P. Frakenthal, *Journal of the Electrochemical Society*, 1972, **119**, 1304, Notes: This gives the mechanism for the 'IR drop model' of crevice corrosion.

K4-3. J.W. Oldfield, W.H. Sutton, *British Corrosion Journal*, 1978, **13**, 13-22, 'Crevice corrosion of stainless steels. A mathematical model.', Notes: This gives the mechanism for the 'passive dissoluion model' of crevice corrosion.

K4-4. J.W. Oldfield, W.H. Sutton, *British Corrosion Journal*, 1978, **13,** 104-111, 'Crevice corrosion of stainless steels. II.Experimental studies.', Notes: This gives the mechanism for the 'passive dissoluion model' of crevice corrosion.

K4-5. S.E. Lott, R.C. Alkire, *Corrosion Science*, 1988, **28,** 479-484, 'The variation of solution composition during the initiation of crevice corrosion on stainless-steel' Notes: This describes how thiosulphate (see also refs. K4-6, K4-7 and K3-15) plays an important part of crevice initiation.

K4-6. S.E. Lott, R.C. Alkire, *Journal of the Electrochemical Society*, 1989, **136,** 973-979, The variation of solution composition during the initiation of crevice corrosion on stainless-steel. 1. Experimental studies'

K4-7. S.E. Lott, R.C. Alkire, *Journal of the electrochemical society*, 1989, **136,** 3256-3262, The role of inclusions on initiation of crevice corrosion of stainless-steel. 2. Theoretical-studies.

K4-8. L. Stockert, H. Boehni, *Materials Science Forum*, 1989, **44/45,** 313-328, 'Susceptibility to crevice corrosion and metastable pitting of stainless steels'

K4-9. B. K. Nash, R.G. Kelly, *Corrosion Science*, 1993, **35,** 817-825, 'Characterisation of the crevice solution chemistry of 304 stainless steel'

K4-10. G.S. Frankel, R.C Newman (editors), 'Critical Factors in Localised Corrosion', *Published by the Electrochemical Society, Pennington, NJ, USA*, 1992, Notes: See article by K. Cho and H.W. Pickering, starting at page 407.

K4-11. M. Suleiman, I.Raguault, R.C. Newman, *Corrosion Science*, 1994, **36,** 479-486, 'The pitting of stainless steel under a rust membrane at very low potentials'

K4-12. P.M. Natishan, R.G. Kelly, G.S. Frankel, R.C Newman (editors), 'Critical Factors in Localised Corrosion II', *Published by the Electrochemical Society, Pennington, NJ, USA*, 1995, Notes: See article by CS. Brossia and R.G. Kelly, starting at page 201.

K4-13. N.J. Laycock, J. Stewart, R.C. Newman, *Corrosion Science*, 1997, **39,** 1791-1809, 'The initiation of crevice corrosion in stainless steels', Notes: Various models for crevice corrosion are noted here.

K4-14. CS. Brossia, R.G. Kelly, *Corrosion*, 1998, **54,** 145-154, 'Influence of alloy sulphur content and bulk electrolyte composition on crevice corrosion initiation of austenitic stainless steel', Notes: sulphide was the only dissolved sulphur species detected during initiation, with sulphite

appearing only in the propagation stage after long times due to homogeneous oxidation of sulphide within the crevice.

5. Electrochemistry at Various Metal Sulphide Electrodes

K5-1. G. S. Eklund, *Journal of the Electrochemical Society*, 1974, **121**, 467-473, 'Initiation of pitting at sulphide inclusions at stainless steel' Notes: chemistry of an MnS electrode in 0.1M NaCl is discussed, as well a possible mechanism for sulphide dissolution. Spheres of elemental sulphur were seen at the MnS electrode when it was polarised at +200 mV vs SCE.

K5-2. H. Keller, H.J. Grabke, H.P. Stoppa, *Werkstoffe und Korrosion-Materials and Corrosion*, 1981, **32**, 275-281, 'Chemical and electrochemical reactions of iron sulphide and manganese sulphide in acid and neutral solutions'

K5-3. A. Ennaoui, S. Fiechter, W. Jaegermann, H. Tributsch, *Journal of the Electrochemical Society*, 1986, **133**, 97-106, 'Photoelectrochemistry of highly quantum effiecient single-crystalline n-FeS_2 (pyrite)'

K5-4. K.K. Mishra, K. Osseo-Asare, *The Journal of the Electrochemical Society*, 1988, **135**, 2505-2509, 'Aspects of interfacial electrochemistry of semiconductor pyrite (FeS_2)'

K5-5. H.W. Nesbitt, I.J. Muir, *Geochimica et Cosmochimica Acta*, 1994, **58**, 4667-4679, 'X-ray photoelectron spectroscopic study of a pristine pyrite surface reacted with water-vapour and air'

K5-6. Y. Su, M.A.A. Schoonen , *Geochimica et Cosmochimica Acta*, 1995, **59**, 4605-4622, The Stability of thiosulphate in the presence of pyrite in low-temperature aqueous-solutions'

K5-7. D.J. Vaughan, K.E.R. England, G.H. Kellsall, , *American Mineralogist*, 1995, **80**, 725-731, Electrochemical oxidation of chalopyrite ($CuFeS_2$) and the related metal-enriched derivatives $Cu_4Fe_5S_8$, $Cu_9Fe_9S_{16}$ and $Cu_9Fe_8S_{16}$', Notes: Oxidation in 0.3M NaCl

K5-8. G. Wittstock, I. Kartio, D. Hirsch, S. Kunze, R. Szargan, *Langmuir*, 1996, **12**, 5709-5721, 'Oxidation of Galena in acetate buffer investigated by atomic force microscopy and photoelectron-spectroscopy', Notes: dissolution of PbS to Pb(II) and hydrosulphide ions. The hydrosulphide ions then undergo oxidation to elemental sulphur.

K5-9. R.A.D. Pattrick, J.F.W. Mosselmans, J.M. Charnock, K.E.R. England, G.H. Helz, C.D. Garner, D.J. Vaughan, *Geochimica et Cosmochimicha*, 1997, **61**, 2023-2036, 'The structure of amorpphous copper sulphide precipitates: An X-ray absorption study'

K5-10. I. Kartio, G. Wittstock, K. Laajalehto, D. Hirsch, J. Simola, T. Laiho, R. Szargan, E. Suoninen, *International Journal of Mineral Processing,* 1997, **51,** 293-301, 'Detection of elemental sulphur on galena oxidised in acidic solution', Notes: AFM images showed that oxidation of galena (PbS) resulted in elemental sulphur being deposited as local accumulations rather than as a uniform layer.

K5-11. D. Wei, K. Osseo-Asare, *The Journal of the Electrochemical Society,* 1997, **144,** 546-553, 'Semiconductor electrochemistry of particular pyrite. Mechanisms and products of dissolution', Notes: Here pyrite particles were used as metal electrodes.

6. Corrosion Resistance / Reduction Measures

K6-1. Q.Y. Pan, W.D. Huang, R.G. Song, Y.H. Zhou, G.L. Zang , *Surface and Coatings Technology,* 1998, **102,** 245-255, 'The improvement of localised corrosion resistance in sensitised stainless steel by laser surface remelting'

K6-2. M.H. Moayed, R.C. Newman, *Corrosion Science,* 1998, **40,** 519-522, 'Aggressive effects of pitting inhibitors on highly alloyed stainless steels', Notes: addition of 0.5M Na_2SO_4 to 1M NaCl inhibits pitting on type 904L stainless steel. In the presence of the inhibitor the enhanced passivation reduces the porosity of the lacy pit cover and helps to retain its local environment'

APPENDICES

APPENDICES

The appendices given here include further details of the experimental method, as well as technical drawings illustrating the construction of the custom made apparatus, lists of the apparatus used, as well as contact addresses for suppliers, and a summary of experimental parameters used. This information has been categorised as follows:

CONTENTS OF THE APPENDICES

Appendix C.

Appendix D.

Appendix E.

Appendix F.

A. LIST OF APPARATUS

A. LIST OF APPARATUS

1. For Electrode Preparation / Use

Silver conductive paint

Conductive silver epoxy

Indium foil, 99.99% pure, Aldrich

Gallium, 99.99% pure, Aldrich

Epoxy resin (Araldite® or Epokwick®)

Permabond SIP (self indicating) primer for epoxy resins

Working electrode mounting cup made of Kel-F

Digital multimeter

Platinum wire-counter electrode, 99.99% pure, 0.5mm diameter
(Advent Research Materials Ltd.)

Reference electrode (SCE): Saturated Calomel Electrode- Hg/Hg_2Cl_2 in sat KCl

Reference electrode (SSE): Hg/Hg_2SO_4 in sat K_2SO_4

Gold wire, 500 μm diameter wire

Gold foil

Screen printed commercial gold microband electrodes

Glass slide (to plate gold)

Gold sputtering machine

Silicon memory chip (256 K EPROM)

p-Type silicon

304L stainless steel, 250 μm diameter wire (Advent Reasearch Materials Ltd.)

316F stainless steel, disc (The Bureau of Analysed Samples Ltd.)

2. For Electrode Polishing

Emery paper- various grades

Diamond polishing wheel

Aluminium oxide polishing papers:

60 μm white, 30 μm green, 9 μm blue, 3 μm pink, 1 μm light green, 0.3 μm grey (Agar Scientific)

Diamond Polishing Pastes:

25 μm brick-red, 14 μm brown, 6 μm yellow, 3 μm green, 1 μm blue, ½ μm grey (Kemet International)

Lubricant Spray for diamond polishing pastes

Alumina Polishing Pastes: 1 μm, 0.3 μm, 0.05 μm

3. For Solution Preparation

Purified water: Triple distilled water or Milli-Q Plus)

Dipotassium hydrogen phosphate (Fluka) microselect grade

Potassium dihydrogen phosphate (Fluka) microselect grade

Potassium hexacyanoferrate (II) trihydrate,

(potassium ferrocyanide) microselect grade > 99.5% (Fluka)

Potassium hexacyanoferrate (III),

(potassium ferricyanide) microselect grade > 99% (Fluka)

HCl (BDH) AnalaR

Sodium perchlorate (BDH) AnalaR

Sodium chloride (BDH) AnalaR

4. Other Solvent Used, for Cleaning etc.

Acetone (BDH) AnalaR

Ethanol (BDH) AnalaR

Nitric Acid (BDH)

5. Apparatus for Water Purification

Aquatron filter and deioniser set
Single distilled water still
Millipore Q185-plus water purification system

6. Instruments for Cyclic Voltammetry and Total Current Measurements

PTFE (teflon®) cell unit
Potentiostat
Waveform generator model PPRI (Hightek Instruments, England)
xyt-Chart recorder, model PM8271 (Philips)
Coaxial cables
12 Bit data logging device model, ADC-100 and computer software (Picotechnology Ltd.)

7. Further Instrumentation for Laser Scanning Experiments

Laser scanning confocal imaging system-
model MRC-600 (Bio Rad) including :
486 P.C., associated software, microscope, argon ion laser- max. power 25 mW
(Several lines are emitted simultaneously. The 2 principle lines are a blue line at 488 nm and a green line at 514 nm with about 10 mW in each of these 2 lines.)
Glass slides / coverslips
Oscilloscope
Amplifier
Offset (black level) box
Neutral density filters

8. Instruments for Noise Reduction

Mu-metal (for lining faraday cages)

NiCd Batteries

Faraday cages-

1. around the cell,
2. around the cell and mini-faraday cage, potentiostat and microscope,
3. around the offset box and preamplifier

Shielded cables (coaxial) with BNC connectors for general instrument to instrument connection, and attached to reference electrodes.

RFI / EMI filtering socket adapters (13A) for plugging mains (non-battery) powered equipment into.

Anti-vibration floating table for scanning laser microscope

9. Instruments for Light Microscope Imaging

Microscope, Manufacturer Carlzeiss

JVC CCD colour video camera (TK-1085E)

Sony Colour Video printer (UP-2200P)

10. Instruments for X-ray Analysis Work

Electron microprobe X ray analysis system:-

Jeol Super Probe (JXA-8600) Electron Probe X-ray microanalyser: including optical microscope, backscattered electron detector, scanning electron microscope system, wavelength dispersive spectrometer for detection with the following analysing crystals, PET (Pentaerythritol), LIF (Lithium fluoride), TAP (Thallium acid Phthalate), STE (Lead Stearate) and associated computer system.

11. Instruments For Calibration Purposes

Of microscopes-

Diamond ruled stage micrometer for reflected light with no coverslip over rulings (Agar Scientific)

Stage micrometer 0.1 mm scale in glass disc mounted in metal slide (Agar Scientific)

Of laser intensity-

Laser power meter

Of neutral density filters-

Lambda-5 UV-visible spectrophotometer

Of the microprobe-

A variety of metal standards of known composition

B. SUMMARY OF SYMBOLS AND EQUATIONS

B. SUMMARY OF SYMBOLS AND EQUATIONS

The symbols and equations, used in this thesis, together with the most typically used units have been listed here:

1. Microscopy and Optical Parameters
2. Thermal Parameters
3. Geometry and Mass
4. Current and Potential
5. Time and Velocity
6. Laser Power / Intensity
7. Energy Levels
8. Diffusion Equations: for electrochemical equations
9. Nernst Equation: for the equilibrium (reversible) potential
10. Butler Volmer equation: for the electrode kinetics
11. Gärtner Equation: for photocurrent generation in semiconductors
12. The Mott-Scottky Equation: for calculating the flat band potential
13. Reference Electrode Conversion: SCE / NHE / SSE
14. Summary of Electronic Symbols

1. Microscopy and Optical Parameters

N_A = numerical aperture (N.A.) of the lens / cm,

n = refractive index / dimensionless

k = extinction coefficient (complex absorption coefficient) / dimensionless

R = normal incident of reflection / dimensionless

this is the fraction of light which is reflected so (1-R) is the fraction of light absorbed by the sample

α = absorption coefficient / dimensionless

$$\alpha = \frac{4\pi\nu k}{c} = \frac{4\pi k}{\lambda}$$

λ = wavelength of laser light / nm, $\lambda = \frac{c}{\nu}$,where c = speed of light and ν = frequency

of light, λ in μm units $= \dfrac{1.2398}{\text{Energy in eV units}}$

2. Thermal Parameters

λ_T = time scale for thermal diffusion / s

$$\lambda_T = \frac{r^2 c_p \rho}{K} = r^2 \times \frac{1}{D}$$

c_p = specific heat capacity / J K^{-1}

D = Thermal diffusivity / cm^2 s^{-1}

$$D = \frac{K}{c_p \rho}$$

K = thermal conductivity / W cm^{-1} K^{-1}

C = Heat capacity / J K^{-1}

$$C = c_p \pi r^2 \rho$$

δT = small change in temperature / K

change in current due to electrode heating: $\delta I = (ia)\dfrac{E_a}{RT^2}\delta T$

T = temperature / K

E_a = activation energy / J

3. Geometry and Mass

laser:

γ = geometrical factor / dimensionless

$$\gamma = \frac{\text{beam radius (r)}}{\text{absorption depth } (\alpha^{-1})}$$

r = laser spot radius / cm

d = 2r = laser spot diameter / cm

$$2r \approx \frac{\lambda}{2N_A}$$

$a = \pi r^2$ = area of laser spot / cm^2

N_A = numerical aperture (N.A.) of the lens

electrode:

ρ = density / g cm^{-3}

w = width of electrode / cm — shortest distance on a band electrode or the diameter of a circular electrode

A = total surface area of electrode / cm

l = length of electrode / cm — the longest distance across a band electrode

d_{line} = distance scanned by the laser over the electrode surface / μm

solution:

m = mass / g

n = number of moles / mol

V = volume / cm^{-3}

c = concentration / mol dm^{-3} — $c = \frac{n}{V}$

units, 1 mol dm^{-3} =1M,

1 x 10^{-3} mol dm^{-3} = 1 mM

ρ = density / g cm^{-3} — $\rho = \frac{m}{V}$

4. Current and Potential

E = potential applied / mV

V_{app} = potential applied, when E is used to represent energy.

dark current:

I = current generated, cyclic voltammetry / A

i = current density / A cm^{-2}

δI = change in dark current produced

E_p = potential difference between the anodic and cathodic peaks on a cyclic voltammogram / mV — for a reversible electrode E_p = 59 mV

photocurrent:

$I_p = I_{photo}$ = photocurrent generated, in an imaging experiment / A,

current with light on - current with light off

dI = current range used to represent 256 greys on a grey scale image

$i_p = i_{photo}$ = photocurrent density / A cm^{-2}

E_{peak} = potential at a peak in the photocurrent / mV

this label was given to any characteristic peak seen on the I_{photo} vs E curve, obtained form photocurrent data

5. Time and Velocity

laser:

v_p = laser scan pseudo-velocity / cm s^{-1} $\qquad v_p = \dfrac{\text{line length}}{\text{line scan time}}$

termed 'pseudo' as the laser has a dwell time at each pixel

τ = laser beam irradiation time / s $\qquad \tau = \dfrac{1}{v_p} 2r, \qquad \tau = \dfrac{t_{line}}{d_{line}} 2r$

$$\tau = \frac{\text{pixel dwell time on the x - axis}}{\text{pixel length on the x - axis}} 2r$$

ν^{-1} = the time factor / dimensionless $\qquad \nu^{-1} = \dfrac{\text{irradiation time}(\tau)}{\text{time scale for thermal diffusion}(\lambda_T)}$

t_{line} = line scan time on scanning laser image / s

cyclic voltammetry:

υ = scan velocity, cyclic voltammetry / mV sec^{-1}

instrumental:

τ_{inst} = limiting response time of an instrument / s $\qquad \tau_{inst} = \dfrac{1}{2\pi f}$

ν = frequency of light / Hz $\qquad$ Units, $1Hz = 1s^{-1}$

f = frequency of mechanical chopper / Hz,

note: 'f' used here so as not to confuse with the scan velocity in cyclic voltammetry

6. Laser Power / Intensity

at laser source:

λ = wavelength of laser light / cm

P = power / Watts

I_o = intensity at the laser source (unfiltered laser intensity) / mW cm^{-2} $\qquad I_o = \frac{P}{a}$

at the neutral density filter:

T_{ND} = transmission of light through the neutral density filter / dimensionless, $T_{ND} = \frac{I_s}{I_o}$

A_{ND} = absorbance of the light by the neutral density filter / dimensionless

$$A_{ND} = \log_{10} \frac{I_s}{I_f} = \log_{10} \frac{1}{T_{ND}} = -\log_{10} T$$

at sample surface:

P_s = incident power at the sample surface / Watts

I_s = incident light intensity at the sample surface / mW cm^{-2}

(after passing through the neutral density filter)

$I_s = 100\% I_o = I_o$ when no neutral density filter is used

in the sample:

$P_{s,abs}$ = power absorbed from the laser beam / Watts

$I_{s,abs}$ = the intensity of light absorbed at the surface / mW cm^{-2}

$I_{s,\,abs} = I_s (1 - R)$, where R = fraction of light reflected

$$I_{s,abs} = \frac{P_s}{\pi r^2}(1 - R)$$, if no neutral density filter is present

then $P_s = P$, the laser power

$$I_{s,abs} = \frac{P_{s,abs}}{\pi r^2}$$

I_f = laser intensity on passing into the sample a distance x. / mW cm^{-2}

$I_f = I_s e^{-\alpha x}$, where α = the absorption coefficient

x = distance travelled by the laser into the sample / cm

7. Energy Levels

E_F = energy of the Fermi-level / eV

E_V = energy of the valence band / eV

E_C = energy of the conductance band / eV

E_{bg} = separation between the conductance and valence band energies / eV

this is the separation between the conductance and valence energies $E_{bg} = E_C - E_V$

V_{fb} = flat band potential / eV,

this is a potential for which the energy drop between the bulk of the electrode and the surface of the electrode is zero.

8. Diffusion Equations: for electrochemical systems

When a reaction occurs at the electrode surface the reactant is left depleted, this gives rise to a concentration difference between the bulk solution and that at the electrode surface which results in the diffusion of any depleted species to the electrode surface.

Fick's 1st law : describes how the ions move towards the electrode;

$$\text{Flux, } J = -D\left(\frac{dc}{dx}\right)$$

Fick's 2nd Law : shows how the movement of ions for a given concentration profile changes with time;

$$\frac{dc}{dt} = D\left(\frac{d^2c}{dx^2}\right)$$

Notes: J = flux = the number of moles of a material passing through a unit area in unit time (mol m^{-2} s^{-1}), D = diffusion coefficient (m^2 s^{-1}), c = concentration (mole m^{-3}), x = distance (m), dc / dx = concentration gradient of solute (mol m^{-4}).

9. Nernst Equation: for the equilibrium (reversible) potential

In a redox reaction looking at the reaction which occurs at just one of the 2 electrodes, a general equation can be given for the half cell:

$$pO + ne^- \rightleftharpoons qR$$

If p and q are the stochiometric coefficients of the reaction, at equilibrium the potential on the left will equal that on the right of the cell. $\Delta\phi$, the potential difference between the two phases, the electrode and electrolyte is given by:

$$\Delta\phi = \Delta\phi^o + \frac{RT}{nF}\ln\left(\frac{a_O{}^p}{a_R{}^q}\right)$$

$\Delta\phi = \phi_{electrode} - \phi_{electrolyte}$

where ϕ = potential, T = temperature, R = Gas Constant, F = Faraday Constant and a = activity (effective concentration) of species.

For example for a whole cell with two metals X and Y:

Left Hand Side	Right Hand Side
$Pt \mid X, X^+ \parallel Y^+, Y \mid Pt$	
oxidation on the left hand side $X \rightarrow X^+ - e^-$	reduction occurs at the right hand side $Y^+ + e^- \rightarrow Y$
overall cell reaction: $X + Y^+ \longrightarrow X^+ + Y$	
$E = \phi_{right} - \phi_{left}$ and $E = E_R - E_L$ (by convention $E_R > E_L$)	
for X, $\Delta\phi_{left} = \Delta\phi^o + \frac{RT}{nF}\ln\frac{a_{X^+}}{a_X}$	for Y, $\Delta\phi_{right} = \Delta\phi^o + \frac{RT}{nF}\ln\frac{a_{Y^+}}{a_Y}$
Subtracting the two above equations gives the **Nernst equation** for a **whole cell** : $E = E^o - \frac{RT}{nF}\ln\left\{\frac{a_{X^+}a_Y}{a_X\, a_{Y^+}}\right\}$	

For cells which include the SHE (standard hydrogen electrode) on the left of the cell.

$$\tfrac{1}{2}H_2 + \text{oxidised states} \rightleftharpoons \text{reduced states} + H^+$$

$$E = E^o - \frac{RT}{nF}\ln\left\{\frac{a_{H^+}\, a_{\text{reduced states}}}{(a_{H_2})^{1/2}\, a_{\text{oxidised states}}}\right\}$$

where $a_{H^+} = a_{H_2} = 1$ (and further inverting the ln term and revering the sign)

$E = E^o + \frac{RT}{nF}\ln\left\{\frac{a_{\text{oxidised states}}}{a_{\text{reduced states}}}\right\}$ If the activity of the oxidised (O) and reduced (R) species are unity then they may be replaced by their concentrations; [O] and [R]:

$$E = E^o + \frac{RT}{nF}\ln\frac{[O]}{[R]}$$

10. The Butler-Volmer Equation: for electrode kinetics

Reaction summary $O + ne^- \rightleftharpoons R$

For the reverse reaction	For the forward reaction
Oxidation reaction, anodic (+VE) current produced $R \xrightarrow{-e^-} O$	Reduction reaction, cathodic (-VE) current produced $O \xrightarrow{+e^-} R$

net current density, $i = i_c + i_a$ (1)

where, $i = nFk[c]$, n = No. of electrons, F = Faradays constant, k = rate constant, $[c]$ = concentration of starting species i_a = anodic current density, i_c = *cathodic current density*

$i_a = +\, nFk_a[R]$	$i_c = -\, nFk_c[O]$

therefore, $i = nFk_a[R] - nFk_c[O]$ (2)

rate constant for the anodic reaction,	rate constant for the cathodic reaction,
$k_a = k_o \exp\frac{nF}{RT}\alpha_a E$	$k_c = k_o \exp\frac{nF}{RT}\alpha_c E$

substituting for k in equation 2,

$$i = nF[R]\cdot k_o \exp\left(\frac{\alpha_a nFE}{RT}\right) - nF[O]\cdot k_o \exp\left(\frac{\alpha_c nFE}{RT}\right) \quad (3)$$

substituting for the overpotential, η = the deviation of the potential from the equilibrium value, $\eta = E - E_{eqm}$ when $\eta = 0$ and $i_a = i_c = i_o$, the exchange current density,

$$i_o = i_a = nF[R]\cdot k_o \exp\left(\frac{\alpha_a nF\eta}{RT}\right) \quad \text{and} \quad i_o = i_c - nF[O]\cdot k_o \exp\left(\frac{\alpha_c nF\eta}{RT}\right)$$

we get the, Butler-Volmer equation: $$i = i_o\left[\exp\left(\frac{\alpha_a nF\eta}{RT}\right) - \exp\left(\frac{-\alpha_c nF\eta}{RT}\right)\right] \quad (4)$$

Simplifications to the above equation:

At high +VE η, when $i_a \gg i_c$	At high -VE η, when $i_c \gg i_a$	At very low overpotentials
$\ln i = \ln i_o + \frac{\alpha_a nF}{RT}\eta$	$-\ln i = \ln i_o - \frac{\alpha_c nF}{RT}\eta$	$i = i_o \frac{nF\eta}{RT}$
$y = c + mx$	$y = -c - mx$	

Tafel Equations

An alternative form of the Butler Volmer equation involving the activation energy can be given, by use of the Arrhenius equation as:

$$i = i_o' \exp\frac{-E_a}{RT}\left[\exp\left(\frac{\alpha_a nF\eta}{RT}\right) - \exp\left(\frac{-\alpha_c nF\eta}{RT}\right)\right]$$

11. Gärtner Equation: for photocurrent generation in semiconductors

$$i_{photo} = qI_{s,abs}\frac{1-e^{-\alpha W}}{1+\alpha L_{min}}$$

i_{photo} = photocurrent density
$I_{s,abs}$ = amount of light entering the semiconductor after it has been corrected for reflection
W = the width of the depletion layer, his is the length across which the energy band bends
L_{min} = the diffusion length for the minority carriers, this is the average length they must move before they are annihilated
q = charge on an electron = 1.60219×10^{-19} C

The width of the space-charge region is given by $W = \left(\frac{2\Delta\emptyset\varepsilon\varepsilon_o}{qN}\right)^{1/2}$

where ε = the relative permitivity of the semiconductor, N = the donor or acceptor density, $\Delta\emptyset$ = potential difference = $V_{app} - V_{fb}$.

A plot of

$-\ln\frac{1-i_{photo}}{I_{s,abs}}$ vs $V-V_{fb}$ should be linear with the slope = α and the intercept = L_{min}.

12. The Mott-Scottky Equation: for calculating the flat band potential

This equation relates to a semiconductor surface in which there is a depletion of majority charge carriers.

$$C_{sc}^{-2} = \frac{2}{qN_d\varepsilon\varepsilon_o}\left(V_{app} - V_{fb} - \frac{kT}{q}\right)$$

C_{sc} = capacitance of the space charge layer, i.e. the capacitance of the length of the semiconductor in which charge carrier depletion and energy band bending occurs.
ε = dielectric constant normal to the electrode surface
ε_o = permittivity of free space
q = electron charge
V_{fb} = flat band potential
V_{app} = applied potential
N_d = doping density
k = Boltzman's constant
T = temperature

This equation can only be used provided the following conditions apply:

1. Carrier inversion has not occurred.
2. The Fermi-level is at least 2kT (0.05 eV) away from the nearest band edge
3. All the donor or acceptor levels are ionised
4. The donor atoms are uniformly distributed in the semiconductor and are immobile

A graph of C^{-2}_{sc} against V_{app} is used to calculate V_{fb} from where $C^{-2}_{sc} = 0$.

13. Reference Electrode Conversion Chart

Reference Electrode Conversion chart for 25°C

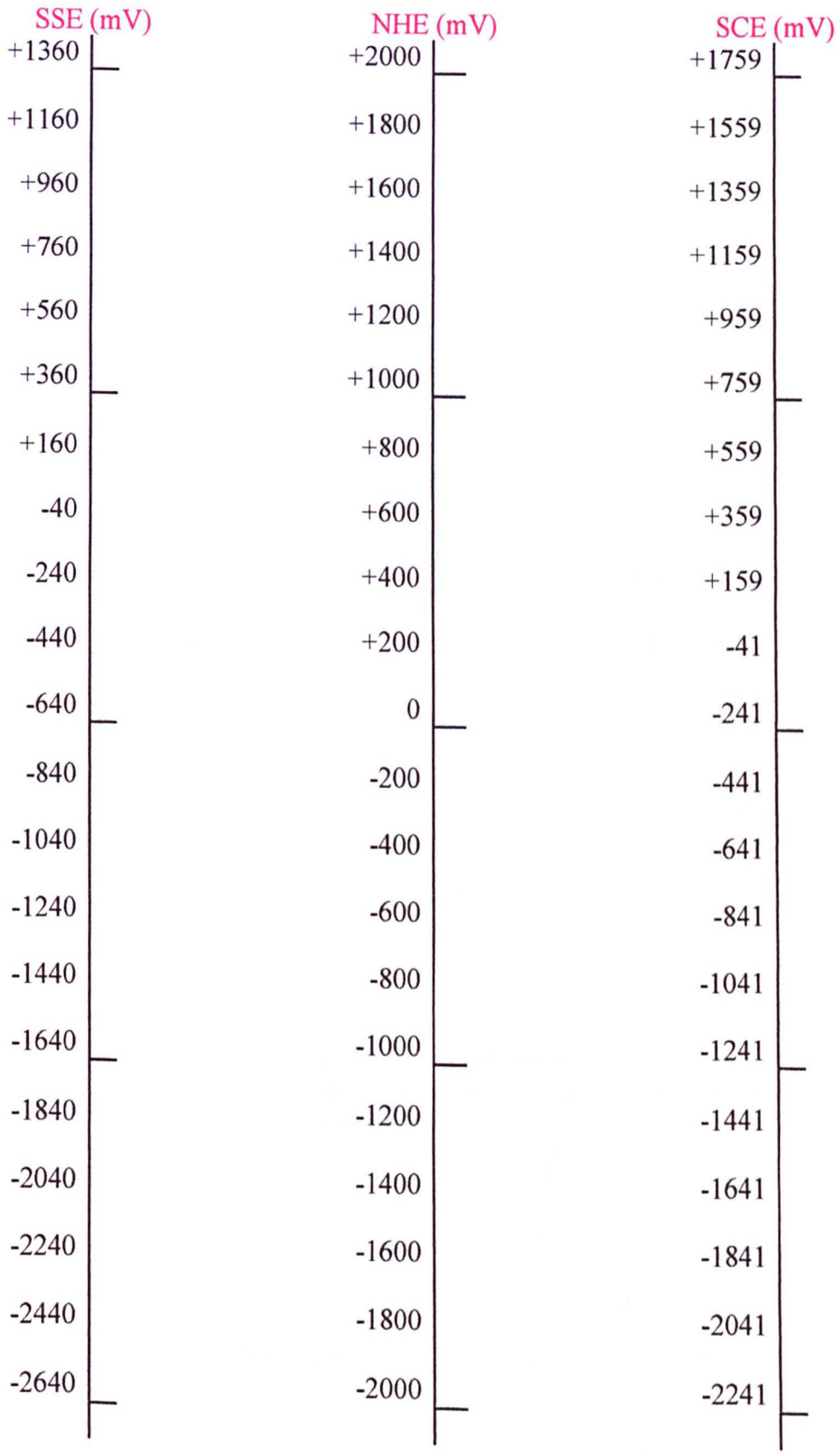

SCE = NHE – 241.2 mV
SSE = NHE – 640 mV,

Note: SSE = Hg/Hg_2SO_4, sat. K_2SO_4

14. Summary of Electronic Symbols

The following is a key to the symbols given in the circuit diagrams shown in Appendix E.

1. BNC CONNECTOR

2. BNC CONNECTOR

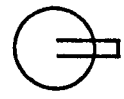

3. SWITCH

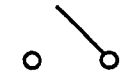

6. RESISTOR

4. BATTERY

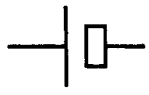

5. BATTERY

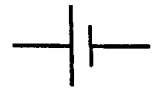

7. VARIABLE POTENTIOMETER

8. VARIABLE POTENTIOMETER

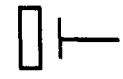

9. VARIABLE RESISTANCE POTENTIOMETER, CONNECTED AS A VARIABLE RESISTOR

10. EARTH

11. CAPACITOR

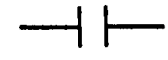

12. A MOVING COIL INDICATOR- this shows if the battery is fully charged, half charged or empty

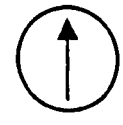

13. ZENA DIODE - a voltage stabiliser

14. LIGHT EMITTING DIODE (LED)

15. OPERATIONAL AMPLIFIER

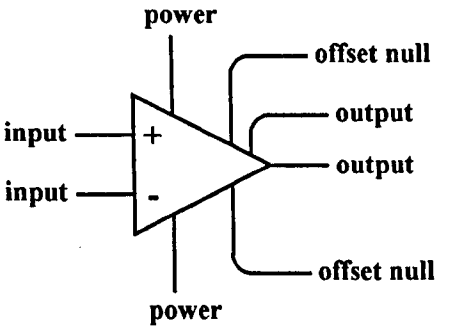

16. A HEADER FOR A PRINTED CIRCUIT BOARD- this provides a means of interconnecting a printed circuit board to other items

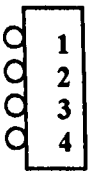

17. SYMBOLS MAKING UP THE ROTARY SWITCH IN THE POTENTIOSTAT

17a.

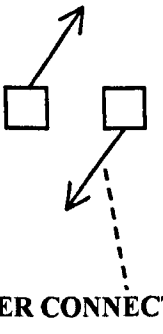

WIPER CONNECTION

17b.

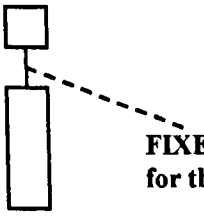

FIXED CONNECTOR- for the wiper to go around

C. TECHNICAL DETAILS OF THE CUSTOM MADE APPARATUS

C. TECHNICAL DETAILS OF THE CUSTOM MADE APPARATUS

The custom made (home made) instruments were constructed in order to carry out the electrochemical experiments with the lowest possible noise gain and with the most efficient response times.

This equipment was constructed by the Electronics Section, Chemistry Department, UCL or the Mechanical workshop based in the Chemistry Department at UCL.

Technical diagrams (in the form of sketches for mechanical equipment and circuit diagrams for electronic equipment) and some photographs have been given as well as some general notes on construction and use.

For further details on how these were used and attached to the other instruments in the overall scheme of things, please see the experimental method (chapter 2).

A summary of the symbols used in the circuit diagrams has been given in Appendix B.

1. Battery Operated Potentiostat

Designed by- Original design by Anthony Kucernak with enhancements in the 1st instant by David Bowman and more design additions by Tasneem Mohiuddin.

Constructed by- Samantha Gardiner (Electronics Section, Chemistry Department, UCL). With smaller additions at later stages Richard Waymark (also of the electronics section, Chemistry Department). Voltmeters for monitoring input and output by Samantha Gardener.

Dimensions- Length = 38.0 cm, width = 26.0 cm, depth = 6.5 cm, for the external box.

Notes on construction and use

The low noise potentiostat was used to pass a current through a chemical cell and the varying current in the cell was monitored via the output of the potentiostat. The potentiostat also maintains a constant voltage between the reference and working electrode by injecting current into the cell solution from the counter electrode.

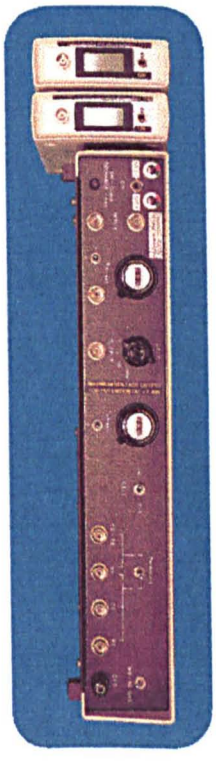

figure C-1

The special features of the potentiostat were, its low noise and ability to pass and measure small currents at fast response.

The potentiostat was used on its side (to save space) in conjunction with battery operated voltmeters attached using Velcro to the potentiostat. The output signal was monitored using voltmeters and if the voltage approached was any where near 7 ½ volts then the μA per volt setting was increased to a greater value (as the potentiostat will saturate at this value and give incorrect results). In addition the

battery status was monitored at all times using a coil meter for each battery, on the front panel of the potentiostat. The deflection for given for each coil meter was 10 volts and a half-way deflection of 5 volts. The batteries were found to run the potentiostat well, when fully charged but when discharged to half the amount or so, the potentiostat started to fail giving incorrect results. So if the half-way deflection point was reached on the coil meters the batteries could not be used. In this case the batteries had to be discharged and recharged either by the back panel on the potentiostat or by removing the batteries and replacing them with ones that had previously been externally discharged and then charged. The externally charged batteries were simply swapped for the depleted batteries by sliding open the top case of the potentiostat.

Another way to check the potentiostat to see if it was working properly, was by using the internal cell setting and applying a range of potentials and then viewing the results on a chart recorder. This gave a straight line graph with current versus voltage line passing through zero with a slope of 10 kΩ, if the potentiostat was working properly and the batteries were sufficiently charged. This method was used to check the state of the potentiostat prior to an experiment, but could not obviously be used mid-experiment, so having viewable coil meters showing the state of the batteries was able to solve this problem.

In use the external or internal cell setting could be selected. For the external cell setting, the 2 or 3 electrode mode of use could be selected by the flick of a switch.

The 'working and reference ground' switch, when turned on, attached the earth shielding from all the coaxial cables coming to and from the potentiostat together.

A block diagram, PCB circuit diagrams, wiring diagrams, and photographs for the potentiostat follow.

POTENTIOSTAT BLOCK DIAGRAM

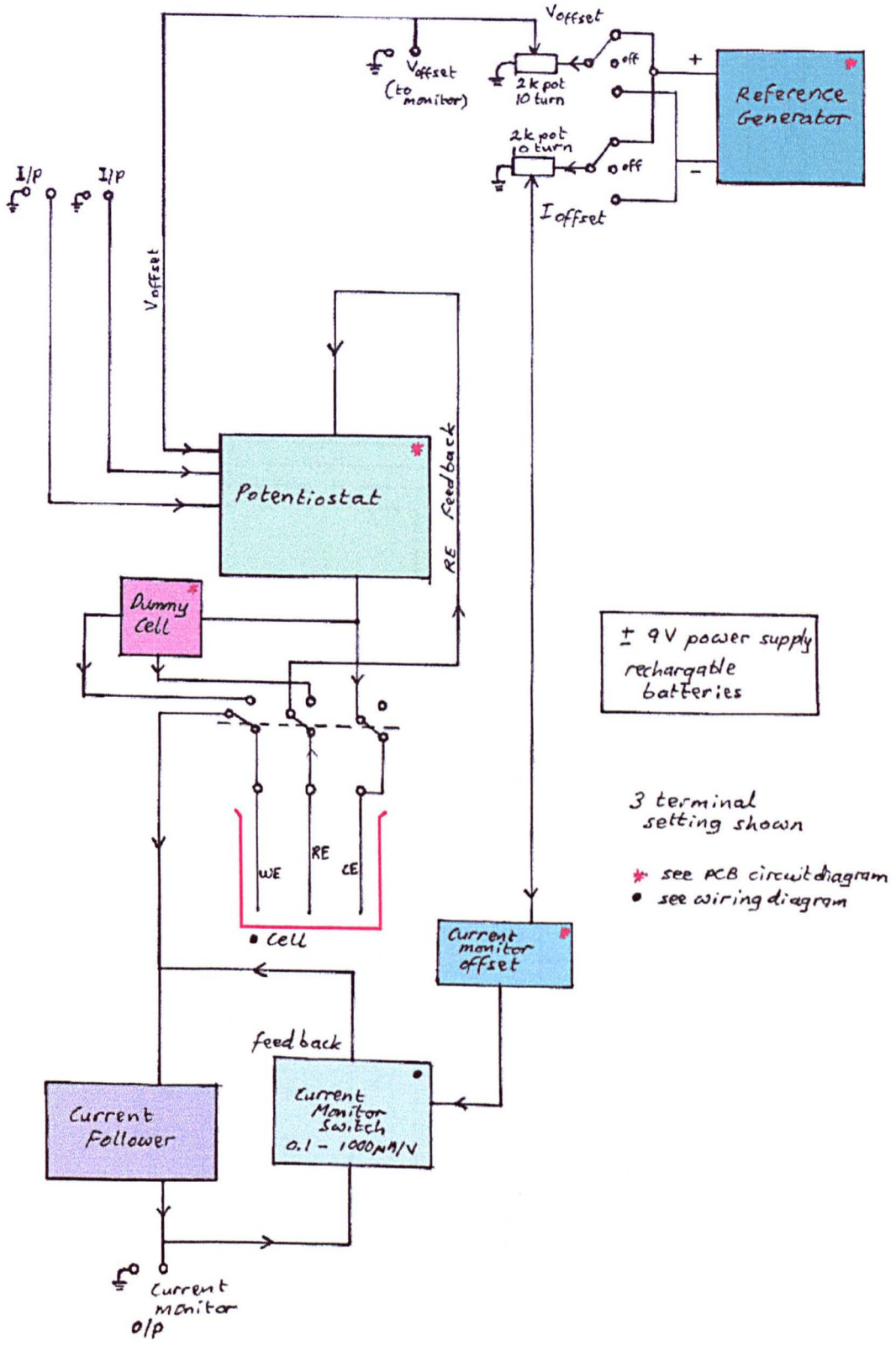

figure C-2

POTENTIOSTAT PCB CIRCUIT DIAGRAM

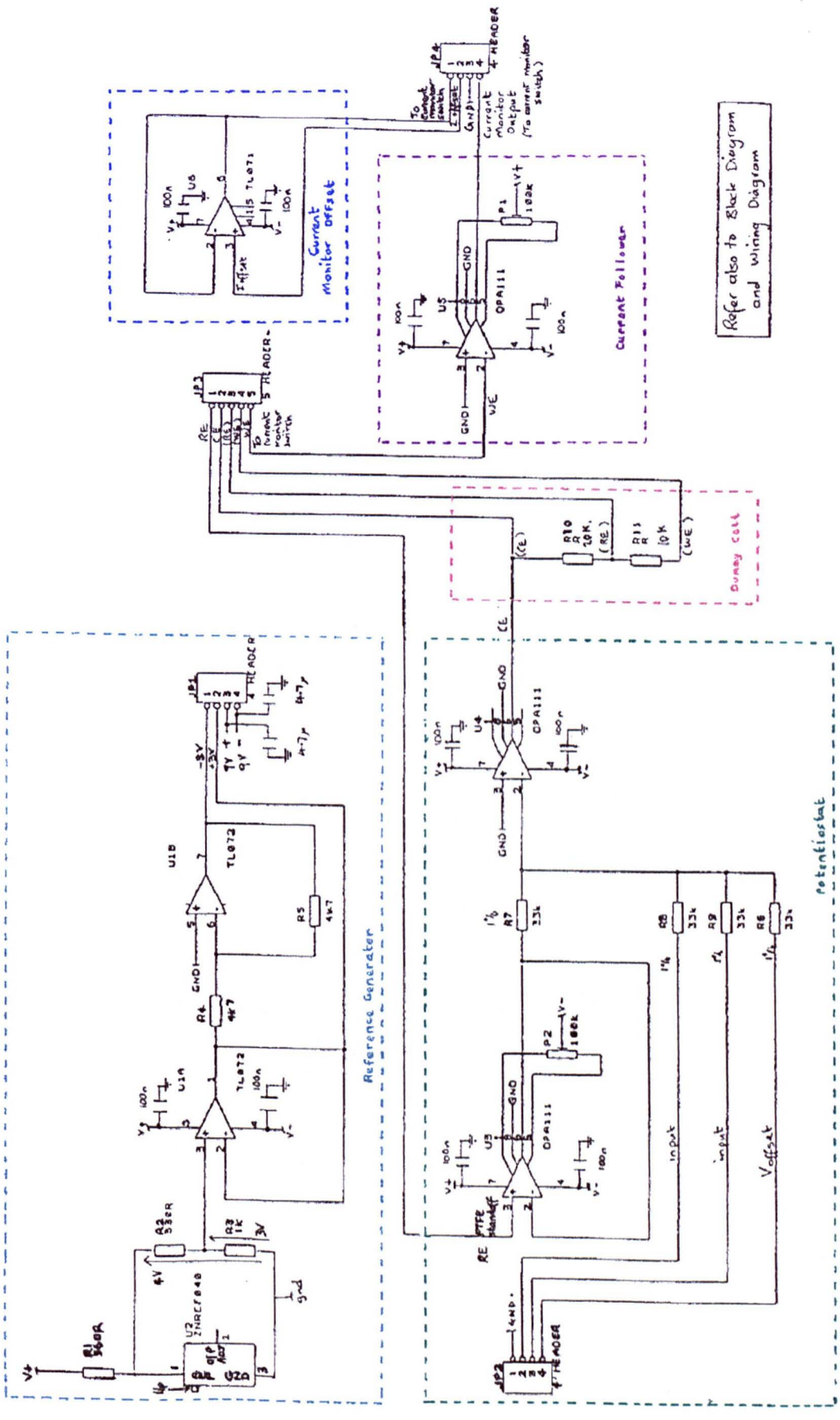

figure C-3

POTENTIOSTAT WIRING DIAGRAM

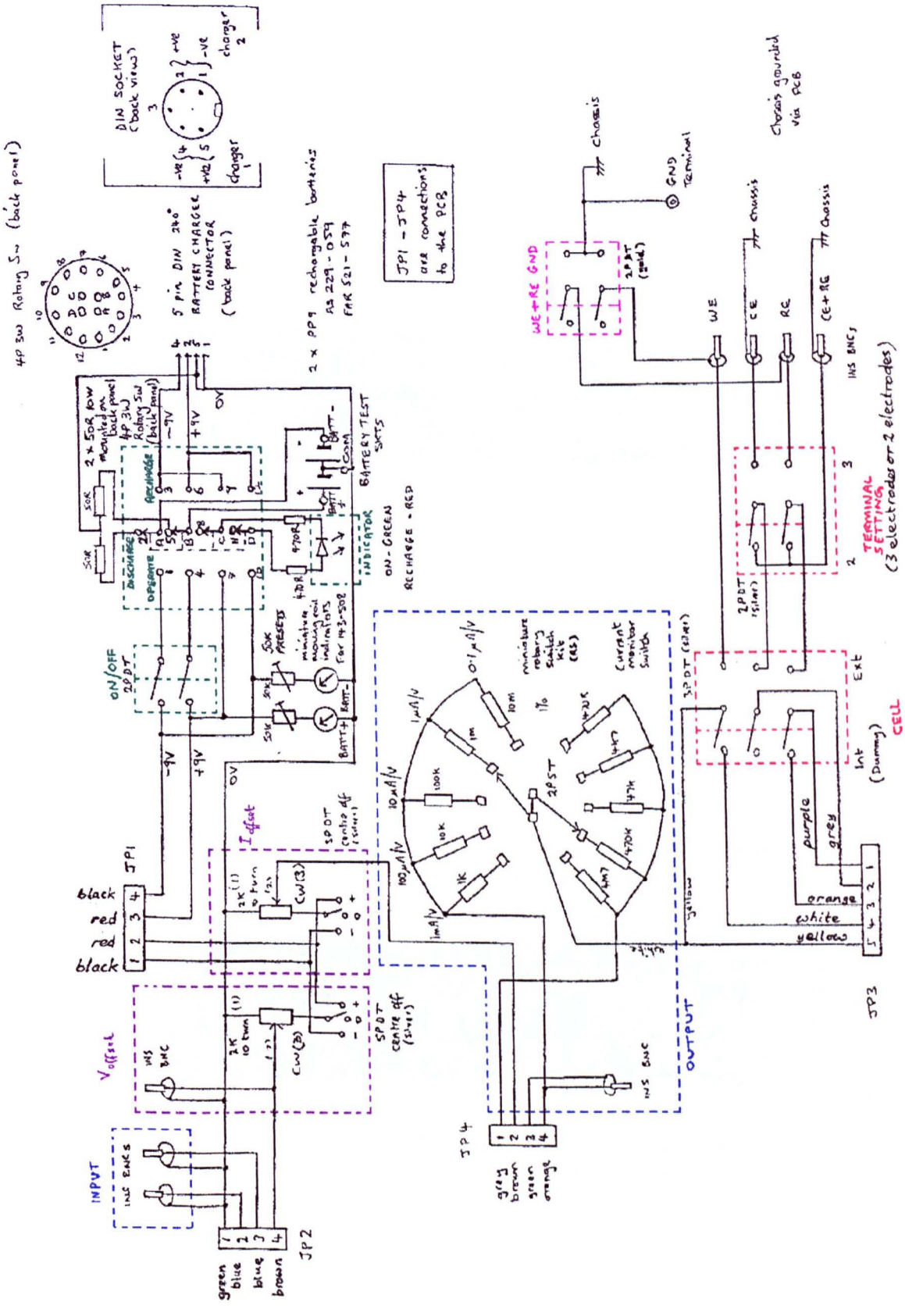

figure C-4

PHOTOGRAPHS SHOWING THE EXTERNAL STRUCTURE OF THE POTENTIOSTAT

a. Front Panel

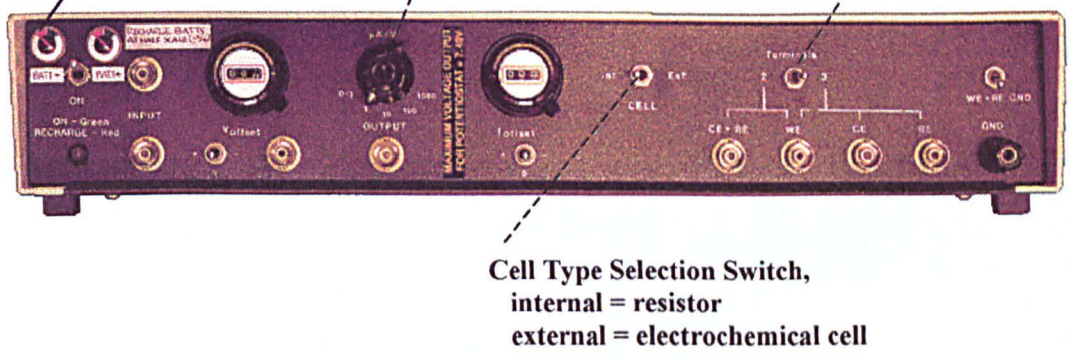

b. Back Panel

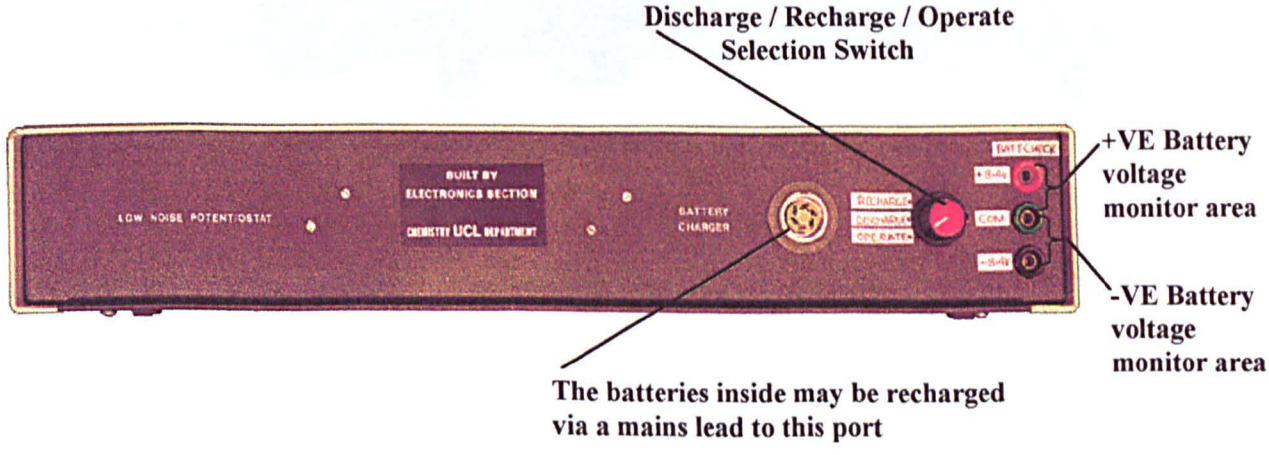

figure C-5

A PHOTOGRAPH SHOWING THE INTERNAL STRUCTURE OF THE POTENTIOSTAT

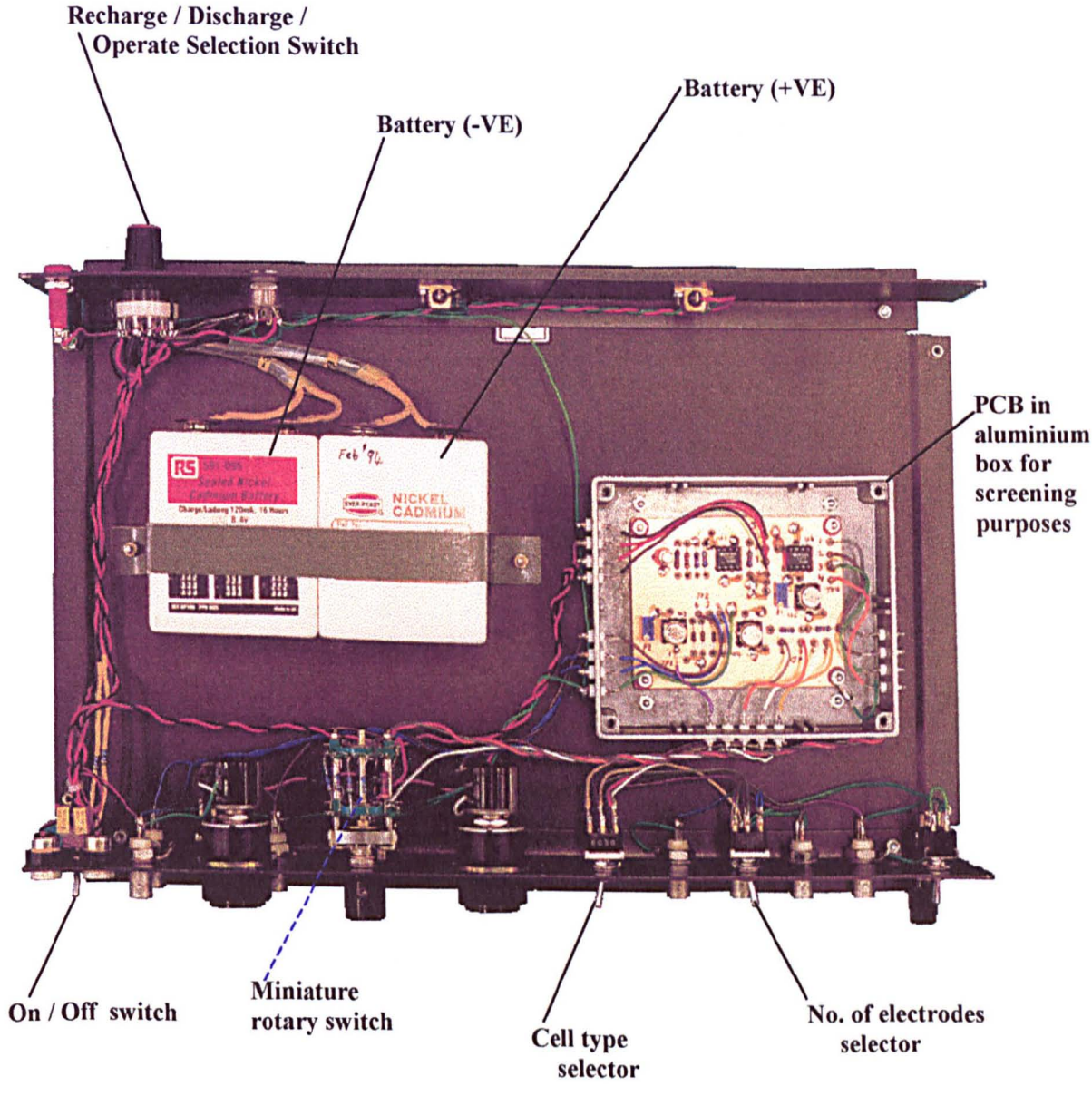

figure C-6

Calculation of the Potentiostat Response Time

In order to calculate the potentiostat response time, a simple impedance experiment was carried out with a 1 MΩ resistor attached to the potentiostat in place of the cell, and a generated amplitude of 0.10 V. In this experiment the effects of varying the frequency, between 10Hz and 100kHz, on the impedance was recorded.

APPARATUS SETUP FOR AC IMPEDANCE ANALYSIS

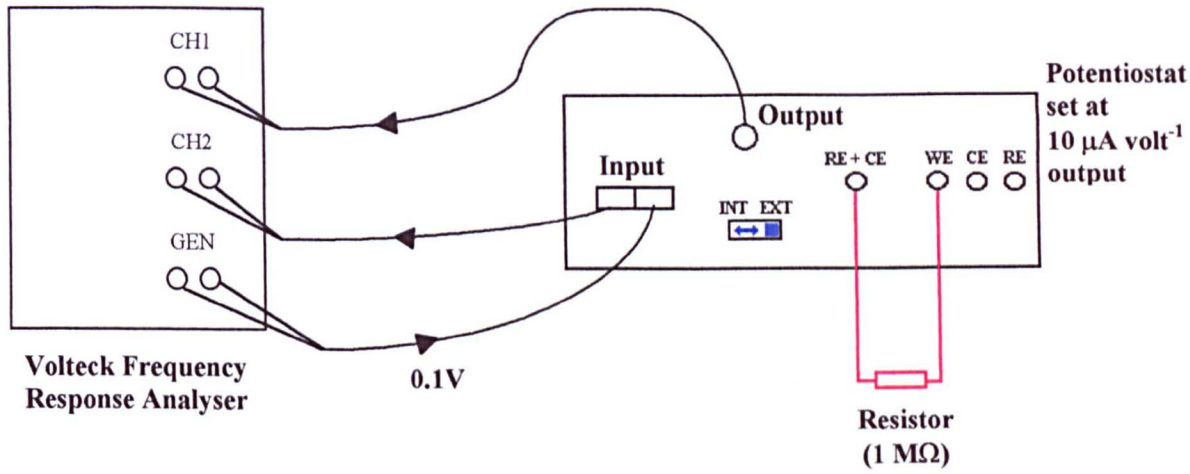

figure C-7

The impedance, z, is given by

$$z = \frac{V_{CH2}}{I_{CH1}}$$

where V_{CH2} = voltage applied, I_{CH1} = current generated

$$\text{gain} = \frac{\text{output}}{\text{input}} = \frac{CH1}{CH2}$$

The gain phase data was collected and recorded for CH2 / CH1 in this system giving inverted results.

A graph was produced from the gain phase data for CH2 / CH1:

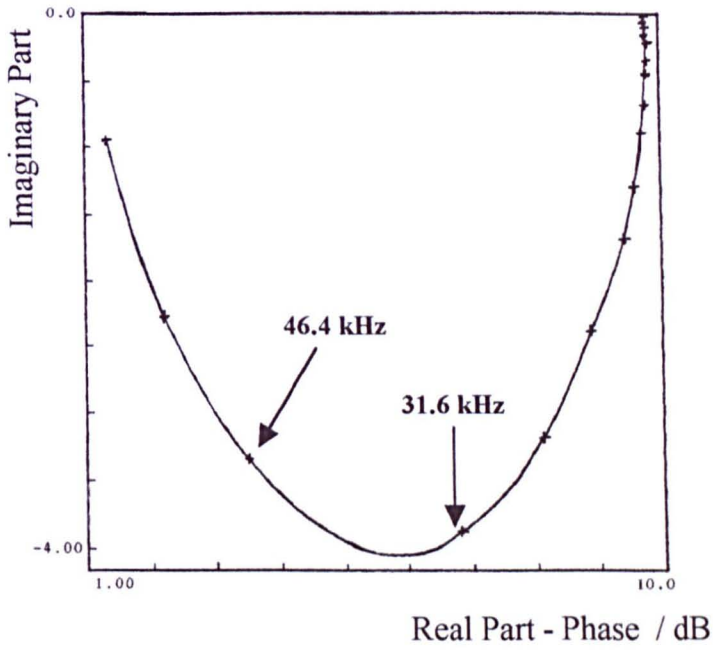

figure C-8

From the graph produced the minimum on the curve will give the response time of the potentiostat.

at 31.6 kHz

$$\omega = 2\pi f$$
$$= 2\pi \times 31600$$
$$= 19848.65$$
$$\frac{1}{\omega} = 5.03 \times 10^{-6} = 5\,\mu s$$

at 46.4 kHz

$$\omega = 2\pi f$$
$$= 2\pi \times 46400$$
$$= 291539.8$$
$$\frac{1}{\omega} = 3.43 \times 10^{-6} = 3\,\mu s$$

This shows that the potentiostat response time was in the region of 4μs.

2. Battery Operated Offset (Black level) Box

Designed by- Original design by Roger Hutton and UCL electronics section later rebuilt with further enhancements suggested by Tasneem Mohiuddin.

Constructed by- Samantha Gardiner of the Electronics Section, Chemistry Department, UCL.

Dimensions- Length = 16.5 cm, height = 12.5 cm, depth = 7.5 cm.

Notes on construction and use

The offset (black level) box was used to adjust the signal coming out of the potentiostat to between 0-1 volt so it can be fed into the computer to form an image from the data. It could be used with the signal inverted or the same way around as it comes into the box. It was used in conjunction with a commercial battery operated pre-amplifier. The offset box was run off four PP9 batteries connected externally to it.

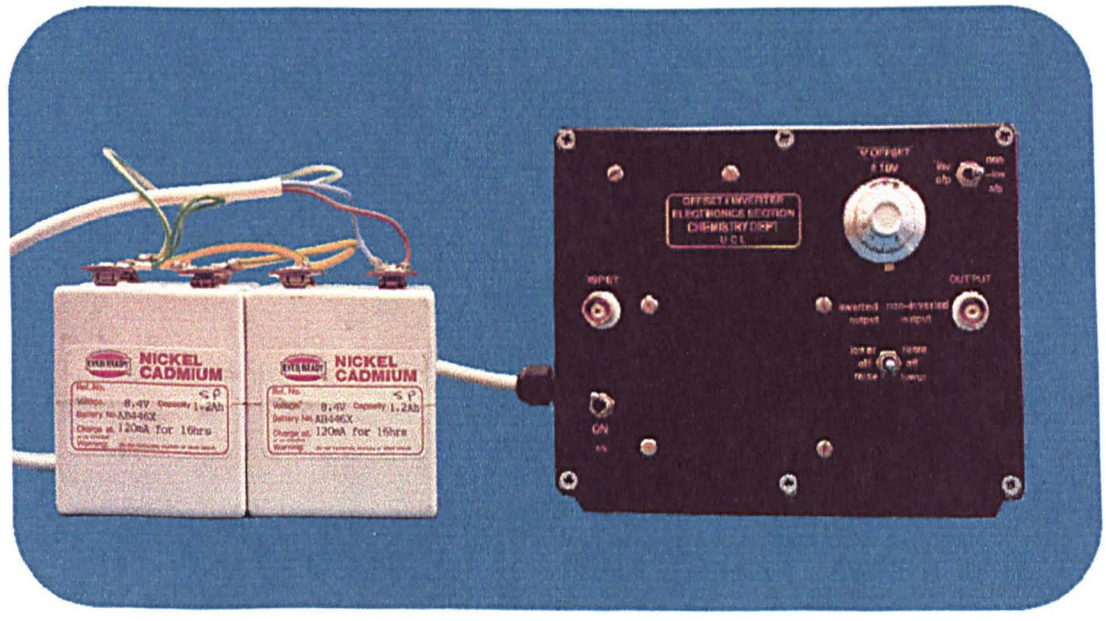

figure C-9

The offset box internally has 2 inputs one from the external apparatus (potentiostat) and one internally from a variable voltage source both variable in amplitude and polarity.

The internal input voltage source had a maximum of ± 10 volts available. So the fraction required from 0 to ± 10 volts was tapped off and added to the input signal.

CIRCUIT DIAGRAMS FOR THE OFFSET BOX

a. Connection to the Batteries

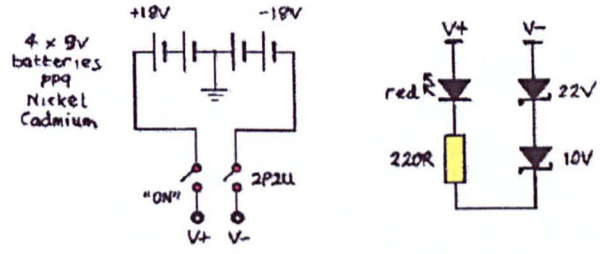

b. The offsetting circuit

(This circuit is an inverting circuit by nature)

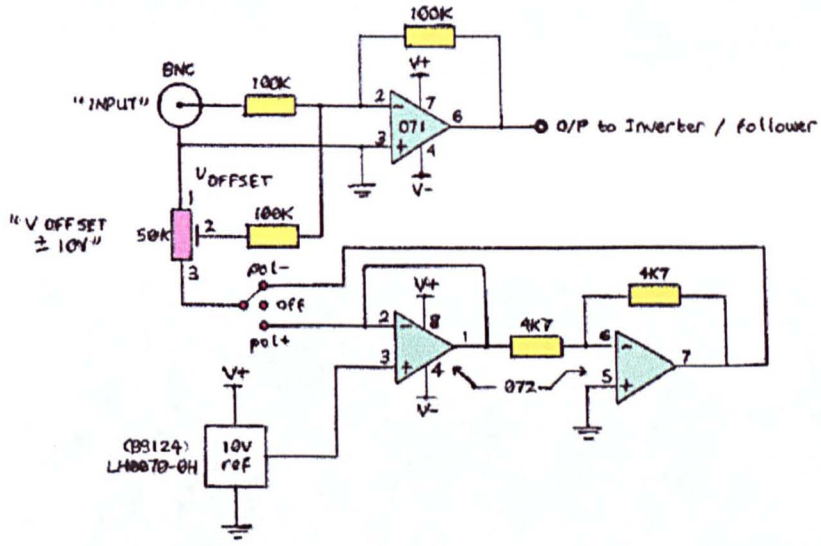

c. The signal inverting circuit

(This allows the signal from the circuit above to be inverted to the correct way)

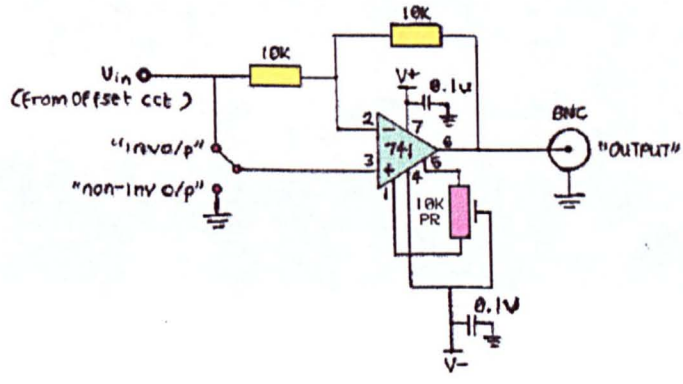

figure C-10

PHOTOGRAPHS SHOWING THE OFFSET BOX STRUCTURE

a. Externally

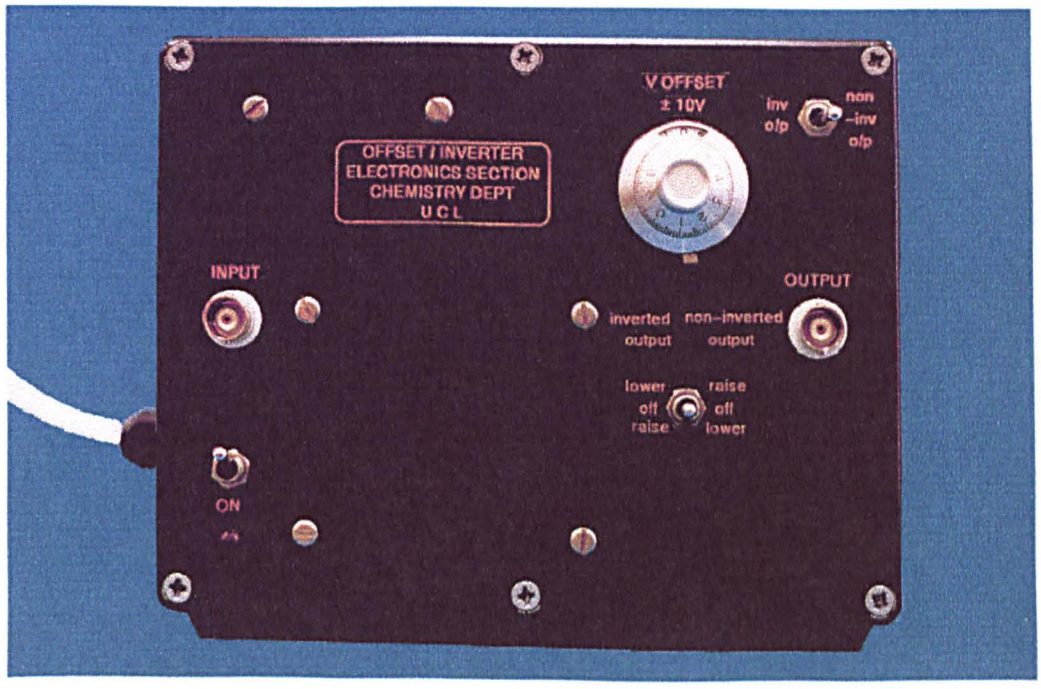

b. Internally

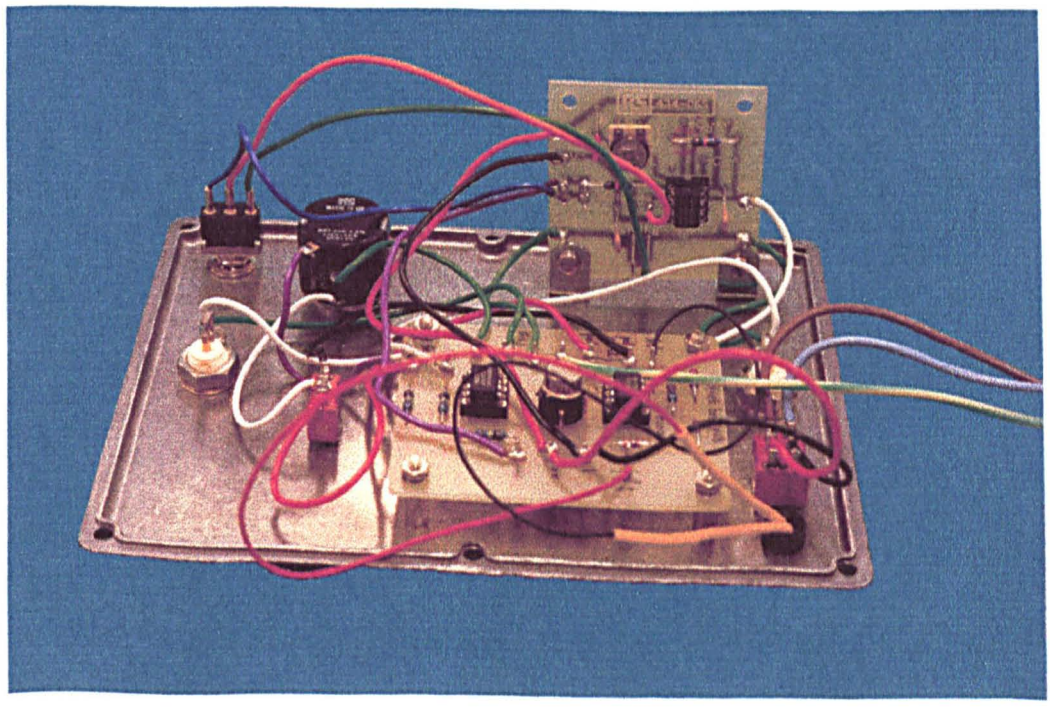

figure C-11

The offset signal was adjustable between 0 and 10 volts with selectable polarity and, was added to the input signal by a unity gain inverting amplifier. This output may be used direct (the nature of the offsetting circuit being an inverting one) or inverted to the same polarity as the in coming signal using a further unity gain amplifier circuit contained in the offset box.

Calibration of the Offset Dial to the Offset Voltage

A fixed voltage was applied directly from the waveform generator to the input of the offset box. The output voltage was then monitored on an accurate digital voltmeter for various settings of the offset dial. The change in the voltage from the input to the output value was then noted as the offset value and a calibration curve drawn.

Offset Dial Position	Offset / V
0.0	0.000
0.5	0.490
1.0	0.958
1.5	1.410
2.0	1.582
2.5	2.289
3.0	2.713
3.5	3.140
4.0	3.563
4.5	3.993
5.0	4.443
5.5	4.883
6.0	5.343
6.5	5.833
7.0	6.323
7.5	6.843
8.0	7.393
8.5	7.983
9.0	8.593
9.5	9.253
10.0	9.983

OFFSET BOX CALIBRATION

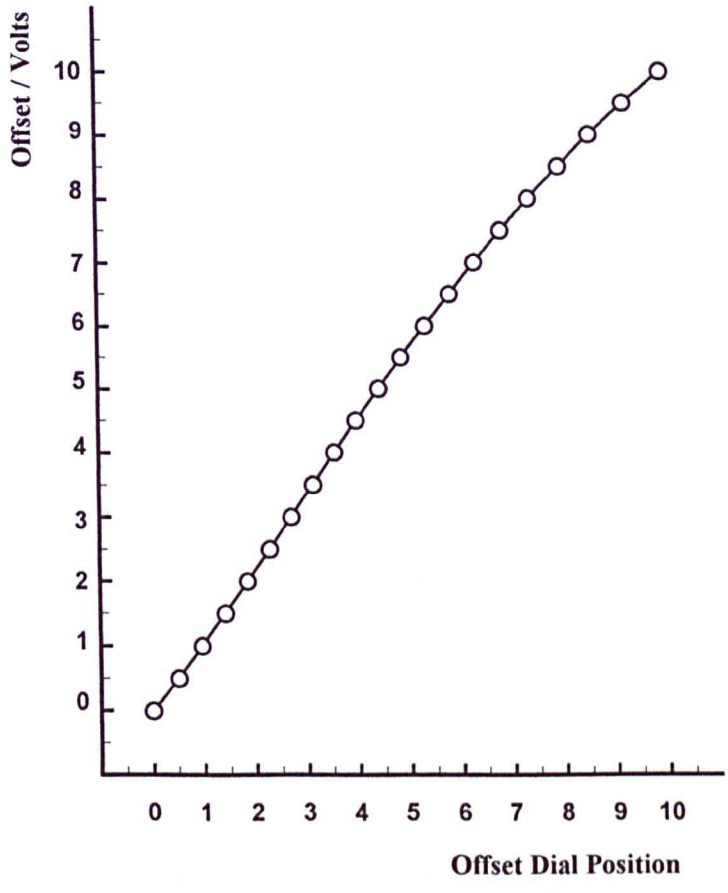

figure C-12

3. Battery Charger and Dischargers

Designed by- Idea by Tasneem Mohiuddin, Richard Waymark (Electronics section, Chemistry Department, UCL) available partly made from RS components.

Constructed by- James (Seumus) Stewart of the Electronics Section, Chemistry Department, UCL.

Dimensions- Length = 9.5 cm, height = 9.5 cm, depth = 12.0 cm.

Notes on construction and use

In order to have low noise pickup on the apparatus, much of the apparatus was run off of PP9 batteries. A charger was constructed allowing 4 batteries at a time to be charged.

CIRCUIT DIAGRAM FOR THE CHARGER

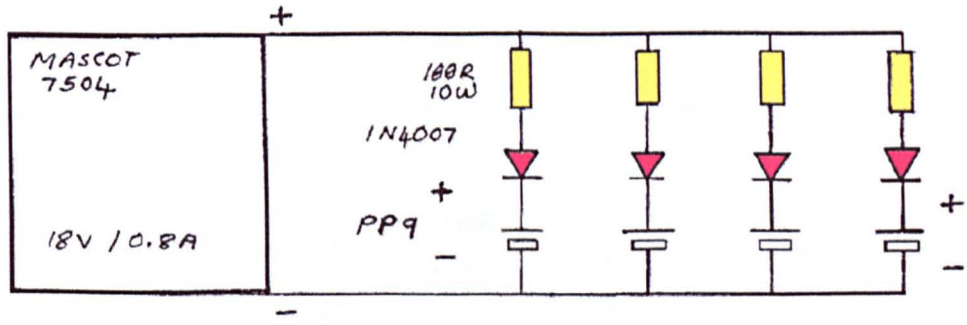

figure C-13

It was found however that the rechargeable batteries developed a 'memory' effect with time. This is when the battery discharges less and less and requires recharging more and more frequently until it can no longer be used.

In order to correct this problem and allow the battery to be used indefinitely at full capacity and in perfect condition battery dischargers were made which could be connected across the batteries positive and negative terminals using PP9 connector press studs.

The nominal voltage for a PP9 battery = 8.4 V but the typical voltage was ~ 10 volts. The batteries were marked as having a capacity of 1.2 Amp hours. So the resistance required to make a discharger was calculated as follows:

If a discharge time of roughly 7-8 hours is required.

$$\text{Current} = \frac{\text{Current Hours}}{\text{Discharge Time}}$$

$$= \frac{1.2 \text{ Amp Hours}}{8 \text{ Hours}}$$

$$= 0.15 \text{ Amps}$$

$$\text{Resistance} = \frac{\text{Voltage}}{\text{Current}} = \frac{8.4 \text{ V}}{0.15 \text{ A}} = 56\Omega$$

A resistance of 50 Ω was selected using two 100 Ω resistors in parallel

CIRCUIT DIAGRAM FOR A DISCHARGER

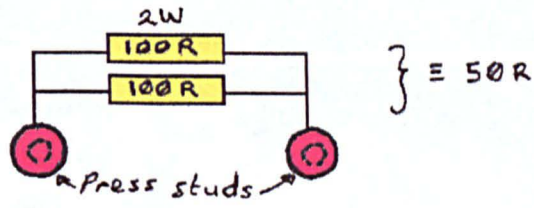

figure C-14

Where,

$$\text{Power dissipated} = \frac{8.4 \text{ x } 8.4}{50} = 1.4 \text{ Watts}$$

A PHOTOGRAPH OF THE EXTERNAL STRUCTURE OF THE BATTERY CHARGER AND SOME DISCHARGERS

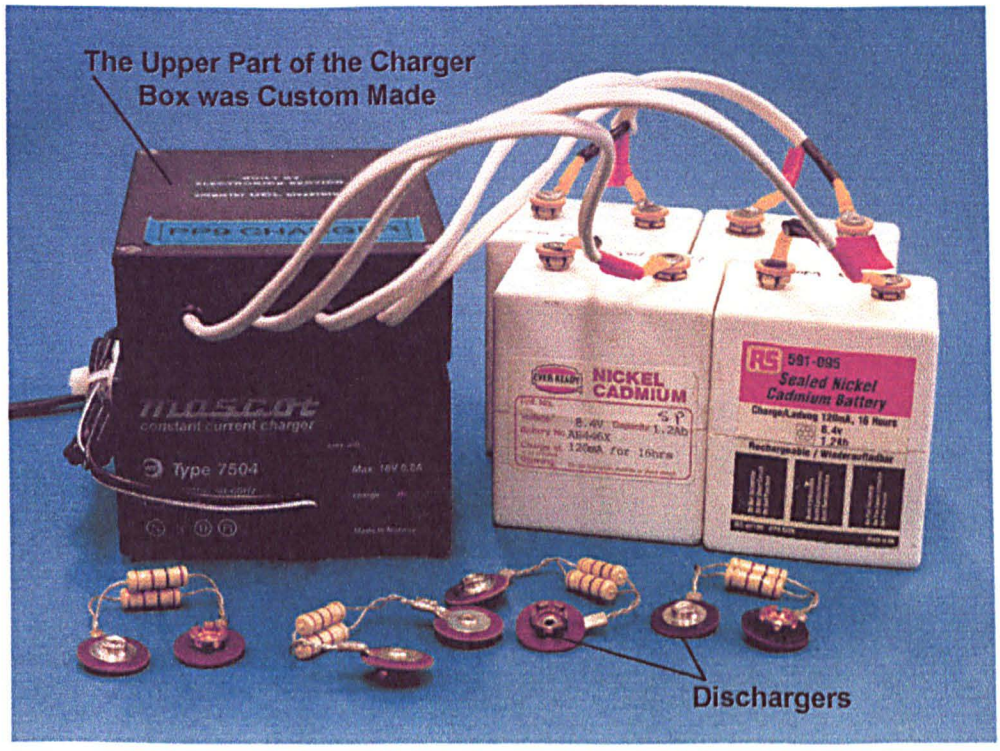

figure C-15

A PHOTOGRAPH SHOWING THE INTERNAL STRUCTURE OF THE CUSTOM MADE PART OF THE BATTERY CHARGER

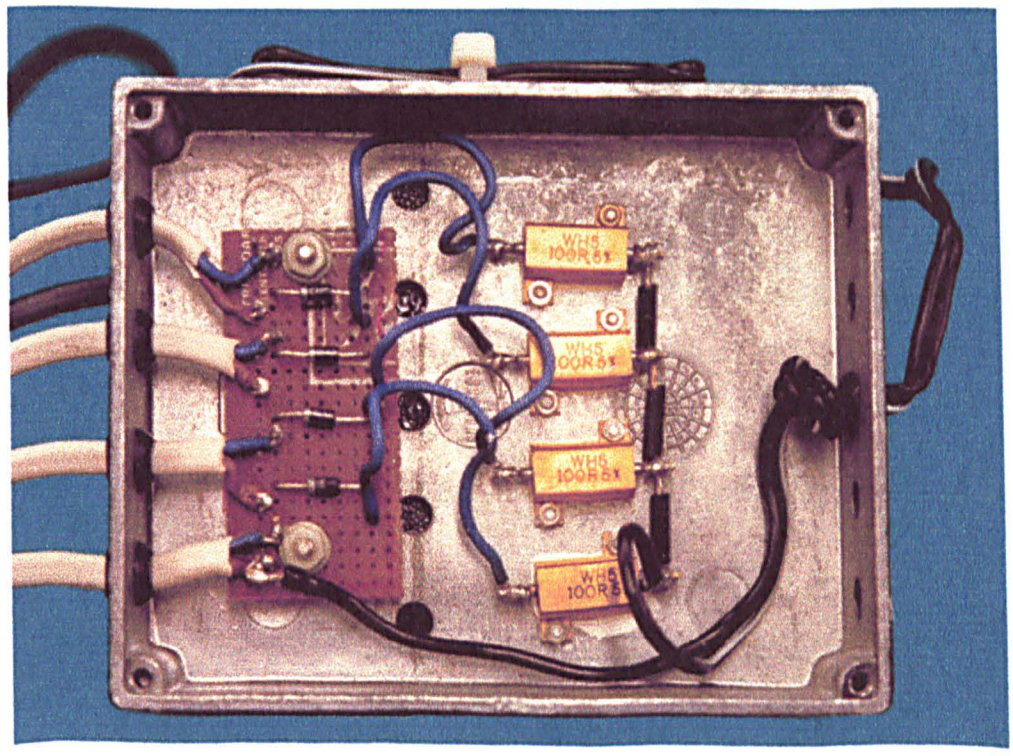

figure C-16

4. Event Marker

Designed by- Original idea by Prof. D.E. Williams, design ideas by Tasneem Mohiuddin and Richard Waymark (Electronics section, Chemistry Department UCL).

Constructed by- Richard Waymark of the Electronics Section, Chemistry Department, UCL.

Notes on construction and use

The event marker was a simple device which gave out a pulse of 1.5 volts when the switch was pressed. This was used to record a parallel signal whilst recording the total current (which was collected simultaneously to the photocurrent signal / images). If any changes were made to the experiment, or any changes observed to the photocurrent image, the event marker button was pressed and a spike was recorded. At the time the event marker was used, a dictaphone message was recorded, to say what had happened, together with an allocated event number.

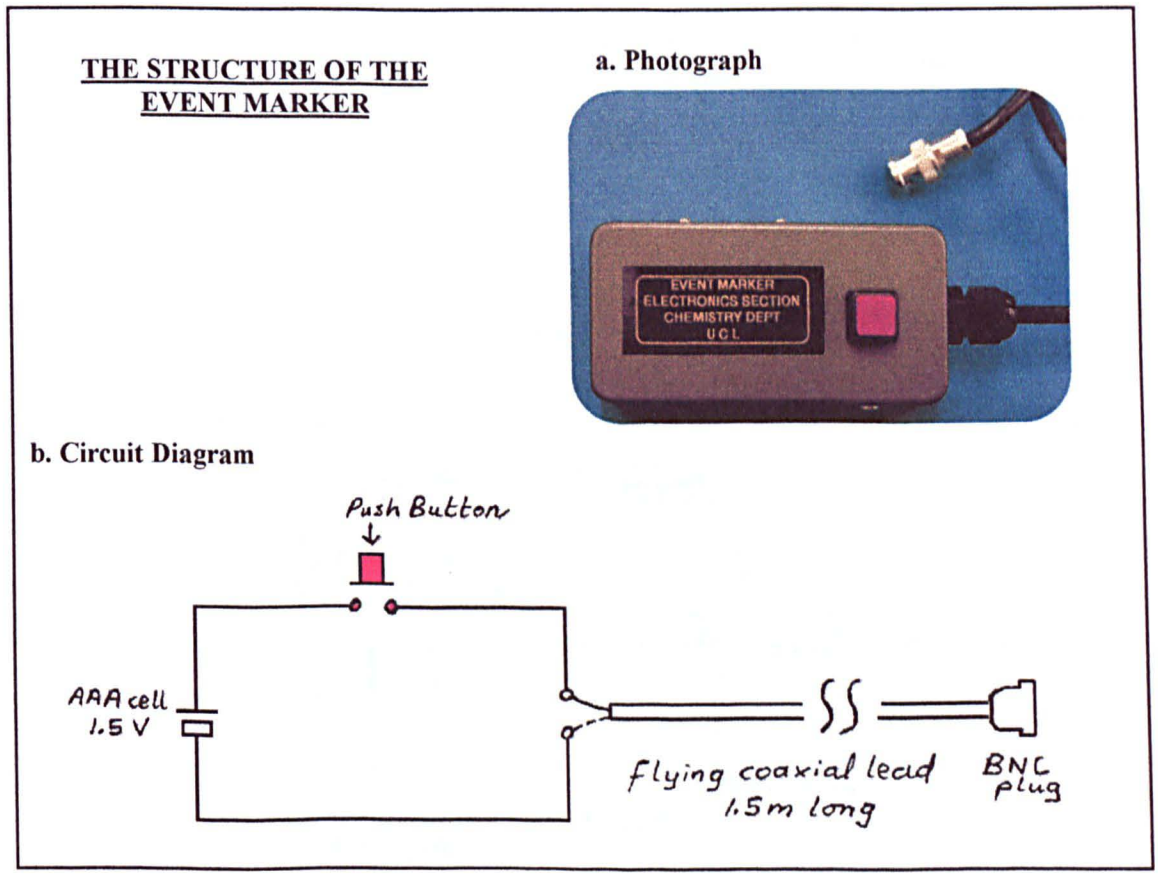

figure C-17

5. The Cell

Designed by- Tasneem Mohiuddin

Constructed by- Frank Ambrose of the Mechanical Workshop Based at the Chemistry Department, UCL.

The cell was constructed primarily from PTFE (teflon®).

THE CELL : **a. MAIN BODY OF THE CELL**

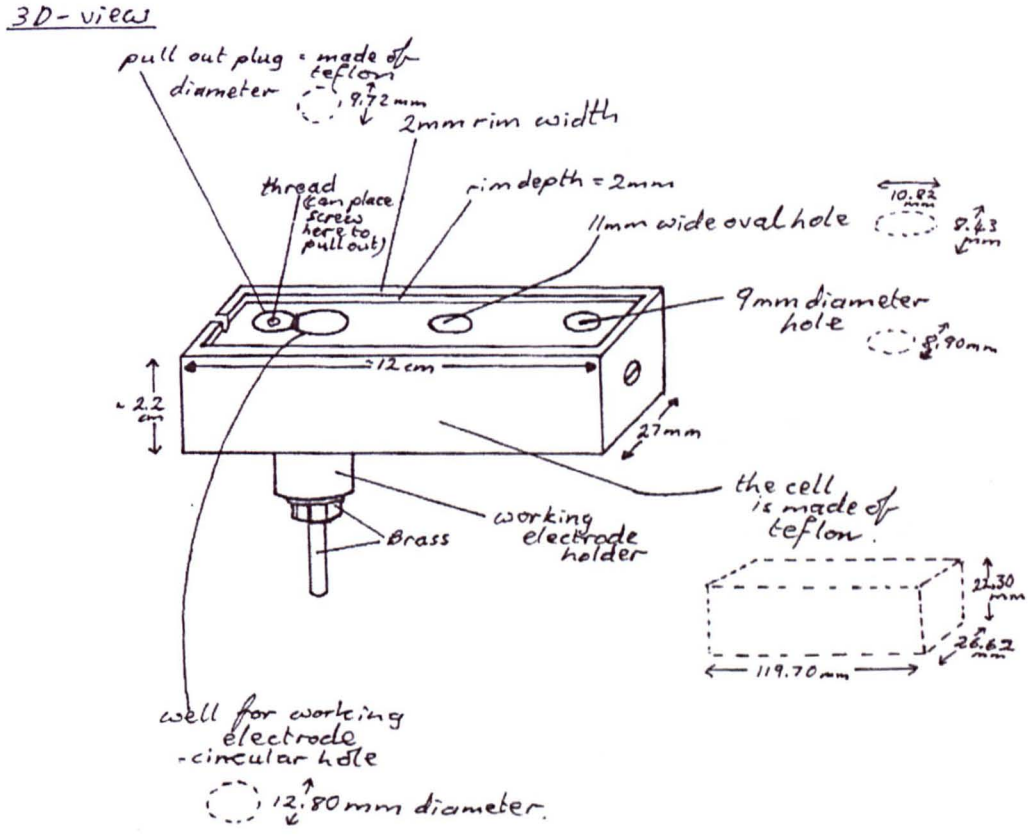

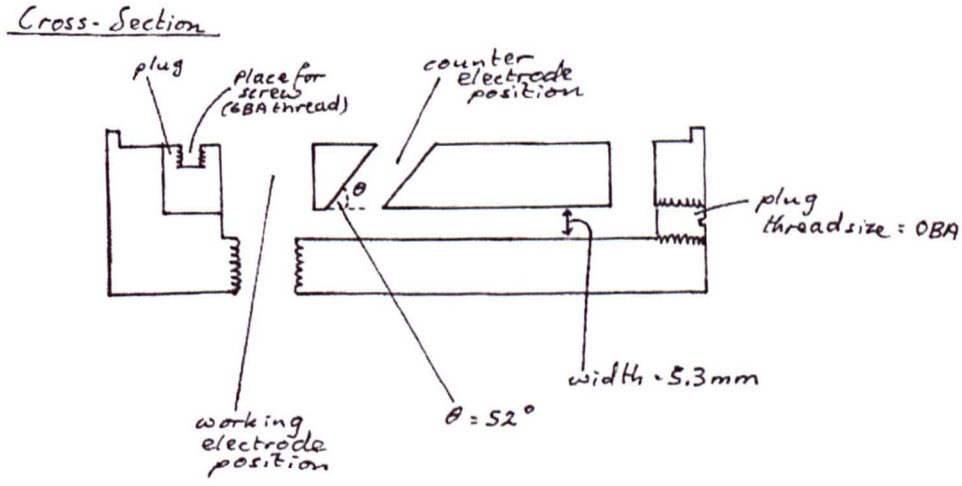

figure C-18

THE CELL : **b. WORKING ELECTRODE HOLDER**

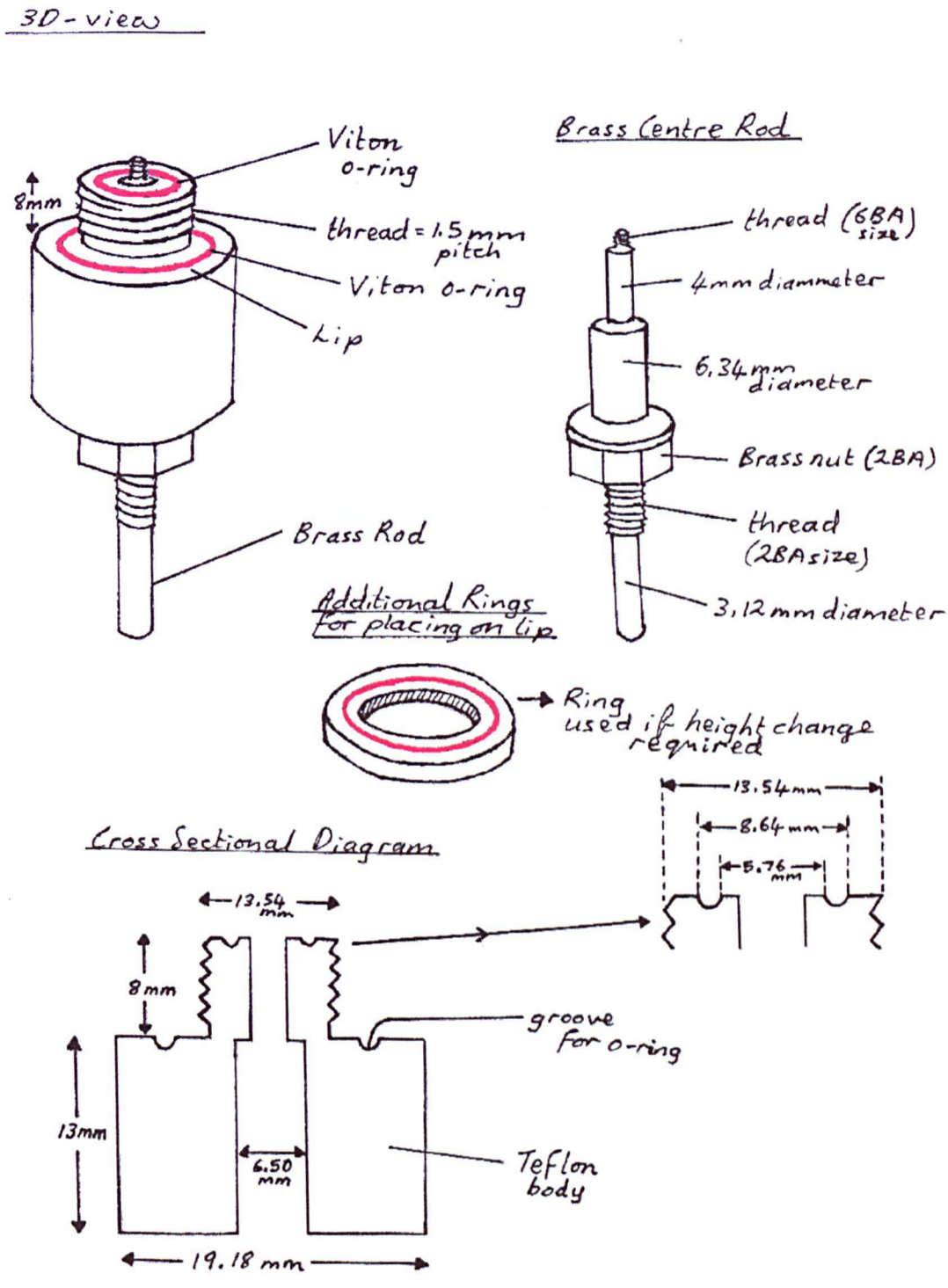

figure C-19

THE CELL : **c. COUNTER ELECTRODE HOLDER**

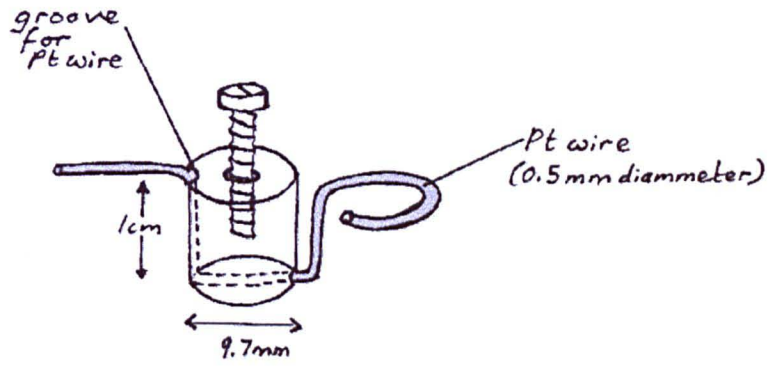

figure C-20

Please see Chapter 2 (Experimental Method) for photographs of the cell.

6. Mini-Faraday Cage for the Cell

Designed by- Tasneem Mohiuddin

Constructed by- Frank Ambrose of the Mechanical Workshop, UCL.

The mini-Faraday cage was designed to fit around the cell and it was constructed from aluminium and lined with mu-metal. Please see Chapter 2 (Experimental Method), figure 2.10, for photographs of this item.

MINI-FARADAY CAGE: **a. MAIN BODY AND LID**

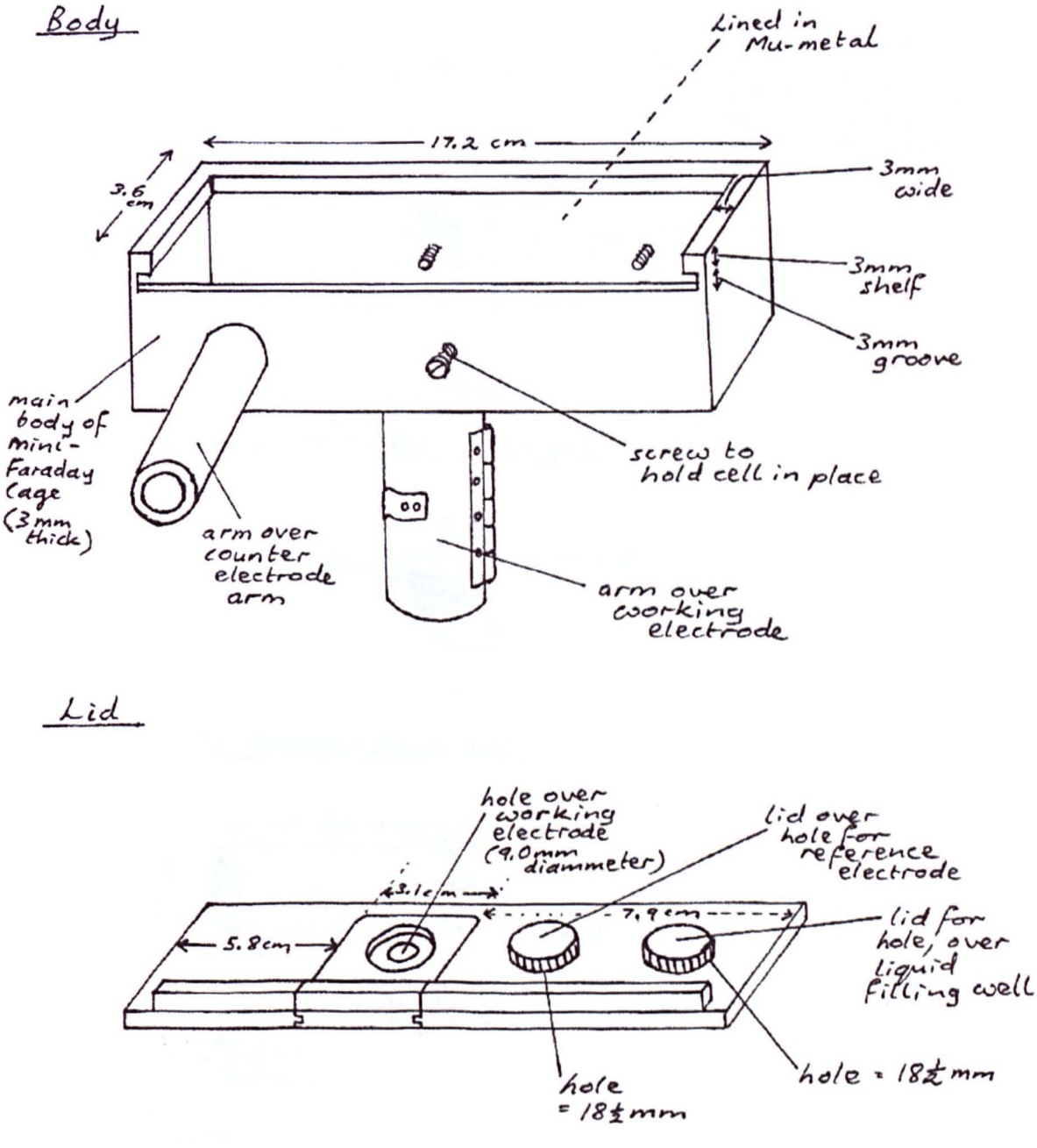

figure C-21

MINI-FARADAY CAGE: **b. REMOVABLE COMPONENTS**

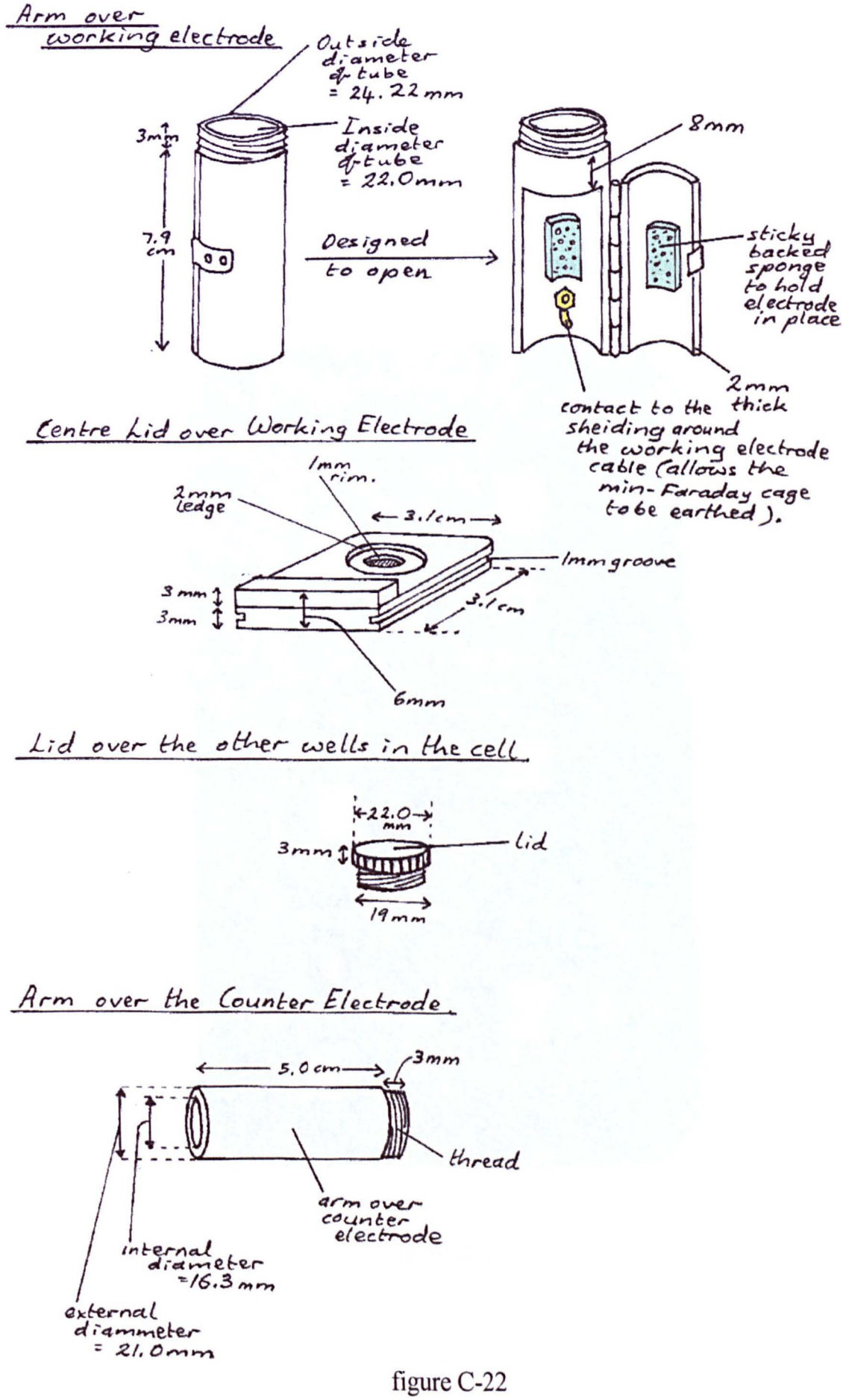

figure C-22

7. Working Electrode Mounting Cups

Designed by- Design enhancements by Tasneem Mohiuddin

Constructed by- Dave Morfett, Roy Northeast, Jim Stevenson of the Mechanical Workshop Based at the Chemistry Department, UCL.

PHOTOGRAPHS OF THE ELECTRODE MOUNTING CUPS

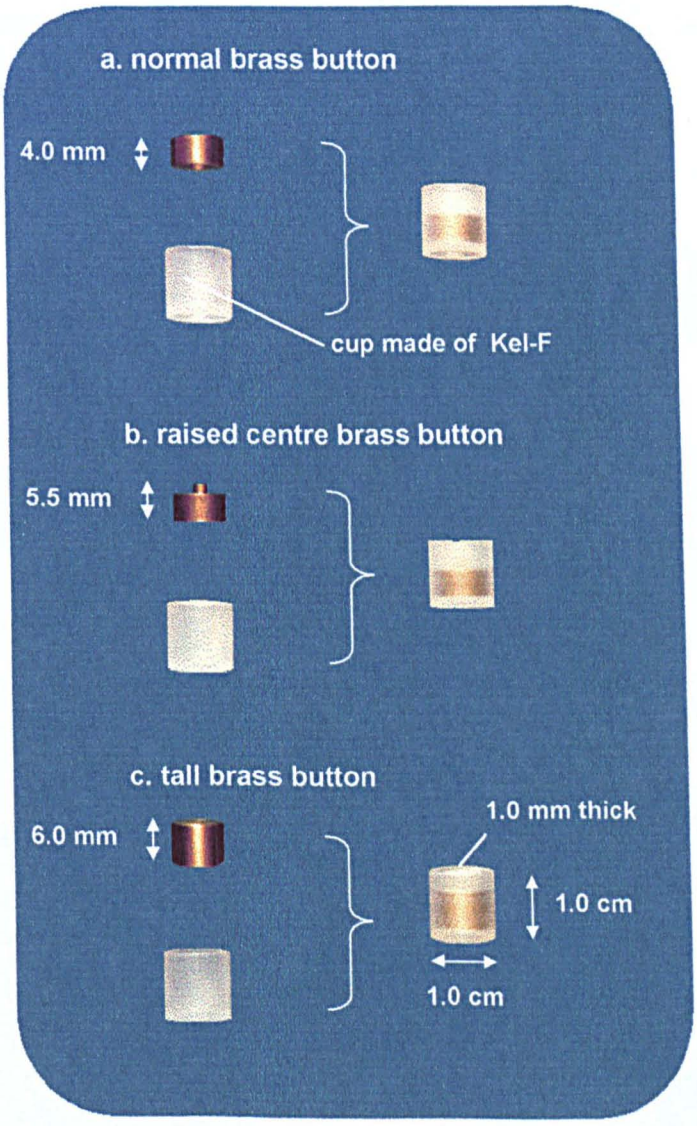

figure C-23

D. PREPARATION OF THE WORKING ELECTRODE

D. PREPARATION OF THE WORKING ELECTRODE

The working electrode consisted of a small piece of sample material (in the form of wire, foil etc) which was inserted into a small plastic, cup shaped, container with a hole in the bottom. The sample material was attached to a conductive brass button placed at the bottom of the cup using silver conductive paint, GaIn eutectic, or alternately made to go straight through the bottom of the cup where it was attached to a conductive pieces of wire using silver conductive paint and covered over the top with epoxy resin.

An electrode preparation technique was devised to give reliably a good electrical contact, avoiding wastage of material and time.

The most important part of the preparation was to obtain a good electrical contact with the brass button. This could be done by having a large as possible surface area of the working electrode material in contact with the brass button, it sits on, and in addition by keeping the piece of metal still and upright and in place throughout the time the silver paint is drying. The type of brass button used was chosen in order to achieve the best results depending on the type of sample being used.

An outline of the steps involved in making the working electrode can be given as follows;

1. Select electrode holding cup and brass button.
2. Cut out sample and bend wire if required to make it stand up.
3. Wash / clean sample.
4. Make an electrical contact from sample to brass button it sits on.
5. Seal in place with resin (and primer if required).
6. Polish electrode.
7. Attach to rod which fits into the electrochemical cell as a whole.

These steps have been discussed in more detail on the following pages.

1. Making the Electrode

Selection of electrode cup type

The electrodes were mounted in electrode cups (of 1 cm height and diameter) fitted with a brass button in the base.

Components:

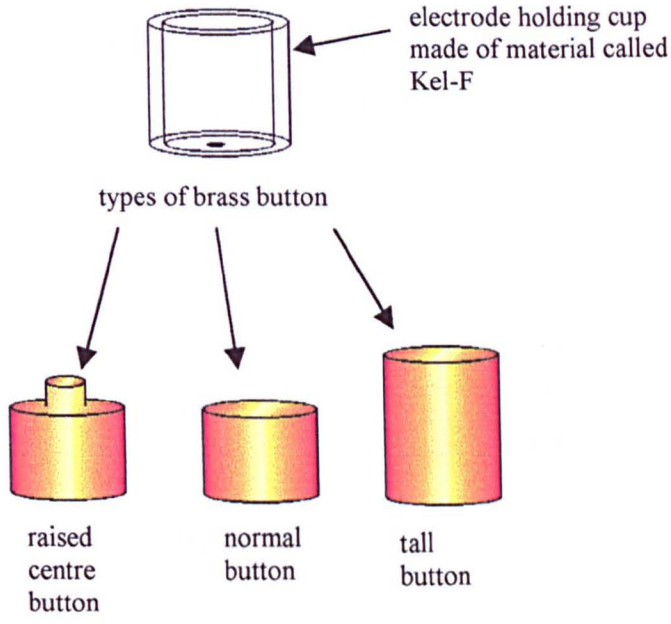

figure D-1

The cup itself was a small container with a hole at the bottom. The cup was made of an inert plastic material, Kel-F. This material was used as it is a very inert substance and like PTFE will not react with most chemicals but has the added advantages of being able to stick to epoxy resin.

The brass button was selected and pushed in down to the bottom of the cup. The type of brass button was chosen depended on the type of sample which was being placed in it.

a) If the sample was easy to bend such as in soft or thin wire, then a normal brass button was selected. The best results were achieved by bending the bottom of the wire into a base so that it can stand up on its own without falling over (figure D-2).

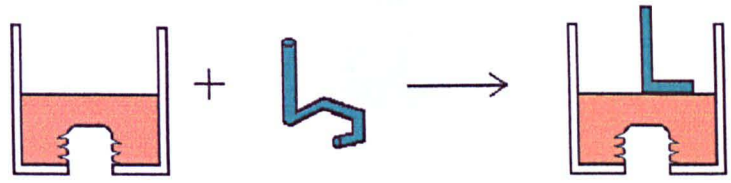

figure D-2

b) If the sample was difficult to bend because it was wider or harder, then a raised centre brass button was used with a small hole having been drilled into the raised centre in order to keep the sample propped up in place (figure D-3).

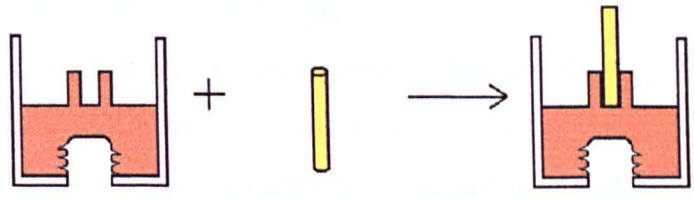

figure D-3

c) Flat samples such as silicon could be mounted on a tall brass button (figure D-4).

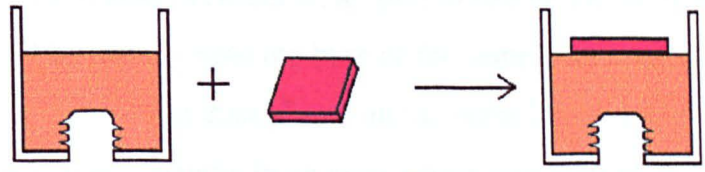

figure D-4

d) In some cases such as for band electrodes the hole at the bottom of the electrode holding cup was elongated into a slit and the electrode was mounted directly through the slit and a wire could then be attached directly to the electrode coming through the bottom of the cup, without the use of a brass button (figure D-5).

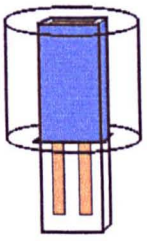

figure D-5

Cleaning the sample

Once the sample has been selected and cut into the right size (to fit the electrode holding cup) and the base of it bent if required, the sample was thoroughly cleaned prior to permanent attachment to the brass button.

The sample was cleaned by first sonicating in ultra pure water (triply distilled or Milli-Q plus) and then sonicating in AnalaR acetone. Prior to sonicating in water and acetone sometimes more extreme measures of cleaning were taken. One such measure would be sonicating in acetic acid first as, used for some stainless steel samples. Where silicon was the selected electrode material chemical etching was used. A drop of HF (30% in water) was placed on the sample for 60 s and then rinsed off using plenty of purified water.

Making electrical contact

A clean pair of fine stainless tweezers were used to handle the sample material. A bit of silver paint was dabbed gently onto the base of the sample and onto the centre of the brass button. This sample was then placed on the brass button and then left to dry in a clean dry place over night (usually in an oven which was kept at 45 °C). This was important as even though it appears to dry to touch on the surface very quickly, the best electrical conductivity is not achieved for at least another 12 hours, and if the resin is poured into the cup too early the silver paint does not fully dry and the best electrical conductivity is not achieved. On occasion conductive silver epoxy was used, if the sample was still proving difficult to mount, as an extra item for holding the electrode in place. In the case of silicon, GaIn eutectic was used instead of silver conductive paint. This was prepared by mixing 1.44 g In : 13.80 g Ga together. This eutectic was then applied to the dull side of a piece of silicon immediately after it had been etched and rinsed using a cotton bud. Then the side with the GaIn eutectic was placed in contact

with the brass button. The time between etching the silicon, and placing the GaIn eutectic on the Si had to be kept short so that a thick oxide layer would not form and degrade the contact.

Sealing the electrode with resin

Once the conductive paint had dried properly the electrode was sealed in place using epoxy resin so that only the sample was in contact with the solution and not any other materials, such as the brass button or conductive paint. Epoxy resin was used as it is a suitably electrochemically inert material.

Prior to pouring in the epoxy resin, a primer was used in some cases such as with stainless steel, where it was especially important to seal the electrode in without any gaps around it to prevent crevice corrosion occurring. The primer used was Permabond SIP®.

In earlier experiments the epoxy resin used was Araldite®. This was a cream coloured resin which was mixed in a 1:1 ratio of resin : hardener (approximately by volume). It was found that this resin was not very hard and easily dissolved in organic cleaning solvents such as acetone or ethanol leaving little holes in the surface of the resin. Therefore these solvents could not be used, except in the case of band electrodes where the metal electrode was already sealed with an insulating material prior to the application of epoxy resin. In later experiments a different epoxy resin was used. This was Epo-kwick® (from Buehler UK Ltd). This was a clear resin which was much easier to handle as it starts of as a much thinner liquid (of water-like consistency) when first mixed so it was easier to pour into the electrode cup. This was mixed in a ratio of 5g resin : 1g hardener (by weight). After weighing out the resin into a disposable plastic cup, the weighing balance was zeroed and then the hardener was dripped into the weighing cup to give 1/5 th the weight that was previously observed for the resin. The cup containing both the resin and the hardener was then tipped to 45° and the resin was stirred using a clean wooden 'lolly' stick, by folding the glue slowly for 2 minutes (and not vigorously stirring) so that there would be very few if any bubbles present in the resin, so stopping any solvent running down the bubbles and hence the sides of an electrode in an experiment. Once mixed the resin which was still a very thin liquid at

this stage, was injected into the electrode cup containing the mounted sample using a disposable 1 ml syringe.

The cup was filled so that the resin just went over the rim of the electrode cup.

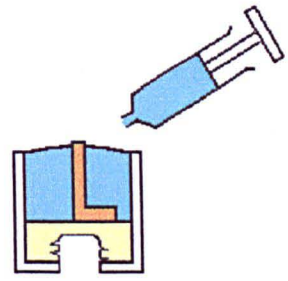

figure D-6

Once the empty space in the cup containing the electrode had been filled with epoxy resin up to the top of the cup and left to dry, in a 45°C oven (over night), the electrode was polished flat.

2. Polishing

Polishing allowed the removal of the surface layers in order to produce as uniform and smooth a surface as possible, and it was carried out by chemical or mechanical treatment.

a) Mechanical Polishing

Mechanical polishing is carried out by polishing on successively finer grades of abrasives.

Initial stage of mechanical polishing

Emery polishing paper (a water proof silicon carbide paper) was used as the initial abrasive. Coarse, medium emery paper was used with purified water as the lubricant. This was done on a polishing wheel with a spring balanced arm which was therefore capable of keeping the electrode flat. Once a flat surface was achieved by machine the sample could be hand polished with even finer grades of emery paper by hand without

ending up with a curved or lop-sided electrode, as which could easily occur if the mechanical wheel had not been at the initial polishing stage.

Intermediate stage of mechanical polishing

After the initial polishing on the wheel finer grades of emery paper were used to polish the electrode by hand, as it was found that the hand polishing gave much better results. It was found that polishing with the right hand in a clockwise direction for a known number of cycles and with the left hand in an anticlockwise direction helped to keep the electrode level (i.e. not tilted) and flat (i.e. not curved). In some cases if the electrode was a very thin layer (e.g. gold foil) it was mounted on very hard material such as a ceramic or glass tile for support. This supporting material was hard to polish using emery paper so the initial polishing was carried out using a diamond polishing wheel followed by 60 μm aluminium oxide paper instead of the emery paper.

Final stage of mechanical polishing

The final stage of the polishing was carried out using finely grained aluminium oxide papers (30 μm, 9 μm, 3 μm, 1 μm, 0.3 μm) resting on a flat piece of glass with purified water (triply distilled or Milil-Q plus) as a lubricant. On occasion, in the very early work the very fine polishing was carried out using aluminium oxide suspensions, of grades 1, 0.3, 0.05 μm, on a polishing cloth with purified water as the lubricant. However the aluminium oxide papers were found to be more effective. Where the electrode was hard (e.g. stainless steel) or mounted on a hard material such as a glass or ceramic tile, diamond polishing pastes, of grades 25, 16, 6, 3, 1, ¼ μm, were used with the lubricant provided. This polishing was carried out on an appropriate polishing cloth stuck down to a piece of flat glass with self adhesive backing. After each stage of polishing (i.e. after each grade of polishing material) debris from the polishing was rinsed off, using a suitable cleaning solvent compatible with the lubricant that was being used in polishing. After each grade of polishing material the sample was first rinsed with the cleaning solvent, and then placed in an ultra sonic bath in the same solvent, and then rinsed with the cleaning solvent again. When the polishing material was emery paper or aluminium oxide, just purified water was used as both the lubricant and as the final cleaning solvent. When the polishing material was diamond polishing paste and, the lubricant used was that provided with the diamond polishing pastes (type-OS), then

AnalaR ethanol was used as the cleaning solvent. The rigorous cleaning was required not only to minimise contamination from one grade of polishing material to the next but, as it is known that dyes contained in the diamond pastes for easy recognition can often be electroactive and similarly small particles of alumina may affect the kinetics of a reaction because of the adsorption of the reactant at the alumina surface.

b) Chemical Polishing

If further polishing is required to remove surface damage from mechanical polishing this can be done by chemical etching. Alternatively if the material comes in a form which is sufficiently smooth to start off with, chemical etching can be used to perfect the surface further without polishing, such as in the case of silicon. Etching is the process of removing surface layers of the semiconductor by a variety of functions including polishing, cleaning the surface, reducing the No. of defects and texturing the surface.

In the experimental work carried out using p-type silicon, prior to each experiment, the silicon electrode was etched for 20s in 30% HF by dripping the solution over the surface then immediately rinsing of the solution with plenty of water.

3. Preparation of Special Electrodes

Homemade pure gold microband electrode

A gold band electrode was prepared from scratch due to the fact that the work conducted with the commercially available screen printed gold microband electrodes showed that they quickly became irreversible, and it was extremely difficult and some times impossible to polish them down to a clean reversible surface again.

a.) In order to prepare this electrode a clean glass microscope slide (depth 1- 1.2 mm) was used. Two sections were cut of this slide each of a width 0.5 cm x 2.6 cm. Then one of these two sections was cut into two halves.

b) Then one whole section (0.5 cm x 2.6 cm) and one half section (0.5 cm x 1.3 cm) of the glass side, were taken and cleaned thoroughly in distilled water and then acetone in an ultra-sonic bath. These were then carefully removed and placed in a clean glass petri-dish. An easily removable sticky label was then cut up into ~ ½ cm strips and then carefully pressed centrally onto the outside perimeter edges (1 mm depth) of the miniature slides.

c) The petri-dish containing these slides was then placed in a gold sputtering machine (which deposits ~ 1 nm per minute) for just over an hour.

d) The sticky labels were then removed from the edges of the glass slide and a small piece of very thin gold foil was cut up, using a clean scalpel and sandwiched between the two gold slides coated with gold, so that the gold coated side of each slide was in contact with the gold foil in the middle.

e) The slides were then held together using a crocodile clip. A ordinary piece of wire was then taken and wound around the end of the gold and glass slide, were the gold was exposed in a slightly lose manor. The wire was then carefully removed and plenty of silver conductive paint was applied to the wound end an then carefully pushed back into place. The silver paint could not be applied by brushing onto the gold surface directly as the gold was very soft and therefore easily brushed off. Once the wire was back in place more silver paint was dropped over the wire which was in contact with the gold. The silver conductive paint was then allowed to dry for a day and then the electrode was tested for an electrical connection from the thin gold band showing at the top where the two glass slides met, through to the exposed end of the wire at the bottom.

f)Then glue (epoxy resin) was placed over the wire / silver conductive paint end of the glass slide to make sure everything was held together securely.

g) This was then inserted into a plastic cup shaped electrode holder (which had a slit cut across the bottom end) and glued in place using epoxy resin.

E. TECHNICAL DETAILS OF THE COMMERCIAL APPARATUS

E. TECHNICAL DETAILS OF THE COMMERCIAL APPARATUS

1. Battery Operated Low Noise Pre-amplifier

This was used in conjunction with the offset box shown in the previous section (Appendix C). Once the signal had been offset to between 0 and 1 volt, the pre-amplifier allowed the signal to be amplified (stretched) so that the variations making up the signal would better the region fill between 0 and 1 volt. This apparatus was run on 2 PP9 rechargeable batteries (10 volt each) contained within it.

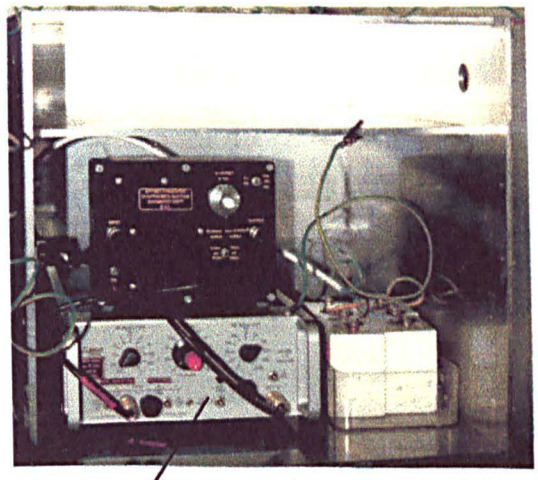

figure E-1

With this the input could be fed directly or inverted depending on which one of two input channels were used. Only the direct non-inverting channel was used (and the second channel had to be set to the off position). In addition any incoming signal could be DC or selected to be just AC. For larger signals just AC was used (silicon work) but for background signals which were fairly small such as in the monitoring of the corrosion of stainless steel DC was used. This is since the background current was zero and having the apparatus set to DC allowed the signal to settle and therefore be processed more quickly than if it is AC.

In addition this unit carried within it low and high frequency filters. The low frequency filter was usually kept open to the lowest amount at 0.03 Hz but the high frequency filter was limited to between 10 kHz and 30 kHz to limit the noise being picked up.

Settings on the pre-amplifier:

1. on the inputs; AC / DC/ GND

2. on the gain; x 10, 20 ,50 ,100 ,200, 500, 1k, 2k, 5k, 10k

3. on the low frequency filter ;

f (Hz)	DC	0.03*	0.1*	0.3*	1	3	10	30	100	300	1000
1/f (s)	——	33.33	10.00	3.33	1.00	0.33	0.10	0.033	0.010	0.003	0.001

4. on the high frequency filter ;

f (Hz)	3	10	30	100	300	1k	3k*	10k*	30k*	100k	300k
1/2πf (μs)	53052	15915	5305	1591	1111	159	53.05	15.91	$5.31^{>P}$	$1.59^{<P}$	0.53

Notes : * represents the values used in the experiments, for the high frequency filter $1/2\pi f = \tau_{inst}$, the limiting characteristic time scale for this instrument and for the low frequency filter, $1/f = t_{lim}$, the cut off time where signal variations taking longer than this time are not recorded. The potentiostat response time = 4 μs. $^{>P}$ represents the potentiostat response time is greater than this, and $^{<P}$ represents the potentiostat response time is lower than this.

Notes on the selection of the high frequency filter

This was adjusted to reduce the amount of electrical noise without the loss of image data. When using the preamplifier optimisation of the high frequency filter was carried out by eye, the filter was lowered starting at the 30 kHz position (30 kHz was selected due to the limiting potentiostat response time) to give the optimum image without loss of image detail. The filter was turned down by watching to see that the noise on the non-electrode area or the 'light off' image was reduced, but the photocurrent image generated over the electrode area was also watched to make sure there is no loss of image features so that the image reached an optimum compromise. If turning the high frequency filter down by a setting resulted in a loss of image features then the setting was turned back up to the next highest frequency filter.

Notes on the selection of the low frequency filter

The low frequency filter was used to eliminate any very slow time variations, so that only changes caused by the laser were observed. Reducing the low frequency filter from 0.03 Hz down to 0.1 Hz or 0.3 Hz did not seem to improve the image, so it was found that it was best to leave the low frequency filter at the lowest possible value (0.03 Hz).

2. Virtual Chart Recorder

In experiments where the effect of the time on the photocurrent image was studied a 12 bit external data logging device (ADC-100 , Picotechnology Limited) was used, by attachment to a computer parallel port. This was used to record the total current output vs time, for the same period of time in which the photocurrent images had been collected.

Data was collected using the combination method of signal averaging where it was possible to specify: average, minimum, maximum or sum, to be recorded as one data value for a selected number of readings. From these techniques, signal averaging was used.

Time taken to collect the data for various amounts of signal averaging:

Number of readings signal averaged	Total sampling time, to collect and average this number of signals / μs
3	240
10	420
20	620
50	1220
100	2220

This technique was found to be useful in looking at the corrosion of stainless steel with time. In this case to eliminate noise, typically for every data point recorded at 1 second intervals, 100 reading were signal averaged (this took up 2220 μs at the beginning of each second) .

3. Scanning Laser Microscope

The laser power and therefore laser light intensity could be reduced by known amounts by the use of neutral density filters. When no filter was present the percentage transmission was 100%. However some of the laser intensity may have been lost along the pathway, due to incorrect alignment, deflection by dust etc.

The neutral density filter provided with the scanning laser microscope come in a rotating wheel of 4 positions. The neutral density, ND, filter value is the absorbance (A) value of the filter concerned, where $A = \log_{10} \frac{1}{T}$. The ND values have been listed in the table below.

A table showing the neutral density filters in the filter wheel:

Position on wheel	ND value (A)	% Transmission (%T)	Transmission (T)
0	0	100	1.00
1	1	10	0.10
2	1.5	3	0.30
3	2	1	0.01

In addition three other filters were also found in our lab. These were calibrated using a UV visible spectrophotometer (Perkin-Elmer Lambda 5). The instrument was first zeroed for air versus air. Then the filter was put in against air and the spectrophotometer scanned between 400 and 600 nm (as around 500 nm was our region of interest) at a scan speed of 120 nm min^{-1}. An almost straight line was recorded between 400 and 600 nm and from this the absorbance was read-off at 500 nm and the transmission calculated from this.

A table showing the additional neutral density filters available:

Filter	Absorbance	Transmission (T)	% Transmission
A	0.265	0.555	55.5 %
B	0.565	0.273	27.3 %
C	0.565	0.273	27.3 %

Any of these filters may be used in combination with each other or with the filters provided by the microscope company in the reduction of argon ion laser light, where:

$$\text{filter A} + \text{filter B} = T_A \times T_B$$

A table showing the properties of the lens available:

lens manufacture	lens magnification	N.A.	working distance (mm)	minimum spot size at $\lambda = 488$ nm (μm)	minimum spot size at $\lambda = 514$ nm (μm)
Nikon	x4	0.13	16.22	1.88	1.98
Bio-Rad	x4	0.12	~13	2.03	2.14
Bio-Rad	x10	0.25	~5	0.98	1.03
Swift	x20	0.40	~2.5	0.61	0.60
Nikon	x40	0.40	14.9	0.61	0.64
Bio-Rad	x40	0.65	~ 0.8	0.38	0.40

Where, minimum spot size, $2r \approx \frac{\lambda_o}{2\ \text{N.A.}}$

The calibration of any lens gave an objective factor which could be manually fed into the microscope software to give the correct size on the image.

A table showing the calibration of the image size to the lens used:

Lens manufacturer	Lens magnification	N.A.	Required Objective Factor	
			x-axis	y-axis*
Bio-Rad	x4	0.12	3.8	4.1
Nikon	x4	0.13	3.7	4.0
Bio-Rad	x10	0.25	9.4	10.2
Swift	x20	0.40	14.3	15.7
Nikon	x40	0.40	27.8	30.5
Bio-Rad	x40	0.65	36.9	40.4

Note: * this is the value for both the y and x axis at faster speeds

The objective factors, listed on the previous page, are for standard slow speed and user selectable slow speeds, but for faster speeds (normal, fast, v.fast) the objective factor value given for the y axis, is the value for the x axis as well. For any electronic zoom and objective lens magnification the pixel size in any direction may be worked out using the formula, and it is done in this way by the microscope's computer program.

$$\text{pixel size} = \frac{15.240}{\text{objective factor}} \div \text{zoom}$$

Typically photocurrent images would be collected using a x4 lens at a zoom of 5.

e.g. x4 Nikon lens (N.A.=0.13)

the objective factor = 3.7 for the x-axis

and the objective factor = 4.0 for the y-axis

If the electronic zoom = 5.0

and the laser scan time = slow

$$\text{The x - axis pixel length} = \frac{15.240}{3.7} \div 5.0 = 0.823\,\mu\text{m}$$

$$\text{The y - axis pixel length} = \frac{15.240}{4.0} \div 5.0 = 0.762\,\mu\text{m}$$

A summary table showing the pixel dwell time for the line scan time selected:

Setting	Dwell Time per Pixel / μs	No of lines per frame	line scan time / ms line^{-1}	Approx. Frame Time
very fast	2.5	¼ of 512 = 125	1.92	¼ s
fast	2.5	½ of 512 = 256	1.92	½ s
normal	2.5	512	1.92	1 s
slow	10	512	7.68	4 s
selectable slow	t_{line} / 768	512	t	512 x t

4. Electron Probe X-ray Microanalyser

a. Instrument Setup for Recording Secondary Electron Images

A BLOCK DIAGRAM SHOWING THE SETUP FOR SEM

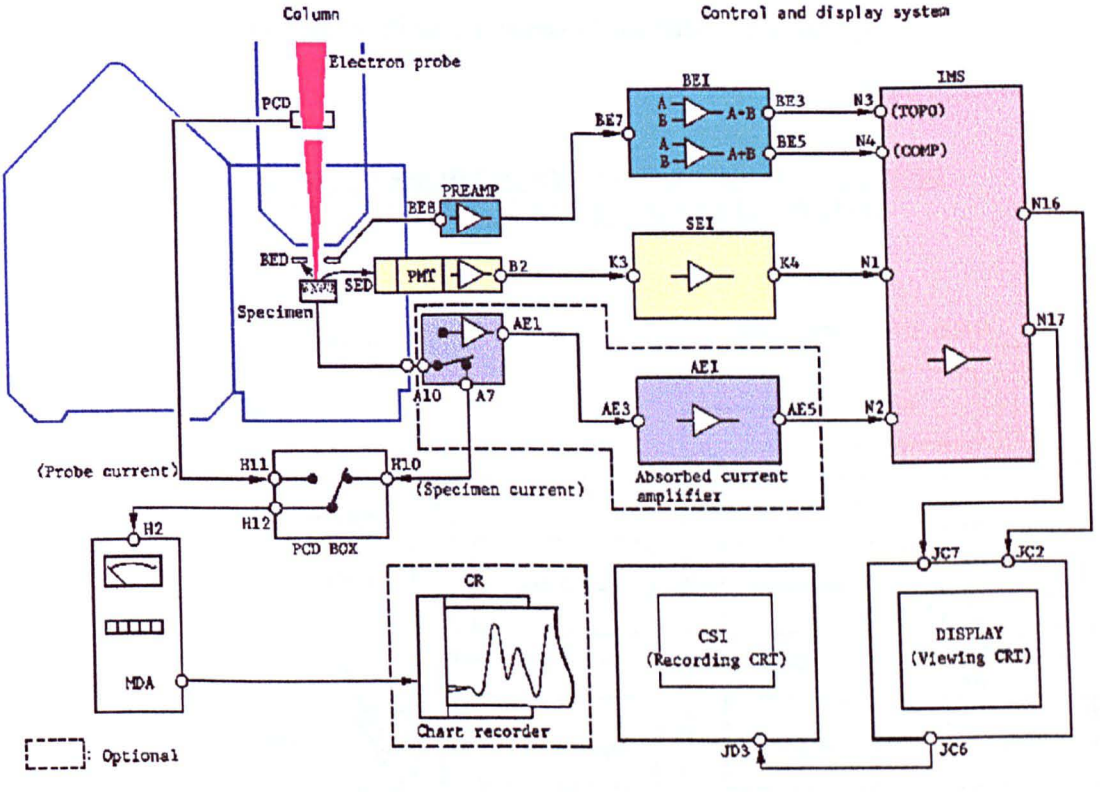

figure E-2

Detection

The secondary and back scattered electrons emitted from the specimen were detected and converted into electrical signals using a secondary electron detector (SED : of the scintillator / photomultiplier type) or a backscattered electron detector (BED : of the doubly divided semiconductor type) respectively. The electrical signal was then fed into the respective video amplifiers. In addition the specimen current was displayed and could then be amplified using an absorbed current amplifier.

Signal Display

After being amplified, the signal was displayed as a line profile or a scanning image. The image type was selected using the image selector (IMS) unit and then displayed on the cathode ray tube (CRT) display.

Image Type / Selection

The image displayed could be a secondary electron image, a backscattered electron image or specimen current image. Usually a secondary electron image was selected. In addition the back scattered electron image could be on of two types topographic or compositional.

b. Instrument Setup for Recording Element Concentration Images

(microprobe maps)

BLOCK DIAGRAM SHOWING THE SETUP FOR MICROPROBE ELEMENTAL CONCENTRATION MAP RECORDING

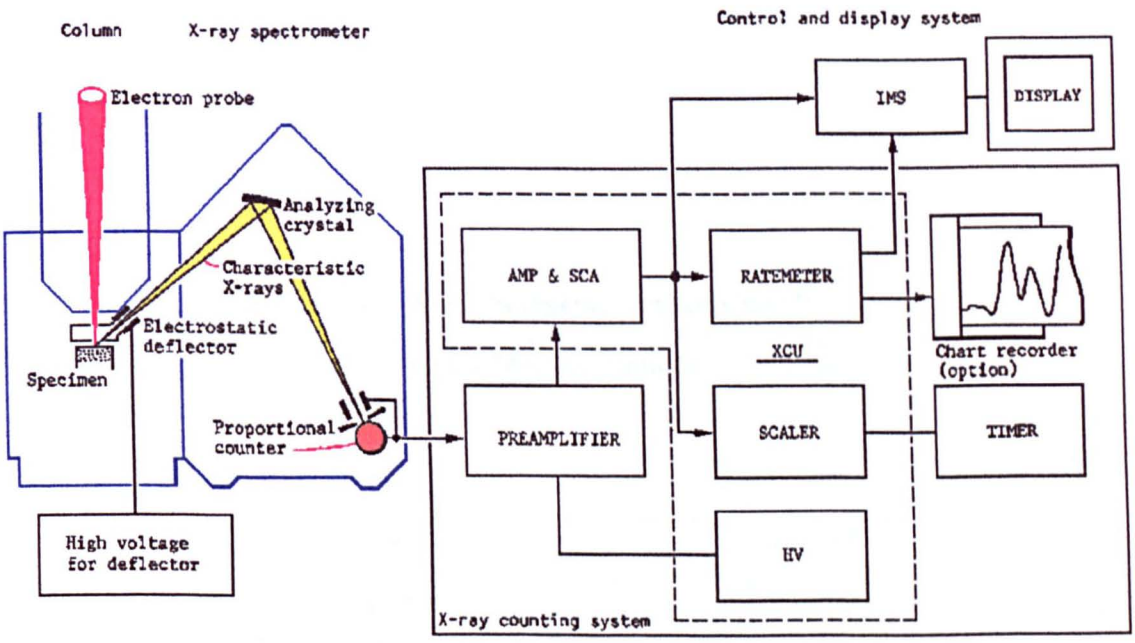

figure E-3

X-ray Detection and Counting System

The characteristic x-rays emitted from the specimen were diffracted by the analysing crystal and then those of the selected wavelength for a particular element entered the detector (a proportional counter), in the x-ray spectrometer, and they were converted into electrical signals.

Amplification of Signals

The signals were then amplified by the pre-amplifier unit and then, the pulse height analysed (by the AMP & SCA unit). The output signal from this was then counted by the scaler and displayed on the ratemeter.

Display

The signal was then saved to the computer, as a 2-dimentional image showing elemental concentration over the surface, and it was viewed directly in time as it was recording, or later as required.

The four detection crystals which were available to use were:-

1. Pentaerythritol (PET)
2. Lithium Fluoride (LIF)
3. Thallium Acid Phthalate (TAP)
4. Lead Stearate (STE)

A table showing the properties of the detecting crystals used:

Crystal	Bragg Diffraction Indices (hkl)	2d (Å)
PET	002	8.742
LIF	200	4.0267
TAP	100	25.757
STE	film	100.4

A summary table of the experimental settings:

	Experimental image type	Acceleration Voltage/ kV	Current / A	typical dwell time
1.	microprobe spot analysis	25	5×10^{-8}	20s
2.	microprobe elemental maps	25	1.3×10^{-7}	100 ms
3.	standard SEM pictures	25	5×10^{-8}	———
4.	special oxygen maps	12	1.3×10^{-7}	100 ms
5.	oxygen and another element combination map	12	1.3×10^{-7}	100 ms
6.	low kV SEM picture	12	5×10^{-8}	———

Diffusion Range at Various Acceleration Voltages

To find the diffusion range a line must be drawn through the density of the material and the acceleration voltage being used, and then extrapolated to find the diffusion range.

DIFFUSION RANGE IN THE MICROPROBE ANALYSIS WORK

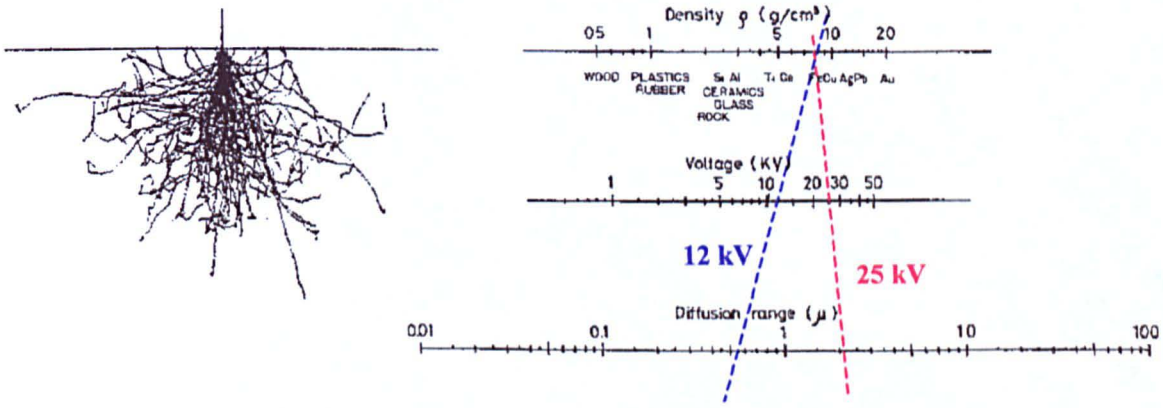

Notes: This diagram was taken from JXA-8600 series Electron Probe X-ray Microanalysis information booklet. The acceleration potential is related to the energy of an electron by the equation: Energy = Acceleration Voltage x Charge of 1 electron. Therefore the energy in keV units has the same value as the acceleration voltage in kV units.

figure E-4

For example,

The density of stainless steel is ~8 g cm^{-3}.

From the above diagram if an acceleration voltage of 12 kV is used to analyse a stainless steel sample then the depth analysed is a fraction of a micrometer, so only a very thin layer at the surface is analysed.

However if an acceleration voltage of 25 kV is used then the depth of the sample analysed is a few micrometers.

F. WATER PURIFICATION SETUP

F. WATER PURIFICATION SETUP

1. Triply Distilled Water

For the earlier work a home made still for providing triply distilled water was used.

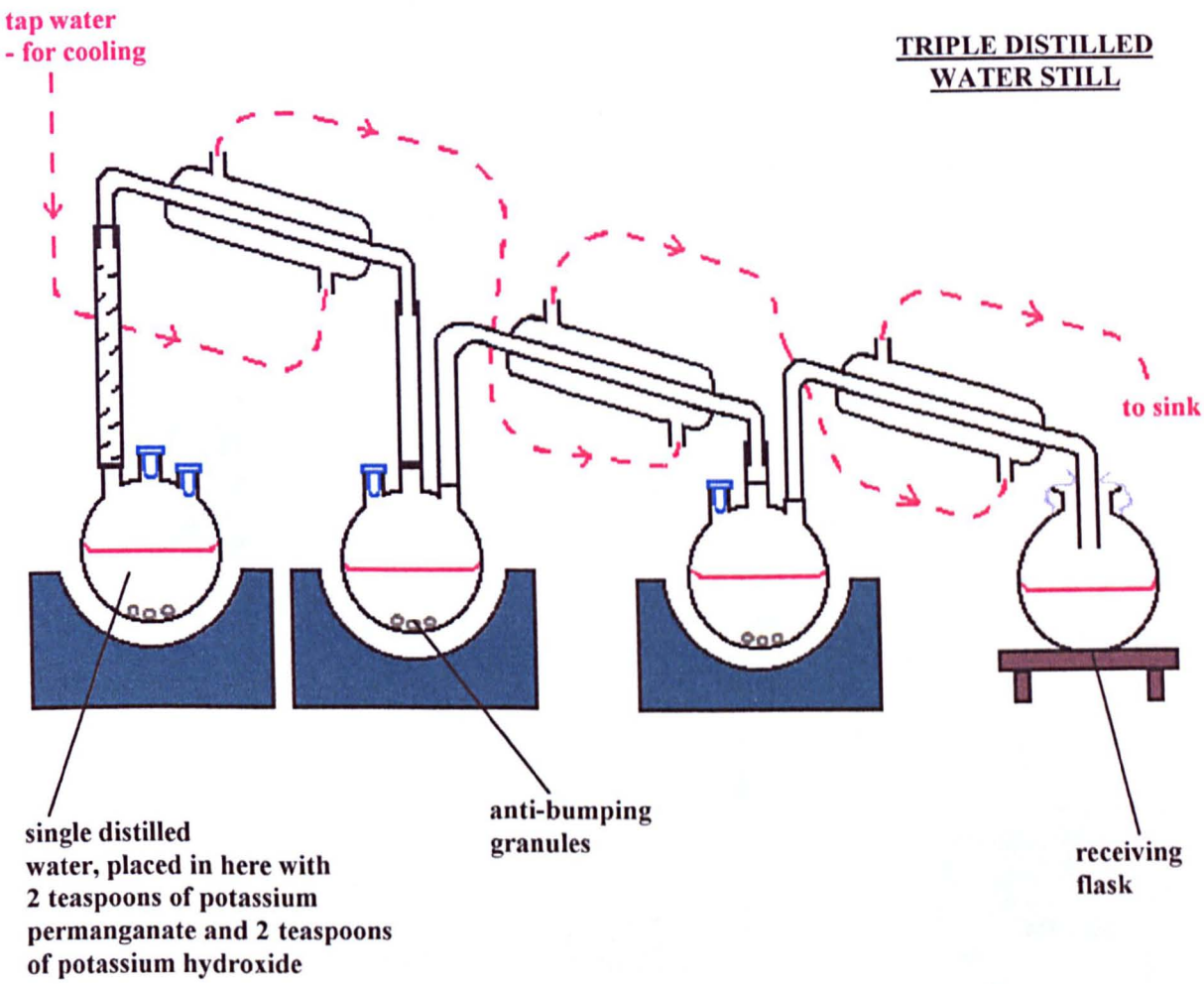

figure F-1

2. Millipore Q-Plus Water

However many problems were encountered with this setup contamination from the feed water (tap water) as if frequently passed into the distilled water. Consequently the system had to be cleaned out at very regular intervals in acid, water, and then distilled water. Even then the quality of the product water was uncertain. Indeed on one occasion when the water managed to get particularly contaminated and some

spectacular photoelectrochemical images showing the poisoning of a gold disc electrode were produced (see Chapter 4, figure 4.25).

A much improved, purification system, was then set up. In this new water purification system a cartridge filter (for filtering out large particles / sand) and deioniser (for removing out mineral ions) were attached to the mains cold water tap. This was required as feeding directly into the single distilled water still damaged it, since the feed water was still so filthy. The filtered water was then fed into a tank from where it was pumped up into the single distilled (using a fish tank pump) water still. Then from here it went into another tank from which it was drawn into a commercial high purity water system. This system was the Millipore-Q185 Plus water purification system.

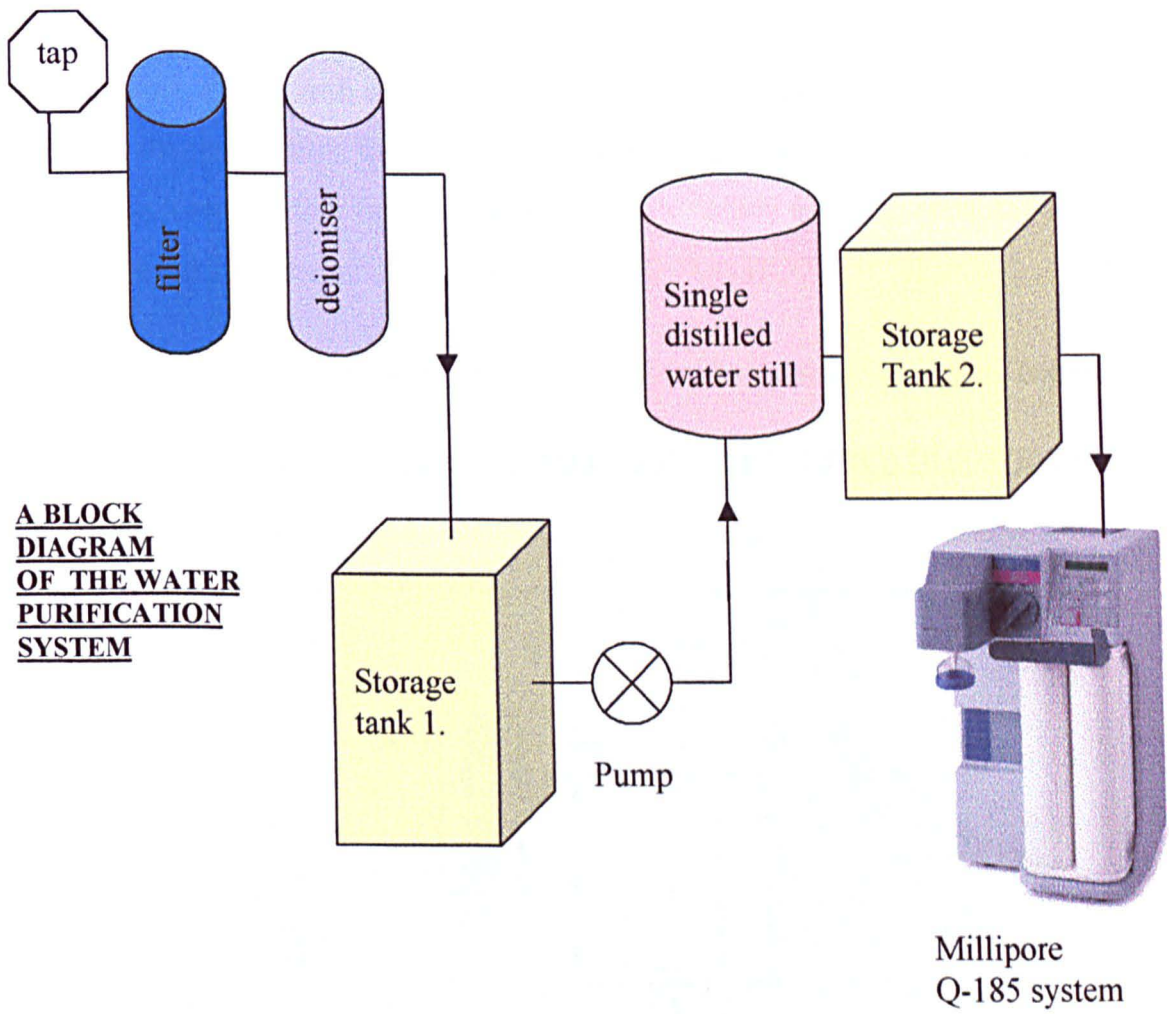

figure F-2

In the millpore Q plus system the water is passed through a system of four filters. These were :

1. activated carbon-to remove dissolved organics,

2. an ion exchange resin to polish out ionic impurities to 18.2 MΩcm resistivity,
3. an organic scavenging material (Organex-Q™) to remove trace organics,
4. a 'Millipak' 0.2μm stacked disc membrane filter cartridge (0.22μm Durapore ® PVDF membrane).

In addition this water was exposed to ultraviolet light in a photo-oxidation chamber in the Millipore Q plus system. The two wavelengths used (185 + 254 nm) were required to generate the short lived but highly reactive hydroxyl free-radicals (OH•)

$$H_2O_2 \xrightarrow{UV,185nm} O_3 \xrightarrow{+H_2O,\ UV\ (254nm)} H_2O + O_2 \xrightarrow{U,\ 254nm} 2OH\bullet \qquad (f.1)$$

OR

$$1½O_2 \xrightarrow{UV,185nm} O_3 \xrightarrow{UV,\ 254nm} O_2 + O\bullet \xrightarrow{+H_2O,\ UV(254nm)} 2OH\bullet \qquad (f.2)$$

The free radicals react with any organic molecules (i.e. initiate photo-oxidation) producing charged organic fragments which may subsequently continue to react in a chain reaction with further free radicals until finally carbon dioxide, water and the bicarbonate ion are generated. $CO_2 + H_2O \leftrightharpoons HCO_3^- + H^+$ (f.3)

So the photooxidation process by UV light results in the decrease in organic content.

A BLOCK DIAGRAM OF THE MILLIPORE-Q WATER PURIFICATION SYSTEM

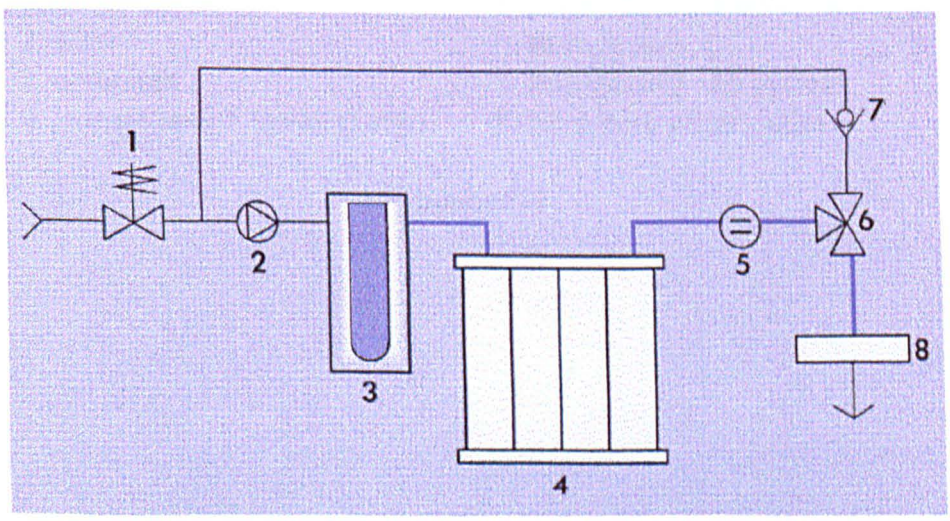

1. Inlet solenoid valve
2. Pump
3. UV photo-oxidation chamber
4. Purification pack
5. Resistivity sensor
6. 3-way valve
7. Check valve
8. Millipak filter unit

figure F-3

In addition the water was never left to stand for large periods of, being automatically recycled through the system for a few minutes every hour.

This system provided up to 1.5 litres min^{-1} of ultra pure water on demand which is at least 18.2 MΩ.cm and with a total organic carbon levels below 5 parts per billion.

A PHOTOGRAPH OF THE WATER PURIFICATION SETUP

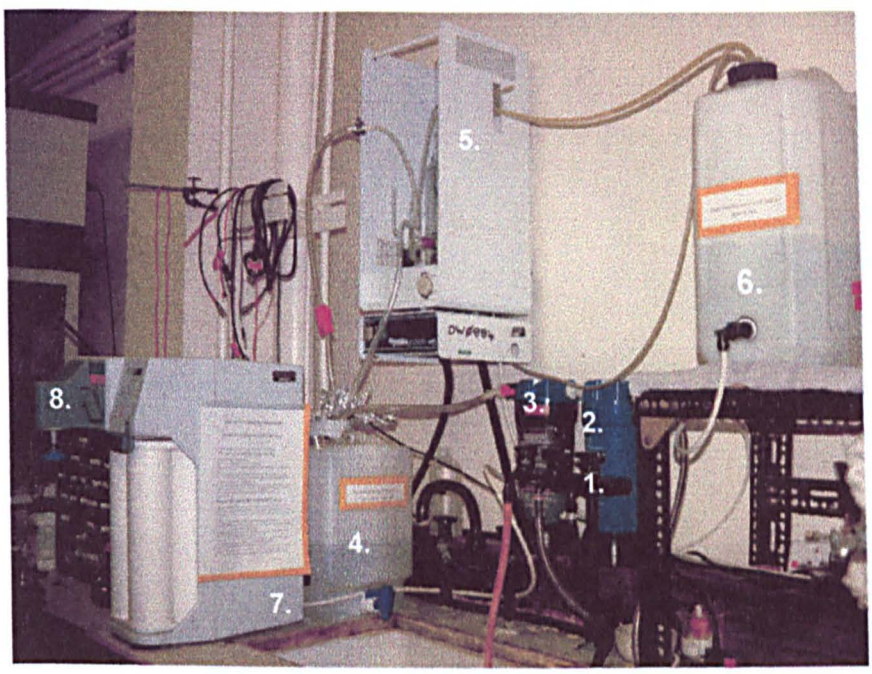

1. water tap
2. filter
3. deioniser
4. storage tank 1. (with pump)
5. single distilled water still
6. storage tank 2.
7. millipore-Q 185 system
8. ultra pure water outlet

figure F-4

G. LASER ALIGNMENT

G. LASER ALIGNMENT

The alignment of the laser source involved very sensitive adjustments of the x and y mirrors so that it comes out of the laser source box perfectly. Then the laser followed a path containing two mirrors in order to reach a small hole on the back of the scanning head of the microscope. Here a beam alignment tool, which is unique to each scanning laser microscope, was used to direct the laser into the microscope scanning head at the correct x, y, z angle. The beam alignment tool is a tube which screws over the end of the scanning head and contains a small hole at either end. The idea is to make the beam go through the centre of both holes, and this can be observed using a slit in the side of the alignment tube.

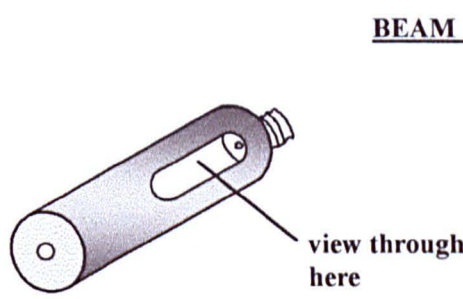

figure G-1

When doing this, the beam may be reduced in power at source so as not to harm the eyes or better still Argon-ion laser protection glasses (orange in colour) may be worn with the laser on full power, but the inside of the black painted tube had to be painted with white correction fluid over the holes of the beam alignment tube in order to be able to see the beam.

Once the laser hit the first mirror in the scanning head properly (centrally). The laser was then aligned through the microscope roughly. The rough alignment was carried out using the laser beam locked in a stationary mode, in the image centre position. This alignment process was a little difficult to do and required a strip of paper to detect the path the beam was following, to ensure that the beam was going along the expected beam path and onto each successive mirror in through scanning head.

Then the fine alignment of the beam through the laser scanning head was carried out by scanning a fairly non reflective object (a piece of pink coloured 3 μm aluminium oxide paper glued onto a glass microscope slide), after focussing with the optical part of the microscope first. The laser was scanned in order to produce a confocal optical image. Whilst scanning each of the four mirrors in the microscope scanning head could be adjusted in turn until the brightest image (of greatest signal) was produced and the image was most central. The first two mirrors could be adjusted in turn, in order to give a central spot, as moving these mirrors out of position shows the edge of a dim circle. Then the next two mirrors were adjusted to give as bright as possible an image.

THE MICROSCOPE SCANNING HEAD

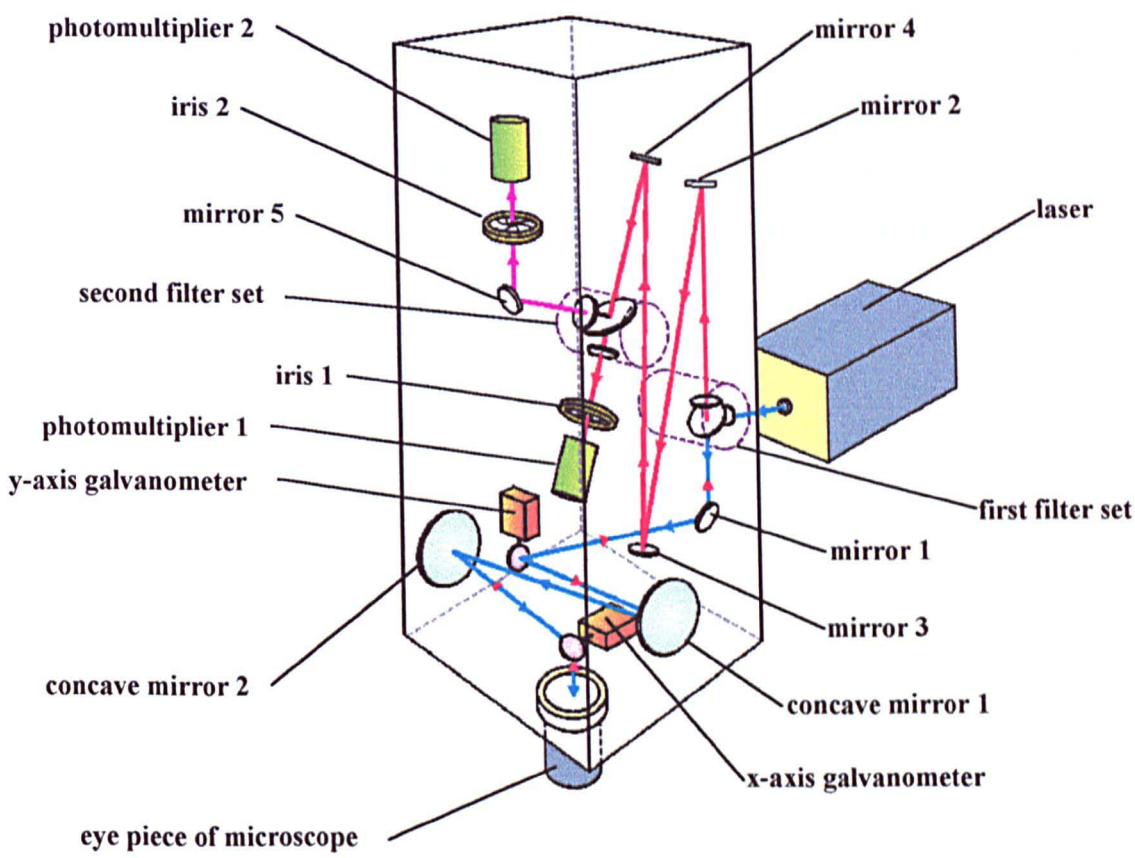

figure G-2

Only the fine alignment was usually required on a regular basis. A major alignment right from the source was required, for example, if the microscope has been moved.

It was also found that the laser power, at the source, varied with room temperature. So it was found that it was best to do the alignment at a known temperature (25 °C) and then to keep the beam power constant by keeping the temperature at 25°C ± 1°C at all times in the laser room (a sectioned off part of the laboratory with no air vents so allowing easy heating of the room). This was easy to do by using a thermostat controlled heater in the winter and a fan or by leaving the doors open in the summer. The temperature was monitored at all times during an experiment using a large digital thermometer and the heating or fan switched on or off as necessary. This was found particularly important for time dependant experiments with stainless steel which were carried out over very long periods of time (many hours). So that like comparison of the images could therefore be carried out at constant laser room temperature and therefore laser power. The laser power was monitored at source by attachment of a digital voltmeter across the two points on the laser casing marked 'power' and making sure that an optimum reading of 2.9 V ± 0.1 V (≡ 25 mW, the maximum laser power) is maintained at all times.

H. COMPUTER TECHNIQUES IN RECORDING AND PROCESSING IMAGES

H. COMPUTER TECHNIQUES IN RECORDING AND PROCESSING IMAGES

In this thesis many of the instruments were used in the collection of data to form various images such as: photocurrent, confocal reflective (optical) and microprobe elemental concentration images. As collecting, recording, and displaying data in the form of images requires the use of computers, this appendix aims to explain the basic concepts in computer imaging (i.e. how the data collected can converted into an image is discussed in this appendix).

1. Collecting Image Data

Computers are used in the first instant to control the instrument involved, from which the data has to be collected. The computer sends out information to allow the probing beam (laser beam or electron beam) to be moved from one point to the next along a line, then back and along the next line down and so on. This technique of moving the beam from one line to the next in a zig-zag pattern is known as raster scanning.

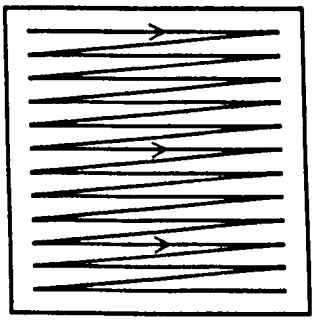

RASTER SCANNING

figure H-1

The computer can also be used to define the number of data points to be collected for each line going from one side of the screen to the other. It is usual to use the computer to pick the size of area to be sampled in terms of the length of a single line (length along x-axis) and the number of lines (length along y-axis) which go to make up an image. The data points are typically collected as the beam moves from left to right, and then the beam moves back to the next line as fast as it can without collecting any data

points, and then the data is collected again as the scanning beam moves from left to right again. This type of data collection is known as the uni-directional scan. The true size of each data point (μm) is given by the magnification selected on the instrument (using various magnification lenses) and by the electronic zoom of the selected image. The highest number of data points the computer software is capable of collecting (e.g. 768 data points per line x 512 lines) is usually used for all the images collected, but due to the changes in the magnification of the lenses and electronic zoom, even though the number of data points remains the same, the real size of each data point will be changed. At the collection stage zooming in electronically can still allow the same number of data points to be collected but zooming in after the data has been collected, and saved in the image processing stage, results in the number of data points on an image being reduced resulting in a reduction of the image resolution being viewed.

Another feature the computer has control over is the time it takes the computer to scan one line. This is known as the line scan time and is controlled by the time required to collect each data point. Each data point gives information for one unit on the digital image and this is known as a pixel. The time spent in collecting each data point is therefore known as the pixel dwell time. So the line scan time or pixel dwell time can be selected when collecting the image (e.g. photocurrent image, confocal reflective image, microprobe concentration map etc).

As the image is collected signal averaging can also be carried out by collecting the image many times and averaging the data recorded.

The features controlled by the computer such as the number of data points, the image size (by electronic zoom), the pixel dwell time and the amount of signal averaging all have to be controlled by information signals sent to the apparatus from the computer. Any feature that needs to be controlled by the computer is sent information using a digital to analogue converter (DAC). The DAC is a device which can change the digital computer signals into analogue potentials. These potentials are then fed into the control section of the apparatus and allow the scanning beam to move at a particular speed and over a specified area repeatedly as requested.

Once the beam has moved over the sample surface a change is caused in a particular property at the surface (e.g. photocurrent generation x-ray emission etc). The changes that occur at the have to be detected by an appropriate detection device. This signal is then converted into an electrical signal. The electrical signal is given by a proportional voltage, where a known voltage corresponds to the detected signal. The whole signal generated is recorded by the detector for a known location of each data point at the time the laser is dwelling on this point. This is done for all the points and the resulting voltage data is sent via an analogue to digital converter (ADC), which converts the voltage signal into a digital signal, to the computer. The computer then converts each data point in the digital signal into a shade of grey or a colour to represent the data value. These coloured points are then mapped out point by point in the same order (positions to one another) as they were collected in order to form an image.

2. Image Display

The digital image as seen on the computer is composed of many small squares known as pixels (picture elements). These are the smallest ellement of a computer display that can be controlled by a computer. A pixel has two values associated with it, the intensity value and the length value.

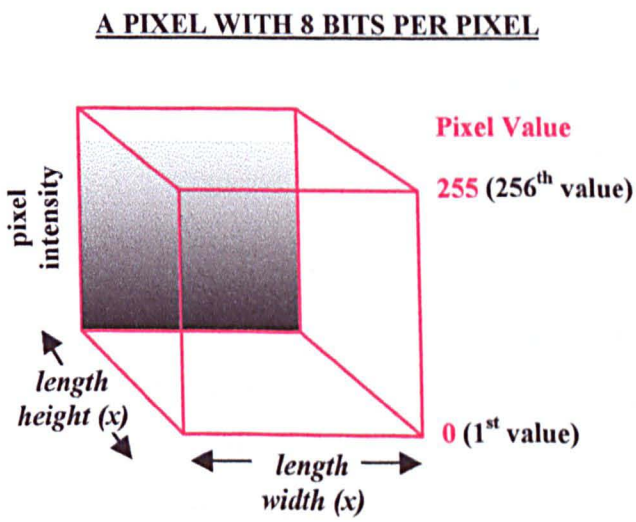

figure H-2

a) Image size

The image size is defined by the number of pixels in the y-direction and the number of pixels in the x-direction (e.g. 768 x 512). This can then be equated to the true size of the sample image by correlating the true length (μm) that represents each pixel length. The smaller the pixel is on the screen the better the resolution will be on the display, so a 768 x 512 pixel image will be much more rifined and of a higher resolution than a 100 x 100 pixel image.

b) Image colours

The pixel intensity defines colours seen on an image. The number of colours that define the pixel intensity depends on the number of bits allocated to 1 pixel. Each bit (binary digit) can have one of two numbers assigned to it, either 0 or 1 and these numbers provide the information the computer requires to define any information it is given. The colour of each pixel is stored as a sequence of one or more bits.

A table showing the number of colours possible:

Bits per Pixel	Number of Colours Possible
1 bit	$2^1 = 2$
2 bit	$2^2 = 4$
3 bit	$2^3 = 8$
4 bit	$2^4 = 16$
8 bit	$2^8 = 256$
16 bit	$2^{16} = 65,536$
24 bit	$2^{24} = 16,777,216$

Each colour is assigned a pixel intensity value number ranging from 0, for the colour representing the lowest value in the scale, up to n_{col} - 1 for a one colour scale. For a linear scale the shade or tone of this from this colour at 0, varies getting lighter untill white is reached for n_{col}-1. However it must be noted that in the computer world zero represents something, whereas in mathematics it represents nothing (or a null) situation, i.e. the zero pixel value has a colour assigned to it.

In scientific experiments images are typically recorded as a **grey scale images** at 8 bit resolution (256 shades of grey). This is used as the greatest number of shades of grey the human eye can resolve between is 256, so if a higher number of greys were used no difference could be resolved by the eye. The grey scale ranges from black through to white. If a linear scale is used then each of the 256 possible values take an assigned pixel value from 0 (1st pixel intensity value) to 255 (the 256th pixel intensity value). Where 0 = black and 255 = white.

A **pseudo-colour scale** image may be recorded directly or may be produced by converting a previously recorded grey scale image during the image processing stage. In a pseudo-colour scale image the pixel intensity values are each assigned a colour (e.g. mid-blue, dark yellow, pale orange, white ect.) instead of just a shade of black or white as in a grey scale image. In some instances it is preferable to use a few contrasting colours to show differences in an image more clearly than would be seen in a grey scale image, but using too many varied colours would leave an image looking diffuse and confused. It was found that the use of 2 to 6 colours to make up the colour scale, with various shades of each colour used, gave the best effect. For example if a pink, green, and blue colour scheme is selected to make up the colour scale we can have 100 shades (tones) of pink 56 shades of green and 100 shades of blue making up the 256 colours in an 8 bit colour image.

A 24 bit colour image is known as a true colour image. Here each colour is thought of as consisting of Red(R), Green(G) and Blue(B) components each with 256 posible values of each. In a true colour scale the colour of the pixel is defined by R(x), G(y), B(z) where x, y, and z all take a value between 0 and 255 (the higher the number the brighter / lighter the colour.

For example with linear changes in red, green and blue :

R(0),G(0),B(0) = Black

R(255),G(255),B(255) = White

R(255), G(0), B(0) = Red

Each pixel value can therefore be assigned a colour defined by R(x), G(y), B(z).

3. Image Analysis

This is the examination of the image data both quantitatively by eye and then quantitatively by analysis of the pixel intensity values. Quantitative analysis is carried out on raw data prior to image processing. Features may be viewed and measured knowing the pixel : true size ratio. Also selected lines and areas may be analysed to show how the pixel intensity changes across a line or what the average pixel intensity is for a selected area. Then correlating the pixel intensity value to the property being measured will allow a direct calculation of changes (e.g. exactly how much photocurrent was generated at a particular location).

4. Image Processing

Image processing is a method by which change are applied typically to a grey scale image, after the image has already been recorded, in order to enhance the variations seen.

a) Adjustments in graphics

Adjustments to the graphics includes adjustment of contrast, gamma and brightness. These parameters can be adjusted individually or in combination. These adjustments can be used to solve problems such as, the data occurring over a very small colour range in the linear grey scale, or the data occurring at mostly one end or the other of the colour scale used.

Adjusting the brightness allows an increase or decrease in all the shades of grey shown, except the value of 255 is not exceeded and the value of 0 is not reduced. So increasing the brightness will make the whole grey scale lighter and decreasing the brightness will make the whole grey scale darker (figure H-3).

CHANGES TO THE IMAGE BRIGHTNESS

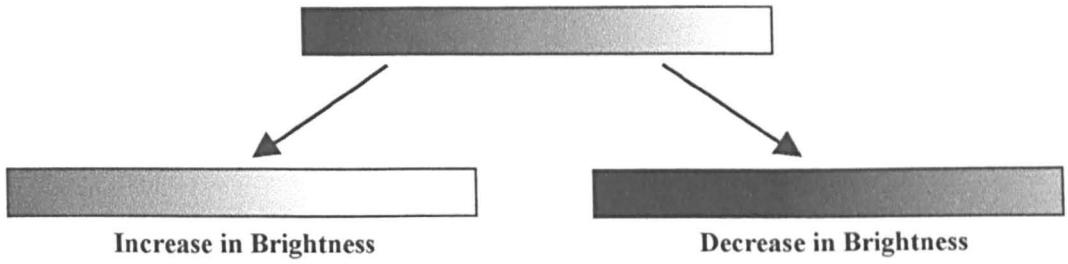

figure H-3

Increasing or enhancing the contrast squashes the 256 grey shades (or colours) into a smaller section of the overall scale. Similarly decreasing the contrast will stretch the grey shades over a wider range of the scale (figure H-4).

CHANGES TO THE IMAGE CONTRAST

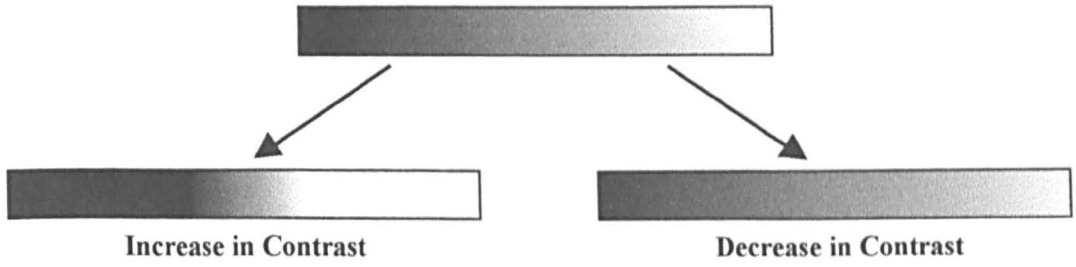

figure H-4

Adjusting the gamma moves the mid-grey position away from the centre (figure H-5).

CHANGES TO THE IMAGE GAMMA SETTINGS

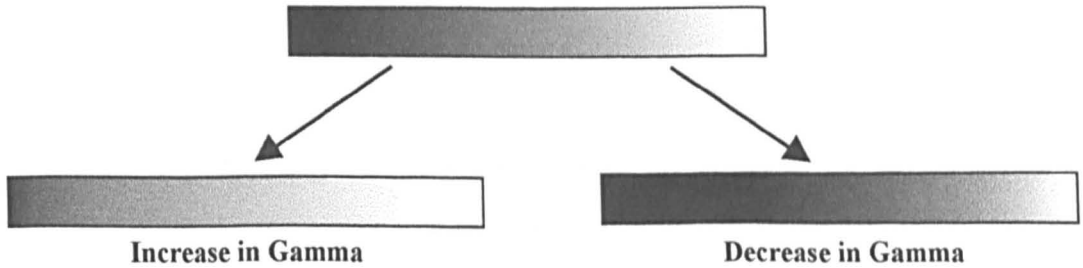

figure H-5

Increasing the gamma shifts the mid-grey towards the bottom of the scale, so making the scale lean predominantly towards the lighter shades of grey. Similarly decreasing

the gamma shifts the mid-grey position closer to the top end of the scale so the scale leans predominantly towards the darker shades of grey.

b) Enlarging a selected area of interest

Other things which can be done to the image include zooming into a selected section of the image if the item of interest is too small to view, provided a sufficient number of pixels are present so there is not a deterioration of the image resolution.

c) Noise reduction

Enhancement to the image can also be made to the image by trying to reduce any effects produced due to unwanted background noise by smoothing the image or better still using FFT (Fast Fourier Transformation) to remove selected frequencies relating to the noise of the image. Another technique which could possibly be used is edge enhancement. This technique enlarges all the pixels above a certain pixel value by multiplying them by a fixed number, whilst all the other pixels with a low pixel intensity value remain the same. This however assumes that all the noise will have very low values compared to the data which will have the high values. If this is not true this technique could result in an image far worse than the original. The application of these techniques are discussed further in Chapter 2 (Experimental Method).

d) Correction from rectangular to square pixels

It is known to be quite common in imaging systems to have a discrepancy in the aspect ratio (x,y), as the aspect ratio provided by the video output by the apparatus does not always correspond to that of the computer generated pixel. So correction to a square pixel from a rectangular one may be carried out by slightly enlarging or reducing the image in one direction (i.e by reduction or enlargement of the pixel, length value, per line length).

e) Conversion of a 2D-image to a 3D-surface plot

Sometimes small changes as seen in a 2D image can be seen more easily if the image is converted an image known as a 3D-surface plot. A 3D surface plot is created by moving the pixels, seen by pixel intensity, into a third dimension. So the x-axis (or x-displacement) shows the width of the image, the y-axis (or y-displacement) shows the height of the image, and the z-axis shows the pixel intensity (colour or shade of grey)

which is related directly to the property that is being measured, for example the photocurrent.

a. A 2D-IMAGE **b. A 3D-SURFACE PLOT**

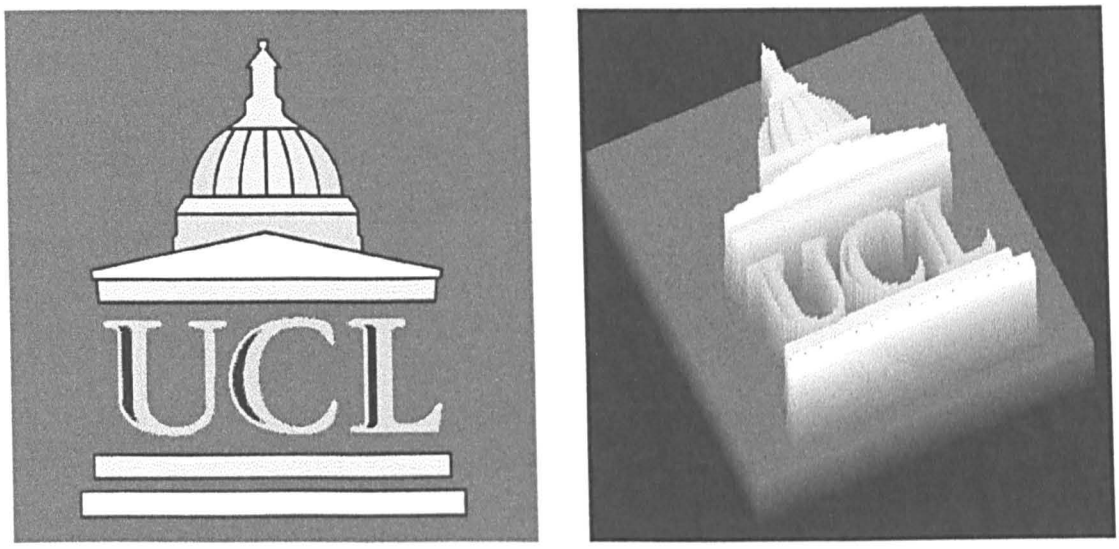

figure H-6

e) Conversion of a grey scale image to a pseudo-colour scale image

If a 8 bit linear grey scale image is converted to a 24 bit colour image the image will be converted from a black and white image to a black and white image which looks exactly the same with all the same tones of grey present in the same spatial locations. However as the colour image is made of red, green and blue scales these can be examined separately. In a 24 bit colour image if the red, green and blue scales are each linear in exactly the same manner they will combine to produce a linear grey scale, but if each component colour scale is made non-linear in a different way to the others then uneven combinations of red, green, and blue will produce different colours for differing pixel values of the colour scale. How the shade of the component colour (represented by 0-255) changes with the colour scale ranging from the minimum pixel value to the maximum can be done by manipulation of graphs known as **tone maps** (on images where colour data is stored straight into the picture data file, e.g. *.tiff, *.jpeg, *bmp pic) or **LUT maps** (where it is stored separately to the picture data file e.g. Bio-Rad *.pic files). The latter much older technique is becoming obsolete nowadays due to greater data storage space on both computer hardware and in the form of removable media.

I. PHYSICAL PROPERTIES OF THE ELECTRODE MATERIALS

I. PHYSICAL PROPERTIES OF THE ELECTRODE MATERIALS

The physical properties of the materials used, at room temperature (25°C), have been divided up into thermal properties, optical properties, and colours and solubilities in this appendix.

1. Thermal Properties

Information and equations regarding the thermal properties of the materials used:

1. The values for

c_p = specific heat capacity (the quantity of heat required to raise 1 mole of the substance by one unit of temperature),

ρ = density (mass per unit volume),

$$K = \text{thermal conductivity} = \frac{\text{heat flow rate x thickness}}{\text{area x temperature difference}}$$

were taken directly from the references listed below

A) CRC hand book 78th edition (1997)

B) Macmillan's Chemical and physical data book (1992)

C) Nuffield Book of Data (1986)

D) www. avestasheffield.com (lists of physical, thermal properties of stainless steel)

2. D = thermal diffusivity, was calculated using

$$D = \frac{K}{c_p \rho},$$

3. λ_T = time scale for thermal diffusion, was calculated using

$$\lambda_T = \frac{r^2 c_p \rho}{K} = r^2 x \frac{1}{D}$$

$$\text{were } 2r \sim \frac{\lambda}{2N_A} = \frac{500x10^{-9}\,m}{0.24} = 2x10^{-6}\,m \qquad \therefore r^2 = 1x10^{-8}\,cm^2$$

Thermal properties for the various materials used in this work:

material *uses*	c_p / J g^{-1} K^{-1}	ρ / g cm^{-3}	K / W cm^{-1} K^{-1}	D / cm^2 s^{-1}	λ_T / s
gold *working electrode*	0.129 ref. A	19.3 ref. A	3.17 ref. A	1.273	7.85×10^{-9}
cadmium *an impurity surrounding screen printed gold*	0.232 ref. A	8.69 ref. A	0.968 ref. A	4.801×10^{-1}	2.08×10^{-8}
silicon *working electrode*	0.705 ref. A	2.33 ref. A	1.48 ref. A	9.010×10^{-1}	1.10×10^{-8}
304 stainless steels (304 L) *working electrode*	0.500 ref. D	7.9 ref. D, A	0.15 ref. A	3.797×10^{-2}	2.633×10^{-7}
316 stainless steels (316F) *working electrode*	0.500 ref. D	8.0 ref. D	0.15 ref. D	3.750×10^{-2}	2.667×10^{-7}
light flint *like the insulator around screen printed gold bands*	0.67 ref. B	3.26 ref. C	7.95×10^{-3} ref. A	3.640×10^{-3}	2.75×10^{-7}
ceramic (95% Al_2O_3) *around screen printed gold bands*	0.774 ref. A	3.8 ref. B, C	0.23 ref. B	7.820×10^{-3}	1.27×10^{-7}
glass (pyrex) *around pure gold band electrodes*	0.85 ref. B	2.23 ref. C	11.30×10^{-3} ref. A	5.961×10^{-3}	1.68×10^{-6}
epoxy resins *general mounting material*	1.05 ref. B	1.11-1.40 ref. B	1.7×10^{-3} - 2.1×10^{-3} ref. B	1.15×10^{-3} - 1.80×10^{-3}	8.70×10^{-6} 5.56×10^{-6}
water *electrolyte solution*	4.181 ref. A	1.00 ref. A.	6.0×10^{-3} ref. A	1.435×10^{-3}	6.88×10^{-6}

2. Optical Properties

Information and equations regarding the optical properties of the materials used:

1. The optical properties at the surface of the electrode materials have been listed as a function of photon energy (eV). To convert energy (eV) to wavelength in μm the equation, $\lambda = 1.2398 / Energy$ was used. The values for the optical properties, n = refractive index, k = extinction coefficient (complex absorption coefficient), R ($\phi = 0$) = normal incidence of reflection were taken directly from the CRC hand book 78th edition (1997)

2. The 2 principal lines in the argon ion laser are:

488 nm (2.541 eV) and 514 nm (2.412 eV)

3. From the information given in the optical properties the absorption coefficient (α) at a given wavelength may be calculated using the Einstein Relationship:

$$\alpha = \frac{4\pi\nu k}{c} = \frac{4\pi k}{\lambda}$$

4. $1eV = 1.60219 \times 10^{-19}$ J

5. Band gap energy = separation between the conductance and valence band energies ($E_{bg} = E_C - E_V$). Incident light of an energy greater than E_g is required to separate an electron-hole pair ($h\nu > E_{bg}$).

Characteristics:

Semi-metals / conductors-	these have an overlap in the conductance and valence bands
True metals / conductors-	these have no band gap (also very small band gaps, >0.1eV are classified as metals)
Semiconductors -	have a small band gap, less than 3eV
Insulators-	have a large band gap, more than 3eV

A table showing the optical properties of silicon, single crystal:

λ / nm	Energy / eV	n	k	R	α / 10^7 m^{-1}
564	2.20	4.123	0.048	0.372	10.695
517	2.40	4.215	0.060	0.380	14.584
496	2.50	4.320	0.073	0.390	18.495
477	2.60	4.442	0.090	0.400	23.710
459	2.70	4.583	0.130	0.412	33.003

note : material type = semiconductor, band gap = 1.125eV = 1.9 x10^{-19} J

A table showing the optical properties of gold, electropolished (110):

λ / nm	Energy / eV	n	k	R	α / 10^7 m^{-1}
564	2.20	0.24	2.54	0.880	5.659
517	2.40	0.50	1.86	0.647	4.521
496	2.50	0.82	1.59	0.438	4.028
477	2.60	1.24	1.54	0.331	4.058
459	2.70	1.43	1.72	0.356	4.710

note: material type = true metal, conductor

3. Colours and Solubilities- for the Stainless Steel Work

The colours and solubilities of MnS and MnO, which are present in stainless steel, as well as and any possible corrosion products of stainless steel e.g. hydroxides and oxides of Fe, Cr and Ni and various Mn salts have been noted here from the following references:

a) 'Revised Nuffeild Advanced Book of Data', 1984, Longman
b) 'Lang's Handbook of Chemistry and Physics' 14th edition,1992, McGraw Hill INC.
c) 'CRC Handbook of Chemistry and Physics 73rd edition,1992-1993'
d) 'Chemistry of the Elements' by N. N. Greenwood and A. Earnshaw, 1986, Pergamon Press

Note: It was found that more recent books such as CRC Handbook of chemistry and Physics, 78th edition 1997-1998', only listed generally whether a material was soluble or not in a particular solvent without giving any values so older books had to be consulted.

Mn containing substances:

With	Ox. State for Mn	Substance	M /g mol^{-1}	Description	Solubility at 25°C (298.15K) unless other wise stated, given as the amount that saturates 100 g (100 cm^{-3}) of water.		
					mass	moles	T, (ref.)
S	II	MnS	87.00	green (a, d), will only exist in this form if all traces of water/ air is removed (d).	0.0006g	6.90×10^{-6}	18°C, (a)
					0.0006g	6.90×10^{-6}	18°C (b)
		$3MnS.H_2O$ (c)	279.01	pale red (a), grey-pink (c), salmon-pink (d)	0.0006g	2.15×10^{-6}	18°C, (c)
S	II	MnS_2	119.06	black (c)	insoluble (c)		
S, O	II	$MnSO_4$	151.00	red (a), redish (c)	52g	3.44×10^{-1}	(a)
					52g	3.44×10^{-1}	(b)
					52g	3.44×10^{-1}	5 °C, (c)

Mn containing substances continued:

With	Ox. State for Mn	Substance	M /g mol^{-1}	Description	Solubility at 25°C (298.15K) unless other wise stated, given as the amount that saturates 100 g (100 cm^{-3}) of water.		
					mass	moles	T, (ref.)
S, O, H_2O	II	$MnSO_4.H_2O$	169.01	pale red (a), pale pink (c)	98.5	5.83×10^{-1}	(a)
					70g	4.1×10^{-1}	(b)
					98.47g	5.83×10^{-1}	48°C, (c)
S,O, H_2O	II	$MnSO_4.5H_2O$	241.07	rose , deliquescent, solid (a) rose (c)	124g	5.14×10^{-1}	(c)
S, O, H_2O	II	$MnSO_4.4H_2O$	223.06	pale red (a), pink (c)	130.0g	5.83×10^{-1}	(a)
					105.3g	4.72×10^{-1}	(c)
O	II	MnO	70.94	green (a, c) grey-green to dark green (d)	insoluble (b, c)		
O	II, IV	Mn_3O_4	228.81	black (a, c)	insoluble (a, c)		
O	III	Mn_2O_3	157.87	black (a)	insoluble (a, c)		
O	IV	MnO_2	86.94	black (a) brown - black (c)	insoluble (a, c)		
O, H	II	$Mn(OH)_2$	88.95	white-pink (a,c)	0.0002g	2.2×10^{-6}	(a)
					0.0002g	2.2×10^{-6}	18°C, (c)
O, H	III	MnO(OH)	87.94	brown-black, rhombic (c)	insoluble (a, c)		
Cl	II	$MnCl_2$	125.84	pale red (a), pink (c), deliquescent (a,c)	63.4g	5.04×10^{-1}	(a)
					74g	5.9×10^{-1}	(b)
					72.3g	5.74×10^{-1}	(c)
Cl, H_2O	II	$MnCl_2.4H_2O$	197.91	pale red, (a), rose (c), deliquescent	121g	6.13×10^{-1}	(a)
					143g	7.22×10^{-1}	(b)
					151g	7.63×10^{-7}	8°C, (c)

Fe containing substances:

With	Ox. State for Fe	Substance	M /g mol^{-1}	Description	Solubility at 25°C (298.15K) unless other wise stated, given as the amount that saturates 100 g (100 cm^{-3}) of water.		
					mass	moles	T, (ref.)
O, H	II	$Fe(OH)_2$	89.86	pale green (a), green or white (c)	0.0006g	6.7×10^{-6}	(a)
					0.00015g	1.67×10^{-6}	18°C, (c)
O	II	FeO	71.85	black (a)	insoluble (a, b)		
O	II, III	Fe_3O_4	231.54	black-red (a)	insoluble (a)		
O, H_2O	II, III	$Fe_3O_4 . xH_2O$	_____	red-brown (c)	insoluble (c)		
O	III	Fe_2O_3	159.69	red-brown (a)	insoluble (a)		
S	II	FeS	87.91	black (a), black-green (c)	0.0004g	5.01×10^{-6}	(a)
					0.0006g	6.83×10^{-6}	18°C, (b)
					0.00062g	7.05×10^{-6}	18°C, (c)
S	II	FeS_2	119.97	yellow (c)	0.00049g	4.08×10^{-6}	(c)
S, O, H_2O	II	$FeSO_4.7H_2O$	278.01	black-green (c)	28.6g	1.03×10^{-1}	(a)
					15.65g	5.63×10^{-2}	(c)
S, O	III	$Fe_2(SO_4)_3$	399.87	yellow (c)	slightly soluble		(c)
Cl	II	$FeCl_2$	126.75	yellow-green (a), green - yellow (c)	80.6g	6.36×10^{-1}	(a)
					62.5g	4.93×10^{-1}	20°C, (b)
					64.4g	5.08×10^{-1}	(c)
Cl, H_2O	II	$FeCl_2 . 2H_2O$	162.78	green (c)	(not given)		
Cl, H_2O	II	$FeCl_2.4H_2O$	198.81	black-green, deliquescent (c)	160.0g	0.805	(a)
					160.1g	0.805	20°C, (c)
Cl	III	$FeCl_3$	162.21	black-brown, deliquescent (a)	74g	4.56×10^{-1}	(b)
					74.4g	4.58×10^{-1}	(c)
Cl, H_2O	III	$FeCl_3.6H_2O$	270.30	brown-yellow, very deliquescent (a,c)	91.9g	3.40×10^{-1}	(c)

Cr containing substances:

With	Ox. State for Cr	Substance	M /g mol^{-1}	Description	Solubility at 25°C (298.15K) unless other wise stated, given as the amount that saturates 100 g (100 cm^{-3}) of water.		
					mass	moles	T, (ref.)
O, H	II	$Cr(OH)_2$	86.01	yellow-brown	insoluble (b)		
O	VI	CrO_3	99.99	dark-red (a), red	61.7	6.17×10^{-1}	(b)
				(c), deliquescent	61.7	6.17×10^{-1}	(c)
O	II	CrO	68.00	black	insoluble (c)		
O	IV	CrO_2	83.90	black	insoluble (b, c)		
O	III	Cr_2O_3	151.99	green (a, c)	1.8×10^{-7}	1.20×10^{-9}	(a)
					insoluble (c)		
O, S, H_2O	II	$CrSO_4 . 7H_2O$	274.16	black	insoluble (c)		
S	II	CrS	84.06	black (c)	insoluble (c)		
S	III	Cr_2S_3	200.17	brown-black (c)	insoluble (c)		
Cl	II	$CrCl_2$	122.90	white , deliquescent (c)	Very soluble (b, c)		

Ni containing substances:

With	Ox. State for Ni	Substance	M /g mol^{-1}	Description	Solubility at 25°C (298.15K) unless other wise stated, given as the amount that saturates 100 g (100 cm^{-3}) of water.		
					mass	moles	T, (ref.)
O	II	NiO	74.69	green-black (a,c)	insoluble (a,c)		
O, H	II	$Ni(OH)_2$	92.70	green (a,c)	0.013g	1.40×10^{-4}	(c)
S	II	NiS	90.75	black (c)	0.00036g	3.97×10^{-5}	18°C (c)
S	I	Ni_3S_2	240.19	pale yellow/ bronze metallic lustre (c).	insoluble (c)		
S	II,III	Ni_3S_4	304.31	grey-black (c)	insoluble (c)		
S, O, H_2O	II	$NiSO_3.6H_2O$	246.84	green (c)	insoluble (c)		
Cl	II	$NiCl_2$	129.60	yellow, deliquescent	61g	4.70×10^{-1}	20°C (b)
					64.2g	4.95×10^{-1}	20°C (c)
Cl, H_2O	II	$NiCl_2.6H_2O$	237.69	green, deliquescent	254g	1.07	20°C (b)
					100g	0.42	20°C (c)
S, O	II	$NiSO_4$	154.75	yellow (a, c)	29.3g	0.189	(a)
					29.3g	0.189	(c)
S, O, H_2O	II	$NiSO_4.7H_2O$	280.85	green (a, c)	75.6g	2.69×10^{-1}	15.5°C, (c)
S, O, H_2O	II	$NiSO_4.6H_2O$	262.84	green (a)	65.52g	2.49×10^{-1}	(c)

J. EXPERIMENTAL PARAMETERS AND SETTINGS FOR THE PHOTOCURRENT AND CONFOCAL IMAGING WORK

J. EXPERIMENTAL PARAMETERS AND SETTINGS FOR THE PHOTOCURRENT AND CONFOCAL OPTICAL IMAGING WORK

The image parameters and experimental settings have been listed by electrode type and chapter of the thesis to which they correspond;

1. Silicon (Chapter 3)
2. Gold (Chapter 4)
3. Stainless Steel- part I, imaging non-corrosive systems (Chapter 5)
4. Stainless Steel- part II, imaging corrosive behaviour (Chapter 6)

Information and equations for calculating the experimental parameters:

1. The sampled image = 768 x 512 pixels in all cases

2. Laser beam minimum spot size = beam diameter

$$2r \approx \frac{\lambda}{2N_A}$$

where 2r = beam diameter (m), wavelength (m), and N_A = numerical aperture of the objective lens

3. Pixel size on a given axis,

$$\text{Pixel size} = \left\{ \frac{15.240}{\text{objective factor}} \div \text{zoom} \right\} \mu\text{m}$$

Where the objective factor (O_f) has been calculated for each lens and for the x and y axis using a graticule. (see technical details for the scanning laser microscope , appendix E).

4. line scan time = pixel dwell time x 768

(where line scan time = t_{line})

5. frame scan time $\approx$ (pixel dwell time x 768) x 512

$\approx$ (line scan time) x No. of lines

6. laser pseudo-velocity $= \dfrac{\text{line length on x - axis}}{\text{line scan time}}$

$$= \frac{768 \times \text{pixel length of x - axis}}{768 \times \text{pixel dwell time}}$$

$$= \frac{\text{pixel length}}{\text{pixel dwell time}}$$

7. Laser beam irradiation time , τ:

this is the time it takes to scan over a length equal to the laser beam diameter

$$\tau = \frac{1}{v_p} 2r$$

$$= \frac{2r}{\text{pixel length on x - axis}} \times \text{pixel dwell time}$$

8. The limiting response time τ_{inst} (in seconds) of an instrument can be given by

$$\tau_{inst} = \frac{1}{2\pi f}$$

where f , is the frequency (in Hz). If several instruments are connected together then the component instrument with the greatest value of f will give the value of τ_{inst} for the overall instrumental setup.

9. $\tau_{inst} \sim 4$ μs for the potentiostat, as calculated using impedance analysis (see technical details of the battery operated potentiostat , Appendix C).

10. Photocurrent scale (μA), represented by a 256 pixel grey scale

= potentiostat setting in μA ÷ preamplifier gain

11. Calculation of the true photocurrent range and therefore sign (+VE / -VE) and size of the photocurrent.

.

This can be calculated by subtracting the average pixel value on the resin part of the photocurrent image from the average pixel value in the electrode area, or more accurately the mid-grey pixel value produced when an image is recorded with the laser light-off can be subtracted from the average pixel value in the electrode area.

On a 0-255 pixel intensity scale, where 0 = 1st value and 255 = 256th value

if the pixel intensity value for the 'light-off' setting (dark images) = d
light-off value = (d + 1) pixels on the 256 grey scale

For a 256 pixel grey scale with a maximum possible photocurrent range, P

$$I_{dark} = (d+1) \times \frac{P}{256}$$

As $I_{photo} = I_{light} - I_{dark}$,

the 'P' nA grey scale ranges from

a maximum of $I_{photo} = (P - I_{dark})$ nA
to a minimum of $I_{photo} = (0 - I_{dark})$ nA

e.g. If on 0-255 scale the 'light off' (dark image) = 148.8 pixels and the grey scale equals to 10 nA

light-off value = 149.8 pixels out of 256 possible values

$$I_{dark} = 149.8 \times \frac{10\,nA}{256} = 5.85\,nA$$

As $I_{photo} = I_{light} - I_{dark}$,

the 10 nA grey scale
ranges from a maximum of I_{photo} = +4 nA
to a minimum of I_{photo} = -6 nA

1. Experimental Parameters for Work on Silicon (as seen in Chapter 3)

SILICON IMAGING
EXPERIMENTS
SUMMARY

A Summary table of the experiments on silicon:

Nº	Sample	Experiment	Conditions
S1	**SILICON MEMORY CHIP (256k EPROM)**	EFFECT OF LIGHT INTENSITY	No solution present, potential = internal bias of potentiostat (0 V), working electrode = Vpp pin of EPROM, Counter / Reference Electrode = GND pin of EPROM.
S2	**p-TYPE SILICON**	EFFECT OF LIGHT INTENSITY AND POTENTIAL	Solution = 1M HCl, light intensity varied between 1 and 100% I_o, potential selected from the range -800 to +300 mV vs SCE, counter electrode = Pt wire open ring.

EXPERIMENT S1

Sample- **SILICON MEMORY CHIP (256k EPROM)**

Solution- none

Experiment- EFFECT OF LIGHT INTENSITY (See Chapter 3 of this thesis)

Potential- internal bias of potentiostat (0 mV)

Light intensity- varied between 1 and 100% I_o

Electrode settings- WE = V_{pp} pin on EPROM, CE / RE = GND pin on EPROM

Table S1-1. Photocurrent and confocal optical image parameters:

Experimental Parameter	Value
Lens	x 10 (Bio-Rad) , $N_A = 0.25$
Laser beam diameter (2r)	1 μm
Electronic Zoom	1.1
Objective Factor	O_f(x-axis) = 9.4 , O_f(y-axis) = 10.2
Pixel Size (x × y)	1.474 x 1.358 μm
Image Area Sampled, 768 x 512 pixels	1132 x 695 μm
Line Length (768 pixels)	1132 μm
Scan Velocity Type	standard slow (F1)
Pixel Dwell Time	10 μs
Line scan time	7.68 ms
Frame Scan Time	3.93 s
Pseudo Laser Velocity , v_p	14.74 cm s^{-1}
Laser Beam Irradiation Time , τ	6.78 μs
Pre-amplifier AC/DC selection*	AC
Pre-amp Low Frequency Filter*	0.03 Hz
Pre-amp High Frequency Filter*	30 kHz (τ_{inst} = 5 μs)

note * applies to the photocurrent image only

Table S1-2. Photocurrent scale:

% I_o , Light Intensity	100	10	3	1
Potentiostat (μA / volt)	10	10	10	10
Pre-amplifier gain	50	50	50	100
256 pixel scale / nA	200	200	200	100

EXPERIMENT S2

Sample (WE)-	**p-TYPE SILICON**
Solution-	1M HCl
Experiment-	EFFECT OF LIGHT INTENSITY AND POTENTIAL (See chapter 3 of this thesis)
Potential-	potential selected from the range -800 to +300 mV vs SCE
Light intensity -	varied between 1 and 100% I_o
RE-	SCE
CE-	Pt wire open ring

Table S2-1. Photocurrent image parameters:

Experimental Parameter	Value
Lens	x 4 (Bio-Rad) , $N_A = 0.12$
Laser beam diameter (2r)	2 μm
Electronic Zoom	1.0
Objective Factor	O_f(x-axis) = 3.8 , O_f(y-axis) = 4.1
Pixel Size (x × y)	4.011 x 3.717 μm
Image Area Sampled, 768 x 512 pixels	3080 x 1903 μm
Line Length (768 pixels)	3080 μm
Scan Velocity Type	standard slow (F1)
Pixel Dwell Time	10 μs
Line scan time	7.68 ms
Frame Scan Time	3.93 s
Pseudo Laser Velocity , v_p	14.74 cm s^{-1}
Laser Beam Irradiation Time , τ	4.98 μs
Pre-amplifier AC/DC selection	AC
Pre-amp Low Frequency Filter	0.3 Hz
Pre-amp High Frequency Filter	30 kHz (τ_{inst} = 5 μs)

The photocurrent scale (256 grey scale) varied (depending on the potential and light intensity selected) from 2 to 50 μA.

2. Experimental Parameters for Work Carried Out on Gold (as seen in Chapter 4)

GOLD IMAGING EXPERIMENTS SUMMARY

A summary table for the experiments on gold:

Nº	Sample	Experiment	Conditions
G1	**SCREEN PRINTED SINGLE GOLD MICROBAND**	EFFECT OF LASER VELOCITY	Solution = 5mM $K_4Fe^{II}(CN)_6$, 0.1M K_2HPO_4, 0.1M KH_2PO_4, light intensity = 100% I_o, potential = +200 mV vs SCE, counter electrode = Pt wire open ring
G2	**SCREEN PRINTED SINGLE GOLD MICROBAND**	HIGH RESOLUTION IMAGING, higher zoom	Solution = 5mM $K_4Fe^{II}(CN)_6$, 0.1M K_2HPO_4, 0.1M KH_2PO_4, light intensity = 100% I_o, potential = +200 mV vs SCE, counter electrode = Pt wire open ring
G3	**GOLD MACRODISC**	EFFECT OF POTENTIAL	Solution = 5mM $K_4Fe^{II}(CN)_6$, 5mM $K_3Fe^{III}(CN)_6$, 0.1M K_2HPO_4, 0.1M KH_2PO_4, light intensity = 100% I_o, potential varied between -300 and +300mV vs SCE, counter electrode = Pt wire open ring
G4	**PURE GOLD MICROBAND**	EFFECT OF POTENTIAL, effect on quantity of photocurrent and apparent width of band on photocurrent image investigated	Solution = 5mM $K_4Fe^{II}(CN)_6$, 0.1M K_2HPO_4, 0.1M KH_2PO_4, light intensity = 100% I_o, potential varied between -100 and +400 mV vs SCE, counter electrode = Pt wire open ring
G5	**SCREEN PRINTED DOUBLE GOLD MICRO BANDS**	EFFECT OF POTENTIAL, for reversible and irreversible (poisoned) systems	Solution = 5mM $K_4Fe^{II}(CN)_6$, 0.1M K_2HPO_4, 0.1M KH_2PO_4, light intensity = 100% I_o, potential varied between -200 and +800 mV vs SCE, counter electrode = Pt wire open ring
G6	**GOLD MACRODISC**	EFFECT OF POISONING	Solution = 5mM $K_4Fe^{II}(CN)_6$, 0.1M K_2HPO_4, 0.1M KH_2PO_4, light intensity = 100% I_o, potential = +200 mV vs SCE, counter electrode = Pt wire open ring

EXPERIMENT G1

Sample (WE)- **SCREEN PRINTED SINGLE GOLD MICROBAND**

Solution- 5mM $K_4Fe^{II}(CN)_6$, 0.1M K_2HPO_4, 0.1M KH_2PO_4

Experiment- EFFECT OF LASER VELOCITY (see Chapter 4)

Potential- + 200 mV vs SCE

Light intensity- 100 % I_o

RE- SCE

CE- Pt wire open ring

Table G1-1. Photocurrent image parameters:

Experimental Parameter	Value
Lens	x 4 (Bio-Rad) , $N_A = 0.12$
Laser beam diameter (2r)	2 μm
Electronic Zoom	x 1.0
Pre-amplifier AC/DC selection	AC
Pre-amp Low Frequency Filter	0.1 Hz
Pre-amp High Frequency Filter	10 kHz (τ_{inst} = 16 μs)

Table G1-2. Photocurrent image parameters showing scan velocity type dependant factors:

Scan Velocity Type	Faster Scan Times	Slower Scan Times
Objective Factor	O_f(x-axis) = 4.1 O_f(y-axis) = 4.1	O_f(x-axis) = 3.8 O_f(y-axis) = 4.1
Pixel Size (x × y)	3.717 x 3.717 μm	4.011 x 3.717 μm
Image Area Sampled 768 x 512 pixels	2855 x 1903 μm	3080 x 1903 μm
Line Length (768 pixels)	2855 μm	3080 μm

Table G1-3. Photocurrent image factors depending on individual laser scan times:

Photocurrent Image	a	b*	c	d	e	f	g
Scan Velocity Type	v. fast	stnd. slow	sel. slow	sel. slow	sel. slow	sel. slow	sel. slow
Line Scan Time / ms line $^{-1}$	1.92	7.68	10.00	23.00	50.00	116.00	114.00
pixel dwell time / μs	2.50	10.00	13.02	29.95	65.10	151.04	182.23
laser pseudo-velocity / cm s $^{-1}$	148.70	40.10	30.80	13.39	6.16	2.66	2.20
laser beam irradiation time , τ / μs	1.35	4.99	6.49	14.93	32.46	75.31	90.87

* Optical image (image h) taken at these settings as well as the photocurrent image.

stnd. slow = standard slow scan time
sel. slow = user selectable / defined slow scan time

Table G1-4. Photocurrent scale :

Potentiostat setting	1 μA = 1 volt
Preamplifier gain	x 20
256 grey scale	50 nA

EXPERIMENT G2

Sample (WE)- **SCREEN PRINTED SINGLE GOLD MICROBAND**

Solution- 5mM $K_4Fe^{II}(CN)_6$, 0.1M K_2HPO_4, 0.1M KH_2PO_4

Experiment- HIGH RESOLUTION IMAGING, higher zoom (see Chapter 4)

Potential- +200 mV vs SCE

Light intensity- 100 % I_o

RE- SCE

CE- Pt wire open ring

Table G2-1. Photocurrent image parameters:

Experimental Parameter	Value
Lens	x 4 (Bio-Rad) , $N_A = 0.12$
Laser beam diameter (2r)	2 μm
Electronic Zoom	x 6.0
Objective Factor	O_f(x-axis) = 3.8 , O_f(y-axis) = 4.1
Pixel Size (x × y)	0.668 x 0.620 μm
Image Area Sampled, 768 x 512 pixels	513 x 476 μm
Line Length (768 pixels)	476 μm
Scan Velocity Type	standard slow (F1)
Pixel Dwell Time	10 μs
Line scan time	7.68 ms
Frame Scan Time	3.93 s
Pseudo Laser Velocity , v_p	2.05 cm s^{-1}
Laser Beam Irradiation Time , τ	29.94 μs
Pre-amplifier AC/DC selection	AC
Pre-amp Low Frequency Filter	0.3 Hz
Pre-amp High Frequency Filter	3 kHz (τ_{inst} = 53 μs)

Table G2-2. Photocurrent scale :

Potentiostat setting	1 μA = 1 volt
Preamplifier gain	x 50
256 pixel scale	20 nA

EXPERIMENT G3

Sample (WE)- **GOLD MACRODISC**

Solution- 5mM $K_4Fe^{II}(CN)_6$, 5mM $K_3Fe^{III}(CN)_6$, 0.1M K_2HPO_4, 0.1M KH_2PO_4.

Experiment- EFFECT OF POTENTIAL (see Chapter 4)

Potential- Varied between -300 and +300 mV vs SCE

Light intensity- 100 % I_o

Other electrodes- RE = SCE, CE = Pt wire open ring

Table G3-1. Photocurrent image parameters:

Experimental Parameter	Value
Lens	x 10 (Bio-Rad) , $N_A = 0.25$
Laser beam diameter (2r)	1 μm
Electronic Zoom	x 1.0
Objective Factor	O_f(x-axis) = 9.4 , O_f(y-axis) = 10.2
Pixel Size (x × y)	1.621 x 1.494 μm
Image Area Sampled, 768 x 512 pixels	1245 x 765 μm
Line Length (768 pixels)	1245 μm
Scan Velocity Type	user defined slow
Pixel Dwell Time	32.6 μs
Line scan time	25 ms
Frame Scan Time	12.8 s
Pseudo Laser Velocity , v_p	4.98 cm s^{-1}
Laser Beam Irradiation Time , τ	20 μs
Pre-amplifier AC/DC selection	AC
Pre-amp Low Frequency Filter	0.03 Hz
Pre-amp High Frequency Filter	10 kHz (τ_{inst} = 16 μs)

Table G3-2. Photocurrent scale :

Potentiostat setting	10 μA = 1 volt
Preamplifier gain	x 50
256 pixel scale	200 nA

EXPERIMENT G4

Sample (WE)- **PURE GOLD SINGLE MICROBAND**

Solution- 5mM $K_4Fe^{II}(CN)_6$, 0.1M K_2HPO_4, 0.1M KH_2PO_4

Experiment- EFFECT OF POTENTIAL (see Chapter 4)

Potential- Varied between -100 and +400 mV vs SCE

Light intensity- 100 % I_o

RE- SCE

CE- Pt wire open ring

Table G4-1. Photocurrent image parameters:

Experimental Parameter	Value
Lens	x 4 (Bio-Rad) , $N_A = 0.12$
Laser beam diameter (2r)	2 μm
Electronic Zoom	x 1.0
Objective Factor	O_f(x-axis) = 3.8 , O_f(y-axis) = 4.1
Pixel Size (x × y)	4.011 x 3.717 μm
Image Area Sampled, 768 x 512 pixels	3080 x 1903 μm
Line Length (768 pixels)	3080 μm
Scan Velocity Type	user defined slow
Pixel Dwell Time	32.6 μs
Line scan time	25 ms
Frame Scan Time	12.8 s
Pseudo Laser Velocity , v_p	12.32 cm s^{-1}
Laser Beam Irradiation Time , τ	16.3 μs
Pre-amplifier AC/DC selection	AC
Pre-amp Low Frequency Filter	0.3 Hz
Pre-amp High Frequency Filter	3 kHz (τ_{inst} = 53 μs)

Table G4-2. Table Photocurrent scale :

Potentiostat setting	10 μA = 1 volt
Preamplifier gain	x 100
256 pixel scale	100 nA

EXPERIMENT G5

Sample (WE)- **SCREEN PRINTED DOUBLE GOLD MICROBANDS**

Solution- 5mM $K_4Fe^{II}(CN)_6$, 0.1M K_2HPO_4, 0.1M KH_2PO_4

Experiment- EFFECT OF POTENTIAL for reversible and irreversible (poisoned) reaction system (see Chapter 4).

Potential- Varied between -200 and +800 mV vs SCE

Light intensity- 100 % I_o

Other electrodes- RE = SCE, CE = Pt wire open ring

Table G5-1. Photocurrent image parameters:

Experimental Parameter	Value
Lens	x 4 (Bio-Rad) , $N_A = 0.12$
Laser beam diameter (2r)	2 μm
Electronic Zoom	x 4.7
Objective Factor	O_f(x-axis) = 3.8 , O_f(y-axis) = 4.1
Pixel Size (x × y)	0.853 x 0.791 μm
Image Area Sampled, 768 x 512 pixels	655 x 405 μm
Line Length (768 pixels)	655 μm
Scan Velocity Type	standard slow (F1)
Pixel Dwell Time	10.00 μs
Line scan time	7.68 ms
Frame Scan Time	3.93 s
Pseudo Laser Velocity , v_p	8.53 cm s^{-1}
Laser Beam Irradiation Time , τ	23.45 μs
Pre-amplifier AC/DC selection	AC
Pre-amp Low Frequency Filter	0.03 Hz
Pre-amp High Frequency Filter	10 kHz (τ_{inst} = 16 μs)

Table G5-2. Photocurrent Scale :

Potentiostat setting	0.1 μA = 1volt
Preamplifier gain	x 50
256 grey scale	2 nA

EXPERIMENT G6

Sample (WE)- **GOLD MACRODISC**

Solution- 5mM $K_4Fe^{II}(CN)_6$, 0.1M K_2HPO_4, 0.1M KH_2PO_4

Experiment- EFFECT OF POISONING (poisoned) (see Chapter 4).

Potential- + 200 mV vs SCE

Light intensity- 100 % I_o

RE- SCE

CE- Pt wire open ring

Table G6-1. Photocurrent image parameters:

Experimental Parameter	Value
Lens	x 4 (Bio-Rad) , $N_A = 0.12$
Laser beam diameter (2r)	2 μm
Electronic Zoom	x 4.5
Objective Factor	O_f(x-axis) = 3.8 , O_f(y-axis) = 4.1
Pixel Size (x × y)	0.891 x 0.826 μm
Image Area Sampled, 768 x 512 pixels	684 x 423 μm
Line Length (768 pixels)	684 μm
Scan Velocity Type	standard slow (F1)
Pixel Dwell Time	10.00 μs
Line scan time	7.68 ms
Frame Scan Time	3.93 s
Pseudo Laser Velocity , v_p	8.91 cm s^{-1}
Laser Beam Irradiation Time , τ	22.45 μs
Pre-amplifier AC/DC selection	AC
Pre-amp Low Frequency Filter	0.03 Hz
Pre-amp High Frequency Filter	10 kHz (τ_{inst} = 16 μs)

Photocurrent Scale : 256 grey scale = 2 nA

3. Experimental Parameters for Work Carried Out on Stainless Steel (as seen in Chapter 5)

STAINLESS STEEL
GENERAL IMAGING
EXPERIMENTS
SUMMARY

A summary table for the experiments on stainless steel:

Nº	Sample	Experiment	Conditions
P1	**304L STAINLESS STEEL**	EFFECT OF POTENTIAL	Solution = 0.3M $NaClO_4$, light intensity = 10% I_o, potential = -900 to +700 mV vs Hg/Hg_2SO_4, sat K_2SO_4, counter electrode = Pt wire open ring.
P2	**316F STAINLESS STEEL**	EFFECT OF POTENTIAL	Solution = 0.3M $NaClO_4$, light intensity = 100% I_o, potential = -900 to +700 mV vs Hg/Hg_2SO_4, sat K_2SO_4, counter electrode = Pt wire open ring.
P3	**316F STAINLESS STEEL**	EFFECT OF LIGHT INTENSITY	Solution = 0.3M $NaClO_4$, light intensity varied between 100% I_o to 1% I_o, potential = +317 mV vs Hg/Hg_2SO_4, sat K_2SO_4, counter electrode = Pt wire open ring.
P4	**304L STAINLESS STEEL**	EFFECT OF LIGHT INTENSITY	Solution = 0.3M $NaClO_4$, light intensity varied between 100% I_o to 1% I_o, potential = 0 mV vs Hg/Hg_2SO_4, sat K_2SO_4, counter electrode = Pt wire open ring.
P5	**304 STAINLESS STEEL**	EFFECT OF LASER VELOCITY	Solution = 0.1M $NaClO_4$, light intensity = 10% I_o, potential = + 448 mV vs Hg/Hg_2SO_4, sat K_2SO_4, counter electrode = Pt wire open ring.

EXPERIMENT P1

Sample (WE)- **304L STAINLESS STEEL**

Solution- 0.3M $NaClO_4$

Experiment- EFFECT OF POTENTIAL (see Chapter 5)

Potential- varied between -900 and +700 mV vs Hg/Hg_2SO_4, sat K_2SO_4

Light intensity- 10% I_o

Other electrodes- RE- Hg/Hg_2SO_4, sat K_2SO_4, CE- Pt wire open ring

Table P1-1. Photocurrent image:

Experimental Parameter	Value
Lens	x4 (Nikon) , $N_A = 0.13$
Laser beam diameter (2r)	2 μm
Electronic Zoom	x 6.0
Objective Factor	O_f(x-axis) = 3.7 , O_f(y-axis) = 4.0
Pixel Size (x × y)	0.686 x 0.635 μm
Image Area Sampled, 768 x 512 pixels	527 x 325 μm
Line Length (768 pixels)	527 μm
Scan Velocity Type	standard slow (F1)
Pixel Dwell Time	10 μs
Line scan time	7.68 ms
Frame Scan Time	3.93 s
Laser Pseudo-Velocity , v_p	6.68 cm s^{-1}
Laser Beam Irradiation Time , τ	29.15 μs
Pre-amplifier AC/DC selection	DC
Pre-amp Low Frequency Filter	0.03 Hz
Pre-amp High Frequency Filter	10 kHz (τ_{inst} = 16 μs)

Table P1-2. Photocurrent scale:

Potentiostat	1 μA = volt
Pre-amplifier gain	x50
256 pixel scale	20 nA
Pixel intensity value on 256 scale	154 pixels = 12.03 nA
Photocurrent range for grey scale	-12 nA to +8 nA

EXPERIMENT P2

Sample (WE)- **316F STAINLESS STEEL**

Solution- 0.3M $NaClO_4$

Experiment- EFFECT OF POTENTIAL (see Chapter 5)

Potential- varied between -900 and +700 mV vs Hg/Hg_2SO_4, sat K_2SO_4

Light intensity- 100% I_o

Other electrodes- RE = Hg/Hg_2SO_4, sat K_2SO_4, CE = Pt wire open ring

Table P2-1. Photocurrent image parameters:

Experimental Parameter	Value
Lens	x4 (Nikon) , $N_A = 0.13$
Laser beam diameter (2r)	2 μm
Electronic Zoom	x 5.0
Objective Factor	O_f(x-axis) = 3.7 , O_f(y-axis) = 4.0
Pixel Size (x × y)	0.824 x 0.762 μm
Image Area Sampled,768 x 512 pixels	633 x 390 μm
Line Length (768 pixels)	633 μm
Scan Velocity Type	standard slow (F1)
Pixel Dwell Time	10 μs
Line scan time	7.68 ms
Frame Scan Time	3.93 s
Pseudo Laser Velocity , v_p	8.24 cm s^{-1}
Laser Beam Irradiation Time , τ	24.27 μs
Pre-amplifier AC/DC selection	DC
Pre-amp Low Frequency Filter	0.03 Hz
Pre-amp High Frequency Filter	10 kHz (τ_{inst} = 16 μs)

Pixel intensity value on 0-255 scale for 'light off' (dark images) = 152

Table P2-2. Photocurrent scale:

Potentiostat	1 μA = volt		
Pre-amplifier gain	x50	x20	x10
256 grey scale pixel scale	20 nA	50 nA	100 nA
Light-off pixel intensity value / 256	152 +1 = 153 pixels		
I_{photo} = 0 (light-off) value on grey scale	12.0 nA	29.8 nA	59.8 nA
Photocurrent range for grey scale	-12 nA to +8 nA	-30 nA to +20 nA	-60 to + 40 nA

EXPERIMENT P3

Sample (WE)- **316F STAINLESS STEEL**

Solution- 0.3M $NaClO_4$

Experiment- EFFECT OF LIGHT INTENSITY (see Chapter 5)

Potential- +317 mV vs Hg/Hg_2SO_4, sat K_2SO_4

Light intensity- varied between 100% I_o and 1% I_o

RE- Hg/Hg_2SO_4, sat K_2SO_4

CE- Pt wire open ring

Table P3-1. Photocurrent image parameters:

Experimental Parameter	Value
Lens	x4 (Nikon) , $N_A = 0.13$
Laser beam diameter (2r)	2 μm
Electronic Zoom	x 5.0
Objective Factor	O_f(x-axis) = 3.7 , O_f(y-axis) = 4.0
Pixel Size (x × y)	0.824 x 0.762 μm
Image Area Sampled, 768 x 512 pixels	633 x 390 μm
Line Length (768 pixels)	633 μm
Scan Velocity Type	standard slow (F1)
Pixel Dwell Time	10 μs
Line scan time	7.68 ms
Frame Scan Time	3.93 s
Pseudo Laser Velocity , v_p	8.24 cm s^{-1}
Laser Beam Irradiation Time , τ	24.27 μs
Pre-amplifier AC/DC selection	DC
Pre-amp Low Frequency Filter	0.03 Hz
Pre-amp High Frequency Filter	10 kHz (τ_{inst} = 16 μs)

Pixel intensity value on 0-255 scale for 'light off' (dark images) = 152

Table P3-2. Photocurrent scale:

% I_o , Light Intensity	100	10	3	1
Potentiostat (μA / volt)	1	1	1	1
Pre-amplifier gain	x10	x50	x50	x50
256 pixel scale / nA	100	20	20	20
Light off value, in 256	153	153	153	153
Light off value on grey scale / nA	59.8	12.0	12.0	12.0
Photocurrent range / nA	-60 to +40	-12 to +8	-12 to +8	-12 to +8

EXPERIMENT P4

Sample (WE)- **304L STAINLESS STEEL**

Solution- 0.3M $NaClO_4$

Experiment EFFECT OF LIGHT INTENSITY (see Chapter 5)

Potential- 0 mV vs Hg/Hg_2SO_4, sat K_2SO_4

Light intensity- varied between 100% I_o and 1% I_o

RE- Hg/Hg_2SO_4, sat K_2SO_4

CE- Pt wire open ring

Table P4-1. Photocurrent image parameters:

Experimental Parameter	Value
Lens	x4 (Nikon) , $N_A = 0.13$
Laser beam diameter (2r)	2 μm
Electronic Zoom	x 6.0
Objective Factor	O_f(x-axis) = 3.7 , O_f(y-axis) = 4.0
Pixel Size (x × y)	0.686 x 0.635 μm
Image Area Sampled, 768 x 512 pixels	527 x 325 μm
Line Length (768 pixels)	527 μm
Scan Velocity Type	standard slow (F1)
Pixel Dwell Time	10 μs
Line scan time	7.68 ms
Frame Scan Time	3.93 s
Pseudo Laser Velocity , v_p	6.68 cm s^{-1}
Laser Beam Irradiation Time , τ	29.15 μs
Pre-amplifier AC/DC selection	DC
Pre-amp Low Frequency Filter	0.03 Hz
Pre-amp High Frequency Filter	10 kHz (τ_{inst} = 16 μs)

Pixel intensity value on 0-255 scale for 'light off' (dark images) = 140.5

Table P4-2. Photocurrent scale:

% I_o , Light Intensity	100	55.5	27.3	10	3	1
Potentiostat (μA / volt)	1	1	1	1	1	1
Pre-amplifier gain	x50	x50	x50	x50	x100	x200
256 pixel scale / nA	20	20	20	20	10	5
Light off value, in 256	141	141	141	141	141	141
Light off value on grey scale / nA	11	11	11	11	5.5	2.8
Photocurrent range / nA	-11 to +39	-11 to +39	-11 to +39	-11 to + 39	-6 to +4	-3 to +2

Table P4-3. Higher resolution confocal optical image:

Confocal Optical Image Experimental Parameter	Value
Lens	x40 (Nikon) , $N_A = 0.40$
Laser beam diameter (2r)	0.6 μm
Electronic Zoom	x 1.0
Objective Factor	O_f(x-axis) = 27.8 , O_f(y-axis) = 30.5
Pixel Size (x × y)	0.548 x 0.500 μm
Image Area Sampled, 768 x 512 pixels	421 x 256 μm
Line Length (768 pixels)	421 μm
Scan Velocity Type	standard slow (F1)
Pixel Dwell Time	10 μs
Line scan time	7.68 ms
Frame Scan Time	3.93 s
Pseudo Laser Velocity , v_p	5.48 cm s^{-1}
Laser Beam Irradiation Time , τ	10.95 μs

EXPERIMENT P5

Sample (WE)- **304L STAINLESS STEEL**

Solution- 0.1M $NaClO_4$

Experiment- EFFECT OF LASER VELOCITY (see Chapter 5)

Potential- + 448 mV vs Hg/Hg_2SO_4, sat K_2SO_4

Light intensity- 10% I_o

RE- Hg/Hg_2SO_4, sat K_2SO_4

CE- Pt wire open ring

Table P5-1. Photocurrent image parameters:

Experimental Parameter	Value
Lens	x4 (Nikon) , $N_A = 0.13$
Laser beam diameter (2r)	2μm
Electronic Zoom	x 6.0
Objective Factor	O_f(x-axis) = 3.7 , O_f(y-axis) = 4.0
Pixel Size (x × y)	0.686 x 0.635 μm
Image Area Sampled, 768 x 512 pixels	527 x 325 μm
Line Length (768 pixels)	527 μm
Scan Velocity Type	'standard slow' or 'user selectable slow'
Pre-amplifier AC/DC selection	DC
Pre-amp Low Frequency Filter	0.03 Hz
Pre-amp High Frequency Filter	10 kHz (τ_{inst} = 16 μs)

Table P5-2. Factors depending on individual laser scan times:

Photocurrent Image	a	b	c	d
Scan Velocity Type	stnd. slow	sel. slow	sel. slow	sel. slow
Line Scan Time / ms line $^{-1}$	7.68	10	20	40
Frame scan time /s	3.93	5.12	10.24	20.48
Pixel dwell time / μs	10.00	13.02	26.04	52.08
Laser pseudo-velocity / cm s $^{-1}$	6.86	5.27	2.64	1.32
Laser beam irradiation time , τ / μs	29.15	37.96	75.92	151.84

Note : stnd. slow = standard slow scan time
sel. slow = user selectable / defined slow scan time

Table P5-3. Photocurrent scale:

Potentiostat setting	1 μA = 1 volt
Preamplifier gain	x100
256 grey scale	10 nA

Pixel intensity value on 0-255 scale for 'light off' (dark images) = 148.8
where 0 = 1st value and 255 = 256th value
∴light-off value = 149.8 pixels on the 256 grey scale

$$I_{dark} = 149.8 \times \frac{10\ nA}{256} = 5.85\ nA$$

As $I_{photo} = I_{light} - I_{dark}$, the 10 nA grey scale
ranges from a maximum of I_{photo} = +4 nA
to a minimum of I_{photo} = -6 nA

4. Experimental Parameters for Work Carried Out on the Corrosion of Stainless Steel (as seen in Chapter 6)

STAINLESS STEEL CORROSION EXPERIMENTS SUMMARY

These experiments were all carried out on 316F stainless steel.

PITTING CORROSION IN JUST $NaClO_4$ ALONE AT A HIGH POTENTIAL:

Nº	Experiment	Conditions
A	EFFECT OF TIME, with $NaClO_4$ alone at a high potential	Solution = 0.1M $NaClO_4$, light intensity = 100% I_o, potential = +173 mV vs Hg/Hg_2SO_4, sat K_2SO_4 then up to +675 mV then back down to +173 m, counter electrode = Pt wire open ring.

PITTING CORROSION WITH A LOW CONCENTRATION OF NaCl PRESENT:

B	EFFECT OF TIME, with a low concentration of NaCl present	Solution = 0.0125M NaCl + 0.02875M $NaClO_4$ (Ionic strength = 0.3M), light intensity = 100% I_o, potential = +175 mV vs Hg/Hg_2SO_4, sat K_2SO_4, counter electrode = Pt wire open ring.
C	EFFECT OF TIME, with a slightly higher concentration of NaCl present at a lower potential	Solution = 0.025M NaCl + 0.275M $NaClO_4$ (Ionic strength = 0.3M), light intensity = 100% I_o, potential = -250 mV vs Hg/Hg_2SO_4, sat K_2SO_4, counter electrode = Pt wire open ring.
D	EFFECT OF TIME, in the presence of NaCl with a lower ionic strength	Solution = 0.025M NaCl + 0.075M $NaClO_4$ (Ionic strength = 0.1M), light intensity =100% I_o , potential = 0 mV vs Hg/Hg_2SO_4, sat K_2SO_4, counter electrode = Pt wire open ring.
E	EFFECT OF TIME, imaging in the presence of NaCl as well as simultaneous monitoring of the total current	Solution = 0.025M NaCl + 0.075M $NaClO_4$ (Ionic strength = 0.1M), light intensity = 100% I_o, potential = 0 mV vs Hg/Hg_2SO_4, sat K_2SO_4, counter electrode = Pt wire open ring.
F	EFFECT OF TIME, imaging in the presence of NaCl with a higher potential, and simultaneous monitoring of the total current	Solution = 0.025M NaCl + 0.075M $NaClO_4$ (Ionic strength = 0.1M), light intensity = 100% I_o, potential = +108 mV vs Hg/Hg_2SO_4, sat K_2SO_4 later increased to +176 mV, counter electrode = Pt wire open ring.

THE OCCURRENCE OF PITTING CORROSION LATER FOLLOWED BY CREVICE CORROSION:

G	EFFECT OF TIME, imaging in the presence of NaCl with a higher potential, and simultaneous monitoring of the total current	Solution = 0.025M NaCl + 0.075M $NaClO_4$ (Ionic strength = 0.1M), light intensity = 100% I_o, potential = +173 mV vs Hg/Hg_2SO_4, sat K_2SO_4 later increased to +252 mV, counter electrode = Pt wire open ring

THE OCCURRENCE OF CREVICE CORROSION IN THE PRESENCE OF NaCl:

H	EFFECT OF TIME, monitored for crevice corrosion imaging in the solution	Solution =0.3M $NaClO_4$ only but electrode exposed to Cl- (from HCl) prior to experiment , light intensity = 100% I_o, potential = -100 mV vs Hg/Hg_2SO_4, sat K_2SO_4, counter electrode = Pt wire open ring.
I	OPTICAL IMAGING, showing the occurrence of sudden crevice corrosion in the presence of a SCE reference electrode	Solution = 0.1M $NaClO_4$ only, light intensity = 100% I_o, potential = -400 mV vs Hg/Hg_2Cl_2, sat KCl, counter electrode = Pt wire open ring. After 35 minutes being polarised at this potential crevice corrosion very suddenly occurred.
J	OPTICAL IMAGING, showing the occurrence of crevice corrosion in the NaCl containing solution even before turning on the potentiostat and applying a potential	Solution = 0.025M NaCl + 0.075M $NaClO_4$ (Ionic strength = 0.1M), light intensity = 100% I_o.

EXPERIMENT A

Sample (WE)- **316F STAINLESS STEEL**

Solution- 0.03M $NaClO_4$

Experiment- EFFECT OF TIME, with $NaClO_4$ alone at a high potential, EXPERIMENT A (see Chapter 6)

Potential- +173 mV then up to +676 for 15 minutes and then back to +173 mV vs Hg/Hg_2SO_4, sat K_2SO_4

Light intensity- 100% I_o

Reference electrode- Hg/Hg_2SO_4, sat K_2SO_4

Counter electrode- Pt wire open ring

Table A-1. Photocurrent image parameters:

Experimental Parameter	Value
Lens	x4 (Nikon) , $N_A = 0.13$
Laser beam diameter (2r)	2 μm
Electronic Zoom	x 5.0
Objective Factor	O_f(x-axis) = 3.7 , O_f(y-axis) = 4.0
Pixel Size (x × y)	0.824 x 0.762 μm
Image Area Sampled, 768 x 512 pixels	633 x 390 μm
Line Length (768 pixels)	633 μm
Scan Velocity Type	standard slow (F1)
Pixel Dwell Time	10 μs
Line scan time	7.68 ms
Frame Scan Time	3.93 s
Pseudo Laser Velocity , v_p	8.24 cm s^{-1}
Laser Beam Irradiation Time , τ	24.27 μs
Pre-amplifier AC/DC selection	DC
Pre-amp Low Frequency Filter	0.03 Hz
Pre-amp High Frequency Filter	10 kHz (τ_{inst} = 16 μs)

Pixel intensity value on 0-255 scale for 'light off' (dark images) = 153.4

Table A-2. Photocurrent scale:

Potentiostat	1 μA / volt
Pre-amplifier gain	x20
256 pixel scale	50 nA
Light off value, in 256	154
Light off value on grey scale	30 nA
Photocurrent range	-30 to +20 nA

Table A-3. Higher resolution confocal optical image:

Experimental Parameter	Value
Lens	x20 (Swift) , $N_A = 0.40$
Laser beam diameter (2r)	0.6 μm
Electronic Zoom	x 1.0
Objective Factor	O_f(x-axis) = 14.3 , O_f(y-axis) = 15.7
Pixel Size (x × y)	1.066 x 0.971 μm
Image Area Sampled, 768 x 512 pixels	818 x 497 μm
Line Length (768 pixels)	818 μm
Scan Velocity Type	standard slow (F1)
Pixel Dwell Time	10 μs
Line scan time	7.68 ms
Frame Scan Time	3.93 s
Pseudo Laser Velocity , v_p	10.65 cm s^{-1}
Laser Beam Irradiation Time , τ	5.63 μs

EXPERIMENT B

Sample (WE)- **316F STAINLESS STEEL**

Solution- 0.0125M NaCl + 0.02875M $NaClO_4$ (Ionic strength = 0.3M

Experiment- EFFECT OF TIME, with a low concentration of NaCl present, EXPERIMENT B (see Chapter 6)

Potential- +175 mV vs Hg/Hg_2SO_4, sat K_2SO_4

Light intensity- 100% I_o

Reference electrode- Hg/Hg_2SO_4, sat K_2SO_4

Counter electrode- Pt wire open ring

Table B-1. Photocurrent image parameters:

Experimental Parameter	Value
Lens	x4 (Nikon) , $N_A = 0.13$
Laser beam diameter (2r)	2 μm
Electronic Zoom	x 5.01
Objective Factor	O_f(x-axis) = 3.7 , O_f(y-axis) = 4.0
Pixel Size (x × y)	0.808 x 0.747 μm
Image Area Sampled, 768 x 512 pixels	620 x 382 μm
Line Length (768 pixels)	620 μm
Scan Velocity Type	standard slow (F1)
Pixel Dwell Time	10 μs
Line scan time	7.68 ms
Frame Scan Time	3.93 s
Pseudo Laser Velocity , v_p	8.07 cm s^{-1}
Laser Beam Irradiation Time , τ	24.75 μs
Pre-amplifier AC/DC selection	DC
Pre-amp Low Frequency Filter	0.03 Hz
Pre-amp High Frequency Filter	10 kHz (τ_{inst} = 16 μs)

Pixel intensity value on 0-255 scale for 'light off' (dark images) = 153.5

Table B-2. Photocurrent scale:

Potentiostat setting	1 μA / volt
Pre-amplifier gain	x10
256 pixel scale / nA	100 nA
Light off value, in 256	154.5
Light off value on grey scale	60.4 nA
Photocurrent range	-60 to +40 nA

EXPERIMENT C

Sample (WE)- **316F STAINLESS STEEL**

Solution- 0.025M NaCl + 0.275M $NaClO_4$ (Ionic strength = 0.3M)

Experiment- EFFECT OF TIME, with a slightly higher concentration of NaCl, EXPERIMENT C (see Chapter 6)

Potential- -250 mV vs Hg/Hg_2SO_4, sat K_2SO_4

Light intensity- 100% I_o

Reference electrode- Hg/Hg_2SO_4, sat K_2SO_4

Counter electrode- Pt wire open ring

Table C-1. Photocurrent image parameters:

Experimental Parameter	Value
Lens	x4 (Nikon) , $N_A = 0.13$
Laser beam diameter (2r)	2 μm
Electronic Zoom	x 5.0
Objective Factor	O_f(x-axis) = 3.7 , O_f(y-axis) = 4.0
Pixel Size (x × y)	0.824 x 0.762 μm
Image Area Sampled, 768 x 512 pixels	633 x 390 μm
Line Length (768 pixels)	633 μm
Scan Velocity Type	standard slow (F1)
Pixel Dwell Time	10 μs
Line scan time	7.68 ms
Frame Scan Time	3.93 s
Pseudo Laser Velocity , v_p	8.24 cm s^{-1}
Laser Beam Irradiation Time , τ	24.27 μs
Pre-amplifier AC/DC selection	DC
Pre-amp Low Frequency Filter	0.03 Hz
Pre-amp High Frequency Filter	10 kHz (τ_{inst} = 16 μs)

Pixel intensity value on 0-255 scale for 'light off' (dark images) = 141.7

Table C-2. Photocurrent scale:

Potentiostat setting	1 μA / volt
Pre-amplifier gain	x20
256 pixel scale	50 nA
Light off value, in 256	142.7
Light off value on grey scale in nA	27.9 nA
Photocurrent range	- 28 nA to + 22 nA

Table C-3. Higher resolution confocal optical images:

Experimental Parameter	High Resolution	Very High Resolution
Lens	x20 (Swift) , $N_A = 0.40$	x40 (Nikon) , $N_A = 0.40$
Laser beam diameter (2r)	0.6 μm	0.6 μm
Electronic Zoom	x 1.0	x 2.4
Objective Factor	O_f(x-axis) = 14.3 ,O_f(y-axis) = 15.7	O_f(x-axis) = 27.8 ,O_f(y-axis) = 30.5
Pixel Size (x × y)	1.066 x 0.971 μm	0.228 x 0.208 μm
Image Area Sampled 768 x 512 pixels	818 x 497 μm	175 x 107 μm
Line Length (768 pixels)	818 μm	175 μm
Scan Velocity Type	standard slow (F1)	standard slow (F1)
Pixel Dwell Time	10 μs	10 μs
Line scan time	7.68 ms	7.68 ms
Frame Scan Time	3.93 s	3.93 s
Pseudo Laser Velocity , v_p	10.65 cm s^{-1}	2.28 cm s^{-1}
Laser Beam Irradiation Time , τ	5.63 μs	26.32 μs

EXPERIMENT D

Sample (WE)- **316F STAINLESS STEEL**

Solution- 0.025M NaCl + 0.075M $NaClO_4$ (Ionic strength = 0.1M)

Experiment- EFFECT OF TIME, in the presence of NaCl with a lower ionic strength, EXPERIMENT D (see Chapter 6)

Potential- 0 mV vs Hg/Hg_2SO_4, sat K_2SO_4

Light intensity- 100% I_o

Reference electrode- Hg/Hg_2SO_4, sat K_2SO_4

Counter electrode- Pt wire open ring

Table D-1. Photocurrent image parameters:

Experimental Parameter	Value
Lens	x4 (Nikon) , $N_A = 0.13$
Laser beam diameter (2r)	2 μm
Electronic Zoom	x 4.6
Objective Factor	O_f(x-axis) = 3.7 , O_f(y-axis) = 4.0
Pixel Size (x × y)	0.895 x 0.828 μm
Image Area Sampled, 768 x 512 pixels	688 x 424 μm
Line Length (768 pixels)	688 μm
Scan Velocity Type	standard slow (F1)
Pixel Dwell Time	10 μs
Line scan time	7.68 ms
Frame Scan Time	3.93 s
Pseudo Laser Velocity , v_p	8.96 cm s^{-1}
Laser Beam Irradiation Time , τ	22.35 μs
Pre-amplifier AC/DC selection	DC
Pre-amp Low Frequency Filter	0.03 Hz
Pre-amp High Frequency Filter	10 kHz (τ_{inst} = 16 μs)

Pixel intensity value on 0-255 scale for 'light off' (dark images) = 140.8

Table D-2. Photocurrent scale:

Potentiostat setting	1 μA / volt		
Pre-amplifier gain	x50	x20	x10
256 pixel scale	20 nA	50 nA	100 nA
Light off value, in 256	141.8		
Light off value on grey scale in nA	11.1 nA	27.7 nA	55.4 nA
Photocurrent range	- 11 nA to + 9 nA	- 28 nA to + 22 nA	- 55 nA to + 45 nA

Table D-3. Higher resolution confocal optical images:

Experimental Parameter	High Resolution	Very High Resolution
Lens	x20 (Swift) , $N_A = 0.40$	x40 (Nikon) , $N_A = 0.40$
Laser beam diameter (2r)	0.6 μm	0.6 μm
Electronic Zoom	x 1.0	x 10.0
Objective Factor	O_f(x-axis) = 14.3 ,O_f(y-axis) = 15.7	O_f(x-axis) = 27.8 ,O_f(y-axis) = 30.5
Pixel Size (x × y)	1.066 x 0.971 μm	0.055 x 0.050 μm
Image Area Sampled 768 x 512 pixels	818 x 497 μm	42 x 26 μm
Line Length (768 pixels)	818 μm	42 μm
Scan Velocity Type	standard slow (F1)	standard slow (F1)
Pixel Dwell Time	10 μs	10 μs
Line scan time	7.68 ms	7.68 ms
Frame Scan Time	3.93 s	3.93 s
Pseudo Laser Velocity , v_p	10.65 cm s^{-1}	0.55 cm s^{-1}
Laser Beam Irradiation Time , τ	5.63 μs	109.09 μs

EXPERIMENT E

Sample (WE)- **316F STAINLESS STEEL**

Solution- 0.025M NaCl + 0.075M $NaClO_4$ (Ionic strength = 0.1M)

Experiment- EFFECT OF TIME, imaging in the presence of NaCl as well as simultaneous monitoring of the total current, EXPERIMENT E (see Chapter 6)

Potential- 0 mV vs Hg/Hg_2SO_4, sat K_2SO_4

Light intensity- 100% I_o

Reference electrode- Hg/Hg_2SO_4, sat K_2SO_4

Counter electrode- Pt wire open ring

Table E-1. Photocurrent image parameters:

Experimental Parameter	Value
Lens	x4 (Nikon) , $N_A = 0.13$
Laser beam diameter (2r)	2 μm
Electronic Zoom	x 5.0
Objective Factor	O_f(x-axis) = 3.7 , , O_f(y-axis) = 4.0
Pixel Size (x × y)	0.824 x 0.762 μm
Image Area Sampled, 768 x 512 pixels	633 x 390 μm
Line Length (768 pixels)	633 μm
Scan Velocity Type	standard slow (F1)
Pixel Dwell Time	10 μs
Line scan time	7.68 ms
Frame Scan Time	3.93 s
Pseudo Laser Velocity , v_p	8.24 cm s^{-1}
Laser Beam Irradiation Time , τ	24.27 μs
Pre-amplifier AC/DC selection	DC
Pre-amp Low Frequency Filter	0.03 Hz
Pre-amp High Frequency Filter	10 kHz (τ_{inst} = 16 μs)

Pixel intensity value on 0-255 scale for 'light off' (dark images) = 140.8

Table E-2. Photocurrent scale:

Potentiostat	1 μA / volt		
Pre-amplifier gain	x100	x50	x20
256 pixel scale	10 nA	20 nA	50nA
Light off value, in 256	141.8		
Light off value on grey scale in nA	5.5 nA	11.1 nA	27.7 nA
Photocurrent range	-6 nA to + 4 nA	-11 nA to + 9 nA	-28 nA to +22 nA

Table E-3 Higher resolution confocal optical images:

Experimental Parameter	Value
Lens	x20 (Swift) , $N_A = 0.40$
Laser beam diameter (2r)	0.6 μm
Electronic Zoom	x 1.0
Objective Factor	O_f(x-axis) = 14.3 , O_f(y-axis) = 15.7
Pixel Size (x × y)	1.066 x 0.971 μm
Image Area Sampled, 768 x 512 pixels	818 x 497 μm
Line Length (768 pixels)	818 μm
Scan Velocity Type	standard slow (F1)
Pixel Dwell Time	10 μs
Line scan time	7.68 ms
Frame Scan Time	3.93 s
Pseudo Laser Velocity , v_p	10.65 cm s^{-1}
Laser Beam Irradiation Time , τ	5.63 μs

EXPERIMENT F

Sample (WE)- **316F STAINLESS STEEL**

Solution- 0.025M NaCl + 0.075M $NaClO_4$ (Ionic strength = 0.1M)

Experiment- EFFECT OF TIME, imaging in the presence of NaCl with a higher potential, and simultaneous monitoring of the total current EXPERIMENT F (see Chapter 6)

Potential- +108 mV later increased to +176 mV vs Hg/Hg_2SO_4, sat K_2SO_4

Light intensity- 100% I_o

Reference electrodes- Hg/Hg_2SO_4, sat K_2SO_4

Counter electrode- Pt wire open ring

Table F-1. Photocurrent image parameters:

Experimental Parameter	Value
Lens	x4 (Nikon) , $N_A = 0.13$
Laser beam diameter (2r)	2 μm
Electronic Zoom	x 4.3
Objective Factor	O_f(x-axis) = 3.7 , O_f(y-axis) = 4.0
Pixel Size (x × y)	0.958 x 0.886 μm
Image Area Sampled, 768 x 512 pixels	763 x 454 μm
Line Length (768 pixels)	763 μm
Scan Velocity Type	standard slow (F1)
Pixel Dwell Time	10 μs
Line scan time	7.68 ms
Frame Scan Time	3.93 s
Pseudo Laser Velocity , v_p	9.93 cm s^{-1}
Laser Beam Irradiation Time , τ	20.88 μs
Pre-amplifier AC/DC selection	DC
Pre-amp Low Frequency Filter	0.03 Hz
Pre-amp High Frequency Filter	10 kHz (τ_{inst} = 16 μs)

Pixel intensity value on 0-255 scale for 'light off' (dark images) = 141

Table F-2. Photocurrent scale:

Potentiostat setting	1 μA / volt		
Pre-amplifier gain	x100	x50	x20
256 pixel scale	10 nA	20 nA	50nA
Light off value, in 256	142		
Light off value on grey scale in nA	5.5 nA	11.1 nA	27.7 nA
Photocurrent range	- 6 nA to + 4 nA	-11 nA to +9 nA	-28 nA to + 22 nA

Table F-3. Higher resolution confocal optical images:

Experimental Parameter	Value
Lens	x20 (Swift) , $N_A = 0.40$
Laser beam diameter (2r)	0.6 μm
Electronic Zoom	x 1.0
Objective Factor	O_f(x-axis) = 14.3 , O_f(y-axis) = 15.7
Pixel Size (x × y)	1.066 x 0.971 μm
Image Area Sampled, 768 x 512 pixels	818 x 497 μm
Line Length (768 pixels)	818 μm
Scan Velocity Type	standard slow (F1)
Pixel Dwell Time	10 μs
Line scan time	7.68 ms
Frame Scan Time	3.93 s
Pseudo Laser Velocity , v_p	10.65 cm s^{-1}
Laser Beam Irradiation Time , τ	5.63 μs

Table F-4. Very high resolution confocal optical images:

Experimental Parameter	Low Electronic Zoom	High Electronic Zoom
Lens	x40 (Swift) , $N_A = 0.40$	x40 (Nikon) , $N_A = 0.40$
Laser beam diameter (2r)	0.6 μm	0.6 μm
Electronic Zoom	x 1.9	x 10.0
Objective Factor	O_f(x-axis) = 27.8 ,O_f(y-axis) = 30.5	O_f(x-axis) = 27.8 ,O_f(y-axis) = 30.5
Pixel Size (x × y)	0.289 x 0.263 μm	0.055 x 0.050 μm
Image Area Sampled 768 x 512 pixels	222 x 135 μm	42 x 26 μm
Line Length (768 pixels)	222 μm	42 μm
Scan Velocity Type	standard slow (F1)	standard slow (F1)
Pixel Dwell Time	10 μs	10 μs
Line scan time	7.68 ms	7.68 ms
Frame Scan Time	3.93 s	3.93 s
Pseudo Laser Velocity , v_p	2.89 cm s^{-1}	0.55 cm s^{-1}
Laser Beam Irradiation Time , τ	20.76 μs	109.09 μs

EXPERIMENT G

Sample (WE)- **316F STAINLESS STEEL**

Solution- 0.025M NaCl + 0.075M $NaClO_4$ (Ionic strength = 0.1M)

Experiment- EFFECT OF TIME, imaging in the presence of NaCl with a higher potential, and simultaneous monitoring of the total current EXPERIMENT G (see Chapter 6)

Potential- +173 mV for some time and then +252 mV for some time vs Hg/Hg_2SO_4, sat K_2SO_4

Light intensity- 100% I_o

Reference electrode- Hg/Hg_2SO_4, sat K_2SO_4

Counter electrode- Pt wire open ring

Table G-1. Photocurrent image parameters:

Experimental Parameter	Value
Lens	x4 (Nikon) , $N_A = 0.13$
Laser beam diameter (2r)	2 μm
Electronic Zoom	x 4.3
Objective Factor	O_f(x-axis) = 3.7 , O_f(y-axis) = 4.0
Pixel Size (x × y)	0.958 x 0.886 μm
Image Area Sampled, 768 x 512 pixels	763 x 454 μm
Line Length (768 pixels)	763 μm
Scan Velocity Type	standard slow (F1)
Pixel Dwell Time	10 μs
Line scan time	7.68 ms
Frame Scan Time	3.93 s
Pseudo Laser Velocity , v_p	9.93 cm s^{-1}
Laser Beam Irradiation Time , τ	20.88 μs
Pre-amplifier AC/DC selection	DC
Pre-amp Low Frequency Filter	0.03 Hz
Pre-amp High Frequency Filter	10 kHz (τ_{inst} = 16 μs)

Pixel intensity value on 0-255 scale for 'light off' (dark images) = 140.5

Table G-2. Photocurrent scale:

Potentiostat setting	1 μA / volt	
Pre-amplifier gain	x50	x20
256 pixel scale	20 nA	50 nA
Light off value, in 256	141.5	
Light off value on grey scale in nA	11.1 nA	27.6 nA
Photocurrent range	- 11 nA to + 9 nA	- 28 nA to + 22 nA

Table G-3. Higher resolution confocal optical images:

Experimental Parameter	Value
Lens	x20 (Swift) , $N_A = 0.40$
Laser beam diameter (2r)	0.6 μm
Electronic Zoom	x 1.0
Objective Factor	O_f(x-axis) = 14.3 , O_f(y-axis) = 15.7
Pixel Size (x × y)	1.066 x 0.971 μm
Image Area Sampled, 768 x 512 pixels	818 x 497 μm
Line Length (768 pixels)	818 μm
Scan Velocity Type	standard slow (F1)
Pixel Dwell Time	10 μs
Line scan time	7.68 ms
Frame Scan Time	3.93 s
Pseudo Laser Velocity , v_p	10.65 cm s^{-1}
Laser Beam Irradiation Time , τ	5.63 μs

EXPERIMENT H

Sample (WE)- **316F STAINLESS STEEL**

Solution- 0.3M $NaClO_4$ only but electrode exposed to Cl- (from HCl) prior to experiment

Experiment- EFFECT OF TIME, monitored for crevice corrosion imaging in the solution, EXPERIMENT H (see Chapter 6)

Potential- -100 mV vs Hg/Hg_2SO_4, sat K_2SO_4

Light intensity- 100% I_o

Reference electrode- Hg/Hg_2SO_4, sat K_2SO_4

Counter electrode- Pt wire open ring

Table H-1. Photocurrent image parameters

Experimental Parameter	Value
Lens	x4 (Nikon) , $N_A = 0.13$
Laser beam diameter (2r)	2 μm
Electronic Zoom	x 5.0
Objective Factor	O_f(x-axis) = 3.7 , O_f(y-axis) = 4.0
Pixel Size (x × y)	0.824 x 0.762 μm
Image Area Sampled, 768 x 512 pixels	633 x 390 μm
Line Length (768 pixels)	633 μm
Scan Velocity Type	standard slow (F1)
Pixel Dwell Time	10 μs
Line scan time	7.68 ms
Frame Scan Time	3.93 s
Pseudo Laser Velocity , v_p	8.24 cm s^{-1}
Laser Beam Irradiation Time , τ	24.27 μs
Pre-amplifier AC/DC selection	DC
Pre-amp Low Frequency Filter	0.03 Hz
Pre-amp High Frequency Filter	10 kHz (τ_{inst} = 16 μs)

Pixel intensity value on 0-255 scale for 'light off' (dark images) = 153.5

Table H-2. Photocurrent scale:

Potentiostat settings	1 μA / volt		
Pre-amplifier gain	x 100	x 50	x 20
256 pixel scale	10 nA	20 nA	50 nA
Light off value, in 256	154.5		
Light off value on grey scale in nA	6.04 nA	12.07 nA	30.18 nA
Photocurrent range	-60 nA to +40 nA	-12 nA to +8 nA	-30 nA to +20 nA

Table H-3. Higher resolution confocal optical images:

Experimental Parameter	Value
Lens	x20 (Swift) , $N_A = 0.40$
Laser beam diameter (2r)	0.6 μm
Electronic Zoom	x 1.0
Objective Factor	O_f(x-axis) = 14.3 , O_f(y-axis) = 15.7
Pixel Size (x × y)	1.066 x 0.971 μm
Image Area Sampled, 768 x 512 pixels	818 x 497 μm
Line Length (768 pixels)	818 μm
Scan Velocity Type	standard slow (F1)
Pixel Dwell Time	10 μs
Line scan time	7.68 ms
Frame Scan Time	3.93 s
Pseudo Laser Velocity , v_p	10.65 cm s^{-1}
Laser Beam Irradiation Time , τ	5.63 μs

EXPERIMENT I

Sample (WE)- **316F STAINLESS STEEL**

Solution- 0.1M $NaClO_4$ only

Experiment- OPTICAL IMAGING, showing the occurrence of sudden crevice corrosion in the presence of a SCE reference electrode.
EXPERIMENT I (see Chapter 6)

Potential- -400 mV vs SCE

Reference electrode- Hg/Hg_2Cl_2, sat KCl (SCE)

Counter electrode- Pt wire open ring

Light intensity- 10% I_o

Table I-1. Confocal optical image parameters:

Experimental Parameter	Value
Lens	x4 (Nikon) , $N_A = 0.13$
Laser beam diameter (2r)	2.0 μm
Electronic Zoom	x 6.9
Objective Factor	O_f(x-axis) = 3.7 , O_f(y-axis) = 4.0
Pixel Size (x × y)	0.597 x 0.552 μm
Image Area Sampled, 768 x 512 pixels	458 x 283 μm
Line Length (768 pixels)	458 μm
Scan Velocity Type	standard slow (F1)
Pixel Dwell Time	10 μs
Line scan time	7.68 ms
Frame Scan Time	3.93 s
Pseudo Laser Velocity , v_p	5.96 cm s^{-1}
Laser Beam Irradiation Time , τ	33.50 μs

EXPERIMENT J

Sample (WE)- **316F STAINLESS STEEL**

Solution- 0.025M NaCl + 0.075M $NaClO_4$ (Ionic strength = 0.1M)

Experiment OPTICAL IMAGING, showing the occurrence of crevice corrosion in the NaCl containing solution even before turning on the potentiostat and applying a potential, EXPERIMENT J (see Chapter 6)

Light intensity- 100% I_o

Table J-1. Confocal optical image parameters:

Experimental Parameter	Value
Lens	x20 (Swift) , $N_A = 0.6$
Laser beam diameter (2r)	0.6 μm
Electronic Zoom	x 1.0
Objective Factor	O_f(x-axis) = 14.3 , O_f(y-axis) = 15.7
Pixel Size (x × y)	1.066 x 0.971 μm
Image Area Sampled, 768 x 512 pixels	818 x 497 μm
Line Length (768 pixels)	818 μm
Scan Velocity Type	standard slow (F1)
Pixel Dwell Time	10 μs
Line scan time	7.68 ms
Frame Scan Time	3.93 s
Pseudo Laser Velocity , v_p	10.65 cm s^{-1}
Laser Beam Irradiation Time , τ	5.63 μs

K. EXPERIMENTAL PARAMETERS AND SETTINGS FOR THE MICROPROBE IMAGING WORK

K. EXPERIMENTAL PARAMETERS AND SETTINGS FOR MICROPROBE IMAGING WORK

This work was carried out on the Joel JXA-8600 Microprobe Analyser. The crystals selected for particular elements, the lines used, the experimental and image parameters given are given in this appendix.

The four detection crystals which were available to use were:

1. Pentaerythritol (PET), 2d = 8.742 Å
2. Lithium Fluoride (LIF), 2d = 4.0267 Å
3. Thallium acid Phthalate (TAP), 2d = 25.757 Å
4. Lead Stearate (STE), 2d = 100.4 Å

The crystal and wavelength required for a particular element was selected from standard tables of data when doing elemental maps, or preferably by selection of much more precise values by calibration of the instrument using known standard elements or alloys. This method of standardisation was particularly important for microprobe spot analysis giving the percentage of any element present, where at any spot the sum of the percentages of all the elements is 100%.

The spectrometer position (L) has been given in 'mm' units. This shows the distance from the x-ray source to the analysing crystal, and it represents the wavelength detecting position of any JEOL spectrometers. The spectrometer position may be related to the wavelength using the following equation:

$$L = \frac{2R}{2d} \cdot N_{th} \lambda$$

Where : 2R = The diameter of the Rowland circle (in millimetres) , 2d = Spacing between the atomic layers in the crystal (in Angstroms), λ = Wavelength (in Angstroms), N_{th} = Order of reflection. For the work given in this thesis N_{th} = 1 and R = 140 mm.

The TAP and STE crystals were held in one spectrometer (Channel 1) and the PET and LIF crystals held in another spectrometer (Channel 2).

1. Work on Gold Screen Printed Microband Electrodes

(See Chapter 3)

Experimental settings:

Parameter	Setting
Acceleration Voltage	20 kV
Current	1.3×10^{-7} A
Movement Type (stage / beam)	Stage
Scan Type	Unidirectional
Pixel Dwell Time	125 ms
Image Area Sampled (1 pixel = 1μm)	250 x 250 μm

Lines and crystals used for each element analysed:

Element	Crystal	Peak / mm	N_{th}	X-ray line	λ / Å	Channel
Al	TAP	90.665	1	Kα	8.341	1
Mg	TAP	107.515	1	Kα	9.891	1
Au	LIF	88.775	1	Lα	1.278	2
Cd	PET	126.700	1	Lα	3.953	2
Cu	LIF	107.150	1	Kα	1.543	2
Zn	LIF	99.810	1	Kα	1.437	2
Si	TAP	77.465	1	Kα	7.127	1
Pb	PET	169.095	1	Mα	5.276	2
Ca	PET	107.540	1	Kα	3.355	2
P	TAP	66.935	1	Kα	6.158	1
Ti	LIF	191.135	1	Kα	2.752	2
Ba	LIF	192.795	1	Lα	2.776	2

Note : The maps were recorded at expected text book values and not at standardised values in this case.

2. Work on Stainless Steel Electrodes (See Chapters 5 and 6)

Details for concentration maps recorded at 25 kV:

Parameter	Setting
Current	1.3×10^{-7} A
Energy of an Electron	25 keV
Movement type (stage / beam)	Stage
Scan Type	Unidirectional
Image Area Sampled (1 pixel = 1μm)	Varied from 60 x 60 μm to 460 x 460 μm the most typical area sampled was 200 x 200 μm
Pixel Dwell Time	Varied from 600 ms to 60 ms the most typical value was 100 ms

Details for concentration maps recorded at 12 kV:

Parameter	Setting
Current	1.3×10^{-7} A
Energy of an Electron	12 keV
Movement type (stage / beam)	Stage
Scan Type	Unidirectional
Image Area Sampled (1 pixel = 1μm)	Varied from 180 x 180 μm to 460 x 460 μm the most typical area sampled was 200 x 200 μm
Pixel Dwell Time	Varied from 300 ms to 75 ms the most typical value was 100 ms

Note : Microprobe spot analysis to show the quantity of the elements present was only conducted at 25 kV using a current of 5×10^{-8} A. This was carried out by movement of the beam to a specific location with a dwell time of 20 s. The same lines were used as were for the concentration maps. (see Chapters 5 and 6). The low kV setting was only used for recording oxygen maps and maps of the principle elements present in significant amounts in the stainless steel.

The lines and crystals typically used for microprobe analysis in order to record element concentration maps as well (as in the use of microprobe spot analysis) have been noted below. The lines used for each element analysis were obtained to 0.001 mm accuracy by calibration against standards with known percentages of elements 100.000%. This calibration was carried out prior to starting each session of microprobe work, as the line positions vary a little from time to time due to the specific conditions at that time. As many experiments were conducted using stainless steels over a long period of time the standardisation process was repeated many times as it was not possible to do the work in one session, so only the typical values have been listed here as a guide to the lines used. More specific values for each element recorded at a particular value have been listed with each individual concentration map shown (see Chapter 6).

Lines and crystals used for each element analysed:

Element	Crystal	Peak / mm	N_{th}	X-ray line	λ / Å	Channel
Fe	LIF	134.34	1	Kα	1.93	2
Cr	LIF	158.94	1	Kα	2.29	2
Al	TAP	91.04	1	Kα	8.38	1
Mn	LIF	145.88	1	Kα	2.10	2
Si	TAP	77.91	1	Kα	7.17	1
S	PET	171.66	1	Kα	5.36	2
Ti	PET	87.70	1	Kα	2.74	2
V	PET	79.84	1	Kα	2.49	2
Cu	LIF	106.84	1	Kα	1.54	2
Mo	PET	172.71	1	Lα	5.39	2
P	PET	196.78	1	Kα	6.14	2
Ni	LIF	115.00	1	Kα	1.66	2
As	TAP	105.43	1	Lα	9.70	1
Co	LIF	124.13	1	Kα	1.79	2
Sn	PET	114.93	1	Lα	3.59	2
O	TAP	256.77	1	Kα	23.62	1
Cl	PET	151.00	1	Kα	4.71	2

L. CONTACT ADDRESSES FOR THE MATERIALS USED

L. CONTACT ADDRESSES FOR THE MATERIALS USED

The supplier names (1.) and the supplier addresses (2.) for the materials used in this thesis have been given in this appendix.

1. Supplier Names

The materials given in this list have been categorised by the following material types:

a. electrode materials
b. substances for electrode mounting
c. electrode storage materials
d. polishing materials
e. solution preparation material /solvents
f. microscopy equipment
g. general equipment used for electrochemical experiments
h. equipment for noise reduction
i. X-ray analysis equipment
j. computer items

a. Electrode materials:

MATERIAL	SUPPLIER NAME	TYPE
Platinum wire- 5mm diameter, 99.99+ % purity, temper hard (used for counter electrode)	Advent Catalogue No- Pt:54087	electrode material
Gold wire 500 μm diameter	Advent	electrode material
P-type Silicon	(free sample given to R.Hutton)	electrode material
Counter electrodes: 1. SCE (Hg/ Hg_2Cl_2, KCl) 2. SSE (Hg/Hg_2SO_4, sat.K_2SO_4) 7mm diameter, shielded low noise cable with BNC end connector	Russel pH limited	electrode material
304L stainless steel 250 μm diameter wire	Advent Catalogue No. 620218	electrode material

MATERIAL	SUPPLIER NAME	TYPE
316F stainless steel disc	Bureau of analysed samples Ltd. Reference No: BCS/SS-CRM No 466/1 (British chemical standard/spectrograpic standard certified reference material)	electrode material

b. Substances for electrode mounting:

MATERIAL	SUPPLIER NAME	TYPE
Sliver Conductive Paint	RS Components Cat. No. 186-3600	electrode mounting
Conductive Silver Epoxy CW2400, Circuit Works, Conductive Epoxy Kit	RS Components catalogue No. 496-265	electrode mounting
Indium Foil 0.5mm thick, 99.99% purity	Aldrich 35, 728-6 [744-74-6]	electrode mounting
Gallium 99.99%	Aldrich 26, 326-5 [744-55-3]	electrode mounting
Kel – F , electrochemically inert material for mounting working electrode material.	Aldtech Polymer Engineering	electrode mounting
Epo-kwick Resin and Hardner This is a clear, hard setting epoxy resin Epo-kwick Resin = 4,4' isoproplidene diphenol epiclorophydrin resin alkyl glycidyl eter poly-acrylate ether Epo-kwick Hardner = Diethylenetriamine 2 hydroxyethylene triamine	Buehler	electrode mounting
Permabond SIP (self indicating) pre-treatment kit	Permabond Adhesives UK Ltd. Spectrum Engineering (local supplier)	electrode mounting

MATERIAL	SUPPLIER NAME	TYPE
Dropping Bottles for storage and application of Epo-kwick Resin and Hardner	Fisher Scientific	electrode mounting
250ml long drop bottle	Kartell part No. 15841DL FSA:BTR-760 070Y	
50ml long drop bottle	Kartell part No. 158011DL FSA:BTR-760 030U	

c. Electrode storage materials:

MATERIAL	SUPPLIER NAME	TYPE
Conductive Carbon tabs 12mm diameter	Agar Cat No. G3347	electrode storage / x-ray
Sample boxes for storing working electrodes 25mm x 25mm x 16mm	Agar Cat No. B3951	electrode storage

d. Polishing materials:

MATERIAL	SUPPLIER NAME	TYPE
Aluminium oxide papers 0.3 μm (grey) 1 μm (light green) 3 μm (pink) 9 μm (blue) 30 μm (green) 60 μm (sand coloured)	Agar Cat. No. B8647 Cat. No. B8646 Cat. No. B8645 Cat. No. B8644 Cat. No. B8642 Cat. No. B8640	polishing
Diamond Polishing Pastes Kemet type KD diamond compound 25 μm (brick-red) 14 μm (brown) 6 μm (yellow) 3 μm (green) 1 μm (blue) ½ μm (grey)	Kemet International Ltd. grade 25-KD-C2 grade 14-KD-C2 grade 6-KD-C2 grade 3-KD-C3 grade 1-KD-C2 grade ¼-KD-C2	polishing
Kemet Lubricating Fluids (for use with diamond polishing pastes) Type OS, solubility oil, a mineral oil based lubricant Type W, solubility water, a water based lubricant	Kemet International Ltd.	polishing

MATERIAL	SUPPLIER NAME	TYPE
Polishing Pads to use with Kemet Polishing Pastes and Aluminium pastes. A very soft nap cloth with a self sticking back KEMET NAP CLOTH	Kemet International Ltd. type NLH	polishing
Emery polishing pads for polishing wheel BRAMET-brand name self adhesive, waterproof, silicon carbide paper discs, diameter 150 cm Grit size 180c (rough) Grit size 320c (medium) Grit size 600 (smooth)	Kemet International Ltd.	polishing
Aluminium oxide pastes Aluminium oxide suspensions (Al_2O_3) in 0.18 litre applicator bottles 1m, type = alpha micropolish® Alumina No. 1C 0.3 m, type = alpha micropolish® Alumina No. 2A 0.05 m, type = gamma micropolish® Alumina No. 3B	Buehler Cat. No. 40-6354-006 Cat. No. 40-6352-006 Cat. No. 40-6353-006	polishing
Waterproof silicon carbide (emery) papers P240 P320 P1000 P1200	from Mechanical Workshop, chemistry Dept. UCL	polising

e. Solution preparation materials / solvents:

MATERIAL	SUPPLIER NAME	TYPE
Milli-Q 185 Plus system, to produce ultra pure water	Millipore (U.K.) Ltd.	solution prep
Single distilled water still : Fistreem™graduate water still manufactured by Fisons Scientific Equipment	Fisher Scientific UK	solution prep
Triple distilled water	homemade	solution prep

MATERIAL	SUPPLIER NAME	TYPE
Aquatron filter and deioniser set. Filter unit : For removing large particles above 10μm (25 litres/min = 1500 litres/hr) Housing for filter unit Element Deioniser unit : for removing inorganic material (conductivity better than 15μS / cm, 60 litres per hr) Housing for ion exchange cartridge Ion exchange cartridge Coupling device : (for attaching filtering and deioniser units together)	Bibby Sterilin Ltd. Cat. No. ADH Cat. No. ADI Cat No. AFH CAT. No. AFI Cat. No. ALC	solution prep
Dipotassium hydrogen phosphate microselect grade > 99% K_2HPO_4, RMM = 136.09	Fluka BioChemika order No. 60354	solution prep
Potassium dihydrogen phosphate microselect grade > 99.5% KH_2PO_4, RMM = 136.09	Fluka BioChemika order No. 60219	solution prep
Potassium hexacyanoferrate (II) trihydrate, *(potassium ferrocyanide)* microselect grade > 99.5% $K_4Fe(CN)_6.3H_2O$, RMM = 422.41	Fluka BioChemika order No. 60279	solution prep
Potassium hexacyanoferrate (III), *(potassium ferricyanide)* microselect grade > 99% $K_3Fe(CN)_6$, RMM = 329.26	Fluka BioChemika order No. 60299	solution prep
HCl BDH AnalaR grade density = 1.18 g cm^{-3} 35.4% wt	BDH	solution prep
Sodium perchlorate BDH AnalaR grade, minimum assay = 99.0% $NaClO_4.H_2O$, RMM = 140.46	BDH Prod No. 10241	solution prep
Sodium Chloride minimum assay = 99.9% BDH AnalaR grade	BDH Prod No. 10241	solution prep

MATERIAL	SUPPLIER NAME	TYPE
Acetone AnalaR grade, minimum assay = 99.5% $(CH_3)_2CO$, RMM = 58.08	BDH	solution
Ethanol AnalaR grade, 99.7-100% V/V, minimum assay = 99.8% (wfw)	BDH	solution

f. Microscopy equipment:

MATERIAL	SUPPLIER NAME	TYPE
Stage Micrometer 0.1 mm scale in glass disc mounted in a metal slide preferably for use with transmitted light	Agar Scientific Ltd Ref No. L4202	microscopy
Diamond ruled stage micrometer for reflected light 1mm scale divided into 100 and 10 μm divisions (lines 3.5 mm long and 1μm wide) note: no cover slip cemented over ruling	Agar Scientific Ltd Ref No. L4211	microscopy
Scanning Laser Microscope: MRC 600 series Laser Scanning Confocal Imaging System	Bio-Rad Laboratories (UK) Ltd	microscopy
Sony Video Graphic Printer UP-860/860CE (instant B/W printer) video paper rolls for above: Type (II) high density 110 x 20 cm roll	Gisborne Microscopy Services Manufacturers Product Code: UPP-110HD	microscopy
Sony Colour Video Printer UP-2200P video paper for above: Sony Video Printing Pack (90 prints + 1 colour ribbon)	Gisborne Microscopy Services Manufacturers Product Code : VMP-90STA	microscopy

MATERIAL	SUPPLIER NAME	TYPE
Super Long Working Distance objectives for scanning laser microscope x 40 – 0.40 NA, plan 4, 14.9 mm working distance, 21.0 mm mechanical tube length x 4 – 0.13 NA, 16.22 mm working distance, 16.0 mm mechanical tube length	Nikon UK Ltd.	microscopy

g. General equipment used for electrochemical experiments:

MATERIAL	SUPPLIER NAME	TYPE
Viton o-rings (for new home-made cell) outer ring: internal diameter = 13mm section (how thick ring is) = 1.5mm inner ring: internal diameter = 5mm section = 1.5 mm	Pimseal	electrochem. general
Digital Timer hr:min:sec	Farnell Components Cat. No. 734-500	electrochem. general
Digital Thermometer	RS Components Cat. No. 427-405	electrochem general
Pre-amplifier model 113, low noise preamplifier runs off rechargable batteries	E G and E Princeton Applied Research	electrochem. general.
Waveform generator PPR1	Hi-Tek Instruments	electrochem. general
Dictaphone Olympus Pearl Corder™ S700 microcasssette™ Recorder	Rymans	electrochem. general
xyt chart recorder Philips, model PM8271 Replacement Pens for above: Black Red	Crown Graphics (UK) Ltd. 1FD26B01-10A (0049583) 1FD26-R (0049585)	electrochem. general
ADC-100 12 bit data logging, parallel port device (with 2 BNC connectors) and computer software- for use as a virtual chart recorder and oscilloscope	Picotechnology Limited	electrochem. general

h. Equipment for noise reduction:

MATERIAL	SUPPLIER NAME	TYPE
Mu-metal: magnetic shielding alloy, Ni77/Fe14/Cu5/Mo4 foil / sheet form, thickness 0.025mm, Light tight	Goodfellows	noise reduction
Rechargeable Batteries PP9 size 8.4 V min,1.2Ah	RS Components	noise reduction
Vibration isolated work station (anti vibration table)	Newport	noise reduction
Surge Suppresser Mains Filter adaptor,13A incorporates a solid-state transient suppresser and RFI filter	RS Components	noise reduction
EMI / RFI shielding paint	RS Components	noise reduction

i. X-ray analysis equipment:

MATERIAL	SUPPLIER NAME	TYPE
Microprobe: JXA-8600 electron probe microanalyser	Jeol (UK) Ltd	X-ray analysis
Analytical Grade Standards of known % weight compositions.	Bureau of analysed samples Ltd.	X-ray analysis

j. Computer items:

MATERIAL	SUPPLIER NAME	TYPE
X-image for windows ver 4.2 Image utility program allows images saved by various scientific instruments to be converted to standard PC formats.	Foster Findlay Associates Ltd	computer
Keyboard / Monitor sharing switch for multiple CPU'S.	Dakota Computer Solutions Ltd.	computer
Optical Discs for storing large amounts of image data	HCS Global	computer

2. Suppler Addresses

The following information has been listed in alphabetical order by company name.

SUPPLIER ADDRESS	MATERIALS	INDEX
Adtech Polymer Engineering Unit 40 Aston Down East Stroud Glos GL6-8HX Tel : 0285-760-504	Kel-F (material for making cups for holding working electrodes)	ADT
Advent Research Materials Ltd Oakfield Industrial Estate, Eynsham, Oxon, OX8 1JA Tel: 01865-884-440 Fax: 01865-884-460 Web: http://www.advent-rm.com	Platinum wire, gold wire, stainless steel	ADV
Agar Scientific Ltd. 66a Cambridge Road, Stanstead, Essex, CM24 8DA England Tel: 01279-813-519	Microscopy materials: sample boxes, conductive carbon tabs, graticule and reflective scales for use in microscopy, aluminium oxide polishing papers.	AGR
Aldrich Chemical Company Inc. The Old Brickyard New Dorset SP8 4XT Tel 01747- 822-211 Fax: 01747-823-779	chemicals: indium, gallium	ALD
Bibby Sterilin Ltd. Tilling Drive, Stone, Staffs, ST15 OSA Tel 01785-812-121 Fax 01785-813-748	Aquatron filter and deioniser set	BIB

SUPPLIER ADDRESS	MATERIALS	INDEX
Bio-Rad Laboratories (UK) Ltd. Bio-Rad House, Maylands Avenue, Hemel Hempstead, Herts HP2 TTD Tel : 01442-232-552 Fax: 01442-259-118 Customer free phone: 0800-181-134	MRC-600 series Laser Scanning Confocal Imaging System	BIO
Buehler UK Ltd. Science Park, University of Warwick, Coventry, CV4 7HS Tel: 01203-692-224 Fax 01203-692-074	Epo-kwick resin and hardner, aluminium oxide pastes.	BUE
Bureau of Analysed Samples Ltd Newham Hall, Newby, Middlesbrough, Cleaveland TS8 9EA Tel: 01642-300-500 Fax: 01642-315-209	metal standards: stainless steel	BUR
Crown Graphics (UK) Ltd Clyde Vale Forest Hill London SE23 3JQ Tel: 0181-699-9200 Fax: 0181-699-3687	Chart recorder pens	CRO
Dakota Computer Solutions Ltd Unit C, 24 Lansdown Grove, London, NW10 1PR	Computer peripherals, switches, leads etc.	DAK

SUPPLIER ADDRESS	MATERIALS	INDEX
Farnell Electronic Components Limited, Canal Road, Leeds LS12 2TU United Kingdom Tel: 0113-263-6311 (sales) Fax: 0113-263-3411 (sales) Internet: http://www.farnellcomponents.com	Electronic components	FAR
Fisher Scientific, UK Bishop Meadow Road Loughborough Leicestershire LE11 5RG Tel: 01509-231-166 Tel: 0161-563-4589	Dropping bottles (resin storage), single distilled water still and components.	FIS
Fluka Chemicals, The Old Brick yard, New Road, Gillingham, Dorset, SP8 4JL Tel: 01747-823-097 Fax 01747-824-596	Chemicals	FLU
Foster Findlay Associates Ltd. Newcastle Technopole Kings Manor Newcastle Upon Tyne NE1 PPA Tel: 0191-201-2180 Fax: 0191-201-2190	X-image for windows ver 4.2 (image conversion utility)	FOS
Gisborne Microscopy Services Oakwood House Brook Lane Brocton Stafford, Stafffs ST17 OZT Tel: 01785-665-858	Replacement video paper cartridges for video printers	GIS

SUPPLIER ADDRESS	MATERIALS	INDEX
Goodfellow Cambridge Limited. Cambridge Science Park, Cambridge, CB4 4DJ, England Tel: 01223-568-068 Fax: 01223-420-639 website:// www.goodfellow.com	Mu-Metal magnetic shielding alloy.	GOO
HCS Global Tel : 0800-252-252 Fax : 0800-125-125 Internet: http://www.hcs.co.uk	Optical Discs	HCS
Hi Tek Instruments Threeways House Ibstone High Wycombe HP14 3XT	PPR1 waveform generator	HIT
Millpore (UK) Ltd. The Boulevard, Blackmoor Lane Watford WD1 8YW Tel: (0923)-816-375 Fax: (0923)-818-297	Millipore Q185 Plus water purification system.	MIL
Nikon UK Limited Nikon House 380 Richmond Road Kingston Upon Thames Surrey KT2 5PR Tel: 0181-541-4440 Fax: 0181-541-4584	Super long working distance objectives	NIK
Permabond adhesives UK Ltd. 01703-629-628	Information on products and local suppliers.	PER

SUPPLIER ADDRESS	MATERIALS	INDEX
Picotechnology Limited Broadway House 149-151 St Neots Road Hardwick Cambs CB3 7QJ Tel: 01954-211-716 Fax: 01954-211-880 Web: http://www.picoteck.co.uk/	Virtual instruments supplied. (ADC 100 data logger)	PIC
Pimseal Brailsford House Knapp Lane St James Square Cheltenham GL50 3QA Tel 01242-222-000 Fax 01242-224-242	Viton-O-Rings	PIM
Jeol (UK) Ltd. Jeol House Grove Park Collindale, London NW9 0JN Tel: 0181-205-6376 Fax: 0181-200-5935	JXA 8600 Electron Probe Microanalyser	JEO
Spectrum Engineering Unit 43 Thurrock Commercial Centre, Purfleet Industrial Park, London Road, Averly South Ockendon, Essex, RM15 4YA	local supplier for permabond SIP primer for Epoxy resins.	SPE
RS Components P.O. Box 99 corby, Nothhants, NN17 9RS Tel: 01536-201-201(sales) Fax: 01536-201-501(sales) General Tel: 01536-201-234	electronic components, silver conductive paint, PP9 Batteries	RSC

SUPPLIER ADDRESS	MATERIALS	INDEX
Russel pH Limited. Station road, Auchtermuchty, Fife, Scotland, KY14 7DP Tel: 01337-828-871 Fax: 01337-828-972	Counter electrodes	RUS